Mössbauer Spectroscopy of Frozen Solutions

Edited by
Attila Vértes
Dénes L. Nagy

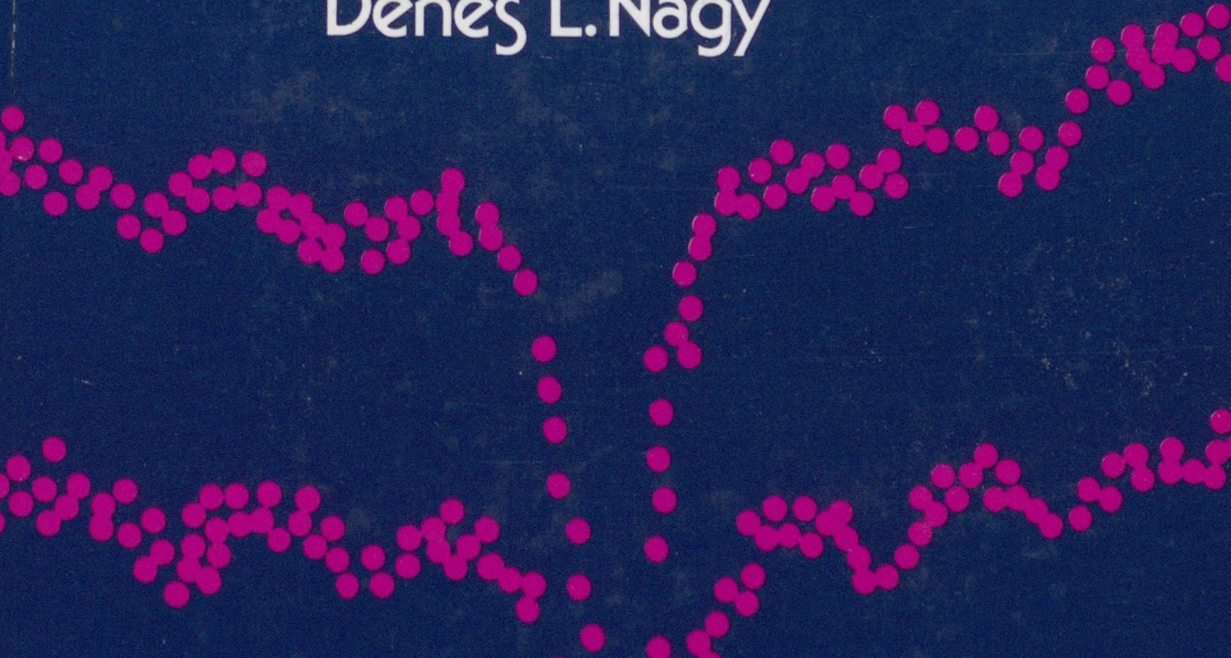

Akadémiai Kiadó, Budapest

MÖSSBAUER SPECTROSCOPY
OF FROZEN SOLUTIONS

Authors:

A. A. ANDREEV
S. V. BONDAREVSKI
S. MØRUP
D. L. NAGY
F. S. NASREDINOV
P. P. SEREGIN
A. VÉRTES

MÖSSBAUER SPECTROSCOPY OF FROZEN SOLUTIONS

EDITED BY
A. VÉRTES
Eötvös Loránd University
and
D. L. NAGY
Central Research Institute for Physics
Budapest, Hungary

1828

AKADÉMIAI KIADÓ · BUDAPEST 1990

ISBN 963 05 5347 3

Printed in Hungary by Akadémiai Kiadó és Nyomda Vállalat

CONTENTS

5. The chemical structure of liquid solutions studied by Mössbauer spectroscopy (A. Vértes) 141

PREFACE

This volume represents an attempt to "square the circle". Although the Mössbauer effect can occur only in solids our aim is to demonstrate how to apply the Mössbauer spectroscopy to the investigation of the chemical structure of solutions.

Chapter 1 introduces the physical foundation and the experimental techniques of Mössbauer spectroscopy concentrating on the most significant questions of its application to frozen solutions. This chapter takes into account that the Mössbauer spectroscopy has already been discussed in a great number of monographs including the theoretical foundation of this method in detail as well.

Solutions can be brought to a frozen state and in this state, if they include Mössbauer-active atoms, it is possible to record Mössbauer spectra. The freezing process can be carried out in a way that the ice formed preserves the most significant chemical features of the solutions as shown in detail in Chapter 2. In this case the Mössbauer method can serve as a rich source of information on the geometrical, chemical and magnetic structure of solutions.

The Mössbauer spectra of solutions and liquids can also be recorded at room temperature if they are diffunded in "thirsty glass" with a pore diameter of 4 nm. This recently developed measuring technique and the related principles are also discussed in Chapter 2.

Chapter 3 deals with relaxation phenomena. These phenomena play a significant part in the interpretation of the Mössbauer spectra of diluted iron-salt solutions.

Chapter 4 shows how to attain subtle pieces of information about the chemical and geometrical environment of the Mössbauer-active ion (e.g.: $^{57}Fe^{2+}$) on the basis of the Mössbauer spectra perturbed with an external magnetic field.

Chapter 5 which is the most extensive part of the book deals with the chemical structure of solutions as investigated by the Mössbauer spectroscopy. Part of the results described in this chapter also appeared in the monograph "Mössbauer spectroscopy, Elsevier, 1979" by Vértes, A., Korecz, L., Burger, K. This volume produces further results in this field.

Chapter 6 reviews investigations of nuclear aftereffects in frozen solutions.

Finally, the subject of Chapter 7 is the investigation of glass-like materials using the Mössbauer effect. Thus this Chapter extends the concept of frozen solutions to glasses as well.

Due to historic reasons and as a result of its outstanding features Chapters 3 and 4 deal with Mössbauer spectroscopy of ^{57}Fe only. Chapter 5, however, also covers Mössbauer studies with tin, europium, iodine, gold and antimony isotopes. In

Chapters 6 and 7 applications of cobalt, tin, tellurium, iodine, americium and other isotopes can also be found.

Our chemical terms follow those recommended by the International Union of Pure and Applied Chemistry (IUPAC); the units and notations follow mainly the International Union of Pure and Applied Physics (IUPAP) proposals unless they lead to units or formula very unusual in Mössbauer spectroscopy.

The authors acknowledge the valuable help of Dr Piroska Fodor–Csányi and Dr Ilona Nagy–Czakó in correcting the manuscript. Thanks are due to Magda Suba, Gabi Bor and Fruzsina Börcsök for their technical assistance, Prof. Sándor Lengyel for his professional and linguistic reading and for his useful advice.

We should like to express our sincere gratitude for all the help offered and accepted from our colleagues.

THE EDITORS

1. PHYSICAL AND TECHNICAL BASES OF MÖSSBAUER SPECTROSCOPY

1.1. INTRODUCTION

The phenomenon of recoil-free resonant emission and absorption of nuclear gamma-rays was discovered in 1958 by Mössbauer [1]. The discovery achieved a resounding success because of its unique relative energy resolution. In the beginning Mössbauer effect was expected to contribute first of all to nuclear physics but later on (especially after the easily detectable resonance of the nuclide ^{57}Fe has been discovered [2, 3]) it turned out that the possible applications of the method are even more important. The first (and perhaps up to now most spectacular) application of the method was the demonstration of the gravitational red shift of gamma-rays [4]. The wide variety of applications in solid state physics and chemistry was open by the demonstration of various hyperfine (magnetic dipole [2], electric quadrupole [5] and isomer [5]) interactions.

Nowadays there are a lot of general works (e.g. [6–14]) on Mössbauer spectroscopy where the foundations and applications are described in detail. Therefore in Chapter 1 we only attempt to give a brief introduction to the theory and methodology of Mössbauer spectroscopy for beginners in the field to an extent which is necessary for the understanding of the further chapters.

1.2. RECOIL-FREE NUCLEAR RESONANCE EMISSION AND ABSORPTION

Consider a fixed nucleus which is in an excited state of energy E_0. If this nucleus is decaying electromagnetically to the ground state a photon of energy E will be emitted with a probability density:

$$W_e(E)=\frac{\Gamma}{2\pi}\,\frac{1}{(E-E_0)^2+\frac{1}{4}\Gamma^2}\,\frac{1}{1+\alpha} \tag{1.1}$$

where α is the coefficient of the internal conversion (the average number of internal conversions is α while one photon is emitted) and Γ is the natural linewidth. Γ is connected to the lifetime τ of the excited state by Heisenberg's uncertainity relation:

$$\Gamma\tau=\hbar \tag{1.2}$$

where $\hbar$ is the Planck constant divided by 2π.

Another similar nucleus which is in the ground state will absorb this photon of energy E with a cross-section:

$$\sigma(E)=\frac{\sigma_0'\Gamma}{4}\,\frac{1}{(E-E_0)^2+\frac{1}{4}\Gamma^2}\,\frac{1}{1+\alpha} \tag{1.3}$$

where $\sigma_0=\sigma_0'/(1+\alpha)$ is the maximum cross-section of the resonance absorption. σ_0' is given by

$$\sigma_0'=2\pi\hbar^2c^2\frac{2I_e+1}{2I_g+1}\,\frac{1}{E_0^2}. \tag{1.4}$$

Here I_e is the nuclear spin of the excited state, I_g is that of the ground state and c is the velocity of light.

The effective cross-section for the resonance absorption is

$$\sigma_{\text{eff}}=\int_0^\infty W_e(E)\sigma(E)\,\mathrm{d}E. \tag{1.5}$$

If the nucleus is free it will receive the recoil energy

$$E_R=\frac{E_0^2}{2Mc^2} \tag{1.6}$$

by the emitted photon where M is the mass of the nucleus. The energy of the photon will be decreased by E_R. Thus, the emission line $W_e'(E)$ appears at the energy E_0-E_R rather than at E_0:

$$W_e'(E)=W_e(E+E_R). \tag{1.7}$$

The line of the absorption cross-section $\sigma'(E)$ will be shifted by the same amount to higher energies:

$$\sigma'(E)=\sigma(E-E_R). \tag{1.8}$$

The effective cross-section is now:

$$\sigma_{\text{eff}}'=\int_0^\infty W_e'(E)\sigma'(E)\,\mathrm{d}E=\int_0^\infty W_e(E+E_R)\sigma(E-E_R)\,\mathrm{d}E, \tag{1.9}$$

which will only be significant if

$$2E_R\lesssim\Gamma. \tag{1.10}$$

(See Fig. 1.1). For many electromagnetic nuclear transitions $E_R\approx10^{-2}\ldots10^{-3}$ eV while $\Gamma\approx10^{-7}\ldots10^{-9}$ eV. Condition (1.10) is not fulfilled at all which is why the cross-section of resonant absorption on free nuclei is extremely small.

The situation will completely be different if the emitting and absorbing nucleus is embedded in solids. In this case the recoil energy will be transferred to the system of lattice vibrations since a few meV are insufficient to knock out an atom from its original site. It was shown by Mössbauer [1] that under such circumstances a processes during which the state of the system of lattice vibrations is unchanged may have a considerable probability. Thus, the emission and absorption of the photon will be recoil-free. This phenomenon is the Mössbauer effect.

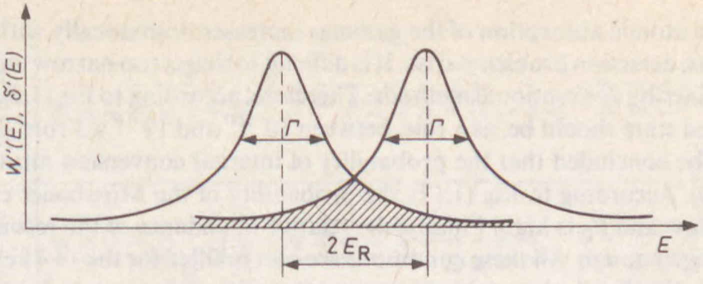

Fig. 1.1. The emission line $W'(E)$ and the absorption line $\sigma'(E)$ of γ-transitions on free nuclei

The probability f of the recoil-free process is essentially described by the same Debye–Waller factor which gives the fraction of elastic processes in X-ray and neutron diffraction:

$$f=\mathrm{e}^{-k^2\langle x^2\rangle}. \tag{1.11}$$

Here k is the wave-number of the photon while $\langle x^2\rangle$ is the mean square displacement of the resonant nucleus in the photon propagation direction.

The theory of the recoil-free fraction will be discussed in somewhat more detail later on in Section 1.6 along with diffusion line broadening effects. At this point it should only be mentioned that in the frame of a concrete model of lattice vibrations the probability of the Mössbauer effect at various temperatures can be calculated.

For a Debye model:

$$f=\exp\left\{\frac{-6E_\mathrm{R}}{k_\mathrm{B}\theta_\mathrm{D}}\left[\frac{1}{4}+\left(\frac{T}{\theta_\mathrm{D}}\right)^2\int\limits_0^{\theta_\mathrm{D}/T}\frac{y\,\mathrm{d}y}{\mathrm{e}^y-1}\right]\right\}. \tag{1.12}$$

Here k_B is the Boltzmann constant, T is the temperature and θ_D is the Debye temperature of the crystal. In practice the asymptotic forms of Eq. (1.12) can be very useful:

$$f=\exp\left[\frac{-E_\mathrm{R}}{k_\mathrm{B}\theta_\mathrm{D}}\left(\frac{3}{2}+\frac{\pi^2T^2}{\theta_\mathrm{D}^2}\right)\right], \quad \text{if} \quad T\ll\theta_\mathrm{D} \tag{1.13}$$

$$f=\exp\left(\frac{-6E_\mathrm{R}T}{k_\mathrm{B}\theta_\mathrm{D}^2}\right) \quad \text{if} \quad T\gtrsim\frac{\theta_\mathrm{D}}{2}. \tag{1.14}$$

It can be seen from Eq. (1.13) that the probability of the Mössbauer effect does not reach unity even at $T=0$:

$$f(T=0)=\exp\left(\frac{-3E_\mathrm{R}}{2k_\mathrm{B}\theta_\mathrm{D}}\right). \tag{1.15}$$

Comparing Eq. (1.15) with Eq. (1.11) one can see that the reason for this fact is that $\langle x^2\rangle>0$ even at $T=0$ because of the quantum-mechanical zero-point motion of nuclei.

A detectable Mössbauer effect can be expected if the value of the product $nf\sigma$ is high enough. Here n is the number of resonant nuclei per unit area of the absorber. From Eqs (1.6), (1.12) and (1.4) one can see that in this case E_0 must not be too high. This is why the effect can hardly be detected at gamma-ray energies above 100 keV. Below ca 5 keV the atomic absorption of the gammas increases dramatically with decreasing energy. Thus, detection problems arise. It is difficult to detect too narrow and too broad resonance lines by conventional methods. Therefore, according to Eq. (1.2), the lifetime of the excited state should be, as a rule, between 10^{-10} and 10^{-6} s. From Eqs (1.1) and (1.3) it can be concluded that the probability of internal conversion must not be too high ($\alpha \lesssim 10$). According to Eq. (1.12), the probability of the Mössbauer effect will be high if T is low and θ_D is high. Finally, the relative abundance of the resonant nuclide should be high enough. All these conditions are best fulfilled for the 14.4 keV transition of ^{57}Fe (Fig. 1.2). Easily detectable Mössbauer transitions have some further nuclides: ^{61}Ni, ^{99}Ru, ^{119}Sn, ^{121}Sb, ^{125}Te, ^{129}I, ^{151}Eu, ^{155}Gd, ^{161}Dy, ^{169}Tm, ^{197}Au, ^{237}Np, etc.

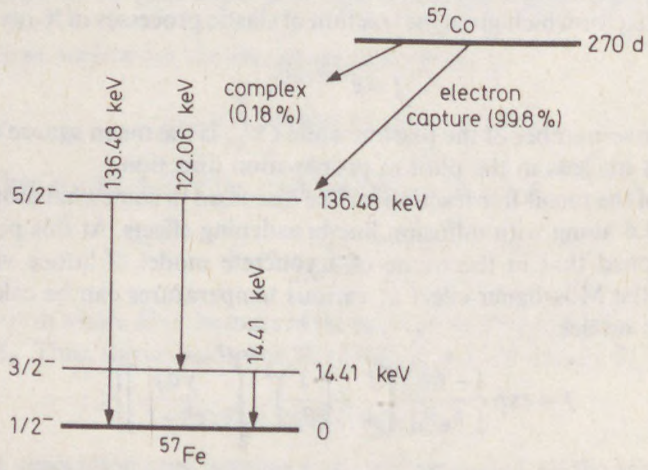

Fig. 1.2. Decay scheme of ^{57}Co

Table 1.1 summarizes the most important parameters of Mössbauer transitions.

Mössbauer effect is generally measured by scanning the absorption lines. In most cases the absorption line is not a Lorentzian centred at E_0 since, as it will be shown in Section 1.3, hyperfine interactions can shift and split it by about 10^{-6} eV. The shape of the absorption line can be scanned by changing the energy of the source along a range in this order of magnitude. The most general way to achieve this change is to move the source. If the source is moving with a velocity v relative to the absorber then the mean energy of photons emitted towards the absorber is

$$E(v) = E_0\left(1 + \frac{v}{c}\right). \tag{1.16}$$

As it can be realized from Table 1.1, in most cases (e.g. ^{57}Fe) the source should be moved with a velocity of several mm s^{-1}.

The photons emitted by the source and crossing the absorber are detected behind the absorber (Fig. 1.3) as a function of the velocity of the source. The number of counts $N(v)$ detected during a certain time is called Mössbauer spectrum. In many cases the

Table 1.1.
Parameters of Mössbauer Transitions*

Nuclide	Gamma energy, keV	Spin and parity of the excited state	Spin and parity of the ground state	Isotope abundance, %	Half life, ns	Linewidth, mm/s	Internal conversion coefficient, α	Maximum resonance cross-section, σ_0, 10^{-20} cm^2
^{40}K	29.56	4^-	3^-	0.012	4.26	2.18	6.6	29
^{57}Fe	14.41	$3/2^-$	$1/2^-$	2.14	97.8	0.194	8.2	257
	136.46	$5/2^-$	$1/2-$	2.14	8.7	0.23	0.14	35
^{61}Ni	67.4	$5/2^-$	$3/2^-$	1.16	5.2	0.78	0.12	72
^{67}Zn	93.32	$1/2^-$	$5/2^-$	4.1	9300	0.00031	0.54	12.2
^{73}Ge	13.26	$5/2^+$	$9/2^+$	7.76	2950	0.00696	1100	0.761
	68.75	$7/2^+$	$9/2^+$	7.76	1.6	2.5	0.229	33.7
^{83}Kr	9.35	$7/2^+$	$9/2^+$	11.55	147	0.199	17.9	118
^{99}Tc	140.51	$7/2^+$	$9/2^+$	0 (β^-)	0.196	9.93	0.104	8.98
^{99}Ru	89.36	$3/2^+$	$5/2^+$	12.7	20.6	0.149	0.42	14.4
^{101}Ru	127.22	$3/2^+$	$5/2^+$	17.1	580	0.00370	0.16	8.7
^{107}Ag	93.08	$7/2^+$	$1/2^-$	51.83	4.43×10^{10}	6.63×10^{-11}	9.4	10.9
^{109}Ag	88	$7/2^+$	$1/2^-$	48.18	3.98×10^{10}	7.81×10^{-11}	9.4	11
^{117}Sn	158.53	$3/2^+$	$1/2^+$	7.6	0.3	5.7	0.159	16.7
^{119}Sn	23.83	$3/2^+$	$1/2^+$	8.58	17.8	0.647	5.12	141
^{121}Sb	37.15	$7/2^+$	$5/2^+$	57.25	3.5	2.1	10.5	20.6
^{125}Te	35.46	$3/2^+$	$1/2^+$	7	1.5	5.2	13.3	27.2
^{127}I	57.6	$7/2^+$	$5/2^+$	100	1.89	2.51	3.7	21
^{129}I	27.77	$5/2^+$	$7/2^+$	0 (β^-)	16.8	0.587	4.9	40
^{129}Xe	39.58	$3/2^+$	$1/2^+$	26.4	1.0	6.8	15	20
^{131}Xe	80.18	$1/2^+$	$3/2^+$	21.2	0.477	7.15	2.1	6.1
^{133}Cs	81.0	$5/2^+$	$7/2^+$	100	6.3	0.54	1.7	10.2
^{133}Ba	12.29	$3/2^+$	$1/2^+$	0 (EC)	8.1	2.7	110	29.2
^{137}La	10.1	$5/2^+$	$7/2^+$	0 (EC)	89	0.30	140	12.8
^{139}La	165.85	$5/2^+$	$7/2^+$	99.911	1.47	1.12	0.22	5.5
^{141}Pr	145.42	$7/2^+$	$5/2^+$	100	1.85	1.02	0.43	10.8
^{145}Nd	67.0	$3/2^-$	$7/2^-$	8.3	33.0	0.124	6.1	3.8
	72.2	$5/2^-$	$7/2^-$	8.3	0.70	5.4	4.9	6.0
^{147}Pm	91.03	$5/2^+$	$7/2^+$	0 (β^-)	2.57	1.17	2.1	7.1

Table 1.1. cont.

Nuclide	Gamma energy, keV	Spin and parity of the excited state	Spin and parity of the ground state	Isotope abundance, %	Half life, ns	Linewidth, mm/s	Internal conversion coefficient, a	Maximum resonance cross-section, σ_0, 10^{-20} cm^2
^{147}Sm	122.1	$5/2^-$	$7/2^-$	15.0 (a)	0.33	6.8	1.0	6.2
^{149}Sm	22.5	$5/2^-$	$7/2^-$	13.83	7.1	1.7	24	14.5
^{151}Sm	65.83	$7/2^-$	$5/2^-$	0 (β^-)	20	0.21	?	?
^{152}Sm	121.78	2^+	0^+	26.72	1.42	1.58	1.3	36
^{153}Sm	35.84	$3/2^-$	$3/2^+$	0 (β^-)	2	3.8	0.30	150
^{154}Sm	81.99	2^+	0^+	22.8	3	1.1	5.05	30.1
^{151}Eu	21.54	$7/2^+$	$5/2^+$	47.82	9.5	1.34	30	23
^{153}Eu	87.37	$7/2^+$	$5/2^+$	52.18	0.7	4.7	6	7
	97.43	$5/2^-$	$5/2^+$	52.18	0.21	13.4	0.42	18.1
	103.18	$3/2^+$	$5/2^+$	52.18	3.8	0.70	1.8	5.5
^{154}Gd	123.14	2^+	0^+	2.15	1.17	1.90	1.2	37
^{155}Gd	60.01	$5/2^-$	$3/2^-$	14.9	0.24	19	9.2	10
	86.54	$5/2^+$	$3/2^-$	14.9	6.32	0.500	0.41	35
	105.31	$3/2^+$	$3/2^-$	14.9	1.16	2.24	0.25	18
^{156}Gd	88.98	2^+	0^+	20.6	2.22	1.38	4.1	30
^{157}Gd	54.5	$5/2^-$	$3/2^-$	15.68	0.187	26.8	10	11
	64.0	$5/2^+$	$3/2^-$	15.68	460	0.0093	7.4	10.7
^{158}Gd	79.51	2^+	0^+	24.7	2.54	1.35	5.94	27.9
^{160}Gd	75.26	2^+	0^+	21.7	2.66	1.37	9.2	21.2
^{159}Tb	58.0	$5/2^+$	$3/2^+$	100	0.06	36	10	9.9
^{160}Dy	86.79	2^+	0^+	2.29	2.01	1.57	4.5	29.4
^{161}Dy	25.66	$5/2^-$	$5/2^+$	18.88	28.5	0.37	2.9	95
	43.84	$7/2^+$	$5/2^+$	18.88	0.78	8.0	5	28
	74.58	$3/2^-$	$5/2^+$	18.88	3.21	1.14	0.46	20.1
^{162}Dy	80.66	2^+	0^+	25.53	2.25	1.51	6.2	26.1
^{164}Dy	73.39	2^+	0^+	28.18	2.39	1.56	10	21
^{165}Ho	94.7	$9/2^-$	$7/2^-$	100	0.022	131	8.6	3.55
^{164}Er	91.39	2^+	0^+	1.56	1.47	2.04	4.23	28.0
^{166}Er	80.57	2^+	0^+	33.41	1.87	1.82	6.5	25.1
^{167}Er	79.32	$9/2^+$	$7/2^+$	22.94	0.119	29.0	5.3	7.7
^{168}Er	79.8	2^+	0^+	27.07	1.88	1.82	14	13

Table 1.1. cont.

Nuclide	Gamma energy, keV	Spin and parity of the excited state	Spin and parity of the ground state	Isotope abundance, %	Half life, ns	Linewidth, mm/s	Internal conversion coefficient, a	Maximum resonance cross-section, σ_0, 10^{-20} cm^2
^{170}Er	78.59	2^+	0^+	14.88	1.89	1.84	7	25
^{169}Tm	8.42	$3/2^+$	$1/2^+$	100	3.9	8.3	220	31.2
^{170}Yb	84.26	2^+	0^+	3	1.60	2.03	6.7	22.4
^{171}Yb	66.72	$3/2^-$	$1/2^-$	14.3	0.8	5.1	11.3	8.9
	75.87	$5/2^-$	$1/2^-$	14.3	1.64	2.20	8.7	13.1
^{172}Yb	78.67	2^+	0^+	21.9	1.8	1.9	9	20
^{174}Yb	76.5	2^+	0^+	31.8	1.8	2.0	10	19
^{176}Yb	82.1	2^+	0^+	12.7	2	1.7	8	20
^{175}Lu	113.81	$9/2^+$	$7/2^+$	97.41	0.10	24	2.3	7.2
^{176}Hf	88.36	2^+	0^+	5.2	1.39	2.23	5.2	25.3
^{177}Hf	112.97	$9/2^-$	$7/2^-$	18.5	0.5	4.8	3	6
^{178}Hf	93.17	2^+	0^+	27.14	1.47	2.00	4.6	25.2
^{180}Hf	93.33	2^+	0^+	35.1	1.51	1.94	5.0	23.4
^{181}Ta	6.23	$9/2^-$	$7/2^+$	99.988	6800	0.0064	46	170
	136.25	$9/2^+$	$7/2^+$	99.988	0.04	50	1.9	5.7
^{180}W	103.6	2^+	0^+	0.13 (*a*)	1.28	2.06	3.5	25.3
^{182}W	100.11	2^+	0^+	26.3	1.38	1.98	3.85	25
^{183}W	46.48	$3/2^-$	$1/2^-$	14.3	0.183	32.2	9	23
	99.08	$5/2^-$	$1/2^-$	14.3	0.975	2.83	4.3	14.1
^{184}W	111.21	2^+	0^+	30.7	1.26	1.95	2.75	26.4
^{186}W	122.3	2^+	0^+	28.6	1.12	2.00	1.6	31
^{187}Re	134.25	$7/2^+$	$5/2^+$	62.60 (β^-)	0.0104	196	2.266	5.542
^{186}Os	137.16	2^+	0^+	1.64 (*a*)	0.83	2.40	1.25	28.9
^{188}Os	155.03	2^+	0^+	13.3	0.71	2.49	0.84	27.7
^{189}Os	36.32	$1/2^-$	$3/2^-$	16.1	0.53	14.2	80	1.15
	69.52	$5/2^-$	$3/2^-$	16.1	1.63	2.41	8	8
	95.33	$3/2^-$	$3/2^-$	16.1	0.23	12.5	6.7	3.5
^{190}Os	186.7	2^+	0^+	26.4	0.367	3.99	?	?
^{191}Ir	82.33	$1/2^+$	$3/2^+$	37.4	3.8	0.87	12.4	1.35
	129.39	$5/2^+$	$3/2^+$	37.4	0.089	23.8	2.4	6.4

Table 1.1. cont.

Nuclide	Gamma energy, keV	Spin and parity of the excited state	Spin and parity of the ground state	Isotope abundance, %	Half life, ns	Linewidth, mm/s	Internal conversion coefficient, α	Maximum resonance cross-section, σ_0, 10^{-20} cm^2
^{193}Ir	73.03	$1/2^+$	$3/2^+$	62.6	6.34	0.591	6.5	3.06
	138.89	$5/2^+$	$3/2^+$	62.6	0.071	27.7	2.3	5.8
^{195}Pt	98.85	$3/2^-$	$1/2^-$	33.8	0.162	17.1	7.2	6.1
	129.78	$5/2^-$	$1/2^-$	33.8	0.67	3.15	1.76	15.8
^{197}Au	77.35	$1/2^+$	$3/2^+$	100	1.89	1.87	4.3	3.9
^{199}Hg	158	$5/2^-$	$1/2^-$	16.9	2.4	0.72	0.2	24
^{201}Hg	32.19	$1/2^-$	$3/2^-$	13.22	0.2	42	60	1.9
^{230}Th	53.20	2^+	0^+	0 (*a*)	0.37	13.9	?	?
^{232}Th	49.37	2^+	0^+	100 (*a*)	0.345	16.1	260	1.92
^{231}Pa	84.2	$5/2^+$	$3/2^-$	0 (*a*)	45.1	0.072	1.83	18.3
^{234}U	43.48	2^+	0^+	0.0055 (*a*)	0.252	25.0	780	0.828
^{236}U	45.24	2^+	0^+	0 (*a*)	0.234	25.8	845	0.706
^{238}U	44.91	2^+	0^+	99.28 (*a*)	0.245	24.9	660	0.917
^{237}Np	59.54	$5/2^-$	$5/2^+$	0 (*a*)	67	0.069	1.1	33
^{239}Pu	57.3	$5/2^+$	$1/2^+$	0 (*a*)	0.101	47.3	?	?
^{243}Am	84.00	$5/2^+$	$5/2^-$	0 (*a*)	2.34	1.39	0.3	27

* Compiled from several issues of the Mössbauer Effect Data Index (J. G. Stevens and V. E. Stevens, University of Asheville, USA) and from the Decay Schemes and Parameters of Mössbauer Isotopes (D. Barb and M. Morariu, Central Institute of Physics, Bucharest, Roumania, 1978).

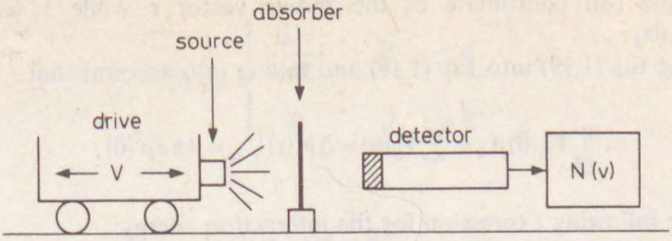

Fig. 1.3. Schematic arrangement of a Mössbauer measurement

normalized spectrum is used:

$$S(v)=\frac{N(\infty)-N(v)}{N(\infty)}. \tag{1.17}$$

Here $v=\infty$ means a velocity far off resonance.

Using Eq. (1.16), the energy in Mössbauer spectroscopy is generally given in velocity units. This convention will be used throughout this book.

1.3. HYPERFINE INTERACTIONS

1.3.1. HYPERFINE SPLITTING OF NUCLEAR LEVELS

Nuclei interact with surrounding electrons. This results in the hyperfine splitting of optical spectra. That is why this kind of interaction is called "hyperfine". The energy of hyperfine interactions generally does not exceed 10^{-6} eV so that before Mössbauer's discovery it was completely impossible to observe directly the hyperfine splitting of nuclear transitions their energy being by about 10 orders of magnitude higher. However, the appearance of a component of natural linewidth in the spectrum of nuclear resonance absorption ensures the necessary resolution.

The study of hyperfine interactions is of basic importance since, as we shall see, it yields many information regarding the electronic structure of the environment of the nucleus.

As a consequence of hyperfine interactions the nucleus is subjected to very intense electric and magnetic fields. These interactions can be described by classical electrodynamics.

The nucleus has an electric charge distribution $e\,\rho(\mathbf{r})$ (e is the charge of the proton; the origin of the coordinate system is the centre of mass of the nucleus). The electrostatic field of external charges (electrons, other ions, etc.) is described by the potential $V'(\mathbf{r})$. The electrostatic energy is then

$$H_{\mathrm{hf}}=e\int\rho(\mathbf{r})\,V'(\mathbf{r})\,\mathrm{d}^3\mathbf{r}\,. \tag{1.18}$$

$V'(\mathbf{r})$ can be expanded in terms of $\mathbf{r}$ around $\mathbf{r}=\mathbf{0}$:

$$V'(\mathbf{r})=V'(\mathbf{0})+\sum_{i=1}^{3}V_i'(\mathbf{0})\,x_i+\frac{1}{2}\sum_{i,k=1}^{3}V_{ik}'(\mathbf{0})\,x_ix_k+\ldots \tag{1.19}$$

Here x_i is the i-th coordinate of the radius vector $\mathbf{r}$ while $V_i' = \partial V'/\partial x_i$ and $V_{ik}' = \partial^2 V'/\partial x_i \partial x_k$.

Substituting Eq. (1.19) into Eq. (1.18) and taking into account that

$$\sum_{i,k} V_{ik}'(\mathbf{0})\,\delta_{ik} = \sum_i V_{ii}'(\mathbf{0}) = \Delta V'(\mathbf{r})\,|_{\mathbf{r}=\mathbf{0}} = 4\pi e \rho'(\mathbf{0}), \tag{1.20}$$

we obtain the following expression for the interaction energy:

$$H_{\mathrm{hf}} = e \int \rho(\mathbf{r}) \left[V'(\mathbf{0}) + \frac{2}{3}\pi r^2 e \rho'(\mathbf{0}) + \sum_i V_i'(\mathbf{0})\,x_i + \right.$$
$$\left. + \frac{1}{2}\sum_{i,k} V_{ik}'(\mathbf{0}) \left(x_i x_k - \delta_{ik}\frac{r^2}{3} \right) \right] \mathrm{d}^3\mathbf{r}. \tag{1.21}$$

Here, $\rho'(\mathbf{0})$ is the density of the negative charges responsible for $V'(\mathbf{r})$ at the origin. Δ is the Laplace operator.

The quadrupole moment tensor of the nucleus is

$$Q_{ik} = \int \rho(\mathbf{r})(3x_i x_k - \delta_{ik} r^2)\,\mathrm{d}^3\mathbf{r} \tag{1.22}$$

with the use of this notation and

$$\langle R^2 \rangle = \frac{\int \rho(\mathbf{r}) r^2 \mathrm{d}^3\mathbf{r}}{\int \rho(\mathbf{r})\mathrm{d}^3\mathbf{r}} = \frac{1}{Z}\int \rho(\mathbf{r}) r^2\,\mathrm{d}^3\mathbf{r} \tag{1.23}$$

the interaction energy becomes

$$H_{\mathrm{hf}} = eZ\,V'(\mathbf{0}) + \frac{2}{3}\pi e^2 Z \rho'(\mathbf{0})\langle R^2 \rangle +$$
$$+ e V_i'(\mathbf{0}) \int \rho(\mathbf{r})\,x_i \mathrm{d}^3\mathbf{r} + \frac{1}{6} e \sum_{i,k} V_{ik}'(\mathbf{0})\,Q_{ik}. \tag{1.24}$$

Here Z is the number of protons in the nucleus.

The third term on the right side of Eq. (1.24) vanishes, the integral being the electric dipole moment of the nucleus. The parity of nuclei is a constant of motion (the nuclear wave function is either even or odd) which is why the charge density function is always even. Therefore the integrand is odd and the integral (the dipole moment) should be zero.

The non-vanishing terms in Eq. (1.24) have very direct meaning. The first term describes the Coulomb energy of a point charge, the second term is the contribution from the finite extension of the nucleus while the last term is the energy of quadrupole interaction.

For the charge density distribution of the nucleus a very simple model is often used: the nucleus is considered to be a homogeneously charged sphere of radius R. Such an approximation can be obviously used only for calculating $\langle R^2 \rangle$ and not of Q_{ik} the latter describing just the deviation of $\rho(\mathbf{r})$ from the spherical symmetry. With the charge distribution

$$\rho(\mathbf{r}) = \begin{cases} \dfrac{3Z}{4\pi R^3} & \text{if } r \le R \\ 0 & \textit{if } r > R \end{cases} \tag{1.25}$$

one obtains

$$\langle R^2 \rangle = \frac{3}{5} R^2 . \tag{1.26}$$

The tensor V'_{ik} is the second derivative of the electrostatic potential. Thus, apart from its sign, it is the vector gradient of the electric field strength. Generally, however, another tensor is called electric field gradient (EFG) which can be obtained from V'_{ik} by eliminating its trace:

$$V_{ik} = V'_{ik} - \frac{1}{3}\delta_{ik} \sum_j V'_{jj} . \tag{1.27}$$

Using Eq. (1.27) and the fact that according to Eq. (1.22)

$$\sum_i Q_{ii} = 0 , \tag{1.28}$$

V'_{ik} can be replaced in Eq. (1.24) by V_{ik}. Using Eq. (1.26) and taking into account that the nucleus has a magnetic dipole moment $\boldsymbol{\mu}$ for the interaction energy, we have the form

$$H_{\text{hf}} = eZ\,V(\mathbf{0}) + \frac{2\pi}{5} e^2 \rho'(\mathbf{0})\, Z R^2 + \frac{1}{6} e \sum_{i,k} V_{ik}(\mathbf{0})\, Q_{ik} - \sum_j \mu_j H_j . \tag{1.29}$$

Here $\mathbf{H}$ is the magnetic field strength acting on the nucleus.

Q_{ik} can be characterized by a single number:

$$Q = \int \rho(\mathbf{r})\, r^2 (3\cos^2\vartheta - 1)\, \mathrm{d}^3\mathbf{r} , \tag{1.30}$$

which is equal to Q_{zz} if Q_{ik} is diagonalized so that the z axis is parallel to the direction of the nuclear spin $\mathbf{I}$. The other two diagonal elements are then $Q_{xx} = Q_{yy} = -Q/2$ since the nucleus is axially symmetric around the z axis.

It can be shown [15] that the equivalent operator of Q_{ik} in quantum mechanics is:

$$\hat{Q}_{ik} = \frac{3Q}{2I(2I-1)} [\hat{I}_i \hat{I}_k + \hat{I}_k \hat{I}_i - \frac{2}{3} \hat{I}^2 \delta_{ik}] . \tag{1.31}$$

In the principal axis system of $V_{ik}(\mathbf{0})$ where

$$V_{ik}(\mathbf{0}) = V_{ii}(\mathbf{0})\, \delta_{ik} \tag{1.32}$$

the equivalent operator of the third term of Eq. (1.29) is

$$\begin{aligned} \hat{H}_Q &= \frac{e}{6} \sum_i V_{ii}(\mathbf{0}) \hat{Q}_{ii} = \frac{eQ}{4I(2I-1)} \sum_i V_{ii}(\mathbf{0}) (2\hat{I}_i^2 - \frac{2}{3} I^2) = \\ &= \frac{eQ}{2I(2I-1)} [V_{xx}(\mathbf{0}) \hat{I}_x^2 + V_{yy}(\mathbf{0}) \hat{I}_y^2 + V_{zz}(\mathbf{0}) \hat{I}_z^2] . \end{aligned} \tag{1.33}$$

Here the property

$$V_{xx}+V_{yy}+V_{zz}=0 \tag{1.34}$$

following from Eq. (1.27) has been used. Equation (1.34) means that only two of V_{xx}, V_{yy} and V_{zz} are independent. (Further on the argument $\mathbf{0}$ of V_{ik} will be omitted.) The coordinate axes are labelled so that

$$|V_{zz}|\geq|V_{yy}|\geq|V_{xx}|. \tag{1.35}$$

The EFG tensor is described by two quantities namely V_{zz} and the asymmetry parameter

$$\eta=\frac{V_{xx}-V_{yy}}{V_{zz}}. \tag{1.36}$$

With the use of these parameters Eq. (1.33) can be re-written as

$$\hat{H}_{\mathrm{Q}}=\frac{eQV_{zz}}{4I(2I-1)}[3\hat{I}_z^2-I(I+1)+\eta(\hat{I}_x^2-\hat{I}_y^2)] \tag{1.37}$$

or

$$\hat{H}_{\mathrm{Q}}=\frac{eQV_{zz}}{4I(2I-1)}[3\hat{I}_z^2-I(I+1)+\frac{\eta}{2}(\hat{I}_+^2+\hat{I}_-^2)] \tag{1.38}$$

where

$$\hat{I}_+=\hat{I}_x+i\hat{I}_y \tag{1.39}$$

$$\hat{I}_-=\hat{I}_x-i\hat{I}_y. \tag{1.40}$$

If the EFG is axially symmetric ($\eta=0$) the eigenstates of $\hat{I}_z$ are the eigenstate of $\hat{H}_{\mathrm{Q}}$ while the eigenvalues are

$$E_{\mathrm{Q}}=\frac{eQV_{zz}}{4I(2I-1)}[3m^2-I(I+1)] \tag{1.41}$$

where m is the magnetic quantum number belonging to $\hat{I}_z$. If $\eta\neq0$ the eigenvalues cannot be given generally in a closed form. In one of the most important cases ($I=3/2$), however, a closed expression exists:

$$E_{\mathrm{Q}}=\frac{eQV_{zz}}{4}\left(m^2-\frac{5}{4}\right)\sqrt{1+\frac{\eta^2}{3}}. \tag{1.42}$$

The last term of Eq. (1.29) describes the Zeeman splitting of nuclear levels:

$$\hat{H}_{\mathrm{M}}=-\hat{\boldsymbol{\mu}}\mathbf{H}=-g\mu_{\mathrm{N}}\hat{\mathbf{I}}\mathbf{H} \tag{1.43}$$

where g is the g-factor of the nuclear level, while μ_{N} is the nuclear magneton. Of course, if the magnetic field is parallel to the z axis the eigenstates of $\hat{H}_{\mathrm{M}}$ are the eigenstates of $\hat{I}_z$ with the eigenvalues

$$E_{\mathrm{M}}=-g\mu_{\mathrm{N}}Hm. \tag{1.44}$$

Coming now to the perturbation of the energy of the γ-transition the excited and the ground state of the nucleus is split corresponding to the eigenvalues of $\hat{H}_{\mathrm{hf}}^{\mathrm{e}}$ and $\hat{H}_{\mathrm{hf}}^{\mathrm{g}}$ where $\hat{H}_{\mathrm{hf}}^{\mathrm{e}}$ and $\hat{H}_{\mathrm{hf}}^{\mathrm{g}}$ denote the Hamiltonian (1.29) in the excited and ground state of the nucleus, respectively. The first term on the right side of Eq. (1.29) being the same in both states of the nucleus does not appear in the transition energy. The second term leads to a shift of the spectral lines:

$$\delta=\frac{2\pi}{3}e^2\rho'(0)\,Z(\langle R_e^2\rangle-\langle R_g^2\rangle)=\frac{2\pi}{5}e^2\rho'(0)\,Z(R_e^2-R_g^2)=$$

$$=\frac{4\pi}{5}e^2\rho'(0)\,ZR^2\frac{\delta R}{R}, \tag{1.45}$$

where R_e and R_g are the nuclear radius in the excited and ground state, respectively; $\delta R=R_e-R_g$, $R=(R_e+R_g)/2$. δ is the isomer shift.

If the EFG is axially symmetric and its axis is parallel to $\mathbf{H}$ then the energy of the transition between the states $|I_e,m_e\rangle$ and $|I_g,m_g\rangle$ is

$$E_0'=E_0+\frac{4\pi}{5}e^2Z\rho'(0)\,R^2\frac{\delta R}{R}+\left\{\frac{Q_e}{4I_e(2I_e-1)}[3m_e^2-I_e(I_e+1)]-\right.$$

$$\left.-\frac{Q_g}{4I_g(2I_g-1)}[3m_g^2-I_g(I_g+1)]\right\}eV_{zz}+(m_g g_g-m_e g_e)\mu_N H \tag{1.46}$$

where the indices g and e refer to the ground and excited states, respectively. The third term (on the right side) of Eq. (1.46) is the electric quadrupole shift (splitting) and the fourth term the magnetic dipole shift (splitting).

In the case of a 1/2→3/2 transition

$$E_0'=E_0+\frac{4\pi}{5}e^2Z\rho'(0)R^2\frac{\delta R}{R}+\frac{eQ_eV_{zz}}{4}\left(m_e^2-\frac{5}{4}\right)+$$

$$+(m_g g_g-m_e g_e)\mu_N H\,. \tag{1.47}$$

All the three perturbing energy terms are the products of a nuclear and a solid-state factor. The positions of the split and shifted resonance lines generally determine the value of every single term of Eq. (1.47). Once the nuclear factors $[R^2(\delta R/R)]$, Q_g, $(m_g g_g-m_e g_e)]$ have been measured the solid-state factors $[\rho'(0), V_{zz}, H]$ can be calculated.

Sources in Mössbauer spectroscopy are mostly substances without electric quadrupole and magnetic dipole interaction. Their spectrum consists, therefore, of a single unsplit line of natural width. Isomer shifts cannot, of course, be switched off. That is why the energy of a photon emitted by the source exceeds the transition energy E_0 of the free nucleus by

$$\delta_s=\frac{4\pi}{5}e^2Z\,|\Psi_s(0)|^2R^2\frac{\delta R}{R} \tag{1.48}$$

where $\Psi_s(0)$ is the wave-function of the electrons at the nucleus in the source.

So, if the absorber has neither electric quadrupole nor magnetic dipole interaction the spectrum will consist of a single line at

$$\delta=\frac{4\pi}{5}e^2Z[|\Psi_a(0)|^2-|\Psi_s(0)|^2]R^2\frac{\delta R}{R} \tag{1.49}$$

where $\Psi_a(0)$ is the wave-function of the electrons at the nucleus in the absorber.

In the case of a 1/2→3/2 dipole transition, if the electric quadrupole interaction differs from zero the spectrum will be a doublet while the magnetic dipole interaction will result in a six-line pattern according to the selection rule $\Delta m = 0, \pm 1$.

In the case of a combined magnetic dipole/electric quadrupole interaction the position of the spectral lines generally cannot be given via closed form even for a 1/2 →3/2 transition. If $|eQV_{zz}| \ll |\boldsymbol{\mu}\mathbf{H}|$ then the first order perturbation theory can be applied. If the EFG is axially symmetric and the angle of **H** to the z axis is ϑ then the eigenvalues of $\hat{H}_Q + \hat{H}_M$ are:

$$E = -g\mu_N H m + (-1)^{|m|+\frac{1}{2}} \frac{eQV_{zz}}{4} \frac{3\cos^2\vartheta - 1}{2} \tag{1.50}$$

The value of ϑ is often unknown. In such cases

$$\varepsilon = \frac{eQV_{zz}}{4} \frac{3\cos^2\vartheta - 1}{2} \tag{1.51}$$

is used. The electric quadrupole interaction shifts the two outermost lines of the sextet by ε while the four inner lines by $-\varepsilon$ (Fig. 1.4). In more complex cases the line positions can only be numerically calculated from the parameters of hyperfine interaction.

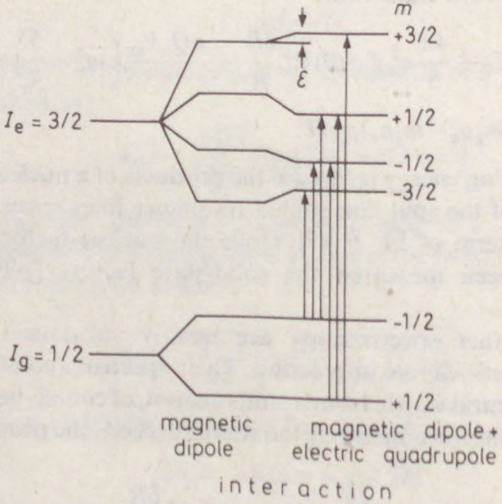

Fig. 1.4. Splitting of a 1/2→3/2 dipole transition in the case of magnetic dipole and combined hyperfine interaction

For a complete description of the spectrum besides the line positions the line intensities are also necessary. We shall come back to this problem in Section 1.5.

The basic problem of Mössbauer spectroscopy is the quantitative description of the electron density, electric field gradient and magnetic field in terms of the electron structure of the crystal.

1.3.2. ISOMER SHIFT

The isomer shift is proportional to the electron density at the nucleus. Classically only the s electrons have a non-vanishing density at the nucleus. Relativistically, however, the $p_{1/2}$ electrons also contribute to the electron density at the nucleus. In most cases this relativistic correction can be neglected.

The relativistic correction of the density of the s electrons is very essential [16]. Instead of Eq. (1.49) the isomer shift is given by

$$\delta = S'(Z)\frac{4\pi}{5}e^2 Z[|\Psi_a(0)|^2 - |\Psi_s(0)|^2]R^2\frac{\delta R}{R} \tag{1.52}$$

where Ψ_a and Ψ_s denote the non-relativistic wave-functions. S' is a rapidly increasing function of Z; its value for Fe is 1.29.

Although only the s electrons have a considerable density at the nucleus the other electrons also contribute to the isomer shift. For example, an increasing number of 3d electrons leads to an enhanced shielding of the 3s electrons and results in a decrease of $|\Psi(0)|^2$. This means an increase in the isomer shift of ^{57}Fe since the 14.4 keV transition of this nucleus the nuclear radius in the excited state is less than that in the ground state. This behaviour offers a possibility for determining the valence state of the investigated ion since, for example, the isomer shift of the high-spin Fe^{3+} ion [electron configuration: $(3d)^5$] differs from that of the high-spin Fe^{2+} ion [electron configuration: $(3d)^6$] by about ten natural linewidths. Figure 1.5 shows some typical isomer shifts of ^{57}Fe. Conventionally the isomer shift of α-Fe at room temperature is chosen to be zero.

The quantitative interpretation of the ^{57}Fe isomer shifts has been attempted many times though the problem has not been completely solved yet. Walker, Wertheim and

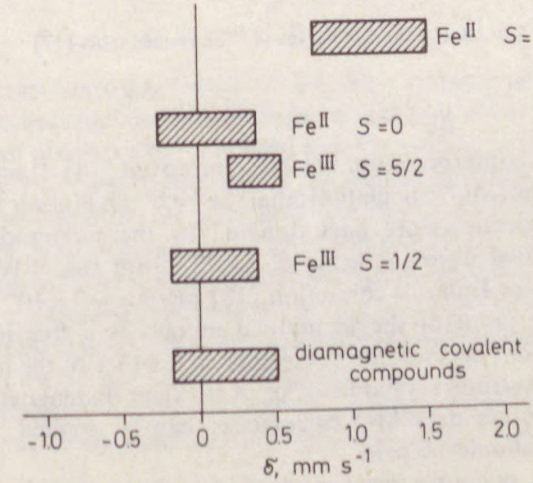

Fig. 1.5. Typical isomer shifts of iron compounds

Jaccarino (WWJ) [17] calculated $|\Psi(\mathbf{0})|^2$ for the $(3d)^5$ and $(3d)^6$ configurations by free ion Hartree–Fock calculations. Then, comparing the obtained values of $|\Psi(\mathbf{0})|^2$ with the isomer shift of some highly ionic Fe^{3+} and Fe^{2+} compounds, respectively, the calibration factor between δ and $|\Psi(\mathbf{0})|^2$ was determined. The chemical bond gets more covalent by the appearence of 4s electrons. Since 4s electrons do not shield considerably the inner s electrons their contribution can be accounted separately. The results of the WWJ model are shown in Fig. 1.6 [17].

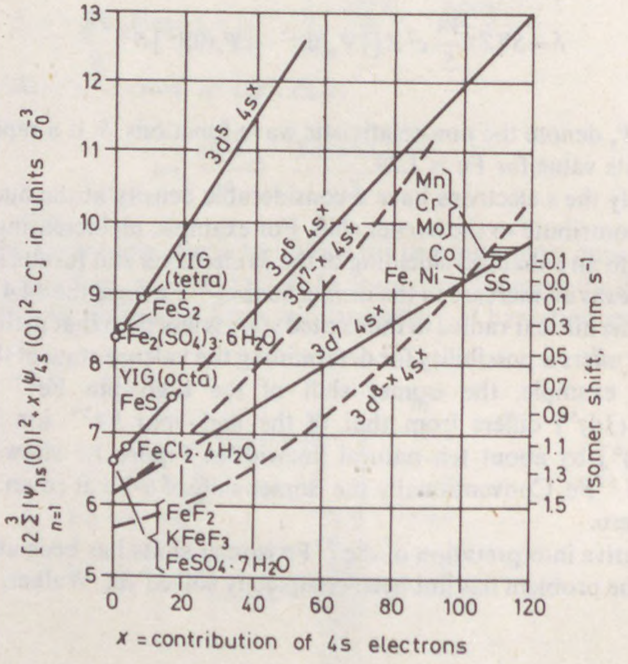

Fig. 1.6. Calibration curves of ^{57}Fe isomer shifts [17]

Later on, the above interpretation has been improved [18]. It has been concluded from molecular orbital (MO) calculations that the Fe^{3+} ion is never fully ionic because at least 0.3–0.4 4s electrons are back-donated by the surrounding ligands. This decreases the estimated absolute value of $\delta R/R$. From the WWJ model $\delta R/R = -18\times10^{-4}$ while after Danon's correction [18] $\delta R/R = -7\times10^{-4}$.

Since the starting point of the mentioned models is a free ion Hartree–Fock calculation, they cannot account for the isomer shift either of the low spin $Fe^{(II)}$ and $Fe^{(III)}$ ions existing in strong crystal fields or of covalent diamagnetic complexes (e.g. ferrocene). In these cases only MO calculations can be applied. Also for metallic systems special care should be paid.

The isomer shift is, of course, pressure-dependent since $|\Psi(\mathbf{0})|^2$ can be changed by compression. This offers a further possibility of estimating $\delta R/R$.

1.3.3. SECOND ORDER DOPPLER SHIFT

A shift of the spectral lines is caused by the second order Doppler effect coming from the thermal motion of atoms. Though this shift is not a consequence of hyperfine interaction it is mentioned here since it cannot be measured independently from the isomer shift.

If a nucleus emitting in its own system a photon of frequency ν is subject to a thermal motion of velocity v_T, then the observed mean frequency is

$$\nu' = \nu\left(1 - \frac{\langle v_T^2 \rangle}{2c^2}\right). \tag{1.53}$$

This leads to a shift of

$$\delta E_{\mathrm{D}} = -\frac{\langle v_T^2 \rangle}{2c^2} E_0 = -\frac{U}{2c^2} E_0 \tag{1.54}$$

of the spectral lines where U is the specific internal energy of the crystal because the mean kinetic energy of a harmonic oscillator is the half of its total energy:

$$\frac{1}{2} M \langle v_T^2 \rangle = \frac{1}{2} M U. \tag{1.55}$$

In the Debye approximation of a lattice containing one kind of atoms [9]:

$$\delta E_{\mathrm{D}} = -\left[\frac{9}{16}\frac{k_{\mathrm{B}}\theta_{\mathrm{D}}}{Mc^2} + \frac{3}{2}\frac{k_{\mathrm{B}}T}{Mc^2} f_{\mathrm{D}}\left(\frac{T}{\theta_{\mathrm{D}}}\right)\right]. \tag{1.56}$$

Here

$$f_{\mathrm{D}}(y) = 3y^3 \int_0^{1/y} \frac{x^3}{e^x - 1}\,\mathrm{d}x \tag{1.57}$$

is the Debye function. Since $f_{\mathrm{D}}(y) = 1$ if $y \gg 1$ at high temperatures the energy of the resonance line is decreasing linearly with increasing temperature. The first term of Eq. (1.56) is independent of temperature showing that the second order Doppler shift does not vanish even at $T = 0$. This is a result of the zero-point motion of the lattice.

The observable second order Doppler shift vanishes if both the temperature and the Debye temperature of source and absorber are equal. This is almost never fulfilled. That is why the total shift of the spectral lines should be called central shift. The isomer shift coming from the Coulomb interaction is only a part (generally the main part) of the central shift. Unfortunately, however, generally the term isomer shift is used for the total shift. Further on we use latter terminology, too.

Similarly to the chemical isomer shift also the second order Doppler shift is pressure-dependent. This pressure-dependence, however, can in most cases be neglected.

1.3.4. QUADRUPOLE SPLITTING

The EFG at the nucleus has two components. First, an EFG is produced by the electrons of the ion concerned while, secondly, the charge distribution of the crystal lattice also contributes to the EFG at the nucleus. An EFG caused by the electrons of its own appears if the ion possesses some electrons of asymmetric charge distribution outside the inner isotropic closed shells. If the local symmetry of the crystal field (i.e. the electrostatic field of the crystal lattice) at the ion is lower than cubic this electrons may cause a considerable EFG.

Instead of V_{zz} and η the EFG is often characterized by

$$q=\frac{V_{zz}}{e} \tag{1.58}$$

and

$$\eta q=\frac{V_{xx}-V_{yy}}{e}. \tag{1.59}$$

The EFG produced by the electrons of the ion (q_{ion} and $\eta_{\text{ion}}q_{\text{ion}}$) is modified by the shielding of the inner (and originally spherically symmetric) electrons. This is described by Sternheimer's antishielding factor R_S [19]. The EFG of the crystal lattice (q_{ion} and $\eta_{\text{ion}}q_{\text{ion}}$) is also modified by the same reason; this is characterized by another antishielding factor of Sternheimer γ_∞ [19]. For most of the ions $0<R_S<1$ while $|\gamma_\infty|$ is often greater than 100.

The EFG at the nucleus is

$$q=(1-R_S)q_{\text{ion}}+(1-\gamma_\infty)q_{\text{latt}} \tag{1.60}$$

and

$$\eta q=(1-R_S)\eta_{\text{ion}}q_{\text{ion}}+(1-\gamma_\infty)\eta_{\text{latt}}q_{\text{latt}}\,. \tag{1.61}$$

The ion contribution (if different from zero) generally exceeds the lattice contribution; the latter, however, is easier to calculate. In point charge approximation the external ions of the lattice are geometrical points at $\mathbf{r}_i$ of charge e_i. Then, using polar coordinates (r_i, ϑ_i, φ_i), the lattice EFG we have in the form

$$q_{\text{latt}}=\frac{1}{e}\sum_i e_i\frac{3\cos^2\vartheta_i-1}{r_i^3} \tag{1.62}$$

and

$$\eta_{\text{latt}}q_{\text{latt}}=\frac{1}{e}\sum_i e_i\frac{3\sin^2\vartheta_i\cos 2\varphi_i}{r_i^3}. \tag{1.63}$$

If the coordinates of the ions are known, say, from X-ray diffraction the lattice contribution of the EFG can be calculated if the e_i charges are also known. This involves some difficulties since the ionic charges can only be obtained by MO calculations.

The ionic contribution can be calculated by using the wave functions of the outer electrons. If the wave function of the valence electrons is $|\Psi\rangle$ then

$$q_{\text{ion}}=-\left\langle\Psi\left|\frac{3\cos^2\vartheta-1}{r^3}\right|\Psi\right\rangle \tag{1.64}$$

and

$$\eta_{\text{ion}} q_{\text{ion}} = -\left\langle \Psi \left| \frac{3\sin^2\vartheta\cos 2\varphi}{r^3} \right| \Psi \right\rangle . \tag{1.65}$$

In the case of hydrogen-like wave functions both Eqs (1.64) and (1.65) are products of an angular and a radial expectation value. The angular part depends on the symmetry of the wave function while the radial part on the radial behaviour of the wave function. The latter which is generally denoted by $\langle r^{-3}\rangle$ is constant for a free ion. If the ion is chemically bound covalency effects reduce $\langle r^{-3}\rangle$.

Coming now to the case of iron, the ground state of the Fe^{3+} ion in weak crystal field is ^6S. The isotropy of this state results in vanishing of the ionic contribution to the EFG. Using Eqs (1.62) and (1.63) we can calculate the lattice contribution in point charge approximation. One obtains relatively small (ca 0.5 mm s^{-1}) temperature-independent quadrupole splittings.

The ground state of the Fe^{2+} ion in weak crystal field is ^5D. This 25-fold degenerate state is split by a cubic crystal field without spin-orbit coupling to an orbital doublet E_g and an orbital triplet T_{2g}. In the most frequent case of octahedral coordination the E_g states lie by about 1 eV above the T_{2g} states. Therefore, their contribution to the EFG at room temperature and below can be neglected.

The EFG values induced by the ^5D states are summarized in Table 1.2.

Table 1.2.
The EFG values induced by the ^5D states of the Fe^{2+} ion

State		q	η
E_g	$d_{x^2-y^2}$	$+(4/7)\langle r^{-3}\rangle$	0
	d_{z^2}	$-(4/7)\langle r^{-3}\rangle$	0
T_{2g}	d_{xy}	$+(4/7)\langle r^{-3}\rangle$	0
	d_{xz}	$-(2/7)\langle r^{-3}\rangle$	+3
	d_{yz}	$-(2/7)\langle r^{-3}\rangle$	−3

In Table 1.2 z axis is chosen to coincide with z axis of the electronic wave-functions, i.e. condition (1.35) has not been used.

If the local symmetry of the nucleus is cubic (which is rarely the case because of the Jahn–Teller effect) the net EFG of the T_{2g} states is 0. A further axial (e.g. trigonal or tetragonal) perturbing crystal field splits the T_{2g} level into an orbital doublet and an orbital singlet. If the ground state is singlet then the absolute value of the quadrupole splitting at $T=0$ is $\Delta E_Q=(4/7)\langle r^{-3}\rangle e^2Q/2$ according to Eq. (1.42). It is also easy to realize that the absolute value of the quadrupole splitting belonging to any T_{2g} doublet is $\Delta E_Q=(2/7)\langle r^{-3}\rangle e^2Q/2$. This results in two typical quadrupole splittings for the Fe^{2+} compounds around 3.6 mm s^{-1} and 1.8 mm s^{-1}. The latter value occurs more rarely since Jahn–Teller effect is going to split the doublet ground state.

At higher temperatures the EFG of the individual levels is thermally averaged which results in a decrease of the quadrupole splitting. The higher-lying states are mixed to the ground state also quantum mechanically first of all via spin-orbit coupling. This also leads to a decrease of the quadrupole splitting as compared to the bare splitting ΔE_Q^0. A further decrease is caused by the covalency of the chemical bond. This is generally taken into account by an appropriate renormalization of $\langle r^{-3} \rangle$.

If the local symmetry (point symmetry) is known the quadrupole splitting measured at the nucleus of a Fe^{2+} ion can be calculated by solving the total ^5D problem. This is equivalent to the diagonalization of a 25×25 complex matrix [20]. In most cases, however, it is sufficient to use T_{2g} approximation. Then, on one hand, only 15×15 matrices should be diagonalized and, on the other hand, it can be shown [21] that in this approximation the absolute value of the quadrupole splitting depends only on the energies of the electronic levels and is independent of the point symmetry.

In strong crystal fields the low-spin modifications of Fe ions exist. The ground state of the low-spin Fe^{3+} ion is $^2T_{2g}$ (five of the six t_{2g} one-electron orbitals are occupied, the e_g orbitals are empty) while that of the low-spin Fe^{2+} ion is $^1A_{1g}$ (the t_{1g} orbitals are filled, the e_g orbitals are empty). That is why the low-spin iron (III) ion resembles the high-spin iron (II) ion while the low-spin iron (II) ion resembles the high-spin iron (III) ion, as far as the quadrupole splitting is concerned.

1.3.5. MAGNETIC HYPERFINE INTERACTION

The magnetic field strength **H** at the nucleus consists of many components:

$$\mathbf{H} = \mathbf{H}_0 - D\mathbf{M} + \frac{4\pi}{3}\mathbf{M} + \mathbf{H}_d + \mathbf{H}_S + \mathbf{H}_L + \mathbf{H}_D \tag{1.66}$$

$\mathbf{H}_0$ is the applied external magnetic field strength. The second term, $-D\mathbf{M}$ is the demagnetization field induced by the magnetization **M** of the sample. It should be noted that this form is exact only for an ellipsoid, a principal axis of which is parallel to the external magnetic field. The third term is the so-called Lorentz field. This is caused by the magnetic dipoles of the sample which are far enough from the atom concerned. The field of nearer dipoles (but not of the own atomic electrons) is $\mathbf{H}_d$ which is zero in the case of cubic point symmetry. Sometimes the third and fourth terms together are called Lorentz field.

The second, third and fourth terms of Eq. (1.66) in non-magnetic materials can always be neglected. Even in magnetic substances, their value generally does not exceed 1T. The most significant contributions to **H** are $\mathbf{H}_S$, $\mathbf{H}_L$ and $\mathbf{H}_D$.

$\mathbf{H}_S$ is the Fermi contact field [22]:

$$H_S = -\frac{8\pi}{3}\mu_B(|\Psi_\uparrow(0)|^2 - |\Psi_\downarrow(0)|^2) = -H_C\langle\hat{S}\rangle \tag{1.67}$$

Here μ_B is the Bohr magneton while $\Psi_\uparrow(\mathbf{r})$ and $\Psi_\downarrow(\mathbf{r})$ is the wave-function of the spin-up and spin-down electrons and S is the atomic spin, respectively. Although only the s electrons appear with a high probability at the nucleus they are polarized by the non-filled magnetic external shells (e.g. 3d, 4f). The number of s electrons is uneffected by this interactions. The radial distribution of the spin-up and spin-down electrons, however, will be different. The polarization is generally only of a few per cents. In insulators, H_S is roughly proportional to the magnetic moment of the own atom of the nucleus. In metals in addition to the core polarization, other atoms also contribute to the internal field by their magnetic moments via polarization of conduction electrons.

$\mathbf{H}_L$ is the magnetic field induced by the orbital momentum $\mathbf{L}$ of the atom:

$$\mathbf{H}_L = -2\mu_B\langle r^{-3}\rangle\langle\hat{\mathbf{L}}\rangle = -H_L\langle\hat{\mathbf{L}}\rangle\,. \tag{1.68}$$

Finally, $\mathbf{H}_D$ is the dipole field induced by the atomic spin $\mathbf{S}$:

$$\mathbf{H}_D = -2\mu_B\langle r^{-3}\rangle\langle\hat{\mathbf{O}}_{SD}\rangle = -H_L\langle\hat{\mathbf{O}}_{SD}\rangle\,, \tag{1.69}$$

where $\hat{\mathbf{O}}_{SD}$ is the spin dipole operator:

$$(\hat{\mathbf{O}}_{SD})_i = \frac{1}{7L(2L-1)}\sum_k\left[\frac{3}{2}(\hat{L}_i\hat{L}_k+\hat{L}_k\hat{L}_i)-L(L+1)\delta_{ik}\right]\hat{S}_k\,. \tag{1.70}$$

1.4. RELAXATION EFFECTS

The shape of the Mössbauer spectrum is substantially influenced by relaxation processes of the atomic electrons. Since Chapter 3 is fully devoted to relaxation phenomena we shall summarize here only their physical bases.

The energy states of a paramagnetic ion are determined by its interaction with the neighbouring ions. As it was shown in Section 1.3 the hyperfine interaction is different in different states of the ion. Since the ion is in thermal equilibrium with its environment it spends a finite time in its stationary states. The transitions between these states are in most cases induced by the interaction of the electron spin with the neighbouring spins (spin-spin relaxation) or with the crystal lattice (spin-lattice relaxation). A significant mechanism of spin-lattice relaxation is the following: the lattice vibrations result in a fluctuating crystal field at the ion which, in turn, influences the expectation value of the electron spin via spin-orbit coupling. This is why for ions of S ground state (e.g. Fe^{3+}) the spin-lattice relaxation is slow as compared to the case of ions with a ground state of non-vanishing orbital momentum (e.g. Fe^{2+}). The spin-spin relaxation is temperature-independent. It depends, however, markedly on the concentration of paramagnetic ions. In contrast to this, the spin-lattice relaxation depends first of all on temperature.

If the ion spends a long time in every single eigenstate the resultant Mössbauer spectrum will be the superposition of the spectra which can be derived from the hyperfine interactions belonging to the eigenstates. If the transition between the eigenstates is fast the hyperfine interaction is averaged and Mössbauer spectrum shows only the averaged hyperfine interaction. At intermediate transition probabilities complex relaxation spectra can be observed. The transition is taken such as "slow" or "fast". It is slower or faster, respectively, than the characteristic time corresponding to the energy of the hyperfine interaction (the time of a Larmor-precession). Relaxation phenomena can be observed in Mössbauer spectrum if the transition time and the Larmor-time are of the same order of magnitude.

The effect of electron spin relaxation upon Mössbauer spectrum was first discussed by Afanasev and Kagan [23]. They completely solved the problem of one-phonon spin-lattice relaxation processes. The density operator formalism used by them allows, in principle, exact solution of relaxation problems. Owing to mathematical difficulties exact formulae exist only in certain cases. This fact justifies the application of various semiclassical models for the determination of Mössbauer spectra in the case of relaxation. In these models the fluctuating environment is classically accounted for. This means that the Hamiltonian of the hyperfine interaction is fluctuating statistically among certain discrete values. The parameters of the individual Hamiltonians (hyperfine magnetic fields, EFG's, etc.) and the stochastic matrix of the statistic process (the relaxation times) determine the Mössbauer spectrum. Within the scope of such semiclassical models the most general solution was given by Blume [24]. Wegener [25] elaborated a perturbation theory of the quantum mechanical model in the case of applied (external) magnetic field. A general description independent of the kind of relaxation, however, limited to high frequencies, was given by Afanasev and Gorobchenko [26]. In their phenomenological model the spectrum consists of some shifted and broadened Lorentzians. The phenomenological parameters of the models are contained in a relaxation matrix reflecting the point symmetry of the resonant nucleus.

The various relaxation models are compared in an excellent review of Wegener [27].

1.5. THE INTENSITY OF RESONANCE LINES

1.5.1. BLACKNESS EFFECT

Besides the positions the intensities of the spectral lines also bear significant information concerning the hyperfine interactions. In the following the factors determining the absolute and relative line intensities will be discussed. The intensity is defined as the area of the absorption line of Eq. (1.17). For a Lorentzian shape it has the value

$$I=\frac{\pi A\Gamma_r}{2} \tag{1.71}$$

where A is the amplitude (height) and Γ_r the full width at half maximum (FWHM) of the resonance line.

If both the source and the absorber are thin and neither the source nor the absorbed lines are split by hyperfine interactions then

$$\Gamma_r=2\Gamma \tag{1.72}$$

Γ being the natural linewidth. Using the data of Table 1.1 in the case of ^{57}Fe and expressed in velocity units $\Gamma_r=0.192\ \mathrm{mm\,s^{-1}}$.

In the case of thick source and/or absorber the shape of the resonance line differs from Lorentzian. When calculating the amplitude and intensity of the resonance line one should take into account that

— the probability of the recoil-free process differs from unity both in the source (f_s) and in the absorber (f_a).

— the gamma-radiation of the resonant transition is weakened by non-reasonant atomic absorption both in the source and in the absorber described by absorption coefficients μ_s and μ_a, respectively,

— recoil-free emitted photons may suffer resonant absorption not only in the absorber but also in the source,

— the resonant absorption—just because of its resonant character—cannot be described by an energy-independent mass absorption coefficient. This results in a non-Lorentzian shape of the resonance line in the case of thick source and/or absorber.

If both the source and the absorber possess lines of natural width Γ and of energy E_0, the transmission (defined as the probability of detecting a photon of the resonant transition behind the absorber) can be given in the following form [28]:

$$T(v)=\mathrm{e}^{-\mu_a t'_a}\left\{(1-f_s)\int_0^\infty \xi(x)\mathrm{e}^{-\mu_s x}\mathrm{d}x+\frac{f_s\Gamma}{2\pi}\int_{-\infty}^{\infty}\exp\left[-f_a\nu_a\sigma_0 t'_a\frac{(\Gamma/2)^2}{(E-E_0)^2+(\Gamma/2)^2}\right]\times\right.$$

$$\times\int_0^\infty\frac{\xi(x)}{[E-E_0(1+v/c)]^2+(\Gamma/2)^2}\times$$

$$\left.\times\exp\left[-\left(f_s\nu_s\sigma_o\frac{(\Gamma/2)^2}{[E-E_0(1+v/c)]^2+(\Gamma/2)^2}+\mu_s\right)x\right]\mathrm{d}x\,\mathrm{d}E\right\} \tag{1.73}$$

ν_s and ν_a being the number of atoms of the resonant isotope in unit volume of source and absorber, respectively, t'_a the thickness of the absorber, $\xi(x)$ the distribution of emitting nuclei in the source as measured perpendicular to the surface of the source and v the velocity of the source relative to the absorber.

In the case of a thin source

$$\xi(x)=\lim_{x'\to+0}\delta(x-x'). \tag{1.74}$$

Substituting Eq. (1.74) into Eq. (1.73) one obtains

$$T(v)=\mathrm{e}^{-\mu_a t'_a}\left\{(1-f_s)+\frac{f_s\Gamma}{2\pi}\int_{-\infty}^{\infty}\exp\left[f_a\nu_a\sigma_0 t'_a\frac{(\Gamma/2)^2}{(E-E_0)^2+(\Gamma/2)^2}\right]\times\right.$$

$$\left.\times\frac{1}{[E-E_0(1+v/c)]^2+(\Gamma/2)^2}\mathrm{d}E\right\} \tag{1.75}$$

The integral in Eq. (1.75) (the so-called "transmission integral") cannot be given in a closed form. However, the amplitude A_T and the intensity I_T of the transmission peak can be expressed as

$$A_T=\frac{T(\infty)-T(0)}{T(\infty)}=f_s\left[1-\exp\left(-\frac{\lambda_a}{2}\right)I_0\left(\frac{\lambda_a}{2}\right)\right] \tag{1.76}$$

and

$$I_T = \int_{-\infty}^{\infty} \frac{T(\infty) - T(v)}{T(\infty)}\,\mathrm{d}v = \frac{\pi \Gamma f_s}{2} \lambda_a \exp\left(-\frac{\lambda_a}{2}\right)\left[I_0\left(\frac{\lambda_a}{2}\right) + I_1\left(\frac{\lambda_a}{2}\right)\right] \tag{1.77}$$

where

$$\lambda_a = \nu_a f_a \sigma_0 t'_a \tag{1.78}$$

is the effective thickness of the absorber while $I_0(y)$ and $I_1(y)$ are the zeroth and first order Bessel functions of an imaginary argument.

With the provision that $T(v)$ can be approximated by a Lorentzian to a reasonable accuracy even for high effective thicknesses, in Eqs (1.76) and (1.77) Γ_r can be obtained by the combination of Eqs (1.76), (1.77) and (1.71):

$$\Gamma_r = \Gamma \frac{\lambda_a \exp\left(-\frac{\lambda_a}{2}\right)\left[I_0\left(\frac{\lambda_a}{2}\right) + I_1\left(\frac{\lambda_a}{2}\right)\right]}{1 - \exp\left(-\frac{\lambda_a}{2}\right) I_0\left(\frac{\lambda_a}{2}\right)}. \tag{1.79}$$

For small effective thicknesses ($\lambda_a \lesssim 2$), Γ_r can be approximated by the first terms of the Taylor expansion of Eq. (1.79):

$$\Gamma_r \approx \Gamma\left(2 + \frac{1}{4}\lambda_a + \frac{1}{96}\lambda_a^2 - \frac{1}{64}\lambda_a^3\right). \tag{1.80}$$

For high effective thicknesses ($\lambda_a \gtrsim 2$) the asymptotic form of the Bessel functions can be used in Eq. (1.79):

$$\Gamma_r \approx 2\Gamma \frac{\lambda_a}{\sqrt{\pi\lambda_a} - 1}. \tag{1.81}$$

Instead of Eqs (1.80) and (1.81) Visscher's semiempirical expression [7] is often used:

$$\Gamma_r = \begin{cases} \Gamma(2.00 + 0.27\,\lambda_a) & \text{if } \; 0 \le \lambda_a \lesssim 5 \\ \Gamma(2.02 + 0.29\,\lambda_a - 0.005\,\lambda_a^2) & \text{if } \; 4 \lesssim \lambda_a \lesssim 10 \end{cases} \tag{1.82}$$

At high effective thicknesses both A_T and I_T can be given in asymptotic forms:

$$A_T = f_s\left(1 - \frac{1}{\sqrt{\pi\lambda_a}}\right), \tag{1.83}$$

$$I_T = \sqrt{\pi}\,\Gamma f_s \sqrt{\lambda_a}. \tag{1.84}$$

If $\lambda_a \to \infty$, A_T tends to the saturation value of the f factor of the source: $A_T = f_s$. This offers the "black absorber" method for measuring f_s. In contrast to A_T, I_T is divergent when $\lambda_a \to \infty$.

Figure 1.7 shows A_T, I_T and Γ_r as functions of the effective thickness of the absorber λ_a. This behaviour is called "blackness effect". Since neither Eq. (1.76) nor Eq. (1.77) is a linear function of λ_a, f_s and λ_a (i.e. f_a) can be determined by measuring A_T or I_T for at least two absorbers of different thicknesses. This way is generally followed when measuring the probability of Mössbauer effect.

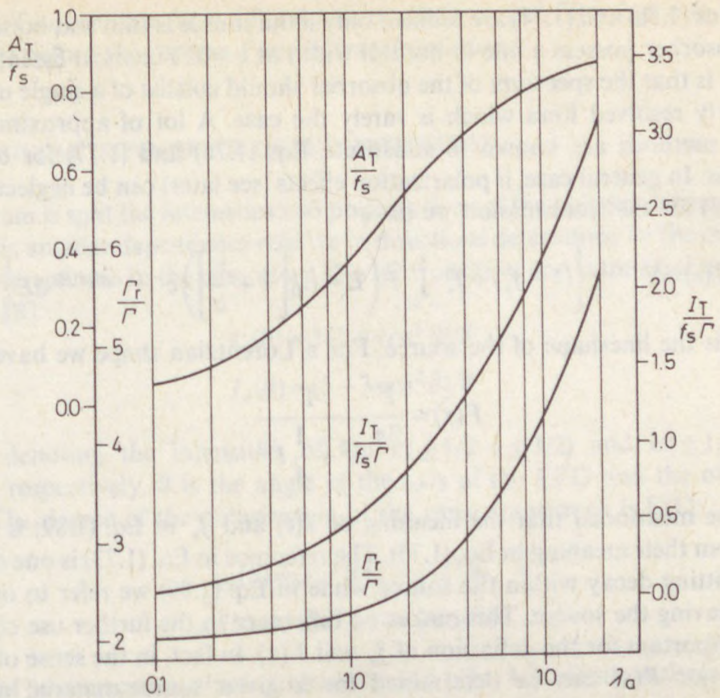

Fig. 1.7. Amplitude A_T, intensity I_T and width Γ_r of the resonance line as functions of the effective thickness of the absorber λ_a

It was supposed above that the measurement is free of background. This is unfortunately never the case. The photons detected behind the absorber originate not only from the transition of interest. A considerable fraction of this background comes from the absorber itself. If the background fraction is denoted by b the measured Mössbauer spectrum becomes

$$N(v)=N(\infty)\left[(1-b)\frac{T(v)}{T(\infty)}+b\right]. \tag{1.85}$$

The normalized spectrum defined by Eq. (1.17) is then

$$S(v)=(1-b)\frac{T(\infty)-T(v)}{T(\infty)}. \tag{1.86}$$

Equation (1.86) compared to Eqs (1.76) and (1.77) leads to the peak amplitude of the normalized spectrum:

$$A_S=(1-b)A_T \tag{1.87}$$

The area of the normalized spectrum is then

$$I_S=(1-b)I_T. \tag{1.88}$$

Equations (1.76) and (1.77) are fulfilled only if the source is thin and both the source and the absorber possess a line of natural width at $v=0$. The most essential of these conditions is that the spectrum of the absorber should consist of a single unsplit or of some clearly resolved lines which is rarely the case. A lot of approximations and numerical methods are known to substitute Eqs (1.76) and (1.77) for overlapping Lorentzians. In general case, if polarization effects (see later) can be neglected, instead of Eq. (1.73) for the transmission we have

$$T(v)=\mathrm{e}^{-\mu_a t'_a}\left\{(1-f_s)+f_s\int_{-\infty}^{\infty} F\left(E-E_0\left[1+\frac{v}{c}\right]\right)\mathrm{e}^{-f_a \nu_a t'_a \sigma(E)}\,\mathrm{d}E\right\}. \tag{1.89}$$

Here $F(x)$ is the lineshape of the source. For a Lorentzian shape we have

$$F(x)=\frac{\Gamma}{2\pi}\frac{1}{x^2+\frac{1}{4}\Gamma^2}. \tag{1.90}$$

It should be mentioned that the meaning of $T(v)$ and f_s in Eq. (1.89) is somewhat different from their meaning in Eq. (1.73). The reference in Eq. (1.73) is one elementary gamma-emitting decay within the source while in Eq. (1.89) we refer to one gamma quantum leaving the source. This makes no difference in the further use of $T(v)$. It is, however, important for the definition of f_s and $F(x)$. In fact, in the sense of Eq. (1.89) neither f_s nor $F(x)$ can be determined for a given source-material at a given temperature, since the self-absorption within the source appearing explicitly in Eq. (1.73) is now included in f_s and $F(x)$. Since the self-absorption is even time-dependent (the source will be enriched in the resonant isotope during the radioactive decay) f_s and $F(x)$ should be determined very carefully if one is going to get $\sigma(E)$ from Eq. (1.89). By the substitution of Eq. (1.89) into Eq. (1.86) the normalized Mössbauer spectrum becomes:

$$S(v)=(1-b)f_s\left\{1-\int_{-\infty}^{\infty} F\left(E-E_0\left[1+\frac{v}{c}\right]\right)\mathrm{e}^{-f_a \nu_a t'_a \sigma(E)}\,\mathrm{d}E\right\}. \tag{1.91}$$

Equation (1.91) is an integral equation for $\sigma(E)$ bearing the physical information. Following the method of Ure and Flinn [29], we can, in principle, easily solve it the integral being a convolution. Using velocity units defined by

$$F_v(v)=F\left(\frac{E_0}{c}v\right)\frac{E_0}{c} \tag{1.92}$$

and

$$\sigma_v(v)=\sigma\left(E_0\left[1+\frac{v}{c}\right]\right) \tag{1.93}$$

one obtains for $\sigma_v(v)$:

$$\sigma_v(v)=\frac{-1}{f_a \nu_a t'_a}\ln \mathscr{F}^{-1}\left\{\frac{1}{\mathscr{F}F_v(v)}\mathscr{F}\left[1-\frac{S(v)}{(1-b)f_s}\right]\right\} \tag{1.94}$$

where $\mathscr{F}$ is the operator of the Fourier transformation. In practice the application of Eq. (1.94) leads to serious mathematical difficulties because of the inherent statistical error of $S(v)$. To overcome these difficulties a carefully chosen filter-function should be used [29, 30] before the inverse Fourier transformation.

1.5.2. ANGULAR DEPENDENCE OF LINE INTENSITIES

If the spectrum is split the intensities and polarizations of the individual lines will have characteristic angular dependence relative to directions determined by the electric and magnetic interactions. In the case of a 1/2→3/2 transition and pure axial quadrupole interaction [8]:

$$I_\pi(\vartheta)=3\,(1+\cos^2\vartheta)/8 \tag{1.95}$$

$$I_\sigma(\vartheta)=(5-3\cos^2\vartheta)/8 \tag{1.96}$$

I_π and I_σ denoting the intensities of the $\pi(\pm 1/2\rightarrow\pm 3/2)$ and $\sigma(\pm 1/2\rightarrow\pm 1/2)$ transitions, respectively. ϑ is the angle of the axis of the EFG and the observation direction. The degree of the polarization of the same transitions is [31]:

$$a_\pi(\vartheta)=\sin^2\vartheta/(1+\cos^2\vartheta)\,, \tag{1.97}$$

$$a_\sigma(\vartheta)=3\sin^2\vartheta/(5-3\cos^2\vartheta)\,. \tag{1.98}$$

In the case of pure magnetic dipole interaction and 1/2→3/2 transition the intensities of the six-line-pattern are [8]:

$$I_{1,6}(\vartheta)=3(1+\cos^2\vartheta)/16 \tag{1.99}$$

$$I_{2,5}(\vartheta)=\sin^2\vartheta/4 \tag{1.100}$$

$$I_{3,4}(\vartheta)=(1+\cos^2\vartheta)/16 \tag{1.101}$$

ϑ being the angle of magnetic field and observation direction.

In the case of pure electric interaction the intensities of the dipole transition can be given by the quadratic form of an "intensity tensor" $\mathbf{I}^{\mathrm{h}}$ [32, 33]:

$$I^{\mathrm{h}}/(I^{\mathrm{h}}+I^{\mathrm{l}})=\mathbf{k}^0\,\mathbf{I}^{\mathrm{h}}\,\mathbf{k}^0 \tag{1.102}$$

I^{h} and I^{l} being the intensities of the higher and lower energy lines, respectively while $\mathbf{k}^0$ is the unity vector parallel to the wave vector of the photon. It can be shown [33] that, for a 1/2→3/2 transition, $\mathrm{Tr}\,\mathbf{I}^{\mathrm{h}}=3/2$.

A general matrix-formalism accounting for the line intensities and polarizations in the case of arbitrary multipolarity of the radiation and arbitrary hyperfine interaction was developed by Spiering [34].

If the crystallites of a polycrystalline sample are randomly oriented the line intensities $\bar{I}$ can be obtained from the former $I(\vartheta)$ (or, in the general case $I(\vartheta,\varphi)$) single crystal or single domain intensities by averaging for the angles:

$$\bar{I}=\frac{1}{4\pi}\int\limits_0^{2\pi}\int\limits_0^{\pi} I(\vartheta,\varphi)\sin\vartheta\,\mathrm{d}\vartheta\,\mathrm{d}\varphi\,. \tag{1.103}$$

Applying Eq. (1.103) for Eqs (1.95) and (1.96) one obtains

$$\bar{I}_\pi = \bar{I}_\sigma . \tag{1.104}$$

Similarly from Eqs (1.99–1.101):

$$\bar{I}_{1,6} : \bar{I}_{2,5} : \bar{I}_{3,4} = 3:2:1 . \tag{1.105}$$

It should be mentioned that Eq. (1.104) holds true generally for pure electric quadrupole interaction and 1/2→3/2 transition. In fact, the macroscopic intensity tensor of a sample with no preferred orientation of the EFG's should be isotropic. Since the trace of a tensor is invariant under rotation it survives the angular averaging, so it is 3/2. Consequently the macroscopic intensity tensor is

$$I^{\mathrm{h}} = \begin{pmatrix} 1/2 & 0 & 0 \\ 0 & 1/2 & 0 \\ 0 & 0 & 1/2 \end{pmatrix} \tag{1.106}$$

i.e. using Eq. (1.103) $\bar{I}^{\mathrm{h}} = 1/2$.

1.5.3. GOLDANSKII–KARYAGIN EFFECT

It was shown first by Goldanskii, Karyagin and co-workers [35, 36] that the anisotropy of lattice vibrations may result in anomalous line intensities, particularly in an asymmetry of the quadrupole doublet of a polycrystalline sample. In fact, if the point symmetry of an atom is less than cubic its mean-square thermal deviation is different along the different crystallographic directions. It follows then from Eq. (1.11) that in such case the probability of the Mössbauer effect will be also angle dependent. This angular dependence $f_\mathrm{a}(\vartheta, \varphi)$ should, however, be taken into account in Eq. (1.103). The new expression giving the averaged line intensities is:

$$\bar{I} = \frac{1}{4\pi} \int_0^{2\pi} \int_0^{\pi} f_\mathrm{a}(\vartheta, \varphi)\, I(\vartheta, \varphi) \sin \vartheta \, \mathrm{d}\vartheta \, \mathrm{d}\varphi \tag{1.107}$$

removing the validity of Eqs (1.104) and (1.105).

For the sake of simplicity let us consider a 1/2→3/2 Mössbauer transition and a pure electric quadrupole interaction of axial symmetry. Let us suppose further that the f factor is also axially symmetric, its symmetry axis coinciding with the EFG axis and that the absorber is thin. The asymmetry of the quadrupole doublet is described [37] by

$$R_\mathrm{q} = \frac{\bar{I}_\pi}{\bar{I}_\sigma} . \tag{1.108}$$

For an axial point symmetry of the resonant nucleus the angular dependence of the f factor is given [38] by

$$f_\mathrm{a}(\vartheta) = \exp\left[-k^2 (\langle z^2 \rangle - \langle x^2 \rangle) \cos^2 \vartheta - k^2 \langle x^2 \rangle \right] \tag{1.109}$$

$\langle z^2 \rangle$ and $\langle x^2 \rangle$ being the mean-square deviations of the resonant nucleus along the z and x direction, respectively, $\mathbf{k}$ the wave-vector of the photon and ϑ its polar angle. Using Eqs (1.95), (1.96), (1.108), (1.109) and the notation $\varepsilon_q = k^2(\langle z^2 \rangle - \langle x^2 \rangle)$, one obtains that

$$R_q = \frac{\int_0^1 (1+u^2)\,e^{-\varepsilon_q u^2}\,du}{\int_0^1 \left(\frac{5}{3} - u^2\right) e^{-\varepsilon_q u^2}\,du}. \tag{1.110}$$

The latter equation can be linearized for $|\varepsilon_q| \lesssim 1$:

$$R_q \approx 1 - \frac{2}{15}\varepsilon_q. \tag{1.111}$$

In the case of pure magnetic dipole interaction the relative line intensities are often described [37] by

$$R_m = \bar{I}_{2,5}/\bar{I}_{3,4}. \tag{1.112}$$

It is easy to realize from Eqs (1.95), (1.96), (1.100), (1.101), (1.107), (1.108) and (1.112) that both R_q and R_m depend only on the same integral α_q of $f_a(\vartheta)$:

$$\alpha_q = \int_0^{\pi/2} f_a(\vartheta) \cos^2\vartheta \sin\vartheta \, d\vartheta \tag{1.113}$$

$$R_q = 3(1+\alpha_q)/(5-3\alpha_q) \tag{1.114}$$

$$R_m = 4(1-\alpha_q)/(1+\alpha_q) \tag{1.115}$$

that is

$$R_m = (3-R_q)/R_q \tag{1.116}$$

Equations (1.110) and (1.116) define the line intensities which are expected for anisotropic lattice vibrations in magnetic materials. The same can be used if the quadrupole interaction is small compared to the magnetic one. In any other case R_q and R_m can be calculated only numerically.

The appearence of anomalous line intensities in Mössbauer spectra as a result of the anisotropy of lattice vibrations is called Goldanskii–Karyagin effect (GKE).

1.5.4. TEXTURE EFFECTS

Many physical quantities are described by vectors and tensors i.e. by items which can be characterized by a direction or directions. Examples are the hyperfine magnetic field, the crystallographic axes, the EFG tensor, etc. There are two extreme cases which are easy to handle in theoretical calculations:

(i) if the above mentioned directions have a parallel (homogeneous) distribution all over the volume of the sample (e.g. single crystal or single ferromagnetic domain), and

(ii) if these directions have no preferred orientation throughout the sample (e.g. ideal polycrystal or paramagnetic material in zero applied field).

In the strict sense, these extreme cases are very rarely realized in nature. An ideal polycrystal occurs as rarely as an ideal single crystal. Mostly an intermediate case is realized, i.e. the above mentioned directions have some preferred orientation. This is called in the general sense *texture*. In crystallography texture is a preferred orientation of the crystal axes of the crystallites.

Texture often plays a very important role, particularly in the macroscopic properties of metals. Correspondingly the theory and the standard methods of the texture measurement (mainly with X-ray diffraction) have been worked out in metallurgy [39].

Like in the case of GKE the angular dependence of the Mössbauer line intensities must not be averaged according to Eq. (1.103) for textured samples. Therefore, also texture leads in Mössbauer spectroscopy to anomalous line intensities. It was shown first by Pfannes and Gonser [40, 41] that a relatively small deviation from isotropy in the distribution of crystallographic axes may lead to a considerable asymmetry of 1/2 →3/2 quadrupole doublets.

To elucidate the effect of texture let us suppose that there is an electric quadrupole interaction of axial symmetry its axis being parallel to the crystallographic c axis with a possible magnetic field also parallel to that axis and that the absorber is thin. We assume further that the texture is also axially symmetric and that the direction of observation is parallel to the texture axis. Finally we suppose that the GKE can be neglected.

The texture in the above case is described [40] by the texture function $D_E(\vartheta)$ which is defined so that the probability of finding a c axis between the polar angles ϑ and $\vartheta + d\vartheta$ is $D_E(\vartheta) \sin\vartheta \, d\vartheta$. Consequently $D_E(\vartheta)$ is normalized so that

$$\int_0^{\pi/2} D_E(\vartheta) \sin\vartheta \, d\vartheta = 1 \,. \tag{1.117}$$

For an isotropic distribution $D_E(\vartheta) \equiv 1$.

The effect of texture is formally equivalent to the anisotropy of lattice vibrations. The intensity anomaly of the spectral lines is given again by Eqs (1.113–1.116) except that $f_a(\vartheta)$ should be replaced by $D_E(\vartheta)$:

$$\alpha_a = \int_0^{\pi/2} D_E(\vartheta) \cos^2\vartheta \sin\vartheta \, d\vartheta \,. \tag{1.118}$$

The above substitution is not quite trivial since $f_a(\vartheta)$ describes the angular dependence of the resonant fraction in the coordinate system of a crystallite while $D_E(\vartheta)$ the distribution of the c axes of the crystallites in the laboratory framework. This difference leads, however, to no difficulty if neither f_a nor D_E depends on the azimutal angle φ. If the direction of observation does not coincide with the texture axis Eq. (1.118) will not hold true any longer. This fact offers a simple possibility to distinguish between GKE and texture. In the case of GKE the observed intensity anomaly does not depend on the position of the absorber relative to the direction of the gamma-rays (except for the trivial change coming from the change of the effective thickness described by Eq. (1.77)). In contrast to this, if the intensity anomaly is caused by texture a rotation of the sample results in an explicite change in the intensity ratios since the texture function is fixed to the sample.

1.6. DIFFUSIONAL BROADENING OF RESONANCE LINES

Atomic motions on a time scale comparable to the nuclear lifetime may lead to a change of the lineshape of the resonance lines. Particularly in glasses diffusion plays an important role. In this chapter we shall discuss the diffusional broadening of resonance lines following the basic paper of Singwi and Sjölander [42].

This general theory of Mössbauer effect only supposes that the nucleus is embedded in some system of atoms. The total Hamiltonian is then

$$\hat{H}_{\mathrm{tot}} = \hat{H} + \hat{H}_{\mathrm{nucl}} + \hat{H}_{\mathrm{rad}} + \hat{H}' + \hat{K} + \hat{H}_{\mathrm{hf}} \tag{1.119}$$

Here $\hat{H}$ is the Hamiltonian of the system of atoms, $\hat{H}_{\mathrm{nucl}}$ that of the nucleus and $\hat{H}_{\mathrm{rad}}$ that of the radiation field. $\hat{H}'$ is the interaction of the nucleus with the radiation field, $\hat{K}$ that of the atomic system with the radiation field and $\hat{H}_{\mathrm{hf}}$ the hyperfine interaction of the nucleus with atoms. If we restrict ourselves to unshifted and unsplit resonance lines and we are not interested in optical transitions the last two terms can be omitted. We shall calculate the cross-section for the absorption of a photon of energy E and wave vector **k**.

In Dirac's formalism, the initial state of the atomic system is $|n_{\mathrm{i}}\rangle$, its final state $|n_{\mathrm{f}}\rangle$, the initial state of the nucleus $|A_{\mathrm{i}})$, its final state $|A_{\mathrm{f}}\rangle$, the initial state of the radiation field $|\mathbf{k}\rangle$, its final state the vacuum $|0\rangle$. The energy eigenvalues are defined by

$$\hat{H}|n_{\mathrm{i}}\rangle = \varepsilon_{n_{\mathrm{i}}}|n_{\mathrm{i}}\rangle \tag{1.120}$$

$$\hat{H}|n_{\mathrm{f}}\rangle = \varepsilon_{n_{\mathrm{f}}}|n_{\mathrm{f}}\rangle \tag{1.121}$$

$$\hat{H}_{\mathrm{nucl}}|A_{\mathrm{i}}\rangle = E_{A_{\mathrm{i}}}|A_{\mathrm{i}}\rangle \tag{1.122}$$

$$\hat{H}_{\mathrm{nucl}}|A_{\mathrm{f}}\rangle = E_{A_{\mathrm{f}}}|A_{\mathrm{f}}\rangle \tag{1.123}$$

$$\hat{H}_{\mathrm{rad}}|\mathbf{k}\rangle = E(\mathbf{k})|\mathbf{k}\rangle \tag{1.124}$$

$$\hat{H}_{\mathrm{rad}}|0\rangle = 0\,. \tag{1.125}$$

The absorption cross-section is given then by Wigner and Weisskopf [43]:

$$\sigma(E) \sim \sum_{n_{\mathrm{i}}, n_{\mathrm{f}}} g_{n_{\mathrm{i}}} \frac{|\langle n_{\mathrm{f}}, A_{\mathrm{f}}, 0|\hat{H}'|\mathbf{k}, A_{\mathrm{i}}, n_{\mathrm{i}}\rangle|^2}{(E_0 - E + \varepsilon_{n_{\mathrm{f}}} - \varepsilon_{n_{\mathrm{i}}})^2 + \Gamma^2/4} \tag{1.126}$$

where $E_0 = E_{A_{\mathrm{i}}} - E_{A_{\mathrm{f}}}$ and Γ is the natural linewidth of the nuclear transition. $g_{n_{\mathrm{i}}}$ is the statistical weight of state $|n_{\mathrm{i}}\rangle$. The matrix element in Eq. (1.126) can be transformed since

$$\hat{H}' = \sum_{j,\mathbf{k}'} C(j, \mathbf{k}')\{\hat{a}_{\mathbf{k}'} \exp[i\mathbf{k}'\mathbf{r}_j] + \hat{a}^{+}_{\mathbf{k}'} \exp[-i\mathbf{k}'\mathbf{r}_j]\} \tag{1.127}$$

$\hat{a}_{\mathbf{k}'}$ and $\hat{a}^{+}_{\mathbf{k}'}$ being the absorption and emission operators of a photon of wave vector $\mathbf{k}'$, respectively, while $\mathbf{r}_j$ is the coordinate vector of the j-th nucleon. The $C(j, \mathbf{k}')$ coefficients contain nuclear operators. On denoting the coordinate vector of the center of mass of the nucleus by $\mathbf{R}_{\mathrm{A}}$ relative coordinates can be defined by

$$\mathbf{r}_j = \mathbf{R}_{\mathrm{A}} + \boldsymbol{\varrho}_j\,. \tag{1.128}$$

Then

$$\begin{aligned}\langle n_\mathrm{f}, A_\mathrm{f}, 0|\hat{H}'|\mathbf{k}, A_\mathrm{i}, n_\mathrm{i}\rangle &= \langle n_\mathrm{f}, A_\mathrm{f}|\sum_j C(j,\mathbf{k})\exp[i\mathbf{k}\mathbf{R}_\mathrm{A}]\exp[i\mathbf{k}\boldsymbol{\rho}_j]|A_\mathrm{i}, n_\mathrm{i}\rangle = \\ &= \langle n_\mathrm{f}|\exp[i\mathbf{k}\mathbf{R}_\mathrm{A}]|n_\mathrm{i}\rangle\,\langle A_\mathrm{f}|\sum_j C(j,\mathbf{k})\exp[i\mathbf{k}\boldsymbol{\rho}_j]|A_\mathrm{i}\rangle\,. \qquad (1.129)\end{aligned}$$

Substituting Eq. (1.129) into Eq. (1.126) and using the same normalization as in Eq. (1.3), we obtain

$$\sigma(E) = \frac{\sigma_o \Gamma^2}{4} \sum_{n_\mathrm{i}, n_\mathrm{f}} g_{n_\mathrm{i}} \frac{|\langle n_\mathrm{f}|\exp[i\mathbf{k}\mathbf{R}_\mathrm{A}]|n_\mathrm{i}\rangle|^2}{(E_0 - E + \varepsilon_{n_\mathrm{f}} - \varepsilon_{n_\mathrm{i}})^2 + \Gamma^2/4}\,. \qquad (1.130)$$

With some algebra, Eq. (1.130) can be brought to the form

$$\sigma(E) = \frac{\sigma_0 \Gamma}{4\hbar} \int_{-\infty}^{\infty} \exp[-\frac{i}{\hbar}(E - E_0)t - \frac{\Gamma}{2\hbar}|t|]\,\langle \exp[-i\mathbf{k}\mathbf{R}_\mathrm{A}(0)]\exp[i\mathbf{k}\mathbf{R}_\mathrm{A}(t)]\rangle_T\,\mathrm{d}t \qquad (1.131)$$

Here

$$\mathbf{R}_\mathrm{A}(t) = \mathrm{e}^{\frac{i}{\hbar}\hat{H}t}\mathbf{R}_\mathrm{A}\mathrm{e}^{-\frac{i}{\hbar}\hat{H}t} \qquad (1.132)$$

while the quantum mechanical and thermal average is denoted by $\langle \ldots \rangle_T$. Equation (1.132) enables us to attribute the meaning "time" to the integration variable t as introduced in Eq. (1.131). Than $\mathbf{R}_\mathrm{A}(t)$ is the coordinate operator of the center of mass of the nucleus as used in Heisenberg's formalism.

Let us calculate the inverse Fourier transform of $\langle \mathrm{e}^{-i\mathbf{k}\mathbf{R}_\mathrm{A}(0)}\,\mathrm{e}^{-i\mathbf{k}\mathbf{R}_\mathrm{A}(t)}\rangle_T$:

$$\begin{aligned}G_\mathrm{s}(\mathbf{r}, t) &= \frac{1}{(2\pi)^3}\int \mathrm{e}^{-i\mathbf{k}\mathbf{r}}\langle \mathrm{e}^{-i\mathbf{k}\mathbf{R}_\mathrm{A}(0)}\,\mathrm{e}^{-i\mathbf{k}\mathbf{R}_\mathrm{A}(t)}\rangle_T\,\mathrm{d}^3\mathbf{k} = \\ &= \langle \int \delta[\mathbf{r} + \mathbf{R}_\mathrm{A}(0) - \mathbf{r}']\,\delta[\mathbf{r}' - \mathbf{R}_\mathrm{A}(t)]\,\mathrm{d}^3\mathbf{r}'\rangle_T \qquad (1.133)\end{aligned}$$

In the classical theory, $G_\mathrm{s}(\mathbf{r}, t)$ describes the correlation of the coordinates of a particle at different instants of time. Consequently, $G_\mathrm{s}(\mathbf{r}, t)$ is the quantummechanical generalization of the self-correlation function.

Using Eq. (1.131) and the Fourier transform of Eq. (1.133), we obtain:

$$\sigma(E) = \frac{\sigma_0 \Gamma}{4\hbar}\int \mathrm{e}^{i(\mathbf{k}\mathbf{r} - \omega t) - \frac{\Gamma}{2\hbar}|t|}\,G_\mathrm{s}(\mathbf{r}, t)\,\mathrm{d}^3\mathbf{r}\,\mathrm{d}t\,, \qquad (1.134)$$

where $\omega = (E - E_0)/\hbar$. The problem of calculation of the absorption cross-section is reduced thereby to the calculation of $G_\mathrm{s}(\mathbf{r}, t)$.

The function $G_\mathrm{s}(\mathbf{r}, t)$ has been calculated by Van Hove [44] for various systems. Particularly for a monoatomic cubic crystal

$$G_\mathrm{s}(\mathbf{r}, t) = \frac{\mathrm{e}^{-\frac{r^2}{2\gamma(t)}}}{(2\pi\gamma(t))^{3/2}} \qquad (1.135)$$

where

$$\gamma(t) = \frac{\hbar^2}{M}\int_0^{\infty}\left[\mathrm{cth}\left(\frac{\nu}{2k_\mathrm{B}T}\right)\left(1 - \cos\frac{\nu t}{\hbar}\right) - i\sin\frac{\nu t}{\hbar}\right]\frac{P(\nu)}{\nu}\,\mathrm{d}\nu \qquad (1.136)$$

M being the mass of one atom while $P(\nu)$ the density of states of phonons normalized to unity. Using Eqs (1.134–136), we obtain

$$\sigma(E)=\frac{\pi\sigma_0\Gamma}{2}\left[\frac{\Gamma}{2\pi}\frac{1}{(E-E_0)^2+\Gamma^2/4}+\sum_{j=1}^{\infty}\frac{(2W)^j}{j!}g_j(E-E_0,T)\right]\mathrm{e}^{-2W} \quad (1.137)$$

where

$$g_1(E,T)=\frac{P(|E|)}{2EF(T)}\left[\operatorname{cth}\left(\frac{E}{2k_\mathrm{B}T}\right)-1\right] \quad (1.138)$$

$$g_n(E,T)=\int_{-\infty}^{\infty} g_1(E-E',T)\,g_{n-1}(E',T)\,\mathrm{d}E' \quad (1.139)$$

$$\Phi(T)=\int_0^{\infty}\frac{P(\nu)}{\nu}\operatorname{cth}\left(\frac{\nu}{2k_\mathrm{B}T}\right)\mathrm{d}\nu \quad (1.140)$$

and

$$2W=\frac{\hbar^2k^2}{2M}\Phi(T) \quad (1.141)$$

The cross-section as given by Eq. (1.137) consists of two terms. The first term describes a sharp absorption line at $E=E_0$ of natural width; this is Mössbauer's recoil-free resonance line. The second term (the sum) describes the transitions involving a change of the phonon-state. The factor e^{-2W} can easily be identified as the Debye–Waller factor f as introduced in Section 1.2.

In the Debye approximation

$$P(\nu)=\begin{cases}\dfrac{3\nu^2}{(k_\mathrm{B}\theta_\mathrm{D})^2} & \text{if} \quad \nu\le k_\mathrm{B}\theta_\mathrm{D}\\ 0 & \text{otherwise}\end{cases} \quad (1.142)$$

Combining Eqs (1.140–142) and Eq. (1.6), we obtain Eq. (1.12).

The diffusion of atoms in a solid will be described in terms of a jump model. Let us denote the mean time which an atom spends in a certain site before jumping to another one by τ_0. Assuming that the jumps are governed by a Markov process. Singwi and Sjölander [42] calculated the appropriate self-correlation function, which, replacing Eq. (1.134) gives

$$\sigma(E)=\frac{\sigma_0\Gamma}{4}\left[\frac{\Gamma+(2\hbar/\tau_0)[1-\alpha(\mathbf{k})]}{(E-E_0)^2+[\Gamma+(2\hbar/\tau_0)(1-\alpha(\mathbf{k}))]^2/4}+\text{phonon terms}\right]\mathrm{e}^{-2W}, \quad (1.143)$$

where

$$\alpha(\mathbf{k})=\int \mathrm{e}^{i\mathbf{kr}}h(\mathbf{r})\,\mathrm{d}^2\mathbf{r} \quad (1.144)$$

$h(\mathbf{r})$ being the probability density of finding an atom after one jump at a distance $\mathbf{r}$ from the origin of the jump.

Equation (1.143) shows that a diffusive motion of resonant nuclei results in a broadening of the Mössbauer line

$$\Delta\Gamma = \frac{2\hbar}{\tau_0}\left[1 - \int e^{i\mathbf{k}\mathbf{r}} h(\mathbf{r})\, d^3\mathbf{r}\right]. \tag{1.145}$$

To estimate the line broadening let us suppose that the jump takes place along any edge of a cube with a probability 1/6. If the interatomic spacing is l, the diffusion coefficient defined by

$$D = \frac{1}{6\tau_0}\int r^2 h(\mathbf{r})\, d^3\mathbf{r} \tag{1.146}$$

is

$$D = \frac{l^2}{6\tau_0}. \tag{1.147}$$

Since in practical cases the integral in Eq. (1.145) is much less then unity, a rough estimate of the diffusion constant from the line broadening is given by

$$D = \frac{l^2}{12\hbar}\Delta\Gamma. \tag{1.148}$$

1.7. EXPERIMENTAL TECHNIQUES

1.7.1. SPECTROMETERS

The Mössbauer spectrum is measured by scanning the absorption cross-section vs. energy. As it was shown in Section 1.2 this can be done by moving the source with velocities of several mm s^{-1} relative to the absorber. In the first years of Mössbauer spectroscopy this was realized with the help of various mechanical and hydraulic systems. With the appearance of electrodynamic drives the latter method became exclusive.

An electrodynamic drive (Fig. 1.8) consists of two electrodynamic loudspeakers. One coil is used, like in the loudspeaker, to generate motion while the other to measure the actual velocity. The latter is used to be fed back to a differential amplifier connected to a velocity generator.

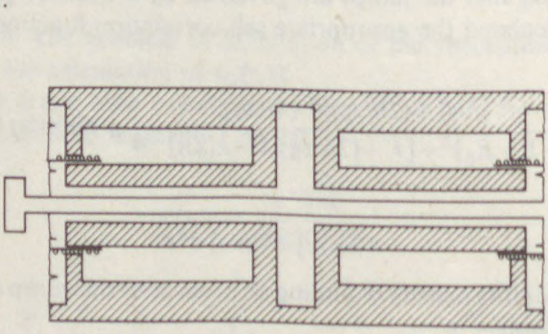

Fig. 1.8. Electrodynamic drive

Photons passing through the absorber are registered with scintillation or proportional counters. Scintillation counters have higher efficiency and less dead time. In contrast to proportional counters they also detect high energy ($\gtrsim 60$ keV) photons which may overload the amplifier. To avoid this, very thin (0.1–0.2 mm) NaI(Tl) scintillation crystals are used. The advantage of proportional counters is the higher resolution and their insensitivity to external magnetic fields. The pulses belonging to the Mössbauer transition are selected by a single-channel analyzer. If this cannot be done because some other γ- or X-ray lines overlap with the Mössbauer line semiconductor detectors or special filters are used.

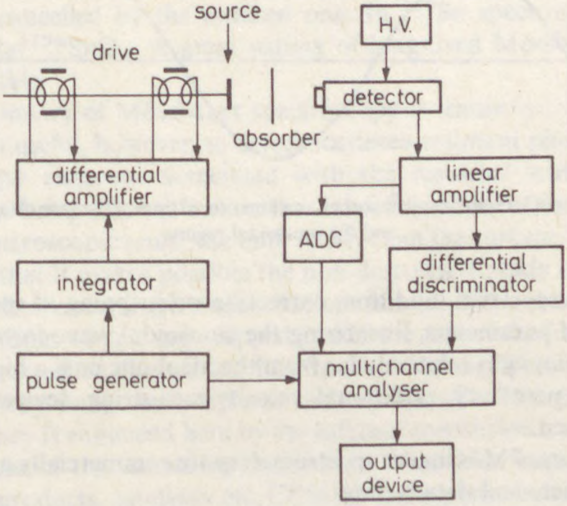

Fig. 1.9. Block scheme of a Mössbauer spectrometer

Up-to-date spectrometers are generally operating in the variable velocity regime. The whole velocity range of interest is scanned many (typically 10 to 50) times per second. The counts detected behind the absorber and selected by the single-channel analyzer are stored in a memory (mostly in the memory of a multichannel analyzer) at an address corresponding to the instantaneous velocity of the source. The memory contains therefore at any time the whole spectrum collected since the start of the measurement. The block scheme of a spectrometer is shown in Fig. 1.9.

An overwhelming majority of Mössbauer spectrometers is operating in the above described "multiscaling regime". The previously used "pulse height modulation regime" [7] is used only to fulfill special requirements.

An undistorted spectrum in the memory of the spectrometer can only be expected if the velocity is a linear function of time [Fig. 1.10(a)]. It is not always easy to realize such a law of motion especially if the velocity is high or the mass to be moved is large. Many spectrometers use a sinusoidal law of motion [Fig. 1.10(b)] to avoid these difficulties. To convert the stored spectrum to linear form mostly numerical methods are used.

Many spectrometers are controlled by small computers or microprocessors. These spectrometers are able not only to control the measurement but also to perform some

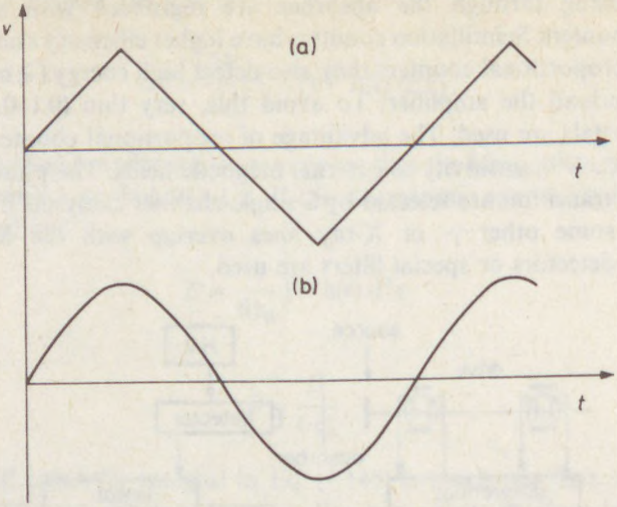

Fig. 1.10. Relative velocity of source and absorber as a function of time in the case of (a) constant acceleration and (b) sinusoidal regime

evaluation of the spectrum (addition, correction or stripping of spectra, fitting them with a number of parameters, linearizing the sinusoidal wave-form, etc.).

If the actual velocity is relatively far from the ideal one or if a high accuracy of the velocity scale is necessary, additional velocity-measuring devices like laser interferometers are used.

Since many types of Mössbauer spectrometers are commercially available we do not go into further technical details here.

Further equipment is necessary to set the temperature of the sample and/or to apply a magnetic field. Above room temperature electric furnaces are used. These are mostly vacuum furnaces to prevent the sample from oxidization. The requirements for the vacuum system are not high: a minimum pressure of 10^{-3} Pa is sufficient. If transformation kinetics are to be studied furnaces of small heat capacity but of high stability should be preferably used.

Below room temperature cryostats cooled with liquid nitrogen, liquid helium or sometimes with dry ice are used. Cryostats (especially exchange gas cryostats) and furnaces are often combined into one unit. This cannot be done with helium-cooled immersion cryostats which are often supplied with superconducting magnets. In such cryostats the movement of the drive is generally transduced to the source by a long rod of about 100 g mass. This results in difficulties with the proper linear velocity waveform as described above.

Since many kinds of cryostats are commercially available one should be careful when choosing the appropriate one for a certain purpose. Many cryostats are, for example, not suitable for studying frozen aqueous solutions since it is impossible to put the pre-cooled sample into the holder so that it does not reach its glass transition temperature which is for such systems at about 160 K.

To apply magnetic fields up to about 1.5 T conventional electromagnets are used. Above this value superconducting magnets are applied. When using magnetic fields one should check if the scattered magnetic field does not affect the drive and/or the detector. On the other hand, in some special cases (e.g. dilute Fe^{3+} systems) the sample should be shielded even against the scattered field of the drive because magnetic fields as low as 10^{-2} T may change the Mössbauer spectrum.

Sources in conventional Mössbauer spectroscopy should have an unsplit and unbroadened line. Moreover, their recoil-less fraction should be as high as possible. In ^{57}Fe spectroscopy this is generally realized by diffusing electrolized ^{57}Co into paramagnetic metals or alloys such as stainless steel, Cr, Pd, Cu, Rh, etc. The two latter hosts are very advantageous because of their narrow line even at 4.2 K. Moreover, they are rather insensitive to scattered magnetic fields at this temperature since the external field is practically cancelled by the induced one. In ^{119}Sn spectroscopy the most suitable source is $Ba^{119m}SnO_3$. A great variety of long-lived Mössbauer sources is commercially available.

The standard geometry of Mössbauer spectroscopy is transmission. It is possible and sometimes even useful, however, to detect scattered resonant photons or X-rays, conversion or Auger electrons associated with the resonant scattering process. Gammas and X-rays bring information on the state of an about 100 μm thick surface layer. This is, in a microscopic sense, the bulk rather than the surface. The importance of this geometry is that it makes possible the non-destructive study of bulk samples.

When detecting electrons a much thinner surface film (ca 100 nm) is seen. Electrons with an energy of about 10 keV are stopped inside the material when coming from deeper. This technique called Conversion Electron Mössbauer Spectroscopy (CEMS) is generally realized by using the sample as the cathode of a flow-gas proportional counter. The efficiency is enhanced here by the internal conversion coefficient α being 8.9 for ^{57}Fe. Because of the increasing importance of surface studies of implanted systems, corrosion products, catalysts, etc. CEMS is getting more and more standard technique shown by the fact that CEMS detectors are produced commercially.

1.7.2. ESTIMATION OF OPTIMUM ABSORBER THICKNESS

If the activity of the source and/or the concentration of resonant nuclei in the absorber is low, Mössbauer lines of appropriate intensity can be produced only with long running times. In such cases it is advisable to estimate the optimum absorber thickness yielding the maximum information per unit of running time.

As it was shown in Section 1.5.1 [cf. Eq. (1.73)] an increase in the layer thickness for a sample of given composition is accompanied by an increase not only of the number of resonant nuclei in the path of the radiation, and hence of the extent of nuclear resonance absorption but also of the non-resonant atomic absorption originating from the shell electrons of all atoms in the sample. An increase in the absorber thickness therefore results in two opposing effects, and it is thus to be expected that (as regards the measurement) there will be an optimum thickness of the absorber.

A number of methods have been developed to determine this layer thickness [45–49]. One of these methods [47, 49] will be described here in detail. The optimum layer thickness is that one for which the shortest time is needed to perform a measurement so that the relative size of the measured effect is greater than a prescribed β times the relative standard statistical deviation of the baseline, i.e. using the notations of Sections 1.2 and 1.5.1:

$$A_s > \frac{\beta}{\sqrt{N(\infty)}} . \qquad (1.149)$$

Here and later on in this chapter it is supposed that, for the sake of simplicity, both the emission and the absorption spectrum consist of single lines of Lorentzian shape and of the same width.

Combining Eqs (1.87) and (1.149), we obtain

$$(1-b)^2 N(\infty) A_T^2 > \beta^2 . \qquad (1.150)$$

To determine the optimum layer thickness t'_{opt} let us assume that the total time of the measurement is t_m using a multichannel analyzer of G channels. Pulses are thus collected in one channel for a time t_m/G assuming that they are fed into each channel for the same time. The number of pulses without background collected by one channel during the whole measurement is

$$N(v) - bN(\infty) = I_x(v) \frac{t_m}{G} , \qquad (1.151)$$

where $I_x(v)$ is the background-free intensity of detected pulses at source velocity v.

At non-resonant velocities only the atomic absorption needs to be considered:

$$I_x(\infty) = I' e^{-\mu_a t'_a} . \qquad (1.152)$$

The absorption coefficient μ_a in Eq. (1.152) refers to the absorption of the Mössbauer line and does not contain the attenuation of the background radiation which also depends on the layer thickness t'_a.

Let us introduce the dimensionless layer thickness by

$$z = \mu_a t'_a . \qquad (1.153)$$

With this notation, Eqs (1.151) and (1.152) give

$$(1-b) N(\infty) = I' e^{-z} \frac{t_m}{G} . \qquad (1.154)$$

If the intensity of the background detected behind the absorber of dimensionless thickness z is denoted by $I_b(z)$ then the number of background pulses collected in one channel during the entire measurement time is

$$bN(\infty) = I_b(z) \frac{t_m}{G} . \qquad (1.155)$$

Adding Eqs (1.154) and (1.155), we obtain the equation:

$$N(\infty) = [I' e^{-z} + I_b(z)] \frac{t_m}{G} \qquad (1.156)$$

and taking square of Eq. (1.154) and dividing it by Eq. (1.156):

$$(1-b)^2 N(\infty)=\frac{I' \mathrm{e}^{-z}}{G\left[1+\frac{I_{\mathrm{b}}(z)}{I'}\mathrm{e}^{z}\right]}t_{\mathrm{m}}. \tag{1.157}$$

Substituting Eq. (1.157) into inequality (1.150) and expressing the minimum necessary measurement time, we arrive at:

$$t_{\mathrm{m}}^{\mathrm{min}}=\left[1+\frac{I_{\mathrm{b}}(z)}{I'}\mathrm{e}^{z}\right]\frac{G\beta^2}{I' A_{\mathrm{T}}^2}\mathrm{e}^{z}. \tag{1.158}$$

Substituting the expression for A_{T} from Eq. (1.76) into Eq. (1.158) and introducing the dimensionless resonant nucleus concentration

$$\gamma=\frac{\lambda_{\mathrm{a}}}{2z} \tag{1.159}$$

one obtains

$$t_{\mathrm{m}}^{\mathrm{min}}=\frac{G\beta^2}{I' f_{\mathrm{s}}^2}[1+g(z)\mathrm{e}^{z}]\frac{\mathrm{e}^{z}}{[1-\mathrm{e}^{-\gamma z}I_0(\gamma z)]^2} \tag{1.160}$$

where the $g(z)$ background ratio is defined by

$$g(z)=\frac{I_{\mathrm{b}}(z)}{I'}. \tag{1.161}$$

If β is fixed and only the effect of the layer thickness is examined, then instead of Eq. (1.160) it is sufficient to consider its thickness-dependent factor, i.e.

$$T(z,\gamma)=[1+g(z)\mathrm{e}^{z}]\frac{\mathrm{e}^{z}}{[1-\mathrm{e}^{-\gamma z}I_0(\gamma z)]^2}. \tag{1.162}$$

Figure 1.11 shows $T(z,\gamma)$ for $b=0$, i.e. when the background is negligible ($g(z)=0$). At low values of γ the minimum for z is fairly sharp, and in such a situation, therefore, it is particularly important to maintain the optimum layer thickness. The latter can be calculated by solving the transcendent equation

$$\frac{\mathrm{d}T}{\mathrm{d}z}=0. \tag{1.163}$$

Figure 1.12 presents the calculated $z_{\mathrm{opt}}(\gamma)$ function for a negligible background. With decreasing γ, the optimal value of z_{opt} tends towards 2. For low values of γ where optimization is most essential the optimum layer thickness is approximately constant and equal to the limiting value

$$\xi=\lim_{\gamma\to 0} z_{\mathrm{opt}}(\gamma). \tag{1.164}$$

In general case when $b\neq 0$, ξ may differ from 2 and is given by the solution of the following equation:

$$\xi=\frac{2}{1+\frac{g(\xi)+g'(\xi)}{g(\xi)+\mathrm{e}^{-\xi}}}, \tag{1.165}$$

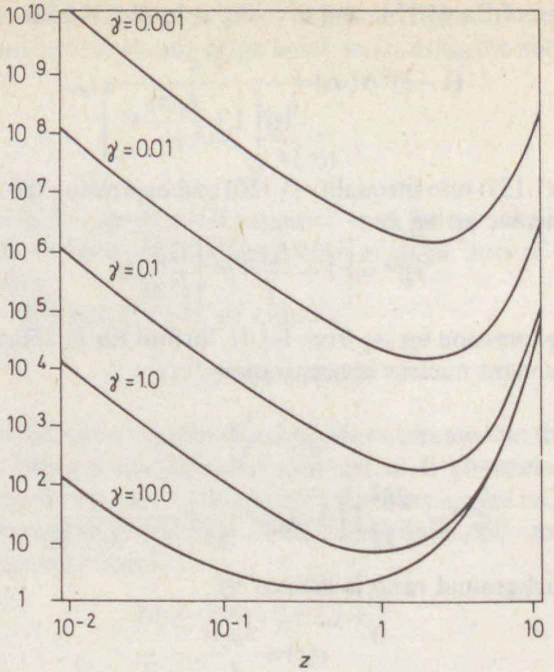

Fig. 1.11. Time factor function $T(z, \gamma)$ of the minimum measurement time plotted against the dimensionless absorber thickness z

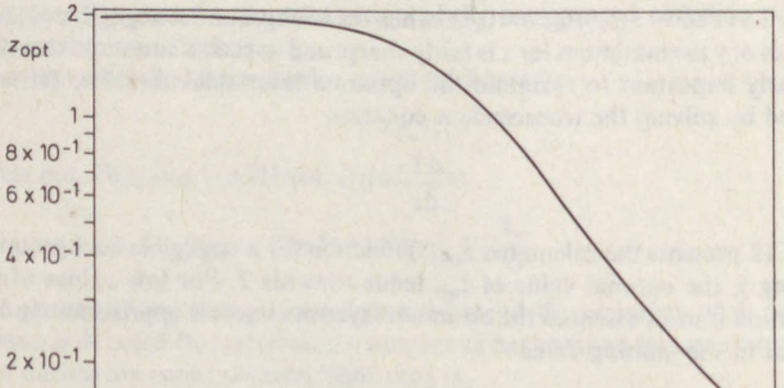

Fig. 1.12. The optimum dimensionless absorber thickness z_{opt} as a function of the dimensionless resonant nucleus concentration γ

where

$$g'(\xi) = \left.\frac{\mathrm{d}g}{\mathrm{d}z}\right|_{z=\xi} \tag{1.166}$$

In general, it is difficult to take the background into consideration in the calculation of ξ from Eq. (1.165), since it is necessary to know the course of $g(z)$. In many cases (e.g. in most ^{57}Fe measurements), however, the background ratio practically does not depend on z, hence $g'(z) \approx 0$ and $g(z) = g_0$ (constant). Equation (1.165) can be then easily solved. The solution is shown in Fig. 1.13. With increasing g_0, ξ decreases from 2 and

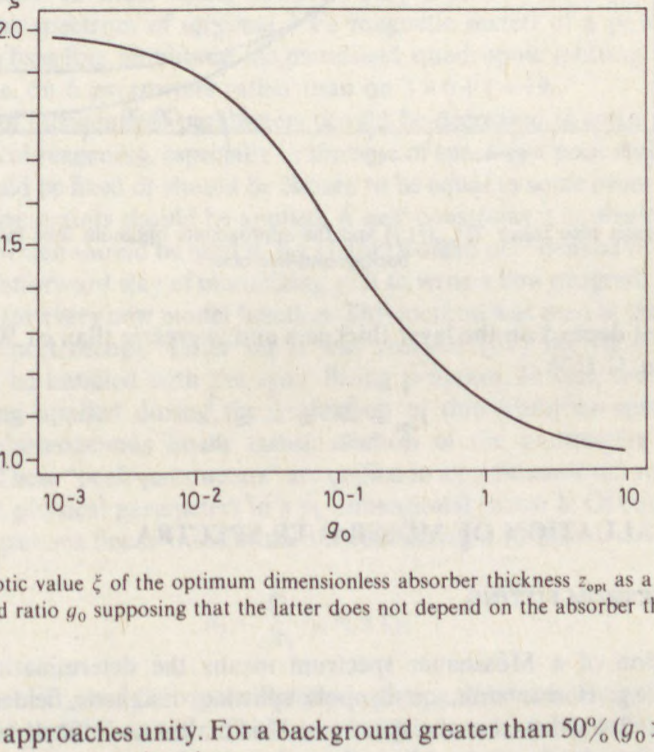

Fig. 1.13. Asymptotic value ξ of the optimum dimensionless absorber thickness z_{opt} as a function of the background ratio g_0 supposing that the latter does not depend on the absorber thickness

asymptotically approaches unity. For a background greater than 50% ($g_0 > 1$) $\xi = 1$ can be taken as a good approximation.

In general case when $g'(z) \neq 0$, the condition for optimum thickness can be given, as well. In this case even $\xi > 2$ may occur.

From a practical aspect, it is important to know how well the value of ξ (readily obtained from the background ratio) replaces z_{opt} which also depends on γ. Figure 1.14 shows the optimum time factor $T(z_{\mathrm{opt}}(\gamma), \gamma)$ and the approximate optimum time factor $T(\xi, \gamma)$ for the background-free case. The two curves start to diverge significantly at γ values for which T is fairly small. The exact meaning of this result as regards time depends on the concrete values of the other parameters in Eq. (1.160). In general, it is a short time. Furthermore, frequently an unrealistically high concentration of resonant nuclei would correspond to such a high value of γ.

The optimum layer thickness has a very simple approximate form if the background

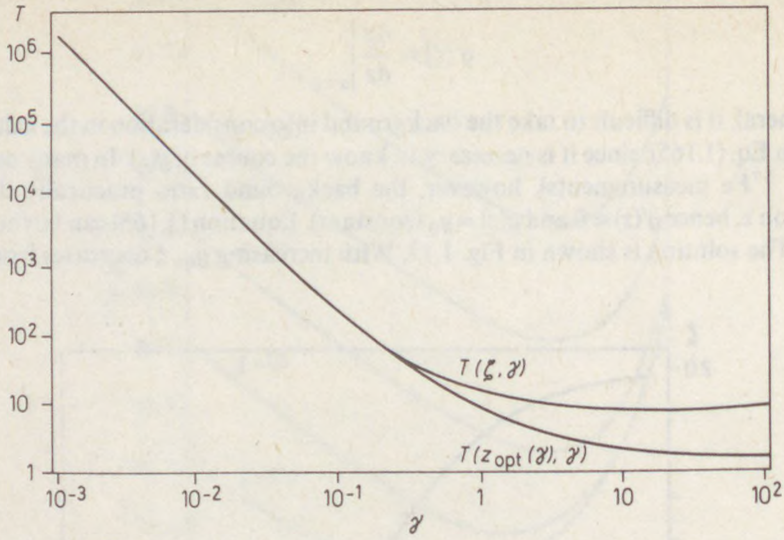

Fig. 1.14. Optimum time factor $T(z_{\mathrm{opt}}(\gamma),\gamma)$ and the approximate optimum time factor $T(\xi,\gamma)$ for the background-free case

ratio does not depend on the layer thickness and is greater than ca 50%. Then, $\xi \approx 1$ and, from Eq. (1.153):

$$t'_{\mathrm{opt}} = \frac{z_{\mathrm{opt}}}{\mu_{\mathrm{a}}} \approx \frac{\xi}{\mu_{\mathrm{a}}} \approx \frac{1}{\mu_{\mathrm{a}}} \tag{1.167}$$

1.8. EVALUATION OF MÖSSBAUER SPECTRA

1.8.1. SPECTRUM FITTING

The evaluation of a Mössbauer spectrum means the determination of physical parameters (e.g. isomer shift, quadrupole splitting, magnetic field strength, peak amplitudes and widths) from the spectrum. This makes no difficulty if the spectrum consists of a few clearly resolved lines. In such cases the parameters can be extracted directly from the spectrum although their correct determination can hardly be performed without computer programs.

More complex spectra can only be evaluated with computer algorithms. This can be done by fitting a function of certain parameters to the spectrum. The fitting is generally made by using the least squares method, i.e. by minimizing

$$\chi^2 = \sum_{i=1}^{G} \frac{1}{N_i} [N_i - \tilde{f}^i(b_1, b_2, \ldots, b_{p_b})]^2 \tag{1.168}$$

for the parameters $b_1, b_2, \ldots b_{p_b}$. Here N_i is the total number of counts in the i-th channel, $\tilde{f}^i(b_1, b_2, \ldots b_{p_b})$ is the value of the model function in the i-th channel and G is the total number of channels.

If the absorber is not too thick the spectrum is a sum of Lorentzians of negative amplitudes superimposed to a base line:

$$\tilde{f}^i = B - \sum_{j=1}^{p} \frac{\Gamma_j^2}{4} \frac{A_j}{(v_i-\delta_j)^2+\Gamma_j^2/4}. \qquad (1.169)$$

The way of evaluation, however, even in this case is not quite trivial. Since Lorentzians have rather long "tails", different peaks of a spectrum can rarely be fitted independently of each other. Simultaneous fitting of p peaks is an iteration process for $p_a = 3p+1$ parameters. This is equivalent to the calculation and inversion of a matrix of order p_a in each iteration step, if Newton's method [50] for minimizing χ^2 of Eq. (1.168) with $\tilde{f}^i$ of Eq. (1.169) is used. In most cases, however, only a few of these parameters are independent. The spectrum of an ideal ^{57}Fe magnetic sextett of a powder sample depends only on base line, amplitude, magnetic field, quadrupole splitting, isomer shift and linewidth i.e. on 6 parameters rather than on $3 \times 6 + 1 = 19$.

The number of independent parameters should be decreased in some other cases, too. With physical reasoning, especially in the case of spectra of poor statistics, some parameters should be fixed or should be chosen to be equal to some other parameters or some other constraints should be applied. A new constraint is equivalent to a new model function which should be used in Eq. (1.168) instead of $\tilde{f}^i$ defined by Eq. (1.169). The most straightforward way of minimizing χ^2 is to write a new program or at least a new subroutine for every new model function. This method was used at the early stage of Mössbauer spectroscopy. Later on it was realized [51] that a great deal of constraints can be handled with the same fitting program. In fact, the majority of constraints being applied during the evaluation of thin absorber spectra can be described as inhomogenous linear transformation of the parameters $B, A_j, \delta_j, \Gamma_j$ $(j = 1, 2, \ldots p)$. These "peak-parameters" are unified in a p_a-dimensional vector **a** while the independent physical parameters in a p_b-dimensional vector **b**. Of course, $p_b \leq p_a$.

The inhomogeneous linear transformation connecting **a** to **b** is:

$$a_j = \sum_{k=1}^{p_b} t_{jk} b_k + c_j, \qquad (1.170)$$

the matrix elements t_{jk} and the vector elements c_j being constants. Every constraint is described by matrix $\boldsymbol{t}$ and vector **c**. The model function can be expressed both in terms of **a** and **b**:

$$f^i(\mathbf{a}) = \tilde{f}^i(\mathbf{b}) \qquad (1.171)$$

The result of the evaluation should be vector **b**. During the numerical calculation one should use therefore $\tilde{f}^i(\mathbf{b})$ and $\partial\tilde{f}^i/\partial b_k$ since minimization procedures generally need the derivatives of the model function. Using Eq. (1.170) both $\tilde{f}^i(\mathbf{b})$ and $\partial\tilde{f}^i/\partial b_k$ can be expressed in terms of $f^i(\mathbf{a})$ and $\partial f^i/\partial a_j$:

$$\tilde{f}^i(\mathbf{b}) = f^i(\mathbf{a}) = f^i(\boldsymbol{t}\mathbf{b}+\mathbf{c}) \qquad (1.172)$$

and

$$\frac{\partial\tilde{f}^i}{\partial b_k} = \sum_{j=1}^{p_a} \left.\frac{\partial f^i}{\partial a_j}\right|_{\mathbf{a}=\boldsymbol{t}\mathbf{b}+\mathbf{c}} t_{jk}. \qquad (1.173)$$

The whole iteration procedure can be performed in the space of **b** by the use of Eqs (1.172) and (1.173). Since **b** contains the physical parameters, the above method directly yields their values, errors and covariance.

There are cases (e.g. thick absorber, electron spin relaxation with medium frequencies) when the model function cannot be given in the form of Eq. (1.169). In some other cases (e.g. combined hyperfine interaction, spectra measured in an applied magnetic field and described in terms of spin Hamiltonian or ligand field parameters) the peak-parameters cannot be given in the form of Eq. (1.170). Then, of course, the above method does not work. The only way of solving the problem is to return to the method of "one function–one program". Up-to-date computers enable us, however, to incorporate many model functions into one large program. In fact, a very versatile program developed by Müller [52] takes the advantages of both described methods by incorporating a lot of subroutines each describing a different theory and by using the method of transformation matrices for applying constraints.

Minimizing χ^2 one is often faced with the problem of poor convergency. The reason for such behaviour is that the minimum of χ^2 as a function of some parameters or of certain combination of some parameters is very "flat". There exist mathematical methods (e.g. [53]) which are convergent even in such "ill-conditioned" cases. At this point, however, a warning should be made. The application of such methods brings one rarely closer to the solution of the physical problem. The above situation means namely that the extraction of more information from the spectrum was attempted than it in fact contains. The solution of the problem is consequently not assuring artificially the convergency but (of course using additional information) decreasing the number of free parameters by applying some constraints.

1.8.2. EVALUATION OF FIELD DISTRIBUTIONS

Mössbauer spectra of non-crystalline solids often consist of broad non-Lorentzian lines. The reason for this fact is a distribution of the parameters of the hyperfine interactions as a result of the non-uniformity of the local environments. To fit such spectra one should construct a model function for the distribution of hyperfine interactions depending on a few parameters. The latter parameters should be adjusted so that the minimum of χ^2 is obtained. To construct a reliable distribution function with good physical arguments is, unfortunately, rather difficult.

Another approach of the evaluation of such spectra is the direct determination of the distribution function from the spectrum. If the problem is one-dimensional, e.g. if only the hyperfine magnetic field has a distribution, the distribution function, at least in principle, can be readily obtained. The probability of the absorption at velocity v for a thin absorber is

$$S(v) = \int_{-\infty}^{\infty} P_d(v') L_s(v - v')\, dv', \qquad (1.174)$$

$P_d(v)$ being the distribution function to be determined and $L_s(v)$ the shape of a spectral line without broadening. Equation (1.174) says that S is the convolution of P_d and L_s. Consequently, denoting the Fourier transforms of S, P_d and L_s by s, p_d and l_s, respectively:

$$s(k)=p_d(k)l_s(k), \tag{1.175}$$

the k frequency being the variable of the Fourier transformation. Now $P_d(v)$ can readily be obtained:

$$P_d(v)=\mathscr{F}^{-1}\frac{s(k)}{l_s(k)}=\mathscr{F}^{-1}\frac{\mathscr{F}\,S(v)}{\mathscr{F}\,L_s(v)} \tag{1.176}$$

$\mathscr{F}$ representing the Fourier transformation. If, e.g.

$$L_s(v)=\frac{\Gamma}{\pi}\frac{1}{v^2+\Gamma^2} \tag{1.177}$$

i.e. a zero-centred Lorentzian of 2Γ width then

$$l_s(k)=e^{-|k|\Gamma}. \tag{1.178}$$

In practice, the solution of integral equation (1.174) is not very easy. Unfortunately, the spectrum and consequently the absorption S can only be measured with a finite statistical error. A direct application of Eq. (1.176) would largely enhance the high frequency part of the error. To overcome this difficulty a filter function $d(k)$ is used. Before the inverse Fourier transformation $s(k)/l_s(k)$ is multiplied by $d(k)$. If $d(k)$ is low enough at high frequencies the statistical error is strongly damped. On the other hand, the multiplication by the filter function modifies the lineshape and leads in the case of a sharp cut-off frequency of the filter function to false (so-called Gibbs) oscillation of $P_d(v)$ [54]. Therefore the shape of $d(k)$ should be chosen with special care. The parameters of $d(k)$ should be determined so that the Gibbs oscillations do not overcome the error of $P_d(v)$. In Mössbauer spectroscopy the filter functions

$$d(k)=\exp(-k^2/2\sigma_d^2) \tag{1.179}$$

and

$$d(k)=\frac{1}{\exp[(k-k_0)\Gamma]+1} \tag{1.180}$$

have been applied with some success [29], [30].

Window's method [55] is closely related to the above Fourier technique. In this procedure the numerical Fourier transformation is replaced by fitting a finite trigonometric series to the spectrum with the least squares method. Another fitting process to determine $P_d(v)$ was suggested by Hesse and Rübartsch [56]. In their method the convolution integral of Eq. (1.174) is replaced by a sum and the values of $P_d(v)$ at discrete points are fitting parameters. This procedure gives thereby directly the distribution function at a finite number of points.

The distribution function of hyperfine interactions in non-crystalline (or just disordered) solids is mostly two-, three- or even more-dimensional. In fact, if an unbroadened spectrum $L_s(v,\delta,\varepsilon,H)$ depends only on the isomer shift δ, the quadrupole splitting ε as defined by Eq. (1.51) and on the magnetic field strengths H then Eq. (1.174) should be replaced by

$$S(v)=\int_0^{\infty}\int_{-\infty}^{\infty}\int_{-\infty}^{\infty} P_d(\delta,\varepsilon,H)L_s(v,\delta,\varepsilon,H)\,d\delta\,d\varepsilon\,dH\,. \tag{1.181}$$

Since $L_s(v, \delta, \varepsilon, H)$ is known the integral equation (1.181) can be, in principle, solved again. Unfortunately, the mathematical difficulties are now even much greater than before. Levitz et al. [57] succeeded in solving the two-dimensional problem by generalizing the method of Hesse and Rübartsch [56]. Their algorithm is very useful when paramagnetic glasses are concerned.

All these methods (Window [55], Hesse and Rübartsch [56], Levitz et al. [57]) are closely related to the Fourier technique. It is no wonder, therefore, that they are very sensitive to proper choice of their internal parameters like the number of terms in the trigonometric series in Window's procedure. If this is not properly done the obtained distribution functions may contain some false peaks similar to the Gibbs oscillations. The inadequate use of the procedures of Window [55] and of Hesse and Rübartsch [56] already led to many controversies particularly as concerning the hyperfine field distribution in ferromagnetic metallic glasses.

An idea of Vincze [58] may bring in some cases closer to the solution of integral Eq. (1.181). This author suggests to get more information regarding $P_d(\delta, \varepsilon, H)$ by measuring the spectra of ferromagnetic glasses at different angles relative to the direction of the magnetization. The samples in this case are magnetized to saturation with a small external magnetic field. By changing the angle of observation one changes the relative line intensities of $L_s(v, \delta, \varepsilon, H)$ but not their line positions. Particularly it is possible therefore to construct two linear combinations of two spectra measured at different angles so that the first contains only the 1st, 3rd, 4th and 6th lines while the second one the 2nd and 5th lines of the original spectra. If the procedure of Levitz et al. [57] is applied for the latter linear combination a two-dimensional projection of $P_d(\delta, \varepsilon, H)$, namely the simultaneous distribution of $\delta - \varepsilon$ and H is obtained.

REFERENCES

1. Mössbauer, R. L., *Z. Physik* **151,** 124 (1958); *Naturwissenschaften* **45,** 538 (1958); *Z. Naturforsch.* **14,** 211 (1958).
2. Pound, R. V. and Rebka, G. A., Jr., *Phys. Rev. Letters* **3,** 554 (1959).
3. Schiffer, J. P. and Marshall, W., *Phys. Rev. Letters* **3,** 556 (1959).
4. Pound, R. V. and Rebka, G. A., Jr., *Phys. Rev. Letters* **4,** 337 (1960).
5. Kistner, O. C. and Sunyar, A. W., *Phys. Rev. Letters* **4,** 412 (1960).
6. Kagan, Yu., *The Mössbauer Effect* (in Russian) Isd. Inostrannoi Literaturi, Moscow, 1962.
7. Frauenfelder, H., *The Mössbauer Effect*, W. A. Benjamin, Inc., New York, 1963.
8. Wertheim, G. K., *Mössbauer Effect, Principles and Applications*, Academic Press, New York, London, 1964.
9. Wegener, H., *Der Mössbauer-Effekt und seine Anwendung in Physik und Chemie*, Bibliographisches Institut AG., Mannheim, 1966.
10. Goldanskii, V. I. and Herber, R. H., *Chemical Applications of Mössbauer Spectroscopy*, Academic Press, New York, London, 1968.
11. Danon, J., *Lectures on the Mössbauer Effect*, Gordon and Breach, New York, London, Paris, 1968.
12. Shpinel, V. Sh., *Resonance of Gamma Rays in Crystals* (In Russian) Isd. Nauka, Moscow, 1969.
13. Greenwood, N. N. and Gibb, T. C., *Mössbauer Spectroscopy*, Chapman and Hall Ltd. London, 1971.
14. Vértes, A., Korecz, L. and Burger, K., *Mössbauer Spectroscopy*, Akadémiai Kiadó, Budapest, 1979.
15. Ramsey, N. F., *Nuclear Moments*, Wiley, New York, 1953.
16. Shirley, D. A., *Rev. Mod. Phys.* 36, 339 (1964).
17. Walker, L. R., Wertheim, G. K. and Jaccarino, V., *Phys. Rev. Letters*, **6,** 98 (1961).

18. Danon, J., *Applications of the Mössbauer Effect in Chemistry and Solid State Physics*, Int. Atomic Energy Agency, Vienna, 1966, p. 89.
19. Sternheimer, R. M., *Phys. Rev.* **84**, 244 (1951).
20. Ingalls, R., *Phys. Rev.* **133**, A787 (1964).
21. Zimmermann, R. and Spiering, H., *Phys. Stat. Sol.* (*b*). **67**, 487 (1975).
22. Fermi, E., *Z. Physik* **60**, 320 (1930).
23. Afanasev, A. M. and Kagan, Yu., *Zh. Eksp. Teor. Fiz.* **45**, 1660 (1963).
24. Blume, M., *Phys. Rev.* **174**, 351 (1968).
25. Wegener, H., *Z. Physik*, **186**, 498 (1965).
26. Afanasev, A. M. and Gorobchenko, V. D., *Zh. Eksp. Teor. Fiz.* **66**, 1406 (1974).
27. Wegener, H., *Proc. Int. Conf. Mössbauer Spectroscopy*, ed. Hrynkiewicz, A. Z. and Sawicki, J. A., Cracow, 1975, vol. 2, p. 257.
28. Margulies, S. and Ehrman, J. R., *Nucl. Instr. Methods* **12**, 131 (1967).
29. Ure, M. C. D. and Flinn, P. A., *Mössbauer Effect Methodology* (ed. by Gruverman, I. J.), Plenum Press, 1971, Vol. 7., p. 245.
30. Nagy, D. L. and Kulcsár, K., *Proc. Conf. Mössbauer Spectrometry* (Dresden, 1971), Physikalische Gesellschaft der DDR, Berlin, 1971, p. 618.
31. Housley, R. M., Gonser, U. and Grant, R. W., *Phys. Rev. Letters* **20**, 1279 (1968).
32. Zimmermann, R., *Chem. Phys. Letters* **34**, 416 (1975).
33. Zimmermann, R., *Nucl. Instr. Methods* **128**, 537 (1975).
34. Spiering, H., *Hyp. Interact.*, **3**, 213 (1977).
35. Goldanskii, V. I., Makarov, E. P. and Khrapov, V. V., *Phys. Letters* **3**, 344 (1963).
36. Goldanskii, V. I., Gorodinskii, G. M., Karyagin, S. V., Korytko, L. A., Krizhanskii, L. M., Makarov, E. F., Suzdalev, I. P. and Krapov, V. V., *Dokl. Akad. Nauk SSSR*, **147**, 127 (1962).
37. Frauenfelder, H., Nagle, D. E., Taylor, R. D., Cohran, D. R. F. and Visscher, W. M., *Phys. Rev.* **126**, 1065 (1962).
38. Kagan, Yu., *Dokl. Akad. Nauk SSSR*, **140**, 794 (1961).
39. Barrett, C. S., *Structure of Metals*, Mc Graw-Hill, New York, 1952.
40. Pfannes, H.-D. and Gonser, U., *Appl. Phys.* **1**, 93 (1973).
41. Pfannes, H.-D. and Gonser, U., *Proc. 5th Int. Conf. Mössbauer Spectroscopy* (Bratislava, 1973), ed. Hucl, M. and Zemcik, T., Czechosl. Atomic Energy Com., Praha, 1975, p. 596.
42. Singwi, K. S. and Sjölander, A., *Phys. Rev.* **120**, 1093 (1960).
43. Weisskopf, V. and Wigner, E., *Z. Physik* **63**, 54 (1930); *ibid* **65**, 18 (1930).
44. Van Hove, L., *Phys. Rev.* **95**, 249 (1954).
45. Shimony, U., *Nucl. Instr. Methods* **37**, 348 (1965).
46. Protop, C. and Nistor, C., *Rev. Roum. Phys.* **12**, 653 (1967).
47. Vértes, A., Fraknóy–Körös, V., Lévay, B., Gelencsér, P. A. and Ranogajec–Komor, M., *Acta Chim. Acad. Sci. Hung.*, **74**, 151 (1972).
48. Nagy, S., Lévay, B. and Vértes, A., *Magy. Kém. Folyóirat* **81**, 4 (1975).
49. Nagy, S., Lévay, B. and Vértes, A., *Acta Chim. Acad. Sci. Hung.*, **85**, 273 (1975).
50. Acton, F. S., *Numerical Methods that Work*, Harper and Row, Publishers, New York, Evanston and London, 1970.
51. Kulcsár, K., Nagy, D. L. and Pócs, L., *Proc. Conf. Mössbauer Spectrometry* (Dresden, 1971), Physikalische Gesellschaft der DDR, Berlin, 1971, p. 594.
52. Müller, E. F., *MOSFUN – Mössbauer Spectra Fitting Program for Universal Theories, Description and User's Guide*, Institut für Anorganische Chemie und Analytische Chemie, Johannes Gutenberg Universität, Mainz, 1980.
53. Marquardt, D. W., *J. Soc. Industr. Appl. Math.* **11**, 431 (1963).
54. Lanczos, C., *Applied Analysis*, Pitman, London, 1957, p. 217.
55. Window, B., *J. Phys. E.: Sci. Instrum.* **4**, 401 (1971).
56. Hesse, J. and Rübartsch, A., *J. Phys. E.: Sci. Instrum.* **7**, 526 (1974).
57. Levitz, P., Bonnin, D., Calas, G. and Legrand, A. P., *J. Phys. E.: Sci. Instrum.* **13**, 427 (1980).
58. Vincze, I., *Solid State Commun.* **25**, 689 (1978).

2. MÖSSBAUER SPECTRA RECORDED IN FROZEN SOLUTIONS

The first Mössbauer spectroscopic studies on frozen solutions were carried out in the early sixties [1–4]. Dézsi et al. [3, 4] attempted to employ Mössbauer atoms incorporated in the ice (as small detectors) to investigate the polymorphic transformation in the ice. During quenching and then slow heating the solutions that contained small amounts of iron(II) and iron(III) salts (ca 0.07 mol kg^{-1} in water) it was found that the Debye–Waller factor (f) of the Mössbauer effect strongly decreases at about -90 °C; on further heating f increases and the Mössbauer spectrum reappears. The new spectrum had other parameters. For example, in $Fe(NH_4)_2(SO_4)_2$ solution the quadrupole splitting decreases from 3.4 to 2.75 mm s^{-1}.

Dézsi and his co-workers [5] also studied the temperature dependence of the Mössbauer effect in frozen solutions of $SnCl_2$ and of $Dy(ClO_4)_3$. In these systems the effect totally disappeared at -90 °C, but further heating it did not lead to the reappearance of the Mössbauer lines.

These investigations found international interest. A number of research groups reproduced the experiments of Dézsi et al. and found that as noted somewhat humourously by Ruby and Pelah [6] frozen solutions of iron(II) salts were found to exhibit identical Mössbauer spectroscopic behaviour in New Haven as well as in Budapest.

The measurements on temperature dependence were repeated by Nozik and Kaplan [7] on $FeCl_2$ and $FeSO_4$ solutions, and by Dilorenzo and Kaplan [8] on $EuCl_3$ solutions. When the temperature of the quenched iron(II) salt solutions was increased from -196 °C until the Mössbauer lines disappeared, the sample was then thermostated at this temperature, the lines of the spectrum reappeared 1–3 h later; in contrast, with $EuCl_3$ solutions the probability of recoil-free nuclear resonance absorption (NRA) began to increase only after about 20 h. Concerning the effect of the rate of cooling on Mössbauer spectrum, it was found that re-heating of slowly cooled solutions did not affect the probability of NRA in the vicinity of about -90 °C.

Dilorenzo and Kaplan further investigated the effects of concentration and of (alien) cations (e.g. Sn^{4+} and Eu^{3+} in Fe^{2+} solutions) on the probability of NRA and on Mössbauer parameters [9]. From their results and earlier X-ray diffraction studies [10], Kaplan et al. came to the conclusion that in a quenched solution, ice with a cubic structure was formed; during keeping the temperature at about -90 °C this structure is transformed into the stable hexagonal polymorphic modification and the transitional decrease in the probability of NRA is caused by the crystal lattice disintegration that accompanies the polymorphic transformation [11], whereas later it became clear that independently of the rate of freezing, the structure of the crystalline ice is hexagonal (see the following section).

Pelah and Ruby [12] studied the temperature dependence of the NRA and the conductivity of a rapidly frozen 0.2 mol dm^{-3} solution of $SnCl_4$. They found that Debye–Waller factor began to decrease quickly at about −90 °C while at the same temperature the conductivity underwent a rapid increase. These two methods of measurement together indicated that at about −90 °C the mobility of the atoms in the ice increases.

The Mössbauer spectroscopic investigations on frozen solutions raised the assumption that the Mössbauer spectra of frozen solutions can provide information on the structures and chemical properties (coordination and bonding conditions) of "liquid" solutions prior to freezing, and on the chemical and electron-exchange reactions that occur in them [13–15].

In order to establish whether this assumption was correct, it was necessary to determine which properties of solutions remain unchanged or only slightly changed after quenching and the extent to which the resulting Mössbauer spectra are characteristic of the initial solution or of the ice.

2.1. EFFECT OF RAPID FREEZING ON THE CHEMICAL STRUCTURES OF SOLUTIONS

To get information on the extent to which Mössbauer spectra of rapidly frozen solutions reflect the chemical properties of the "liquid" solution, we can compare Mössbauer spectra of a series of frozen solutions in which characteristic differences were observed in some chemical property.

As an example, both the nature and the amount of coordination ions in iron(III) salt solutions are known to vary with the pH and with the anion. In the presence of the perchlorate anion, only $[Fe(H_2O)_6]^{3+}$ is present in solutions of $pH \leq 0$, whereas at increasing $pH > 0$ there is a continuous increase in the concentrations of $[Fe(OH)(H_2O)_5]^{2+}$, $[Fe(OH)_2(H_2O)_4]^{+}$ and $[Fe_2(OH)_2(H_2O)_8]^{4+}$ [16]. Mössbauer spectra of these frozen solutions strongly indicate chemical changes in the "liquid" solutions [17, 18].

If the Cl^- concentration in an aqueous 0.5 mol dm^{-3} $FeCl_2$ solution is increased by the addition of LiCl, then at a Cl^- concentration of 17 mol dm^{-3} in water the quadrupole splitting of Mössbauer spectrum will change from 3.25 to 2.45 mm s^{-1}. This indicates that at $Cl^- > 17$ mol dm^{-3} in water the Cl^- participates in the inner ligand sphere of the iron [15].

Several publications demonstrate that the coordination as well as chemical bonding conditions and the oxidation states in solutions are reflected in the Mössbauer spectra recorded after rapid freezing [19–21].

It should be mentioned that even in the event of rapid freezing, kinetically unstable equilibria may shift during cooling. In this case Mössbauer spectra for the frozen solution reflect the structure not of the initial solution.

Some publications studied the dependence of the structure of the ice and of Mössbauer spectra on the rate of freezing. Ruby et al. studied how the Mössbauer parameters of a frozen $SnCl_4$ solution of a concentration of 0.22 mol dm^{-3} depend on the freezing rate [22]. They found that above a value of $\sim 8\,K\,s^{-1}$ Mössbauer parameters are independent of the cooling rate, but below this threshold value the isomer shift increases progressively with the lengthening of the freezing time, and at a cooling rate of $\sim 10^{-3}\,K\,s^{-1}$ Mössbauer parameters corresponded to those of the crystal hydrate $SnCl_4 \cdot 5H_2O$. These results suggest that eutectic or crystal hydrate aggregates can be formed by slow cooling, whereas rapid freezing leads to solidification of the original or similar structure of the solution.

Dézsi et al. [23] reproduced the above experiments with $Fe(NH_4)_2(SO_4)_2$ solutions and they found that more components (eutectic and crystal hydrate) were formed in the ice on slow freezing (at 2 and 7 K min^{-1}).

Mørup et al. used aqueous solutions of $Fe(NO_3)_3$, HNO_3 and $NaNO_3$ of concentrations of 0.5, 2.0 and 3.0 mol dm^{-3}, respectively and found that the freezing rate higher than 570 K min^{-1} resulted a glassy state [24]. This result supports again that $\sim$8–10 K s^{-1} is the critical rate of freezing. To get further information on the mechanism of freezing, differential thermal analytical (DTA) examinations [23–27] were carried out on frozen solutions, as well. Measurements on iron salt solutions revealed that, in the event of heating after rapid freezing, the DTA curve first gave rise to one or more exotherm peaks indicative of crystallization, and then an endotherm one indicative of melting [23, 25, 26]. With slowly cooled solutions (when the crystallization processes may take place in the course of the cooling), there are no exotherm peaks on the DTA curve.

These experimental results demonstrate that in rapidly cooled aqueous solutions, a glass-like ice is formed in the environment of the ions; this ice preserves the structure (or quasi-structure) of the liquid. When it is heated, a supercooled liquid is produced, from which a eutectic, crystal hydrate, ice, etc., may next crystallize out. A typical DTA curve of the quenched aqueous solution of iron(II) perchlorate is given in Fig. 2.1 [27].

The crystallization of the amorphous (glass) phase on an increase in temperature in rapidly frozen iron(II) chloride solutions was studied by Brunot et al. [28, 29]. They

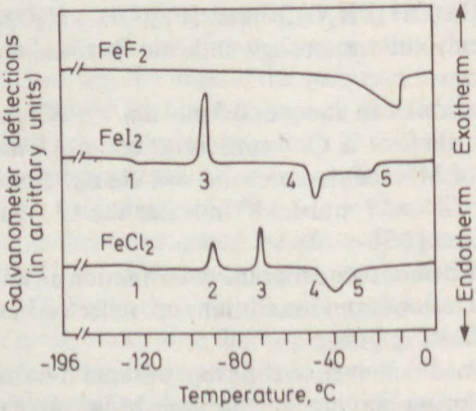

Fig. 2.1. Differential thermal analytical curves of various frozen aqueous solutions. Mole fractions: FeF_2 0.0328, $FeCl_2$ 0.0700, FeI_2 0.0700. The observed transitions: glass transition (1), crystallization of ice (2), crystallization of eutectic (3), melting of eutectic (4), melting of ice (5)

used Mössbauer effect, X-ray diffraction and differential scanning calorimetry. They found that in rapidly frozen solutions the Mössbauer atoms are surrounded by a glassy phase. Fröhlich and Keszthelyi [30] later demonstrated that the X-ray diffraction examinations reported by Brunot et al. [29] were not reproducible, as the change in intensity of the scattered photons is determined primarily not by the glass-crystalline phase transition, but by the parameters that characterize the random distribution of the surfaces of the phase spaces.

Simopoulos et al. [31] found that the rapid freezing of a solution of $FeCl_2$ in methanol resulted in a "solidified" solution structure. Thus, methanol also was found in a glass forming material.

The determination of the structures of frozen solutions can be further refined on the basis of neutron-diffraction and microscopic examinations [32, 33], which reveal that in a frozen system glass-like solidified solution layers and ice layers of hexagonal structure alternate. The amount of the glass-like phase increases in comparison with that of the crystalline ice with an increase in the cooling rate or the concentration of the solution. The structure of the ice is independent of the rate of freezing, however, in contrast to Nozik and Kaplan's finding [11] only ice of hexagonal structure could be detected in the quenched samples [32].

Cameron et al. [26] demonstrated that Mössbauer spectra recorded at various temperatures in iron(II) perchlorate solutions frozen at high pressure do not differ from

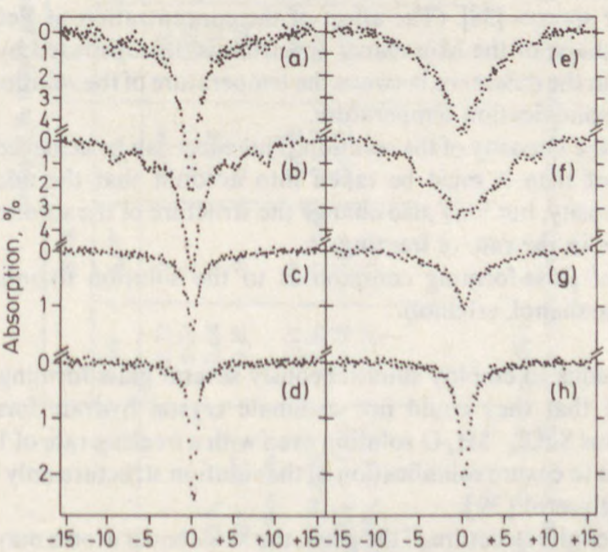

Fig. 2.2. Mössbauer spectra of frozen aqueous solutions of $FeCl_3$ at 80 K. Mole ratio: (a), (e) = 0.045; (b), (f) = 0.035; (c), (g) = 0.05; (d), (h) = 0.05 but these spectra were recorded after exposure at 200 K for 1 h. (a), (b), (c) and (d) were obtained in applied field at a strength of 5 mT and for (e), (f), (g) and (h) 1.24 T [24] was used. Spectra (b) and (f) showed the longest time of the paramagnetic spin relaxation demonstrating the glass formation. At a higher concentration [(a) and (e)] the stronger spin-spin interaction decreased again the time of spin-relaxation

the spectra of solutions frozen at 10^5 Pa, even though freezing at high pressure results in a cubic ice structure. Consequently, the structure of the ice does not affect the Mössbauer parameters of the frozen solution, as the immediate environment of the Mössbauer atoms involves not crystalline, but glass-like ice.

Fröhlich and Keszthelyi used DTA to determine quantitatively how many water molecules surround an iron(II) ion in the amorphous phase in rapidly frozen solutions [34]. They found that each iron(II) ion is associated with 15–18 molecules of water. It must be pointed out that the freezing may result in some segregation of the Mössbauer atoms. This process can be detected by means of paramagnetic spin relaxation in solutions that contain iron(III) ion, as an increasingly closer approach of the iron(III) ions increases the spin-spin interaction and the frequency of spin relaxation, which results in the disappearance of the magnetic hyperfine structure [35]. The segregation can be effectively inhibited by the use of additives, such as glycerol, probably as a consequence of a decrease in the diffusion coefficient of the iron(III) ion [36].

For 0.67 mol dm^{-3} aqueous $Fe(No_3)_3$ solutions (pH = 1.2), Du Fresne et al. found that both the increase in the rate of freezing and the addition of ethanol to the solution resulted in a decrease of the segregation [37].

The most important factors that promote glass formation are as follows:

(*a*) An increase in the concentration of the solute up to the eutectic composition. At this concentration the probability of glass formation has a maximum. This effect has been utilized, for example, to determine the phase diagrams of two-component systems from Mössbauer spectra [38]. (The effect of the concentration of $FeCl_3$ in aqueous solution on the shape of the Mössbauer spectrum is demonstrated by Fig. 2.2 [24].)

(*b*) A decrease in the difference between the temperature of the solution prior to rapid freezing and its solidification temperature.

(*c*) Increase in the viscosity of the solution. This effect can be achieved with additives (e.g. glycerol), but then it must be taken into account that the additive not only increases the viscosity, but may also change the structure of the solution under study.

(*d*) An increase in the rate of freezing.

(*e*) Addition of glass-forming compounds to the solution to inhibit ice crystal formation (e.g. methanol, ethanol).

It is advantageous to employ simultaneously several glass forming effects. Cohen and West found that they could not eliminate crystal hydrate formation in 0.22 mol dm^{-3} aqueous $SnCl_4 \cdot 5H_2O$ solution even with a freezing rate of 1000 K s^{-1}, and it proved possible to ensure solidification of the solution structure only by the addition of methanol or glycerol [39].

Due to the indefinite structure of the glass, the Mössbauer atoms may be present in a number of different positions in frozen solutions [40].

Table 2.1.
Mössbauer parameters of the studied systems

Sample	Trapped in thirsty glass						Frozen solution			Crystalline	
	293 K			80 K			80 K			293 K	
	$\delta^{(a)}$	$\Delta E^{(b)}$	$I^{(c)}$	$\delta^{(a)}$	$\Delta E^{(b)}$	$I^{(c)}$	$\delta^{(a)}$	$\Delta E^{(b)}$	$I^{(c)}$	$\delta^{(a)}$	$\Delta E^{(b)}$
$SnCl_4$	0.72	0	0.029	0.82	0	0.15	0.80	0	0.297		
	−0.20	0	0.023	−0.02	0	0.11					
0.01 mol dm^{-3} SnI_4 in CCl_4	−0.04	0	0.011	0.13	0	0.138	1.60	0	0.087		
0.01 mol dm^{-3} SnI_4 in dmf + CCl_4	−0.10	0	0.015	0.00	0	0.149	0.76	0	0.063		
0.01 mol dm^{-3} SnI_4 in 1 mol dm^{-3} $C_2H_5OH + CCl_4$	−0.11	0	0.036	0.02	0	0.251					
50 − 50 w.-% Fe $(CO)_5 + CH_3OH$	0.35	0.79	0.003	0.47	0.84	0.01	−0.08	2.52			
0.01 mol dm^{-3} $[Fe(bpy)_3]Cl_2$ in H_2O	0.30	0.30	0.002	0.35	0.33	0.021	0.35	0.34	0.022		
0.5 mol dm^{-3} $[Fe(H_2O)_6]SO_4$ in H_2O	1.25	3.17					1.35	3.28			
$[Fe(bpy)_3]Cl_2$ crystalline										0.28	0.31
$FeSO_4 \cdot 7H_2O$ crystalline$^{(d)}$										1.25	3.20
$FeSO_4 \cdot H_2O$ crystalline										1.23	2.70
$FeSO_4$										1.31	2.94

dmf = dimethylformamide, bpy = 2,2′-bipyridine

(*a*) Isomer shift referred to SnO_2 and α-iron, respectively, reproducibility ±0.01 mm s^{-1}

(*b*) Quadrupole splitting

(*c*) Integral intensity

(*d*) In this compound the Fe^{2+} has the same hexaaqua ligand sphere as in solution. The components with 0.01 mol dm^{-3} concentrations were prepared from enriched ^{119}Sn and ^{57}Fe, respectively

2.2. MÖSSBAUER SPECTROSCOPY OF LIQUIDS TRAPPED IN THE PORES OF THIRSTY GLASS

CAPILLARY MÖSSBAUER SPECTROSCOPY (CMS)

The preceding section showed that Mössbauer spectroscopy can be used for the study of the chemical properties of solutions and liquids and for the investigation of chemical reactions occurring in the liquid phase if the studied system was quenched to a frozen state before recording of the Mössbauer spectrum. Nevertheless Mössbauer spectra of liquids can be recorded at room temperature if the molecules of liquids are trapped in the cavities of a special porous silicate glass of a mean pore diameter of 4 nm [41–43].

The used "Corning–Vycor 2930" type thirsty glass has about 28% void space of their total volume [44].

Liquids containing Mössbauer active elements can be divided into three groups on the basis of their Mössbauer parameters recorded in the thirsty glass carrier at room temperature (see Table 2.1).

(*a*) Mössbauer parameters for the quenched (frozen) solutions or liquids are similar to those measured for the solutions of liquids trapped in the porous glass. The differences between the Mössbauer parameters achieved at the temperature of liquid nitrogen and at room temperature in the glass carrier are mostly due to the second order Doppler shift that is to the normal temperature dependence. Such kinds of systems are the aqueous solutions of Mössbauer active salts.

(*b*) Mössbauer parameters measured in the frozen state and in the carrier at room temperature are considerably different, e.g. SnI_4 dissolved in carbon tetrachloride or pentacarbonyl iron a liquid itself (see Table 2.1).

(*c*) Mössbauer spectra recorded in the porous glass consist of two components. One of these is identical or very similar to that measured in a quenched (frozen) solution or liquid the other one differs from it. Such kind of a system is $SnCl_4$ (see Fig. 2.3).

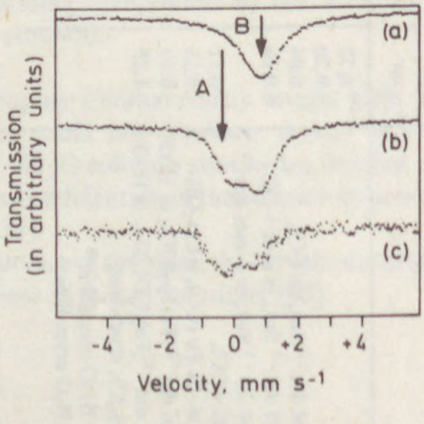

Fig. 2.3. Mössbauer spectra of $SnCl_4$ samples; (a) frozen and measured at 80 K, (b) trapped in the pores of thirsty glass, measured at 80 K, (c) trapped in the pores of thirsty glass, measured at room temperature. Arrow A stands for $SnCl_4$ on the surface of the thirsty glass and B stands for the bulk $SnCl_4$

On the basis of the experimental data in systems characteristic of group (*a*) only the solvent molecules (e.g. water) can be supposed to be in chemical interaction with the wall of the capillaries in the glass and the Mössbauer active species (e.g. Fe^{II}) have the same near surroundings (first coordination sphere) they have in normal liquid state [see Fig. 2.4(a)].

In systems characteristic of the group (*b*) all Mössbauer active atoms trapped in the carrier are in direct chemical interaction with the wall of its cavities (e.g. SnI_4, see Fig. 2.4(b)].

In systems characteristic of group (*c*) only one part of Mössbauer active molecules is in direct chemical interaction with the wall of the pores in the carrier, the remaining part shows Mössbauer parameters characteristic of the free species. This situation is realized, e.g. when the liquid, trapped in the pores, consists of only the Mössbauer active molecules [e.g. $SnCl_4$, see Fig. 2.4(c)].

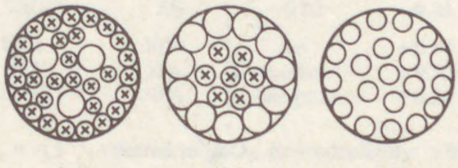

Fig. 2.4. Typical positions of Mössbauer active molecules in the cavities: ○ represents the Mössbauer active ions or molecules (e.g. $[^{57}Fe^{II}(bpy)_3]^{2+}$, $^{119}SnI_4$, $^{119}SnCl_4$, etc.) and X represents the solvent molecules (H_2O, CCl, etc.)

The recoilless gamma-resonance absorption can take place in the Mössbauer active molecules absorbed directly on the wall of the cavities in the glass carrier due to the interaction between the silicate oxygen of the wall and the absorbed species.

On the other hand, in the molecules located in the second or third layers to the capillary wall the Debye–Waller factor will depend on the direction of the recoil. (It should be mentioned that there is space only for the formation of a few layers of molecules between the walls of the cavities of the porous glasses.)

It is interesting to mention that the relative intensity of the line A in Fig. 2.3 is higher at room temperature due to the effect of the direct interaction between the inner surface of the thirsty glass and the $SnCl_4$ molecules. On the other hand the Debye–Waller factor of the bulk $SnCl_4$ molecules decreases considerably when the temperature increases from nitrogen to room temperature.

A relatively high Debye–Waller factor was recorded for $Na_2Sn(OH)_6$ aqueous solution in thirsty glass carrier at room temperature [45]. $[Sn(OH)_6]^{2-}$ ions are known to have H-bonded cluster structure in aqueous solution. Consequently, it can be supposed that hydrogen bonding increases the Debye–Waller factor of the solute in the thirsty glass.

Hydrogen bondings can exist also between the oxygen atoms of the silicate surface of the thirsty glass and the molecules of the solute. This bond can also promote Mössbauer effect in the thirsty glass. The Mössbauer spectra of $Na_2Sn(OH)_6$ are given in Fig. 2.5. The spectra show that the effect of the wall of the glass did not result in a new

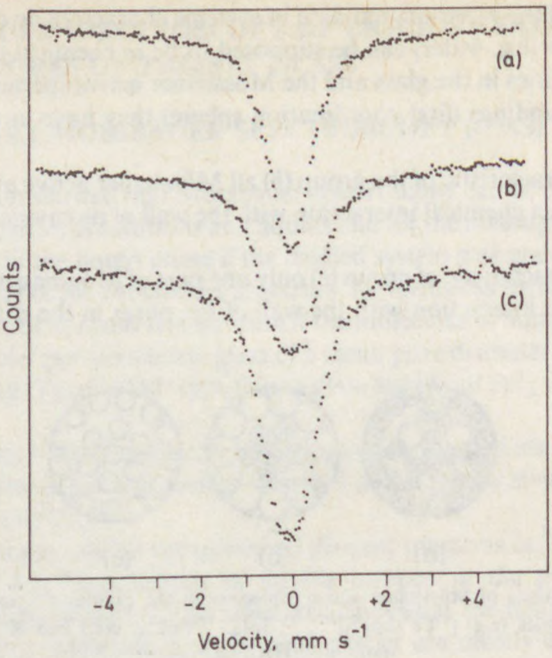

Fig. 2.5. Mössbauer spectra of the aqueous solution of 1 mol dm^{-3} $Na_2Sn(OH)_6$: (a) frozen solution measured at 80 K. Isomer shift (IS) = -0.017 mm s^{-1} (relative to SnO_2) and half width (Γ) = 1.04 mm s^{-1}, (b) solution trapped in thirsty glass measured at 80 K. IS = -0.005 mm s^{-1}, Γ = 1.56 mm s^{-1}, (c) solution trapped in thirsty glass measured at room temperature. IS = -0.05, Γ = 1.4 mm s^{-1}

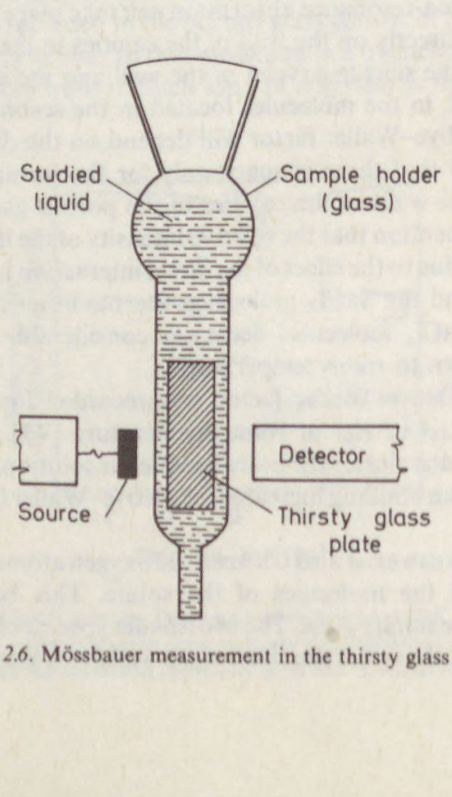

Fig. 2.6. Mössbauer measurement in the thirsty glass

Table 2.2.
Mössbauer parameters of aqueous $SnCl_4$ solutions

Composition			Trapped in thirsty glass		Frozen solution
$SnCl_4$ mol dm^{-3}	Reagent	mol dm^{-3}	293 K	80 K	80 K
			IS*	IS*	IS*
1.0	–	–	−0.13	+0.09	+0.16
3.0	–	–	−0.02	+0.20	+0.24
1.0	NaCl	4.0	+0.02	+0.22	+0.32
1.0	LiCl	10.0	+0.01	+0.23	+0.30
1.0	NaOH	0.1	−0.09	+0.11	+0.15
1.0	NaOH	3.0	−0.02	+0.04	+0.06
1.0	HCl	30%	no	+0.49	+0.43
3.0	HCl	30%	recoilless	+0.50	+0.49
1.0	HNO_3	30%	absorption	+0.26	+0.29

* IS: isomer shift, mm s^{-1}, referred to SnO_2. Reproducibility: ±0.02 mm s^{-1}

line and only a line broadening was detected in the thirsty glass. An indirect evidence of the role of the hydrogen bonding was achieved also by the destruction of this bondings by HCl or HNO_3 addition to the aqueous solution of $SnCl_4$. As it is demonstrated in Table 2.2., the Debye–Waller factor became practically zero in the thirsty glass at room temperature when acid was added to the solution.

The Mössbauer measurement in the thirsty glass is demonstrated in Fig. 2.6.

REFERENCES

1. Kerler, W., Neuwirt, W., Fluck, E., Kuhn, P. and Zimmermann, B., *Z. Physik*, **173**, 321 (1962).
2. Hazony, Y. and Bukshpan, S., *Rev. Mod. Phys.*, **36**, 360 (1964).
3. Dézsi, I., Keszthelyi, L., Molnár, B. and Pócs, L., *Phys. Lett.*, **18**, 28 (1965); *KFKI Közlemények*, **9**, 1967.
4. Dézsi, I., Keszthelyi, L., Pócs, L. and Korecz, L., *Phys. Lett.*, **14**, 14 (1965).
5. Dézsi, I., Eissa, N. A., Keszthelyi, L., Molnár, B. and Nagy, D. L., *Phys. Stat. Sol.*, **30**, 215 (1968).
6. Ruby, S. L. and Pelah, I., *Crystals, Supercooled Liquids and Glasses in Frozen Aqueous Solutions. Mössbauer Effect Methodology*, ed. Gruverman, I. J. **6**, 21 (1971).
7. Nozik, A. I. and Kaplan, M., *J. Chem. Phys.* **47**, 2960 (1967).
8. Dilorenzo, I. V. and Kaplan, M., *Chem. Phys. Lett.* **2**, 509 (1968)
9. Dilorenzo, I. V. and Kaplan, M., *Chem. Phys. Lett.* **3**, 216 (1969).
10. Weltman, H. I., Report No. AD 423175. Defense Documentation Center for Scientific and Technical Information, Camerion Station, Va., 1963.
11. Nozik, A. I. and Kaplan, M., *Chem. Phys. Lett.*, **1**, 391 (1967).
12. Pelah, I. and Ruby, S. L., *J. Chem. Phys.*, **51**, 383 (1969).
13. Goldanskii, V. I., Okhlobystin, O. Yu., Rochev, V. Ya. and Khrapov, V. V., *J. Organometal. Chem.*, **4**, 160 (1965).
14. Schnorr, H. and Kriegsmann, H., *Proc. Conf. Appl. Mössbauer Effect, Tihany* (Hungary), 1969. Akadémiai Kiadó, Budapest, 1971, p. 629; Proc. Conf. Mössbauer Spectroscopy. Dresden, 1971, p. 474.
15. Vértes, A., *Acta Chim. Acad. Sci. Hung.*, **63**, 9 (1970)
16. Mulay, L. N. and Selwood, P. W., *J. Am. Chem. Soc.*, **77**, 2693 (1955).

17. Dézsi, I., Vértes, A. and Komor, M., *Inorg. Nucl. Chem. Lett.* **4,** 649 (1968).

18. Vértes, A., Suba, M. and Komor, M., *Radiochem. Radioanal. Lett.*, **3,** 365 (1970).

19. Vértes, A., Burger, K. and Dézsi, I., *Fifth Hungarian Complex Chemistry Colloquium*, Siófok, 1969.

20. Burger, K. and Vértes, A., *Proc. Second Conf. Coord. Chem.* Bratislava 1–5 December, 1969, p. 39.

21. Vértes, A., *Chemical Society Meeting, Southampton*, 23–25 September, 1969.

22. Ruby, S. L., Tseng, P. K. and Iluva-Sheng Cheng, Li, N. C., *Chem. Phys. Lett.* **2,** 39 (1968).

23. Dézsi, I., Keszthelyi, L., Nagy, D. L., *Proc. Conf. Appl. Mössbauer Effect, Tihany* (Hungary), 1969. Akadémiai Kiadó, Budapest, 1971, p. 607.

24. Mørup, S., Knudsen, J. E., Nielsen, M. K. and Trumpy, G., *J. Chem. Phys.*, **65,** 536 (1976).

25. Nagy, G. and Dézsi, I., *J. Thermal Analysis*, **2,** 159 (1970).

26. Cameron, I. A., Keszthelyi, I., Nagy, G., Kacsóh, L., *J. Chem. Phys.*, **58,** 4610 (1973).

27. Dézsi, I., Szűcs, I. and Molnár, B., *Second Seeheim Workshop on Mössbauer Spectroscopy*, May, 23–26, 1983, p. 16.

28. Brunot, B., Hauser, U., Neuwirth, W. and Bolz, J., *Z. Physik*, **249,** 125 (1971).

29. Brunot, B., Hauser, U. and Neuwirth, W., *Z. Physik*, **249,** 134 (1971).

30. Fröhlich, K. and Keszthelyi, L., *Z. Physik*, **259,** 301 (1973).

31. Simopoulos, A., Wickman, H., Kostikas, A. and Petridis, D., *Chem. Phys. Lett.*, **7,** 615 (1970).

32. Arnold, G. P., Finch, E. D., Rabidean, S. W. and Wenzel, R. G., *J. Chem. Phys.*, **49,** 4365 (1968).

33. Rohatgi, P. K., Jain, S. M. and Adamx, C. M., *Ind. Eng. Chem. Fundamentals*, **7,** 72 (1968).

34. Fröhlich, K. and Keszthelyi, L., *J. Chem. Phys.*, **58,** 4614 (1973).

35. Vértes, A. and Parak, F., *J. Chem. Soc. Dalton Trans.*, 2062 (1972).

36. Bibicu, I., Dézsi, I., Lohner, T. and Nagy, D. L., *Proc. 5th Int. Conf. Mössbauer Spectrometry*. Bratislava, Czechoslovakia, 1973, p. 247.

37. Du Fresne, A., Knudsen, J. M., Moreira, J. E. and Skeff-Neto, K., *Chem. Phys. Lett.*, **20,** 108 (1973).

38. Plaatchinda, A. S. and Makarov, E. F., *Chem. Phys. Lett.*, **25,** 364 (1974).

39. Cohen, R. L. and West, K. W., *Chem. Phys. Lett.*, **13,** 482 (1972).

40. Ruby, S. L., *Proc. Int. Conf. Appl. Mössbauer Effect*, Ayeleth Hashahar, Israel, 28–31 August 1972.

41. Burger, K., Vértes, A. and Zay, I., *Inorganica Chimica Acta*, **76,** L247 (1983).

42. Burger, K. and Vértes, A., *Nature*, **306,** 353 (1983).

43. Vértes, A., Burger, K., Takács, L. and Horváth, I., *J. Radional. Nucl. Chem. Letters*, **86,** 195 (1984).

44. Espe, W., *Materials of High Vacuum Technology*, Pergamon, Oxford, 1968. p. 414.

45. Burger, K., Nemes-Vetéssy, Zs., Vértes, A., Suba, M., Krausz, D.: Inorganica Chimica Acta, **148,** 223 (1988).

3. RELAXATION PHENOMENA IN FROZEN SOLUTIONS

3.1. INTRODUCTION

As discussed in Chapter 1, the interaction between the electronic and nuclear magnetic moments of a paramagnetic ion gives rise to a magnetic hyperfine interaction. This magnetic hyperfine interaction can often be described in terms of an effective magnetic field at the nucleus. In paramagnetic materials, however, the magnitude and the direction of this magnetic hyperfine field are not fixed, but fluctuate because of paramagnetic relaxation processes.

Mössbauer spectra of paramagnetic materials are very sensitive to paramagnetic relaxation when the relaxation time is of the order of 10^{-10}–10^{-7} s.

Two types of electronic relaxation processes contribute to the relaxation in paramagnetic compounds, namely spin-lattice relaxation processes and spin-spin relaxation processes. Spin-lattice relaxation originates from the interaction between phonons and the paramagnetic ions. Since the population of the phonon states depends on temperature, the spin-lattice relaxation time also depends on temperature. Spin-spin relaxation arises from the magnetic interaction among the paramagnetic ions. The spin-spin relaxation time therefore decreases with increasing concentration of magnetic ions, but it is essentially independent of the temperature.

In many iron-containing crystalline compounds the paramagnetic relaxation time is shorter than 10^{-10}s because of fast spin-spin relaxation. Moreover, in iron(II) compounds, the spin-lattice relaxation is also normally very fast, even at low temperatures. However, in materials with a low concentration of iron(III) ions the relaxation time may be of the order of magnitude that can be studied by Mössbauer spectroscopy. Therefore, relaxation effects can be observed in Mössbauer studies of frozen solutions with a sufficiently low concentration of Fe^{3+} ions. The use of Mössbauer spectroscopy for studies of relaxation phenomena has recently been reviewed [1, 2].

This chapter deals with paramagnetic relaxation phenomena in frozen solutions. In Section 3.2 we discuss the spin Hamiltonian of Fe^{3+} ions and the electronic eigenstates among which the relaxation takes place.

In very dilute systems the relaxation time may be so long that paramagnetic hyperfine split Mössbauer spectra can be obtained at low temperatures. The information that can be obtained from this type of Mössbauer spectra is the subject of Section 3.3.

Section 3.4. deals with the theories for Mössbauer relaxation spectra. In Section 3.5 and 3.6 Mössbauer studies of spin-spin and spin-lattice relaxation in frozen solutions are reviewed. Dimeric, trimeric and polymeric coordination entities are characterized by a strong exchange coupling among the magnetic ions. The relaxation of such coordination entities is the subject of Section 3.7. Finally, in Section 3.8 it is discussed how crystallization and glass formation during cooling of solutions can be elucidated by studies of spin-spin relaxation.

Since almost all Mössbauer studies of relaxation effects in frozen solutions have been made with Fe^{3+}, in this chapter only iron(III) coordination entities will be discussed.

3.2. THE SPIN HAMILTONIAN OF Fe^{3+} IONS

The total spin Hamiltonian $\hat{H}$ of a Fe^{3+} ion in the high-spin state $\left(S=\frac{5}{2}\right)$ can be written as a sum of the electronic Zeeman interaction, $\hat{H}_Z$, the crystal field interaction $\hat{H}_{cf}$, the magnetic dipole-dipole interaction $\hat{H}_{dd}$ and the exchange interaction $\hat{H}_{ex}$ with the neighbouring ions, and the hyperfine interaction, $\hat{H}_h$ [3, 4]. In the following the influence of the various terms on the electronic eigenstates will be discussed.

3.2.1. THE CRYSTAL FIELD INTERACTION

A Fe^{3+} ion in its ^6S ground state ($S=\frac{5}{2}$, $L=0$) has a spherically symmetric distribution of electronic charge. Therefore, even when the ion is found in non-cubic surroundings, the electric interactions with the neighbouring ions, i.e. the crystal field interaction is relatively small and the splitting of the ^6S ground state does normally not exceed 10 cm^{-1}.

The crystal field spin Hamiltonian $\hat{H}_{cf}$ can be expressed as a sum of an axial term, $\hat{H}_{ax}$, a rhombohedral term, $\hat{H}_{rh}$ and a cubic term, $\hat{H}_{cub}$ [1, 3, 4]:

$$\hat{H}_{cf}=\hat{H}_{ax}+\hat{H}_{rh}+\hat{H}_{cub} \tag{3.1}$$

where

$$\hat{H}_{ax}=D\left\{\hat{S}_{z'}^2-\frac{1}{3}S(S+1)\right\} \tag{3.2}$$

$$\hat{H}_{rh}=E(\hat{S}_{x'}^2-\hat{S}_{y'}^2) \tag{3.3}$$

$$\hat{H}_{cub}=\frac{1}{6}a\left\{\hat{S}_\xi^4+\hat{S}_\eta^4+\hat{S}_\zeta^4-\frac{1}{5}S(S+1)(3S^2+3S-1)\right\}. \tag{3.4}$$

The fourth order axial term is in most cases negligible, and it is therefore omitted in the present discussion.

Conventionally, the principal axes of the crystal field interaction, x', y', z' are chosen so that $E<D$. It is convenient to define:

$$\lambda=\frac{E}{D}, \quad \mu=\frac{a}{D}. \tag{3.5}$$

Furthermore, we define the parameter Δ_{cf} as the total energy splitting due to $\hat{H}_{cf}$. Generally, $\hat{H}_{ax}$ is the dominating term of $\hat{H}_{cf}$ and D is normally of the order of 0.01–1.0

cm^{-1} in Fe^{3+} coordination entities. The Hamiltonian $\hat{H}_{cf}$ gives rise to a splitting of the electronic ground state into three Kramers doublets.

3.2.2. ELECTRONIC ZEEMAN INTERACTION

The Hamiltonian describing the Zeeman interaction of the electronic spin with an external magnetic field **H** is given by:

$$\hat{H}_Z = g\mu_B \mathbf{H} \cdot \mathbf{S} \tag{3.6}$$

where μ_B is the Bohr magneton and g is close to the free electron value (2.0023). It is convenient to introduce:

$$\Delta_Z = 2g\mu_B HS \tag{3.7}$$

which is the total Zeeman splitting for $\Delta_{cf} = 0$.

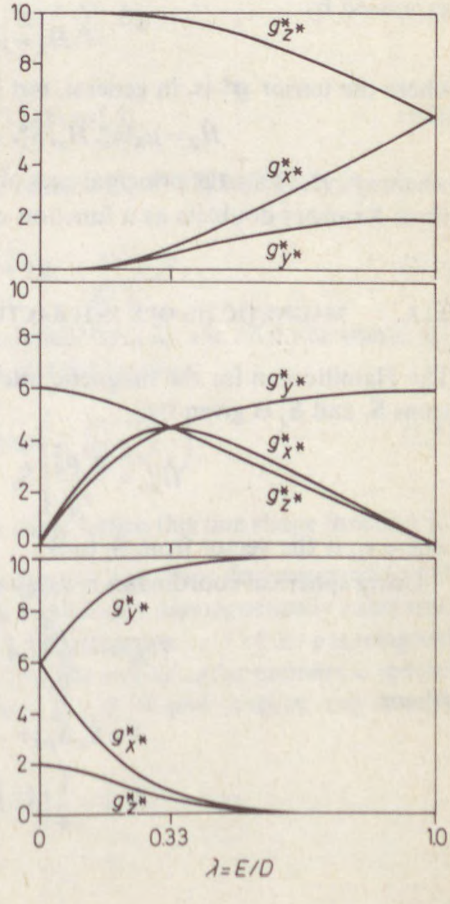

Fig. 3.1. The values of $g_{x^*}^*$, $g_{y^*}^*$ and $g_{z^*}^*$ for the three Kramers doublets of a Fe^{3+} ion as a function of $\lambda = E/D$. It is assumed that the cubic splitting parameter a is negligible [1]

When $\Delta_Z \gg \Delta_{cf}$, the electronic eigenstates are (to a good approximation) the eigenstates of $\hat{S}_z$, the z direction being defined by the applied field **H**. When the crystal field interaction has the simple form $\hat{H}_{cf} = \hat{H}_{ax} = D\left\{\hat{S}_{z'}^2 - \frac{1}{3}S(S+1)\right\}$ and $\Delta_Z \gg \Delta_{cf}$, the eigenvalues of $\hat{H}_{cf} + \hat{H}_Z$ can easily be calculated by use of first order perturbation theory which gives [5]:

$$E_M = g\mu_B HM + D\left(\frac{3\cos^2\theta - 1}{2}\right)\left\{M^2 - \frac{1}{3}S(S+1)\right\} \tag{3.8}$$

where M is an eigenvalue of $\hat{S}_z$ and θ is the angle between the z' direction, defined as the symmetry axis of the crystal field interaction, and the z direction, defined by the applied magnetic field.

If $\Delta_Z \lesssim \Delta_{cf}$, calculation of the energy levels and the eigenstates will be more complicated. Even for $\Delta_Z \ll \Delta_{cf}$, an external field has a decisive influence on the eigenstates, because it lifts the degeneracy of the Kramer's doublets. In this case, it is convenient to consider each Kramer's doublet separately. Often, a fictitious spin operator $\hat{\mathbf{S}}^*\left(S^* = \frac{1}{2}\right)$ is introduced for each doublet. The Zeeman interaction is then expressed by:

$$\hat{H}_Z = \mu_B \mathbf{H} \cdot \boldsymbol{g}^* \cdot \hat{\mathbf{S}}^* \tag{3.9}$$

where the tensor $\boldsymbol{g}^*$ is, in general, not isotropic. Equation (3.9) can also be written:

$$\hat{H}_Z = \mu_B(g^*_{x^*} H_{x^*} \hat{S}^*_{x^*} + g^*_{y^*} H_{y^*} \hat{S}^*_{y^*} + g^*_{z^*} H_{z^*} \hat{S}^*_{z^*}), \tag{3.10}$$

where x^*, y^*, z^* are the principal axes of the tensor $\boldsymbol{g}^*$. The values of $g^*_{x^*}$, $g^*_{y^*}$, $g^*_{z^*}$ for the three Kramers doublets as a function of $\lambda = E/D$ are shown in Fig. 3.1.

3.2.3. MAGNETIC DIPOLE INTERACTION

The Hamiltonian for the magnetic interaction between two paramagnetic ions with spins $\mathbf{S}_i$ and $\mathbf{S}_j$ is given by:

$$\hat{H}^{ij}_{dd} = \frac{g^2\mu_B^2}{r_{ij}^3}\left[\hat{\mathbf{S}}_i \cdot \hat{\mathbf{S}}_j - \frac{3(\mathbf{r}_{ij}\cdot\hat{\mathbf{S}}_i)(\mathbf{r}_{ij}\cdot\hat{\mathbf{S}}_j)}{r_{ij}^2}\right] \tag{3.11}$$

where $\mathbf{r}_{ij}$ is the vector from $\mathbf{S}_i$ to $\mathbf{S}_j$.

Using spherical coordinates r, θ, ϕ, we may write the Hamiltonian in the form [4]:

$$\hat{H}^{ij}_{dd} = \frac{g^2\mu_B^2}{r_{ij}^3}[\hat{A} + \hat{B} + \hat{C} + \hat{D} + \hat{E} + \hat{F}] \tag{3.12}$$

where

$$\hat{A} = \hat{S}_{iz}\hat{S}_{jz}(1 - 3\cos^2\theta), \tag{3.13}$$

$$\hat{B} = -\frac{1}{4}[\hat{S}_i^+\hat{S}_j^- + \hat{S}_i^-\hat{S}_j^+](1 - 3\cos^2\theta), \tag{3.14}$$

$$\hat{C} = -\frac{3}{2}[\hat{S}_i^+ \hat{S}_{jz} + \hat{S}_{iz}\hat{S}_j^+] \sin\theta \cos\theta \, e^{-i\phi}, \tag{3.15}$$

$$\hat{D} = -\frac{3}{2}[\hat{S}_i^- \hat{S}_{jz} + \hat{S}_{iz}\hat{S}_j^-] \sin\theta \cos\theta \, e^{i\phi}, \tag{3.16}$$

$$\hat{E} = -\frac{3}{4}\hat{S}_i^+ \hat{S}_j^+ \sin^2\theta \, e^{-2i\phi}, \tag{3.17}$$

$$\hat{F} = -\frac{3}{4}\hat{S}_i^- \hat{S}_j^- \sin^2\theta \, e^{2i\phi}. \tag{3.18}$$

The influence of the magnetic dipole interaction on the paramagnetic ions has been discussed in detail by several authors. The pioneer work was done by van Vleck [6, 7]. Most of the early work was carried out in order to explain the line shape and line width of ESR lines. Therefore, the effect of $\hat{H}_{\mathrm{dd}}$ is often expressed in terms of the second order moment $\langle \Delta\nu^2 \rangle$ and the fourth order moment $\langle \Delta\nu^4 \rangle$ of the ESR line shape function. For an assembly of identical paramagnetic ions with a large external magnetic field applied in the z-direction ($\Delta_Z \gg \Delta_{\mathrm{cf}}$) van Vleck finds in the high temperature limit [7]:

$$\langle \Delta\nu^2 \rangle = \frac{1}{3} S(S+1) h^{-2} \sum_{j(\neq i)} B_{ij}^2 \tag{3.19}$$

where

$$B_{ij} = \frac{3}{2} g^2 \mu_{\mathrm{B}}^2 r_{ij}^{-3} (1 - 3\cos^2\theta). \tag{3.20}$$

With a powder sample, it is customary to replace Eq. (3.19) by its average over a sphere:

$$\langle \Delta\nu^2 \rangle = \frac{3}{5} g^4 \mu_{\mathrm{B}}{}^4 S(S+1) h^{-2} \sum_{j(\neq i)} r_{ij}^{-6}. \tag{3.21}$$

In practice, it is useful to have a simple analytical form for the ESR line shape, $g(\nu)$. Often, it is assumed that the shape function $g(\nu)$ is Gaussian:

$$g(\nu) = (2\pi\langle \Delta\nu^2 \rangle)^{-1/2} \exp\left(-\frac{(\nu - \nu_0)^2}{2\langle \Delta\nu^2 \rangle} \right). \tag{3.22}$$

For ions with spin $S = \frac{1}{2}$ forming a simple cubic lattice this line shape function is a good approximation [7]. However, in other cases the line shape deviates considerably from that given by Eq. (3.22). For instance, in a randomly diamagnetically substituted sample the line shape is rather Lorentzian [8]. If the fraction $1 - f$ of the paramagnetic ions are replaced at random by diamagnetic ions, the second order moment is reduced by a factor equal to f, because the summation in Eq. (3.19) now is taken only over the fraction f of the lattice sites [8].

3.2.4. EXCHANGE INTERACTION

The exchange interaction between two ions with spins $\mathbf{S}_i$ and $\mathbf{S}_j$ is usually expressed by the Heisenberg Hamiltonian:

$$\hat{H}_{\mathrm{ex}}^{ij} = -2J_{ij}\hat{\mathbf{S}}_i \cdot \hat{\mathbf{S}}_j. \tag{3.23}$$

The total contribution of the exchange interaction to the spin Hamiltonian of the ion i is then expressed by:

$$\hat{H}_{\mathrm{ex}} = -2\hat{\mathbf{S}}_i \cdot (\sum_j J_{ij}\hat{\mathbf{S}}_j). \tag{3.24}$$

Since J_{ij} depends on the overlap between the electronic wave functions of the ions i and j, $\hat{H}_{\mathrm{ex}}^{ij}$ is normally negligible for all pairs of ions except nearest neighbour magnetic ions. In frozen solutions the distance between the magnetic ions is normally so large that the exchange interaction is insignificant.

3.2.5. HYPERFINE INTERACTION OF Fe^{3+} IONS

Generally, the hyperfine interaction is much smaller than the other terms of the spin Hamiltonian of a Fe^{3+} ion. Therefore, except for special cases, it has little influence on the electronic wave functions. However, Mössbauer spectroscopy gives direct information about the hyperfine interaction and thereby allows an investigation of the electronic wave functions.

The influence of the magnetic hyperfine interaction on the nucleus can often be expressed in terms of an effective field at the nucleus, which is given as a sum of several contributions:

$$\mathbf{H}_{\mathrm{n}} = \mathbf{H} + \mathbf{H}_i + \mathbf{H}_L + \mathbf{H}_S + \mathbf{H}_{\mathrm{c}} \tag{3.25}$$

where $\mathbf{H}$ is the external field, $\mathbf{H}_i$ is the dipolar field from the neighbouring ions discussed in Section 3.2.3, $\mathbf{H}_L$ is the field due to the orbital motion of electrons around the nucleus, $\mathbf{H}_S$ is the dipolar field from the spins of the electrons of the Mössbauer ion, and $\mathbf{H}_{\mathrm{c}}$ is the Fermi contact term.

For Fe^{3+} ions, $\mathbf{H}_{\mathrm{c}}$ is generally much larger than the other terms in Eq. (3.25). $\mathbf{H}_{\mathrm{c}}$ is determined by the difference in electron density of electrons with "spin up" and "spin down" at the nucleus.

The effective field approximation [Eq. (3.25)] is only valid for a strongly anisotropic Kramers doublet ($g^*_{z^*} \gg g^*_{x^*}, g^*_{y^*}$) or in the presence of an external magnetic field which causes an energy splitting of the electronic states that is much larger than the energy splitting due to the hyperfine interaction ($\Delta_Z \gg g_{\mathrm{n}}\mu_{\mathrm{N}}H_{\mathrm{n}}I$) ($g_{\mathrm{n}}$ is the nuclear g-factor, μ_{N} is the nuclear magneton and I is the spin of the nucleus). For Fe^{3+} the Hamiltonian for the magnetic interaction between the nucleus and the surrounding electrons may be written [9]:

$$\hat{H}_{\mathrm{m}} = A_{\mathrm{n}}\hat{\mathbf{S}} \cdot \hat{\mathbf{I}}. \tag{3.26}$$

By use of Mössbauer spectroscopy the value of A_{n}($= A_{\mathrm{e}}, A_{\mathrm{g}}$ for the excited and the ground state, respectively) can be found from the maximum magnetic hyperfine splitting in the presence of a strong applied field ($\Delta_Z \gg \Delta_{\mathrm{cf}}$) [9–11]. In this case we find for the nuclear Zeeman Hamiltonian:

$$\hat{H}_{\mathrm{Zn}} = A_{\mathrm{n}} M \hat{I}_z + g_{\mathrm{n}} \mu_{\mathrm{N}} H \hat{I}_z = g_{\mathrm{n}} \mu_{\mathrm{N}} (H_{\mathrm{hf}} + H) \hat{I}_z , \tag{3.27}$$

where the magnetic hypefine field H_{hf} is given by:

$$H_{\mathrm{hf}} = \frac{A_{\mathrm{n}}}{g_{\mathrm{n}} \mu_{\mathrm{N}}} M \equiv a_0 M . \tag{3.28}$$

For small external fields for which $A_{\mathrm{n}} \ll \Delta_{\mathrm{Z}} \ll \Delta_{\mathrm{cf}}$ it is convenient to consider the Kramers doublets separately and to express the magnetic hyperfine interaction in terms of the effective spin quantum number S^* of the doublet in question (see Section 3.2.2):

$$\hat{H}_{\mathrm{m}} = \hat{\mathbf{S}}^* \cdot \boldsymbol{A}_{\mathrm{n}}^* \cdot \hat{I} \tag{3.29}$$

where

$$\boldsymbol{A}_{\mathrm{n}}^* = \frac{1}{2} A_{\mathrm{n}} \boldsymbol{g}^* \tag{3.30}$$

($\boldsymbol{g}^*$ is defined in Eq. (3.9) and shown in Fig. 3.1 as a function of λ). The effective magnetic hyperfine field is then given by [10–12]:

$$H_{\mathrm{hf}} = \frac{a_0 S}{10} \left(\frac{g_{x^*}^{*4} H_{x^*}^2 + g_{y^*}^{*4} H_{y^*}^2 + g_{z^*}^{*4} H_{z^*}^2}{g_{x^*}^{*2} H_{x^*}^2 + g_{y^*}^{*2} H_{y^*}^2 + g_{z^*}^{*2} H_{z^*}^2} \right)^{1/2} \tag{3.31}$$

where x^*, y^*, z^* are the principal axes of the tensor $\boldsymbol{g}^*$.

The direction of H_{hf} can be found from [10–12]:

$$H_{\mathrm{hf},x^*} : H_{\mathrm{hf},y^*} : H_{\mathrm{hf},z^*} = g_{x^*}^{*2} H_{x^*} : g_{y^*}^{*2} H_{y^*} : g_{z^*}^{*2} H_{z^*} . \tag{3.32}$$

In addition to the magnetic hyperfine interaction the electric field gradient at the nucleus also gives rise to a hyperfine interaction if the nucleus has a finite electric quadrupole moment.

The Hamiltonian describing the nuclear quadrupole interaction is given by:

$$\hat{H}_{\mathrm{Q}} = \frac{eQ_{\mathrm{n}} V_{zz}}{4I(2I-1)} [3\hat{I}_z^2 - I(I+1) + \eta(\hat{I}_+^2 + \hat{I}_-^2)/2] \tag{3.33}$$

where eQ_{n} is the electric quadrupole moment of the nucleus, V_{zz} is the z-component of the electric field gradient (EFG), and

$$\eta = \frac{V_{xx} - V_{yy}}{V_{zz}} . \tag{3.34}$$

Here, the x, y, z directions are defined as the principal axes of the electric field gradient tensors and

$$|V_{zz}| \geq |V_{yy}| ; \; |V_{xx}| . \tag{3.35}$$

In the case of Fe^{3+} the electric field gradient only has contributions from the neighbouring ions (see Chapter 1). Therefore the nuclear quadrupole interaction in iron(III) ions is, in general, small.

3.3. PARAMAGNETIC HYPERFINE SPLIT MÖSSBAUER SPECTRA OF Fe^{3+} COORDINATION ENTITIES

When the relaxation time in a paramagnetic material is long, ($\gtrsim$ 100 ns) it is possible to observe magnetically hyperfine split Mössbauer spectra of Fe^{3+} coordination entities. Such spectra are very sensitive to the relative magnitude of the terms in the total spin Hamiltonian:

$$\hat{H}=\hat{H}_{\mathrm{cf}}+\hat{H}_{\mathrm{Z}}+\hat{H}_{\mathrm{dd}}+\hat{H}_{\mathrm{ex}}+\hat{H}_{\mathrm{h}}. \tag{3.36}$$

As discussed above, $\hat{H}_{\mathrm{cf}}$ gives rise to a splitting of the ionic ground state into three Kramers doublets. The eigenstates of the electronic system depend critically on small perturbations that lift the degeneracy of the doublets. For $\hat{H}_{\mathrm{Z}}=\hat{H}_{\mathrm{dd}}=\hat{H}_{\mathrm{ex}}=0$ the hyperfine interaction alone lifts the degeneracy. The spectrum is then very sensitive to the values of the parameters λ and μ defined in Eq. (3.5). The magnetic hyperfine interaction gives rise to a splitting of the order of 10^{-7} eV. Applied magnetic field strengths of the order of only 0.001 T result in a Zeeman splitting of the ionic states of the same size. Such fields have a significant influence on the spectrum and are in fact difficult to avoid [12, 13]. For instance, the random dipolar fields from the ligand nuclei can easily be of this size and the dipolar fields due to neighbouring paramagnetic ions may be considerably larger.

If a field strength of about 0.01 T is applied, the electronic Zeeman interaction with the applied field is large compared to the hyperfine interaction and the Zeeman interaction with the dipolar fields. Then the electronic eigenstates are essentially determined by $\hat{H}_{\mathrm{cf}}$ and $\hat{H}_{\mathrm{Z}}$. Normally, the crystal field splitting is large compared to the Zeeman splitting for fields of this size. The Mössbauer spectrum then consists of three Zeeman split components each described by an effective magnetic field, the size and direction of which are given by Eqs (3.31) and (3.32).

When the electronic Zeeman splitting is increased and becomes comparable to the crystal field splitting, the electronic eigenstates, and therefore also the size and direction of the hyperfine field, depend on the relative size of Δ_{cf} and Δ_{Z}. Finally, for $\Delta_{\mathrm{Z}} \gg \Delta_{\mathrm{cf}}$, the electronic eigenstates are essentially determined by $\hat{H}_{\mathrm{Z}}$. In this simple case the Mössbauer spectrum can be described in terms of six Zeeman split components with effective magnetic fields given by:

$$H_{\mathrm{n}}=H+\frac{A_{\mathrm{n}}}{g_{\mathrm{n}}\mu_{\mathrm{N}}}M=H+a_0 M. \tag{3.37}$$

An investigation of the spectrum as a function of the applied field allows a determination of all the parameters of the total spin Hamiltonian [11]. If the spectra are obtained at low temperatures, the relative areas of the spectral components from the electronic states are weighted with appropriate Boltzmann factors.

A detailed study of the iron(III) hexaaqua coordination entity $[Fe(H_2O)_6]^{3+}$, in frozen aqueous solutions has been performed by Knudsen [10, 11, 13]. He prepared absorbers with low concentrations of Fe^{3+} and studied the magnetic field dependence of the spectra at 78 K and at 4.5 K. The samples were prepared with different glass formers (e.g. glycerol and different nitrates) in order to ensure formation of homogeneous glasses (see Section 3.7).

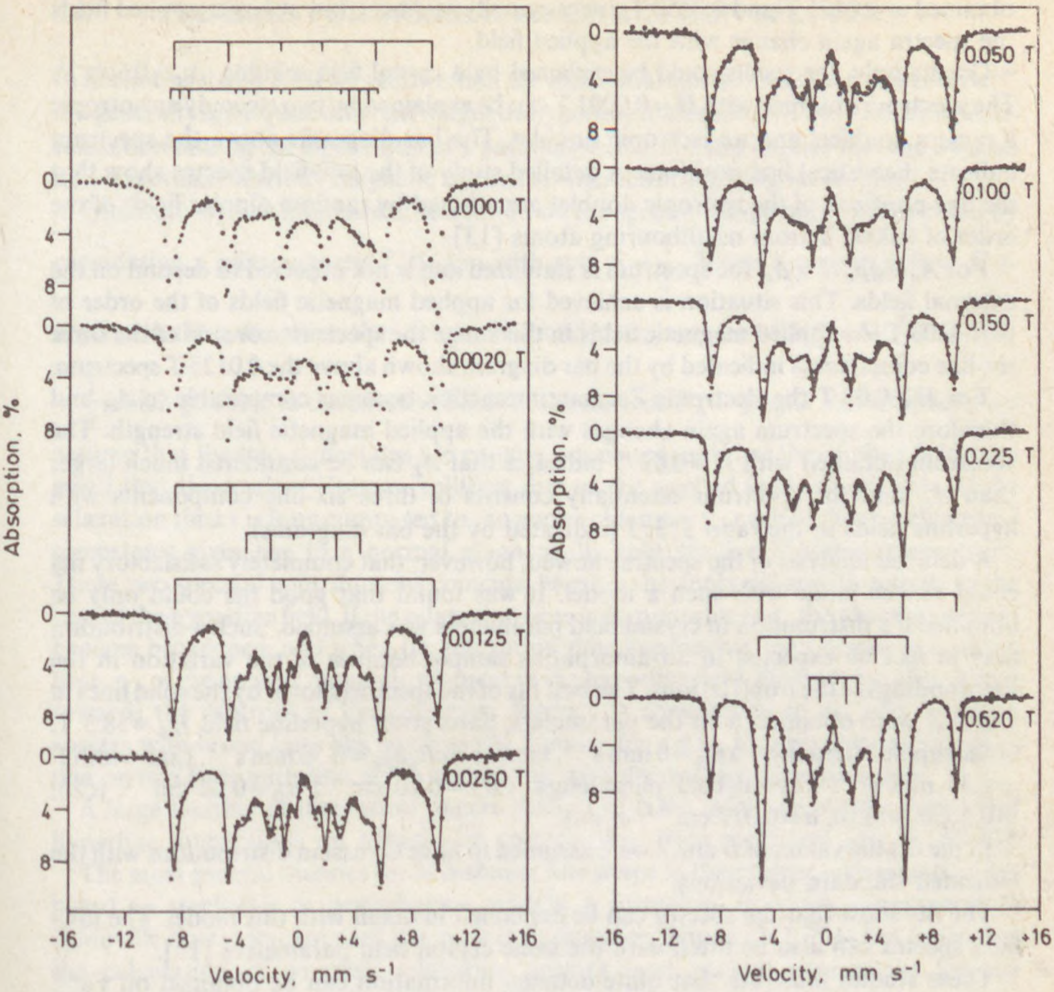

Fig. 3.2. Mössbauer spectra of an absorber of a frozen aqueous solution with 0.03 mol dm^{-3} $Fe(NO_3)_3$, 0.5 mol dm^{-3} HNO_3, 5.4 mol dm^{-3} $LiNO_3$ obtained at 4.5 K with various applied transverse magnetic fields. The full curves show a theoretical fit. The bar diagram above the 0.0001 T and the 0.0125 T spectra show a simplified interpretation in terms of spectra related to the three Kramers doublets. The bar diagram above the 0.620 T spectrum shows an interpretation in terms of three magnetically split spectra with transverse hyperfine fields in in the ratio 5 : 3 : 1. The line intensitites are indicated by the lengths of the bars (adapted from [11])

Typical spectra of an absorber containing 0.03 mol dm^{-3} $Fe(NO_3)_3$, 0.5 mol dm^{-3} HNO_3 and 5.4 mol dm^{-3} $LiNO_3$ are shown in Fig. 3.2. The spectra were obtained at 4.5 K. At $H = 0.0001$ T the spectrum essentially consists of a six-line component superimposed with an asymmetric component.

The spectra are drastically changed when the applied magnetic field strength is increased. For $H \gtrsim 0.01$ T the spectra are symmetric. It was found that the spectra obtained at 0.0125 T and 0.0250 T are essentially identical, but at larger applied fields the spectra again change with the applied field.

Qualitatively, the results could be explained by a crystal field splitting, $\Delta_{\mathrm{cf}} \simeq 0.6 \mathrm{cm}^{-1}$. The spectrum obtained with $H = 0.0001$ T can be explained by two strongly anisotropic Kramers doublets and an isotropic doublet. The bar diagrams above the spectrum indicate theoretical line positions. A detailed study of the low-field spectra show that the line positions of the isotropic doublet are affected by random dipolar fields of the order of 0.0006 T from neighbouring atoms [13].

For $A_{\mathrm{n}} \ll g\mu_{\mathrm{B}} H \ll \Delta_{\mathrm{cf}}$ the spectrum is stabilized and is not expected to depend on the external fields. This situation is achieved for applied magnetic fields of the order of 0.01–0.03 T. At applied magnetic fields in this range the spectrum consists of the three six-line components indicated by the bar diagram shown above the 0.0125 T spectrum.

For $H \gtrsim 0.05$ T the electronic Zeeman interaction becomes comparable to Δ_{cf} and therefore the spectrum again changes with the applied magnetic field strength. The spectrum obtained with $H = 0.62$ T indicates that Δ_{Z} can be considered much larger than Δ_{cf} and the spectrum essentially consists of three six-line components with hyperfine fields in the ratio 5 : 3 : 1 (indicated by the bar diagrams).

A detailed analysis of the spectra showed, however, that completely satisfactory fits could not be made with such a model. It was found that good fits could only be obtained if a distribution in crystal field parameters was assumed. Such a distribution may in fact be expected in an amorphous sample because of the variation in the surroundings of the iron(III) ions. The best fits of the spectra (shown by the solid lines in Fig. 3.2) were obtained with the parameters: Saturation hyperfine field $H_0 = 58.5$ T. Quadrupole interaction $\Delta E_{\mathrm{Q}} = 0 \mathrm{~mm~s}^{-1}$. Isomer shift, $\delta_{\mathrm{Fe}} = 0.50 \mathrm{~mm~s}^{-1}$. Line width $\Gamma = 0.34 \mathrm{~mm~s}^{-1}$. Crystal field parameters: $\langle D \rangle = 0.10 \mathrm{~cm}^{-1}$; $\sigma_D = 0.02 \mathrm{~cm}^{-1}$, $|\langle \lambda \rangle| = 0.20$; $\sigma_\lambda = 0.10$, $a = 0.017 \mathrm{~cm}^{-1}$; $\sigma_a = 0$.

In the fits the values of D and λ were assumed to have Gaussian distributions with the indicated standard deviations.

The fits show that the spectra can be explained in detail with this model. The low-field spectra can also be fitted with the same crystal field parameters [13].

These studies illustrate that quite detailed information can be obtained on Fe^{3+} coordination entities with slow paramagnetic relaxation. It is of particular interest that the variation in the local environments of the Fe^{3+} ions can be studied by this method.

Mössbauer studies of dilute frozen aqueous solutions have appeared useful for studies of other inorganic and organic iron coordination entities [9, 14–19]. In such studies it is essential that a homogeneous glass be formed upon freezing. This can be achieved by a sufficiently rapid cooling and by adding a glass-former to the solution. This is discussed in some detail in Section 3.8.

It should be emphasized that it is necessary to study the field dependence of the Mössbauer spectra in order to determine the saturation hyperfine field and the crystal field parameters by use of Mössbauer spectroscopy. In particular, in zero applied magnetic field strenght the maximum magnetic hyperfine splitting depends critically on the crystal field parameters and does therefore not give direct information about the parameter A_{n} in Eq. (3.26).

3.4. THEORIES FOR MÖSSBAUER RELAXATION SPECTRA

In Sections 3.2 and 3.3 it was shown that the individual electronic eigenstates of a Fe^{3+} ion generally have quite different magnetic hyperfine interactions. Thus, the presence of relaxation among the eigenstates of a paramagnetic Fe^{3+} ion implies that the nucleus may experience various magnetic hyperfine interactions during its lifetime.

Qualitatively, the influence of relaxation on the spectral shape may be illustrated by considering a paramagnetic ^{57}Fe ion with spin $S=\frac{1}{2}$. When a magnetic field H is applied in the z direction, the ion can be found in eigenstates with $S_z=+\frac{1}{2}$ and $S_z=-\frac{1}{2}$ which give rise to the effective fields at the nucleus $H_n=\pm a_0/2$. For simplicity we assume that the two eigenstates are equally populated and that the applied field is so small that the nuclear Zeeman splitting due to the applied field is negligible. If the relaxation time τ is long compared to the nuclear lifetime, τ_n, each of the two electronic eigenstates gives rise to a normal magnetically split six-line Mössbauer spectrum. These two spectral contributions coincide, because they only differ with respect to the sign of the hyperfine field. If the relaxation time is comparable to τ_n the absorption lines become broadened, and when the relaxation time approaches the Larmor precession time, τ_L, of the nuclear magnetic moment in the hyperfine field, the lines are also shifted towards the centroid of the spectrum. When τ is comparable to τ_L, very complex spectra with broad lines can be observed. Finally, for $\tau \ll \tau_L$, the spectrum collapses to one or two lines with line width decreasing with decreasing relaxation time.

A large number of theoretical papers dealing with the influence of time-dependent hyperfine interactions on Mössbauer spectra have been published [e.g. 9, 20–42].

The most general theories for Mössbauer line shape in the presence of relaxation are based on stochastic or perturbation models. A formalism in which superoperators (Liouville operators) are used has been introduced by Blume [31]. This has facilitated the calculation of complex relaxation spectra, and general expressions for the Mössbauer line shape in the presence of magnetic relaxation have been derived.

Clauser and Blume [32] considered a system described by a Hamiltonian $\hat{H}_0$ containing all the time-independent interactions of the nucleus and the surrounding electrons, and a time-dependent Hamiltonian which gives rise to transitions among the eigenstates of $\hat{H}_0$ at random instants of time.

The result of the calculations is formally expressed by:

$$I(\omega)=\langle \hat{A}^{+}\left(\frac{1}{2}\Gamma_{\text{nat}}-\mathrm{i}\omega-\hat{W}-\mathrm{i}\hat{H}_0^{\times}\right)^{-1}\hat{A}\rangle \tag{3.38}$$

Where Γ_{nat} is the natural line width, $\hat{W}$ is a superoperator describing the relaxation among the eigenstates of the system, $\hat{H}_0^{\times}$ is the Liouville operator corresponding to the Hamiltonian $\hat{H}_0$, and $\hat{A}$ is an operator describing the interaction of the system with the electromagnetic field. Equation (3.38) may also be expressed in terms of matrix elements:

$$I(\omega)=\sum_{\substack{\mu,\nu\\ \mu',\nu'}} p(\nu)\langle\nu|\hat{A}^{+}|\mu\rangle\left(\mu\nu\left|\left(\frac{1}{2}\Gamma_{\text{nat}}-\mathrm{i}\omega-\hat{W}-\mathrm{i}\hat{H}_0^{\times}\right)^{-1}\right|\mu'\nu'\right)\langle\mu'|\hat{A}|\nu'\rangle \tag{3.39}$$

where $p(\nu)$ is the probability that the system initially is in the state $|\nu\rangle$.

It has been shown by Clauser [33] that a relaxation spectrum can be expressed by the sum of a number of resonance lines with positions and widths determined by the real and imaginary parts of the eigenvalues of the superoperator $-\hat{H}_0^{\times}+\mathrm{i}\hat{W}-\frac{1}{2}\mathrm{i}\Gamma_{\text{nat}}$, and the intensities of the lines are obtained from matrix elements of the eigenvectors of the same superoperator.

The calculation of theoretical Mössbauer spectra is particularly simple if the magnetic hyperfine interaction can be described by an effective magnetic field which fluctuates only along the z direction (longitudinal relaxation), and if the electric field gradient is axially symmetric with its symmetry axis parallel to the same direction [25]. The matrix in Eq. (3.38) then splits up in a number of block matrices (with dimension determined by the number of electronic states), one for each of the nuclear transitions. Under these circumstances $\hat{H}_{\text{h}}$ is given by:

$$\hat{H}_{\text{h}}=Q'\{3\hat{I}_z^2-I(I+1)\}-g_{\text{n}}\mu_{\text{N}}\hat{I}_zH_{\text{n}}(t) \tag{3.40}$$

where $Q'=\dfrac{eQ_{\text{n}}V_{zz}}{4I(2I-1)}$ and the magnetic field at the nucleus, $H_{\text{n}}(t)$ is a random function of time. For a Fe^{3+} ion in the high spin state $\left(S=\frac{5}{2}\right)$ in a large applied field $(\Delta_Z \gg \Delta_{\text{cf}})$ $H_{\text{n}}(t)$ can take six different values which are given by:

$$H_{\text{n}}=a_0M+H$$
$$\left(M=\frac{5}{2},\frac{3}{2},\frac{1}{2},-\frac{1}{2},-\frac{3}{2},-\frac{5}{2}\right) \tag{3.41}$$

The spectral component corresponding to a specific nuclear transition $m_{\text{g}}\rightarrow m_{\text{e}}$ may then be calculated using an expression of the form

$$I(\omega)=\text{Re}\{\sum_{M,M'} p(M)A_{MM'}^{-1}(\omega)\}\,. \tag{3.42}$$

Here, $p(M)$ is the thermal population of the electronic state $|M\rangle$, and the matrix elements $A_{MM'}$ are given by:

$$A_{MM'}=[\mathrm{i}(\omega_M-\omega)+\frac{1}{2}\Gamma_{\text{nat}}]\,\delta_{M,M'}-\Omega_{MM'} \tag{3.43}$$

where $\hbar\omega_M$ is the nuclear transition energy when the ion is in the state M, and $\Omega_{MM'}$ is the transition probability rate for the ionic spin transition $|M\rangle\rightarrow|M'\rangle$, with $\Omega_{MM}=-\sum_{M'(\neq M)}\Omega_{MM'}$.

3.5. SPIN-SPIN RELAXATION

In paramagnetic materials the magnetic relaxation frequency of the paramagnetic ions is determined by contributions from both the spin-spin and the spin-lattice relaxation processes. The spin-spin relaxation frequency is essentially independent of the temperature whereas the spin-lattice relaxation frequency increases with increasing temperature. At sufficiently low temperatures the spin-lattice relaxation frequency can often be considered negligible compared to the spin-spin relaxation frequency and it is convenient to study spin-spin relaxation phenomena under such circumstances. Often the spin-lattice relaxation of Fe^{3+} ions is negligible even at 80 K (see Section 3.6), and therefore detailed studies of spin-spin relaxation may be carried out at this temperature.

In this section the theory of cross-relaxation by Bloembergen et al. [43] and its consequences for the relaxation of Fe^{3+} ions in frozen solutions is discussed, and a number of experimental studies are presented. Although the theory by Bloembergen et al. may not be correct in detail, it has been found that at least qualitatively it can explain the observed dependence of the spin-spin relaxation time on temperature, applied magnetic fields, crystal field interaction, and concentration of Fe^{3+} ions and other paramagnetic ions.

3.5.1. CROSS-RELAXATION PROCESSES

Bloembergen et al. [43] derived an expression for the probability per unit time for a process, which results in a transition of an ion i from the state $|M_a^i\rangle$ to the state $|M_{a+\alpha}^i\rangle$ accompanied by a transition of another ion j from the state $|M_b^j\rangle$ to $|M_{b+\beta}^j\rangle$. The process results in an increase in the crystal field and Zeeman energy of the ion i by an amount E_α^i and a decrease in energy of the ion j by an amount E_β^j. It is assumed that the energy difference $E_\alpha^i - E_\beta^j$ is taken up by the magnetic dipolar energy of the whole spin system. If the shape functions of the two transitions α and β are Gaussian with second-order moments $(\Delta E_\alpha^i)^2$ and $(\Delta E_\beta^j)^2$, respectively, the expression for the transition probability can be written:

$$\Omega_{\mathrm{ss}}^{ij} = \frac{(2\pi)^{-1/2}}{\hbar} \frac{|\langle M_{a+\alpha}^i, M_{b+\beta}^j|\hat{H}_{\mathrm{dd}}^{ij}|M_a^i, M_b^j\rangle|^2}{[(\Delta E_\alpha^i)^2 + (\Delta E_\beta^j)^2]^{1/2}} \exp\left(-\frac{(E_\alpha^i - E_\beta^j)^2}{2[(\Delta E_\alpha^i)^2 + (\Delta E_\beta^j)^2]}\right) p_j(M_b^j). \tag{3.44}$$

Here, $\hat{H}_{\mathrm{dd}}^{ij}$ is the Hamiltonian describing the magnetic dipolar interaction between the two ions i and j, given by Eq. (3.11) and $p_j(M_b^j)$ is the probability for the ion j to be in the initial state $|M_b^j\rangle$. Figure 3.3 shows a schematic illustration of a cross-relaxation process.

The assumption of Gaussian line shapes for the transitions is generally not correct (see Section 3.2). Equation (3.44) may therefore be considered a crude approximation to the real transition probability.

The total transition probability Ω_{ss}^i for a transition of a Mössbauer ion, $|M_a^i\rangle \rightarrow |M_{a+\alpha}^i\rangle$ is obtained by adding up contributions from all the energy levels of all the

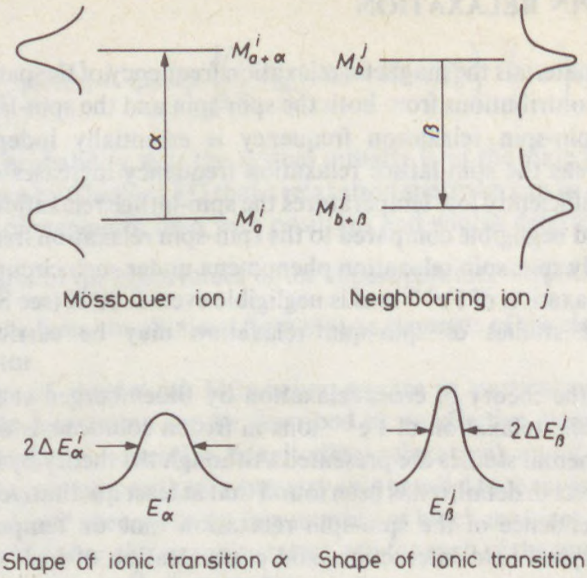

Fig. 3.3. Schematic illustration of a cross-relaxation process, by which the Mössbauer ion i performs a transition α, accompanied by a transition β of a neighbouring paramagnetic ion j (adapted from [5])

neighbouring paramagnetic ions, j. We then find:

$$\Omega^i_{ss}=\frac{(2\pi)^{-1/2}}{\hbar}\sum_{j,M^j_b}\frac{|\langle M^i_{a+\alpha},M^j_{b+\beta}|\hat{H}^{ij}_{dd}|M^i_a,M^j_b\rangle|^2}{\Delta E^{ij}_{\alpha\beta}}\exp\left[-\frac{(E^i_\alpha-E^j_\beta)^2}{2(\Delta E^{ij}_{\alpha\beta})^2}\right]p_j(M^j_b) \tag{3.45}$$

where we have introduced $\Delta E^{ij}_{\alpha\beta}=[(\Delta E^i_\alpha)^2+(\Delta E^j_\beta)^2]^{1/2}$.

When a large magnetic field strength is applied ($\Delta_Z \gg \Delta_{cf}$) the ionic states are to a good approximation the pure Zeeman states. In this case the relative transition probabilities for the transition of Mössbauer ion, $|M^i_a\rangle \rightarrow |M^i_{a+\alpha}\rangle$ may be calculated, if we assume that the values of $\Delta E^{ij}_{\alpha\beta}$ are identical for all the transitions. The terms of $\hat{H}^{ij}_{dd}$ which give rise to cross-relaxation are those of the term $\hat{B}$ of the Hamiltonian of the magnetic dipolar interaction [Eq. (3.14)]. This term contains the spin operator $\hat{S}^+_i\hat{S}^-_j+\hat{S}^-_i\hat{S}^+_j$ that allows transitions for which:

$$\Delta M=M^i_a-M^i_{a+\alpha}=-(M^j_b-M^j_{b+\beta})=\pm 1\,. \tag{3.46}$$

If the value of $(E^i_\alpha-E^j_\beta)$ is independent of the initial state of the ion j, $|M^j_b\rangle$, the transition probabilities for the transitions $M^i_a \rightarrow M^i_a \pm 1$ are proportional to [5]:

$$\sum_{M^j_b}|\langle M^i_a\pm 1, M^j_b\mp 1|\hat{S}^+_i\hat{S}^-_j+\hat{S}^-_i\hat{S}^+_j|M^i_a,M^j_b\rangle|^2=35\,[S(S+1)-M^i_a(M^i_a\pm 1)]\,. \tag{3.47}$$

This is the case, for example, when the two ions i and j have negligible crystal field splittings and identical g-factors.

Another important case is found when the crystal field interaction is large compared to the level broadening, and the ions i and j have identical energy levels. In this case only equivalent transitions, i.e. transitions for which $M^j_b = M^i_{a+\alpha}$ and $M^i_a = M^j_{b+\beta}$ have a finite probability. The transition probability rate is then proportional to [5]:

$$|\langle (M^i_{a+\alpha} = M^i_a \pm 1), (M^j_{b+\beta} = M^i_a)| \hat{S}_i^+ \hat{S}_j^- + \hat{S}_i^- \hat{S}_j^+ | M^i_a, (M^j_b = M^i_a \pm 1)\rangle|^2 =$$
$$[S(S+1) - M^i_a(M^i_a \pm 1)]^2 . \tag{3.48}$$

The relative transition probabilities for the individual transitions of a Fe^{3+} ion in these two cases are given in Table 3.1.

It has been pointed out [5] that some special effects may be observed in amorphous frozen solutions. In such samples the crystal field splittings of the individual Fe^{3+} ions are not very different [11]. However, the orientations of the crystal field axes of neighbouring ions will generally not be correlated. In this case, the relative transition probabilities in the presence of a large applied magnetic field may be different from those given in Table 3.1. This can be illustrated by considering the case of an axial crystal field Hamiltonian given by Eq. (3.2). If $\Delta_{\mathrm{cf}} \ll \Delta_{\mathrm{Z}}$ we may estimate the transition energies $E = E^i_\alpha$ and $E = E^j_\beta$ by using first order perturbation theory [Eq. (3.8)] [5]:

$$\begin{aligned} E\left(\frac{5}{2} \rightleftarrows \frac{3}{2}\right) &= g\mu_{\mathrm{B}} H + 4D' \\ E\left(\frac{3}{2} \rightleftarrows \frac{1}{2}\right) &= g\mu_{\mathrm{B}} H + 2D' \\ E\left(\frac{1}{2} \rightleftarrows -\frac{1}{2}\right) &= g\mu_{\mathrm{B}} H \\ E\left(-\frac{1}{2} \rightleftarrows -\frac{3}{2}\right) &= g\mu_{\mathrm{B}} H - 2D' \\ E\left(-\frac{3}{2} \rightleftarrows -\frac{5}{2}\right) &= g\mu_{\mathrm{B}} H - 4D' \end{aligned} \tag{3.49}$$

where

$$D' = D\,\frac{3\cos^2\theta - 1}{2} \tag{3.50}$$

and θ is the angle between the crystal field axis and the magnetic field direction.

Equations (3.49) can be written as a single expression which can be shown to be independent of the total spin of the ion [5]:

$$E(M \rightleftarrows M-1) = g\mu_{\mathrm{B}} H + (2M-1)D' . \tag{3.51}$$

The Eqs (3.49) and (3.51) remain valid even if a rhombic term $\lambda D(\hat{S}_x^2 - \hat{S}_y^2)$ is present in the crystal field Hamiltonian, but then a term proportional to λD has to be added to D' in Eq. (3.50).

In an amorphous material a cross-relaxation process, by which the Mössbauer ion i performs a specific transition $M^i_a \rightarrow M^i_a - 1$ (or $M^i_a \rightarrow M^i_a + 1$) with transition energy E^i_α, can take place, if a neighbouring ion j performs a transition $M^j_b \rightarrow M^j_b + 1$ (or $M^j_b \rightarrow M^j_b - 1$) with transition energy E^j_β close to E^i_α. Due to the random energy displacements [Eqs (3.49) and (3.51)] connected with the random orientations of the crystal field axes,

Table 3.1.
Definition of transition probability rates for the electronic transitions of the Mössbauer ion Only the transitions for which $\Delta M > 0$ are given. For $\Delta M < 0$ the rates are given by $\Omega_{MM'} = \Omega_{M'M} \exp(-2\mu_B H(M' - M)/kT)$

Electronic transition a of Mössbauer ion	Transition probability rate	Spin-spin relaxation probability rates	
$M_a \to M_{a+\alpha}$		$\Omega^i_{ss} \sim S(S+1) - M_a(M_a - 1)$	$\Omega^i_{ss} \sim [S(S+1) - M_a(M_a - 1)]^2$
$\frac{5}{2} \to \frac{3}{2}$	Ω^1_{ss}	$5\Omega'_{ss}$	$25\Omega''_{ss}$
$-\frac{3}{2} \to -\frac{5}{2}$			
$\frac{3}{2} \to \frac{1}{2}$	Ω^2_{ss}	$8\Omega'_{ss}$	$64\Omega''_{ss}$
$-\frac{1}{2} \to -\frac{3}{2}$			
$\frac{1}{2} \to -\frac{1}{2}$	Ω^3_{ss}	$9\Omega'_{ss}$	$81\Omega''_{ss}$

it might be assumed as a first approximation that there is no preference to a specific value of M^j_b. Thus, the relative transition probabilities should be given by $\Omega^1_{ss} : \Omega^2_{ss} : \Omega^3_{ss} = 5:8:9$ (see Table 3.1). However, a more detailed analysis shows that in an amorphous sample the ratio $\Omega^1_{ss} : \Omega^2_{ss} : \Omega^3_{ss}$ may differ from $5:8:9$ [5]. For two ions with identical g-factors we find by inserting Eq. (3.51) into Eq. (3.45):

$$\Omega^i_{ss} = \frac{(2\pi)^{-1/2}}{\hbar} \sum_{j, M^j_b} \frac{|\langle M^i_{a+\alpha'} M^j_{b+\beta} | \hat{H}^{ij}_{dd} | M^i_{a'} M^j_b \rangle|^2}{\Delta E^{ij}_{\alpha\beta}} \times$$

$$\times \exp\left[-\frac{[(2M^i_a \mp 1)D'_i - (2M^j_b \pm 1)D'_j]^2}{2(\Delta E^{ij}_{\alpha\beta})^2} \right] p_j(M^j_b) . \qquad (3.52)$$

According to Eq. (3.49) D'_i and D'_j may assume any values in the intervals $-D_i/2 \leq D'_i \leq D_i$ and $-D_j/2 \leq D'_j \leq D_j$, depending on the angles θ_i and θ_j. The average values of the distributions are $\langle D'_i \rangle = \langle D'_j \rangle = 0$. If $|2M^i_a \mp 1|$ is small, there is a relatively high probability that the exponent in Eq. (3.52) is close to zero, whereas a large value of $|2M^i_a \mp 1|$ results in a smaller probability for the exponent to be close to zero. Thus, the exponential factor of Eq. (3.52) may result in an increase in the $\pm\frac{1}{2} \rightleftarrows \mp\frac{1}{2}$ and $\pm\frac{3}{2} \rightleftarrows \pm\frac{1}{2}$ transition probabilities relative to the $\pm\frac{5}{2} \rightleftarrows \pm\frac{3}{2}$ transition probabilities. This leads to a deviation from $\Omega^1_{ss} : \Omega^2_{ss} : \Omega^3_{ss} = 5:8:9$. The size of the effect depends on the values of D_i, D_j, and $\Delta E^{ij}_{\alpha\beta}$.

In particular, it should be noted that according to Eq. (3.49) the energy of the $\frac{1}{2} \rightleftarrows -\frac{1}{2}$ transitions is independent of D'. Therefore, these transitions should have a finite probability for any pair of ions when $\Delta_Z \gg \Delta_{cf}$.

It should finally be mentioned that spin-spin relaxation processes that involve only a transition of a single ion may be important, if the energy difference between two states $|M^i_a\rangle$ and $|M^i_{a+\alpha}\rangle$ is comparable to or smaller than ΔE^i_α. Thus, in small applied fields these processes may give significant contributions to the total relaxation rate [43].

3.5.2. TEMPERATURE DEPENDENCE OF THE SPIN-SPIN RELAXATION TIME

The dipole-dipole and exchange interactions, which are responsible for spin-spin relaxation, are essentially independent of temperature. Therefore, the spin-spin relaxation time is generally independent of temperature. However, at low temperatures ($kT \lesssim \Delta_{cf}$) the populations of the Kramers doublets are temperature dependent and this may affect the spin-spin relaxation time.

Consider for example an iron(III) compound with a large crystal field splitting ($\Delta_{cf} \gg \Delta E^{ij}_{\alpha\beta}$) and with axial crystal field Hamiltonian ($\hat{H}_{cf} = \hat{H}_{ax} = D[\hat{S}_z^2 - \frac{1}{3}S(S+1)]$). All of the Fe^{3+} ions are assumed to have identical crystal field splittings, i.e. the value of the exponent of Eq. (3.45) $(E^i_\alpha - E^j_\beta)^2/2(\Delta E^{ij}_{\alpha\beta})^2$, equals zero for equivalent transitions of two ions i and j, but is much greater than unity for inequivalent transitions of the two ions. Thus only equivalent transitions have a finite probability and for these transitions the exponential factor of Eq. (3.45) equals one. For $D > 0$ the $\left|\pm\frac{1}{2}\right\rangle$ doublet has the lowest energy. At temperatures for which $kT \simeq \Delta_{cf}$ the populations of the individual doublets depend significantly on temperature, and with decreasing temperature the population increases for the $\left|\pm\frac{1}{2}\right\rangle$ states which have the greatest transition probabilities (see Table 3.1). This leads to a shorter average relaxation time for the ions. It can be seen from Eq. (3.45) that the population factor $p_j(M^j_b)$, is also explicitly affecting the relaxation frequency. For $D > 0$, this also gives rise to an increase of the relaxation frequency with decreasing temperature.

In compounds in which $D < 0$ the $\left|\pm\frac{5}{2}\right\rangle$ doublet has a higher population than the other doublets at low temperatures. As only $\Delta M = \pm 1$ transitions are allowed, relaxation between a $\left|+\frac{5}{2}\right\rangle$ state and a $\left|-\frac{5}{2}\right\rangle$ state must go through all the other states. Therefore, if the population of the $\left|\pm\frac{1}{2}\right\rangle$ doublet is negligible, the spin correlation-time becomes very long.

3.5.3. MAGNETIC FIELD DEPENDENCE OF THE SPIN-SPIN RELAXATION TIME

Mössbauer studies of amorphous frozen aqueous solutions of Fe^{3+} salts at 78 K have shown an increase in the relaxation time with increasing applied magnetic field [1, 2, 44, 45]. As an example of this effect Fig. 3.4 shows Mössbauer spectra of an amorphous frozen aquous solution of $Fe(NO_3)_3$ with a concentration of 0.043 mol $Fe(NO_3)_3$ per mol H_2O. The spectra were obtained at 80 K in zero applied magnetic field and at $H = 1.4$ T [44]. The latter spectrum exhibits clear satellite lines at about $\pm 9\ \mathrm{mm\,s^{-1}}$ but these lines are not present in the spectrum obtained in zero field. This difference is a clear indication of an increasing relaxation time when the external magnetic field is applied.

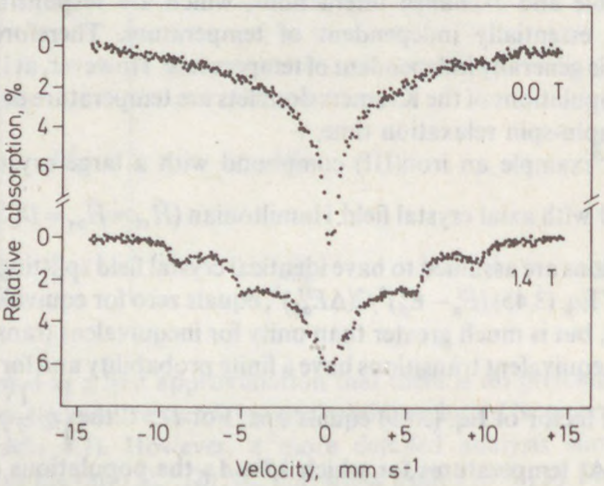

Fig. 3.4. Mössbauer spectra of a frozen aqueous solution of $Fe(NO_3)_3$ with a concentration of 0.043 mol $Fe(NO_3)_3$ per mol H_2O. The spectra were obtained at 80 K in zero applied field and in a magnetic field of 1.4 T (adapted from [44])

This effect can be explained by the model for cross-relaxation [Eq. (3.44)]. In zero field all the Fe^{3+} ions have approximately the same energy splitting (see Section 3.3). When the external field is applied the energy splittings of the iron(III) ions depend on the angle between the applied field and the crystal field axis [see Eqs (3.49)–(3.51)]. Since the orientation of the Fe^{3+} coordination entities is random (due to the amorphous nature of the samples) two neighbouring complexes will in general have quite different energy splittings when the external field is applied, and this explains the increase in the relaxation time [1, 2, 44, 45].

Sontheimer et al. [46] studied in detail the magnetic field dependence of the spin-spin relaxation time in frozen aqueous solutions of $Fe(NO_3)_3$ and $Fe(ClO_4)_3$. The measurements were made at 4.2 K in applied magnetic field strengths up to 8.0 T. Some of the experimental results are shown in Fig. 3.5. Since Δ_{cf} can be considered negligible compared to Δ_Z for fields larger than about 2.0 T the spectra could be fitted with the model for longitudinal relaxation (see Section 3.4). Figure 3.6 shows the spin-spin

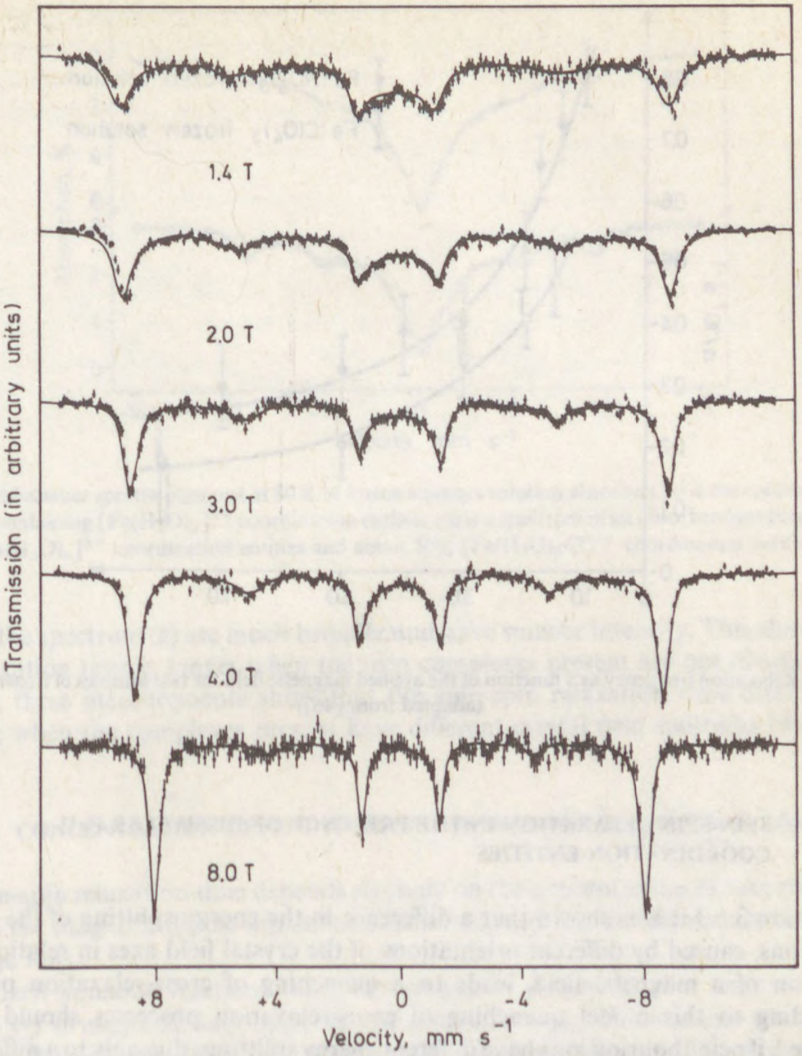

Fig. 3.5. Mössbauer spectra of a frozen aqueous solution of $Fe(NO_3)_3$ obtained at 4.2 K at different applied magnetic fields (adapted from [46])

relaxation frequency as a function of the applied magnetic field. For both samples the relaxation frequency decreases with increasing applied magnetic field, in accordance with the theory for cross-relaxation discussed in Section 3.5.1.

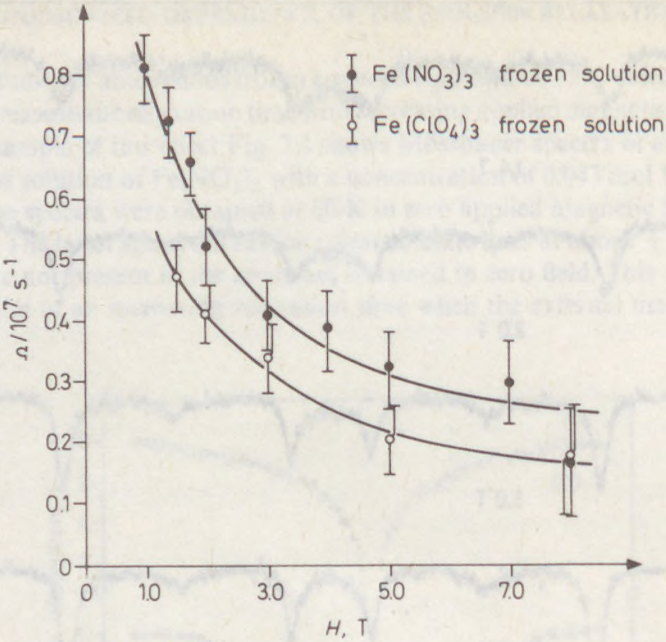

Fig. 3.6. Relaxation frequency as a function of the applied magnetic field for two samples of frozen solutions (adapted from [46])

3.5.4. SPIN-SPIN RELAXATION IN THE PRESENCE OF DISSIMILAR Fe^{3+} COORDINATION ENTITIES

In Section 3.5.3 it was shown that a difference in the energy splitting of the levels of Fe^{3+} ions, caused by different orientations of the crystal field axes in relation to the direction of a magnetic field, leads to a quenching of cross-relaxation processes. According to this model quenching of cross-relaxation processes should also be expected, if neighbouring ions have different energy splittings due only to a difference in their crystal field splittings.

In order to investigate this, Mørup and Knudsen compared the spin-spin relaxation in two different absorbers of frozen aqueous solutions [47]. One of them contained 1.5 mol dm^{-3} $Fe(NO_3)_3$, 0.9 mol dm^{-3} $HClO_4$, 30% glycerol and the other one 1.5 mol dm^{-3} $Fe(NO_3)_3$, 0.9 mol dm^{-3} HCl, 30% glycerol. In the first absorber only $[Fe(H_2O)_6]^{3+}$ coordination entities are formed, whereas in the second absorber about 50% of the Fe^{3+} ions are found in $[Fe(H_2O)_6]^{3+}$ coordination entities and the remaining Fe^{3+} ions in $[FeCl(H_2O)_5]^{2+}$ coordination entities which have a different crystal field splitting. The glycerol was added in order to ensure formation of a homogeneous glass during freezing (see Section 3.8).

Mössbauer spectra of the two absorbers at 80 K are shown in Fig. 3.7. The spectrum (b) of the absorber containing HCl shows distinct satellite lines, whereas the satellite

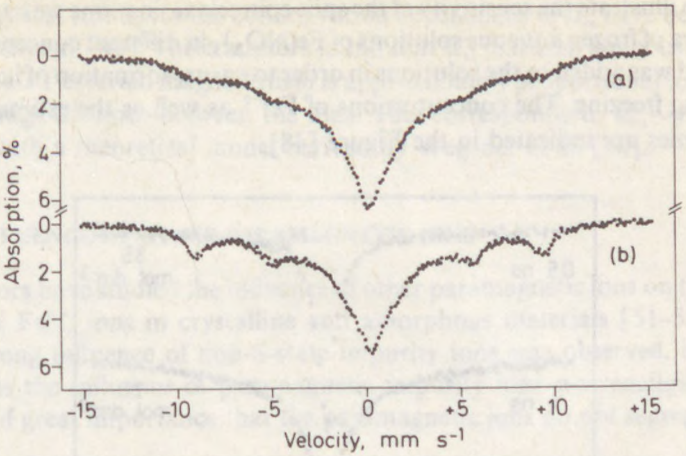

Fig. 3.7. Mössbauer spectra obtained at 80 K of frozen aqueous solution absorbers (a) is the spectrum of an absorber containing $[Fe(H_2O)_6]^{3+}$ coordination entities, (b) is a spectrum of an absorber containing about 50% $[Fe(H_2O)_6]^{3+}$ coordination entities and about 50% $[Fe(H_2O)_5Cl]^{2+}$ coordination entities [47]

lines of the spectrum (a) are much broader and have smaller intensity. This shows that the relaxation time is longer when the iron complexes present are not identical.

Thus, these measurements show that the spin-spin relaxation time does in fact increase when the complexes present have different crystal field splittings [47].

3.5.5. CONCENTRATION DEPENDENCE OF THE SPIN-SPIN RELAXATION TIME

The spin-spin relaxation time depends strongly on the concentration of magnetic ions because the magnetic dipole-dipole interaction depends on the distance between the magnetic ions.

In frozen aqueous solutions the dilution may be described as a removal of the fraction 1-f of magnetic ions, while the remaining fraction f still occupies the original positions. It can be shown that the second order moments ΔE^i_α and ΔE^j_β are reduced by a factor f upon the magnetic dilution [8]. In addition, in the expression for the transition probability, Eq. (3.45) the summation over j must be replaced by a summation over the remaining fraction f of ions, j'. For $E^i_\alpha - E^j_\beta = 0$, we then find [45]:

$$\Omega'_{ss}(f) \simeq \Omega'_{ss}(f=1) f^{1/2} . \qquad (3.53)$$

In an amorphous sample we generally find that $E^i_\alpha - E^j_\beta \neq 0$, even for $H=0$ [11]. Moreover, when an external magnetic field is applied $|E^i_\alpha - E^j_\beta|$ generally increases (see Section 3.5.3). This gives rise to an enhanced concentration dependence of Ω'_{ss} [45]. Therefore, the effect of magnetic dilution on Ω'_{ss} in frozen solutions is much more complex than indicated by Eq. (3.53). It must also be realized that each ion in a glass has its unique surroundings of magnetic ions. Therefore, the relaxation times of different ions are not identical and this also complicates the situation.

In order to illustrate the sensitivity of the spin-spin relaxation time we have in Fig. 3.8 shown spectra of frozen aqueous solutions of $Fe(NO_3)_3$ in different concentration at 80 K. Nitric acid was added to the solutions in order to ensure formation of homogeneous glasses during freezing. The concentrations of Fe^{3+} as well as the estimated average relaxation times are indicated in the Figure [48].

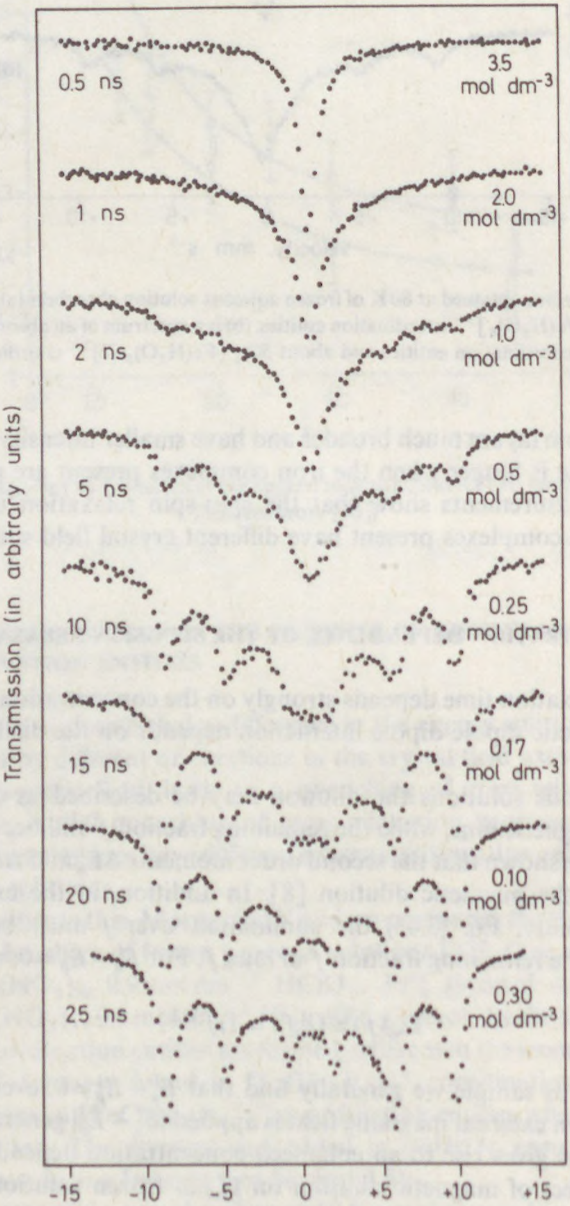

Fig. 3.8. Mössbauer spectra of some aqueous $Fe(NO_3)_3 + HNO_3$ glasses. The iron concentration and an estimate of the relaxation time are indicated [48]

Some numerical results for the concentration dependence of Ω_{ss} have been obtained by Sontheimer et al. [49]. These authors found that Ω'_{ss} in frozen aqueous solutions of $Fe(NO_3)_3$ in a 2 T external magnetic field is approximately proportional to R^{-6}, where R is the average distance between the ions. This corresponds to $\Omega'_{ss} \sim f^2$, and is in accordance with a theoretical model derived by Wegener et al. [50].

3.5.6. INFLUENCE OF OTHER PARAMAGNETIC IONS

Several authors have studied the influence of other paramagnetic ions on the spin-spin relaxation of Fe^{3+} ions in crystalline and amorphous materials [51–55]. In some studies a strong influence of non-S-state impurity ions was observed, but in other investigations the influence of paramagnetic impurity ions was negligible. In such studies it is of great importance that the paramagnetic ions do not segregate to form

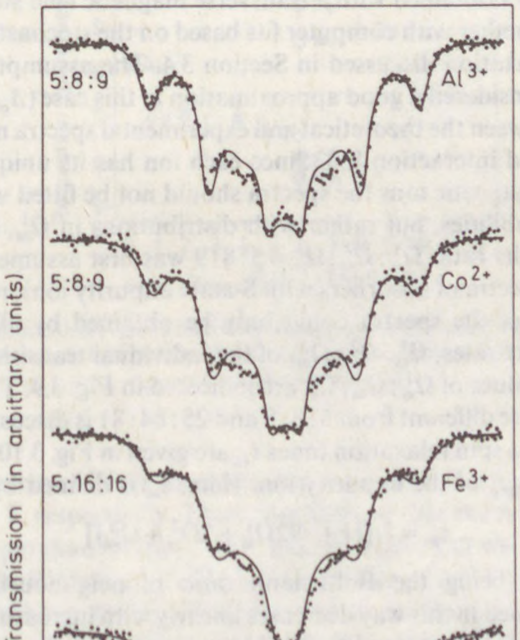

Fig. 3.9. Mössbauer spectra of absorbers with 0.95 mol dm^{-3} Fe^{3+} ions and 0.95 mol dm^{-3} impurity ions obtained at 80 K with a transverse field of 1.23 T. The solid curves show the corresponding fits calculated by means of the relaxation model explained in the text. The ratios $\Omega^1_{ss}:\Omega^2_{ss}:\Omega^3_{ss}$ are indicated [5]

clusters with high local concentrations. This is most easily achieved in amorphous frozen solutions. A detailed study of spin-spin relaxation in frozen aqeuous solutions has been carried out by Bhargava et al. [5]. These authors obtained Mössbauer spectra of amorphous frozen aqueous solutions of Fe^{3+} ions together with other ions such as Al^{3+}, Cu^{2+}, Cr^{3+}, Co^{2+}, Mn^{2+}, Gd^{3+}, and Dy^{3+}, hereafter referred to as impurity ions [5]. The absorbers were prepared by rapid freezing of aqueous solutions of the composition: 0.95 mol dm^{-3} $Fe(NO_3)_3$, 0.95 mol dm^{-3} HNO_3, 0.95 mol dm^{-3} impurity nitrate, and 19% (by volume) glycerol. The glycerol was added in order to ensure that the solutions solidified as glasses with a uniform distribution of the paramagnetic ions. At this concentration of paramagnetic ions the Mössbauer spectra are significantly influenced by spin-spin relaxation. The spectra were obtained with transverse magnetic fields of 0.014 T and 1.23 T. In all the measurements the absorber temperature was 80 K. At this temperature spin-lattice relaxation is negligible compared to the spin-spin relaxation (see Section 3.6).

Some of the spectra obtained with a transverse magnetic field strength of 1.23 T are shown in Fig. 3.9 together with computer fits based on the stochastic relaxation model for longitudinal relaxation discussed in Section 3.4. The assumption of longitudinal relaxation can be considered a good approximation in this case ($\Delta_{cf}/\Delta_Z \simeq 0.10$), but the small deviations between the theoretical and experimental spectra may be explained by the finite crystal field interaction [5]. Since each ion has its unique surroundings of neighbouring paramagnetic ions the spectra should not be fitted with sharp values of the transition probabilities, but rather with distributions in Ω^1_{ss}, Ω^2_{ss} and Ω^3_{ss}. In the theoretical spectra the ratio $\Omega^1_{ss}:\Omega^2_{ss}:\Omega^3_{ss} = 5:8:9$ was first assumed. It was, however, found that for the spectra of absorbers with S-state impurity ions, reasonably good fits of the central part of the spectra could only be obtained by allowing the relative transition probability rates, $\Omega^1_{ss}:\Omega^2_{ss}:\Omega^3_{ss}$, of the individual transitions to deviate from 5:8:9. The actual values of $\Omega^1_{ss}:\Omega^2_{ss}:\Omega^3_{ss}$ are indicated in Fig. 3.9. The reason for ratios of $\Omega^1_{ss}:\Omega^2_{ss}:\Omega^3_{ss}$ that are different from 5:8:9 and 25:64:81 is discussed in Section 3.5.1.

The estimated spin-spin relaxation times τ_{ss} are given in Fig. 3.10 as a function of the magnetic moment μ_{imp} of the impurity ion. Here, τ_{ss} is defined by the relation:

$$\tau_{ss} = 5/[(1+s)(2\Omega^1_{ss} + 2\Omega^2_{ss} + \Omega^3_{ss})] \tag{3.54}$$

$s = \exp(-g\mu_B H/kT)$ being the Boltzmann ratio of neighbouring Zeeman levels. Roughly, τ_{ss} determined in this way decreases linearly with increasing μ_{imp}, if the results for the S-state impurity ions (Mn^{2+}, Gd^{3+}) are not included.

For none of the absorbers the theoretical spectra were in complete agreement with the experimental ones. This introduces some extra uncertainty in the determination of the actual value of τ_{ss}. However, the differences in the relaxation times can be observed qualitatively even by visual inspection. A qualitative description of the differences may therefore be useful. A decrease in relaxation time leads first to a broadening and inward motion of the Mössbauer lines and subsequently to a collapse of the splitting. Thus, the ratio W between the total area and the absorption intensity in the centre of the spectrum can be taken as a crude measure of the relaxation time [5, 45]. This parameter is also useful for a description of the changes in the weak field spectra ($H = 0.014$ T) since the values of the relaxation frequencies cannot easily be determined from these spectra because the relaxation is not longitudinal.

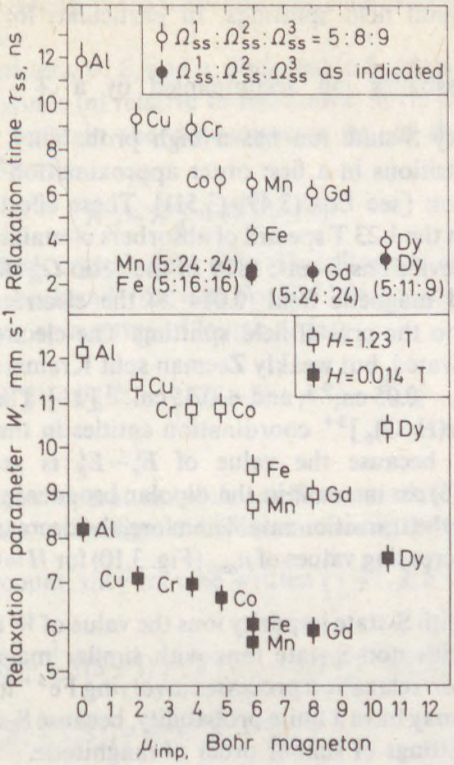

Fig. 3.10. Spin-spin relaxation times τ_{ss} and relaxation parameters W deduced from the spectra of absorbers with 0.95 mol dm^{-3} Fe^{3+} ion and 0.95 mol dm^{-3} impurity ion, shown as a function of the magnetic moment μ_{imp} of the impurity ion [5]

In Fig. 3.10 the values of W are shown for the various impurity ions at external fields of 0.014 T and 1.23 T, respectively. These results show that the relaxation time for the 1.23 T spectra is longer than for the 0.014 T spectra. This effect was discussed in Section 3.5.3. The changes in W with μ_{imp} will be quite similar at 0.014 T and 1.23 T and will follow roughly the behaviour of τ_{ss}, if the free parameter fits ($\Omega^1_{ss} : \Omega^2_{ss} : \Omega^3_{ss}$ as indicated) are used for the absorbers with S-state impurities. Apparently, Dy^{3+} at 0.014 T presents an exception.

The results obtained at $H = 1.23$ T can be explained by the increase in $\Delta E^{ij}_{\alpha\beta}$ with increasing values of μ_{imp}. According to Eq. (3.44) this leads to an increase in Ω^{ij}_{ss} for a cross-relaxation process involving two Fe^{3+} ions. However, the presence of paramagnetic impurity ions may also lead to cross-relaxation processes involving a Fe^{3+} ion and an impurity ion. Since non-S-state ions generally have crystal field splittings which are considerably larger than those of the Fe^{3+} ions, the value of $(E^i_\alpha - E^j_\beta)$ will be large for such a process. Therefore, these processes will generally have a very small probability. However, for S-state impurity ions the probability of cross-relaxation involving a Fe^{3+} ion and an impurity ion may not be negligible. This is because the g-factors of S-state ions are always close to 2.0 and S-state ions generally have quite small crystal field splittings. In particular, for $\Delta_Z \gg \Delta_{cf}$ a $\pm\frac{1}{2}\rightarrow\mp\frac{1}{2}$ transition of a Mössbauer ion accompanied by a $\mp\frac{1}{2}\rightarrow\pm\frac{1}{2}$ transition of a neighbouring impurity S-state ion has a high probability, because the transition energies of these transitions in a first order approximation are independent of the crystal field interaction [see Eqs (3.49)–(3.51)]. These effects may explain the fast relaxation observed in the 1.23 T spectra of absorbers containing S-state impurity ions as well as the large deviations from 5 : 8 : 9 of the ratio $\Omega^1_{ss}:\Omega^2_{ss}:\Omega^3_{ss}$.

In a small applied magnetic field (0.014 T) the electronic Zeeman splitting is negligible compared to the crystal field splitting. The electronic states can then be described as well separated, but weakly Zeeman split Kramers doublets with energies of about $-0.29\ \mathrm{cm}^{-1}$, $-0.05\ \mathrm{cm}^{-1}$, and $+0.35\ \mathrm{cm}^{-1}$ [11]. The variation in the crystal field splittings for $[\mathrm{Fe(H_2O)_6}]^{3+}$ coordination entities in the glass [11] reduces the cross-relaxation rate because the value of $E^i_\alpha - E^j_\beta$ is generally non-vanishing. According to Eq. (3.45) an increase in the dipolar broadenings (ΔE^i_α) and (ΔE^j_β) will result in an increase in the transition rate. Therefore, the decrease in relaxation time (the decrease in W) with increasing values of μ_{imp} (Fig. 3.10) for $H = 0.014$ T is in accordance with Eq. (3.45).

For the absorbers with S-state impurity ions the value of W at $H = 0.014$ T is smaller than for absorbers with non-S-state ions with similar magnetic moments. This is presumably due to cross-relaxation processes involving $\mathrm{Fe^{3+}}$ ions and S-state impurity ions. These processes may have a finite probability, because S-state ions generally have small crystal field splittings of similar order of magnitude.

At $H = 0.014$ T the relaxation may also have a contribution from single spin-flip processes, by which transitions take place between the two states of a Kramers doublet. The relaxation rate for these processes will also increase with increasing dipole interaction with the neighbouring paramagnetic ions [43].

3.6. SPIN-LATTICE RELAXATION

Spin-lattice relaxation is induced by modulations of the crystal field due to thermal oscillations of the ligands [3, 4, 56]. Spin-lattice relaxation of paramagnetic ions is normally investigated by means of ESR. This method is mainly applicable for long relaxation times $\tau \gtrsim 10^{-6}$ s, i.e. at low temperatures. Since ^{57}Fe Mössbauer spectroscopy is sensitive to relaxation effects for relaxation times in the range of 10^{-10} s $< \tau < 10^{-7}$ s studies of spin-lattice relaxation can be extended to higher temperatures and, as shown in this section, new types of spin-lattice relaxation processes may therefore be observed.

3.6.1. SPIN-LATTICE RELAXATION PROCESSES

For high-spin $\mathrm{Fe^{3+}}$ ions the coupling between the spin and the lattice is weak because of the spherical charge symmetry of the ^{6}S ground state. This leads to small crystal field splittings and long spin-lattice relaxation times τ_{sl}, and τ_{sl} is often in the range where the Mössbauer spectrum is sensitive to the relaxation, even at temperatures of the order of the Debye temperature.

The crystal field parameters, D, E, and a, discussed in Section 3.2.1 are functions of the positions $\mathbf{r}_n$ of the ligands (n) relative to the central ferric ions, and may thus be expressed by a Taylor series in the displacements $\Delta\mathbf{r}_n$ of the ligands from their equilibrium positions [57–62]:

$$\hat{H}_{\mathrm{cf}} = \hat{H}_{\mathrm{cf}}^{(0)} + \hat{H}_{\mathrm{cf}}^{(1)} + \hat{H}_{\mathrm{cf}}^{(2)} \tag{3.55}$$

Here, $\hat{H}_{\mathrm{cf}}^{(0)}$ is the static crystal field spin Hamiltonian corresponding to the equilibrium positions of the ligands ($\Delta\mathbf{r}_n = 0$). For Fe^{3+} in non-cubic surroundings $\hat{H}_{\mathrm{cf}}^{(0)}$ can be written (neglecting spin terms of fourth order):

$$\hat{H}_{\mathrm{cf}}^{(0)} = D\left\{\hat{S}_{z'}^2 - \frac{1}{3}S(S+1) + \lambda(\hat{S}_{x'}^2 - \hat{S}_{y'}^2)\right\} \tag{3.56}$$

(see Section 3.2.1).

$\hat{H}_{\mathrm{cf}}^{(1)}$ and $\hat{H}_{\mathrm{cf}}^{(2)}$ are spin operators with coefficients that depend linearly and quadratically, respectively, on the ligand displacements $\Delta\mathbf{r}_n$. If spin terms up to second order are taken into account, they may be written $\left(i=1,2; S=\frac{5}{2}\right)$:

$$\hat{H}_{\mathrm{cf}}^{(i)} = \hat{d}^{(i)}\left(\hat{S}_z^2 - \frac{1}{3}S(S+1)\right) + \hat{e}^{(i)}(\hat{S}_x^2 - \hat{S}_y^2) + \hat{f}^{(i)}(\hat{S}_x\hat{S}_y + \hat{S}_y\hat{S}_x) + \hat{g}^{(i)}(\hat{S}_x\hat{S}_z + \hat{S}_z\hat{S}_x) + \hat{h}^{(i)}(\hat{S}_y\hat{S}_z + \hat{S}_z\hat{S}_y) \tag{3.57}$$

where the z-axis can be chosen in the direction of the applied magnetic field. The operators $\hat{d}$, $\hat{e}$, $\hat{f}$, $\hat{g}$, and $\hat{h}$ act on the phonon states only, and depend linearly ($i=1$) and quadratically ($i=2$), respectively, on the ligand displacements, $\Delta\mathbf{r}_n \cdot \hat{H}_{\mathrm{cf}}^{(1)} + \hat{H}_{\mathrm{cf}}^{(2)}$ thus represents a coupling between the electronic spin of the iron(III) ion and the phonon bath. It gives rise to electronic transitions $|M\rangle \rightarrow |M'\rangle$ among the eigenstates, $|M\rangle$, $|M'\rangle$, of the static spin Hamiltonian, accompanied by simultaneous transitions among the lattice states $|n_1, n_2, \ldots n_q, \ldots n_r, \ldots\rangle$ with conservation of the total energy, i.e. the change in total phonon energy must balance the electronic transition energy $\Delta \equiv E_M - E_{M'}$ (here $n_1, n_2, \ldots n_q, \ldots n_r, \ldots$ are the occupation numbers of the phonon states $1, 2, \ldots, q, \ldots, r, \ldots$).

First order perturbation by $\hat{H}_{\mathrm{cf}}^{(1)}$ results in direct one-phonon processes, in which a spin transition is accompanied by the creation or annihilation of a single phonon, the phonon energy $h\omega_{\mathrm{q}}$ being exchanged with the spin transition energy Δ.

For a Debye solid this leads to a relaxation rate $\tau_{\mathrm{sl}}^{-1} \propto \Delta^2 T$ for $kT \gg \Delta$. If the Zeeman splitting is large compared to the crystal field splitting, the transition energy Δ is approximately a multiple of $2\mu_{\mathrm{B}}H$, so that $\tau_{\mathrm{sl}}^{-1} \propto H^2 T$. For a Debye solid the direct process is only important at temperatures well below the Debye temperature θ_{D}, because only low energy phonon states, with $h\omega_q = \Delta$, contribute.

At higher temperatures the two-phonon (Raman) processes become the more important ones. In such a process a phonon with energy $h\omega_q$ is annihilated and a phonon with energy $h\omega_r$ is created. The energy deficiency $h\omega_q - h\omega_r$ is taken up in a transition of the electronic spin. The first order Raman process results from first order perturbation by $\hat{H}^{(2)}_{\text{cf}}$.

In the simple Debye approximation for the phonon spectrum the corresponding temperature dependence has the form (for $kT \gg \Delta$):

$$W^{(2)}_{MM'} \propto \int_0^{\omega_D} \frac{\omega^6 \exp(\hbar\omega/kT)\,d\omega}{\{\exp(\hbar\omega/kT)-1\}^2}. \tag{3.58}$$

which gives $\tau_{\text{sl}}^{-1} \propto T^7$ for $T \ll \theta_D$ and $\tau_{\text{sl}}^{-1} \propto T^2$ for $T \gtrsim \theta_D$. If $\Delta_Z \gg \Delta_{\text{cf}}$, there is no dependence on H. The simple Debye model is expected to hold for acoustic phonons at most. For optical phonons the Einstein model is more appropriate. This leads to the expression:

$$W^{(2)}_{MM'} \propto \frac{\exp(-\theta_E/T)}{\{1-\exp(-\theta_E/T)\}^2} \tag{3.59}$$

where θ_E is the Einstein temperature. For $T \ll \theta_E$, we find $\tau_{\text{sl}}^{-1} \propto \exp(-\theta_E/T)$, and for $T \gtrsim \theta_E$, we find that $\tau_{\text{sl}}^{-1} \propto T^2$. For $\Delta_Z \gg \Delta_{\text{cf}}$ no dependence on H is expected.

Finally, an Orbach process is defined as a two-phonon relaxation process which occurs via population of an excited electronic state of energy E_0. The temperature dependence is given by [3]:

$$\tau_{\text{sl}}^{-1} \propto \frac{1}{\exp(E_0/kT)-1}. \tag{3.60}$$

The Orbach process is essentially insensitive to applied magnetic fields. This process is not expected to be important for Fe^{3+} because of the lack of appropriate excited electronic states.

If a large magnetic field is applied ($\Delta_Z \gg \Delta_{\text{cf}}$), the electronic eigenstates $|M\rangle$ of the static Hamiltonian are the six Zeeman states with spin projections $S_z = M$ in the applied field direction. The electronic part of the matrix elements of the perturbation

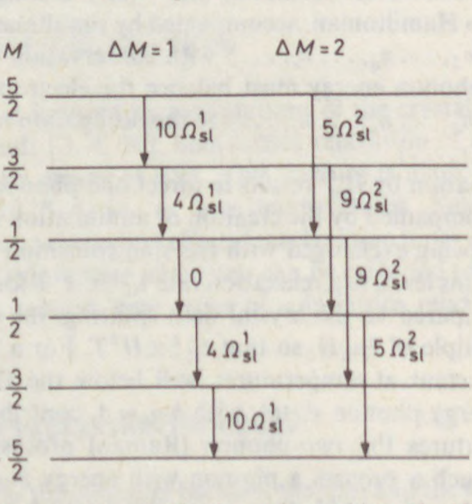

Fig. 3.11. Transition probability rates $W_{MM'}$ for the electronic transitions $M \rightarrow M'$ of the Mössbauer ion due to spin-lattice relaxation [61]

operators $\hat{H}_{\text{cf}}^{(i)}$ between the eigenstates $|M\rangle$ can then easily be calculated using the expansion given by Eq. (3.57). The squared matrix elements of the spin operators of Eq. (3.57) give the relative transition probability rates for the direct processes and for the first order Raman processes $M \rightarrow M'$ [59–62]. The results are given in Fig. 3.11.

Only the transitions for $\Delta M = M - M' > 0$ are shown. The rates for $\Delta M < 0$ are given by

$$W_{MM'} = W_{M'M} \exp[-2\mu_B H(M' - M)/kT]. \tag{3.61}$$

It can be seen that the spin-lattice relaxation is described by the two parameters Ω_{s1}^{1} and Ω_{s1}^{2}, associated with the transition $\Delta M = \pm 1$ and $\Delta M = \pm 2$, respectively. It appears from Fig. 3.11 that the transition probability rate is zero for the processes $\mp \frac{1}{2} \rightleftarrows \pm \frac{1}{2}$.

3.6.2. SPIN-LATTICE RELAXATION IN FROZEN AQUEOUS SOLUTIONS

The influence of spin-lattice relaxation on the Mössbauer spectra of frozen aqueous solutions has been observed in several samples containing Fe^{3+} ions [44, 45, 63, 64].

Spectra of frozen aqueous solutions with different concentrations of FeCl_3 (from 2 mol FeCl_3 per 100 mol water to 6 mol FeCl_3 per 100 mol water) were found to be essentially independent of temperature below about 120 K. Thus, $\tau_{\text{sl}} \gg \tau_{\text{ss}}$ for $T < 120$ K. Above 120 K the spectra showed a clear decrease in relaxation time with increasing temperatures indicating the influence of the spin-lattice relaxation [45]. A similar result was found for frozen aqueous solutions of $\text{Fe(NO}_3)_3$ [44, 63].

A detailed study of spin-lattice relaxation in a frozen aqueous solution has been made by Knudsen and Mørup [64, 65]. When the iron concentration in the samples is low, the spin-spin relaxation time is long compared to the nuclear Larmor precession time of the ^{57}Fe nucleus. Then the observed relaxation effects can be attributed to spin-lattice relaxation. The sample were therefore prepared with a low (0.03 mol dm^{-3}) concentration of Fe^{3+} which was added as a nitrate to a 0.5 mol dm^{-3} HNO_3 solution in order to ensure that the iron was present as $[\text{Fe(H}_2\text{O)}_6]^{3+}$ coordination entities. The solution was prepared with glycerol in order to ensure formation of a homogeneous glass.

Figure 3.12. shows Mössbauer spectra of the sample at different temperatures. The spectra were obtained with a transverse field $H = 1.23$ T, which is large enough to ensure that the electronic eigenstates are approximately the pure Zeeman states, $M = \pm\frac{5}{2}, \pm\frac{3}{2}$ and $\pm\frac{1}{2}$. Therefore the spectra were fitted with the simple model for longitudinal relaxation described in Section 3.4. This model gives reasonably good fits at low temperatures. Small deviations between theoretical and experimental spectra are presumably due to the finite size of the crystal field parameters ($D/2\mu_B H \simeq 0.10$) [64, 65].

It is remarkable that the spectra obtained above T_g, could not be fitted with a constant line width of the fundamental Lorentzian lines and the line width was

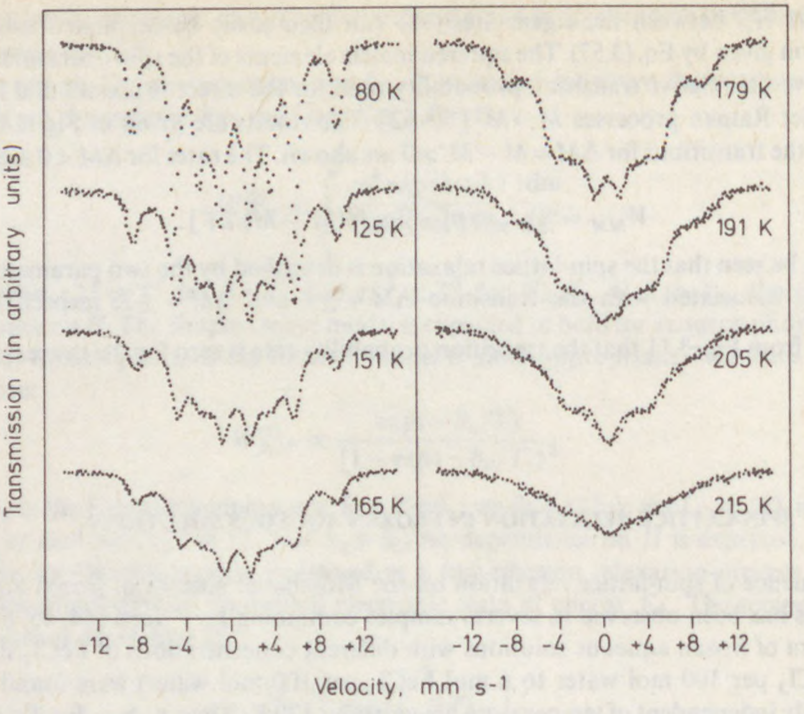

Fig. 3.12. Mössbauer spectra of a frozen aqueous solution of $Fe(NO_3)_3$ prepared with glycerol as a glass-former. The spectra were obtained in a transverse applied magnetic field of 1.23 T at the temperatures indicated (adapted from [65])

therefore allowed to vary with temperature. In several studies of Fe^{2+} coordination entities in viscous liquids a similar tendency has been observed and explained in terms of diffusional broadening (see e.g. [66–74]).

The Mössbauer line width (FWHM) in the spectrum of a viscous liquid is given by

$$\Gamma = \Gamma_{nat} + 2\frac{E^2}{\hbar c^2} D_0 \qquad (3.62)$$

where Γ_{nat} is the natural line width, E is the gamma ray energy and D_0 is the diffusion coefficient [75].

It was also found that the f-factor decreases rapidly with increasing temperature above T_g, indicating a strong increase in the vibrational amplitude of the Fe^{3+} ions. Such effects has also been seen in several previous studies of frozen solutions [66, 68–73].

Figure 3.13 shows the spin-lattice relaxation frequency as a function of temperature in a double logaritmic plot. Below T_g, Ω is approximately proportional to T^2. This indicates that the spin-lattice relaxation is due to Raman processes and that the characteristic temperature of the lattice vibrations that are responsible for the relaxation is relatively low.

A detailed analysis of the temperature dependence of Ω_{sl} below T_g on the basis of the

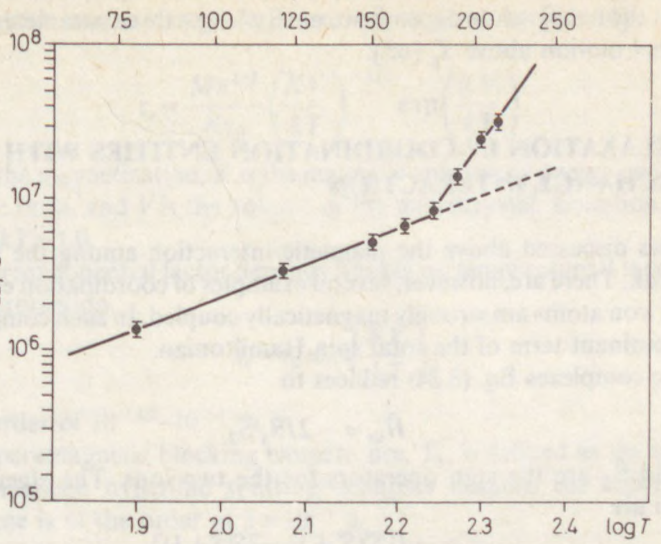

Fig. 3.13. Temperature dependence of the spin-lattice relaxation frequency estimated from the spectra shown in Fig. 3.12 (adapted from [65])

Debye model for the phonon spectrum yielded a Debye temperature $\theta_D \approx 125$ K. This Debye temperature is somewhat lower than the Debye temperature obtained on the basis of the temperature dependence of the spectral area ($\theta_D \simeq 160 \pm 20$ K). However, since the Debye model is only a rough approximation to the real phonon spectrum it is not surprising that the two different methods give different results.

Above T_g the spin-lattice relaxation frequency increases rapidly, indicating that a new type of spin-lattice relaxation processes is present in the supercooled liquid. This result might be explained by spin-lattice relaxation via internal vibrations in the $[Fe(H_2O)_6]^{3+}$ coordination entities. This type of relaxation might become more important than the relaxation via the acoustical phonons above a certain temperature, because of its stronger temperature dependence [65].

If the new relaxation processes, seen above T_g, were due to internal vibrations in the $[Fe(H_2O)_6]^{3+}$ coordination entity one would expect that the characteristic temperature T_0 should be of the order of 450 K as in alum [61]. However, an analysis of the results yielded the value $T_0 \simeq 2100$ K. Therefore it seems more likely that another type of spin-lattice relaxation is responsible for the results.

Since the new type of spin-lattice relaxation is present only above T_g it seems probable that it is associated with the diffusional motion in the supercooled liquid. Therefore the temperature dependence of Ω was compared with those of the f-factor and the diffusion coefficient, D_0 which were also obtained from the Mössbauer spectra measured at $T > T_g$.

The results showed that the temperature dependence of the new spin-lattice relaxation processes, the increased vibrational amplitude of the Fe^{3+} ions above T_g, and the diffusion coefficient could be described by the same activation energy, $\Delta E = 0.2$

eV corresponding to a characteristic temperature of about 2100 K. This result strongly suggests that the temperature dependence of all of these three parameters are related to the diffusional motion above T_g [65].

3.7. RELAXATION IN COORDINATION ENTITIES WITH STRONG EXCHANGE INTERACTION

In the studies discussed above the magnetic interaction among the Fe^{3+} ions was relatively weak. There are, however, several examples of coordination entities in which two or more iron atoms are strongly magnetically coupled. In such complexes $\hat{H}_{ex}$ may be the predominant term of the total spin Hamiltonian.

In dimeric complexes Eq. (3.24) reduces to

$$\hat{H}_{ex} = -2J\hat{\mathbf{S}}_1\hat{\mathbf{S}}_2 \tag{3.63}$$

where $\hat{\mathbf{S}}_1$ and $\hat{\mathbf{S}}_2$ are the spin operators for the two ions. The eigenvalues of this Hamiltonian are

$$E = -J[S'(S'+1) - 2S(S+1)] \tag{3.64}$$

where S' is the total spin quantum number for the coordination entity. For negative values of J, the lowest state corresponds to $S' = 0$. Therefore such coordination entities are diamagnetic at very low temperatures and consequently the Mössbauer spectrum does not exhibit magnetic splitting. At low temperatures the application of an external magnetic field only results in a magnetic field at the nucleus equal to the applied magnetic field. Therefore, such dimeric complexes can be identified by Mössbauer spectroscopy.

In a study of frozen aqueous solutions of $Fe(ClO_4)_3$ at different pH values Dézsi et al. [76] observed the presence of a dimeric coordination entity at a pH value of 1.45. This coordination entity has later been investigated in detail [77–79] and it has been identified as a mono-oxy bridged dimer, $[(H_2O)_5Fe—O—Fe(H_2O)_5]^{4+}$ with an exchange coupling constant of the order of $\sim 100\ cm^{-1}$ [78].

Dimeric coordination entities have also been observed in non-aqueous solutions of Fe^{3+}. For example Vértes et al. [14] have found the presence of such coordination entities in frozen solutions of $FeCl_3$ in pyridine.

At temperatures $T \gtrsim |J|/k$ not only the lowest state of a dimeric coordination entity is populated. Since the excited states of the dimer are paramagnetic the magnetic hyperfine interaction is non-vanishing in these states. Therefore magnetic relaxation effects may be observed when the thermal energy is of the same order of magnitude as the exchange interaction.

Trimeric coordination entities have also been observed in frozen solutions. Such coordination entities behave similar to the dimeric coordination entities, but these coordination entities are paramagnetic at all temperatures.

In several studies of frozen solutions the appearence of microcrystalline precipitates has been observed [76, 78, 80, 81]. In such samples another type of relaxation, superparamagnetic relaxation, may be observed.

The superparamagnetic relaxation time, i.e., the relaxation time for transitions of the magnetization vector between the two easy directions of magnetization for a microcrystal with uniaxial magnetic anisotropy is given by [82–84]:

$$\tau_s = \frac{M\pi^{1/2}}{K\gamma_0}\left(\frac{KV}{kT}\right)^{-1/2} \exp\left(\frac{KV}{kT}\right). \tag{3.65}$$

Here M is the magnetization, K is the magnetic anisotropy energy constant, γ_0 is the gyromagnetic ratio, and V is the volume of the microcrystal. Equation (3.65) is valid only for $KV/kT > 1.0$.

Since the preexponential factor depends weakly on temperature it is common to use the simpler expression

$$\tau_s = \tau_0 \exp\left(\frac{KV}{kT}\right). \tag{3.66}$$

τ_0 is of the order of 10^{-10}–10^{-12} s.

The superparamagnetic blocking temperature, T_B, is defined as the temperature at which the magnetic hyperfine splitting collapses because the superparamagnetic relaxation time is of the order of 5×10^{-9} s.

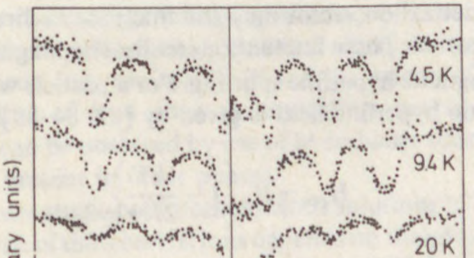

Fig. 3.14. Temperature dependence of Mössbauer spectrum of an aqueous solution of 0.04 mol dm^{-3} $(Fe(ClO_4)_3$ and 3 mol dm^{-3} $NaClO_4$ (pH = 2.3) [76, 80]

In practice a sample of microcrystals always exhibits a particle size distribution. Because of the exponential dependence of the superparamagnetic relaxation time on KV/kT this results in a very broad distribution in relaxation times. Consequently, most of the particles in the sample may either have relaxation times shorter than 10^{-9} s or longer than 10^{-7} s. Experimental spectra therefore often consist of a superposition of a six-line component due to the larger particles and a single-line or a doublet component due to the smaller particles. The particles with intermediate relaxation times (10^{-9}–10^{-7} s) yield very broad components of low intensity which are not easily resolved.

A typical example of superparamagnetic relaxation in precipitates is shown in Fig. 3.14. These spectra were obtained from a solution of 0.04 mol dm^{-3} $Fe(ClO_4)_3$ + 3 mol dm^{-3} $NaClO_4$ (pH = 2.3), which was allowed to stand for four weeks at room temperature [76, 80]. At 4.5 K the spectrum consists of a six-line component and a weak paramagnetic component. This indicates that most of the particles are below the blocking temperature. At higher temperatures the relative area of the paramagnetic component increases at the expense of the six-line component. This illustrates how an increasing number of particles become superparamagnetic when the temperature is increased. Vértes et al. [80] estimated the particle size distribution from the spectra, assuming that the magnetic anisotropy energy constant was independent of the particle size.

Below T_B the magnetization vector may still fluctuate in directions close to an easy direction of magnetization. These fluctuations (collective magnetic excitations) lead to a reduction in the magnetic hyperfine splitting. For a particle with uniaxial anisotropy the observed magnetic hyperfine field is given by [82, 84–88]:

$$H_{\text{obs}} \simeq H_0 \left\{ 1 - \frac{kT}{2KV} \right\}. \tag{3.67}$$

From the reduction in the magnetic hyperfine splitting it is possible to determine the value of the parameter KV.

3.8. STUDIES OF CRYSTALLIZATION AND GLASS FORMATION

3.8.1. NUCLEATION AND GROWTH OF CRYSTALS

Freezing of an aqueous solution may result in the formation of various solid phases depending on the cooling rate and the initial composition. The thermodynamically stable state below the liquidus temperature T_l is crystalline. This state is, however, obtained only if the cooling rate is low enough to allow both nucleation of microcrystals and subsequent crystal growth.

The temperature dependence of the nucleation rate I in a supercooled liquid may be written [89, 90]:

$$I \propto \exp\{(-F^* + Q)/kT\}. \tag{3.68}$$

Here, Q is an activation energy for short range diffusion and atomic rearrangements and F^* is the free energy barrier which must be surmounted, when a new liquid-solid interface is created. The energy barrier F^* is to a good approximation proportional to $(T_l - T)^{-2}$ ($T_l - T$ is the supercooling).

Just below the liquidus temperature T_l the nucleation rate increases with the supercooling, but at low temperatures the influence of the activation energy Q is dominating and causes a rapid decrease in nucleation rate.

The rate of crystal growth is often assumed to be proportional to $(T_l - T)/\eta_0 \cdot \eta_0$ is the viscosity of the supercooled liquid and it depends exponentially on the reciprocal temperature. Hence, the crystal growth rate, like the nucleation rate, first increases with the supercooling, has a maximum at a certain temperature, and approaches zero at further cooling due to the exponential temperature dependence of the transport properties of the liquid.

If crystallization does not take place during cooling, the diffusion rate gradually decreases because of the increase in the viscosity. Below the glass temperature, T_g, the diffusion is negligible and a metastable glass phase is formed.

When pure water is cooled by conventional methods to sufficiently low temperatures, it always crystallizes into ice. However, if for example a salt is dissolved in water, or if a suitable alcohol is added, the freezing point is lowered, and this may cause a decrease in the rates of nucleation and crystal growth at a given supercooling. Hence, the solution may solidify into a glass at ordinary cooling rates.

If only a glass is formed during the cooling of an aqueous solution of a iron(III) salt, the iron ions are uniformly distributed. However, if crystallization of ice takes place during cooling, the iron ions are mainly found in regions of higher concentration, because the solubility of iron ions in crystalline ice is very low. Therefore, crystallization of ice can be observed by use of Mössbauer spectroscopy, although the Mössbauer ions are present in other phases.

In several Mössbauer studies of frozen aqueous solutions of Fe^{3+} it has been found that the relaxation time of the iron(III) ions depends on the composition of the solution in a complex way. For example, Vértes and Parak [15] found a dependence of the relaxation time on the anion concentration and the pH value. Ohya and Ono [91] found that the spin-spin relaxation time in frozen aqueous solutions of iron(III) perchlorate was independent of the concentration of iron(III) ions for a wide range of concentrations. Platchinda and Makarov [92] found that heating at 200 K of solutions which had been rapidly cooled in liquid nitrogen resulted in a substantial decrease in the relaxation time. In a subsequent paper the same authors later showed that the relaxation time of Fe^{3+} in aqueous solutions of HCl and $FeCl_3$ depends critically on the concentration. The longest relaxation time was observed in solutions with the eutectic composition [93].

3.8.2. THE $FeCl_3$—H_2O SYSTEM

In order to investigate basic features of the amorphous and crystalline states in frozen aqueous solutions, Mørup et al. studied in detail the $FeCl_3 + H_2O$ system [45]. Figure 2.2 shows some typical spectra of absorbers with various concentrations.

The absorbers were frozen by immersion into liquid nitrogen, and the freezing time, defined as the time after which violent boiling ceased, was about 10 s. The spectra were obtained at 80 K in external fields of 1.24 T and in the remanent field, which was about 0.005 T. Most of the spectra consist essentially of a single line, broadened by electronic relaxation. In some cases satellite lines can be seen, indicating a partly resolved magnetic hyperfine structure, but in all cases the relaxation time is so short that the line width of the spectrum (FWHM), Γ, can be used as a rough measure of the relaxation time. From the temperature dependence of the spectra it was concluded that spin-lattice relaxation can be neglected at 80 K.

In Fig. 3.15 is shown the phase diagram of $FeCl_3 + H_2O$. The glass curve (the glass temperature as a function of composition) is included [94].

In the same figure is shown the Mössbauer line width (FWHM) at 80 K as a function of the concentration, x. Results are given for the absorbers before and after heating to 200 K for one hour. It can be seen that the Mössbauer line width (and thus the spin-spin relaxation time) of the absorbers before heating to 200 K exhibits a pronounced maximum for $x \simeq 3.5$. By visual inspection it was found that the absorbers with $x \geq 3.5$ were transparent with some cracks, indicating that a glassy state was formed by rapid cooling of these absorbers. However, the less concentrated absorbers were opaque and seemed to consist of a large number of small crystals. Heating of the absorbers with $x < 5.5$ to 200 K for one hour resulted in an irreversible line narrowing in accordance with the observations by Plachinda and Makarov [92]. The more concentrated absorbers were, however, unaffected by this treatment.

The fast frozen absorbers with $x \geq 3.5$ all had a glassy appearance and the line width decreases with increasing iron concentration in accordance with the expected influence of spin-spin relaxation in a system with a uniform distribution of paramagnetic ions. These absorbers therefore seem to be glasses with a uniform distribution of the iron(III) ions.

The dilute absorbers ($x < 3.0$) were opaque, indicating that some crystallization of ice had taken place during the cooling. Before heating to 200 K, all these absorbers showed identical Mössbauer line widths, namely about 1.6 mm s^{-1} at $H = 0.005$ T and 3.3 mm s^{-1} at $H = 1.24$ T. These values are identical to those of a homogeneous glass with $x \simeq 5.5$ (see Fig. 3.15). The results therefore indicate that before heating to 200 K the iron is found in amorphous regions with a composition corresponding to $x \simeq 5.5$, independent of the initial composition of the solutions. Similar results have been found in studies of frozen aqueous solutions of $Fe(ClO_4)_3$ [91] and in other systems [95].

After heating to 200 K for one hour and recooling to 78 K the Mössbauer spectra of the samples with $x < 5.0$ had changed irreversibly whereas the spectra of the more concentrated samples were unaffected by this treatment. For all the spectra with $x < 5.0$ the line width decreased to $\Gamma \simeq 1.2$ mm s^{-1} at 0.005 T and $\Gamma = 1.5$ mm s^{-1} at 1.24 T. These values are identical to those of a homogeneous glass with $x \simeq 7.3$ and this suggests that the Fe^{3+} ions are present in a glass with a local concentration corresponding to $x \simeq 7.3$ in all these samples.

On the basis of these observations a simple model can be evalutated for the kinetics of the freezing process in the $FeCl_3 - H_2O$ system [45]. When a sample of an initial concentration, $x < 3.0$ is cooled, nucleation and growth of ice crystals initiate at a certain supercooling. As the temperature is decreased the crystal growth continues, while the iron concentration in the liquid increases following a curve below the hypoeutectic liquidus curve of the equilibrium phase diagram. The detailed relation

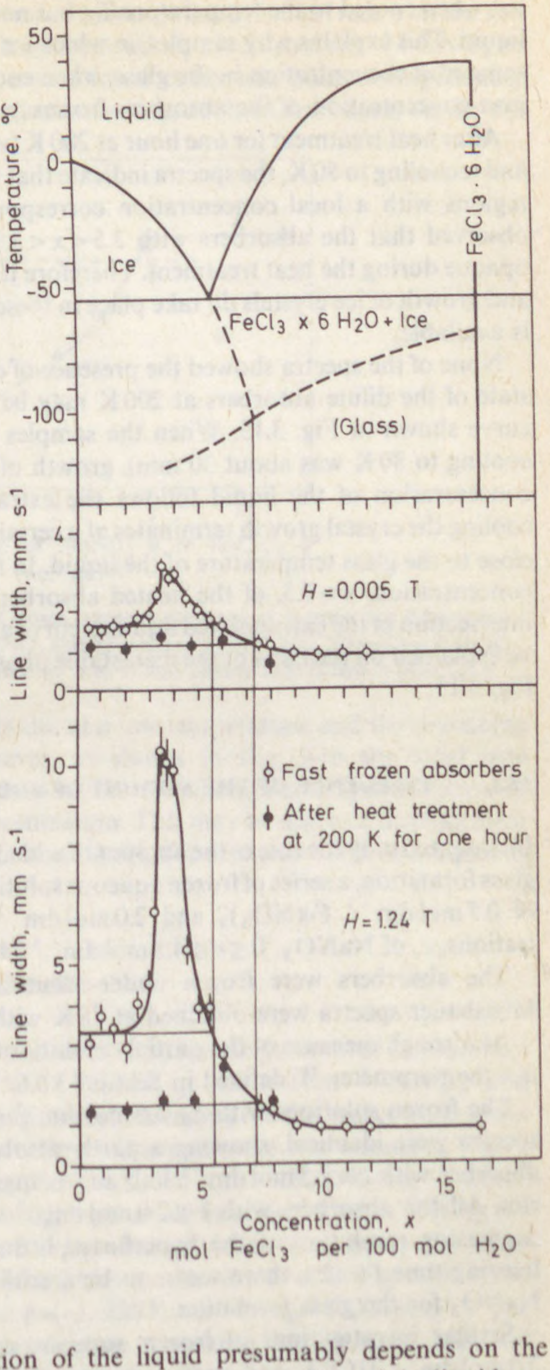

Fig. 3.15. The upper part of the figure shows the phase diagram of the $FeCl_3$—H_2O system. The dotted lines indicate the metastable phase diagram including the extrapolated hypoeutectic liquidus curve and the glass curve. In the lower part of the figure the Mössbauer line width (FWHM) of frozen aqueous solutions of $FeCl_3$ is shown at 80 K at applied fields of 0.005 T and 1.24 T as a function of the concentration (adapted from [45])

between temperature and composition of the liquid presumably depends on the freezing rate. At a certain temperature T_0 and a certain composition of the liquid, x_0, the crystal growth rate becomes slow compared to the cooling rate and eventually the remaining liquid solidifies into a glass with $x \simeq x_0$. According to this model, samples with different initial concentrations $x < 3.0$ will only differ with respect to the amount of ice, when cooled to the temperature T_0, but not with respect to the composition of the liquid. This explains why samples, in which ice crystallizes during cooling, all have the same iron concentration in the glass, when cooled at the same cooling rate. The local iron concentration of the absorbers frozen in about 10 s is $x_0 \simeq 5.5$.

After heat treatment for one hour at 200 K (which is above the glass temperature T_g) and recooling to 80 K, the spectra indicate that the Fe^{3+} ions are present in amorphous regions with a local concentration corresponding to $x = 7.3$. Furthermore, it was observed that the absorbers with $3.5 < x < 5.0$, which initially were glassy, became opaque during the heat treatment. Therefore it can be concluded that both nucleation and growth of ice crystals do take place in these samples at 200 K, when sufficient time is available.

None of the spectra showed the presence of crystalline $FeCl_3 \cdot 6H_2O$. Therefore the state of the dilute absorbers at 200 K may be found from the extrapolated liquidus curve shown in Fig. 3.15. When the samples are recooled slowly (cooling time for cooling to 80 K was about 30 min), growth of ice crystals may take place, while the concentration of the liquid follows the extrapolated liquidus curve. During slow cooling the crystal growth terminates at a certain temperature, which is supposed to be close to the glass temperature of the liquid. In fact, it is seen in Fig. 3.15 that the local concentration, $x \simeq 7.3$, of the heated absorbers is close to the concentration at the intersection of the extrapolated liquidus curve and the glass curve. Thus, the results can be explained on the basis of the metastable phase diagram shown by the dotted lines in Fig. 3.15.

3.8.3. INFLUENCE OF THE AMOUNT OF ADDED GLASS FORMER

In order to study the role of the amount of added glass former on the crystallization and glass formation, a series of frozen aqueous solutions was prepared with a concentration of 0.5 mol dm^{-3} $Fe(NO_3)_3$ and 2.0 mol dm^{-3} HNO_3, but with different concentrations, c, of $NaNO_3$, $0 \leq c \leq 4.5$ mol dm^{-3} [45].

The absorbers were frozen under identical conditions (freezing time $t \simeq 12$ s). Mössbauer spectra were obtained at 78 K without applied magnetic field.

As a rough measure of the partial resolution of the magnetic hyperfine splitting we use the parameter W defined in Section 3.5.6.

The frozen solutions with $c \geq 3.0$ mol dm^{-3} all had a glassy appearence, and their spectra were identical, showing a partly resolved magnetic hyperfine splitting. The absorber with $c = 2.5$ mol dm^{-3} had an opaque central part, surrounded by a glassy rim. All the absorbers with $c \leq 2.0$ mol dm^{-3} were opaque, and their spectra show decreasing resolution of the hyperfine splitting with decreasing c. With the given freezing time $t \simeq 12$ s, there seems to be a critical concentration $c \simeq 3.0$ mol dm^{-3} of $NaNO_3$ for the glass formation.

Similar investigations of frozen aqueous solutions of 0.5 mol dm^{-3} $Fe(ClO_4)_3$, 2.0 mol dm^{-3} $HClO_4$ and various concentrations c of $NaClO_4$ indicated a critical concentration for glass formation, $c \simeq 1.0$ mol dm^{-3}. The parameter W obtained from the spectra of the samples prepared with the two glass formers are shown in Fig. 3.16.

These results may be interpreted in terms of a change in nucleation rate with the salt concentration. In the solutions with salt concentrations $c > 3.0\,\mathrm{mol\,dm^{-3}}$ $NaNO_3$ or $c > 1.0\,\mathrm{mol\,dm^{-3}}$ $NaClO_4$, respectively, nucleation does not take place during freezing ($t = 12\,\mathrm{s}$). In more dilute solutions nucleation and growth of ice occur. As in the solutions of $FeCl_3$ crystallization terminates at a low temperature, and the remaining solution solidifies into a glass. However, as shown in Fig. 3.16 the local iron concentration in the fast frozen solutions of the multicompound system seems to increase with decreasing initial salt concentration. This may be due to a displacement of the equilibrium between ice and solution as the relative amounts of the non-aqueous components are changed.

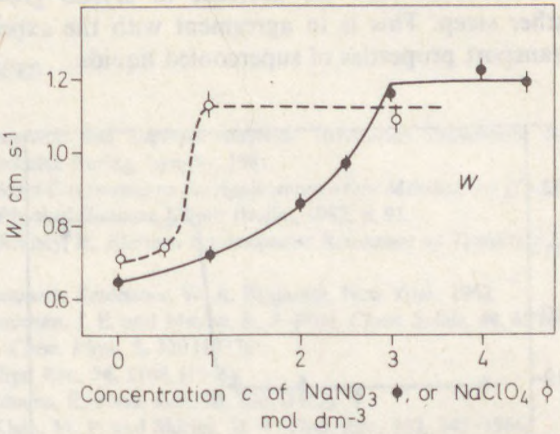

Fig. 3.16. Hyperfine resolution parameter W of frozen aqueous solutions of composition $0.5\,\mathrm{mol\,dm^{-3}}$ $Fe(NO_3)_3$, $2.0\,\mathrm{mol\,dm^{-3}}$ HNO_3, $c\,\mathrm{mol\,dm^{-3}}$ $NaNO_3$ and $0.5\,\mathrm{mol\,dm^{-3}}$ $Fe(ClO_4)_3$, $2.0\,\mathrm{mol\,dm^{-3}}$ $HClO_4$, $c\,\mathrm{mol\,dm^{-3}}$ $NaClO_4$. The spectra were obtained at 78 K in zero applied field (adapted from [45])

3.8.4. INFLUENCE OF THE FREEZING RATE

The role of the freezing conditions has been studied by freezing a number of absorbers of identical composition, [$0.5\,\mathrm{mol\,dm^{-3}}$ $Fe(NO_3)_3$, $2.0\,\mathrm{mol\,dm^{-3}}$ HNO_3 and $3.0\,\mathrm{mol\,dm^{-3}}$ $NaNO_3$] at various freezing rates by changing the thermal contact to the liquid nitrogen bath [45]. During the cooling the temperature was measured with a thermocouple inside the absorber (except for the fastest rate $r \simeq 5000\,\mathrm{K\,min^{-1}}$, which was obtained by dipping into liquid nitrogen pieces of filter paper made wet by the solution). The freezing rate, r, was defined as the average rate in the temperature range 273 K–125 K. The parameter W of the Mössbauer spectra is shown in Fig. 3.17. It can be seen that there exists a critical rate, $r = r_0$, $220\,\mathrm{K\,min^{-1}} < r_0 < 570\,\mathrm{K\,min^{-1}}$. The quickly frozen absorbers ($r > r_0$) had a glassy apperance and showed identical Mössbauer spectra, whereas the slowly frozen absorbers ($r < r_0$) were opaque and showed identical spectra with less resolved magnetic hyperfine splitting.

The dependence of the final state on the freezing rate, illustrated in Fig. 3.17 indicates that nucleation of ice does occur for cooling rates smaller than $r=r_0$. The results also show that the parameter W is independent of the freezing rate for $r<r_0$. Thus the amount of crystallized ice seems to be independent of the cooling rate over at least two decades. Hence, we conclude that the decrease in crystal growth rate at low temperatures is rather steep. This is in agreement with the expected exponential behaviour of the transport properties of supercooled liquids.

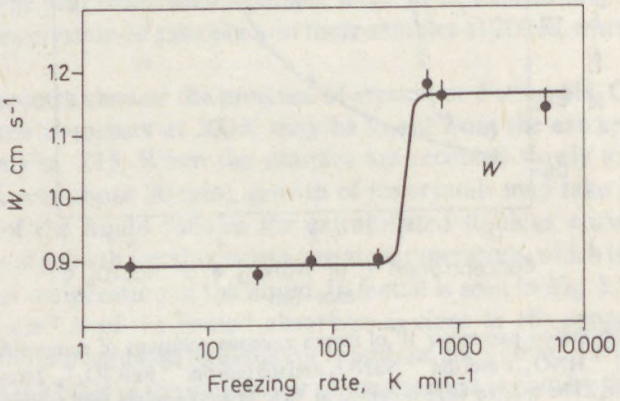

Fig. 3.17. Hyperfine resolution parameters W of frozen aqueous solutions of 0.5 mol dm^{-3} $(Fe(NO_3)_3$, 2.0 mol dm^{-3} HNO_3, 3.0 mol dm^{-3} $NaNO_3$ as a function of the freezing rate. The spectra were obtained at 78 K in zero applied field (adapted from [45])

3.9. CONCLUSIONS

Paramagnetic relaxation processes in frozen solutions are, as discussed above, in some respects different from the relaxation process observed in crystalline compounds. One example is the increase in the spin-spin relaxation time with increasing applied magnetic fields discussed in Section 3.5. This effect is explained by the amorphous nature of the samples.

It is of particular interest that the dependence of the spin-spin relaxation time on the local concentration of paramagnetic ions can be used to obtain information about crystallization and glass formation during freezing of solutions.

Spin-lattice relaxation can conveniently be studied in frozen solutions with a low concentration of paramagnetic ions. Below the glass temperature the spin-lattice relaxation seems to be dominated by processes similar to those observed in crystalline compounds. Above the glass temperature a new type of spin-lattice relaxation has been observed. This spin-lattic relaxation seems to be related to the diffusional motion of the complexes in the supercooled liquid.

Mössbauer spectroscopy is also very useful for studies of precipitates in frozen solutions. In particular the superparamagnetic behaviour of ultrafine magnetic precipitates gives information about particle size and magnetic anisotropy.

At low temperatures Mössbauer spectra of magnetically dilute frozen solutions exhibit a well-resolved magnetic hyperfine splitting. Studies of the magnetic field dependence of such spectra give detailed information about the structure of the complexes.

REFERENCES

1. Mørup, S., *Paramagnetic and Superparamagnetic Relaxation Phenomena Studied by Mössbauer Spectroscopy*, Polyteknisk Forlag, Lyngby, 1981.
2. Mørup, S., *International Conference on the Applications of the Mössbauer Effect*, Proc. Indian National Science Academy, Physical Sciences, Jaipur (India), 1982, p. 91.
3. Abragam, A. and Bleaney, B., *Electron Paramagnetic Resonance of Transition Ions*, Clarendon Press, Oxford, 1970.
4. Pake, G. E., *Paramagnetic Resonance*, W. A. Benjamin, New York, 1962.
5. Bhargava, S. C., Knudsen, J. E. and Mørup, S., *J. Phys. Chem. Solids*, **40**, 45 (1979).
6. van Vleck, J. H., *J. Chem. Phys.*, **5**, 320 (1937).
7. van Vleck, J. H., *Phys. Rev.*, **74**, 1168, (1948).
8. Kittel, C. and Abrahams, E., *Phys. Rev.*, **90**, 238, (1953).
9. Wickman, H. H., Klein, M. P. and Shirley, D. A. *Phys. Rev.*, **152**, 345 (1966).
10. Knudsen, J. E., *J. Physique Colloque*, **37**, C6–735 (1976).
11. Knudsen, J. E., *J. Phys. Chem. Solids*, **38**, 883, (1977).
12. Afanas'ev, A. M., Gorobchenko, V. D., Dézsi, I., Lukashevich, I. and Filippov, N. I., *Zh. Eksp. Teor. Fiz.*, **62**, 673 (1972); *Sov. Phys. JETP*, **35**, 355 (1972).
13. Knudsen, J. E., *J. Phys. Chem. Solids*, **41**, 545 (1980).
14. Vértes, A., Nagy-Czakó, I. and Burger, K., *J. Phys. Chem.*, **84**, 1469 (1978).
15. Vértes, A. and Parak, F., *J. Chem. Soc., Dalton Trans.* 2062 (1972).
16. Simopoulos, A., Wickman, H. H., Petrides, D. and Kostikas, A., in *"Hyperfine Interactions in Excited Nuclei"*, eds. Goldring, G. and Kalish, R. Gordon and Breach, London, 1971, p. 873.
17. Knudsen, J. E. and Mørup, S., *J. Physique Colloque*, **37**, C6–535 (1976).
18. Mørup, S. and Knudsen, J. E., *Acta Chim. Acad. Sci. Hung.* **121**, 147 (1986).
19. Spartalian, K. and Carrano, C. J., *J. Chem. Phys.*, **78**, 4811 (1983).
20. Afanas'ev, A. M. and Kagan, Y., *Zh. Eksp. Teor. Fiz.*, **45**, 1660 (1963). *Sov. Phys. JETP.*, **18**, 1139 (1964).
21. Kagan, Y. and Afanas'ev, A. M., *Zh. Eksp. Teor. Fiz.*, **47**, 1108 (1964). *Sov. Phys. JETP.*, **20**, 743 (1965).
22. Wegener, H., *Z. Phys.*, **186**, 498 (1965).
23. Wickman, H. H., *Mössbauer Effect Methodology*, Vol. 2. Ed. Gruverman, I., Plenum Press, New York, 1966, p. 39.
24. Blume, M., *Phys. Rev. Lett.*, **14**, 96 (1965).
25. Blume, M. and Tjon, J. A., *Phys. Rev.*, **165**, 446 (1968).
26. M. Blume, *Hyperfine Structure and Nuclear Radiations*, eds. Matthias, E. and Shirley, D., North-Holland, Amsterdam, 1968, p. 911.
27. van Zorge, B. C., Caspers, W. J. and Dekker, A. J., *Phys. Stat. Sol.*, **18**, 761 (1966).
28. Gabriel, H., *Phys. Stat. Sol.*, **23**, 195 (1967).
29. Gabriel, H., Bosse, J. and Rander, K., *Phys. Stat. Sol.*, **27**, 301 (1968).
30. Bradford, E. and Marshall, W., *Proc. Phys. Soc.*, **87**, 731 (1966).
31. Blume, M., *Phys. Rev.*, **174**, 351 (1968).
32. Clauser, M. J. and Blume, M., *Phys. Rev.* **B3**, 583 (1971).
33. Clauser, M. J., *Phys. Rev.* **B3**, 3748 (1971).
34. Schwegler, H., *Phys. Stat. Sol.*, **41**, 353 (1970).
35. Schwegler, H., *Fortschritte der Physik*, **20**, 251 (1972).
36. Hirst, L. L., *J. Phys. Chem. Solids*, **31**, 655 (1970).
37. Hartman-Boutron, F., *Phys. Rev.* **B5**, 2113 (1974).
38. Dattagupta, S., *Phys. Rev.* **B12**, 3584 (1975).

39. Dattagupta, S., *Phys. Rev.* **B12,** 47 (1975).

40. Afanas'ev, A. M. and Onishchenko, E. U., *Zh. Eksp. Teor. Fiz.*, **74,** 1115 (1978), *Sov. Phys. JETP*, **47,** 585 (1978).

41. Hartman-Boutron, F., *Ann. de Phys.*, **9,** 285 (1975).

42. Dattagupta, S., *Hyperfine Interactions*, **11,** 77 (1981).

43. Bloembergen, N., Shapiro, S., Pershan, P. S. and Artman, J. O., *Phys. Rev.*, **114,** 445 (1959).

44. Mørup, S. and Thrane, N., *Chem. Phys. Lett.*, **21,** 363 (1973).

45. Mørup, S., Knudsen, J. E., Nielsen, M. K. and Trumpy, G., *J. Chem. Phys.*, **65,** 536 (1976).

46. Sontheimer, F., Nagy, D. L., Dézsi, I., Lohner, T., Ritter, G., Seyboth, D. and Wegener, H., *J. Physique Colloque*, **35,** C6–443 (1974).

47. Mørup, S. and Knudsen, J. E., *Chem. Phys. Lett.*, **40,** 292 (1976).

48. Knudsen, J. E., unpublished results.

49. Sontheimer, F., Seyboth, D. and Wegener, H., *Proceedings International Conference on Mössbauer Spectroscopy*, eds. Hrynkiewicz, A. Z. and Sawicki, J. A., Cracow, 1975, p. 399.

50. Wegener, H., Wimmer, K., Seyboth, D. and Zeman, N., *Hyperfine Interactions*, **12,** 15 (1982).

51. Date, S. K., *J. Phys. Soc. Japan*, **30,** 1203 (1971).

52. Srivastava, J. K. and Prasad, K. G., *Phys. Lett.*, **40** A, 37 (1972).

53. Ohya, T. and Ôno, K., *J. Phys. Soc. Japan*, **28,** 1092 (1970).

54. Goldanskii, V. I., Novikov, G. V., Mikhailov, A. I., Trukhtanov, V. A. and Abdrashitov, E. F., *Zh. Eksp. Teor. Fiz. Pis. Red.* **12,** 464 *JETP Lett.*, **12,** 323 (1970).

55. Date, S. K., Keune, W., Engelman, H., Gonser, U. and Dézsi, I., *J. Physique Colloque*, **37,** C6–117 (1976).

56. van Vleck, J. H., *Phys. Rev.*, **57,** 426 (1940).

57. Orbach, R., *Proc. Royal Soc. A.*, **264,** 458 (1961).

58. Al'tschuler, S. A. and Kozyrev, B. M., *Electron Paramagnetic Resonance in Compounds of Transition Elements*, Wiley New York, 1974.

59. Suzdalev, I. P., Afanas'ev, A. M., Plachinda, A. S., Goldanskii, V. I. and Makarov, E. F., *Zh. Eksp. Teor. Fiz.*, **55,** 1752 (1968). *Sov. Phys. JETP*, **28,** 923 (1969).

60. Svetozarov, V. V., *Fiz. Tverd. Tela*, **12,** 1054 (1970). *Sov. Phys. Solid State*, **12,** 826 (1970).

61. Bhargava, S. C., Knudsen, J. E. and Mørup, S., *J. Phys. C.*, **12,** 2879 (1979).

62. Svetozarov, V. V., *Fiz. Tverd. Tela*, **13,** 1263 (1971). *Sov. Phys. Solid State*, **13,** 1057 (1971).

63. Mørup, S., *Mössbauer Effect Methodology*, eds Gruverman, I. J., Seidel, C. W. and Dieterly, D. K., Plenum Press, New York, 1974, Vol. 9., p. 127.

64. Knudsen, J. E. and Mørup, S., *Proceedings of International Conference on Mössbauer Spectroscopy, Bucharest*, Romania, ed. Barb, D. and Tarina, D., 1977, Vol. 1., p. 205.

65. Mørup, S. and Knudsen, J. E., *J. Phys. C.* **18,** 2943 (1985).

66. Jensen, J. H., *Phys. Kondens Material*, **13,** 273 (1971).

67. Ruby, S. L., Love, J. C., Flinn, P. A. and Zabransky, B. J. *Appl. Phys. Lett.*, **27,** 320 (1975).

68. Ruby, S. L., Zabransky, B. J. and Flinn, P. A., *J. Physique Colloque*, **37,** C6–745 (1976).

69. Flinn, P. A., Zabransky, B. J. and Ruby, S. L., *J. Physique Colloque*, **37,** C6–739 (1976).

70. Vasques, A. and Flinn, P. A., *J. Chem. Phys.*, **72,** 1958 (1980).

71. Frauenfelder, H., Petzko, G. A. and Tsernoglou, O. *Nature*, **280,** 558 (1979).

72. Keller, H. and Debrunner, P. G., *Phys. Rev. Lett.*, **45,** 68 (1980).

73. Knapp, F. W., Fischer, S. F. and Parak, F., *J. Chem. Phys.*, **86,** 5042 (1982).

74. Parak, F., Knapp, E. W. and Kucheida, D., *J. Mol. Biol.*, **161,** 177 (1982).

75. Singwi, K. S. and Sjölander, A., *Phys, Rev.*, **120,** 1093 (1960).

76. Dézsi, I., Gorobchenko, V., Komor, M., Vértes, A. and Tsirskishviei, K., *Acta Chim. Acad. Sci. Hung.* **70,** 329 (1971).

77. Dufresne, A., Knudsen, J. M., Moreira, J. E. and Skeff Neto, K., *Chem. Phys. Lett.* **20,** 108 (1973).

78. Knudsen, J. E., Larsen, E., Moreira, J. E. and Faurskov Nielsen, O., *Acta Chem. Scand. A.*, **29,** 833 (1975).

79. Chaves, F. A. B. and Garg, V. K., *J. Inorg. Nucl. Chem.*, **37,** 2283 (1975).

80. Vértes, A., Ranogajec–Komor, M. and Gelencsér, P., *Acta Chem. Acad. Hung.*, **77,** 55 (1973).

81. Ohya, T. and Ôno, K., *J. Chem. Phys.*, **57,** 3210 (1972).

82. Mørup, S., Dumesic, J. A. and Topsøe, H., in: *Applications of Mössbauer Spectroscopy*, Vol. 2., ed. Cohen, R. L., Academic Press, New York, 1980, p. 1.

83. Dormann, J. L., *Rev. Phys. Appl.*, **16,** 275 (1981).

84. Mørup, S., Topsøe, H. and Clausen, B. S., *Phys. Scripta*, **25,** 713 (1982).

85. Morrish, A. H. and Haneda, K., *J. Magn. Magn. Mat.*, **35,** 105 (1983).
86. Mørup, S. and Topsøe, H., *Appl. Phys.*, **11,** 63 (1976).
87. Mørup, S., Topsøe, H. and Lipka, J., *J. Physique Colloque*, **37,** C6–287 (1976).
88. Mørup, S., *J. Magn. Magn. Mat.*, **37,** 39 (1983).
89. Rawson, H., *Inorganic Glass–Forming Systems*, Academic Press, New York, 1967.
90. Doremus, R. H., *Glass Science*, Wiley, New York, 1973.
91. Ohya, T. and Ôno, K., *J. Phys. Soc. Japan*, **34,** 376 (1973).
92. Plachinda, A. S. and Makarov, E. F., *Chem. Phys. Lett.*, **15,** 627 (1972)d.
93. Plachinda, A. S. and Makarov, E. F., *Chem. Phys. Lett.*, **25,** 364 (1974).
94. Angell, G. A. and Sare, E. J., *J. Chem. Phys.*, **52,** 1058 (1970).
95. Vuillard, G., *Ann. Chim.* (*Paris*), **2,** 233 (1957).

4. SHORT RANGE ORDER IN FROZEN AQUEOUS SOLUTIONS OF IRON(II) SALTS

4.1. INTRODUCTION

Mössbauer spectroscopy is sensitive to the local order around the resonant nucleus. The parameters of the hyperfine interaction bear a great deal of structural information. In an ordered crystal sharp resonance lines appear in Mössbauer spectrum.

In the vitreous state the resonance lines are usually very broad due to the distribution of the hyperfine fields. Examples are ferromagnetic metallic glasses [1], glassy ferrous halogenides [2], chalcogenide glasses [3], etc.

Mössbauer parameters of frozen aqueous solutions of various high-spin iron(II) salts in the vitreous state show, however, a surprizing uniformity (see Table 4.1). Moreover, the resonance lines are rather narrow (ca 0.4 mm/s^{-1}). Therefore, in the early stage of Mössbauer studies, it was suggested [5, 12] that the local environment of the Fe^{2+} ion was crystalline in this state.

Even so, a great deal of structural information could be gained from conventional Mössbauer studies on frozen aqueous solutions of high-spin iron(II) salts. The uniformity of the spectra reflects in some sense the uniformity of the environments of the Fe^{2+} ions. The main conclusion of these studies was that, at least in the first

Table 4.1.
Mössbauer parameters of frozen aqueous solutions of some high-spin ferrous salts as quenched to liquid N_2

Salt	Isomer shift,* δ mm/s	Quadrupole splitting, ΔE_Q mm/s	Literature
$FeCl_2$	1.31	3.30	[4]
	1.27	3.26	[5]
	1.38	3.35	[7]
	–	3.32	[8]
	1.30	3.10	[9]
	1.38	3.32	[10]
$FeBr_2$	1.35	3.25	[9]
FeI_2	1.35	3.25	[9]
FeF_2	1.32	3.27	[11]
$Fe(ClO_4)_2$	1.43	3.40	[4]
	–	3.32	[6]
$FeSO_4$	1.41	3.30	[4]
	1.33	3.45	[5]
$Fe(NH_4)_2(SO_4)_2$	1.46	3.40	[4]

* Relative to α-Fe at 295 K.

approximation, all Fe^{2+} ions are forming $[Fe(H_2O)_6]^{2+}$ coordination entities of octahedral geometry [13].

The disappearence of Mössbauer effect around 170 K [12] and the appearance of the glass transition in the DTA curves at the same temperature [7, 14] have proved that the environment of the Fe^{2+} ions was originally amorphous. Therefore, at least two questions remained open:

(i) why is it that—presumably random—distortion of the water octahedra do not result in a considerable line broadening;

(ii) why cannot a strong anionic effect be observed although it is well-known that small anions like Cl^- do form aqua coordination entities with divalent transition metal cations while large anions like ClO_4^- do not?

The aim of this chapter is to attempt to answer the above questions using the method of "magnetically perturbed Mössbauer spectra", i.e. Mössbauer spectroscopy at low temperatures and in high external magnetic fields.

4.2. THE MÖSSBAUER SPECTRUM OF Fe^{2+} IN EXTERNAL MAGNETIC FIELDS

A Mössbauer spectrum reflects the hyperfine interaction of the nucleus with its environment. In the case of an Fe^{2+} ion—due to its sixth d electron—the major contribution to the hyperfine interaction comes from the 3d electrons. Therefore, the calculation of the Mössbauer spectrum of an Fe^{2+} ion involves three steps:

(i) solution of the problem of the electron shell with regard to the ligand field (electric field of the surrounding ligands), spin-orbit coupling and external magnetic field,

(ii) calculation of the EFG and of the induced magnetic fields for the individual electronic levels and, in the case of fast relaxation, the calculation of their statistical average, and

(iii) calculation of the splitting of the nuclear levels and of the transition probabilities, i.e. the calculation of the spectrum.

To carry out these calculations rather sophisticated computer programs needed especially in the case when the iron(II) ion is in a polycrystal or even in an amorphous substance. In the first case one has to average over the relative directions of the crystal axes, while in the second case, additionally, the distribution of the ligand field should be taken into account. Such computer programs have been first developed in the Erlangen group by Spiering and his co-workers [15, 16]. In the following, the way of such calculations will be described.

4.2.1. ELECTRONIC HAMILTONIAN AND SPLITTING OF THE GROUND STATE

As already mentioned in Section 1.3.4, the ground state of a free Fe^{2+} ion is, according to Hund's rule, ^5D (five spins up and one spin down). This high spin state is stable in weak crystal fields. Some textbooks discuss the ligand field theory of transition metal ions [17–19] even as applied especially for Mössbauer spectroscopy [20]. Therefore, we are going to deal only with the aspects here which are relevant for the $[Fe(H_2O)_6]^{2+}$ coordination ion.

In the case of weak crystal fields (the crystal field is weaker than the Coulomb interaction of the electrons) the ^5D electronic system is described by the following Hamiltonian:

$$\hat{H}_{el} = \hat{H}_c + \hat{H}_{so} + \hat{H}_z + \hat{H}_{ss}. \tag{4.1}$$

Here $\hat{H}_c$ is the crystal field, $\hat{H}_{so}$ is the spin-orbit coupling, $\hat{H}_z$ is the Zeeman effect in the external magnetic field and $\hat{H}_{ss}$ is the spin-spin coupling of the electrons. The strength of the interactions described by the individual terms in Eq. (4.1) is for each term approximately one order of magnitude lower than for the preceding term.

The crystal field Hamiltonian $\hat{H}_c$ can be split up into terms ordered according to a decrease in symmetry. In the case of octahedrally coordinated Fe^{2+} ions the strongest component of the crystal field is the cubic one (point group O_h). This interaction ($\hat{H}_{O_h}$) results in a splitting (ca 10^4 cm^{-1}) of the ^5D state into an orbital triplet $^5T_{2g}$ and an orbital doublet ^5E_g. In octahedral coordination ions the triplet is the lower lying state (cf. Fig. 4.1).

If the symmetry is decreased the new point group is some subgroup of O_h. In the case of the $[Fe(H_2O)_6]^{2+}$ coordination ion the symmetry is usually not far from trigonal (the octahedron is distorted along a C_3 axis). The ^5E_g state remains degenerate in the presence of a crystal field of D_{3d} symmetry ($\hat{H}_{D_{3d}}$). The $^5T_{2g}$ triplet, however, will split into an orbital singlet $^5A_{1g}$ and an orbital doublet ^5E_g. Typical trigonal splittings are

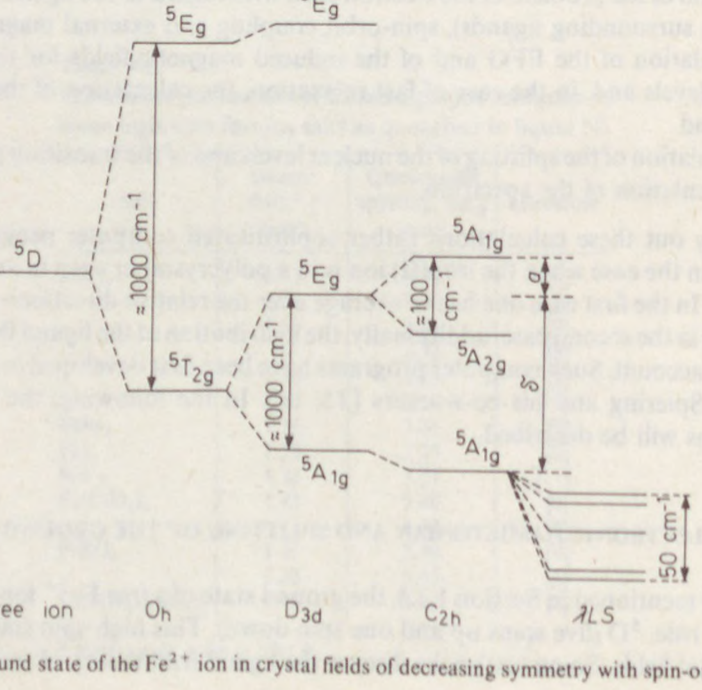

Fig. 4.1. The ground state of the Fe^{2+} ion in crystal fields of decreasing symmetry with spin-orbit coupling

$\lesssim 10^3\ \mathrm{cm}^{-1}$. If the octahedron is streched along the C_3 axis the doublet is the ground state, while, if it is compressed, the singlet.

If the symmetry is further decreased (e.g. to C_{2h}) all orbital degeneracy is removed. This component of the crystal field ($\hat{H}_{C_{2h}}$) splits the doublets into singlets the typical splitting being ca $10^2\ \mathrm{cm}^{-1}$.

In the above example $\hat{H}_c$ consists of three terms:

$$\hat{H}_c = \hat{H}_{O_h} + \hat{H}_{D_{3d}} + \hat{H}_{C_{2h}} \tag{4.2}$$

The spin-orbit coupling

$$\hat{H}_{so} = \lambda \mathbf{LS} \tag{4.3}$$

partly removes the fivefold spin degeneracy. The spin-orbit coupling constant is $\lambda = -114\ \mathrm{cm}^{-1}$ for the free Fe^{2+} ion [21].

An external magnetic field **H** completely removes the spin degeneracy by the Zeeman effect:

$$\hat{H}_z = \mu_B(\mathbf{L} + 2\mathbf{S})\mathbf{H} \tag{4.4}$$

μ_B being the Bohr magneton. The corresponding shift of the levels is $\lesssim 5\ \mathrm{cm}^{-1}$ for magnetic fields < 4T.

The last term of $\hat{H}_{el}$ in Eq. (4.1) describes the spin-spin interaction.

$$\hat{H}_{ss} = \rho\left[(\mathbf{LS})^2 + \frac{1}{2}\mathbf{LS} - \frac{1}{3}L(L+1)S(S+1)\right]. \tag{4.5}$$

The coupling constant ρ is, however, rather low: $0.18\ \mathrm{cm}^{-1}$ from the theory [22] and $0.95\ \mathrm{cm}^{-1}$ from the experiment [23] where higher order terms of the spin orbit coupling also contribute to the measurement [24]. Therefore, this interaction will be neglected.

Up to this point we have assumed that the electrons of the Fe^{2+} ion do not overlap with the electrons of the ligands. This is never the case and this fact (the covalency of the chemical bond) should be taken into account in the Hamiltonian $\hat{H}_{el}$. If the binding is nearly ionic which is certainly the case for the iron(II) hexaqua coordination entity the usual way to account for covalency is to multiply all constants containing radial integrals by the square of the covalency parameter $\alpha < 1$. The compression or expansion of the radial wave function can be taken into account in the same way.

To solve the Schrödinger equation with $\hat{H}_{el}$ relating to ^5D state we have to diagonalize a 25×25 matrix. (All the other terms are lying so high that they are neither thermally populated nor mixed to the ground term via spin-orbit interaction.) Also the ^5E_g orbital doublet is lying so high (ca $10^4\ \mathrm{cm}^{-1}$) that it is never thermally populated. Its spin-orbit admixture to the $^5T_{2g}$ triplet is of 1% only which may play some role in special cases. As a rule, however, this contribution can also be neglected thereby restricting the problem to the $^5T_{2g}$ space i.e. to the diagonalization of a 15×15 matrix.

The matrix elements of the magnetic field operator $\hat{H}_z$ are small as compared to the orbital splitting of the $^5T_{2g}$ state. Therefore $\hat{H}_z$ has been diagonalized within the space of five spin states which are split by the spin-orbit coupling $\hat{H}_{so}$. In our case of polycrystalline or glassy materials measured at low temperatures only the five lowest eigenstates and eigenvalues are calculated for the different directions of the magnetic field with respect to the crystalline field.

We return to the concrete form of the matrices in Section 2.3.

4.2.2. HYPERFINE INTERACTIONS AND MÖSSBAUER SPECTRUM

The electric field gradient and the internal magnetic field strength are calculated as described in Sections 1.3.4 and 1.3.5. In the case of iron(II) frozen aqueous solutions the large quadrupole splitting clearly shows that the orbital ground state is a singlet, the higher states being depopulated at 4.2 K. Therefore both the valence EGF (see Eqs 1.64, 1.65) and the hyperfine field components (see Eqs 1.67–69) can be calculated as thermal averages from the lowest-lying spin quintet resulting mainly from the ground state orbital singlet. A lot of computer time can be saved by calculating the valence EGF from the lowest five spin states without external magnetic field. This is why the magnetic perturbation needs to be calculated only for the lowest five states, from which the induced magnetic fields are then determined. This is the only part of the calculation which should be performed for all directions of the external magnetic field.

There is no simple way for a reliable calculation of the lattice EFG (see Eqs 1.62, 1.63). Since it is much less than the ionic contribution in an Fe^{2+} ion, we are just neglecting it.

Once the EFG and the effective magnetic field at the nucleus are known it is possible to calculate Mössbauer spectrum of any direction of the γ-quanta. The principles of such a calculation have already been described in Chapter 1. In the general case, when $\hat{H}_Q$ and $\hat{H}_M$ do not commute all the eight possible transitions in Fig. 1.4 are allowed. These eight-line spectra are calculated by solving the eigenvalue problems of $\hat{H}_Q + \hat{H}_M$ for the nuclear excited ($I = 3/2$) and ground ($I = 1/2$) state for many directions of the external field. The resultant spectrum is the average [25] of these spectra. For the calculation of the absorption spectra polarization and blackness effects (see Sections 1.5.1 and 1.5.2) have also been taken into account [26].

4.2.3. NORMAL COORDINATES AND SYMMETRY OF THE CRYSTAL FIELD

The hyperfine interaction of the ^{57}Fe nucleus depends on certain matrix elements which in turn depend on the wave functions of the Fe^{2+} ion. For a certain point symmetry, there exist some restrictions for the angular part of the wave function. These restrictions may considerably reduce the number of free parameters in the wave functions. Therefore it may be possible to get information on the local symmetry of the Fe^{2+} ion from the shape of Mössbauer spectra. Our final aim is to determine the distortions of the $[Fe(H_2O)_6]^{2+}$ coordination ion from magnetically perturbed Mössbauer spectra or, in the case of glassy frozen solutions, the distribution of these distortions.

The normal distortions (or, dynamically, the normal vibrations) of the hexaaqua coordination entity can be classified according to the irreducible representations of the cubic point group O_h [27]. Six of the 21 degrees of freedom are translation and rotation the rest being $A_{1g} + E_g + T_{2g} + 2T_{1u} + T_{2u}$. We are interested in the interaction of 3d electrons with the crystal field of the distorted octahedron. Since the d electrons are of even parity, first order matrix elements of odd normal distortions (T_{1u} and T_{2u}) vanish. A_{1g} distortions are of cubic symmetry and will not, therefore, influence the relative energies of the T_{2g} substates. The other two distortions E_g and T_{2g} interact with the T_{2g}

electronic state. The crystal field Hamiltonian can be parametrized in terms of the ε_g and τ_{2g} normal coordinates (the distortions will be denoted hereafter by the corresponding small greek letters) [28]:

$$\hat{H}_c = \frac{L_\varepsilon}{2\sqrt{3}} \begin{pmatrix} u-\sqrt{3}v & 0 & 0 \\ 0 & u+\sqrt{3}v & 0 \\ 0 & 0 & -2u \end{pmatrix} - \frac{L_\tau}{\sqrt{6}} \begin{pmatrix} 0 & \zeta & \eta \\ \zeta & 0 & \xi \\ \eta & \xi & 0 \end{pmatrix}. \tag{4.6}$$

Here u and v are the ε while ξ, η, ζ the τ normal coordinates as shown in Fig. 4.2. The normal coordinates are dimensionless since they are expressed in units of $\sqrt{\frac{\hbar}{M\omega}}$, M being the mass of a water molecule and ω the vibration frequency of the corresponding normal mode. L_ε and L_τ are the reduced matrix elements of the ε- and τ-mode coupling, respectively. As base functions the real orbital eigenfunctions $|yz\rangle$, $|xz\rangle$ and $|xy\rangle$ [17] have been used where the coordinate axes are pointing towards the vertices of the undistorted octahedron.

In order to find relations between point symmetry and $\hat{H}_c$ the relations of normal distortions and symmetry should be discussed.

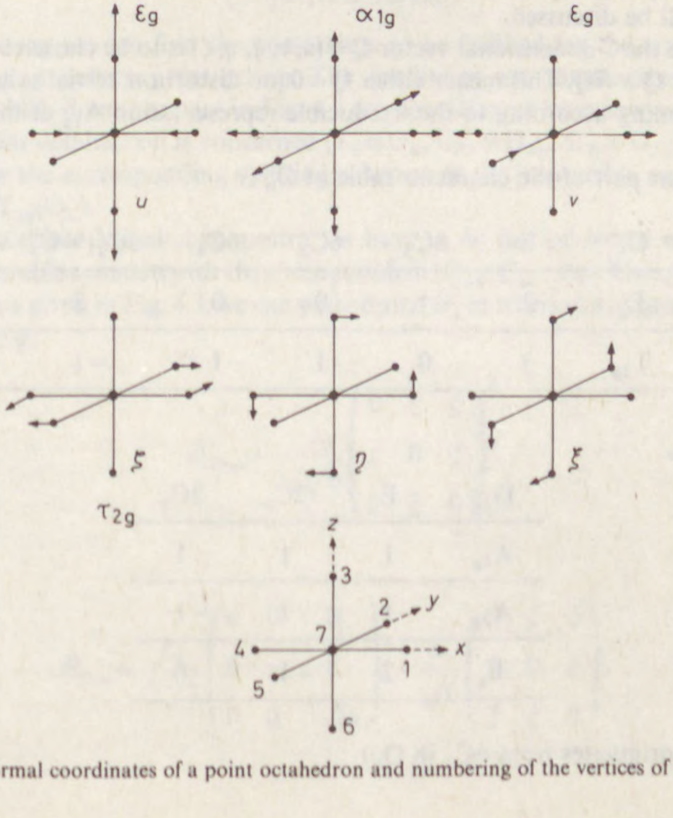

Fig. 4.2. Even normal coordinates of a point octahedron and numbering of the vertices of the octahedron

If the vertices of the water octahedron are numbered as shown in Fig. 4.2 the ε and τ distortions can be expressed as linear combinations of the Cartesian coordinates of the deviations of the single water molecules:

$$u=\frac{1}{\sqrt{12}}(-X_1-Y_2+2Z_3+X_4+Y_5-2Z_6)$$

$$v=\frac{1}{2}(X_1-Y_2-X_4+Y_5), \tag{4.7}$$

$$\xi=\frac{1}{2}(Z_2+Y_3-Z_5-Y_6)$$

$$\eta=\frac{1}{2}(Z_1+X_3-Z_4-X_6)$$

$$\zeta=\frac{1}{2}(Y_1+X_2-Y_4-X_5). \tag{4.8}$$

(We shall consider the water molecules to be geometrical points.) Obviously, if and only if $u=v=\xi=\eta=\zeta=0$ the octahedron is undistorted and the point symmetry at the central ion is O_h. We should like to find the conditions which the normal distortions should fulfil so that the symmetry group is a prescribed subgroup of O_h. This can be done with simple group-theoretical methods. To show an example the case of D_{3d} symmetry will be discussed.

In this case the 5-dimensional vector $\mathbf{Q}=(u, v, \xi, \eta, \zeta)$ is to be chosen so that for all $\boldsymbol{R}\in D_{3d}$ holds: $\mathbf{Q}=\boldsymbol{R}\mathbf{Q}$. This means either $\mathbf{Q}=\mathbf{0}$ (no distortion: trivial solution) or that $\mathbf{Q}$ is transforming according to the irreducible representation A_{1g} of the group D_{3d} (invariant).

The relevant part of the character table of O_h is:

O_h	E	$8C_3$	$6C_2$	$6C_4$	$3C_2(=C_4^2)$
E_g	2	−1	0	0	2
T_{2g}	3	0	1	−1	−1

while for D_{3d}:

D_{3d}	E	$2C_3$	$3C_2$
A_{1g}	1	1	1
A_{2g}	1	1	−1
E_g	2	−1	0

($3C_2$ in D_{3d} originates from $6C_2$ in O_h)

Consequently:

$$E_g(O_h) \rightarrow E_g(D_{3d}), \tag{4.9}$$

$$T_{2g}(O_h) \rightarrow A_{1g}(D_{3d}) + E_g(D_{3d}) \tag{4.10}$$

This means that $E_g(O_h)$ does not contain $A_{1g}(D_{3d})$; in words there is no invariant in this case. Therefore, the only solution is the trivial one: $u=v=0$. On the other hand, there exists one invariant for the τ-coordinates. To find out the form of this invariant we have to look at the transformation properties of ξ, η and ζ as expressed in Eqs (4.7).

A 120° rotation along the C_3 axis means the following transformation for the Cartesian axes:

$$X \rightarrow Z; \quad Y \rightarrow X; \quad Z \rightarrow Y \tag{4.11}$$

and for the indices:

$$1 \rightarrow 3; \quad 2 \rightarrow 1; \quad 3 \rightarrow 2; \quad 4 \rightarrow 6; \quad 6 \rightarrow 5; \quad 5 \rightarrow 4. \tag{4.12}$$

Performing transformations (4.11) and (4.12) in Eq. (4.8), we get:

$$\xi \rightarrow \zeta; \quad \eta \rightarrow \xi; \quad \zeta \rightarrow \eta \tag{4.13}$$

or, in other words, $\xi = \eta = \zeta =$ arbitrary number. This is the only invariant in D_{3d} which is why the conditions for D_{3d} symmetry are:

$$u = v = 0$$

$$\xi = \eta = \zeta = \text{arbitrary}. \tag{4.14}$$

In the same way we can find the constraints to be fulfilled for the ε and τ normal coordinates in a certain point group. The conditions are summarized in Fig. 4.3. Subgroups which do not appear in Fig. 4.3 are not different from those appearing, as long as a point octahedron is concerned ($T_h \equiv O_h$, $C_{4h} \equiv D_{4h}$, $C_{3i} \equiv D_{3d}$). Figures 4.4 and 4.5 show the corresponding splitting schemes of the irreducible representations $E_g(O_h)$ and $T_{2g}(O_h)$.

Now, to calculate Mössbauer spectra, we have to do the following: we choose the highest reasonable symmetry for the given problem (D_{3d}, C_{2h}, etc.). Using Eq. (4.6) and the constraints given in Fig. 4.3, we can write down $\hat{H}_c$ in terms of a reduced number of parameters, e.g.:

$$\hat{H}_{D_{3d}} = -\frac{L_\tau}{\sqrt{6}} \begin{pmatrix} 0 & \xi & \xi \\ \xi & 0 & \xi \\ \xi & \xi & 0 \end{pmatrix} \tag{4.15}$$

or

$$\hat{H}_{C_{2h}} = \frac{L_\varepsilon}{2\sqrt{3}} \begin{pmatrix} u & 0 & 0 \\ 0 & u & 0 \\ 0 & 0 & -2u \end{pmatrix} - \frac{L_\tau}{\sqrt{6}} \begin{pmatrix} 0 & \zeta & \xi \\ \zeta & 0 & \xi \\ \xi & \xi & 0 \end{pmatrix}. \tag{4.16}$$

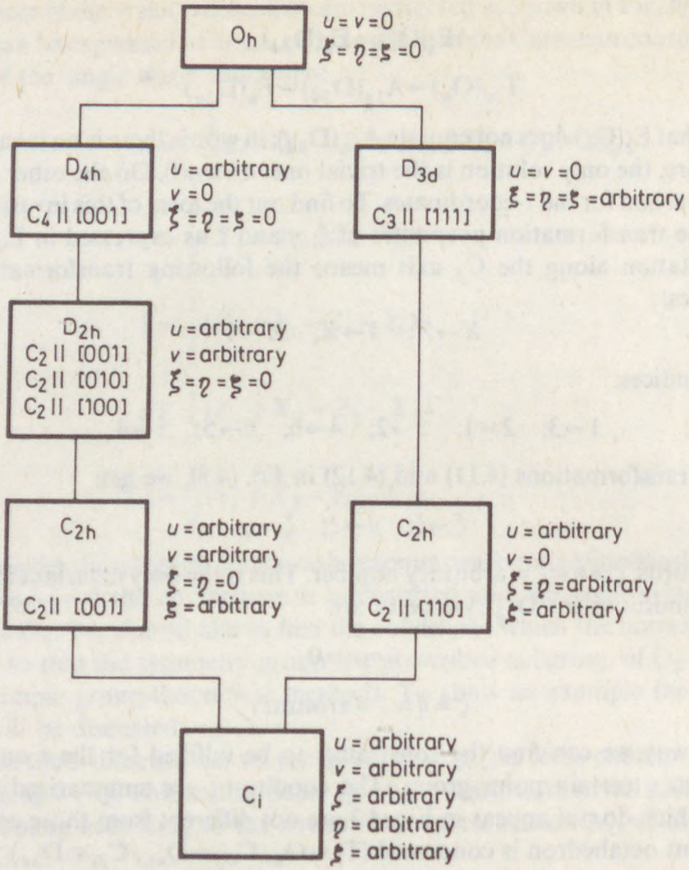

Fig. 4.3. Constraints for the normal coordinates in case of decreasing symmetry in a point octahedron

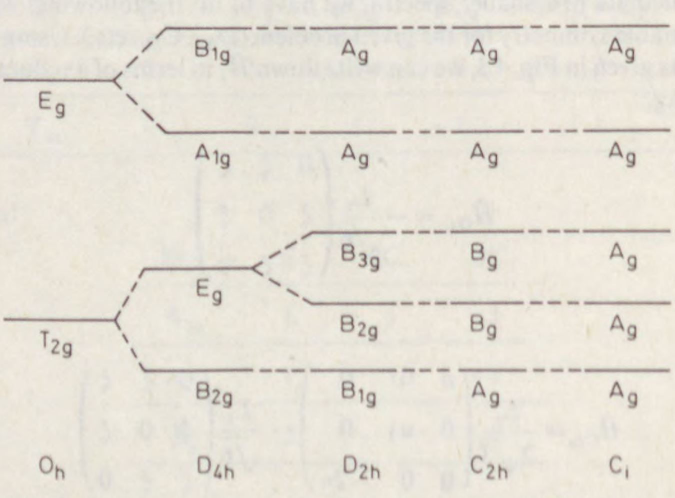

Fig. 4.4. Splitting of the irreducible representations of the cubic point group O_h with decreasing symmetry (tetragonal branch)

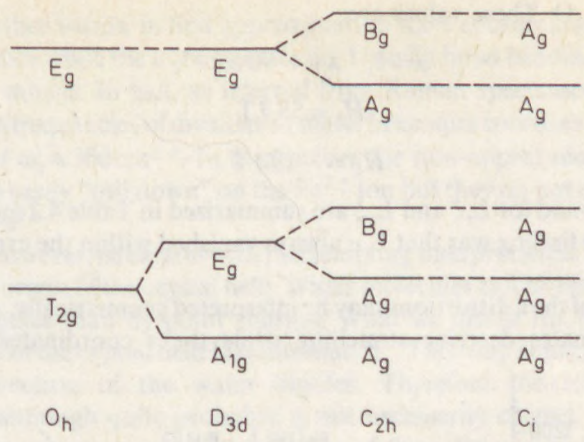

Fig. 4.5. Splitting of the irreducible representations of the cubic point group O_h with decreasing symmetry (trigonal branch)

In the crystal field Hamiltonian the reduced matrix elements L_ε and L_τ always appear in company of the normal coordinates as their coefficients. Therefore, their values do not play any role in the calculations as long as we are interested in the products of normal coordinates and reduced matrix elements only. $\hat{H}_{D_{3d}}$ has one free parameter $L_\tau \xi$ while $\hat{H}_{C_{2h}}$ has three: $L_\varepsilon u$, $L_\tau \xi$ and $L_\tau \zeta$. Having made some guess for these parameters we can solve the Schrödinger equation with $\hat{H}_{el}$ of Eq. (4.1) and proceed as described in Sections 4.2.1 and 4.2.2.

A systematic study on a series of iron(II) crystalline hydrates all containing the $[Fe(H_2O)_6]^{2+}$ ion has been made on polycrystalline samples by Spiering and other members of the Erlangen group [15, 16, 29, 30]. The substances investigated: $Fe[SiF_6] \cdot 6H_2O$, $Fe(ClO_4)_2 \cdot 6H_2O$, $Fe[BF_4]_2 \cdot 6H_2O$, Fe in $Co[BF_4]_2 \cdot 6H_2O$ and $FeCl_2 \cdot 9H_2O$ all have a trigonal symmetry in good approximation with the exception of the last compound whose crystal structure is not known.

In spite of this, any attempt to describe the spectra with $\hat{H}_{D_{3d}}$ failed. The next lower symmetry is then C_{2h}. In fact, all polycrystalline spectra could be reasonably well described supposing a C_{2h} point symmetry for the iron(II) ion.

The parameters used in this procedure belong to two different groups: *a*) the covalency parameter α, the spin-orbit coupling constant λ and the hyperfine coupling constants H_L and H_C are properties of the $[Fe(H_2O)_6]^{2+}$ ion itself and should be the same for all compounds; *b*) the normal coordinates of the octahedron (or, more exactly, of the crystal field) depend on the surroundings and may be different from compound to compound.

The best values for α, λ, H_L and H_C were obtained [30] from a simultaneous evaluation of magnetic susceptibility, specific heat, far infrared (FIR) ESR and single crystal Mössbauer data with and without magnetic field on $Fe(NH_4)_2(SO_4)_2 \cdot 6H_2O$ and of magnetically perturbed polycrystalline Mössbauer spectra and FIR–ESR data on $Fe[SiF_6]\cdot 6H_2O$. These values are:

$$\alpha=1, \quad \lambda=-90\,\mathrm{cm}^{-1},$$
$$H_L=55.7\,\mathrm{T}$$
$$H_C=-29.1\,\mathrm{T}. \tag{4.17}$$

The best values found for $L_\tau\xi$ and $L_\tau\xi$ are summarized in Table 4.2 and shown in Fig. 4.6. A remarkable finding was that $L_\varepsilon u$ always vanished within the experimental error [30].

The vanishing of the ε distortions may be interpreted geometrically. As shown in Fig. 4.2 the ε coordinates describe stretching while the τ coordinates bond bending

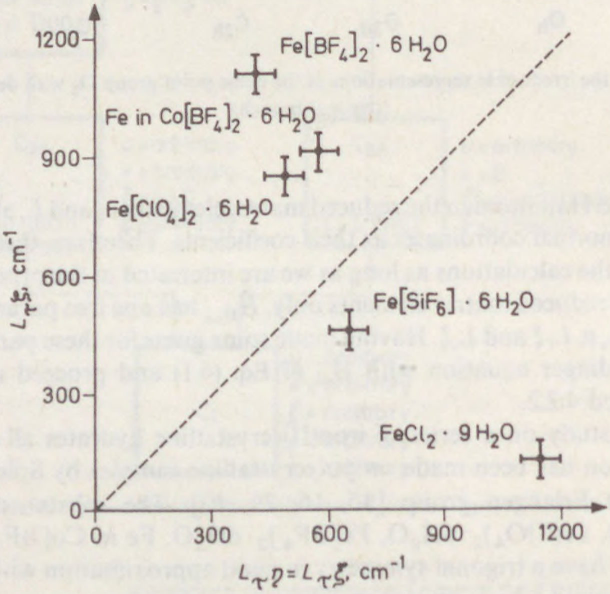

Fig. 4.6. Ligand field parameters of various ferrous hexaaqua coordination entities. The dotted line corresponds to $\xi=\eta=\zeta$ (D_{3d} symmetry)

Table 4.2
Ligand field parameters of the $Fe[(H_2O)_6]^{2+}$ ion

Compound	$L_\tau\xi$ cm^{-1}	$L_\tau\zeta$ cm^{-1}	$\delta+a$ cm^{-1}	$\delta-a$ cm^{-1}
$Fe[BF_4]_2\cdot 6H_2O$	400 ± 40	1110 ± 40	650 ± 20	1000 ± 20
$Fe(ClO_4)_2\cdot 6H_2O$	480 ± 40	850 ± 40	650 ± 20	850 ± 20
Fe in				
$Co[BF_4]_2\cdot 6H_2O$	570 ± 40	910 ± 40	760 ± 20	940 ± 20
$Fe[SiF_6]\cdot 6H_2O$	650 ± 20	455 ± 20	770 ± 10	670 ± 10
$FeCl_2\cdot 9H_2O$	1140 ± 50	125 ± 20	1310 ± 25	730 ± 25

$\delta+a$ and $\delta-a$ are the splittings of the orbital levels (see Fig. 4.1) calculated from $L_\tau\xi$ and $L_\tau\zeta$ by diagonalizing $\hat{H}_{C_{2h}}$ of Eq. (4.16).

distortions. In other words, in first approximation the τ coordinates do not affect the iron-water distance while the ε coordinates do. Usually bond bending modes are softer than stretching modes. In fact, as inferred from Raman spectroscopy data [31–33] typical vibration frequencies of divalent 3d metal hexaaqua coordination entities are $\omega_\tau \approx 200\,\mathrm{cm}^{-1}$ and $\omega_\varepsilon \approx 300\,\mathrm{cm}^{-1}$. In this picture the non-appearance of u means that water molecules easily "roll down" on the Fe^{2+} ion but they do not easily change their distance from Fe^{2+}.

One should, however, be careful with this tempting interpretation. Finally, we do not really know the origin of the crystal field. Water molecules can be better approximated by extended dipoles than by point charges. What we did in Eq. (4.6) was simply a parametrization of the crystal field Hamiltonian $\hat{H}_c$. This may or may not be influenced e.g. by the direction of the water dipoles. Therefore the simple geometrical interpretation, although quite probable, is not necessarily correct.

The C_{2h} point symmetry and the vanishing of the ε distortions is by no means an absolutely general property of the $[Fe(H_2O)_6]^{2+}$ ion. Various data measured on single crystals of Mohr's salt ($Fe(NH_4)_2(SO_4)_2 \cdot 6H_2O$) can only be understood [34] admitting ε coordinates in $\hat{H}_c$. The absolute value of the ε coordinates is, however, less than that of the τ coordinates. Room temperature X-ray data [35] on the same compound show that Fe^{2+} occupies a site of no symmetry at all. Even so, the C_{2h} symmetry without ε distortions is a fair approximation of reality and deviations are exceptions rather than the rule.

4.3. MAGNETICALLY PERTURBED SPECTRA OF IRON(II) FROZEN AQUEOUS SOLUTIONS

The method of magnetically perturbed Mössbauer spectra as described in the previous section has proved to be rather informative for the distortions of the $[Fe(H_2O)_6]^{2+}$ ion in crystalline hydrates. Since short range order is a central problem in amorphous systems the method as applied to frozen aqueous solutions containing the Fe^{2+} ion seems to be promising. In this section we shall show first how magnetically perturbed spectra in amorphous systems should be calculated. Thereafter the spectra of $Fe(ClO_4)_2$ frozen aqueous solution will be discussed and the distribution of the normal distortions in this system will be determined. Finally, applications of the method to other problems (hydration, complex formation, glass formation) will be presented.

4.3.1. CALCULATION OF MAGNETICALLY PERTURBED SPECTRA OF Fe^{2+} IN AMORPHOUS SYSTEMS

In amorphous systems the environment of the Fe^{2+} ion is no longer uniform. Therefore, when applying the method to such systems first an assumption should be made for the distribution of the distortions of the water octahedra around the Fe^{2+} ion. Then many distorted octahedra should be constructed (e.g. by the Monte Carlo technique) and the Mössbauer spectra for all octahedra must be calculated (as described in Section 4.2) and summed up. The remaining ligand field parameters and the bare quadrupole splitting ΔE_Q^0 are then obtained in an iterative procedure by fitting the zero-field and magnetic-field spectra alternately.

There is a further problem concerning the quadrupole interaction. Since the lattice EFG has been neglected in the previous Section and since the quadrupole moment Q of the 14.4 keV nuclear level in ^{57}Fe is not known to a satisfactory accuracy, the bare quadrupole splitting $\Delta E_Q^0 = \frac{eQV_{zz}}{2}$ [see Eq. (1.42)] has been chosen so that it reproduced the measured quadrupole splitting when no external magnetic field was applied. This resulted, of course, in the fact that ΔE_Q^0 turned out to be somewhat (by ca $\pm 10\%$) different for different substances.

In the case of frozen aqueous solutions we cannot prescribe the value of the quadrupole splitting since the resonance lines are slightly and asymetrically broadened also in the absence of a magnetic field. This leads to the purely technical complication that ΔE_Q^0 should be handled as one of the model parameters. If the other model parameters are known we estimate ΔE_Q^0 and calculate the spectrum in zero field. If necessary the parameters are corrected and a new zero-field spectrum is calculated. When a good fit has been found the high-field spectra are calculated and compared with the experimental data. If necessary, new model parameters are chosen, new zero-field spectra are calculated, etc. The obvious way to fit simultaneously all measured spectra results, unfortunately, in programs demanding irrealistically long computer times.

4.3.2. DISTRIBUTION OF THE DISTORTIONS OF THE $[Fe(H_2O)_6]^{2+}$ ION IN FROZEN AQUEOUS SOLUTIONS OF $Fe(ClO_4)_2$

4.3.2.1. Experimental results

The distribution of the distortions of the water octahedron should obviously be studied on systems where the Fe^{2+} ion is completely hydrated forming exclusively $[Fe(H_2O)_6]^{2+}$ ions. Unfortunately, no X-ray diffraction measurements have been made till now on frozen aqueous solutions of iron(II) salts. In the liquid state, however, X-ray data [36] show that all Fe^{2+} ions are fully hydrated in an aqueous $Fe(ClO_4)_2$ solution. The presence of unperturbed hexaaqua coordination entities has been confirmed in liquid aqueous solutions of other divalent transition metal perchlorates, too [36–38]. Therefore, frozen aqueous solution of $Fe(ClO_4)_2$ has been chosen as model substance.

To ensure the highest possible glass-forming ability without adding glass former to the solution the concentration of $Fe(ClO_4)_2 \cdot 6H_2O$ dissolved in water was chosen to be 7.2 mol percent corresponding to the eutectic composition [14]. Samples with four different freezing rates have been prepared. The lowest rate (ca 0.3 K s^{-1}) was achieved by cooling the sample being in contact with a liquid nitrogen cooled brass block. A faster rate (ca 30 K s^{-1}) was ensured by immersing the absorber containing ca 0.5 ml solution into liquid nitrogen. An even faster rate (ca 100 K s^{-1}) was achieved by soaking up the solution with a filter paper and immersing it into liquid nitrogen. The sample was prepared of three filter paper sheets. To ensure the highest cooling rate (estimated to be $\gtrsim 10^3$ K s^{-1}) the solution was injected into a liquid nitrogen cooled rotating cylinder. A further sample with ca 30 K s^{-1} cooling rate has been prepared from a dilute solution containing 3.5 mg ml^{-1} ^{57}Fe in solution. The iron in $Fe(ClO_4)_2$ was enriched in ^{57}Fe to 80% in the latter case. In dilute solutions the local concentration of the frozen solution around the Fe^{2+} ion cannot be given definitely; it should be close to the minimum concentration of the glass formation [39] or to the eutectic concentration.

Mössbauer spectra have been taken in a liquid helium bath cryostat supplied with a superconducting coil. The applied magnetic field was parallel to the propagation direction of the gamma quanta. The source was ^{57}Co in Rh matrix at 295 K.

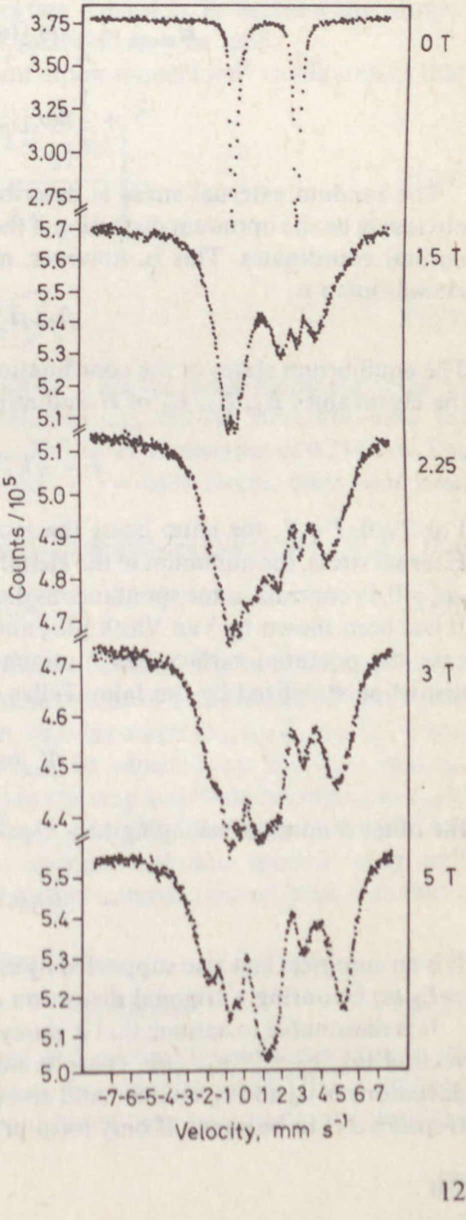

Fig. 4.7. Mössbauer spectra of a eutectic frozen aqueous solution of $Fe(ClO_4)_2$ at 4.2 K in various longitudinal applied magnetic fields

Spectra of the slowly ($0.3\ \mathrm{K\,s^{-1}}$) cooled sample are shown in Fig. 4.7. The corresponding spectra of the other four samples did not differ significantly.

4.3.2.2. Discussion

A direct way to calculate the distribution of the normal distortions of the water octahedron is to determine the normal coordinates belonging to the minimum of the free energy when the coordination entity is exposed to random external stresses. The elastic energy can be written in this case as

$$\hat{H}_{\mathrm{elastic}}=\frac{1}{2}\hbar\omega_{\varepsilon}[(u-u_0)^2+(v+v_0)^2]+$$
$$+\frac{1}{2}\hbar\omega_{\tau}[(\xi-\xi_0)^2+(\eta-\eta_0)^2+(\zeta-\zeta_0)^2]\,. \tag{4.18}$$

The random external stress is described here by $(u_0, v_0, \xi_0, \eta_0, \zeta_0)$. This would obviously be the optimum distortion if the electronic energy $\hat{H}_{\mathrm{e}}$ did not depend on the normal coordinates. This is, however, not the case (see Eq. (4.6)) and so the total Hamiltonian is:

$$\hat{H}=\hat{H}_{\mathrm{elastic}}+\hat{H}_{\mathrm{c}}\,. \tag{4.19}$$

The equilibrium states of the coordination entity can be calculated by determination the eigenvalues E_1, E_2, E_3 of $\hat{H}$ and minimization of the Helmholtz function

$$F=-kT\ln\sum_{i=1}^{3}\mathrm{e}^{-\frac{E_i}{kT}}\,. \tag{4.20}$$

For $T=0$, $F=E_1$ the latter being the ground state energy. Even in the absence of an external stress, the minimum of the Helmholtz function does not belong to $u=v=\xi=\eta=\zeta=0$, in contrast, some spontaneous distortion (Jahn–Teller effect) is always present. It has been shown by Van Vleck [40] and by Öpick and Pryce [41] that in the above case the potential surface has 7 minimum points three of which belong to a D_4 distortion stabilized by the Jahn–Teller energy

$$E_{\mathrm{JT}}(\varepsilon)=\frac{L_{\varepsilon}^2}{6\hbar\omega_{\varepsilon}} \tag{4.21}$$

the other 4 minima belonging to a D_3 distortion stabilized by

$$E_{\mathrm{JT}}(\tau)=\frac{L_{\tau}^2}{9\hbar\omega_{\tau}}\,. \tag{4.22}$$

It is an empirical fact also supported by calculations [42] that for $[\mathrm{Fe(H_2O)_6}]^{2+}$ $E_{\mathrm{JT}}(\tau)>E_{\mathrm{JT}}(\varepsilon)$ favouring a trigonal distortion of the complex.

It is reasonable to assume that a glassy environment can be represented by random vectors $(u_0, v_0, \xi_0, \eta_0, \zeta_0)$. There is no reason, however, to choose the standard deviations of u_0 and v_0 on one hand and of ξ_0, η_0 and ζ_0 on the other hand (σ_{ε} and σ_{τ}, respectively) to be equal. If only local properties are concerned it may be justified to compare the glass structure to a snapshot of thermal vibrations at a certain effective temperature T_0, i.e.

$$\frac{1}{2}\hbar\omega_\varepsilon\sigma_\varepsilon^2=\frac{1}{2}\hbar\omega_\tau\sigma_\tau^2=\frac{1}{2}k_B T_0\,. \tag{4.23}$$

In principle, $\hat{H}$ of Eq. (4.19) does not contain any further unknown parameters since the vibration frequencies ω_ε and ω_τ can be measured by optical spectroscopy while the reduced matrix elements L_ε and L_τ [i.e. $E_{JT}(\varepsilon)$ and $E_{JT}(\tau)$; see Eqs (4.21) and (4.22)] can be calculated. Unfortunately, no data of ω_ε and ω_τ for $[Fe(H_2O)_6]^{2+}$ are available for frozen aqueous solutions of Fe(II) salts. Also, the Jahn–Teller energies calculated by Bersuker [42] clearly contradict to the values of the trigonal splitting observed in various ferrous hexaaqua coordination entities (see Table 4.2). To decrease the number of the free parameters, however, two further relations may be used:

(i) It can be calculated [28] in terms of a point dipole model for d^6 configuration that

$$\frac{E_{JT}(\varepsilon)}{E_{JT}(\tau)}=\frac{9}{4}\frac{\omega_\tau^2}{\omega_\varepsilon^2}\left(\frac{1-\frac{25}{27}\eta_d}{1-\frac{5}{9}\eta_d}\right)^2 \tag{4.24}$$

where

$$\eta_d=\frac{3}{2}\frac{\langle r^4\rangle}{R^2\langle r^2\rangle} \tag{4.25}$$

R being the ligand-ion distance while $\langle r^2\rangle$ and $\langle r^4\rangle$ are the radial momenta of the 3d electrons. To estimate R in the frozen solution e.g. crystal structure data for $FeSiF_6\cdot 6H_2O$ [43] can be used suggesting an Fe^{2+}—H_2O distance of 0.214 nm. The calculated values $\langle r^2\rangle=1.390$ atomic units and $\langle r^4\rangle=4.498$ atomic units have been published [44]. Thus, $\eta_g=0.30$.

(ii) It is an empirical rule [28] for ionic coordination entities like $[Fe(H_2O)_6]^{2+}$ that

$$\omega_\tau/\omega_\varepsilon\approx 0.4\,. \tag{4.26}$$

To determine the distribution of the five normal coordinates u, v, ξ, η, ζ one has to generate random vectors $(u_0, v_0, \xi_0, \eta_0, \zeta_0)$ characterized by standard deviations σ_ε and σ_τ and has to solve the minimization problem for every single $(u_0, v_0, \xi_0, \eta_0, \zeta_0)$. Using Eqs (4.23–26) there remain 3 parameters only to be adjusted, e.g. $E_{JT}(\tau)$, ω_τ and σ_τ.

A series of spectra has been calculated [45] in this way and those belonging to $E_{JT}(\tau) = 140\ \mathrm{cm}^{-1}$, $\omega_\tau=150\ \mathrm{cm}^{-1}$ and $\sigma_\tau=0.60$ (i.e. to $E_{JT}(\varepsilon)=37.9\ \mathrm{cm}^{-1}$, $\omega_\varepsilon=375\ \mathrm{cm}^{-1}$ and $\sigma_\varepsilon=0.38$) reproduce the $Fe(ClO_4)_2$ frozen aqueous solution spectra fairly well. Unfortunately, however, in this set of parameters an internal contradiction is involved [31, 46].

The condition for a static Jahn–Teller effect is that

$$E_{JT}(\varepsilon)\gg\hbar\omega_\varepsilon \qquad \text{and} \qquad E_{JT}(\tau)\gg\hbar\omega_\tau\,, \tag{4.27}$$

otherwise the potential wells are not separated and no local bound states exist. In the previous calculation it was silently assumed that conditions (4.27) are fulfilled, otherwise a dynamical Jahn–Teller calculation should have been performed resulting in enormous computations. The above set of parameters does not fulfil these conditions which is why it cannot be considered as conclusive.

There exist Raman spectroscopy data for ω_ε and ω_τ in divalent transition metal hexaaqua coordination entities, among others in $\mathrm{Fe[SiF_6]\cdot 6H_2O}$ [33]. Using such data which are all [31–33] about $\omega_\varepsilon = 300\ \mathrm{cm^{-1}}$ and $\omega_\tau = 200\ \mathrm{cm^{-1}}$ one can immediately realize that Eq. (4.26) is not fulfilled. Recalculating Bersuker's data [43] with these frequencies one obtains $E_{\mathrm{JT}}(\varepsilon) = 237\ \mathrm{cm^{-1}}$ and $E_{\mathrm{JT}}(\tau) = 290\ \mathrm{cm^{-1}}$ corresponding to $L_\varepsilon = 653\ \mathrm{cm^{-1}}$ and $L_\tau = 723\ \mathrm{cm^{-1}}$. The situation is now somewhat better than before, but condition (4.27) for a purely static case is still not fulfilled. Moreover

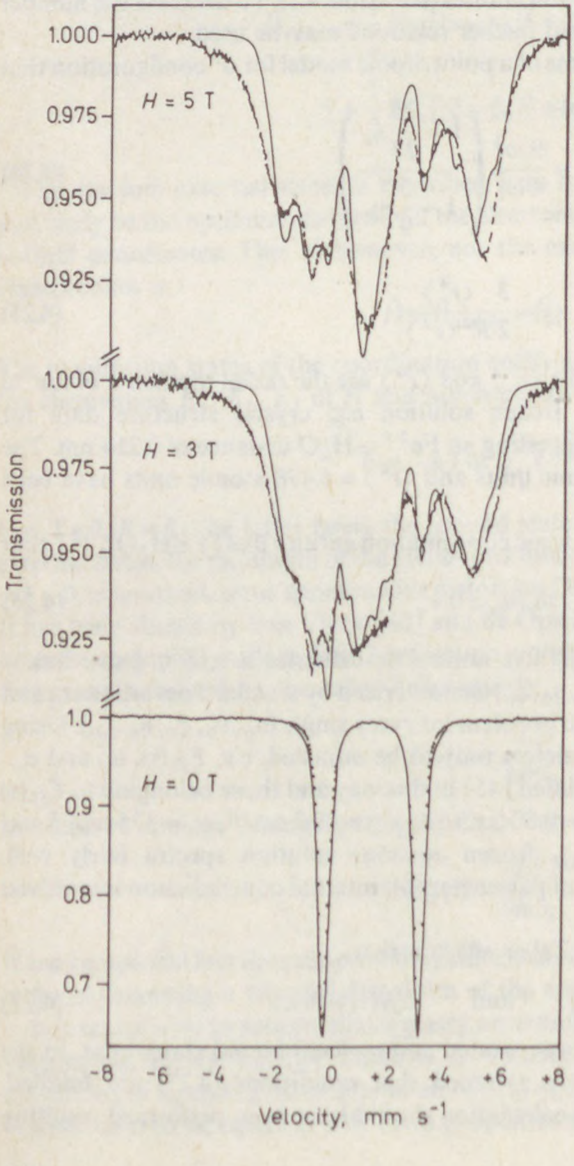

Fig. 4.8. Measured and calculated [see Eq. (4.28)] Mössbauer spectra of a frozen aqueous solution of $\mathrm{Fe(ClO_4)_2}$ in longitudinal magnetic fields at 4.2 K

the spectra calculated with the above values do not fit to the measured ones unless the Jahn–Teller energies are reduced. Although this may be justified in view of covalency effects in this case conditions (4.27) are even less fulfilled. We may conclude, therefore, that the $Fe(ClO_4)_2$ frozen aqueous solution spectra cannot be understood consistently in terms of a static Jahn–Teller calculation.

Since a dynamic Jahn–Teller calculation would raise insurmountable computational difficulties another heuristic approach will be used to find out the distribution of the normal distortions[47].

As described in Section 4.2.3 the spectra of a series of iron(II) crystal hydrates could be well described supposing a C_{2h} symmetry without ε-distortions ($u=0$). We may believe, therefore, that this tendency is an inherent property of the $[Fe(H_20)_6]^{2+}$ ion. Therefore it can be used as a constraint when generating a random vector (u, v, ξ, η, ζ). Having in mind that for C_{2h} symmetry we have the constraints: $v=0$ and $\xi=\eta$ (cf. Fig. 4.3); this means that the distribution is only two dimensional: $(u, v, \xi, \eta, \zeta)=(0, 0, \xi, \xi, \zeta)$. The pairs (ξ, ζ) have been generated by a random number generator yielding two Gaussian distributions with expectation values ξ_0 and ζ_0 with a common variance σ_τ. Using the parameters of Eq. (4.17), the best fit of the measured spectra (see Fig. 4.8) was achieved [47] with

$$L_\tau\xi_0=950\,\mathrm{cm}^{-1}, \quad L_\tau\zeta_0=0, \quad L_\tau\sigma_\tau=150\,\mathrm{cm}^{-1} \tag{4.28}$$

along with the bare quadrupole splitting $\Delta E_Q^0=3.94$ mm/s. This corresponds to mean orbital energies (see Fig. 4.1) of $\delta+a=1100\,\mathrm{cm}^{-1}$ and $\delta-a=550\,\mathrm{cm}^{-1}$. These values are not far from those reported by Neuwirth and Schröder [10] $\delta+a=(700 \pm 100)\,\mathrm{cm}^{-1}$ and $\delta-a=(450\pm 80)\,\mathrm{cm}^{-1}$ obtained from the temperature dependence of the quadrupole splitting in frozen aqueous solution of $FeCl_2$.

Since all the important details of the spectra could be reasonably well reproduced with four free parameters only, this can be considered as an evidence that iron(II) hexaaqua coordination entities in fact obey C_{2h} symmetry with no ε-distortions in $Fe(ClO_4)_2$ frozen aqueous solutions.

If one compares the expectation values of the normal distortions in Eq. (4.28) with the values in Table 4.2, they are not far from the normal coordinates found for $FeCl_2 \cdot 9H_2O$. Therefore, if the short range order around the Fe^{2+} ion can be described in terms of a quasicrystalline model, the basic crystal structure should be close to that of $FeCl_2 \cdot 9H_20$ which is, unfortunately, not yet known.

The Monte Carlo calculation which resulted in the parameters of Eq. (4.28) yields the EFG parameters $\eta=(V_{xx}-V_{yy})/V_{zz}$ and V_{zz}. Following the suggestion of Czjzek [48] their distribution can well be represented in polar coordinates r and ϕ which are defined by

$$V_{zz}=r\cos\left(\frac{\pi}{6}-\phi\right) \qquad \eta=\sqrt{3}\tan\left(\frac{\pi}{6}-\phi\right) \quad \text{for} \quad V_{zz}>0$$

$$V_{zz}=-r\cos\left(\frac{\pi}{6}+\phi\right) \qquad \eta=\sqrt{3}\tan\left(\frac{\pi}{6}+\phi\right) \quad \text{for} \quad V_{zz}<0. \tag{4.29}$$

This distribution is shown in Fig. 4.9 for 60 subspectra of the Monte Carlo calculation. The points appear in the $V_{zz}<0$ sector. Since the orbital ground state is a singlet, the large quadrupole splitting being typical for this case, this means that the

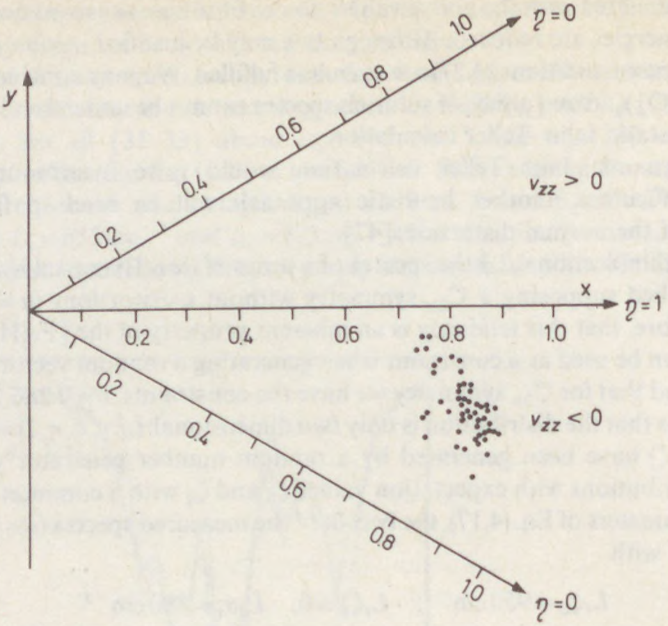

Fig. 4.9. Distribution of the EFG of FAS of $Fe(ClO_4)_2$ represented on a "Czjzek's plot" [48]

basical symmetry is not very far from trigonal. This might be a consequence of the Jahn–Teller effect.

The quadrupole splitting on a Czjzek-plot is proportional to r. It is easy to see that in spite of the broad distribution of η and V_{zz} the distribution of ΔE_Q is relatively narrow apart from a few points appearing at lower values of r and being responsible for the long low-velocity tail of the zero field spectrum.

Using the measured Raman frequency $\omega_\tau = 200\,\mathrm{cm}^{-1}$ and the recalculated reduced matrix element $L_\tau = 723\,\mathrm{cm}^{-1}$ we can estimate the geometrical distortions of the octahedron the parameters being

$$\xi_0 = \eta_0 = 0.013\,\mathrm{nm}; \quad \zeta_0 = 0; \quad \sigma_\tau = 0.002\,\mathrm{nm}. \tag{4.30}$$

Unfortunately, this data cannot directly be compared with X-ray data. Even if the normal coordinates of the crystal field can directly be related to the distortions of the octahedron, Mössbauer data are insensitive to odd and to A_{1g} distortions which may be, in principle, comparable to the observed distortions.

4.3.3. HYDRATION, COORDINATION FORMATION AND GLASS FORMATION STUDIES

Different anions are known to have different ability to enter the first coordination shell of the cation forming thereby so-called inner-shell coordination entities. Usually one or more water molecules of the hexaaqua coordination entity are then replaced by an anion or by an atom belonging to an anionic molecule. Such tendency of halogenide ions is expected to increase with increasing concentration and increasing electronegativity (i.e. with decreasing ionic radius). To study such phenomena the investigation of ternary systems with variable concentration of the anions should be informative.

Changing the anion in the solution and particularly the addition of a third component may change the geometry and the glass-forming tendency (GFT) of the system. Therefore any change observed in Mössbauer spectra should be carefully analyzed whether it should be ascribed to inner-shell coordination entity formation, to a change of the geometry, or to a change in GFT.

4.3.3.1. Binary systems [46, 49]

Solutions have been prepared by dissolving the appropriate quantity of the iron(II) salt in distilled water. The "dilute" solutions prepared from iron enriched in ^{57}Fe up to 80% contained 3.5 mg/ml ^{57}Fe in solution. The concentrated solutions have been prepared from natural iron. The pH values were 2 or somewhat below that value. The samples have been quenched by immersing them into liquid nitrogen (cooling rate ca 30 K s^{-1}). The experimental conditions of the measurements were the same as described in Section 4.3.2.1. Spectra have been measured in $H = 0, 1, 2, 3, 4$ and 5 T. The parameters of the zero-field measurements are summarized in Table 4.3.

Table 4.3.
Concentrations and zero-field Mössbauer parameters of frozen aqueous solutions of some iron (II) salts at 4.2 K

Salt	Molality, m mol/kg	Quadrupole splitting, ΔE_Q mm/s	Isomer shift*, δ mm/s
FeF_2	1.3(3)	3.40(1)	1.41(1)
$FeCl_2$	0.08	3.18(1)	1.37(1)
$FeBr_2$	0.08	3.28(1)	1.39(1)
FeI_2	0.08	3.32(1)	1.39(1)
$Fe(ClO_4)_2$	0.08	3.36(1)	1.39(1)
$Fe[SiF_6]$	1.18(2)	3.35(1)	1.39(1)
$FeSO_4$	1.15	3.33(1)	1.36(1)
$Fe(NH_4)_2(SO_4)_2$	0.48(1)	3.35(1)	1.39(1)
$Fe(NH_4)_2(SO_4)_2$	1.41(1)	3.34(1)	1.43(1)

* Relative to α-Fe at 295 K.

Some representative spectra measured in an external field of 5 T are shown in Fig. 4.10. In contrast to the zero-field spectra, those measured in external fields consist of broad lines similarly to the spectra of the eutectic $Fe(ClO_4)_2$ described in Section 4.3.2. Although there is not much difference between the spectra, significant effects of the anions can be seen. This is most pronounced in the case of $FeCl_2$ (see e.g. the depth ratio of the two rightmost peaks).

As described in Section 4.3.2.1, one has good reasons to believe that the spectrum of the dilute $Fe(ClO_4)_2$ frozen aqueous solution is rather typical for the spectra of

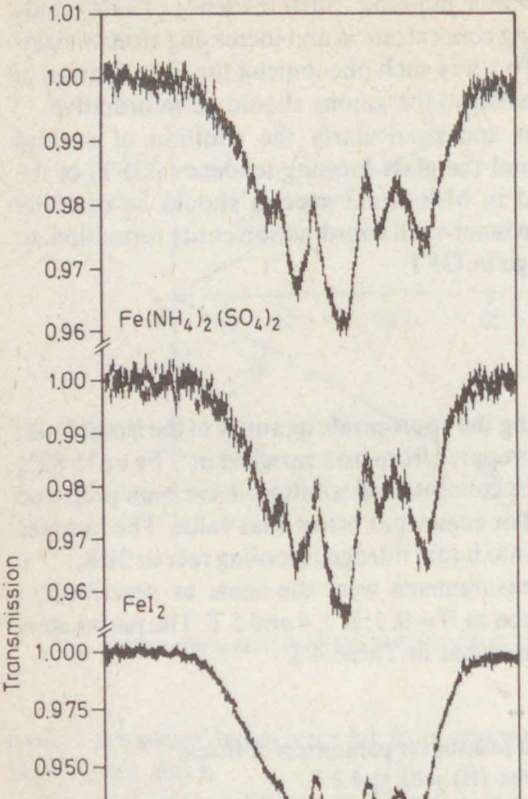

Fig. 4.10. Mössbauer spectra of frozen aqueous solutions of some iron(II) salts in longitudinal magnetic fields at 5 T at 4.2 K

unperturbed $[Fe(H_2O)_6]^{2+}$ coordination entities in a glassy environment. The other limiting case is that of $FeCl_2$ in frozen aqueous solution. With the only exception of the FeF_2 frozen aqueous solution all other spectra can reasonably well be described as a linear combination of the above two spectra. Thus, a systematic change of the spectra in the series of iron(II) halogenides can be observed. Frozen aqueous solutions containing anions of higher radii and of lower electronegativity show spectra similar to those of the $Fe(ClO_4)_2$ frozen aqueous solution. However, no significant concentration dependence of the fraction of unperturbed $[Fe(H_2O)_6]^{2+}$ coordination entities could be found in the investigated cases.

It would be important to know what the "perturbed" complexes are. It is possible that Cl^- ions enter the first coordination sphere of Fe^{2+} forming inner shell coordination entities, e.g. $[Fe(H_2O)_5]^{2+}\ Cl^-$, $[Fe(H_2O)_4]^{2+}\ 2Cl^-$, etc. with it. In fact, such a behaviour has been established for $NiCl_2$ [50–53] and $CoCl_2$ [53, 54]. Moreover, the magnetically perturbed Mössbauer spectra of the Fe^{2+} species do not differ significantly in frozen aqueous solutions of $FeCl_2$ and $^{57}CoCl_2$ [55].

The random ligand field model, which was suited for describing the $Fe(ClO_4)_2$ frozen aqueous solution spectra (see Section 4.3.2) failed to explain the $FeCl_2$ frozen aqueous solution spectra. Even so what we can state is that in the case of $FeCl_2$ the ligand field at the Fe^{2+} ion is not the same as in the case of $Fe(ClO_4)_2$ (i.e. there is a tendency of crystallization or a change in the geometry) and/or the Fe^{2+} ions form inner shell coordination entities with Cl^- ions. To give a more definite answer ternary systems have to be studied.

4.3.3.2. Ternary systems [49, 56]

It is known [57, 58] that, when LiCl is added to a liquid aqueous solution of $CoCl_2$, the concentration of inner shell chloro coordination entities of Co^{2+} is increasing with increasing LiCl concentration. At very high concentrations of LiCl, the frozen aqueous solution of $FeCl_2$ and LiCl shows an abrupt change of the quadrupole splitting [13] probably due to the forming of tetrahedral $[FeCl_4]^{2-}$ coordination entities. Similar behaviour was detected by X-ray diffraction studies [57] of aqueous solutions of $CoCl_2$ and LiCl. Therefore, it is expected that the concentration of inner shell chloro coordination entities of Fe^{2+} can be increased by increasing LiCl concentration in the $FeCl_2$—LiCl—H_2O system. If the characteristics of the magnetically perturbed Mössbauer spectra of the $FeCl_2$ frozen aqueous solution can be ascribed to the

Table 4.4.
Concentrations and zero-field Mössbauer parameters of frozen $FeCl_2$—LiCl—H_2O systems at 4.2 K

Molality, *m* ($FeCl_2$) mol/kg	$\frac{[Cl^-]}{[Fe^{2+}]}$	Quadrupole splitting, ΔE_Q mm/s	Isomer shift*, δ mm/s
1.00(1)	4	3.22(1)	1.37(1)
1.00(1)	5	3.34(1)	1.39(1)
1.04(1)	6	3.35(1)	1.39(1)
1.00(1)	7	3.33(2)	1.39(1)
0.51(1)	14	3.36(1)	1.39(1)
0.24(1)	28	3.38(2)	1.40(1)

* Relative to α-Fe at 295 K.

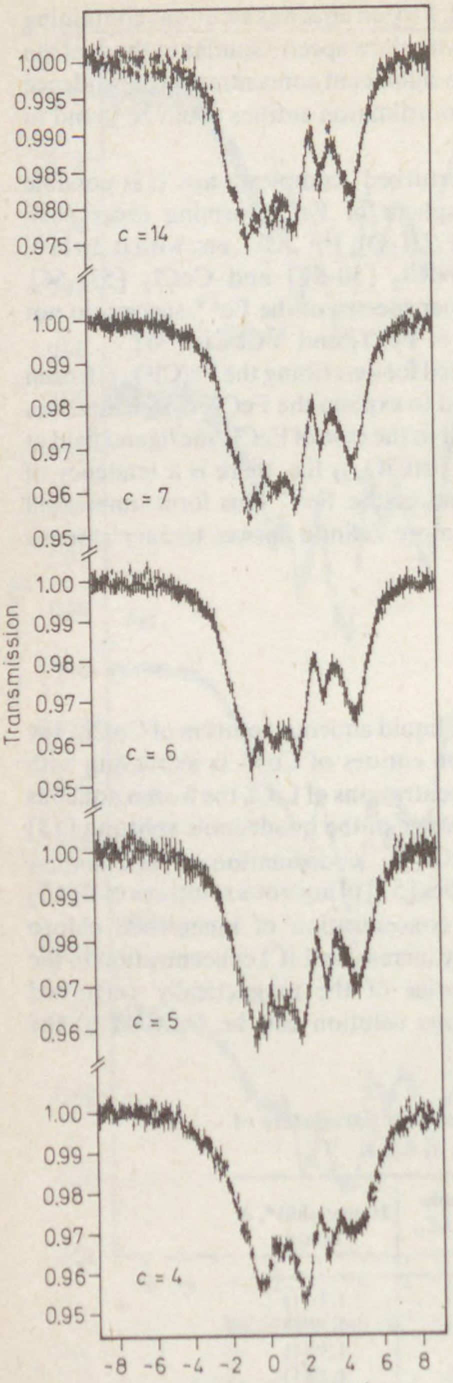

Fig. 4.11. Mössbauer spectra of the frozen $FeCl_2$–$LiCl-H_2O$ system in longitudinal magnetic fields of 3 T at 4.2 K

c = concentration ratio $[Cl^-]/[Fe^{2+}]$

presence of inner shell chloro coordination entities then those characteristics are expected to be even more pronounced at higher LiCl concentrations.

Solutions and absorbers have been prepared on the usual way. Concentrations of $FeCl_2$ and LiCl and zero-field Mössbauer parameters of the frozen $FeCl_2$—LiCl—H_2O system at 4.2 K are summarized in Table 4.4.

Some magnetically perturbed Mössbauer spectra of the same system are shown in Fig. 4.11. They show, surprisingly, just the opposite behaviour as expected. At higher concentrations of LiCl the spectra almost do not differ at all from those of the $Fe(ClO_4)_2$ frozen aqueous solution.

LiCl, however, not only may have the tendency of increasing the number of Cl^- ions in the first coordination shell of Fe^{2+} it is also known [39] to be an excellent glass-former. Frozen aqueous solutions of LiCl have one of the broadest concentration range of glass formation [39]. Moreover, as shown by Ruffolo and Boolchand [3], the GFT (GFT = glass-forming tendency) of a system may be manifested in the Mössbauer spectrum. Therefore, it is possible that the observed behaviour of the $FeCl_2$—LiCl—H_2O system is due to an increase of the GFT and/or to a change in the local geometry with increasing LiCl concentration. To decide whether this is the case, a third component should be added to the aqueous solutions of iron(II) salts which is not expected to change the first coordination shell of Fe^{2+} but which is known to be a glass-former. Glycerol is such a substance.

Table 4.5.
Concentrations and zero-field Mössbauer parameters of frozen iron (II) salt—glycerol—H_2O systems at 4.2 K

Salt	Molality, m mol/kg	Volume ratio, φ H_2O/glycerol	Quadrupole splitting ΔE_Q mm/s	Isomer shift*, δ mm/s
FeF_2	0.57(2)	1 : 1	3.34(1)	1.39(1)
$FeCl_2$	1.62	1 : 1	3.31(1)	1.39(1)
$FeCl_2$	0.035	1 : 1	3.33(1)	1.39(1)
$Fe(ClO_4)_2$	1.31	1 : 1	3.33(1)	1.39(1)
$Fe(ClO_4)_2$	0.035	1 : 1	3.34(1)	1.39(1)
$Fe(ClO_4)_2$	2.37	5 : 1	3.36(1)	1.39(1)
$Fe(ClO_4)_2$	0.064	5 : 1	3.32(1)	1.39(1)

* Relative to α-Fe at 295 K

The volume ratio of H_2O and glycerol was 1 : 1 or 5 : 1. Samples have been prepared in the usual way. Zero-field Mössbauer parameters are summarized in Table 4.5.

It is remarkable that no difference within the experimental error can be observed between the zero-field parameters of the different samples in Table 4.5. Also, the magnetically perturbed spectra, some of which are shown in Fig. 4.12, do not show significant differences as compared to the spectra of $Fe(ClO_4)_2$ frozen aqueous solutions.

Therefore, we may conclude that magnetically perturbed Mössbauer spectra of frozen aqueous solutions of iron(II) salts are sensitive to the GFT of the system which may be related to the local geometry around the Fe^{2+} ion but they do not reflect the presence of, say, a halogenide ion in the first coordination sphere of Fe^{2+}. This finding

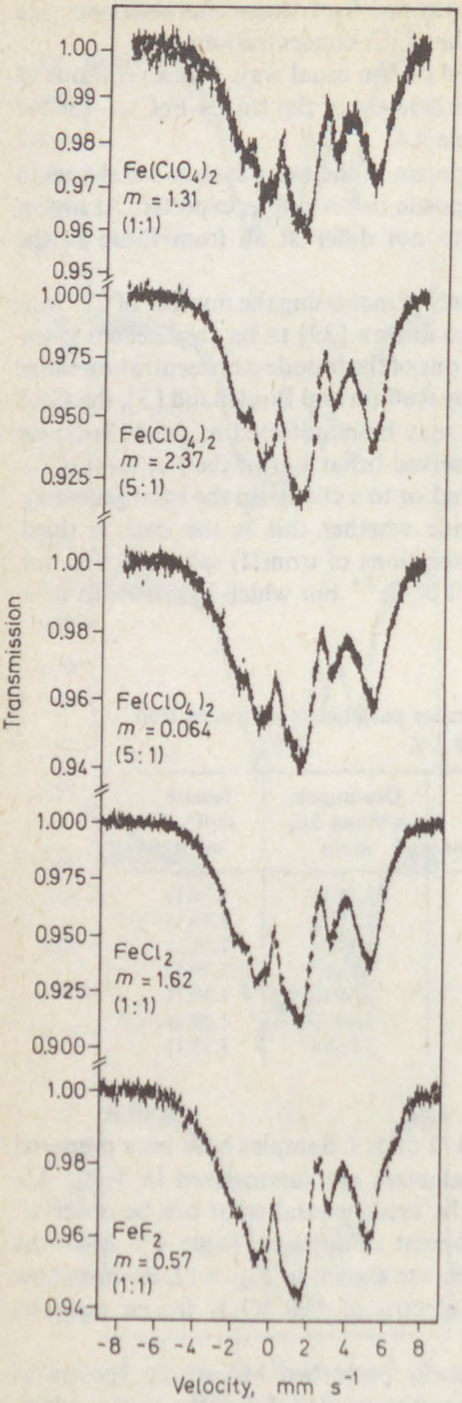

Fig. 4.12. Mössbauer spectra of some frozen iron(II) salt-H_2O-glycerol solutions of different molalities (m) and volume ratios (H_2O/glycerol) in 5 T longitudinal magnetic field at 4.2 K

can be explained by the fact that the mean orbital splitting of Fe^{2+} in frozen aqueous solutions is rather high [ca 820 cm^{-1}, corresponding to $L_\tau\xi_0 = 950$ cm^{-1}; see Eq. (4.28)]. Also the C_{2h} symmetry is low enough that it easily can be retained if one or two vertices of the octahedron are occupied by halogenide ions (Mössbauer spectroscopy is insensitive to the violation of inversion symmetry in the case of d electrons).

In conclusion, the above findings can be explained as follows:

(i) Magnetically perturbed Mössbauer spectra of iron(II) salts in a purely glassy state do not differ from one another, a typical representative being the frozen aqueous solution of $Fe(ClO_4)_2$. Particularly, no effect of the formation of inner shell coordination entities can be observed if the system is prevented from a tendency of crystallization.

(ii) In the series of halogenides the GFT is decreasing with decreasing anionic radii and increasing electronegativity. An extreme example is FeF_2 where no glass formation can be observed in DTA measurements at all [11]. Magnetically perturbed Mössbauer spectra of this system are similar to those of $FeF_2 \cdot 4H_2O$ [49]. In the other halogenides the line positions are not far from those of $FeCl_2 \cdot 9H_2O$ [30].

(iii) If the GFT of the system is increased by adding some glass-former to it the number of unperturbed "glassy" $[Fe(H_2O)_6]^{2+}$ coordination entities is increasing. Therefore the word "unperturbed" means throughout this Section "in glassy environment" rather then "with no inner shell coordination entity".

REFERENCES

1. Fujita, F. E., in: Application of Nuclear Techniques to the Studies of Amorphous Metals (U. Gonser, ed.), *Atomic Energy Review*, Supplement No. 1., 173 (1981).
2. Litterst, F. J., Kalvius, G. M. and Boyle, A. J. F., *J. Physique Colloque*, **35**, C6–403 (1974).
3. Ruffolo, D. and Boolchand, P., *Phys. Rev. Letters*, **55**, 242 (1985).
4. Dézsi, I., Keszthelyi, L., Pócs, L. and Korecz, L., *Phys. Letters*, **14**, 14 (1965).
5. Nozik, A. J. and Kaplan, M., *J. Chem. Phys.*, **47**, 2960 (1967).
6. Cameron, J. A., Keszthelyi, L., Nagy, G. and Kacsóh, L., *Chem. Phys. Letters*, **8**, 628 (1971).
7. Ruby, S. L., Zabransky, B. J. and Stevens, G. J., *J. Chem. Phys.*, **54**, 4559 (1971).
8. Brunot, B., Hauser, U., Neuwirth, W. and Bolz, J., *Z. Physik*, **249**, 125 (1971).
9. Dézsi, I., *Report KFKI*, 72–52 (1972).
10. Neuwirth, W. and Schröder, H.-J., *Z. Physik, B.*, **23**, 71 (1976).
11. Dézsi, I., Szűcs, I. S. and Molnár, B. in: "*Applications of the Mössbauer Effect*", Vol. 3., Proc. Int. Conf. Appl. Mössbauer Effect, Alma-Ata (1983), eds: Kagan, Yu. M. and Lyubutin, I. S., Gordon and Breach Sci. Publ., New York, 1986., p. 1279.
12. Dézsi, I., Keszthelyi, L., Molnár, B. and Pócs, L., *Phys. Letters*, **18**, 28 (1965).
13. Vértes, A., *Acta Chim. Hung.*, **63**, 9 (1970).
14. Nagy, G., Kacsóh, L., Nyeste, J. and Dézsi, I., *J. Thermal Analysis*, **4**, 251 (1972).
15. Spiering, H., Zimmermann, R., Ritter, G., *Phys. Stat. Sol.*, (b) **62**, 123 (1974).
16. Spiering, H., Nagy, D. L. and Zimmermann, R., *J. Physique*, **35**, C–231 (1974).
17. Ballhausen, C. J., *Introduction to Ligand Field Theory*, McGraw-Hill, New York, London, 1962.
18. Abragam, A. and Bleaney, B., *Electron Paramagnetic Resonance of Transition Ions*, eds Marshall, W., Wilkingson, D. H., Clarendon Press, Oxford, 1970.
19. Griffith, J. S., *The Theory of Transition Metal Ions*, Cambridge University Press, 1964.
20. Price, D. C. and Varret, F., in: *Advances in Mössbauer Spectroscopy*, eds Thosar, B. V., Iyengar, P. K., Elsevier, Amsterdam, 1983.

21. Blume, M. and Watson, R. E., *Proc. Roy. Soc. A.*, **271**, 565 (1962).
22. Watson, R. E. and Blume, M., *Phys. Rev. A.*, **139**, 1209 (1965).
23. Pryce, M. H. L., *Phys. Rev.*, **80**, 1107 (1950).
24. Trees, R. E., *Phys. Rev.*, **82**, 683 (1951).
25. Hasselbach, K. M. and Spiering, H., *Nucl. Instr. Methods*, **176**, 537 (1980).
26. Spiering, H. and Witzgall, R., *Hyp. Int.*, **5**, 265 (1978).
27. Landau, L. D. and Lifshitz, E. M., *Quantum Mechanics*, Pergamon Press, Inc., New York, 1958.
28. Englman, R., *The Jahn-Teller Effect in Molecules and Crystals*, Wiley Interscience, New York, 1972.
29. Spiering, H., Dézsi, I. and Nagy, D. L., *J. Physique Colloque*, **37**, C6–571 (1976).
30. Doerfler, R., Leupold, O., Nagy, D. L., Ritter, G., Spiering, H. and Zimmermann, R., *Hyp. Int.*, **15/16**, 831 (1983).
31. Jäger, J. and Schaak, G., *Z. Naturforsch.*, **28a**, 738 (1973).
32. Jenkins, T. E. and Lewis, J., *Phys. Scripta*, **18**, 351 (1978).
33. Lewis, J. and Jenkins, T. E., *J. Raman Spectroscopy*, **8**, 111 (1979).
34. Doerfler, R., private communication
35. Montgomery, H., Chastain, R. V., Natt, J., Witkovska, A. and Lingafelter, E., *Acta Cryst.*, **22**, 775 (1967).
36. Ohtaki, H., Yamaguchi, T. and Maeda, M., *Bull. Chem. Soc. Japan*, **49**, 701 (1976).
37. Ohtaki, H. and Maeda, M., *Bull. Chem. Soc. Japan*, **47**, 2197 (1974).
38. Neilson, G. W., Newsome, J. R. and Sandström, M., *J. Chem. Soc. Faraday Trans.*, **77**, 1245 (1981).
39. Angell, C. A. and Sare, E. J., *J. Chem. Phys.*, **52**, 1058 (1970).
40. van Vleck, J. H., *J. Chem. Phys.*, **7**, 72 (1939).
41. Öpick, U. and Pryce, M. H. L., *Proc. Roy. Soc.*, **A238**, 425 (1957).
42. Bersuker, I. B., *Teor. I. Eksper. Khim.*, **1**, 5 (1965).
43. Hamilton, W. C., *Acta Cryst.*, **15**, 353 (1962).
44. Fraga, S., Karowski, J. and Saxena, K. M. S., *Handbook of Atomic Data*, Elsevier, Amsterdam, 1976.
45. Nagy, D. L., Horváth, D., Ritter, R., Spiering, H., Szücs, I. S. and Volland, U., *Nucl. Instr. Meth.*, **199**, 223 (1982).
46. Domes, H., Diplomarbeit, Universität Erlangen–Nürnberg, 1984 (unpublished).
47. Domes, H., Leupold, O., Nagy, D. L., Ritter, G., Spiering, H., Molnár, B. and Szücs, I. S., *J. Chem. Phys.*, **85**, 7294 (1986).
48. Czjzek, G., *Hyp. Int.* **14**, 189 (1983).
49. Szücs, I. S., Dézsi, I., Leupold, U., Ritter, G. and Molnár, B., *Int. Conf. Appl. Mössbauer Effect, Leuven*, 1985, Abstracts 1.52.
50. Marchand, N. H. and Thosi, M. P., *Phys. Letters*, **50A**, 224 (1974).
51. Fontana, M. P., Maisiano, G., Migliardo, P. and Wanderlingh, F., *Solid State Commun.*, **23**, 489 (1977).
52. Fontana, M. P., Maisiano, G., Migliardo, P. and Wanderlingh, F., *J. Chem. Phys.*, **69**, 676 (1978).
53. Magini, M., *J. Chem. Phys.*, **74**, 2523 (1981).
54. Wertz, D. L. and Knuh, R. V., *J. Chem. Phys.*, **50**, 4313 (1969).
55. Nagy, D. L., in: *Trends in Mössbauer Spectroscopy; Lectures Presented at the Second Seeheim Workshop on Mössbauer Spectroscopy*, eds Gütlich, P. and Kalvius, G. M., Johannes Gutenberg Universität Mainz, FRG, 1983, p. 241.
56. Leupold, O., private communication
57. Lee, H.-G., Matsumoto, Y., Yamaguchi, T. and Ohtaki, H., *Bull. Chem. Soc. Japan*, **56**, 443 (1983).
58. Musina, A., Paschina, G., Piccaluge, G. and Magini, M., *J. Chem. Phys.*, **80**, 2772 (1984).

5. CHEMICAL STRUCTURE OF LIQUID SOLUTIONS STUDIED BY MÖSSBAUER SPECTROSCOPY

5.1. HYDRATION STUDIES, FORMATION OF AQUA COORDINATION ENTITIES

The first general model describing the structures of aqueous solutions has been constructed successfully only for dilute solutions of strong electrolytes [1]. The Debye–Hückel theory takes into account the interaction of Coulomb electrostatic forces between the ions, and regards the solvent as a homogeneous dielectric. Theoretical considerations on more concentrated solutions as ion-pair theory [2], restricted interaction site model (RISM) [3], reference hypernetted chain (RHNC), molecular dynamics (MD), Monte Carlo method [4], etc. can give information about the thermodynamic parameters of electrolyte solutions (excess internal energy, heat capacity, osmotic coefficient, etc.) but in general these do not result in a description of the microstructures of such solutions.

Thus reliable information on hydration and solvation, these important characteristics of solution structures, can be obtained by means of appropriate experiments and measurements. There are many types of such investigations as equilibrium, kinetic, thermodynamic, etc. The methods used are X-ray, neutron- and electron-diffraction, NMR, IR (infrared spectroscopy), conductivity, spectrophotometry, etc. In accordance with its importance, this topic has been dealt with by a large number of workers, several thousand relevant publications having appeared so far. However, only a few monographs and reviews have been published [5–7].

On the basis of Chapter 2 it can be said that the coordination conditions between the individual atoms, ions and molecules remain completely or almost unchanged during rapid freezing under optimal conditions, the solution structure thus being "frozen-in" or rigidified. In this way, Mössbauer spectroscopy can provide direct information on the coordination conditions as a consequence of hydration and solvation. Mössbauer spectroscopy, therefore, is an advantageous supplement to previously used methods of examining solution structures, and permits the study of the electronic structures of hydrated and solvated Mössbauer atoms.

5.1.1. HYDRATION OF IRON SALTS

Quenched aqueous solutions of a few iron(II) compounds were investigated by Mössbauer technique. For example, studies were carried out on aqueous solutions of $FeCl_2$, $FeSO_4$ and $Fe(ClO_4)_2$ and on the three-component systems $FeCl_2$—LiCl—H_2O, $FeCl_2$—KCl—H_2O, $FeCl_2$—KF—H_2O, $FeCl_2$—NaF—H_2O, $FeSO_4$—$C_6H_{11}NO$ (caprolactam)—H_2O) (in which the LiCl, KCl, KF, NaF and caprolactam served to decrease the activity of water), $FeCl_2$—CH_3COOH—H_2O and $FeSO_4$—CH_3COOH—H_2O [8].

Table 5.1.
Mössbauer parameters of quenched aqueous iron(II) salt solutions

No.	The composition of the solution in water	Quadrupole splitting, ΔE mm s^{-1}	Isomer shift, δ (Relative to α-iron) mm s^{-1}	Half width, Γ mm s^{-1}	Literature
1.	0.01 mol dm^{-3} $^{57}Fe(ClO_4)_2$ + 0.1 mol dm^{-3} $HClO_4$	3.300 ± 0.009	1.383 ± 0.004	0.49 ± 0.01	[14]
2.	0.01 mol dm^{-3} $^{57}Fe(ClO_4)_2$ + 0.1 mol dm^{-3} $HClO_4$ + 5.6 wt.-% glycerol	3.262 ± 0.004	1.357 ± 0.002	0.381 ± 0.006	
3.	0.01 mol dm^{-3} $^{57}Fe(ClO_4)_2$ + 0.1 mol dm^{-3} $HClO_4$ + 9.64 wt.-% glycerol	3.244 ± 0.004	1.354 ± 0.002	0.391 ± 0.006	
4.	0.01 mol dm^{-3} $^{57}FeSO_4$ + 0.1 mol dm^{-3} H_2SO_4	3.307 ± 0.003	1.367 ± 0.002	0.389 ± 0.005	
5.	0.01 mol dm^{-3} $^{57}FeSO_4$ + 0.1 mol dm^{-3} H_2SO_4 + 4.33 wt.-% glycerol	3.276 ± 0.004	1.361 ± 0.002	0.395 ± 0.006	
6.	0.01 mol dm^{-3} $^{57}FeSO_4$ + 0.1 mol dm^{-3} H_2SO_4 + 10.52 wt.-% glycerol	3.275 ± 0.004	1.367 ± 0.002	0.406 ± 0.006	
7.	0.01 mol dm^{-3} $^{57}FeCl_2$ + 0.1 mol dm^{-3} HCl	3.17 ± 0.01	1.346 ± 0.005	0.39 ± 0.02	[14]
8.	0.01 mol dm^{-3} $^{57}FeCl_2$ + 0.1 mol dm^{-3} HCl + 4.41 wt.-% glycerol	3.245 ± 0.007	1.354 ± 0.004	0.36 ± 0.01	
9.	0.01 mol dm^{-3} $^{57}FeCl_2$ + 0.1 mol dm^{-3} HCl + 9.0 wt.-% glycerol	3.252 ± 0.005	1.360 ± 0.003	0.368 ± 0.008	
10.	1.0 mol dm^{-3} $Fe(ClO_4)_2$ + 0.5 mol dm^{-3} $HClO_4$	3.322 ± 0.005	1.375 ± 0.003	0.423 ± 0.008	
11.	0.5 mol dm^{-3} $Fe(ClO_4)_2$ + 1.0 mol dm^{-3} $HClO_4$	3.348 ± 0.004	1.376 ± 0.002	0.382 ± 0.007	
12.	1.0 mol dm^{-3} $Fe(ClO_4)_2$ + 1.0 mol dm^{-3} $HClO_4$	3.319 ± 0.005	1.373 ± 0.002	0.427 ± 0.008	
13.	1.0 mol dm^{-3} $FeSO_4$ 1.0 mol dm^{-3} H_2SO_4	3.314 ± 0.005	1.368 ± 0.003	0.435 ± 0.008	
14.	0.5 mol dm^{-3} $FeSO_4$ 0.1 mol dm^{-3} H_2SO_4	3.346 ± 0.003	1.391 ± 0.002	0.406 ± 0.005	
15.	0.316 mol dm^{-3} $FeSO_4$ + 0.158 mol dm^{-3} H_2SO_4	3.309 ± 0.004	1.374 ± 0.002	0.388 ± 0.006	[14]
16.	0.1 mol dm^{-3} $FeSO_4$ + 0.1 mol dm^{-3} H_2SO_4	3.322 ± 0.007	1.366 ± 0.003	0.38 ± 0.01	

Table 5.1. cont.

No.	The composition of the solution in water	Quadrupole splitting, ΔE mm s^{-1}	Isomer shift, δ (Relative to α-iron) mm s^{-1}	Half width, Γ mm s^{-1}	Literature
17.	0.02 mol dm^{-3} $^{57}FeCl_2$ + 4 mol dm^{-3} NaCl	3.226 ± 0.009	1.375 ± 0.005	0.52 ± 0.02	[13]
18.	0.36 mol dm^{-3} $FeCl_2$	3.219 ± 0.006	1.367 ± 0.003	0.46 ± 0.01	
19.	0.34 mol dm^{-3} $FeCl_2$ + 0.93 mol dm^{-3} NaCl	3.206 ± 0.006	1.377 ± 0.003	0.479 ± 0.009	
20.	0.33 mol dm^{-3} $FeCl_2$ + 1.78 mol dm^{-3} NaCl	3.214 ± 0.008	1.370 ± 0.004	0.42 ± 0.01	
21.	0.33 mol dm^{-3} $FeCl_2$ + 4 mol dm^{-3} NaCl 0.5 mol dm^{-3} CH_3COOH + 0.5 mol dm^{-3} CH_3COONa	3.110 ± 0.009	1.367 ± 0.004	0.55 ± 0.001	
22.	0.02 mol dm^{-3} $Fe(ClO_4)_2$ + 4 mol dm^{-3} $NaClO_4$	3.323 ± 0.005	1.384 ± 0.002	0.416 ± 0.008	
23.	0.02 mol dm^{-3} $Fe(ClO_4)_2$ + 4 mol dm^{-3} $NaClO_4$ + 0.5 mol dm^{-3} CH_3COOH + 0.5 mol dm^{-3} CH_3COONa	3.118 ± 0.008	1.366 ± 0.004	0.48 ± 0.01	[11]
24.	0.37 mol dm^{-3} $FeCl_2$ in 50—50 wt.-% H_2O—D_2O mixture	3.229 ± 0.007	1.346 ± 0.007	0.46 ± 0.02	[11]
25.	0.37 mol dm^{-3} $FeCl_2$ in D_2O	3.220 ± 0.005	1.345 ± 0.005	0.46 ± 0.02	
26.	0.37 mol dm^{-3} $FeCl_2$ in H_2O	3.221 ± 0.007	1.345 ± 0.007	0.45 ± 0.02	
27.	0.26 mol dm^{-3} $FeSO_4$ in H_2O	3.41 ± 0.06	1.36 ± 0.03	0.41 ± 0.09	
28.	0.26 mol dm^{-3} $FeSO_4$ in D_2O	3.31 ± 0.04	1.36 ± 0.02	0.40 ± 0.02	
29.	0.26 mol dm^{-3} $FeSO_4$ in 50—50 wt.-% H_2O—D_2O mixture	3.42 ± 0.05	1.36 ± 0.02	0.39 ± 0.08	
30.	$FeSO_4$ crystalline	3.11	1.40		[15]
31.	$FeSO_4 \cdot H_2O$ crystalline	3.04	1.36		
32.	$FeSO_4 \cdot 4H_2O$ crystalline	3.51	1.39		
33.	$FeSO_4 \cdot 7H_2O$ crystalline	3.60	1.41		
34.	$FeCl_2$ crystalline	1.23	1.01		
35.	$FeCl_2 \cdot 2H_2O$ crystalline	2.59	1.20		
36.	$FeCl_2 \cdot 4H_2O$ crystalline	3.08	1.33		

The results permit to draw the following conclusions.

The Mössbauer parameters of aqueous iron(II) salt solutions containing various anions (Cl^-, SO_4^{2-}, ClO_4^-) have practically the same value, hence it can be concluded that most part of Fe^{2+} in the above solutions is probably present in the form of the hexaaqua coordination entity. Even a significant increase of the concentration of the iron(II) salt does not lead to the break-down of the species $[Fe(H_2O)_6]^{2+}$. However, if the activity a_0 of the water is decreased by some additive, then it is possible to reach an a_0 value where the quadrupole splitting (ΔE) of the solution changes; this is an indication that some change has occurred in the structure of the hydrate layer of Fe^{2+}. If LiCl is used to decrease a_0, then with the condition $a_0 < 0.2$ (the concentration of LiCl is more than ~30 wt.-%), the considerable decrease in $\Delta E \approx 0.8$ mm s^{-1} is due to Cl^- which occupies some of the coordination sites of the iron. This remarkable change of ΔE includes the possibility of an octahedral–tetrahedral transformation and $[FeCl_4]^-$ anion formation, as well. The chloride coordination is supported by the sign of the change of ΔE, as this can be brought into a good agreement with the nephelauxetic effect of chloride [9, 10].

The Mössbauer parameters of the quenched solutions of different iron(II) salts are given in Table 5.1. One of the Mössbauer spectra is shown in Fig. 5.1(a). The results show that the anions as well as the additional compounds (sodium acetate, acetic acid, glycerol) have a slight effect on the Mössbauer parameters. The value of this effect can give information about the position of the coordinated ions or molecules, whether they are in the first or second ligand sphere of iron(II) ion.

It should be mentioned that Mössbauer parameters different from those given in Table 5.1 have also been published, for the quadrupole splitting of $FeSO_4$ solution, for example, the values 3.521 mm s^{-1} [11] and 3.6 mm s^{-1} [12]. The origin of the differences is—probably—that during the freezing of the solution small particles of crystalline iron(II) salt hydrates can also be formed. These results show the importance of the application of glass forming materials. It should be noted, at the same time, that the applied glycerol can also slightly modify the results of the measurements.

X-ray diffraction measurements have been carried out in 1 molar aqueous solution of $Fe(ClO_4)_2$, $FeCl_2$ and $FeSO_4$ at room temperature [16]. These experiments yielded a

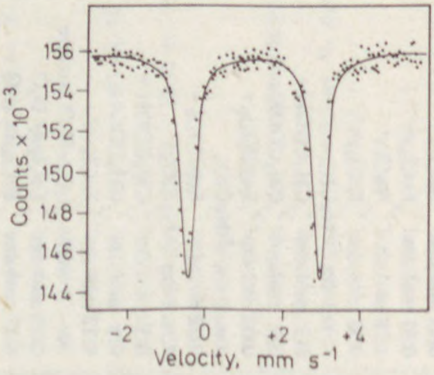

Fig. 5.1(a) Mössbauer spectrum of the aqueous frozen solution of 0.5 mol dm^{-3} $FeSO_4$ + 0.1 mol dm^{-3} H_2SO_4, recorded at the temperature of liquid nitrogen

0, 0.2 and 0.4 mole rations of $Fe(H_2O)_5A^+$ coordination compound in perchlorate, sulfate and chloride solutions, respectively (where A stands for anion) [16]. Whereas the Mössbauer spectra of the same solutions recorded at liquid nitrogen temperature showed only one component (one doublet) and their parameters were very similar. [See Table 5.1 and Fig. 5.1(a)]. Candidates of the explanation of the contradiction between the X-ray and Mössbauer results can be the shift of the equilibrium between $[Fe(H_2O)_6]^{2+}$ and $[Fe(H_2O)_5A]^+$ during the quenching of the solutions or the supposition that the Mössbauer parameters of hexaaqua iron(II) and mono-chloro- or mono-sulfato-pentaaqua coordination compounds of iron(II) are very close to each other. The solution of this puzzle needs further investigation. (For example, calculations of the electric field gradient at Fe^{II} nucleus in $[Fe(H_2O)_6]^{2+}$ and $[Fe(H_2O)_5A]^+$ could be useful.)

The results obtained for solutions containing acetic acid [8] suggest that the iron in solution is predominantly present in the form $[Fe(H_2O)_6]^{2+}$ up to an acetic acid content of 40 wt.-%. In a solution containing 45.20 wt.-% of acetic acid, however, a new

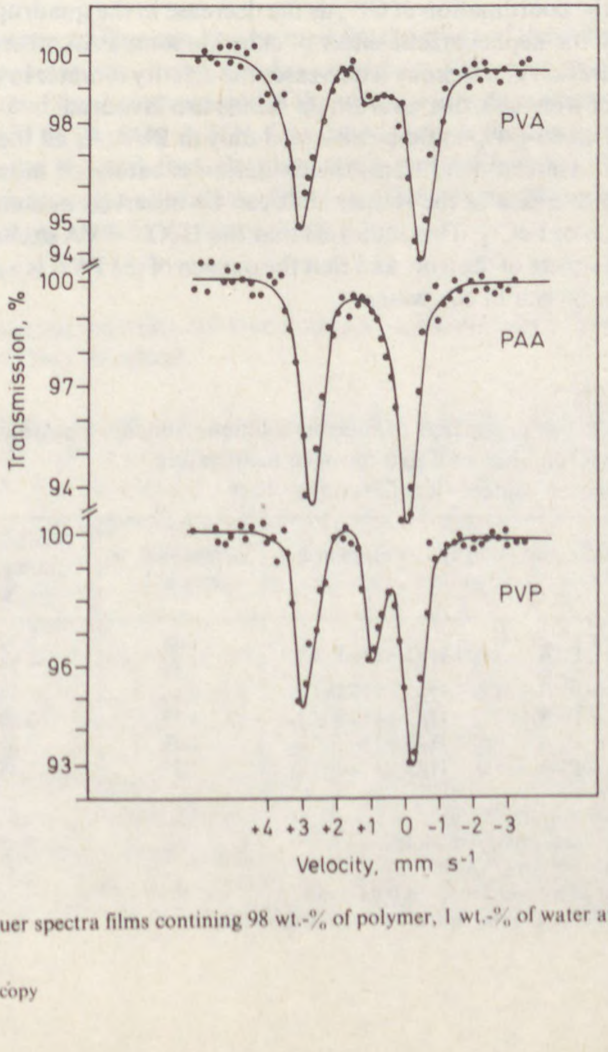

Fig. 5.1(b) Mössbauer spectra films contining 98 wt.-% of polymer, 1 wt.-% of water and 1 wt.-% of $FeCl_2$

spectrum, with a quadrupole splitting of 2.47 mm s^{-1}, appears as well. If a constant Debye–Waller factor may be assumed, then about 10–15% of the iron(II) ions in the solution has a structure different from that of the hexaaqua coordination entity. In acetic anhydride the total amount of iron(II) ions in the solution exhibits a Mössbauer spectrum with the relatively low quadrupole splitting of 2.43 mm s^{-1}. Hence it is likely that in concentrated acetic acid solutions the $[Fe(H_2O)_6]^{2+}$ ion is substituted by an iron(II) coordination ion of a different structure. The concentration of the latter ion increases with increasing acetic acid concentration at the expense of hexaaqua ion up to the moment, when only the coordination compound is present in acetic anhydride, with the probable structure $[FeCl_2(CH_3COOH)_4]$.

Information on the physicochemical properties of the polymers can be acquired [17] by the Mössbauer spectroscopic study of aqueous solutions containing both polymers and Mössbauer atoms, or films prepared from these solutions. The studied solutions and films contained polyvinyl alcohol (PVA), polyvinylpyrrolidine (PVP) and polyacrylamide (PAA). The results are presented in Fig. 5.1(b) and Table 5.2 (the data refer to a stainless steel radiation source).

The experimental results showed a considerable decrease in ΔE observed in the PAA film indicating the coordination of Cl^-, as the decrease in the quadrupole splitting can be explained by the nephelauxetic effect of chloride ions. PAA, therefore, undergoes appreciable hydration and thereby it decreases the activity of water in the system. Thus, the formation of iron–chlorine coordinate bonds are favoured.

Oxidation up to 40 ± 4% could be observed only in PVP. As all the three films were prepared under identical conditions, the oxidation is catalyzed mostly by PVP.

With PVA, a decrease of the isomer shift can be observed in comparison with an aqueous solution of $FeCl_2$. This indicates that the H_2O—PVA exchange proceeds in the inner ligand sphere of the iron, and that the oxygen of the PVA is a stronger electron donor than the oxygen of the water.

Table 5.2

Mössbauer parameters of aqueous solutions containing polymers and iron(II) chloride at liquid nitrogen temperature

Radiation source: ^{57}Co in stainless steel

Composition of system examined wt.-%	Isomer shift, δ mm s^{-1}	Quadrupole splitting, ΔE mm s^{-1}
98% PAA + 1% H_2O + 1% $FeCl_2$	1.48 1.48	2.79 3.29
98% PVP + 1% H_2O + 1% $FeCl_2$	0.46	1.24
7% PVA + 92% H_2O + 1% $FeCl_2$	1.29	3.20
89.5% PVA + 9.5% H_2O + 1% $FeCl_2$	1.31	3.29
98% PVA + 1% H_2O + 1% $FeCl_2$	1.37	3.48

PAA = polyacrylamide
PVP = polyvinylpyrrolidine
PVA = polyvinyl alcohol
Error of measurements: ± 0.03 mm s^{-1}
The Fe^{III}/Fe^{II} ratio in the PVP film was 40 : 60.

The first coordination sphere of the iron remains unchanged on the dissolution of low-spin iron compounds. Accordingly, the isomer shifts of low-spin iron(II) and iron(III) compounds are the same in the solid state and in solution, while the quadrupole splittings change to a slight extent as a result of dissolution. This phenomenon has been observed in aqueous solutions of

$$Na_2[Fe(CN)_5(NO)] \cdot 2H_2O \text{ [18]}$$

$$Na_3[Fe(CN)_5(C_6H_5NO)] \cdot 2H_2O \text{ [19]},$$

$$Li_3[Fe(CN)_6] \cdot 4H_2O \text{ [20]}$$

and

$$Na_3[Fe(CN)_6] \cdot H_2O \text{ [20]}.$$

Dominques and Danon [20] published the Mössbauer parameters of $K_3[Fe(CN)_6]$ to be the same in solution and in the solid state, viz, $\Delta E = 0.445$ mm s^{-1}. Papp et al., used glycerol or a phosphonium salt to eliminate segregation and a quadrupole splitting of 1.07 mm s^{-1} was measured in aqueous solutions of $K_3[Fe(CN)_6]$ [21]. This high quadrupole splitting can be explained by the hydration of the ligand resulting in their polarization.

The Mössbauer technique can also be used for the study of the diffusion of iron ions in cold aqueous solutions. Ruby and his coauthors [22] used the Mössbauer line broadening method for measurements of the temperature dependence of the diffusion coefficient of Fe^{2+} in $(H_3PO_4 \cdot 3.27\,H_2O)$ mixed liquid in the temperature range 185-215 K. The results showed that the jumps are not defined by the size of lattice dimensions in contrast to crystalline diffusion. The temperature dependence of the diffusion coefficients showed Arrhenius' law.

5.1.2. MÖSSBAUER SPECTRA OF THE FROZEN AQUEOUS SOLUTIONS OF TIN HALOGENIDES

As known, in tin halogenide compounds the electron orbitals of tin corresponding to the principal quantum numbers $n \leq 4$ are completely occupied $[(1s)^2 (2s)^2 (2p)^6 (3s)^2 (3p)^6 (3d)^{10} (4s)^2 (4p)^6 (4d)^{10}]$, and any change in the electronic structure of tin as a consequence of formation of chemical bonds, therefore, arises primarily in the 5s, 5p and 5d orbitals. Hence, the Mössbauer parameters (the isomer shift, δ, and the quadrupole splitting, ΔE) of tin are determined by the configuration of the 5s, 5p and 5d electrons.

According to Donaldson and Senior [23], the shielding effect of each 5p electron on the 5s electrons is 10% (one 5p electron reduces the value of $|\Psi_{5,s}(0)|^2$ by 10%). It follows that the s electron density at the ^{119}Sn nucleus, and hence the isomer shift (δ), are highest for pure ionic Sn^{2+} $(5s)^2$ compounds ($\delta \approx +5.6$ mm s^{-1}), and lowest for the pure ionic Sn^{4+} $(5s)^0$ electronic structure ($\delta \approx -3$ mm s^{-1}). The values are referred to an α-Sn radiation source and liquid air temperature. The "pure" ionic state is of course only hypothetical in tin compounds and hence the above δ values are the results of extrapolation. For ^{119}Sn nuclei, therefore, the isomer shift may vary within a wide interval of ca. 8 mm s^{-1}, depending on the 5s 5p 5d electronic configuration.

Gibb and Greenwood assumed that ΔE will increase if the atoms bound to the tin have different electronegativities or these atoms show different donor acceptor properties [24]. However, the results of more recent measurements by Zuckerman have demonstrated that this assumption does not hold in all cases [25] and accordingly it cannot be regarded as being generally valid.

Recording Mössbauer spectra of quickfrozen samples prepared from hydrochloric and perchloric acid solutions of $SnCl_2 \cdot 2H_2O$, it was found that the variation in the hydrochloric acid concentration did not cause a change higher than the limiting experimental error in the Mössbauer parameters until a lower threshold concentration was reached, viz., $[HCl] > 0.1$ mol dm^{-3} [26]. As an example, the Mössbauer spectrum of a solution containing 2.3 mol dm^{-3} of HCl and 2.15 mol dm^{-3} of $SnCl_2$ has $\delta = 3.25$ mm s^{-1}, $\Delta E = 0.98$ mm s^{-1} (radiation source: $BaSnO_3$). Measurable changes occurred in the Mössbauer spectra when hydrolysis commenced as a result of the decrease of the acid concentration. The Mössbauer parameters of a 2.10 mol dm^{-3} solution of $SnCl_2$ prepared in 0.09 mol dm^{-3} HCl are: $\delta = 3.76$ mm s^{-1}, $\Delta E = 0.65$ mm s^{-1}.

A change of the anion of the acid used in the solution did not cause a detectable difference in the Mössbauer spectra. In the range 0.05–4 mol dm^{-3}, the concentration of the tin salt also does not influence δ and ΔE to an extent that exceeds the limits of experimental error [26].

If the isomer shifts of the above frozen $SnCl_2$ solutions are compared with the corresponding Mössbauer parameters of crystalline $SnCl_2$ [27] ($\delta = 4.17$ mm s^{-1}; relative to $BaSnO_3$) the tin(II) ion in the solutions will show a less ionic character than in crystalline state. In the solution, therefore, there is a greater occupancy of the 5p and 5d electron orbitals. The empirical diagram given by Donaldson and Senior [23] reveals that the sp^3 character for the shell $n = 5$ (n is the principal quantum number) in the tin atom is 10% higher in $SnCl_2$ solutions than in crystalline $SnCl_2$. Donaldson and Senior [23] regarded the electronic structure of α–Sn as 100% sp^3 and that of the pure ionic $(5s)^2$ state as 0% sp^3 configuration, and assumed a linear correlation between the "sp^3 character" and the δ values. The considerable decrease in the isomer shift further indicates that the coordination number of the tin(II) ion increases during dissolution, an octahedral structure develops.

In water solutions of tin(IV)-salts, the isomer shift does not depend on the anion present in the solution and it is by 0.6 mm s^{-1} lower than in pure $SnCl_4$, and about 1.2 mm s^{-1} lower than in crystalline SnI_4. This means that in the aqueous solutions of the tin(IV) salt the electron density at the tin nucleus is lower than in these two tin(IV) halogenides. The reason is the formation of hexaaqua-coordinated tin(IV) species in the solution, which decreases the electron density at the nucleus by increasing the extent of occupation of the orbitals shielding the 5s orbital.

The effect of a second salt on the Mössbauer spectrum of a frozen aqueous solution of $SnCl_4$ was studied by Takeda et al. [28]. They found that the following salts changed the isomer shift of the frozen 0.4 mol dm^{-3} $SnCl_4$ solution. The magnitude of this change had the following order: $LiCl > AlCl_3 > MnCl_2 > MgCl_2 > ZnCl_2 > MgSO_4 > Mg(NO_3)_2$. The sequence suggests an increasing coordination of the anions to the central Sn atom.

5.1.3. HYDRATION OF EUROPIUM(III) CHLORIDE

Europium(III) chloride solutions have been investigated by various authors [29–36]. The stability constants of $EuCl_x^{(3-x)+}$ are also known [30]. Mössbauer spectroscopic studies provide useful information on the interaction between europium and its inner ligand sphere.

The quadrupole interaction results in eight lines in the Mössbauer spectrum of ^{151}Eu. The positions of these lines do not differ substantially, and they appear therefore, as one broadened line. The population of the levels related to the various magnetic quantum numbers (m_i) is not uniform, and therefore the intensities of the eight lines differ; which makes the determination of the isomer shifts difficult [37]. The centre of gravity of the broad line resulting from superposition of several peaks is frequently considered as the average isomer shift (δ_{eff}). It is suitable for comparisons within a given series of measurements.

Table 5.3.

Mössbauer parameters of rapidly frozen europium(III) salt solutions at liquid nitrogen temperature

Radiation source: $^{151}EuF_3$

No.	Molality in water mol kg^{-1}	Average isomer shift, δ_{eff} mm s^{-1}	Half width, Γ mm s^{-1}	Literature
1.	0.8 $Eu(ClO_4)_3 + 4\ HClO_4$	0.321 ± 0.015	3.30 ± 0.09	
2.	0.7 $Eu(ClO_4)_3 + 2.5\ HClO_4$	0.347 ± 0.017	2.86 ± 0.09	[38]
3.	1.4 $EuCl_3$	0.300 ± 0.015	3.31 ± 0.09	
4.	1.79 $EuCl_3 + 7.33\ LiCl$	0.240 ± 0.069	3.66 ± 0.46	
5.	1.4 $EuCl_3 + 10.5\ LiCl$	0.254 ± 0.014	2.86 ± 0.08	
6.	1.0 $EuCl_3 + 7.9\ LiCl + 2.2\ HCl$	0.134 ± 0.042	2.95 ± 0.23	
7.	$EuCl_3$ crystalline	0.083 ± 0.008	2.81 ± 0.04	
8.	$EuCl_3 \cdot 6H_2O$ crystalline	0.495 ± 0.040	3.01 ± 0.15	
9.	0.5 Eu $(ClO_4)_3 + 3\ HClO_4$	0.34 ± 0.05		
10.	0.5 $Eu(ClO_4)_3$ at pH = 1	0.31 ± 0.05		[39]
11.	0.5 $Eu(ClO_4)_3$ at pH = 4	0.21 ± 0.05		
12.	0.5 $Eu(ClO_4)_3$ at pH = 7	0.14 ± 0.05		
13.	0.5 $Eu(ClO_4)_3 + 1.5\ HClO_4 + 1.5\ NaCl$	0.12 ± 0.05		
14.	0.5 $Eu(ClO_4)_3 + 1.5\ HClO_4 + 5.0\ NaCl$	0.16 ± 0.05		
15.	0.5 $Eu(ClO_4)_3 + 1.5\ HClO_4 +$ saturated NaCl	0.15 ± 0.05		
16.	0.5 $Eu(ClO_4)_3 + 1.5\ HClO_4 + 1.5\ NaBr$	0.17 ± 0.05		
17.	0.5 $Eu(ClO_4)_3 + 1.5\ HClO_4 + 5.0\ NaBr$	0.17 ± 0.05		
18.	0.5 $Eu(ClO_4)_3 + 1.5\ HClO_4 + 1.0\ NaI$	0.27 ± 0.05		
19.	0.5 $Eu(ClO_4)_3 + 1.5\ HClO_4 + 2.0\ NaI$	0.21 ± 0.05		

From the data in Table 5.3 it can be seen that an increase of the halogenide concentration or the pH leads to a decrease of δ_{eff}, indicating that the coordination of halogenides results in a decrease in the electron density at the nucleus, and hence in the occupation of the orbitals (4f, 5d) that shield the s orbitals [38, 39]. The same tendency can be observed on comparison of the δ values of the $EuCl_3 \cdot 6H_2O$ and anhydrous $EuCl_3$ (see Table 5.3), as in the latter case, when only chloride is coordinated to the europium, δ is substantially lower than in the hexahydrate, when most of the coordination sites of the europium are occupied by water molecules. (One of the Mössbauer spectra is shown in Fig. 5.2.)

The results in Table 5.3 also show that a decrease of the pH leads to a substantial increase of the coordination of chloride ions. In measurement No. 5, for example, the Cl^- concentration was higher than in measurement No. 6, nevertheless, the δ_{eff} values indicate stronger chloride coordination in measurement No. 6. This effect can be explained by the higher H^+ concentration in the latter solution.

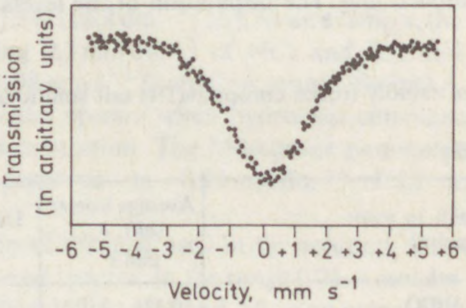

Fig. 5.2. Mössbauer spectrum of aqueous solution of 0.5 mol dm^{-3} $Eu(ClO_4)_3$ at pH = 4.0 and at 80 K

The isomer shift δ_{eff} strongly depends on the nature of the halogenides and only to a very slight extent on their concentration, suggesting that the number of coordinated halogenides (X = Cl, Br, I) is < 3. The values of the isomeric shifts show the following order of covalency effect: Cl > Br > I. Comparing the results for different pH it can be concluded that both Eu^{III}—OH and Eu^{III}—X bonds decrease δ_{eff}.

Yamanchi et al. used Mössbauer technique to follow the photooxidation of Eu^{II} ions in aqueous solution to Eu^{III} ions in the presence of Cl^- anions [40]. They used the light of 300 nm wavelength and the Mössbauer spectra were recorded at 78 K. Adding 5 mol dm^{-3} LiCl to the solution, the freezing of the liquid resulted in a glassy state and the Mössbauer line of Eu^{II} very intensively broadened. The explanation of this phenomenon is that the LiCl hindered the segregation of 0.28 mol dm^{-3} Eu^{II} and the dispersed Eu^{II} ions, which have one unpaired $(5d)^1$ electron, have a relatively slow paramagnetic spin relaxation.

REFERENCES

1. Debye, P., Hückel, E., *Z. Physik*, **24**, 185 (1923).
2. Stillinger, F. H. and Lovett, R., *J. Chem. Phys.*, **48**, 3858 (1968).
3. Rossky, P. J., *Ann. Rev. Phys. Chem.* **36**, 321 (1985).
4. Dogonadze, R. R., Kálmán, E., Kornyshev, A. A. and Ulstrup, J., *The Chemical Physics of Solvation* Part A. Theory of Solvation, Elsevier, (1985.
5. Erdey-Grúz, T., *Transport Processes in Aqueous Solutions* (in Hungarian), Akadémiai Kiadó, Budapest, 1971.
6. Horne, R. A., *Water and Aqueous Solutions*, Wiley-Interscience, New York, London, Sydney, Toronto, 1972.

7. *Symposium on the Structure of Liquids and Solutions*, 27–30 August, 1984, Veszprém, Hungary.
8. Vértes, A., *Acta Chim. Acad. Sci. Hung.*, **63**, 9 (1970).
9. Burger, K., Vértes, A., Papp-Molnár, E., *Acta Chim. Acad. Sci. Hung.*, **57**, 257 (1968); *Magy. Kém. Folyóirat*, **74**, 365 (1968).
10. Jørgensen, C. K., *Absorption Spectra and Chemical Bonding in Complexes*, Pergamon Press, Oxford, 1962; *Structure and Bonding*, **1**, 3 (1966).
11. Vértes, A., *Radiochem. Radioanal. Letters*, **40**, 405 (1979).
12. Korolev, V. V. and Bazhin, I. M., *Zh. Neorg. Khim.*, **20**, 701 (1975).
13. Vértes, A., Czakó-Nagy, I. and Kravtsov, V. I., *Radiochem. Radioanal. Letters*, **43**, 93 (1980).
14. Vértes, A., Unpublished results.
15. Vértes, A., Székely, T. and Tarnóczy, T., *Acta Chim. Acad. Sci. Hung.*, **63**, 1 (1970).
16. Kálmán, E., Radnai, T., Pálinkás, G., Hajdú, F., Vértes, A., *Electrochimica Acta*, **33**, 1223 (1988).
17. Vértes, A. and Nagy, M., *Radiochem. Radioanal. Lett.*, **9**, 221 (1972).
18. Mundt, W. A. and Sonnino, T., *J. Chem. Phys.*, **50**, 3127 (1969).
19. Dézsi, I., Molnár, B., Szalay, T. and Jászberényi, I., *Chem. Phys. Lett.*, **18**, 598 (1973).
20. Dominques, P. H. and Danon, J., *Chem. Phys. Lett.*, **13**, 365 (1972).
21. Papp, S., Kvintovics, T., Nagy, F. and Vértes, A., *Acta Chim. Acad. Sci. Hung.*, **87**, 343 (1975).
22. Ruby, S. L., Love, J. C., Flinn, P. A. and Zabransky, B. J., *Applied Physics Letters*, **27**, 320 (1975).
23. Donaldson, F. and Senior, B. J., *J. Chem. Soc. A*, 1796 (1966).
24. Gibb, T. C. and Greenwood, N. N., *J. Chem. Soc. A*, 43 (1966).
25. Zuckerman, S. S., *Advances in Organometallic Chemistry*, **9**, 21 (1970).
26. Vértes, A., Győri, E., Gál, M. and Suba, M., *Magy. Kém. Folyóirat*, **77**, 189 (1971).
27. Donaldson, J. D. and Nicholson, D. G., *J. Chem. Soc.* A, 145 (1970).
28. Takeda, M., Kanno, H. and Tominaga, T., *J. Physique.*, **40**, C2–345 (1979).
29. Irving, H. and Khapkor, P., *J. Inorg. Nucl. Chem.*, **26**, 1561 (1964).
30. Choppin, C. R. and Unrein, P. I., *J. Inorg. Nucl. Chem.*, **25**, 387 (1963).
31. Basel, B. M., Patil, S. K. and Sharma, J. D., *J. Inorg. Nucl. Chem.*, **26**, 993 (1964).
32. Gallagher, P. K., *J. Chem. Phys.*, **41**, 3061 (1964).
33. Sayre, E. V., Miller, D. G. and Freed, S., *J. Chem. Phys.*, **26**, 109 (1957).
34. Miller, D. G., Sayre, E. V. and Freed, S., *J. Chem. Phys.*, **29**, 454 (1958).
35. Tereshin, G. S., *Zh. Neorg. Khim.*, **12**, 2401 (1967).
36. Ferraro, J. R., Basile, L. J. and Kovacic, D., *Inorg. Chem.*, **5**, 391 (1966).
37. Goodman, B. A., Greenwood, N. N. and Turner, G. E., *Chem. Phys. Lett.*, **5**, 181 (1970).
38. Greenwood, N. N., Turner, G. E. and Vértes, A., *Inorg. Nucl. Chem. Lett.*, **7**, 389 (1971).
39. Vértes, A., Music, S. and Nagy-Czakó, I., *Radiochem. Radioanal. Letters*, **30**, 35 (1977).
40. Yamauchi, S., Minai, Y. and Tominaga, T., *J. Radioanal. Nucl. Chem. Letters*, **93**, 237 (1985).

5.2. MÖSSBAUER SPECTRA AS A MEANS OF SOLVATION STUDIES

In the systematization of organic solvents and in the discovery of general regularities of the solvation process, significant results were achieved by Gutmann [1], who classified solvents in accordance with their donor characters (donicities) and dielectric properties.

As a measure of the donor property of a solvent, he considered the calorimetrically measured reaction heat (in kJ mol^{-1}) for the solvation of $SbCl_5$ by the donor solvent (the calorimetric measurement was carried out in a dilute solution prepared with an inert solvent of low relative permittivity (ε_r), in order to eliminate side-reactions such as dissociation). He termed the enthalpy of solvation the donor number (DN), or donicity. A higher donicity, therefore, represents a greater ability for the formation of a donor-acceptor covalent bond between the solvent and solute. Denoting the dissolved salt by MA and the donor solvent molecule by D, a solvation process can be described by the following equation:

$$\mathrm{MA} + n\mathrm{D} \rightleftharpoons (\mathrm{MD}_n)^+\mathrm{A}^- . \qquad (5.1)$$

The equilibrium constant of Eq. (5.1) depends on the DN of the solvent.

The dissociation of the dissolved salt is known to depend primarily on the relative permittivity (ε_r); in the case of solutes containing covalent bonds, however, ion dissociation is also promoted by a higher DN. Solvent molecules of high donicity in the solvate in Eq. (5.1) weaken the covalent bond M—A, and in this way the dipolar solvent molecules can easily separate the cation and anion from one another. The above solvate, therefore, undergoes a further transformation:

$$[(\mathrm{MD}_n)^+\mathrm{A}^-] + (k+1)\mathrm{D} \rightleftharpoons [\mathrm{MD}_{n+1}]^+ + [\mathrm{AD}_k]^- . \qquad (5.2)$$

By addition of Eqs (5.1) and (5.2), we obtain:

$$\mathrm{MA} + (n+k+1)\mathrm{D} \rightleftharpoons [\mathrm{MD}_{n+1}]^+ + [\mathrm{AD}_k]^- . \qquad (5.3)$$

The dissociation coefficient of MA is thus determined jointly by the DN and ε_r.

When metal salts are dissolved in various solvents, two fundamental effects determine the electronic structure and hence the Mössbauer spectrum of the metal: (*a*) the coordination of the solvent molecules to the cation and (*b*) the extent of association between the cation and its anion. Accordingly, Mössbauer spectra primarily yield information regarding these two effects.

5.2.1. SOLVATION OF IRON SALTS

In early applications of Mössbauer spectroscopy to the study of solvation processes and metal solvates, one of the model systems were the rapidly frozen solutions of iron(II) salts in different nonaqueous solvents [2, 3]. Some characteristic experimental results are presented in Table 5.4.

In methanol ice, iron(II) sulfate gave a Mössbauer spectrum coinciding with that for iron(II) chloride, whereas in ethylene glycol ice the Mössbauer parameters of the two salts differed. In methanolic solution, therefore, these two iron(II) salts form iron(II) solvate coordination entities of the same composition, while in ethylene glycol solution the composition of the coordination sphere of the iron(II) ion depends on the anion, i.e. anions also participate in the inner coordination sphere.

Table 5.4.

Mössbauer parameters of rapidly frozen iron salt solutions at liquid nitrogen temperature

Radiation source: ^{57}Co in stainless steel

No.	Solute	Solvent	Quadrupole splitting, ΔE mm s^{-1}	Isomer shift*, δ mm s^{-1}
1.	$FeCl_2$	Methanol	3.50	1.41
2.	$FeSO_4$	Methanol	3.44	1.37
3.	$FeCl_2$	Ethylene glycol	3.20	1.20
4.	$FeSO_4$	Ethylene glycol	3.06	1.48
5.	$FeCl_2 \cdot 4H_2O$	Methanol	3.24	1.48
6.	$FeCl_2$	Methanol + water	3.33	1.40
7.	$FeCl_2$	Pyridine	3.48	1.26
8.	$FeCl_2$	Formamide	1.89	1.43
9.	$FeCl_2$	Dimethylformamide	2.12	1.21
10.	$FeCl_2 \cdot 4H_2O$	Formamide	2.71	1.41
11.	$FeCl_2 \cdot 4H_2O$	Dimethylformamide	2.67	1.25
12.	$FeCl_2$	Dimethyl sulfoxide	2.36	1.34
13.	$FeCl_2$	Hexamethylphosphoric triamide	2.77	1.16
14.	$FeCl_2$	Tributyl phosphate	2.77	1.35
15.	$FeCl_2$	Acetonitrile	2.95	1.29

* Relative to stainless steel. Concentrations: 0.7 mol kg^{-1} for $FeCl_2$ salts, or saturated solutions if the solubility was less than 0.04 mol kg^{-1} for $FeSO_4$.

When iron(II) chloride tetrahydrate ($FeCl_2 \cdot 4H_2O$) was dissolved in methanol, Mössbauer parameters differed by more than the experimental error from those measured for methanolic solutions of anhydrous iron(II) chloride. If the calculated amount of water was added to the methanolic solution of anhydrous iron(II) chloride (four molecules of water per iron atom) and the solution was frozen after being aged for 24 hours, the resulting Mössbauer spectrum was nearly the same as that of an absolute methanolic solution of $FeCl_2 \cdot 4H_2O$. These experimental results show that the affinity of the water molecules for iron(II) is thus so much greater than that of the methanol molecules that even under extreme concentration conditions the solvation equilibrium is shifted in the direction of the formation of coordination entity that also contains water molecules.

Comparison of the isomer shifts of frozen solutions of anhydrous iron(II) chloride in pyridine, ethylene glycol or dimethylformamide with the corresponding values measured in aqueous, methanol or formamide solutions clearly shows that in the former solutions (in which, as conductivity data [2] indicate, the chloride ion is probably also bound in the first coordination sphere of the iron) the isomer shifts are lower than in the latter solutions, in which the chloride is not coordinated to the iron(II) ion.

The relatively low ΔE values of anhydrous iron(II) chloride solutions in formamide or dimethylformamide show that the solvate sheath that contains the formamide or dimethylformamide molecules increases the symmetry of the electron cloud of the central iron atom. The difference between the δ values relating to the formamide and dimethylformamide solvents can be interpreted on the basis of conductivity measurements as follows: in the formamide solvate the chloride ions are not present in the first coordination sphere of the iron(II) ion, while in the dimethylformamide solvate also the chloride ions are bound directly to the iron(II) ion, and, as a consequence of their high nephelauxetic effect, increase the s electron density at the central iron nucleus.

The Mössbauer parameters measured in the formamide–$FeCl_2 \cdot 4H_2O$ and dimethylformamide–$FeCl_2 \cdot H_2O$ systems reveal that these solvents form mixed solvates with water. From the Mössbauer measurements (see Nos 6–9 in Table 5.4) it can be concluded that the chloride ion is involved in the inner ligand sphere in these solvents.

When pyridine is saturated with LiCl, the Mössbauer spectrum of the $FeCl_2$ solution remains unchanged, indicating that an increase in the chloride concentration does not result in further chloride coordination. In hexamethylphosphoric triamide saturated with LiCl, the Mössbauer parameters change to $\Delta E = 2.88$ mm s^{-1} and $\delta = 0.78$ mm s^{-1}. The considerable decrease of the isomer shift shows that chloride ions are coordinated to the iron in the solution saturated with chloride [3].

De Vries et al. [4] studied the effect of solvation on the Mössbauer parameters in bis(*N*,*N*-diethyldithiocarbamato)iron(III) chloride, $[Fe(dtc)_2]Cl$ and the tetrabutylammonium salts of bis(maleonitriledithiolato)ferrate(III) and bis(toluenedithiolato) ferrate(III). They compared the Mössbauer parameters of the coordination entities measured in the solid state and in frozen solutions prepared with various solvents, and demonstrated that the quadrupole splitting of the coordination entities are lower in solution than in the solid state, and roughly agree with the value for $[Fe(dtc)_3]$ in which iron is octahedrally coordinated. It was concluded from the experimental results that the 5-coordinated iron in the solid-state is transformed into 6-coordinated iron in the solution. (For example, at liquid nitrogen temperature the quadrupole splittings of $[Fe(dtc)_3]$ and $[Fe(dtc)_2]Cl$ are 0.52 mm s^{-1} and 2.76 mm s^{-1}, respectively in solid state and they are 0.66 mm s^{-1} and 0.70 mm s^{-1} in dimethylformamide solutions.) Mössbauer spectra of the $[Fe^{III}(dtc)_x]X_y$ (where X is a halogenide) in tetrahydrofuran were studied by Malliaris et al. [5] in the temperature range between 4.2 and 300 K. Analysis of the Mössbauer parameters shows that in the solvated coordination entity the Fe^{III} has $S = 5/2$ spin quantum number and lies in the plane of the four sulfur atoms [5].

Mössbauer study of the paramagnetic spin-relaxation can give information about the structure of iron(III) salt solutions.

When the positions of Fe^{III} ions are far apart in the frozen solutions a spectrum with magnetic hyperfine structure (MHS) will be observed due to the slow paramagnetic spin relaxation. This is the case of mononuclear solvates at low concentrations. On the other hand, when the iron(III) ions are close together, such as in dimers or polymers, the MHS is diminished because of the resulting decrease of spin-spin relaxation time.

Mössbauer spectra show that iron(III) chloride is in dimeric or polymeric form in benzene, nitrobenzene and partially in acetone, acetonitrile, pyridine, and dimethylformamide (dmf), while it is monomeric in ethanol. The stability of dimeric solvates generally increases with the increase of the donicity of the solvent, but the stability of the iron-pyridine dimeric solvate is much higher than it could be explained by donicity [6].

Inclination to monomer formation depends on the donicity and relative permittivity of the solvent. The order in decreasing inclination is: ethanol, dimethylformamide, pyridine, acetone, acetonitrile, nitrobenzene and benzene. Some of the spectra are shown in Fig. 5.3.

The transversely applied magnetic field strength of 0.88 T resulted in splitting of the central line only in the acetone solution of iron(III) chloride in the case of the studied solvents. This proves that in dimeric solvates, with the exception of acetone dimer, the iron(III) atoms are antiferromagnetically coupled (see Fig. 5.4).

Frozen solutions of 0.1 mol dm^{-3} tris(acetylacetonato)iron(III), $[Fe(acac)_3]$ in benzene, toluene, ethylbenzene and cumene were also studied [7]. The Mössbauer spectra recorded at 78 K showed magnetic hyperfine structure in toluene, ethylbenzene and cumene, but only paramagnetic structure could be obtained in benzene. These experimental results gave the evidence that the $[Fe(acac)_3]$ had a polymer structure in benzene, but was uniformly dispersed in the other three solvents.

The Mössbauer spectrum of the frozen solution of 0.1 mol dm^{-3} $FeCl_3$ in isopropyl alcohol possesses MHS, demonstrating again mononuclear structure. By water addition to the solution before freezing the MHS collapses and only a doublet appears in the Mössbauer spectrum ($\Delta E = 0.77$ mm s^{-1} and $\delta = 0.48$ mm s^{-1}). This is a proof for dimer formation in the solution at the presence of water [8]. (This experiment is an excellent demonstration of the usefulness of Mössbauer technique in solution chemistry.)

Marques and Matos recorded the Mössbauer spectra of $FeCl_3$ in toluene in the presence of hydrogen chloride and trilauroylamine hydrochloride (R_3NHCl, $R = CH_3—[CH_2]_{10}—CO—$) [9]. The authors identified $R_3NH[FeCl_4]$ and $[FeCl_3(R_3N)]$ coordination entities. $R_3NH[FeCl_4]$ appeared in the solution at high HCl concentrations (8 mol dm^{-3}). There is a special type of solvation when the solvent is added to ion-exchanger containing Mössbauer active ions. In such cases the Mössbauer spectra give information about the position of the ion-exchanged atoms in the ion-exchange materials [10–15]. For example Dickson and Rees recorded the Mössbauer spectra of iron(II) ions exchanged into sodium-A zeolite after successive additions of small amounts of ethanol [15]. The results gave evidence that two molecules of solvent coordinate to each iron(II) ion. This experimental result allowed conclusions about the position of iron(II) ion in the lattice of sodium-A zeolite. The

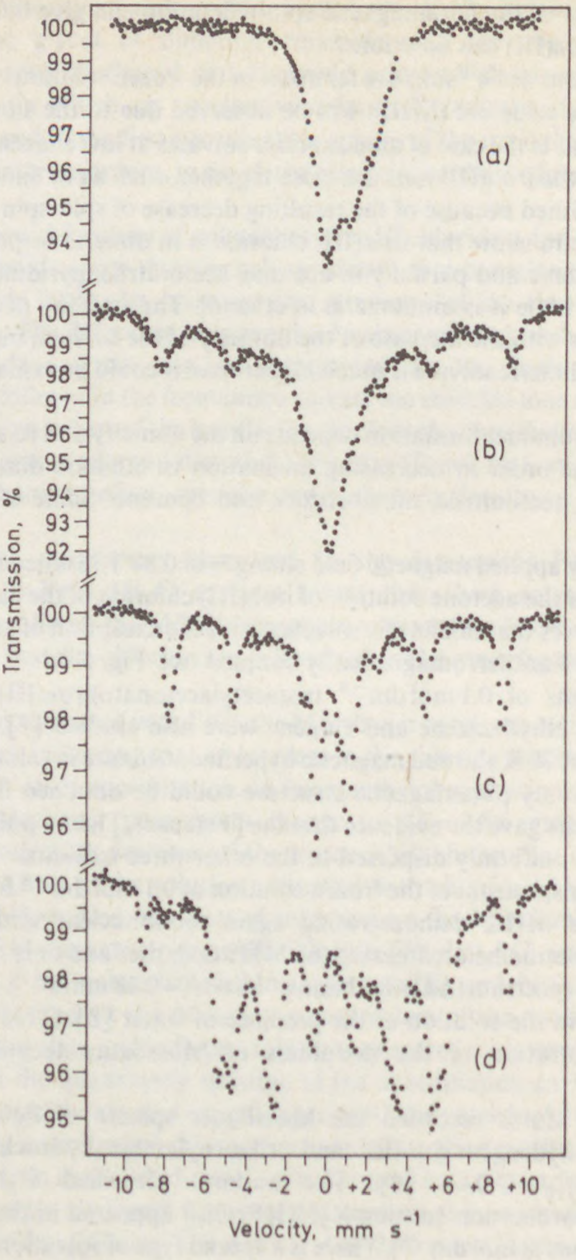

Fig. 5.3. Mössbauer spectra of $FeCl_3$ solutions at 4.2 K. (a) 1.4×10^{-2} mol dm^{-3} $FeCl_3$ in benzene; (b) 1.0 $\times 10^{-2}$ mol dm^{-3} $FeCl_3$ in acetone; (c) 1.4×10^{-2} mol dm^{-3} $FeCl_3$ in pyridine; (d) 1.4×10^{-2} mol dm^{-3} $FeCl_3$ in ethanol

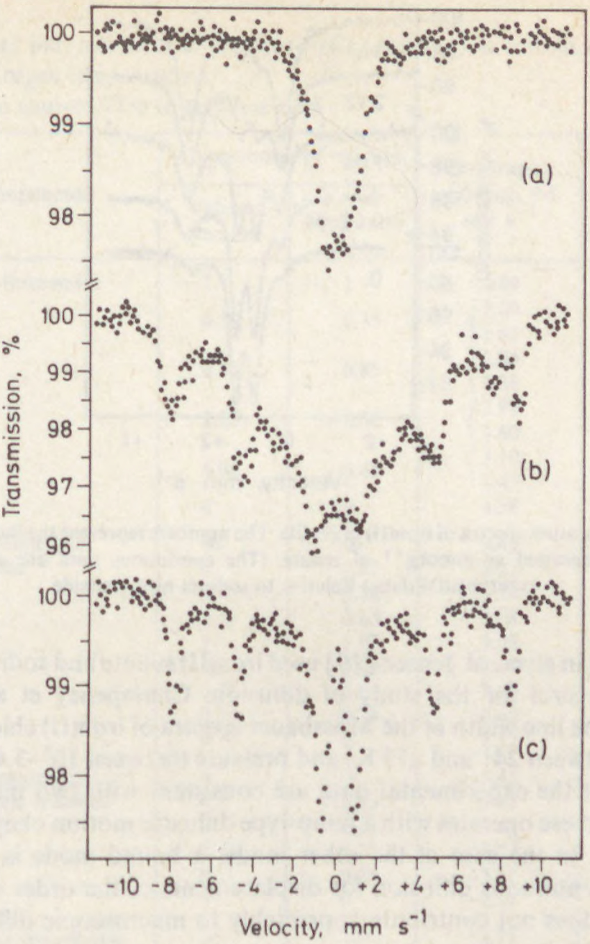

Fig. 5.4. Mössbauer spectra of $FeCl_3$ solutions at 4.2 K and at 0.88 T applied magnetic flux density. (a) 1.4 $\times 10^{-2}$ mol dm^{-3} $FeCl_3$ in benzene; (b) 1.0 $\times 10^{-2}$ mol dm^{-3} $FeCl_3$ in acetone; (c) 1.4 $\times 10^{-2}$ mol dm^{-3} $FeCl_3$ in pyridine

unsolvated iron(II) ions showed isomer shift of 1.09 mm s^{-1} (relative to sodium nitroprusside at room temperature) and quadrupole splitting of 0.46 mm s^{-1} in the lattice of zeolite. These parameters increased after ethanol adsorption: the isomer shift was 1.40 mm s^{-1} and 2.30 mm s^{-1} was measured for the quadrupole splitting of the solvated iron(II) ions. The spectra are demonstrated in Fig. 5.5.

The dependence of the line broadening of the Mössbauer spectra of frozen solutions on the temperature informs about the motion namely about the diffusion of the dissolved Mössbauer active atoms. (The model of this correlation is given in Section 1.6.) The diffusion of cobalt(II) chloride in glycerol was studied by Craig and Sutin [16] using the emission Mössbauer technique. The motion of iron(II) and iron(III) sulfate was measured by Elliot et al. [17] and that of iron(II) chloride was studied by Abras

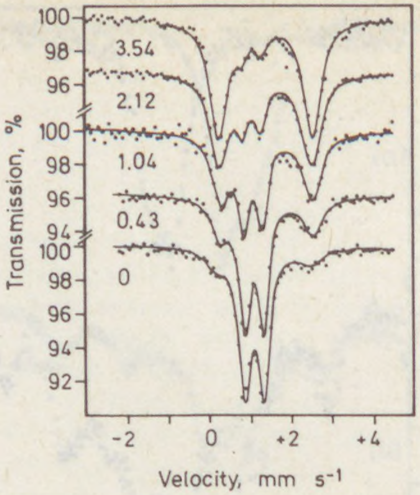

Fig. 5.5. Room temperature spectra of iron(II) in zeolite. The numbers represent the increasing quantities of adsorbed ethanol expressed as mmol g^{-1} of zeolite. (The continuous lines are computer fits of the experimental data.) Relative to sodium nitroprusside

and Mullen [18] in glycerol. Jensen [19] used iron(II) sulfate and sodium nitroprusside dissolved in glycerol for the study of diffusion. Champeney et al. measured the dependence of the line width of the Mössbauer spectra of iron(II) chloride solution on temperature (between 241 and 273 K) and pressure (between 10^5–3.45×10^8 Pa) [20]. They found that the experimental data are consistent with two models collaterally applied. One of these operates with a jump-type diffusive motion obeying the Einstein-Stokes relation. In the case of the other model a bound mode is supposed which approximates continuous diffusion for displacements of the order of 0.3×10^{-10} m. This, however, does not contribute appreciably to macroscopic diffusion.

5.2.1.1. Solvation studies of anhydrous iron(II) chloride in solvent mixtures

Anhydrous iron(II) chloride was dissolved in methanol–formamide, methanol–dimethylformamide, hexamethylphosphoric triamide $\{[(CH_3)_2N]_3PO\}$–pyridine and hexamethylphosphoric triamide–water mixtures of various compositions occurring in solvent mixtures [3, 21]. The results are presented in Table 5.5, and as an example, the spectra for hexamethylphosphoric triamide–water mixtures are shown in Fig. 5.6 [3, 21].

According to the results for the methanol-formamide mixtures, the spectral component with the lower quadrupole splitting (ΔE) exhibits a value close to that measured in pure formamide solution (see Table 5.5). This component is, therefore, a line pair originating from a solvate sheath consisting largely of formamide molecules. The higher ΔE value can be attributed to a solvate layer that consists mainly of methanol molecules, as this value lies close to the ΔE value for the pure methanolic solution. It should be noted that the higher and lower ΔE values cannot completely be

Table 5.5.
Mössbauer parameters of anhydrous $FeCl_2$ dissolved in solvent mixtures, at liquid nitrogen temperature
Radiation source: ^{57}Co in stainless steel

Components	Composition of mixture		Quadrupole splitting, ΔE mm s^{-1}	Isomer shift, δ mm s^{-1}
	Volume fraction	Mole ratio		
Methanol-formamide	1	1	1.89	1.43
	0.39	0.35	2.80 1.45	1.50
	0.94	0.85	2.86 1.36	1.41
	2.25	2.02	2.92 1.60	1.40
	6.06	5.45	3.10 1.45	1.47
	0	0	3.58	1.34
Methanol-dimethyl-formamide	∞	∞	3.45	1.33
	4	7.71	3.27	1.33
	3	5.78	3.14	1.33
	2	3.85	3.08	1.32
	1	1.92	3.03	1.32
	0.5	0.96	3.00	1.31
	0.33	0.64	2.93	1.31
	0.25	0.79	2.63	1.25
	0	0	2.12	1.21
Pyridine-hexamethyl-phosphoric triamide	∞	∞	3.45	1.25
	9	19.93	3.45	1.22
	3	6.64	3.44	1.23
	0.33	0.73	3.42	1.23
	0.11	0.24	3.41	1.22
	0	0	2.77	1.16
Hexamethyl-phosphoric triamide-water	∞	∞	2.77	1.16
	487	49.94	2.72	1.18
	139	14.24	2.77	1.14
	78	7.97	3.24 2.28	1.40 1.16
	17	1.74	3.24 2.72	1.46 1.20
	5.3	0.54	3.20 2.72	1.48 1.19
	0	0	3.20	1.51

identified with the quadrupole splitting values $\Delta E = 3.50 \pm 0.05$ and 1.89 ± 0.05 mm s^{-1} for pure methanolic solution and pure formamide solution, respectively. The difference between the quadrupole splittings obtained in the pure solvents and in the mixtures can be explained by the formation of a mixed solvate sheath.

It is worth noting that for all the compositions of the mixture the intensities of the lines relating to the lower ΔE values are smaller than those of the lines relating to the higher ΔE values [21]. Assuming that the probability (f) of recoilless absorption is equal for all solvate sheaths in a given solvent mixture, this experimental fact shows

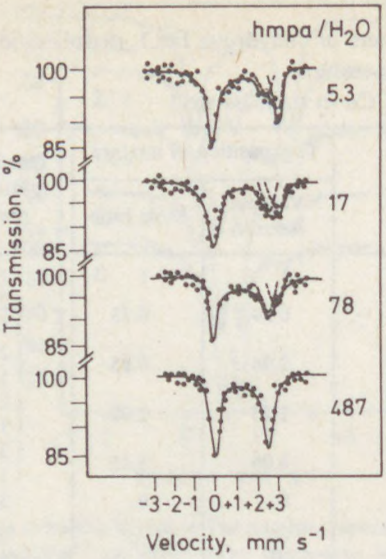

Fig. 5.6. Mössbauer spectra of $FeCl_2$ in hexamethylphosphoric triamide (hmpa)-water mixtures at various mole ratios, at liquid nitrogen temperature

that the relative amount of the solvate (containing more methanol molecules) corresponding to the higher ΔE value is in every instance higher than that of the solvate (containing more formamide molecules) corresponding to the lower ΔE value. It can be seen from the spectra, however, that with a decrease in the ratio of formamide in the mixture the relative intensity of the line pair relating to the lower ΔE value decreases, indicating equilibrium between the two types of solvate coordination entities.

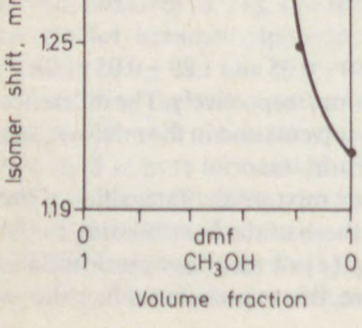

Fig. 5.7. Dependence of the isomer shift of $FeCl_2$ on the composition of the solvent in dimethylformamide (dmf)-methanol mixtures

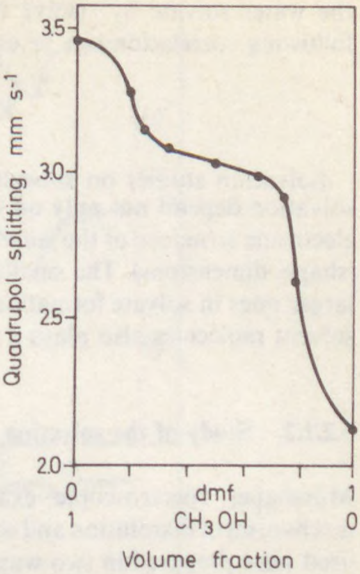

Fig. 5.8. Dependence of the quadrupole splitting of $FeCl_2$ on the composition of the solvent in dimethylformamide (dmf)-methanol mixtures

Separation of the Mössbauer spectra in dimethylformamide–methanol mixtures into components was not possible, as the presence of various types of solvates is indicated only by the broadening of the lines. The Mössbauer parameters obtained in solvent mixtures of various compositions are presented in Table 5.5 and in Figs 5.7 and 5.8.

From the δ and ΔE values, it can be concluded that in a methanol–dmf mixture containing ca 75 vol.-% dimethylformamide there is a sudden change in the composition of the solvate sheath, and that at a dimethylformamide concentration of less than ca 75 vol.-% (mole ratio 0.64 : 1) the methanol predominates in the inner ligand sphere of the iron(II).

The δ and ΔE values of Mössbauer spectra recorded in pyridine–hexamethylphosphoric triamide mixtures agreed with the data recorded in pure pyridine, even for a hexamethylphosphoric triamide content of 90 vol.-% (mole ratio 0.24 : 1). It follows from this result that pyridine is bound to iron(II) more covalently than hexamethylphosphoric triamide.

All the Mössbauer spectra recorded in hexamethylphosphoric triamide–water mixtures revealed the superposition of two spectral components (see Fig. 5.6), and the Mössbauer parameters of these agreed with the parameters of Mössbauer spectra recorded in pure water or in pure hexamethylphosphoric triamide, demonstrating that in this solvent mixture the bulk of the iron(II) is present in the forms of pure water and pure hexamethylphosphoric triamide solvates. As regards the quantitative proportions of the individual components, it can be stated that in hexamethylphosphoric triamide–water mixture (volume fraction 17 : 1, mole ratio 1.74 : 1) the amounts of the two types of solvates are the same; in mixtures rich in water the "water solvate" will increasingly predominate.

If the mole ratio of hexamethylphosphoric triamide to water in the solution is denoted by r(sln), and the mole ratios of the hexamethylphosphoric triamide solvate to the water solvate by $r(\text{solv})$, then from the intensities of the Mössbauer lines the following correlation can be established:

$$K = \frac{r(\text{solv})}{r(\text{sln})} = 0.57 \pm 0.03. \tag{5.4}$$

Solvation studies on solvent mixtures showed that the course and result of the solvation depend not only on the cation and anion of the dissolved salt and on the electronic structure of the solvent molecules, but also on their geometrical properties (shape, dimensions). The smaller solvent molecules take part more actively than the larger ones in solvate formation. In the formation of mixed solvates the fitting of the solvent molecules also plays a significant role.

5.2.1.2. Study of the solvation of iron in acetic acid by Mössbauer spectroscopy

Mössbauer spectroscopic examinations have contributed to the study of the mechanism of dissolution and solvation of iron in glacial acetic acid [22]. The solutions used were prepared in two ways: (*a*) In the course of the dissolution, oxygen was led through the solvent (dissolution process A). (*b*) Hydrogen was bubbled through the solvent during the dissolution (dissolution process B). In solution A, only iron(III) ions were present in the system and in solution B, both iron(III) and iron(II) ions appeared [22] (see Fig. 5.9).

In process A, the solution after dissolution was dark brown, and then gradually became paler. The decrease in intensity of the colour of the solution could be followed spectrophotometrically, see Fig. 5.10 (the absorption curve exhibited a maximum at 650 nm, and measurements were therefore made at this wavelength).

The colour of solution B was lighter, and no colour change or precipitate formation was observed even after several weeks. When solutions A and B were diluted by water, the δ values did not change, but the ΔE values decreased substantially, indicating coordination of the water. In the case of solution A, although the quadrupole splitting decreased from 0.60 to 0.43 mm s^{-1} after the addition of water [22], it did not decrease close to zero, as occurred in the case of solution B. (In solution B the lack of quadrupole splitting can be attributed to a totally symmetric ligand sphere around the iron(III) ion, as is the case of $[\text{Fe(H}_2\text{O)}_6]^{3+}$ ion.) This shows that the composition of the solvate sheath in solution A changes; thus, in this instance the water molecules force out the acetate ions and acetic acid molecules from the inner ligand sphere of the iron(III) ions, but in addition the iron atom is bound to some other inner ligand component which the water molecules cannot displace. This effect suggests the presence of hydroxo ligand in the coordination entity.

Also the Mössbauer parameters of the iron(II) ion depend on the composition of the aqueous acetic acid solution and this suggests an equilibrium among water and acetic acid molecules and OH^- and CH_3COO^- ions in the ligand sphere of iron(II) ion. The Mössbauer parameters of three frozen iron-acetic acid-water solutions are given in Table 5.6. The higher concentration of acetic acid resulted in a strong decrease of the quadrupole splitting due to the coordination of CH_3COO^- and CH_3COOH to the iron(II) ion.

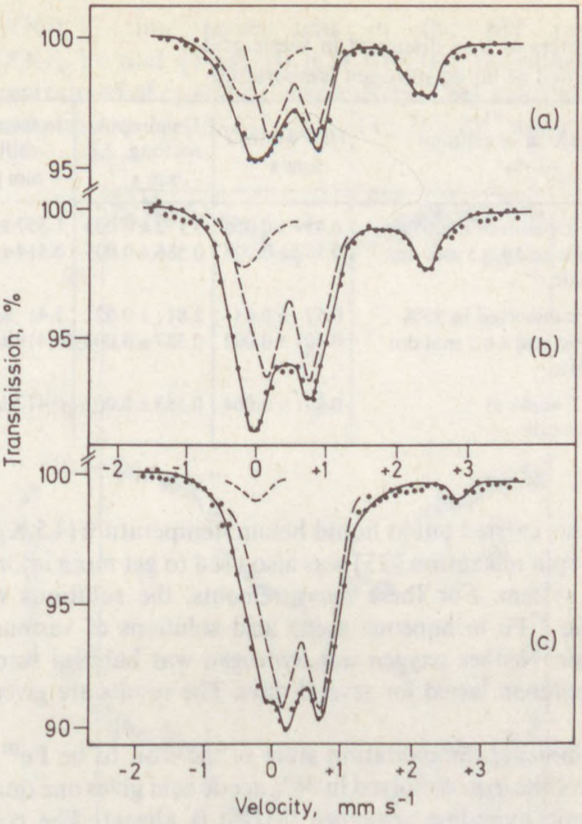

Fig. 5.9. Mössbauer spectrum of solution B at liquid nitrogen temperature. (a) Immediately after dissolution; (b) after ageing for 1 d, and (c) after ageing for 1 week. Radiation source: ^{57}Co in stainless steel

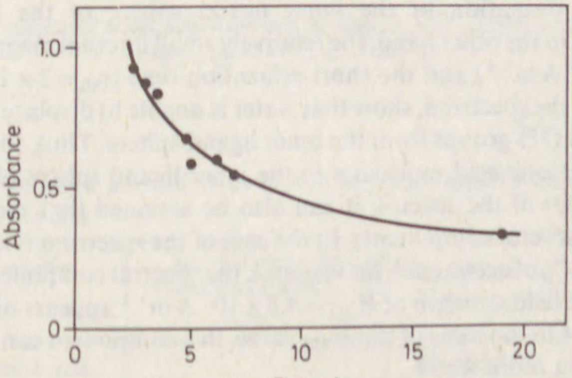

Fig. 5.10. Variation of the absorbance of solution A with time at 650 nm

Table 5.6.
Mössbauer parameters of iron dissolved in acetic acid
Spectra were recorded at liquid nitrogen temperature

No.	Composition of solution wt.-%	Half width, Γ mm s^{-1}	Quadrupole splitting, ΔE mm s^{-1}	Isomer shift, δ mm s^{-1}	Area percentage of Fe^{II} line
1.	Enriched ^{57}Fe dissolved in 20% aqueous acetic acid + 0.5 mol dm^{-1} sodium acetate	0.439 ± 0.008 0.337 ± 0.008	3.172 ± 0.005 0.586 ± 0.005	1.357 ± 0.002 0.514 ± 0.003	62.01
2.	Enriched ^{57}Fe dissolved in 95% aqueous acetic acid + 0.5 mol dm^{-3} sodium acetate	0.57 ± 0.03 0.409 ± 0.002	2.81 ± 0.02 0.587 ± 0.001	1.41 ± 0.01 0.419 ± 0.001	12.54
3.	No. 1, aged 2 weeks at room temperature	0.341 ± 0.004	0.583 ± 0.002	0.412 ± 0.001	

In measurements carried out at liquid helium temperature (4.5 K) the phenomenon of paramagnetic spin relaxation [23] was also used to get more information about the iron-acetic acid system. For these measurements, the solutions were prepared by dissolving metallic ^{57}Fe in aqueous acetic acid solutions of various compositions in the presence of air. Neither oxygen nor hydrogen was bubbled through the solution, and thus the dissolution lasted for several days. The results are given in Fig. 5.11 and Table 5.7.

The δ values indicate the oxidation state of the iron to be Fe^{III}. Nearly the total amount (> 90%) of the iron dissolved in 96% acetic acid gives one quadrupole line pair, and thus magnetic hyperfine structure (MHS) is absent. The comparatively high quadrupole splitting ($\Delta E = 0.58$ mm s^{-1}) demonstrates that the iron solvate is a coordination entity of mixed ligand. As the iron was dissolved in acetic acid in the presence of air or oxygen, this absence of MHS suggests that under such conditions polymer formation commences in the solution after dissolution.

In systems that contain 35 or 60 wt.-% water, the bulk of the dissolved iron forms species which exhibit MHS. In these two instances the water molecules are also involved in the formation of the inner ligand sphere of the iron, and inhibit polymerization. On the other hand, the relatively small internal magnetic field strength ($H_{5/2} = 3.98 \times 10^7$ A m^{-1}) and the short relaxation time ($\tau_{SR} = 2 \times 10^{-9}$ s), calculated from the shape of the spectrum, show that water is unable to displace the more strongly covalently bound OH groups from the inner ligand sphere. Thus, the water molecules replace only the acetic acid molecules in the inner ligand sphere of the iron(III) ion.

From the shapes of the spectra, it can also be assumed that they result from the superposition of several components. In the case of the spectrum relating to a solution containing 40 wt.-% of acetic acid, for instance, the spectral component representing an internal magnetic field strength of $H_{5/2} = 4.3 \times 10^7$ A m^{-1} appears only with fairly low intensity (ca 5%). On the basis of the $H_{5/2}$ value, this component can be ascribed to the solvate containing more water.

Nikolskii et al. [24] considered that in an aqueous solution of 3 mol dm^{-3} of acetic acid and of 2.4×10^{-2} mol dm^{-3} Fe(ClO$_4$)$_3$ in the pH range of 1.5–3 the

$[Fe_3(OH)_2(CH_3COO)_6]^+$ ion exists and in the pH range 3–4 both $[Fe_3(OH)_2(CH_3COO)_6]^+$ and $[Fe_3(OH)_2(CH_3COO)_7]$ coordination entities are present with concentrations of c_1 and c_2, respectively. They calculated the formation constants of the complexes: $c_1 a_H^2 c_{Fe^{3+}}^{-3} c_{CH_3COO^-}^{-6} = (3 \pm 2) \times 10^{19}$ and $c_1^{-1} c_2 c_{CH_3COO^-}^{-1} = 3$.

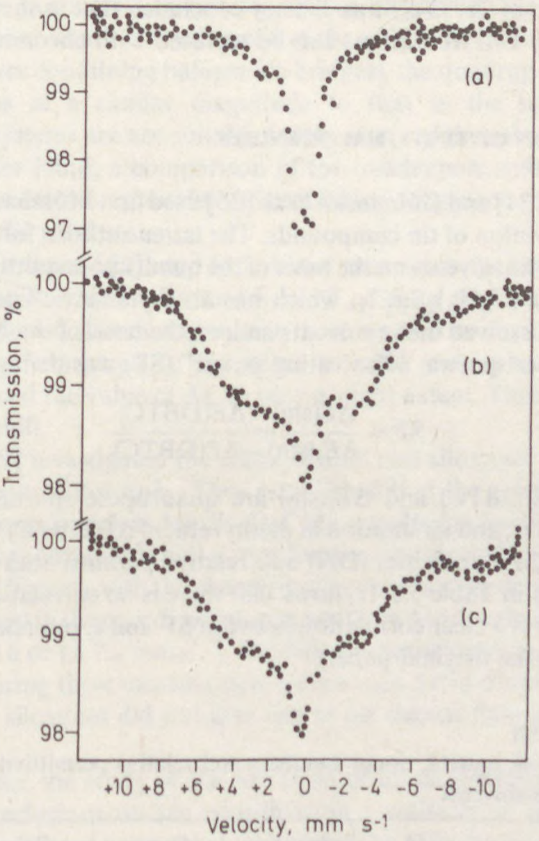

Fig. 5.11. Mössbauer spectra of acetic acid-water-iron systems at 4.5 K. Acetic acid concentration: (a) 96 wt.-%, (b) 65 wt.-%, (c) 40 wt.-%

Table 5.7.
Mössbauer spectra of acetic acid solutions of iron at liquid helium temperature
Radiation source: $^{57}Co(Pt)$

Composition of solution in water wt.-%	Internal magnetic field strength, $H_{5/2}$ A m^{-1}	Isomer shift, δ mm s^{-1}	Quadrupole splitting, ΔE mm s^{-1}
0.2% Fe + 96% acetic acid		0.194 ± 0.008	0.58 ± 0.05
0.2% Fe + 65% acetic acid	$(3.98 \pm 0.119) \times 10^7$		
0.2% Fe + 40% acetic acid	$(4.30 \pm 0.119) \times 10^7$		

In these calculations the authors supposed that the mononuclear hexaaquairon(III) ion has a sextet due to the paramagnetic spin relaxation and the different polynuclear complexes have different doublets in the Mössbauer spectrum.

On adding $Cr(ClO_4)_3$ to the solution, they found that the increase in the concentration of Cr^{III} ion in the solution changed the Mössbauer parameters until the concentration ratio of Cr^{III}/Fe^{III} was 2. They concluded that in the heteropolynuclear coordination entity two iron atoms can be replaced with chromium [24].

5.2.2. SOLVATION OF TIN(IV) HALOGENIDES

Aleksandrov et al. [24] and Goldanskii et al. [26] used first Mössbauer spectroscopy to investigate the solvation of tin compounds. The latter authors, for instance, classified seven dipolar, aprotic solvents on the basis of the quadrupole splitting of the dibutyltin dichloride (DBTC), $(C_4H_9)_2SnCl_2$, which has an asymmetric ligand sphere in pure state. DBTC was dissolved in the solvents and, on the basis of the ΔE values, obtained from the Mössbauer spectra, a "solvating power" (SP) was defined:

$$SP = \frac{\Delta E(\mathrm{sln}) - \Delta E(\mathrm{DBTC})}{\Delta E_e(\mathrm{sln}) - \Delta E(\mathrm{DBTC})} \tag{5.5}$$

where $\Delta E(\mathrm{sln})$, $\Delta E(\mathrm{DBTC})$ and $\Delta E_e(\mathrm{sln})$ are quadrupole splittings relating to the solution, pure DBTC, and its solution in diethyl ether [$\Delta E(\mathrm{DBTC}) = 3.4\ \mathrm{mm\ s^{-1}}$]. The solvating powers (SP), donicities (DN) and relative permittivities (ε_r) of the solvents examined are listed in Table 5.8. It shows that there is no correlation between SP and DN, but that there is a clear correlation between SP and ε_r (no reference was made to this correlation in the original paper).

Table 5.8.
Solvating powers, donor numbers and relative permittivities for various solvents

Solvent	Solvating power SP	Donor number DN	Relative permittivity ε_r
Diethyl ether	1.0	19.2	4.3
Diethoxyethane	6.0		
Tetrahydrofuran	7.0	20.0	7.6
Dimethyl ether	10.0		
Hexamethylphosphoric triamide	15.5	38.8	30.0
Dimethylformamide	16.0	26.6	36.1
Dimethyl sulfoxide	18.0	29.8	45.0

Later, studies have also been carried out on the solution of some R_3SnX compounds (where $R = CH_3$, methyl (Me); C_2H_5, ethyl (Et) or C_6H_5, phenyl (Ph) and X = F, Cl, Br or I) in some dipolar solvents, and it was found that the sequence of solvating powers was similar as that in Table 5.8 [27]. The authors measured also the sequence of the solvation ability of the solutes: $(C_4H_9)_2SnCl_2 > (C_6H_5)_3SnI > (C_2H_5)_3SnBr > (C_2H_5)_3SnI$, where C_4H_9 is butyl (Bu).

The actual reason for the change in quadrupole splitting due to solvation of the alkyl tin halogenides is that the molecule in the solid state contains tetrahedrally coordinated tin atom, which becomes 5 or 6 coordinated in solution by coordination of the solvent molecule. In contrast, in systems such as Ph_3SnF, Et_3SnF and Et_3SnCl, in which the tin has a coordination number of 5 in the solid state (these compounds have polynuclear structures containing halogenide bridges), the quadrupole splitting in the frozen solution was of a similar magnitude to that in the solid sample [27]. Accordingly, these systems are not suitable for the study of the solvating ability of the solvent. On the other hand, a comparison of the quadrupole splittings of the solid sample and its frozen solution provides indirect information as to whether the sample was monomeric in the solid state.

Schnorr and Kriegsmann [28] used Mössbauer spectroscopy to study the solvation of R_nSnCl_{4-n} (where R = Me or Bu and $n = 1$, 2 or 3) in acetonitrile, benzene and cyclohexane. It was found that in acetonitrile there was a considerable increase of the quadrupole splitting, compared to the value in solid state whereas benzene and cyclohexane influenced the value of ΔE to only a slight extent. These solvents did not change the isomer shift.

Csákvári et al. [29] investigated the alkoxysilanes and siloxanes as donor solvents against the reference acceptor SnI_4. They established that the solvation of the bulky organosilicon compounds such as $Me_3Si{-}O{-}CMe_3$ resulted in a coordination number of 5, while the smaller compounds had a coordination number of 6. The isomer shift of the tin varied almost linearly with the change in the coordination number of the tin(IV). More exactly, a change in the coordination number from 4 to 5, or from 4 to 6, leads to a decrease in δ of ca 0.6 or ca 1.2 mm s^{-1}, respectively. Significant quadrupole splitting was not observed during these measurements, even with 5 coordination, therefore, the coordination of the siloxanes did not give rise to an electric field gradient at the tin nucleus.

In certain instances, the study of the solvation of tin coordination entities can be utilized to draw conclusions on the coordination conditions in solid coordination entities. For example, Nesmeyanov et al. compared the Mössbauer spectra of R_3SnR' (where $R = C_2H_5{-}$ or $C_6H_5{-}$ and $R' = C_6H_5{-}S{-}$ or $NC_5H_4{-}S{-}$) recorded in the solid state and in solution in pyridine [30]. They found that in the solid state the ΔE values of the 4-pyridylthiostannane derivatives were higher by 1 mm s^{-1} than those for the corresponding phenylthiostannane coordination entities, whereas in frozen solution the Mössbauer parameters of the two types of coordination entity were very similar and, in addition, exhibited a good agreement with the δ and ΔE data for the solid 4-pyridylthiostannane derivatives. It was concluded that in solid state the tin had a coordination number of 4 in the phenylthiostannane coordination entity, and 5 in the 4-pyridylthiostannane (the nitrogen is also coordinated). On dissolution in pyridine, however, coordination of the nitrogen atom of the solvent molecules similarly leads to a coordination number of 5.

Herber and Goscinny [31] carried out ^{57}Fe and ^{119}Sn Mössbauer spectroscopic study of $[\pi\text{-}C_5H_5Fe(CO)_2]SnCl_3$ in the solid state and in poly(methyl methacrylate) solution and found that dissolution did not change the Mössbauer parameters. On this basis, they established that the unusually low value of 2.4 nm obtained for the Sn—Fe bond distance by diffraction methods could be attributed not to intermolecular, but to intramolecular interactions, as the former would be eliminated on dissolution.

A comparison of the quadrupole splittings of tin organic compounds in the solid state and in pyridine solution gave information on the structure of the solid compound [32, 33]. The change in the quadrupole splitting demonstrates the coordination of the pyridine solvent, and indicates that the coordination sphere of the tin is not saturated in the solid state.

Table 5.9.

Mössbauer parameters relating to the tin in tin(IV) halogenide solutions at liqud nitrogen temperature, donor numbers and relative permittivities of the solvents
Radiation source: $Ba\,^{119m}Sn_3O_3$

Reference acceptor	Solvent	Isomer shift*, δ mm s^{-1}	Half width, Γ mm s^{-1}	Donor number, DN	Relative permittivity, ε_r
$SnCl_4$	Dimethyl sulfoxide	0.32	1.18	29.8	45.0
	Dimethylformamide	0.29	1.11	26.6	36.1
	Tributyl phosphate	0.24	1.50	23.7	6.8
	Acetonitrile	0.64	1.19	14.1	38.1
	Pure $SnCl_4$	0.83	1.02		
$Sn\,I_4$	Ethanol	0.40	1.25	30.4	24.3
	Dimethyl sulfoxide	0.48	1.37	29.8	45.0
	Dimethylformamide	0.51	1.81	26.6	36.1
	Tributyl phosphate	1.09	1.60	23.7	6.8
		1.50			
	Carbon tetrachloride	1.64	1.25	0	2.2
	SnI_4 crystalline	1.50	0.98		

* The error of the measurements was ±0.08 mm s^{-1}. The measured values represent the average isomer shifts produced by the superposition of the components in the solution.

Mössbauer spectra of frozen solutions of $SnCl_4$ and SnI_4 were recorded by Vértes et al. [34] (see Table 5.9). The line broadening is due to the fact that a number of solvates are in equilibrium in the solution as a result of the stepwise dissociation of the tin(IV) halogenides and the Mössbauer lines corresponding to these solvates are superimposed.

The isomer shifts of $SnCl_4$ in frozen dimethyl sulfoxide, dimethylformamide and tributyl phosphate solutions agree, within experimental error, while for SnI_4 the isomer shifts measured in dimethyl sulphoxide dimethylformamide and ethanol are nearly equal. The Gutmann donicities of the solvents listed lie between 20 and 30. For both tin compounds, a further decrease in the donicity of the solvent leads to an increase in the isomer shift, indicating an increase in the electron density at the tin nucleus due to the decreased population in the shielding orbitals. This effect showed up in acetonitrile solution for $SnCl_4$, and in tributyl phosphate and carbon tetrachloride solutions for SnI_4 (it should be emphasized that the last two solvents have low relative permittivity, whereas that of acetonitrile is high).

Table 5.10

Mössbauer spectral parameters for methyltin halogenides dissolved in various solvents [35]

Solvent	DN	ε_r	Solute	Donor/methyltin halogenide						Neat donor	
				1/1		2/1		5/1			
				ΔE	δ	ΔE	δ	ΔE	δ	ΔE	δ
Solvent-free			Me_2SnCl_2							3.60	1.59
CH_2Cl_2		9.1	Me_2SnCl_2							3.55	1.64
dee	19.2	4.3	Me_2SnCl_2	3.75	1.75	3.81	1.78	3.80	1.73	3.80	1.75
dme	—	—	Me_2SnCl_2	4.05	1.74	4.05	1.74	4.05	1.74	4.05	1.74
thf	20.0	7.6	Me_2SnCl_2	3.75	1.61	3.92	1.61	4.04	1.66	3.92	1.66
Dioxane	—	—	Me_2SnCl_2	3.70	1.67	3.75	1.67	3.77	1.67	3.77	1.67
Acetone	17.0	20.7	Me_2SnCl_2	3.61	1.69	3.85	1.75	3.85	1.75	3.85	1.75
dmf	26.6	36.1	Me_2SnCl_2	3.68	1.66	4.30	1.69	4.30	1.69	4.25	1.66
dmso	29.8	45.0	Me_2SnCl_2	3.91	1.60	4.33	1.64	4.33	1.64	4.40	1.60
hmpa	38.8	30.0	Me_2SnCl_2	4.05	1.55	4.45	1.54	4.45	1.50	4.36	1.50
Pyridine	33.1	12.3	Me_2SnCl_2	3.84	1.63	4.05	1.60	4.05	1.60	4.05	1.60
Solvent-free			Me_2SnBr_2							3.40	1.62
CH_2Cl_2	—	9.1	Me_2SnBr_2							3.64	1.64
dee	19.2	4.3	Me_2SnBr_2	3.63	1.81	3.63	1.81	3.57	1.78	3.57	1.78
dme	—	—	Me_2SnBr_2	4.14	1.70	4.22	1.70	4.22	1.70	4.22	1.70
thf	20.0	7.6	Me_2SnBr_2	3.57	1.79	3.92	1.79	3.98	1.82	3.86	1.87
Dioxane	—	—	Me_2SnBr_2	3.55	1.56	3.62	1.52	3.62	1.52	3.63	1.59
Acetone	17.0	20.7	Me_2SnBr_2	3.61	1.80	3.82	1.86	3.82	1.86	3.85	1.81
dmf	26.6	36.1	Me_2SnBr_2	3.61	1.63	4.36	1.77	4.36	1.77	4.30	1.75
dmso	29.8	45.0	Me_2SnBr_2	3.63	1.64	4.49	1.64	4.32	1.64	4.40	1.58
hmpa	38.8	30.0	Me_2SnBr_2	3.84	1.08	4.40	1.56	4.45	1.56	4.40	1.56
Pyridine	33.1	12.3	Me_2SnBr_2	3.76	1.74	3.90	1.67	3.98	1.70	3.98	1.63
Solvent-free			$MeSnCl_3$							2.07	1.32
CH_2Cl_2		9.1	$MeSnCl_3$							1.94	1.36
dee	19.2	4.3	$MeSnCl_3$	2.18	1.19	2.14	1.21	2.21	1.14	2.15	1.18
dme	—	—	$MeSnCl_3$	2.43	1.18	2.40	1.12	2.40	1.12	2.40	1.12
thf	20.0	7.6	$MeSnCl_3$	2.08	1.21	2.37	1.15	2.34	1.12	2.37	1.15
Dioxane	—	—	$MeSnCl_3$	2.44	1.15	2.44	1.15	2.50	1.18	2.43	1.14
Acetone	17.0	20.7	$MeSnCl_3$	2.30	1.15	2.40	1.16	2.44	1.18	2.44	1.18
dmf	26.6	36.1	$MeSnCl_3$	2.08	1.14	1.97	0.98	1.92	0.94	1.89	0.89
dmso	29.8	45.0	$MeSnCl_3$	2.03	1.05	1.96	0.91	1.96	0.88	1.97	0.90
hmpa	38.8	30.0	$MeSnCl_3$	2.00	1.03	2.17	0.80	2.17	0.80	2.35	0.89
Pyridine	33.1	12.3	$MeSnCl_3$	1.91	1.01	1.89	0.95	1.94	0.97	1.86	0.93
Solvent-free			$MeSnBr_3$							1.75	1.44
CH_2Cl_2		9.1	$MeSnBr_3$							1.94	1.36
dee	19.2	4.3	$MeSnBr_3$	1.96	1.37	2.07	1.39	2.07	1.39	2.14	1.39
dme	—	—	$MeSnBr_3$	2.43	1.32	2.46	1.33	2.48	1.37	2.46	1.33
thf	20.0	7.6	$MeSnBr_3$	2.12	1.32	2.37	1.27	2.37	1.27	2.42	1.34
Dioxane	—	—	$MeSnBr_3$	2.18	1.34	2.18	1.34	2.22	1.35	2.18	1.34
Acetone	17.0	20.7	$MeSnBr_3$	2.14	1.36	2.25	1.37	2.32	1.34	2.36	1.36
dmf	26.6	36.1	$MeSnBr_3$	1.88	1.18	1.88	0.96	1.83	0.97	1.77	0.94
dmso	29.8	45.0	$MeSnBr_3$	1.99	1.34	2.03	1.05	2.00	1.06	1.96	1.08
hmpa	38.8	30.0	$MeSnBr_3$	2.10	1.12	2.25	1.12	2.27	0.93	2.31	1.05
Pyridine	33.1	12.3	$MeSnBr_3$	1.77	1.05	1.74	1.03	1.83	1.05	1.74	0.98

DN = donor number, ε_r = relative permittivity, ΔE = quadrupole splitting, δ = isomer shift. dee = diethyl ether, dme = dimethoxyethane, thf = tetrahydrofuran, dmf = dimethylformamide, dmso = dimethyl sulfoxide, Me = methyl, hmpa = hexamethylphosphoric triamide.

It is interesting that the isomer shift of SnI_4 dissolved in CCl_4 is higher than that of crystalline SnI_4, which indicates that SnI_4 dissolved in CCl_4 maintains its tetrahedral structure.

The isomer shifts measured in frozen solutions of the two tin halogenides prepared with the same solvent exhibited differences greater than the limit of experimental error. This result indicates that even in a solution prepared with a solvent of high relative permittivity and donicity, such as dimethyl sulfoxide, for at least one of the tin compounds the halogenide is involved in the coordination sphere of the tin.

It can be seen from the data in Table 5.9 that there is undoubtedly a correlation between the donicities of the solvents and the isomer shifts. However, significant effects are also exerted on the isomer shifts by several other factors (affecting the electronic structure of the reference acceptor), such as dissociation reactions influenced by the relative permittivity of the solvent.

Petrosyan et al. [35] studied the intermolecular interactions of methyltin halogenides with electron-donor solvents. For dimethyltin dihalogenides, the quadrupole splittings have been found to be more informative whereas with methyltin trihalogenides the trend of the isomer shifts are coinciding for the various reference molecules as it is demonstrated by Table 5.10.

In methyltin trihalogenide systems, the isomer shifts decreased with coordination of the solvent, indicating a decrease in the electron density at the tin nucleus. This effect is probably due to an increase in the polarity of the tin-halogenide bond, or a greater shielding effect due to the occupation of the 5d orbitals. Both explanations can be correlated with the sequence of changes in donor ability for the coordinated solvents. Thus, the decreasing sequence of isomer shifts may denote an increasing sequence of solvent donor strengths.

The decrease of ΔE of the trihalogenides on coordination of solvent molecules can be explained by the difference in the ionic character of the Sn-halogenide bonds measured by nuclear quadrupole resonance (NQR) technique [36, 37]. The alkyltin trihalogenides contain two types of tin-halogenide bond, the ionic characters of which differ due to the presence of halogen bridges in the molecular associates. Due to the coordination of donor solvents, the difference between the two types of tin-halogenide bond decreases, which leads to a decrease in the electric field gradient and hence in the quadrupole splitting. This effect is greater in the case of chlorides.

5.2.2.1. Mössbauer spectroscopic investigations of solvation of tin(IV) halogenides in solvent mixtures

A better understanding of the correlation between the Mössbauer parameters and the donicity of the solvent can be expected from a study of systems in which a low and nearly constant value of the relative permittivity is ensured. It is therefore useful to compare the Mössbauer parameters in mixtures of the studied solvents with a given inert solvent (e.g. CH_2Cl_2; $\varepsilon_r = 9.1$ and CCl_4; $\varepsilon_r = 2.2$). The low ε_r ensures that the tin(IV) halogenide does not dissociate in the solutions, and thus changes in the Mössbauer parameters can be attributed exclusively, or at least predominantly, to the solvation of the tin(IV) halogenide. The results of such investigations, with SnI_4 as the reference

Table 5.11

Isomer shifts of solvates of SnI_4 with various solvents, and Gutmann donor numbers of the solvents [36]

Donor solvent	Isomer shift, δ mm s^{-1}	Donor number DN
Carbon tetrachloride	1.64	0.0
Nitrobenzene	1.40	4.4
Acetonitrile	1.04	14.1
Acetone	0.95	17.0
Ethyl acetate	0.96	17.1
Dimethylformamide	0.65	26.6
Hexamethylphosphoric triamide	0.56	38.8

Error of the measurements: ± 0.05 mm s^{-1}.

acceptor, are presented in Table 5.11. In these studies the concentration of the $^{119}SnI_4$ was 0.02 and that of the donor solvent was 1 mol kg^{-1} in CCl_4.

It can be established from the data in Table 5.11 that there is a correlation between the isomer shift of the SnI_4 and the solvent donicity (see Fig. 5.12).

By utilizing the data in Table 5.11 and the Fermi–Segré–Goudsmith equation, the population of the 5d electron orbitals of the tin in the solvates can be estimated [38]. The calculation involves substantial approximations, but nevertheless the results (Table 5.12) yield important information.

By means of spectrophotometric and conductivity measurements, Gaizer and Beck investigated solutions of SnI_4 in mixtures of CCl_4 and dimethylformamide (dmf) [39]. In CCl_4 the SnI_4 is very weakly solvated; then, as a result of the addition of dmf, $SnI_4 \cdot 2$ dmf is formed, which is partly precipitated. Addition of further dmf to the mixture leads to dissociation, i.e. formation of a solvate, $[SnI_{4-x}(dmf)_{2+x}]^{x+}$ and the precipitate dissolves. Mayer and Gutmann showed that in SnI_4 solutions dmf favours

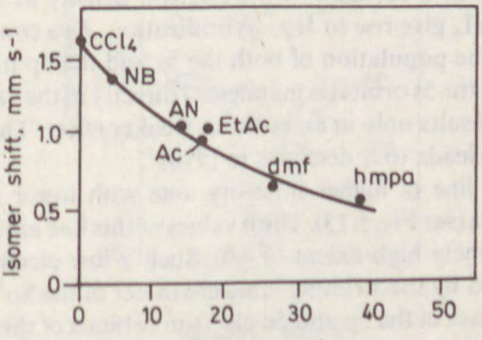

Fig. 5.12. Dependence of the isomer shift of SnI_4 in carbon tetrachloride-donor solvent mixtures on the donor number of the solvent [38]. NB = nitrobenzene, AN = acetonitrile, EtAc = ethyl acetate, dmf = dimethylformamide, hmpa = hexamethylphosphoric triamide, Ac = acetone

Table 5.12.
Estimated lower and upper limits of population of 5d orbitals in the solvates SnI_4D_2 [36]

Donor solvent	Number of electrons x
Nitrobenzene	0.31 – 0.35
Acetonitrile	1.15 – 1.20
Acetone	1.33 – 1.43
Ethyl acetate	1.15 – 1.20
Dimethylformamide	1.96 – 2.15
Hexamethylphosphoric triamide	2.13 – 2.35

autocomplex formation [40], which takes place according to the following mechanism:

$$SnI_4 \cdot 2dmf + dmf \rightleftharpoons [SnI_3(dmf)_3]^+ + I^- \qquad (5.6a)$$

$$SnI_4 \cdot 2dmf + 2I^- \rightleftharpoons [SnI_6]^{2-} + 2dmf. \qquad (5.6b)$$

In the view of these authors, addition of further dmf again results in a decrease of the amount of the hexaiodostannate ion.

These results initiated a Mössbauer spectroscopic examination of the system [41]. The following conclusions can be drawn from the experimental results listed in Table 5.13. Adding 0.04 mol kg^{-1} of dmf to a CCl_4 solution containing 0.02 mol kg^{-1} of SnI_4, then a precipitate of composition $SnI_4 \cdot 2dmf$ is formed. The δ value of the precipitate shows that the coordination of the dmf causes a very strong decrease in the electron density at the tin nucleus, which is a result of the occupation of the 5p and 5d orbitals shielding the s orbitals.

At higher dmf concentrations, no precipitate formation is observed and the δ values measured for the rapidly frozen solutions exhibit a slight tendency to decrease as the dmf concentration increases. This is connected with the increase of the concentration of the coordination entities $[SnI_x(dmf)_{6-x}]^{(4-x)+}$ if $(1 \le x < 4)$, and thus the exchange of I atoms for dmf results in a decrease in the electron density at the nucleus. The four iodine atoms in the SnI_4 give rise to $5sp^3$ hybridization. As a consequence of the I-dmf exchange, therefore, the population of both the 5s and the 5p orbitals decreases. The effect of the change on the 5s orbital is manifested directly in the value of the isomer shift while the other case results only in an indirect, weaker effect. The resultant of the two opposing effects thus leads to a decrease in $|\Psi(0)|^2$.

In addition to the line of higher intensity, one with lower intensity can also be observed in the spectra (see Fig. 5.13). The δ values of this line are shifted in the negative direction to an extremely high extent ($\delta < 0$). Such a low electron density at the tin nucleus may be caused by the strongly ionic character of the Sn^{IV} ($|\Psi_{5s}(0)|^2 \sim 0$), or by the extensive occupation of the 5p and 5d electron orbitals of the tin atom. The former would be explained by complete dissociation ($[Sn(dmf)_6]^{4+}$) and the latter by autocomplex formation ($[SnI_6]^{2-}$).

According to Greenwood et al., the population of the 5d orbital of the tin in $[SnI_6]^{2-}$ in the solid state corresponds to 1.181 electrons, while in SnI_4 the 5d orbital is

Table 5.13.
Mössbauer parameters of SnI_4 in carbon tetrachloride-dimethylformamide (dmf) solvent mixtures at liquid nitrogen temperature
Radiation source: Ba $^{119m}SnO_3$

No.	Composition of solution mol kg^{-1} CCl_4		Isomer shift, δ mm s^{-1}	Area %
	$^{119}SnI_4$	dmf		
1.	0.020	0.00	1.64	
2.	0.020	0.04	0.69*	
3.	0.022	1.10	0.63	97 ± 1
			< 0	
4.	0.024	3.12	0.70	94 ± 2
			< 0**	6 ± 2
5.	0.023	4.62	0.59	87 ± 2
			< 0	13 ± 2
6.	0.024	6.93	0.55	95 ± 2
			< 0	5 ± 2
7.	0.022	pure dmf	0.56	92 ± 2
			< 0	8 ± 2
8.***	0.023	4.62	0.26	69 ± 2
			< 0	31 ± 2

* Precipitation occurred; the value refers to prepared precipitate.
** Isomer shift: $-0.15 > \delta > -0.30$ mm s^{-1}.
*** Solution saturated with NaI (0.14 mol kg^{-1}).

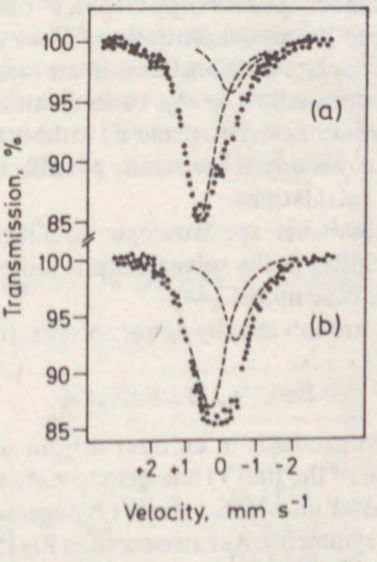

Fig. 5.13. Mössbauer spectrum of $^{119}SnI_4$ and dimethylformamide (dmf) in CCl_4 solution at liquid nitrogen temperature. (a) 0.023 mol kg^{-1} of $^{119}SnI_4$ and 4.62 mol kg^{-1} of dmf; (b) 0.023 mol kg^{-1} of $^{119}SnI_4$; 4.62 mol kg^{-1} of dmf and 0.14 mol kg^{-1} of NaI

almost empty [42]. Further, as the lines with $\delta < 0$ exhibit a maximum intensity at a dmf concentration of 4.62 mol kg^{-1} and then, after a temporary decrease, their intensity again increases, it appears obvious that the lines with $\delta < 0$ represent the ion $[SnI_6]^{2-}$ at lower dmf concentrations and the $[Sn(dmf)_6]^{4+}$ coordination ion at higher dmf concentrations.

The presence of $[SnI_6]^{2-}$ in solution was also strongly suggested by a further experiment in which the intensity of the line with $\delta < 0$ increased substantially when the solution No. 5 in Table 5.13 was saturated with NaI (0.14 mol kg^{-1}). That is an increase in the concentration of I^- shifts the equilibrium (5.6b) towards the formation of ions that contain more iodine (see Fig. 5.13 and Table 5.13, measurement 8).

5.2.3. DETERMINATION OF EQUILIBRIUM CONSTANTS ON THE BASIS OF MÖSSBAUER SPECTRA

In stepwise solvation reactions the electronic structures of the coordination entities existing in solution may be different (primarily because of the different symmetries of the coordination spheres) and so the individual species may each appear as separate lines in the Mössbauer spectrum of the frozen solution. The spectral characteristics of the individual solvates can be obtained by appropriate computer resolution of the total spectrum.

Assuming that the Debye-Waller factors of the various coordination entities in a solution are the same, the areas under the curves can be regarded as being directly proportional to the concentrations of the species relating to them. Simple calculation from these data yields the equilibrium constants of the stepwise solvation processes [43, 44].

The advantage of Mössbauer spectroscopy is that, in contrast to the generally used methods, in which the equilibrium concentration of one (or at most two) species is determined and used to calculate the constants, in an ideal situation the Mössbauer spectrum permits the determination of the concentrations of all solvates present. Hence, the equilibrium constants can be calculated without formation curves, and from fewer experimental data. In this way, it is virtually possible to eliminate the uncertainty of model selection in the calculations.

In one of the first Mössbauer spectroscopic equilibrium studies the solvation equilibrium constants of $SnBr_4$ in the solvents acetic anhydride, acetonitrile, acetone and tetrahydrofuran were determined [44].

The tin(IV) halogenides are solvated by donor solvents (D) in one step, according to the following equation:

$$SnX_4 + 2D \rightleftharpoons SnX_4D_2 . \qquad (5.7)$$

If the solvation reaction proceeds in an inert solvent of low relative permittivity, which inhibits dissociation of the tin(IV) halogenide, only two species will form in the solution, viz., the tetrahedral unsolvated tin(IV) halogenide and its solvated species with distorted octahedral symmetry. As can be seen in Fig. 5.14, the Mössbauer lines of these two species can be well distinguished from each other, and thus the spectrum proved suitable for the determination of the equilibrium constant of the above equilibrium.

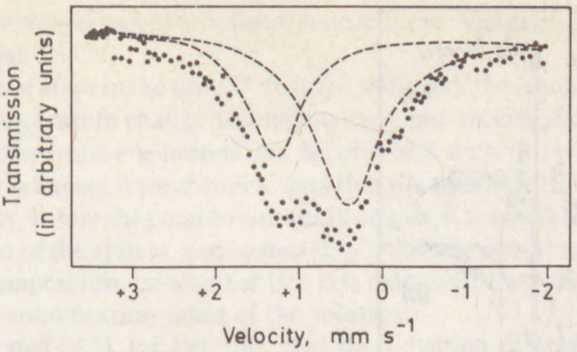

Fig. 5.14. Mössbauer spectrum of $SnBr_4$ containing 0.18 mol kg^{-1} of $SnBr_4$ + 1.0 mol kg^{-1} of acetic anhydride in benzene, at liquid nitrogen temperature. Radiation source: Ba $^{119m}SnO_3$

Of course, if the relative permittivity of the donor solvent is appreciable, an increase in its concentration will lead to dissociation of the tin(IV) halogenide also, and the coordination ions $[SnX_{4-k}D_{2+k}]^{k+}$ will also appear in the solution and lines corresponding to these ions will be observed in the Mössbauer spectrum. These conditions are illustrated in Fig. 5.15.

The solvation equilibrium constants of tin(IV) bromide are listed in Table 5.14, together with the donicities and relative permittivity of the solvents. It can be seen even from these few data that the stability of the solvate increases with an increase in the donicity of the solvent, but it can be assumed that other factors (steric requirements, polarizability, etc.) also act on the solvation.

In principle, the method can be used to investigate equilibria that are much more complicated than that above. If the concentrations of only one or a few solvates can be determined from the Mössbauer spectra even in a system that contains several stepwise-formed solvates, then the dependence on the ligand concentration (or possibly the donor solvent concentration) of the areas under the Mössbauer lines assigned to the individual species can be used to calculate the Bjerrum formation functions, from

Table 5.14.
Mössbauer parameters and equilibrium constants of solvates $SnBr_4D_2$ in various donor solvents
The temperature before rapid freezing was 5°C

Solvent	Donor number, DN	Relative permittivity, ε_r	Isomer shift, δ mm s^{-1}		Equilibrium constant, K kg^2 mol^{-2}
			$SnBr_4$	$SnBr_4D_2$	
Acetic anhydride	10.5	20.7	1.22 ± 0.08	0.413 ± 0.09	3.2
Acetonitrile	14.1	38.0	1.237 ± 0.05	0.358 ± 0.02	25.2
Acetone	17.0	20.7	1.176 ± 0.08	0.247 ± 0.04	38.9
Tetrahydrofuran	20.0	7.6	1.281 ± 0.04	0.220 ± 0.01	93.2

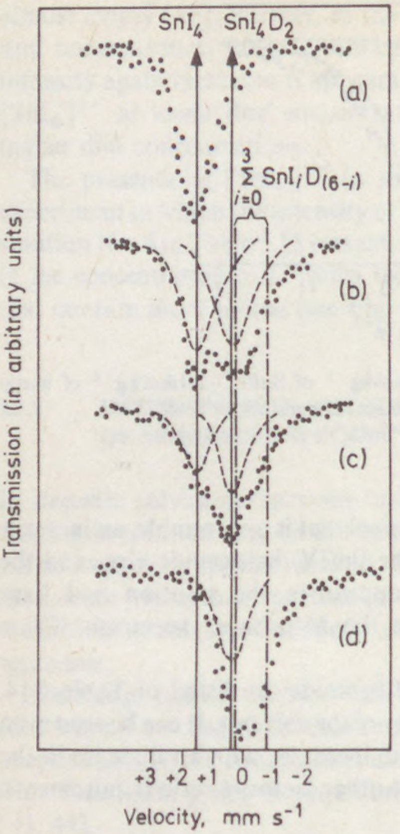

Fig. 5.15. Mössbauer spectra of $^{119}SnI_4$ solutions at liquid nitrogen temperature. (a) 0.02 mol kg^{-1} of $^{119}SnI_4$ in CCl_4; (b) 0.02 mol kg^{-1} $^{119}SnI_4$ + 0.1 mol kg^{-1} of isopropoxysilane in CCl_4; (c) 0.02 mol kg^{-1} $^{119}SnI_4$ + 0.5 mol kg^{-1} isopropoxysilane in CCl_4; (d) 0.02 mol kg^{-1} of $^{119}SnI_4$ + 1 mol kg^{-1} isopropoxysilane in CCl_4. Radiation source: $Ba^{119m}SnO_3$

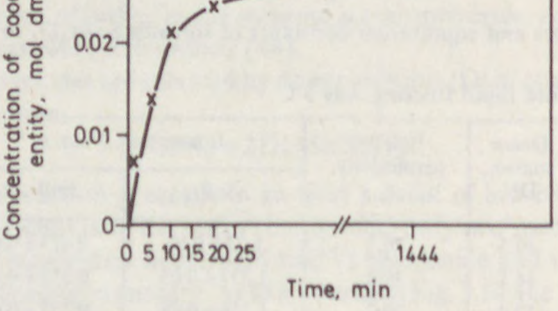

Fig. 5.16. Kinetic curve for solvation of SnI_4 by tetrahydrofuran (thf). 0.098 mol dm^{-3} SnI_4 + 0.623 mol dm^{-3} thf

which the equilibrium data can be obtained in accordance with the rules of classical equilibrium analysis.

A possible source of error in the procedure is the shifting of the equilibria in solution as a result of the temperature change accompanying rapid freezing. Equilibrium data relating to room-temperature solutions can be obtained with this method only for systems for which it is known from chemical data that the equilibria do not shift during cooling. Accordingly, before the equilibrium study proper, it is advisable to carry out a kinetic investigation of the system, and to decide whether the equilibrium data can be referred to room temperature or whether (for fast reactions) they correspond to the temperature of the solidification point of the solution.

It was demonstrated [45], for example, that the solvation of tin(IV) bromide by donor solvents is an instantaneous reaction. Thus, the data in Table 5.14 refer to 5 °C. In contrast, the solvation of tin(IV) iodide by tetrahydrofuran is a much slower process. As can be seen from the kinetic curve in Fig. 5.16, a period of about 1 h is necessary for the establishment of the solvation equilibrium. Hence, as the rapid freezing requires at most only a few seconds, in this case the Mössbauer spectrum of a rapidly frozen solution yields equilibrium data that are valid for the room temperature system. The rate constants (k) of the solvation reaction

$$\mathrm{SnI_4 + 2D \underset{k_2}{\overset{k_1}{\rightleftharpoons}} SnI_4D_2} \tag{5.8}$$

can be determined from the data obtained from kinetic measurements (at 5 °C, $k_1 = 1.1 \pm 0.3\,\mathrm{min^{-1}\,mol^{-2}}$ and $k_2 = 0.06 \pm 0.02\,\mathrm{min^{-1}}$ in benzene). From these constants, the equilibrium constant is calculated to be $K = 18.3 \pm 2.0\,\mathrm{mol^{-2}}$. The temperature dependence of the equilibrium constant yields a value of $-16.75 \pm 4\,\mathrm{kJ\,mol^{-1}}$ for the heat of solvation.

More detailed study of the solvation of $SnBr_4$ and SnI_4 indicated a concentration dependence of the equilibrium constants determined from the Mössbauer spectra and Eq. (5.7) which suggested that solvation proceeds in two steps [45]:

$$\mathrm{SnX_4 + D \rightleftharpoons SnX_4D} \tag{5.9a}$$

$$\mathrm{SnX_4D + D \rightleftharpoons SnX_4D_2} \tag{5.9b}$$

To clarify this problem Mössbauer measurements were extended to the entire measurable concentration range of the solvation of $SnBr_4$ with acetic anhydride and of SnI_4 with tetrahydrofuran (thf), respectively.

When determining the equilibrium constants of the process corresponding to stepwise formation of the coordination entity the following facts were considered: if during solvation the formation of a tin coordination entity with a coordination number of 5 must also be considered, then the corresponding peak in the Mössbauer spectrum should be situated between the peaks of the nonsolvated SnX_4 and of the tin coordination entity with a coordination number of 6. According to other findings published by Csákváry et al. [29] the isomer shift changes linearly with the coordination number, thus it might be assumed that the peak believed hitherto to be proportional only to the concentration of SnX_4D_2, represents also half of the concentration of the SnX_4D coordination entity present in the system (while the other half of this coordination entity is contained in the peak corresponding to SnX_4). For the study of the system under investigation the following function was introduced [45]:

$$\alpha' = \frac{1/2[MD]+[MD_2]}{[M]+[MD]+[MD_2]} = \frac{\text{area corresponding to the solvate coordination entities in the Mössbauer spectrum}}{\text{total area of the Mössbauer spectrum}} \tag{5.10}$$

where M is SnX_4.

Substitution of the stepwise equilibrium constants

$$K_1 = [MD]/[M][D] \tag{5.11}$$

and

$$K_2 = [MD_2]/[MD][D] \tag{5.12}$$

gives:

$$\alpha' = \frac{1/2K_1[D] + K_1K_2[D]^2}{1 + K_1[D] + K_1K_2[D]^2}. \tag{5.13}$$

The α' values can be obtained by the Mössbauer spectra and e.g. the dependence of α' on log [D] is shown in Fig. 5.17 for the SnI_4—thf—benzene system. The K_1 and K_2 can be calculated as fitting parameters.

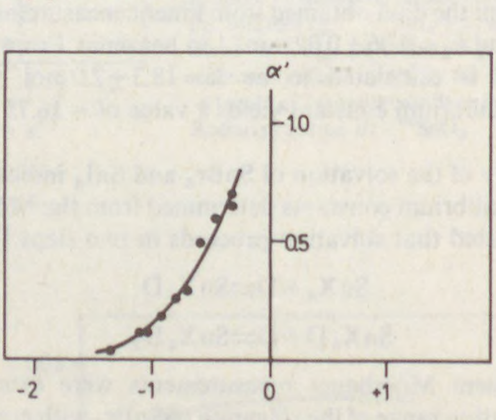

Fig. 5.17. Formation curve of solvated coordination entities in the SnI_4-thf-benzene system. The points are the experimentally obtained data, the full line is the fitting curve.

The stepwise stability constant of the SnI_4—thf system determined according to this method are at 5 °C as follows:

$$K_1 = 0.9 \pm 0.2\,\text{mol}^{-1}$$

and

$$K_2 = 13.1 \pm 1.6\,\text{mol}^{-1}$$

in kg of benzene and the $SnBr_4$-acetic anhydride system in kg of benzene:

$$K_1 = 0.8 \pm 0.2\,\mathrm{mol}^{-1}$$

and

$$K_2 = 4.0 \pm 0.6\,\mathrm{mol}^{-1}.$$

Naturally, other complex equilibria (and not only those of solvation reactions) can also be investigated by Mössbauer spectroscopy. In these studies the Mössbauer parameters provide information not only on the equilibrium data, but also on the electronic structures and symmetries of the stepwise-formed species.

A special case of the dissolution of tin in organic solvents is when small particles ($\sim$7.5 nm) of electrocondensed metallic tin were mixed with organic solvents: hexane, cyclohexane, toluene, benzene, acetone and 1-propanol [46]. The Mössbauer spectra of the frozen suspension showed that the particles consist of β-Sn and SnO_2 of about 79% and 21%, respectively [46]. Dissolving iron (instead of tin) in the same organic solvents, the composition of the particles was α-iron and different iron carbides [47]. The type of carbides depended on the solvents used.

REFERENCES

1. Gutmann, V., *Coordination Chemistry in Non-Aqueous Solutions.* Springer-Verlag, Vienna, New York, 1968.
2. Burger, K., Vértes, A. and Czakó–Nagy, I., *Acta Chim. Acad. Sci. Hung.*, **63,** 115 (1970); *Magy. Kém. Folyóirat*, **75,** 257 (1969).
3. Vértes, A., Burger, K., Molnár, B. and Pálfalvy, M., *J. Inorg. Nucl. Chem.*, **35,** 691 (1973).
4. De Vries, J. L. K. F., Trooster, J. M. and De Boer, E., *Inorg. Chem.*, **10,** 81 (1971).
5. Mulliaris, A. and Niarchos, D., *Inorg. Chem.*, **15,** 1340 (1976).
6. Vértes, A., Czakó–Nagy, I. and Burger, K., *J. Phys. Chem.*, **82,** 1469 (1978).
7. Sakai, Y., Nishioji, H., Yamanchi, S. and Tominaga, T., *Radiochem. Radioanal. Letters*, **53,** 215 (1982).
8. Rodriquez, F., Moreno, M., Fayet, J. C. and Varret, F., *Z. Naturforsch.*, **38a,** 701 (1983).
9. Marques, N. and de Matos, A. P., *J. Inorg. Nucl. Chem.*, **43,** 2285 (1981).
10. Imshennik, V. K., Afanasev, A. M., Goldanskii, V. I., Makarov, E. F., Platshinda, A. S. and Suzdalev, I. P., *Fig. Tverd. Tela*, **15,** 2656 (1973).
11. Suzdalev, I. P., Afanasev, A. M., Platshinda, A. S., Goldanskii, V. I. and Makarov, E. F., *Zh. Eksp. Teor. Fiz.*, **55,** 1752 (1968).
12. Suzdalev, I. P., Korneev, V. P. and Krupjanskii, Yu. F., *Zh. Eksp. Teor. Fiz.*, **57,** 438 (1969).
13. Kornejev, V. P., Suzdalev, I. P., Goldanskii, B. I., Kurnejeva, T. Ya., Makarov, E. F. and Platskinda, A. S., *Fiz. Tverd. Tela*, **13,** 354 (1972).
14. Peev, T., *Bulg. J. Phys.*, **4,** 391 (1976).
15. Dickson, B. L., Rees, L. V. C., *J. Chem. Soc. Faraday I.*, **2,** 2060 (1974).
16. Craig, P. P. and Sutin, N., *Phys. Rev. Lett.*, **11,** 460 (1963).
17. Elliott, J. A., Hall, H. E. and Bunbury, D. St. P., *Proc. Phys. Soc.*, **89,** 595 (1966).
18. Abras, A. and Mullen, J. G., *Phys. Rev.*, **A6,** 2343 (1972).
19. Jensen, J. H., *Phys. Kondens. Mater.*, **13,** 273 (1971).
20. Champeney, D. C., Higgy, E. S. M. and Ross, R. G., *J. Phys. C.: Solid State Phys.*, **8,** 507 (1975).
21. Vértes, A., Burger, K. and Suba, M., *Acta Chim. Acad. Sci. Hung.*, **63,** 123 (1970); *Magy. Kém. Folyóirat*, **75,** 317 (1969).
22. Vértes, A., Kiss, L. and Varsányi, M., *Acta Chim. Acad. Sci. Hung.*, **65,** 67 (1970); *Magy. Kém. Folyóirat*, **76,** 145 (1970).
23. Vértes, A. and Parak, F., *J. Chem. Soc. Dalton Trans.*, 2062 (1972).
24. Nikolskii, B. P., Kalyamin, A. V., Kuvshinov, V. A., Ralchevskii, V. V., Tomilov, S. B. and Yakubov, Ch. M., *Dokl. Akad. Nauk SSSR*, **219,** 659 (1974).

25. Aleksandrov, Yu., Dorfman, G., Lependina, O. L., Mitrofanov, K. P., Plotnikov, M. V., Polak, L. S., Temkin, A. Ya. and Shpinel, V. S., *Zh. Fiz. Khim.*, **38**, 2190 (1964).

26. Goldanskii, V. I., Okhlobystin, O. Yu., Rochev, V. Ya. and Kravcov, V. V., *J. Organometal. Chem.*, **4**, 160 (1965).

27. Goldanskii, V. I., Rochev, V. Ya., Khrapov, V. V., Kravtsov, D. N. and Bochlina, E. M., *Dokl. Akad. Nauk SSSR*, **191**, 134 (1970).

28. Schnorr, H. and Kriegsmann, H., *Proc. Conf. Appl. Mössbauer Effect, Tihany* (Hungary), Akadémiai Kiadó, Budapest, 1971, p. 629; *Proc. Conf. Mössbauer Spectrometry, Dresden*, 1971, p. 474.

29. Csákvári, B., Csákvári, É., Gömöry, P. and Vértes, A., *J. Radioanal. Chem.*, **25**, 275 (1975).

30. Nesmeyanov, A. N., Goldanskii, V. J., Khrapov, V. V., Rochev, V. Ya., Kravtsov, D. N. and Rokhlena, E. M., *Izv. Akademii Nauk SSSR, Ser. Chim.*, 793 (1968).

31. Herber, R. H. and Goscinny, Y., *Inorg. Chem.*, **7**, 1293 (1968).

32. Poller, R. C. and Ruddick, J. N. R., *J. Chem. Soc. Dalton Trans.*, 555 (1972).

33. Poller, R. C. and Ruddick, J. N. R., *J. Organometal. Chem.*, **39**, 121 (1972).

34. Vértes, A. and Burger, K., *J. Inorg. Nucl. Chem.*, **34**, 3665 (1972).

35. Petrosyan, V. S., Yashina, N. S., Sacharov, S. G., Rentov, O. A., Rochev, V. Ya. and Goldanskii, V. J., *J. Organometal. Chem.*, **52**, 333 (1973).

36. Petrosyan, V. S., Yashina, N. S., Rentov, O. A., Bryuchova, E. V. and Semin, G. K., *J. Organometal. Chem.*, **52**, 321 (1973).

37. Maksyutin, Yu. K., Guryanova, Ye. N. and Semin, G. K., *Usp. Khim.*, **4**, 727 (1970).

38. Vértes, A. and Nagy, S., *Magy. Kém. Folyóirat*, **79**, 23 (1973).

39. Gaizer, F. and Beck. M. T., *J. Inorg. Nucl. Chem.*, **29**, 21 (1967).

40. Mayer, U. and Gutmann, V., *Mh. Chem.*, **101**, 887 (1970).

41. Vértes, A., Gaizer, F. and Beck, M. T., *Magy. Kém. Folyóirat*, **79**, 310 (1973).

42. Greenwood, N. N., Perkins, P. G. and Wall, D. H., *Symp. Faraday Soc.*, **1**, 51 (1967).

43. Burger, K., Fluck, E. and Vértes, A., *Abstracts IV. Internat. Conf. on Non-aqueous Solutions*, Vienna, 1974, p. 9.

44. Vértes, A., Nagy, S., Czakó–Nagy, I. and Csákvári, É., *J. Phys. Chem.*, **79**, 149 (1975).

45. Vértes, A., Czakó–Nagy, I. and Burger, K., *J. Phys. Chem.*, **80**, 1314 (1976).

46. Plachinda, A. S., Pisarenko, O. I., Makarov, E. F. and Lunina, M. A., *Zh. Fiz. Khim.*, **50**, 1832 (1976).

47. Plachinda, A. S., Pisarenko, O. I., Suzdalev, I. P., Lunina, M. A. and Makarov, E. F., *Zh. Fiz. Khim.*, **48**, 2485 (1974).

5.3. COORDINATION COMPOUND FORMATION IN SOLUTIONS

It is very difficult to draw a strict line between the formation reactions of coordination compounds and solvation phenomena in solutions. A solvate can be regarded as a coordination entity if the donor solvent is bound to the solvated ion by an electron pair of the donor atom.

In the case of coordination formation a coordinate bond is established between the central atom and the ligand, the electron configurations of both being altered, and this change can be followed by the Mössbauer spectrum. In such a case, Mössbauer spectroscopy is suitable for the study of coordination entities formed in solutions.

5.3.1. FORMATION OF COORDINATION COMPOUNDS WITH IRON CENTRAL ATOM

In reactions that lead to the formation of a low-spin coordination entity, the Mössbauer spectrum of the frozen solution reveals the clear separation of the Mössbauer lines of the high-spin metal ion and the low-spin metal coordination compound. This effect was shown by the studies of Vértes et al. [1] on the formation of the iron(II)-bipyridine coordination entity. For example in frozen aqueous solution the Mössbauer data for iron(II) chloride are $\delta = 1.40\,\mathrm{mm\,s^{-1}}$, $\Delta E = 3.28\,\mathrm{mm\,s^{-1}}$. In contrast to this, the low-spin coordination entity $[\mathrm{Fe(bpy)_3}]^{2+}$ formed by the addition of 2,2′-bipyridine before freezing has the values $\delta = 0.46\,\mathrm{mm\,s^{-1}}$ and $\Delta E = 0.33\,\mathrm{mm\,s^{-1}}$ (relative to stainless steel).

Figures 5.18(a), (b) and (c) show the spectra of solutions in which the amount of 2,2′-bipyridine was insufficient to bind the iron quantitatively in the form of the 2,2′-bipyridine coordination compound (see Table 5.15). The superimposed spectra obtained in these cases can be resolved into two components, one of which can in each case be identified with the spectrum obtained in an aqueous solution of iron(II) chloride, while the other component is the Mössbauer spectrum of $[\mathrm{Fe(bpy)_3}]^{2+}$. The ratios of the intensities of the two components agree well with the stoichiometric ratios of the amounts of 2,2′-bipyridine complex and the residual uncoordinated iron(II) ion. This indicates that the probabilities of recoil-free resonance absorption are nearly the same for the two components.

The above results, consequently, show that in the solutions examined the inner coordination sphere of the iron(II) ion consists either of water molecules or of bipyridine molecules, and mixed ligand coordination compounds are not present in detectable amounts (i.e. their amount is less than 1–2%). This result agrees well with the known stability constants for the iron(II)-2,2′-bipyridine coordination entities [2, 3], viz., $\log \beta_3 = 17.45$, $\log K_1 \approx 4$ and $\log K_2 < 5$.

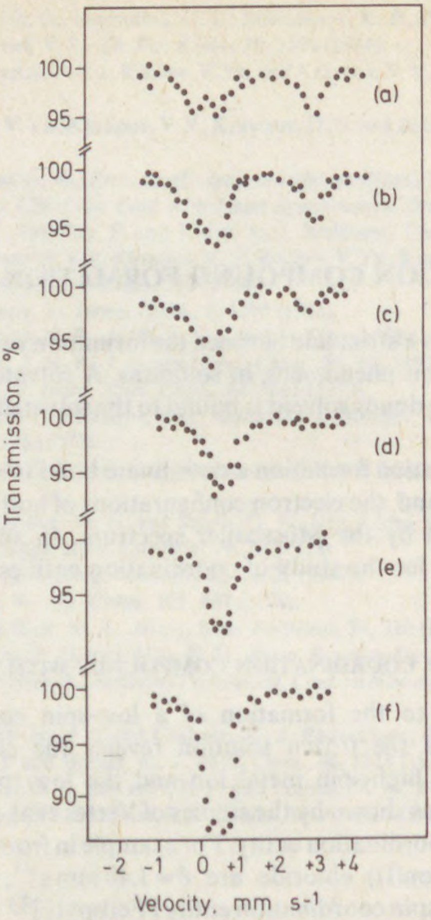

Fig. 5.18. Mössbauer spectra of frozen aqueous solutions of $FeCl_2$ and 2,2′-bipyridine at liquid air temperature. The concentrations of the solutions are given in Table 5.15 (with the notations of the solutions). Curve (f) is the Mössbauer spectrum of the anhydrous coordination entity prepared from solution (e).

The Mössbauer parameters for the coordination cation $[Fe(bpy)_3]^{2+}$ in frozen solution and in the solid state were found to be identical within the limits of experimental error [1, 4]. This result demonstrates that this inner coordination sphere does not change during dissolution and freezing.

Silver et al. have studied the coordination formation of $FeCl_3$ with phenol, and with phenol derivatives (4-methylphenol, 2-nitrophenol, 4-nitrophenol, pyrocatechol, hydroquinone) in dry methanol and also in the presence of water traces [5]. The initiation of this work was that the addition of iron(III) chloride to dilute solutions of phenols results in a blue, violet or red colour, a well-known phenomenon often used as a test for the aromatic hydroxy group. Mössbauer spectra recorded at liquid nitrogen temperature showed the same effect in all the phenols studied: water addition lead to the formation of iron(II). Exceptions were pyrocatechol and hydroquinone, in which iron(II) was formed even in dry methanol due to the water formed by self-condensation.

Table 5.15.
Dependence of the ratio of high and low spin iron compounds from the mole ratio of 2,2′-bipyridine and $FeCl_2$

Mole ratio of 2,2′-bipyridine and $FeCl_2$ in the solution, normalized to amount of substance expressed in moles of $FeCl_2$	Ratio of iron atoms remaining free in solution or participating in coordination formation, normalized to the concentration of the coordination entity*	
	Based on stoichiometric calculation	Calculated from intensities of Mössbauer spectral lines**
0.75	3.00	3.21
1.51	0.99	1.09
2.40	0.25	0.23
3.01	0.00	0.00
3.60	0.00	0.00

* Assuming that only $[Fe(bpy)_3]^{2+}$ coordination ions are present in the solution [2,3].
** The error in the area calculation is ± 5%.

The formation of colours (mentioned above) was explained by the reduction of iron(III) to iron(II) [5].

Fanning and coauthors carried out measurements in a frozen aqueous solution of $K_3[Fe^{III}Spc]\cdot 0.5\,KOH\cdot 4H_2O$ of $2\,mmol\,dm^{-3}$ concentration at 120 K (where Spc = 4,4′,4″,4‴-sulfophthalocyanine). Mössbauer parameters $0.23\,mm\,s^{-1}$ and $1.70\,mm\,s^{-1}$ were obtained for the isomer shift (relative to ^{57}Co in copper) and

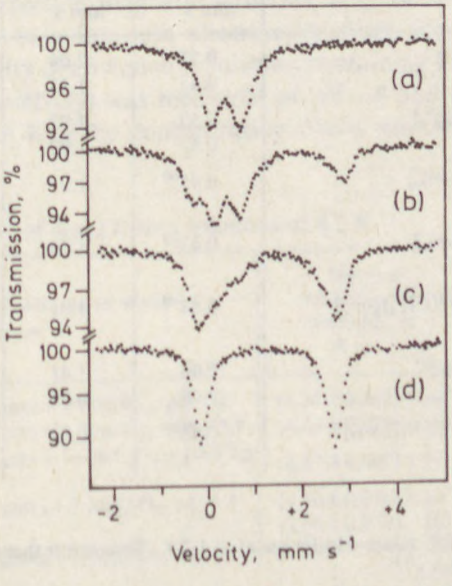

Fig. 5.19. Mössbauer spectra of auqeous solutions of $K[^{57}Fe(C_2O_4)_2(H_2O)_2]$ at 77 K. (a) Unirradiated solution; after photoirradiation for (b) 3 s, (c) 10 s, and (d) 60 s [7]. Radiation source: ^{57}Co in copper

quadrupole splitting, respectively [6]. These results indicated the presence of a low-spin octahedral coordination entity.

Sato and Tominaga used the Mössbauer technique for the study of the mechanism of the photolysis of bis- and tris(oxalato)ferrate(III) aqueous solutions. The Mössbauer spectra of the solutions quenched immediately after the irradiation showed the formation of iron(II) coordination entities and these experimental results gave evidence that iron(II) species are metastable intermediate products in the photolysis of iron(III) oxalate [7]. A series of spectra are given in Fig. 5.19.

The stepwise formation of the oxalatoferrate(II) coordination ions could be followed by the Mössbauer technique. Vértes et al. [8] measured the Mössbauer parameters of frozen aqueous solutions of $Fe(C_2O_4)$ at different concentrations of $Na_2(C_2O_4)$. As the concentration of the $C_2O_4^{2-}$ anions increased in the solution also the concentration of the $[Fe(C_2O_4)_2]^{2-}$ and $[Fe(C_2O_4)_3]^{4-}$ coordination ions increased and this resulted in an increase of the quadrupole splitting of the frozen solution up to $\Delta E = 2.7$ mm s^{-1}. (The ΔE value is 2.03 mm s^{-1} for the solid $Fe(C_2O_4) \cdot 2H_2O$.) The actual value of the quadrupole splitting can give information about the ratio of the concentration of the different coordination ions.

The comparison of Mössbauer spectra of coordination compounds measured in solid state and in frozen solution frequently can give useful information about the

Table 5.16.
Mössbauer parameters for $[Fe_4S_4(SR)_4]^{3-}$ clusters at 4.2 K
Spectra fitted by two doublets [9]

Compounds	Solid state		CH_3CN solution	
	δ(a) mm s^{-1}	ΔE(b) mm s^{-1}	δ(a) mm s^{-1}	ΔE(b) mm s^{-1}
$(Et_4N)_3[Fe_4S_4(S{-}C_6H_5)_4]$(c)	0.52 0.45	2.04 1.13	0.51 0.46	2.01 1.11
$(Me_4N)_3[Fe_4S_4(S{-}C_6H_4Me\text{-}o)_4]$	0.50 0.43	1.93 1.09	0.54 0.44	1.67 1.02
$(Me_4N)_3[Fe_4S_4(S{-}C_6H_4Me\text{-}m)_4]$	0.45(d)	1.01	0.53 0.45	1.70 0.99
$(Me_4N)_3[Fe_4S_4(S{-}C_6H_4Me\text{-}p)_4]$	0.43(d)	1.06	0.53 0.45	1.70 0.99
$(Et_4N)_3[Fe_4S_4\{S{-}C_6H_4{-}CH(CH_3)_2\text{-}p\}_4]$	0.44(d)	1.01	0.50 0.45	1.90 1.06
$(Et_4N)_3[Fe_4S_4(S{-}CH_2C_6H_5)_4]$(c)	0.48 0.48	1.41 0.93	0.52 0.47	2.01 1.12
$(Et_4N)_3[Fe_4S_4(S{-}CH_2{-}C_6H_4OMe\text{-}p)_4]$	0.43(d)	0.86	0.50 0.45	1.90 1.06

Et $= C_2H_5$, Me $= CH_3$

(*a*) ±0.02 mm s^{-1}; isomer shift relative to Fe metal at 4.2 K. To convert these values to Fe metal at room temperature, add 0.12 mm s^{-1}.

(*b*) Quadrupole splitting; ±0.03 mm s^{-1}.

(*c*) Data from literature [10] corrected to refer to Fe metal at 4.2 K.

(*d*) Fit assuming one quadrupole doublet.

structure of the studied species. Laskowski et al. compared the Mössbauer spectra of solid $(R'_4-N)_3[Fe_4S_4(SR)_4]$ with those in frozen acetonitrile solutions [9] where R' $=CH_3$, C_2H_5 and $R=C_6H_5$; *o*-, *m*- or *p*-CH_3—C_6H_4—; *p*-$(CH_3)_2CH$—C_6H_4—; C_6H_5—CH_2—; *p*-CH_3O—C_6H_4—CH_2— [9]. These compounds were used as models of ferredoxin proteins for the study of the structural change in electron transfer reactions. The obtained results are listed in Table 5.16. The Mössbauer parameters of solid materials and those of frozen solutions are nearly equal which suggests that the electronic structure of iron (in the inner ligand sphere) is similar in the solid state and in the frozen solution [9].

In addition to the isomer shift and quadrupole splitting, in paramagnetic systems the magnetic hyperfine structure (MHS) of the Mössbauer spectrum can also provide information on the electronic structure of coordination entities in frozen solutions, and primarily on the covalency of the coordinate bonds. As pointed out previously, at liquid helium temperature the probability of spin-lattice relaxation decreases strongly. If the frequency of spin-spin relaxation is also decreased by appropriate lowering of the concentration of the Mössbauer atom, e.g. the iron(III) ion, then the Mössbauer spectrum of the solution will also exhibit MHS, and accordingly, extra information can be obtained on the structures of the species in solution.

If the aqueous solution of iron(III) salts contains also ethylenediaminetetraacetic acid (H_4edta) or nitrilotriacetic acid (H_3nta), iron-acetate bonds will be formed. The Mössbauer parameters of frozen solutions measured at 4.2 K are tabulated in Table 5.17 [11].

The Mössbauer spectra of H_3nta solutions of various pH values are presented in Fig. 5.20. For pH = 4 the spectrum can be decomposed into a quadrupole pair of lines and a spectrum component showing Zeeman splitting.

The lack of a hyperfine magnetic structure may be due either to dimerization (polymerization) or to a low-spin electron structure. To clarify this problem the magnetic susceptibility of an aqueous solution containing $FeCl_3$ and H_3nta (0.33 and 0.68 mol kg^{-1}, respectively) was measured at pH = 4 and in a temperature interval between 95 and 259 K. (The concentration could not be as low as that used for

Table 5.17.
Mössbauer parameters of some frozen solutions at 4.2 K

Composition of solution in water mol dm^{-3}	Internal magnetic field strength, H A m^{-1}	Isomer shift*, δ mm s^{-1}	Qadrupole splitting, ΔE mm s^{-1}
0.02 $Fe(ClO_4)_3$ + 0.06 H_3nta + 1 $NaClO_4$: pH = 4	$(4.34\pm0.002)\times10^7$	0.13 ± 0.01	1.43 ± 0.017
0.02 $Fe(ClO_4)_3$ + 0.06 H_3nta + 1 $NaClO_4$: pH = 2.5	$(4.40\pm0.014)\times10^7$	0.15 ± 0.03	0.036 ± 0.03
0.02 $Fe(ClO_4)_3$ + 0.06 H_3nta + 1 ($NaClO_4$ + $HClO_4$) pH = 1	$(4.43\pm0.009)\times10^7$		
0.02 $Fe(ClO_4)_3$ + 0.05 H_4edta + 1 $NaClO_4$: pH = 4	$(4.30\pm0.016)\times10^7$ $(3.68\pm0.032)\times10^7$		
0.02 $Fe(ClO_4)_3$ + 0.05 H_4edta + 1 $NaClO_4$: pH = 3	$(4.30\pm0.014)\times10^7$		

* Relative to $^{57}Co(Pt)$ source.
H_3nta = nitrilotriacetic acid.
H_4edta = ethylenediaminetetraacetic acid.

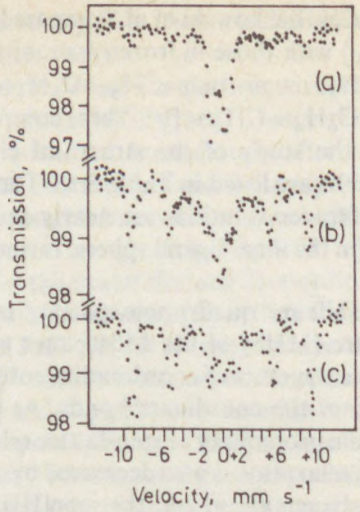

Fig. 5.20. Mössbauer spectra of frozen solutions of nitrilotriacetic acid at 4.2 K at different pH
pH: (a) 4.0, (b) 2.5, (c) 1.
Radiation source: ^{57}Co(Pt)

Mössbauer measurements, since in the case of such very low concentrations the error of susceptibility measurements is too high.) The experimental result followed the Curie–Weiss law. A value of $2.8 \pm 0.2\,\mu_B$ (Bohr magneton) was obtained for spin only [11].

This value indicates an electron structure with a low spin number which, however, does not unambiguously exclude the possibility of dimerization (polymerization), since in the dimer (or polymer) the spin of some iron atoms may have an opposite orientation [12]. The relatively high Weiss constant also points to an antiferromagnetic interaction and, therefore, when these experimental results are compared, it appears that the quadrupole pair of lines can be identified with a polynuclear coordination ion.

The great quadrupole splitting pertaining to the coordination entity without magnetic hyperfine structure (MHS) ($1.45 \pm 0.02\,\mathrm{mm\,s^{-1}}$) shows that the internal ligand sphere, i.e. the electron structure of iron is highly asymmetric. From the decomposition of the spectra the following values of the line area were obtained at different pH values for the component without MHS (which represents the dimer in the solution).

pH = 1.0	68.9 ± 4.5%
pH = 2.5	58.5 ± 14%
pH = 1.0	0%

Mössbauer spectra of the solution containing H_4edta are shown in Fig. 5.21 where it can be seen that in solution at pH = 4 the outer lines are doubled: $(H_{5/2})_{\mathrm{I}} = 4.3 \times 10^7\,\mathrm{A\,m^{-1}}$ and $(H_{5/2})_{\mathrm{II}} = 3.7 \times 10^7\,\mathrm{A\,m^{-1}}$. The internal magnetic field strength of $3.7 \times 10^7\,\mathrm{A\,m^{-1}}$ indicates a strong covalency effect. X-ray diffraction [13] and Mössbauer spectroscopic [14] measurements led some workers to the conclusion that the iron(III) in the coordination ion Na[Fe(OH)$_2$(H$_2$edta)]$\cdot n\,$H$_2$O has a coordination number

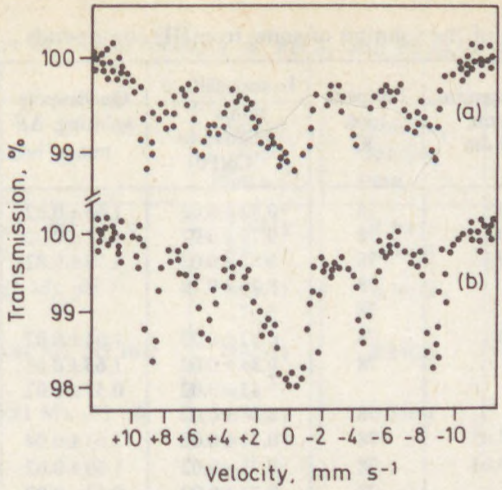

Fig. 5.21. Mössbauer spectra of solutions containing ethylenediaminetetraacetic acid at 4.5 K. pH: (a) 4.0, (b) 3.0. Radiation source: ^{57}Co(Pt)

equal to seven. Accordingly, the possibility cannot be excluded that the iron may also have a coordination number seven in solution. In this instance $(H_{5/2})_{II}$ refers to the 7 coordinated entity and $(H_{5/2})_{I}$ to the 6 coordinated entity. X-ray examinations show that in the latter the EDTA occupies only five coordination sites, the sixth being occupied by a water molecule. Hence, the stability (covalency) of this coordination entity is clearly lower than that of the 7 coordinate entity formed at higher pH values. This conclusion is also supported by the $H_{5/2}$ values. At pH = 3, only the lines corresponding to $(H_{5/2})_{I}$ appear, whereas at pH = 4 the ratio of the concentrations of the two coordination entities is 14.6 : 11.5 (in more acidic solutions the number of non-coordinating acetate groups is naturally higher).

De Arajou et al. [15] investigated the Mössbauer spectra of frozen Fe^{III} salt-H_4edta solutions. They supposed that at higher pH values the iron is coordinated not only to edta, but also to OH^- ions.

Kachanova et al. [16] also studied the pH dependence of the Mössbauer spectra of the frozen solution of Fe^{III} salt-H_4edta at 80 K in the concentration range of $4 \times 10^{-3} - 2 \times 10^{-2}$ mol dm^{-3}. They found MHS in the spectrum at pH = 2 and only a quadrupole doublet appeared in the spectrum at the higher value pH = 10 ($\Delta E = 1.58$ mm s^{-1}). The relatively large quadrupole splitting was attributed to the formation of seven-coordinated iron(III), but this assumption contradicts the results of Spijkerman et al. [14], who measured a difference in the quadrupole splitting in six- and seven-coordinated salts of Fe–H_4edta to be 0.33 mm s^{-1}.

Stein and Marinsky [17] measured the Mössbauer spectra of several iron(III) polyaminocarboxylates in the solid, polyelectrolyte (75% trimethylstyrylammonium chloride and 25% styrene), ion exchanger (Dowex A-1) and solution phases as a function of the pH. The results for the frozen solutions are tabulated in Table 5.18(a). The higher quadrupole splittings (over 1 mm s^{-1}) were interpreted by dimerization

Table 5.18(a)

Mössbauer parameters of the solution of some iron(III) compounds

Compounds	Concentration, mol dm^{-3}	Temperature, K	Isomer shift, δ mm s^{-1} Relative to ^{57}Co(Pd)	Quadrupole splitting, ΔE mm s^{-1}	pH	Area, %	Half width, Γ mm s^{-1}
$N(C_2H_5)_4[Fe(edta)]$	0.1	78	0.82 ± 0.02	1.65 ± 0.02	9.0		
$N(C_3H_7)_4[Fe(edta)]$	0.1	78	0.79 ± 0.02	1.67 ± 0.02	9.0		
$N(C_4H_9)_4[Fe(edta)]$	0.1	78	0.82 ± 0.02	1.70 ± 0.02	9.0		
		78	0.76 ± 0.10		3.0		1.14
Fe^{III} + cdta*		78	0.62		7.3		1.82
Fe^{III}(Hedta)	0.1	78	0.82 ± 0.02	1.64 ± 0.02	9.0		
		78	0.84 ± 0.02	1.65 ± 0.02	3.3	45	
			0.83 ± 0.02	0.57 ± 0.02		55	
		78	0.85 ± 0.02		0.7		0.95
Fe^{III}(nta)	0.05	78	0.71 ± 0.02	1.63 ± 0.04	3.5		0.65
Fe^{III}(nta)	0.05	78	0.71 ± 0.02	1.60 ± 0.02	7.0		
freshly prepared		78	0.71 ± 0.02	0.52 ± 0.02	3.0		
5 days			0.77 ± 0.02				0.63
30 days			0.76 ± 0.02				0.79
$Fe^{III} + K^+$ + nta*		77	0,77	1.39	6.0		
$Fe^{III} + Na^+$ + nta*		77	0.55	1.68	5.3		
Fe^{III}(nta)		77	0.66	0.70	9.1		

* Data taken from the publication of Rabinowitz et al. [18(a)]. The measured samples were lyophilized powder.

cdta = cyclohexylenedinitrilotetraacetic acid.

which results in a unidirectional delocalization of π electrons in the Fe–O–Fe three-center bond that creates a large asymmetry in the electric field gradient at the iron nucleus. The authors did not report any appearance of the MHS in the spectra due—probably—to the applied relatively high concentration of the paramagnetic iron(III) (fast spin-spin relaxation) and temperature not low enough of the measurements (fast spin-lattice relaxation). The published Mössbauer parameter values [17] were similar for polyelectrolyte and resin samples equilibrated with solutions of the same pH value and also with the frozen solutions. This result indicates that the structure of the studied coordination entities are the same or very similar in the polyelectrolyte, in the resin and in the solution.

Silver et al. measured the Mössbauer parameters of frozen solutions of protoporphyrin IX iron(II) coordination compounds containing ligands as phenol, catechol, fluoride, acetone and triphenylphosphine [18(b)]. The obtained isomer shift (relative to iron) and quadrupole splitting at 80 K were in the range of 1.01–1.04 mm s^{-1} and 4.11–4.34 mm s^{-1}, respectively. These data are consistent with the high spin iron(II) electronic structure and with five coordinate environments. The large quadrupole splitting suggests the existence of the five-coordinated iron(II). In the case of acetone ligand a part of iron(II) transformed into iron(III).

Keypour et al. published some results on the interaction of iron(III) and ascorbic acid as a function of pH in pure water, pure methanol and mixtures of these solvents [18(c)].

Table 5.18(b)

Mössbauer parameters of frozen solution of $FeCl_3$ and ascorbic acid in methanol-water mixture at 80 K

Composition	Isomer shift (mm s^{-1})	Quadrupole splitting (mm s^{-1})	Half width (mm s^{-1})	Line area (%)
1. $FeCl_3$(0.1 M)+H_2Asc(0.2 M), pH 4 (95% methanol/water)	1.37(1) 0.51(2)	3.34(1) 0.59(3)	0.20(1) 0.19(3)	86.7(2.4) 13.3(2.4)
2. $FeCl_3$(0.1 M)+H_2Asc(1 M), pH 2 (water)	1.39(1)	3.33(2)	0.21(2)	100
3. $FeCl_3$(0.2 M)+Na_2Asc(1 M), pH 10.0 (methanol)	0.49(2)	0.81(2)	0.22(2)	100
4. $FeCl_3$(0.2 M)+Na_2Asc(1 M), pH 1.0 (methanol)	1.36(1)	3.55(1)	0.20(1)	100

Mössbauer data indicated that the iron(III) is reduced at low pH to iron(II). The obtained Mössbauer parameters are given in Table 5.18(b). Stopped flow spectrophotometry have been used to follow the mechanism of the above reactions and evidence was shown for blue intermediates in the reduction pathway of iron at low pH values.

5.3.2. COORDINATION FORMATION WITH TIN CENTRAL ATOM

It is known from equilibrium studies [19, 20] that if tin(IV) iodide is dissolved in liquid tin(IV) chloride at room temperature, then mixed coordination entities are formed. The Mössbauer spectra of some frozen mixtures of $SnCl_4$ and SnI_4 of different compositions, show, in agreement with the equilibrium measurements that dissolution of SnI_4 in $SnCl_4$ leads to the formation of mixed Sn(IV) halogenides of composition $SnCl_xI_{4-x}$, where $x \leq 4$ [21]. It can be established further that in a given $SnCl_4$—SnI_4 mixture, x may assume at least two values (this follows from the fact of superposition).

This result is in agreement with those obtained in Raman spectroscopic [22, 23], molecular light scattering [24] and NMR [25] studies.

Katada et al. measured the Mössbauer parameters of frozen aqueous solutions of hexahalogenostannate(IV) coordination entities. The compositions of the solutions were the following: $3\,SnF_4+100\,HF+300\,H_2O$, $6\,SnCl_4+100\,HCl+600\,H_2O$, $6\,SnBr_4+100\,HBr+600\,H_2O$ and $3\,SnX_4+3\,SnY_4+50\,HX+50\,HY+600\,H_2O$ (where X and Y stand for two of F, Cl and Br). The summary of the experimental results is given in Fig. 5.22 [26].

Cheng and coauthors supposed that the isomer shifts of frozen aqueous solutions of tin halogenides are linearly related to the average number of the coordinated halogenides [27–30]. This working hypothesis was the basis of the estimation of several equilibrium, stability and formation constants in the aqueous tin halogenide solutions. A series of experiments is given in Fig. 5.23 [27] and some of the stability constants of tin halogenides are given in Table 5.19.

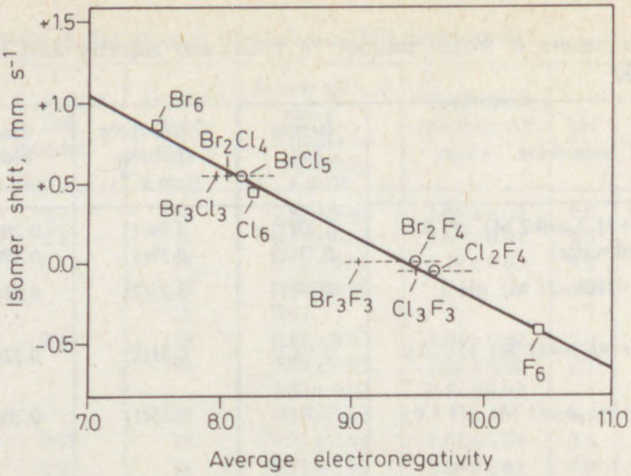

Fig. 5.22. Relation between isomer shift and the average electronegativity. $[SnBr_3F_3]^{2-}$ is represented by Br_3F_3 in the figure. The straight line is based on the data of the $[SnX_6]^{2-}$ ions (□). The circle (○) indicates the most probable configuration stabilized in each mixed halogenide solution. The spectra were recorded at 77 K. Isomer shifts are given relative to $BaSnO_3$.

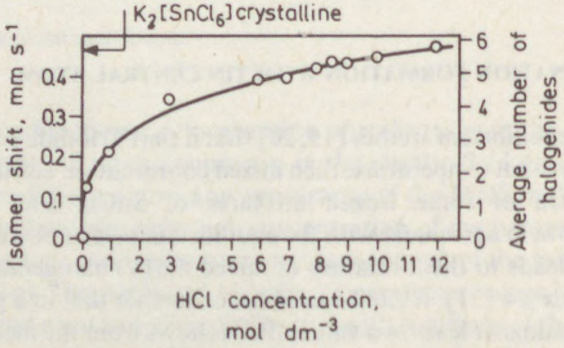

Fig. 5.23. Correlation of isomer shift, average number of halogenides and HCl concentration for aqueous solution of 0.04 mol dm^{-3} tin(IV) chloride. Isomer shift is with respect to $BaSnO_3$ at room temperature.

The formalism of the calculations was based on Bjerrum's formation function [31]. (This technique was first used by Vértes et al. to obtain stability constants on the basis of Mössbauer spectra [32].)

Cheng wrote the measured isomer shift as [27]:

$$\delta = \sum_{i=0}^{N} x_i \delta_i \qquad (5.14a)$$

where N is the maximum of the halogenide coordination, x is the mole fraction of SnX_n.

Using linear relation between the average number of the coordinated halogenides ($\bar{n}$)

Table 5.19.
Stability constants obtained by Mössbauer spectroscopy in aqueous solutions of tin halogenides:

$$K_n = \frac{[\mathrm{SnX}_n]}{[\mathrm{SnX}_{n-1}][\mathrm{X}]}$$

where X is the halogenide and $\beta = K_1.K_2. \ldots . K_n$

System	K_1	K_2	K_3	K_4	K_5	K_6	β	Literature
SnF_4—HF—H_2O							3.3×10^{24}	27
$SnCl_4$—HCl—H_2O	20.3	6.3	1.5	0.6	0.2	0.1	2.3	29
$Sn(ClO_4)_2$—HF—H_2O	3.6×10^4	2.5×10^3	1.8×10^2				1.6×10^{10}	28
	2.6×10^4	3.1×10^3	3.7×10^2				3.0×10^{10}	
$K[SnBr_3]$—HBr—H_2O	22	3	0.4				2	30

In the case of $Sn(ClO_4)_2$—HF—H_2O system the first row was obtained on the basis of the isomer shift (σ) and the second one on the basis of the quadrupole splitting (ΔE). The isomer shift and the quadrupole splitting were 3.55 mm s^{-1} and 1.50 mm s^{-1}, respectively in the solution of 0.53 mol dm^{-3} $Sn(ClO_4)_2$ + 0.59 mol dm^{-3} $HClO_4$ and in the saturated HF solution they changed to $\sigma = 3.19$ mm s^{-1} and $\Delta E = 1.83$ mm s^{-1}.

and the isomer shift:

$$\delta = \delta_0 + \bar{n}(\delta_N - \delta_0)/N \tag{5.14b}$$

where δ_0 is the partial isomer shift of tin ion without any halogenide coordination (totally aquacoordinated tin) which can be measured in the aqueous solution of tin perchlorate and δ_N is the isomer shift of the totally halogen-coordinated tin which can be measured in the solution saturated with halogenide. $\bar{n}$ can be written:

$$\bar{n} = \frac{[\mathrm{SnX}] + 2[\mathrm{SnX}_2] + \ldots N[\mathrm{SnX}_N]}{[\mathrm{Sn}] + [\mathrm{SnX}] + [\mathrm{SnX}_2] + \ldots [\mathrm{SnX}_N]}. \tag{5.15a}$$

Using the stability constants $\left(K_n = \dfrac{[\mathrm{SnX}_n]}{[\mathrm{SnX}_{n-1}][\mathrm{X}]}\right)$ and their products ($\beta_i = K_1 \cdot K_2 \cdot \ldots K_i$)

$$\bar{n} = \frac{\sum_1^N i\beta_i[\mathrm{X}]^i}{\sum_0^N \beta_i[\mathrm{X}]^i} = \frac{\sum_1^N i\beta_i[\mathrm{X}]^i}{1 + \sum_1^N \beta_i[\mathrm{X}_i]^i}. \tag{5.15b}$$

Combination of Eqs (5.14b) and (5.15b) gives:

$$\delta = \delta_0 + \frac{\sum_1^N i\beta_i[\mathrm{X}]^i}{1 + \sum_1^N \beta_i[\mathrm{X}]^i} \frac{\delta_N - \delta_0}{N}. \tag{5.16}$$

Eq. 5.16 gives a function between the measured isomer shifts and the concentration of uncoordinated halogenides in the solution (see Fig. 5.23). The β_i values and the stability constants can be obtained as fitting parameters.

The Mössbauer studies by Cohen and West [33, 34] reflect the formation and subsequent decomposition of a polynuclear coordination entity in solution. Their results are illustrated in Fig. 5.24. Figure 5.24(a) shows the spectrum of a frozen solution of $SnCl_2$ in hydrochloric acid at liquid nitrogen temperature. If the solution is frozen after the addition of a Pd^{II} salt, the Mössbauer spectrum changes substantially, as seen in Fig. 5.24(b). This change corresponds to the formation of a polynuclear Sn—Pd coordination entity, which decomposes spontaneously in solution ($Sn^{2+} + Pd^{2+} = Sn^{4+} + Pd$); this decomposition is reflected by Fig. 5.24(c). With an appropriate spectral series, it was even possible to follow the kinetics of this intramolecular redox reaction.

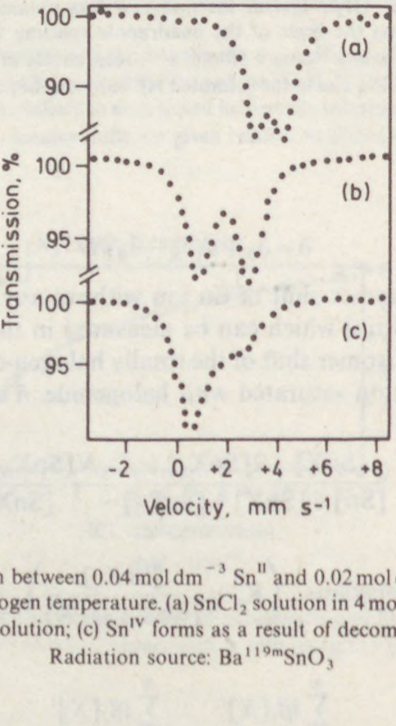

Fig. 5.24. Following of reaction between 0.04 mol dm^{-3} Sn^{II} and 0.02 mol dm^{-3} Pd^{II} in HCl medium via Mössbauer spectra at liquid nitrogen temperature. (a) $SnCl_2$ solution in 4 mol dm^{-3} aqueous HCl; (b) $SnCl_2 + PdCl_2$ solution; (c) Sn^{IV} forms as a result of decomposition.
Radiation source: $Ba^{119m}SnO_3$

Antonov et al. used both spectrophotometry and Mössbauer spectroscopy for the study of the formation of iridium-tin dinuclear coordination entities in the aqueous solution of hydrochloric acid [35]. The samples studied by them were prepared by dissolution of 3×10^{-2} mol dm^{-3} $IrCl_3$ in a solution of 3 mol dm^{-3} HCl and $SnCl_2$ with various concentrations between 3×10^{-2} and 3.6×10^{-1} mol dm^{-3}.

Mössbauer spectra of the frozen solutions showed superposition and it was an evidence that different coordination ions were present in the solution. The ratio of the line intensities depended on the concentration of Sn^{II}. (The concentration of Ir^{III} was constant during the experiment.) On the basis of the comparison of the spectrophotometrical and Mössbauer results the author concluded that the following equilibrium takes place in the solution [35]:

$$[\mathrm{IrCl_4(SnCl_3)_2}]^{3-} + 3[\mathrm{SnCl_3}]^{-} \rightleftharpoons [\mathrm{IrCl(SnCl_3)_5}]^{3-} + 3\mathrm{Cl}^{-}. \qquad (5.17)$$

Mathieu and his coauthors studied the effect of sodium pyrophosphate on the Mössbauer parameters of a frozen aqueous solution of $SnCl_2$ [35(a)]. They found that the isomer shift was 3.56 mm s^{-1} and the quadrupole splitting 1.14 mm s^{-1} in 1.87×10^{-2} mol dm^{-3} $SnCl_2$ solution at 77 K. The addition of sodium pyrophosphate changed these values to 3.19 mm s^{-1} and 1.76 mm s^{-1}, respectively. These measurements proved the formation of Sn^{II}-pyrophosphate coordination compound in the solution.

5.3.3. COORDINATION COMPOUND AND ION FORMATION WITH Eu, I AND Au MÖSSBAUER ACTIVE ATOMS

Mössbauer spectroscopy has the advantage that it can be applied to the investigation of frozen solutions prepared with any solvent. For example, Broun et al. [36] used this method to examine the ice produced by the rapid freezing of europium solutions prepared with liquid ammonia. The Mössbauer spectra of the frozen solutions were recorded in the temperature range 1.6–78 K. It was found that the isomer shift of $[Eu(NH_3)_6]$ relative to the Eu_2O_3 radiation source is -12.5 mm s^{-1} while that of the other Eu—NH_3 coordination entity in solution is -13.7 mm s^{-1}. These isomer shifts indicate the divalent $(4f)^7$ electron configuration, but they are more positive than the value found for purely ionic Eu^{2+} compounds, viz., -14.5 mm s^{-1}. The isomer shifts remained unchanged throughout the temperature range considered. At the temperature of liquid helium and below, $[Eu(NH_3)_6]$ exhibited a magnetic hyperfine structure, with an internal magnetic field strength of 2.3×10^7 A m^{-1} (this value is lower than that found for ionic Eu^{2+} compounds, viz. 2.6×10^7 A m^{-1}). On the basis of their results, Broun et al. supported the earlier assumption relating to $[Eu(NH_3)_6]$, that the valency electrons of Eu form a conductance band, and that $[Eu(NH_3)_6]$ is therefore of a metallic nature.

Sakai and his coauthors investigated the Mössbauer spectra of the frozen solution of ^{129}I in carbon disulfide at the presence of donor molecules [37]. The molecular I_2 and the donor molecules form charge-transfer coordination entities in the disulfide solution and the Mössbauer parameters of those recorded at 16 K are tabulated in Table 5.20. Three of the spectra are shown in Fig. 5.25. The main conclusions of the measurements were the following. When the donor molecules formed n–σ type charge-transfer coordination entity with I_2 (triethylamine and pyridine) two chemical positions of iodine appeared in the Mössbauer spectra (see Table 5.20). They correspond to the bridging and terminal iodines. The benzene and methylated benzene gives π–σ type coordination entities with I_2 molecules. The Mössbauer spectra of such coordination entities show only one position of iodine. The acceptor orbital of iodine was supposed to be an spd hybrid. Using the Mössbauer parameters the authors calculated also the charge densities and charge distributions of iodine.

The Mössbauer technique was used for the study of coordination between gold and

Table 5.20.
The Mössbauer parameters for the charge-transfer coordination entities

Composition	Quadrupole coupling constant[(a)], MHz	Isomer shift[(b)], δ mm s^{-1}	η %	Literature
I_2 in CS_2	−2242 ± 20	0.93 ± 0.04	11 ± 5	[37]
Triethylamine-I_2 (A)	−2604 ± 20	1.56 ± 0.05		[37]
(B)	−1261 ± 20	0.40 ± 0.05	9 ± 5	
Pyridine-I_2 (A)	−2631 ± 20	1.82 ± 0.04	10 ± 5	[37]
(B)	−1439 ± 20	0.39 ± 0.04		
Pyridine-I_2 (A)	−2600 ± 30	1.40 ± 0.07		[38]
(B)	−1300 ± 15	0.28 ± 0.05		
Benzene-I_2	−2253 ± 20	0.94 ± 0.05	11 ± 5	[37]
Benzene-I_2	−2412 ± 2	0.76 ± 0.05		[39]
Mesitylene-I_2	−2297 ± 20	0.89 ± 0.05	10 ± 5	[37]
Hexamethylbenzene-I_2	−2371 ± 20	0.84 ± 0.05	7 ± 5	[37]

(*a*) It is converted to ^{127}I.
(*b*) The isomer shift is relative to the ZnTe source.

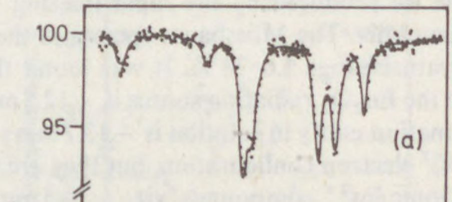

Fig. 5.25. Mössbauer spectra of ^{129}I at 16 K. (a) I_2 in CS_2 (free iodine molecule); (b) pyridine-I_2 coordination entity in CS_2; (c) triethylamine-I_2 coordination entity in CS_2 [37].

SR = thiomaleate = $SCH(CO_2H)CH_2CO_2H$ in solution [40]. The previous NMR data indicated the presence of $[Au_4(SR)_7]^{3-}$ coordination ion in the solution although the Mössbauer data suggested a simpler formation, e.g. AuSR. The ^{197}Au isotope was used for the Mössbauer measurements.

REFERENCES

1. Vértes, A., Dézsi, I. and Suba, M., *Acta Chim. Acad. Sci. Hung.*, **64**, 347 (1970); *Magy. Kém. Folyóirat*, **76**, 133 (1970).
2. Anderegg, G., *Helv. Chim. Acta*, **46**, 2397 (1963).
3. Bayendale, J. H. and George, P., *Trans. Faraday, Soc.*, **46**, 55 (1950).
4. Epstein, L. M., *J. Chem. Phys.*, **40**, 435 (1963).
5. Silver, J., Morrison, I. E. G. and Rees, L. V. C., *Inorg. Nucl. Chem. Letters*, **15**, 433 (1979).
6. Fanning, J. C., Park, G. B., James, C. G. and Heatley, W. R., *J. Inorg. Nucl. Chem.*, **42**, 343 (1980).
7. Sato, H. and Tominaga, T., *Bulletin of the Chemical Society of Japan*, **52**, 1402 (1979).
8. Vértes, A., Burger, K. and Bognár, L., *Acta Chim. Acad. Sci. Hung.*, **66**, 209 (1970).
9. Laskowski, E. J., Reynolds, J. G., Frankel, R. B., Foner, S., Papaefthymion, G. C. and Holm, R. H., *J. Am. Chem. Soc.*, **101**, 6562 (1979).
10. Laskowski, E. J., Frankel, R. B., Gillum, W. O., Papaefthymion, G. C., Renand, J., Ibers, J. A. and Holm, R. H., *J. Am. Chem. Soc.*, **100**, 5322 (1978).
11. Vértes, A. and Parak, F., *J. Chem. Soc. Dalton Trans.*, 2062 (1972).
12. Figgis, B. N. and Lewis, J., *Progr. Inorg. Chem.*, **6**, 37 (1964); Reiff, W. M., Long, G. J. and Baker, W. A., *J. Am. Chem. Soc.*, **90**, 6347 (1968).
13. Lind, M. O. and Hoard, J. L., *Inorg. Chem.*, **3**, 34 (1964).
14. Spijkerman, I. I., Hall, L. H. and Lambert, I. L., *J. Am. Chem. Soc.*, **90**, 2039 (1968).
15. De Arajou, F. T., Dufresne, A., De Lima, G. and Knudsen, I. M., *Chem. Phys. Lett.*, **7**, 333 (1970).
16. Kachanova, Zh. T., Stukan, R. A. and Purmaly, A. P., *Teor. Eksp. Khim.* (*Kiew*) **6**, 280 (1970).
17. Stein, G. E. and Marinsky, J. A., *J. Inorg. Nucl. Chem.*, **37**, 2421 (1975).

18(a). Rabinowitz, I. N., Davis, F. F. and Herber, R. H., *J. Am. Chem. Soc.*, **88**, 4346 (1966).

18(b). Silver, J., Lukas, B. and Al. Jaff, G., *Inorganica Chimica Acta*, **91**, 125 (1984).

18(c). Keypour, H., Silver, J., Wilson, M. T. and Hamed, M. Y., *Inorganica Chimica Acta*, **125**, 97 (1986).

19. Beck, M. T. and Huhn, P., *Acta Chim. Acad. Sci. Hung.*, **51**, 7 (1967).
20. Gaizer, F., Kovács, E. and Beck, M. T., *Magy. Kém. Folyóirat*, **77**, 347 (1971).
21. Vértes, A., Győri, E., Gál, M. and Suba, M., *Magy. Kém. Folyóirat*, **77**, 189 (1971).
22. Trumpy, B., *Z. Phys.*, **66**, 790 (1930).
23. Dellwaule, M. L., Buisset, M. B. and Deihaye, M., *J. Am. Chem. Soc.*, **74**, 5768 (1952).
24. Fabelinskii, I. L., *Molekularnoje Rasseyaniye Sveta*, Nauka Moscow, 1965.
25. Burke, J. J. and Lauterbur, P. C., *J. Am. Chem. Soc.*, **83**, 326 (1961).
26. Katada, M., Kanno, H. and Sano, H., *Polyhedron*, **2**, 104 (1983).
27. Cheng, H. S., *Radiochem. Radioanal. Letters*, **49**, 161 (1981).
28. Cheng, H. S., Hsu, Y. C., Chang, Y. C. and Wet, H. H., *Ibid*, **49**, 167 (1981).
29. Cheng, H. S., *Ibid*, **47**, 167 (1981).
30. Hsu, C. M., Cheng, H. S., Luh, H. and Chen, M. Y., *J. Chinese Chemical Society*, **31**, 211 (1984).
31. Bjerrum, N., *Z. Anorg. Chem.*, **119**, 179 (1921).
32. Vértes, A., Nagy-Czakó, I. and Burger, K., *J. Phys. Chem.*, **80**, 1314 (1976).
33. Cohen, R. L. and West, K. W., *J. Electrochem. Soc.*, **119**, 433 (1972).
34. Cohen, R. L., *Science*, **178**, 828 (1972).
35. Antonov, P. G., Kukushkin, Yu. N., Skredov, V. F. and Vasilyev, L. N., *Koord. Khim.*, **5**, 561 (1979).

35(a). Mathieu, L., Bussiere, P., Christofidis, D., Porthault, M. and Berger, M., *Radiochem. Radioan. Letters.*, **40**, 223 (1979).

36. Brown, J. P., Cohen, R. L. and West, K. W., *Mössbauer Effect Methodology*, Vol. 8, ed. Gruverman, I. J. and C. W. Seidel, Plenum Press, New York, 1973, p. 3.
37. Sakai, H., Maeda, Y., Ichiba, S. and Negita, H., *J. Chem. Phys.*, **72**, 6192 (1980).
38. Wynter, C. I., Hill, J., Bledsoe, W., Shenoy, G. K. and Ruby, S., *J. Chem. Phys.*, **50**, 3872 (1969).
39. Maeda, Y., Sakai, H., Ichiba, S., Katada, M. and Negita, H., *Anner. Rep. Res. Reactor Inst. Kyoto Univ.*, **6**, 64 (1973).
40. Moss, K., McAuliffe, C. A., Parish, R. V. and Sayegh, L., *Abstr. Second Seeheim Workshop on Mössbauer Spectroscopy*, 23–26 May, 1983, p. 56.

5.4. TRACER MÖSSBAUER SPECTROSCOPY

ELECTRON-EXCHANGE REACTIONS STUDIED BY THE MÖSSBAUER EFFECT

The combination of Mössbauer spectroscopy with the radioactive tracer technique makes a special method which provides more complex information than the simple tracer method alone. The study of the electron exchange in solution is an excellent example for the demonstration of the advantages of "Tracer Mössbauer Spectroscopy".

The study of electron exchange between elements of the same atomic number but different oxidation states was made possible earlier by the use of radioactive tracers [1–4]. In this technique the component in one of the oxidation states is labelled by means of a radioactive or stable isotope; then, after the exchange time, the components in the different oxidation states are separated by chemical methods (precipitation, extraction, etc.), and the amount of the isotope used for labelling is determined in one or both components by radioactivity or mass-spectrometric measurement.

The Mössbauer method is suitable for following the progress of the electron-exchange continuously, without the separation of the exchange components, and can therefore be applied with advantage in studies of either liquid or solid-state reactions [5].

The possibility of the application of Mössbauer effect instead of isotopic labelling was pointed out by Stukan et al. [6].

5.4.1. ELECTRON EXCHANGE BETWEEN TIN(II) AND TIN(IV) SPECIES

The basis of the method is described here on an example of the electron-exchange between Sn^{II} and Sn^{IV}.

Only certain isotopes of a given element are capable of undergoing the nuclear resonance absorption of γ-rays (e.g. ^{119}Sn in the case of tin isotopes) and these isotopes form only a small proportion of the elements as occurring in nature (^{119}Sn makes 8.5% of natural tin). It is possible to enrich the nuclides adequate for nuclear resonance absorption, up to nearly 100% of Mössbauer active atoms. Solutions prepared from these enriched isotopes may yield Mössbauer spectra with suitably high line intensities, even at concentrations as low as 10^{-3} mol dm^{-3}. If a solution of the same concentration is prepared from the same element, with the naturally-occurring composition, the line intensity of the resulting Mössbauer spectrum is virtually zero.

Figure 5.26 shows the Mössbauer spectra of a solution containing 0.063 mol dm^{-3} of $SnCl_4$ and 0.057 mol dm^{-3} of $SnCl_2$, frozen after two different times. The Sn^{II} and Sn^{IV}

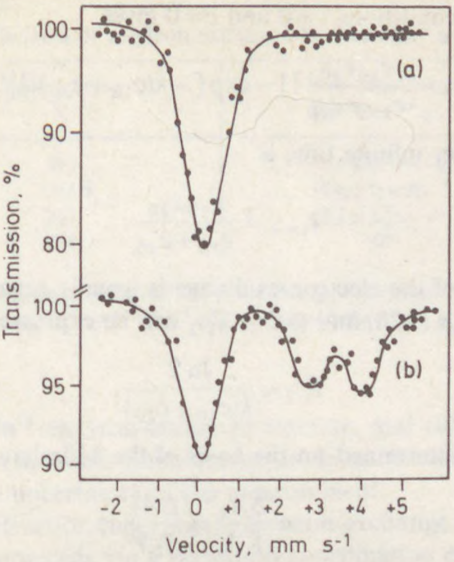

Fig. 5.26. Mössbauer spectra at liquid air temperature of 0.063 mol dm^{-3} $^{119}SnCl_4$ + 0.057 mol dm^{-3} $SnCl_2$ aqueous solution. Time of the electron-exchange: (a) 2 s, (b) 3.9 × 10^3 s. Radiation source: $Ba^{119}SnO_3$

solutions were mixed only a short time before the freezing necessary for the recording of the Mössbauer spectra; the electron-exchange time is less than 3 s. The $SnCl_4$ solution was made from ^{119}Sn enriched to 92%, and accordingly the Sn^{IV} line (isomer shift, $\delta = 0.20$ mm s^{-1}) appears with a high intensity in the spectra, whereas the corresponding line ($\delta = 3.4$ mm s^{-1}) for $SnCl_2$ solution, prepared from natural tin, is not visible. As a result of the electron-exchange, however, an increasing amount of $^{119}Sn^{IV}$ is converted into Sn^{II}, and thus the intensity of the line corresponding to Sn^{IV} decreases, while that corresponding to Sn^{II} increases with time, to limiting values. The spectrum in Fig. 5.26(b) belongs to the mixture of $SnCl_4$ and $SnCl_2$. This sample was kept for 65 min at 20°C before it was frozen. A part of the ^{119}Sn was converted from Sn^{IV} into Sn^{II} due to the electron exchange, and thus the intensity of the line pair corresponding to the latter (quadrupole splitting, $\Delta E = 0.95$ mm s^{-1}) increased considerably.

The equation for the electron-exchange of ^{119}Sn is

$$^{119}Sn^{IV} + Sn^{II} \underset{k}{\overset{k}{\rightleftarrows}} Sn^{IV} + {}^{119}Sn^{II}. \qquad (5.18)$$

(Sn without mass number denotes natural tin.)

The rate of the transfer $^{119}Sn^{IV} \rightarrow {}^{119}Sn^{II}$ can be written as

$$\frac{dc}{dt} = k(c_{10} - c)(c_{20} - c) - kc^2 \qquad (5.19)$$

where c is the $^{119}Sn^{II}$ concentration (mol dm^{-3}), t is time (s), c_{10} is the $^{119}Sn^{IV}$ concentration at time $t = 0$ and c_{20} is the Sn^{II} concentration at time $t = 0$. Solution of Eq.

(5.19) with the initial conditions $t=0$ and $c=0$ gives

$$c=\frac{c_{10}c_{20}}{c_{10}+c_{20}}\{1-\exp[-k(c_{10}+c_{20})t]\}\,. \tag{5.20}$$

The concentration after infinite time is

$$c_{t=\infty}=\frac{c_{10}\,c_{20}}{c_{10}+c_{20}}\,. \tag{5.21}$$

The half life ($T_{1/2}$) of the electron-exchange is usually regarded as the time when $c/c_{t=\infty}=0.5$. From Eqs (5.20) and (5.21), $T_{1/2}$ can be expressed as

$$T_{1/2}=\frac{\ln 2}{k(c_{10}+c_{20})}\,. \tag{5.22}$$

The c values can be determined on the basis of the Mössbauer spectra

$$c=\frac{\Delta A_1}{f_1\,V}=\frac{\Delta A_2}{f_2\,V} \tag{5.23}$$

where ΔA_1 and ΔA_2 (cm^2) are the decrease or increase in the areas of the Mössbauer line or line pair (in the case of quadrupole splitting) relating to $\mathrm{Sn^{IV}}$ and $\mathrm{Sn^{II}}$, respectively, during the electron-exchange time t, and f_1 and f_2 are quantities proportional to the Debye–Waller factor and denote the areas (cm^2) of the lines relating to 1 mol of $\mathrm{Sn^{IV}}$ and $\mathrm{Sn^{II}}$, respectively; V is the volume of absorber subjected to the γ-radiation.

The results showed [5] that $f_1=f_2$.

$$c_{10}=\frac{A_{10}}{fV} \tag{5.24}$$

where A_{10} is the area of the $\mathrm{Sn^{IV}}$ line at time $t=0$. From Eqs (5.23) and (5.24)

$$c=c_{10}\frac{\Delta A}{A_{10}}\,. \tag{5.25}$$

In this way, the c values relating to the individual points of time t can be determined from c_{10}, A_{10} and the ΔA values measured at different times. From Eqs (5.20) and (5.25), the rate constant of the electron exchange is given by

$$k=-\frac{1}{Bt}\ln\left(1-\frac{\Delta AB}{A_{10}c_{20}}\right) \tag{5.26}$$

where $B=c_{10}+c_{20}$.

The samples and at the same time the electron-exchange reaction are quenched to the temperature of liquid nitrogen and the Mössbauer measurements can be carried out at this temperature.

Table 5.21 gives the results for the electron-exchange between $\mathrm{Sn^{II}}$ and $\mathrm{Sn^{IV}}$ in hydrochloric acid solution with a concentration of 10 mol dm^{-3} [5].

The activation energy (E_a) of the electron-exchange is 92 ± 8 kJ mol^{-1}. It should be noted that Browne et al. [7] used the isotopic tracer technique to measure the rate

Table 5.21.
Rate coefficients of electron-exchange between Sn^{II} and Sn^{IV}

Temperature K	Rate constant, k $dm^3\ mol^{-1}\ s^{-1}$
293	$(7.5 \pm 0.8) \times 10^{-3}$
273.5	$(4 \pm 1.1) \times 10^{-4}$
243	$(2.5 \pm 1.2) \times 10^{-6}$
204	0*

* During the reaction time of 100 h the change in the ratio of the line intensities of Sn^{II} and $^{119}Sn^{IV}$ did not exceed the error of measurement.

constants of the Sn^{II}–Sn^{IV} electron-exchange reaction, and calculated an activation energy of 46 kJ mol^{-1}. The tracer technique necessitates chemical separation and this circumstance raises the uncertainty of the measurement.

The relatively high activation energy of the electron-exchange reaction indicates that the electron-exchange proceeds via a transition coordination entity, probably in the following steps:

$$[^{119}SnCl_6]^{2-} + [SnCl_4]^{2-} \rightarrow [^{119}SnSnCl_{10}]^{4-} \rightarrow$$
$$\rightarrow [^{119}SnCl_4]^{2-} + [SnCl_6]^{2-}.$$

5.4.2. ELECTRON-EXCHANGE REACTIONS BETWEEN IRON(II) CHLORIDE AND IRON(III) CHLORIDE IN FORMAMIDE SOLUTION

The mechanisms of electron transfer reactions can be divided into two main groups, depending on whether indirect or direct electron transfer is assumed. In the indirect mechanism, the electron transfer is mediated by some atom, molecule, ion or radical [8–11], while in the direct mechanism the electron-exchange reaction is influenced by the Coulombic repulsion between the dipolar solvent and the ion participating in the electron transfer reaction [12–17].

By variation of the solvent it can be determined whether the electron-exchange reaction will proceed by a direct or an indirect mechanism. The measurements can be carried out in an analogous manner to that described in Section 5.4.1.

In anhydrous formamide solution it was found that if freezing is carried out 48 h after the mixing of $^{57}FeCl_3$ and $FeCl_2$ solutions, Mössbauer lines corresponding to $^{57}FeCl_2$ will not appear, and thus a measurable extent of electron-exchange cannot be detected under such conditions [18]. Although some water addition makes possible the electron exchange in this system.

Figure 5.27 shows the Mössbauer spectrum of a solution containing 0.01 mol kg^{-1} of $^{57}FeCl_3$, 0.01 mol kg^{-1} of $FeCl_2$ and 8 wt.-% of water, after an electron-exchange reaction time of 20 s.

In an anhydrous formamide solution of $^{57}FeCl_3$, the iron(III) exhibits a magnetic hyperfine structure, and thus its electron-spin relaxation time (τ_R) is longer than the

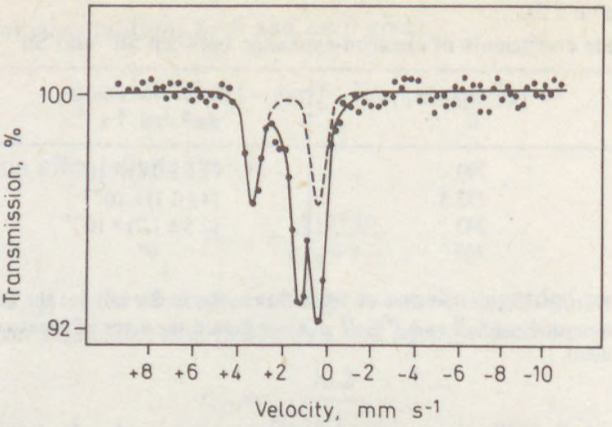

Fig. 5.27. Mössbauer spectrum of formamide solution containing 8 wt.-% H_2O, 0.01 mol kg^{-1} of $^{57}FeCl_3$ and 0.01 mol kg^{-1} of $FeCl_2$ at liquid nitrogen temperature. Electron-exchange reaction time is 20 s. The solutions were allowed to stand for 1 week prior to mixing. Radiation source: ^{57}Co in stainless steel

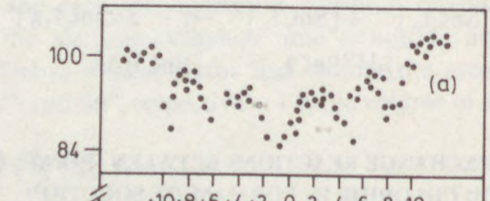

Fig. 5.28. Mössbauer spectra of formamide solution containing 9.07 wt.-% of H_2O and 0.02 mol kg^{-1} of $^{57}FeCl_3$ at liquid nitrogen temperature. (a) Fresh solution, (b) after standing for 6 d. The internal magnetic field strength was 4.46×10^{-7} A m^{-1}, which indicates that at most one chloride is situated in the inner ligand sphere of the iron.

Larmor precession time and the average lifetime of the ^{57}Fe nucleus in the excited state. After the addition of water, the magnetic hyperfine structure progressively disappears, and finally only a quadrupole line pair is seen in the Mössbauer spectrum. Figure 5.28 shows the Mössbauer spectrum of a freshly prepared 0.02 mol kg^{-1} ^{57}FeCl$_3$ solution containing 9.07 wt.-% of water and that after staying for 6 days.

The disappearance of the magnetic hyperfine structure (the decrease in the relaxation time) proves that the water promotes dimerization (or possibly polymerization) in the solution, and thus the probability of spin-spin interaction increases [19]. Further, this result clearly indicates that the inner ligand sphere of the iron undergoes a change after the addition of water; some of the formamide molecules are replaced by water molecules. The above results show that electron-exchange takes place between the resulting iron(III) and iron(II) mixed solvates, whereas the rate constant of electron-exchange in the anhydrous formamide solution is virtually zero.

The measurements clearly demonstrate that the electron exchange between Fe^{II} and Fe^{III} in the water-formamide mixture proceeds according to an indirect mechanism.

REFERENCES

1. Matusek, M., Jaros, F. and Tochstein, A., *Chem. List.*, **63,** 188, 317, 435 (1969).
2. Baulch, D. L., Dainton, F. S., Ledward, D. A. and Sugier, H., *Trans. Faraday Soc.*, **62,** 2200 (1966).
3. Horne, R. A., *J. Inorg. Nucl. Chem.*, **25,** 1139 (1963).
4. Nitzan, E. and Wahl, A. C., *J. Inorg. Nucl. Chem.*, **28,** 3069 (1966).
5. Vértes, A., *Radiochem. Radioanal. Lett.*, **4,** 337 (1970); *Magy. Kém. Folyóirat*, **77,** 344 (1971); *Proc. Conf. Mössbauer Spectrometry, Dresden,* 1971, p. 535.
6. Stukan, R. A., Goldanskii, V. I. and Makarov, E. F., *Dokl. Akad. Nauk SSSR*, **165,** 1347 (1965).
7. Browne, C. J., Craig, R. P. and Davidson, N.: *J. Am. Chem. Soc.*, **73,** 1946 (1951).
8. Dodson, R. W., *J. Phys. Chem.*, **56,** 863 (1952).
9. Reynolds, W. L. and Lumby, R. J., *Chem. Phys.*, **23,** 2560 (1955).
10. Horne, R. A. and Axelrod, E. H., *J. Chem. Phys.*, **40,** 1518 (1964).
11. Ruff, I., *J. Phys. Chem.*, **69,** 3183 (1965); *Acta Chim. Acad. Sci. Hung.*, **47,** 241 (1966); *Ibid*, **47,** 255 (1966); *Ibid*, **52,** 251 (1967); *J. Phys. Chem.*, **72,** 1792 (1968); *Quart. Rev.*, **22,** 199 (1968).
12. Marcus, R. J., Zwolinski, B. J. and Eyring, H., *J. Phys. Chem.*, **58,** 432 (1954).
13. Marcus, R. J., *Chem. Phys.*, **24,** 966 (1956); *J. Chem. Phys.*, **26,** 867 (1967); *Canad. J. Chem.*, **37,** 155 (1959); *Discuss. Faraday Soc.*, **29,** 21 (1960); *J. Phys. Chem.*, **67,** 853 (1963).
14. Hush, N. S., *Trans. Faraday Soc.*, **57,** 557 (1961).
15. Levich, V. G. and Dogonadze, R. R., *Dokl. Akad. Nauk. SSSR*, **124,** 123 (1959).
16. Dogonadze, R. R., *Dokl. Akad. Nauk SSSR*, **153,** 1368 (1960).
17. Dogonadze, R. R. and Chismadzhev, Y. A., *Dokl. Akad. Nauk SSSR*, **144,** 1077 (1962).
18. Vértes, A. and Suba, M., *Acta Chim. Acad. Sci. Hung.*, **74,** 439 (1972).
19. Vértes, A. and Parak, F., *J. Chem. Soc., Dalton Trans.*, 2062 (1972).

5.5. HYDROLYSIS STUDIES BY MÖSSBAUER SPECTROSCOPY

Decreasing the hydrogen ion concentration in an aqueous salt solution, hydroxide ligands may be formed in the hydrated ions, accompanied by the release of protons. This phenomenon in frequently observed in the case of cations, e.g.

$$[Fe(H_2O)_6]^{3+} \rightarrow [Fe(OH)(H_2O)_5]^{2+} + H^+$$

but also some uncharged coordination entities or anions are inclined to hydrolysis, e.g.

$$[SbCl_4(H_2O)_2]^- \rightarrow [SbCl_4(OH)(H_2O)]^{2-} + H^+.$$

In the study of hydrolysis it is often necessary to determine the structures and amounts of the coordination ions formed or transformed in aqueous solutions as a result of a pH change. This section illustrates the application of Mössbauer spectroscopy in such studies presenting the example of some iron and antimony salt solutions.

5.5.1. HYDROLYSIS OF IRON(III) SALTS

The hydrolysis of iron(III) salts attracted the interest of scientists several decades ago, as the great amount of papers published since that time shows. The most important methods applied were magnetic measurements [1–6], potentiometric titration [7] and spectrophotometry [8, 9, 12, 13]. The results obtained and conclusions drawn led to certain contradictions, and, in addition, a number of problems, particularly pertaining to solutions of higher concentration, were not considered. These circumstances motivated the use of Mössbauer spectroscopy in this field [14–16, 19, 20, 22].

The most important parameters that affect the hydrolysis of iron(III) salts are the pH, the anion effect, ionic strength (concentration conditions), time of ageing and temperature. An account is given below of how the effects of these parameters on the hydrolysis of the iron(III) ion can be examined by Mössbauer spectroscopy. (If the total electrolyte concentration (c) is not otherwise mentioned, then $c = 2\,\mathrm{mol\,dm^{-3}}$ is assumed in the following discussion.)

5.5.1.1. Effect of the hydrogen ion concentration on the hydrolysis of iron(III) salts

The previous magnetic [1], spectrophotometric [9] and potentiometric [7] measurements showed that various species (coordination ions) were formed in solutions of iron(III) salts when the pH was changed. In perchlorate and nitrate solutions the following species were assumed:

$$[Fe(H_2O)_6]^{3+}, \quad [Fe(OH)(H_2O)_5]^{2+}, \quad [Fe(OH)_2(H_2O)_4]^{+}$$

and a dimer which may have the composition of

$$[Fe_2(OH)_2(H_2O)_8]^{4+} \quad \text{or} \quad [Fe_2O(H_2O)_{10}]^{4+}.$$

The structure of the dimer was described alternatively as

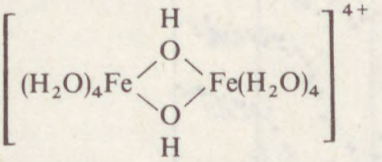

or $[(H_2O)_5Fe—O—Fe(H_2O)_5]^{4+}$.

Knudsen et al., using Mössbauer spectroscopy and vibrational spectroscopy, characterized the dimer as decaaquaoxodiiron coordination entity [10]. They found that the quadrupole doublet of 1.67 mm s^{-1} which appears at $1 < pH < 2$ belongs to the dimer and another doublet of 0.66 mm s^{-1} ($pH > 1.8$) represents the trimer and polynuclear species. Their main argument was that $[Fe\,edta]_2O$ has also an oxo bridge and a quadrupole splitting of 1.66 mm s^{-1}.

This picture was supported by the measurements of Ohya and Ono [11], by Nikolskii et al. [23] and by Du Fresne et al. [37]. Nevertheless other authors [17, 20, 38] supposed that the smaller quadrupole doublet belonged to the dimer and the higher one to an intermediate coordination entity. The contradiction of the results may be resolved by the compromising hypothesis that the first step of dimer formation is:

$$2[Fe(OH)(H_2O)_5]^{2+} \rightarrow [(H_2O)_5Fe—O—Fe(H_2O)_5]^{4+}$$

and, at higher pH values, this dimer may transform to the dihydroxo form:

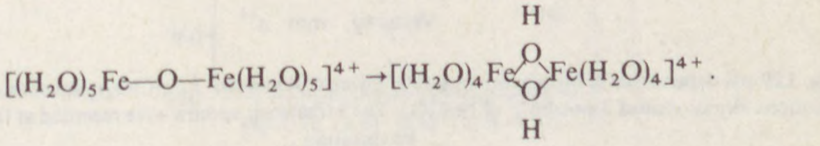

$$[(H_2O)_5Fe—O—Fe(H_2O)_5]^{4+} \rightarrow [(H_2O)_4Fe(\mu\text{-}OH)_2Fe(H_2O)_4]^{4+}.$$

According to this supposition, the quadrupole splitting of ~ 1.6 mm s^{-1} is attributed to the decaaquaoxodiiron coordination entity and the ~0.6 mm s^{-1} doublet to the dihydroxo coordination entity. (The polymer formation needs longer time as it will be shown in Chapter 5.5.1.5.). Dézsi et al. showed that the quadrupole splitting of *trans*-$[Fe(OH)_2(H_2O)_4]^{+}$ may be also about 1.6 mm s^{-1} [17, 22], although the concentration of such a species is so small [7] that it, probably, is not visible in the Mössbauer spectrum.

The Mössbauer spectra of aqueous solutions of $Fe(ClO_4)_3$ are shown in Fig. 5.29 [22]. These spectra were recorded at liquid nitrogen temperature. The lines of the Mössbauer spectrum apparently disappear at pH values below 0.2. The explanation being that in this concentration range the average distance between the iron atoms of the mononuclear iron species is ca 3×10^{-7} cm. This is the distance where the spin-spin interaction is already negligible (in other words, the probability of spin-spin relaxation

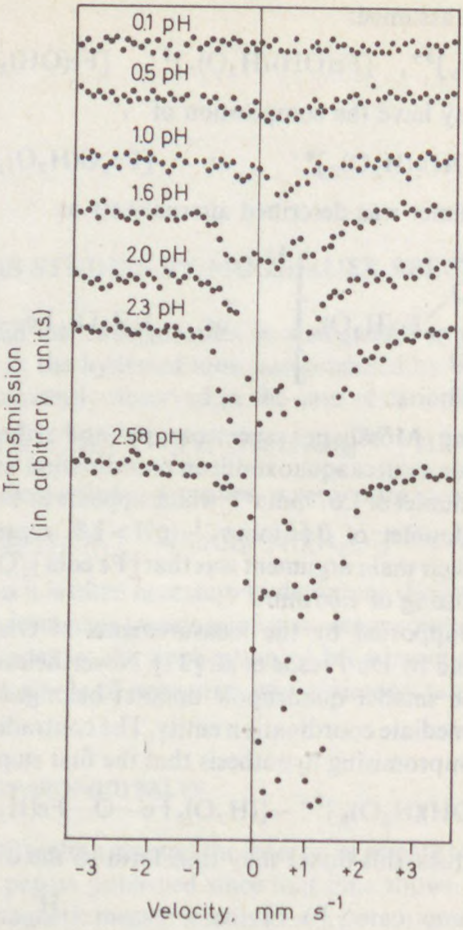

Fig. 5.29. pH dependence of Mössbauer spectra of frozen 0.04 mol dm^{-3} $Fe(ClO_4)_3$ aqueous solutions. The solutions also contained 3 mol dm^{-3} of $NaClO_4$. The Mössbauer spectra were recorded at liquid nitrogen temperature.

is low). Therefore, an increase in the spin-relaxation time (τ_R) results in the magnetic hyperfine structure of the spectrum. On the basis of the discussion given in the section dealing with paramagnetic spin relaxation, it can be seen that in such a situation the intensity of the Mössbauer effect (related to the total amount of iron) is distributed over a fairly large number of lines in the interval -10 to $+10$ mm s^{-1} in accordance with Kramer's doublets. At lower pH values (<0.5), all of the iron species can be regarded as monomeric, while for pH values higher than 2.00 about 90% of the iron (see later) is present in the solution as dimer. The spin-spin interaction in the dimer increases the probability of spin-spin relaxation, which prevents the development of the magnetic hyperfine structure, and thus only one quadrupole doublet appears in the Mössbauer spectrum. Hence, at pH > 2 the depth of the Mössbauer lines is ca 20%, while plotted on the same scale and velocity range (-3 to $+3$ mm s^{-1}), lines with a depth of 0.5–1% can

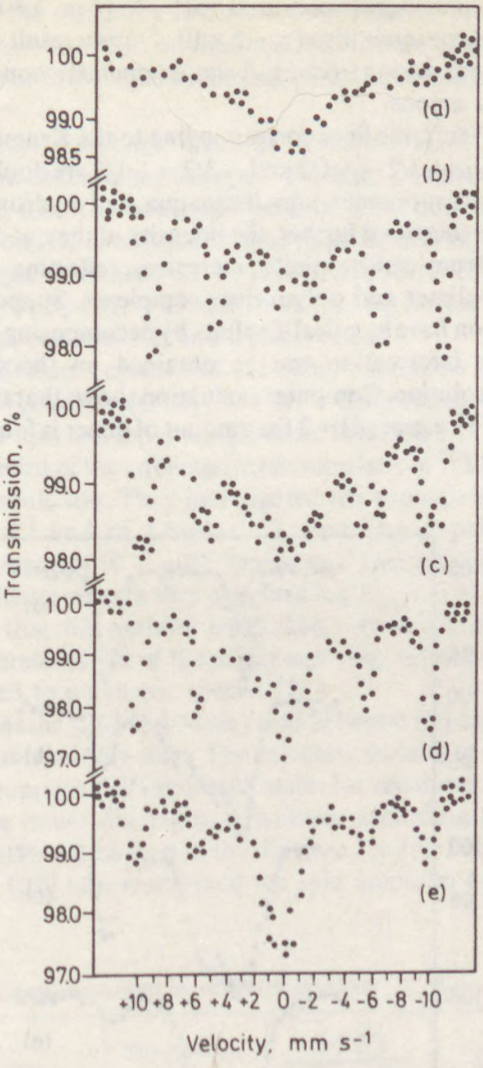

Fig. 5.30. Mössbauer spectra of 0.05 mol kg^{-1} $Fe(ClO_4)_3$ solutions at 4.5 K.
pH: (a) ~0; (b) 0.5; (c) 1.0; (d) 2.0; (e) 2.3.
Radiation source: $^{57}Co(Pt)$

no longer be observed in the spectra at $pH < 0.5$. By increasing the time of the measurement or the number of counts per channel (ca 10^6–10^7), however, a Mössbauer spectrum exhibiting definite magnetic splitting can also be recorded in strongly acidic solutions at 80 K [14]. On a further decrease of the temperature, the frequency of spin-lattice relaxation may also be reduced, which results in additional refinement of the MHS [15, 16]. Figure 5.30 shows the Mössbauer spectra of $Fe(ClO_4)_3$ solutions of a concentration of 0.05 mol kg^{-1} at different pH values and at the temperature of liquid helium (4.5 K).

In strongly acidic perchlorate solutions (pH = 0) [Fig. 5.30(a)], the frequency of paramagnetic spin relaxation is high ($\tau_R \sim 5 \times 10^{-9}$ s) as a result of the segregation that occurs in these solutions during freezing. A similar phenomenon cannot be observed in the presence of other anions.

At pH = 1 [Fig. 5.30(c)], the lines corresponding to the Kramer's doublet $S_z = \pm 5/2$ and the transitions $m_i = +3/2 \rightarrow +1/2$ and $-3/2 \rightarrow -1/2$ are doubled, indicating that in the same time various monomer ions (hexaaqua and hydroxo) are present in the solution. As the pH is increased further, the intensity of the quadrupole line pair in the center of the spectrum substantially increases, reflecting the increase of the concentration of the dimer and polynuclear complexes. Supposing that the various iron ions in the solution have identical f values, by decomposing the spectra in Fig. 5.30 into its components information can be obtained on the concentrations of the coordination ions in solution. Computer evaluation shows that the uncertainty of these data is rather high [16], e.g. at pH = 2 the amount of dimer is found to be 60 ± 15% and at pH = 2.3 it is 67 ± 14%.

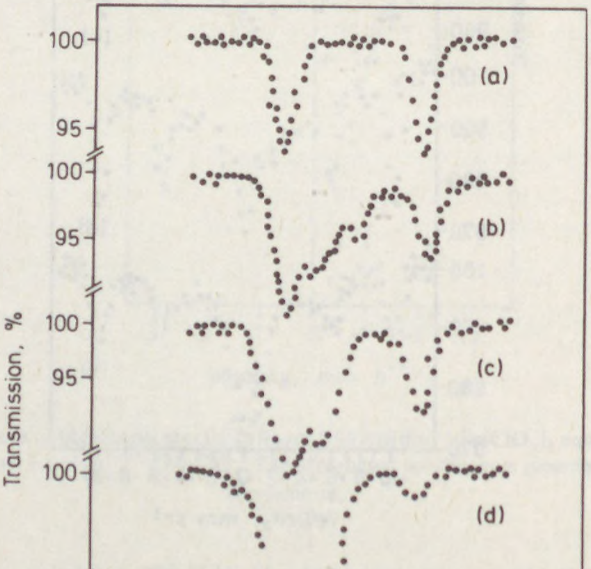

Fig. 5.31. Mössbauer spectra of mixtures of $^{57}Fe(ClO_4)_3$ and $Fe(ClO_4)_2$ solutions immediately after mixing. pH: (a) 0.1, (b) 1.1, (c) 1.8, (d) 2.2

Information about the concentration of the coordination ions formed in aqueous iron(III) perchlorate solutions can be obtained with the aid of a method based on the combined application of Mössbauer spectroscopy and electron exchange experiments [19, 20].

An iron(II) salt solution prepared from the isotope ^{56}Fe is added to an iron(III) solution prepared from the enriched isotope ^{57}Fe. After establishment of the electron-exchange equilibrium, the Mössbauer spectra (Fig. 5.31) were used to determine the proportions of the iron(III) coordination ions capable and of those not capable to electron-exchange (e.g. dimers cannot take part in electron exchange). By Mössbauer spectroscopy a value of $E_\alpha = 31.77\,\mathrm{kJ\,mol^{-1}}$ was found for the activation energy of electron exchange between iron(III) and iron(II) [21].

Values of the equilibrium constant of the dimer formation K_{22} according to the equation: $2Fe^{3+} + 2H_2O \rightleftharpoons [Fe_2(OH)_2]^{4+} + 2H^+$ determined by various methods (including Mössbauer spectroscopy) are given in Table 5.22.

The Mössbauer spectra of the aqueous frozen solutions of iron(III) perchlorate were studied by Nikolski et al., too. They investigated the dependence of the areas of the doublets (ca $0.4\,\mathrm{mm\,s^{-1}}$ and ca $1.6\,\mathrm{mm\,s^{-1}}$) appearing at $\mathrm{pH} < 2$ on the iron(III) concentration (in the range of $10^{-2} - 10^{-1}\,\mathrm{mol\,dm^{-3}}$) and pH (in the range 0.4–2). On the basis of the Mössbauer spectra they obtained $\log K_{22} = -3.1 \pm 0.2$. This low value was due to the fact, that the authors had taken into account only the doublet of $\sim 1.6\,\mathrm{mm\,s^{-1}}$ as a representative of the dimer and they supposed that the doublet of $\sim 0.6\,\mathrm{mm\,s^{-1}}$ belonged to polymeric species [23].

Máthé and Bakk-Máthé [26] and Mulay and Selwood [9] calculated the values of K_{22} from magnetic susceptibility data. The calculations lead to significantly different values, because they supposed different spin states for the dimer. Namely, Mulay and Selwood regarded the dimer diamagnetic, whereas according to Máthé and Bakk-Máthé [26] the spin state of the iron in the dimer is $S = 3/2$. Magnetic measurements made by Lázár et al. [27] have confirmed the spin quantum number $S = 3/2$.

Table 5.22.
Dimer equilibrium constants measured by different workers

Method of measurement	Temperature, °C	$NaClO_4$ concentration, $\mathrm{mol\,dm^{-3}}$	$K_{22} \times 10^3$	Literature
Proton magnetic relaxation	22		1.0	[24]
Potentiometry	25	3	1.22 ± 0.1	[7]
Spectrophotometry	25	1	1.9 ± 0.6	[8]
	25	3	2.6	
Potentiometry	25	3	4.4	[25]
Magnetic susceptibility	25	3	7.3 ± 0.8	[9]
	15	3	6.7	
Proton magnetic relaxation	20		10	[5]
Mössbauer spectroscopy			0.75	[23]
Mössbauer spectroscopy	20	3	13.5 ± 5	[18]
Spectrophotometry and magnetic susceptibility	25	3	75 ± 10	[6]
Mössbauer spectroscopy			1.0 ± 0.1	[23]
Magnetic susceptibility	25	3	32	[26]

Zvyagintsev and Lyachmanov [25] determined the thermodynamic characteristics of dimer formation by potentiometric equilibrium measurements at 25, 35 and 45 °C, and found $\Delta H = 47\,\mathrm{kJ\,mol^{-1}}$.

In the Mössbauer spectroscopic studies [18] of K_{22} (at 25, 35, 45 and 55 °C) a value of $\Delta H = 18\,\mathrm{kJ\,mol^{-1}}$ was found for the enthalpy of formation of the dimer.

The difference between the data obtained by the two procedures can be explained by the fact that at higher pH (>2.2) and at higher temperatures the iron(III) ion relatively rapidly polymerizes in the aqueous solution. Ultracentrifugation and dialysis measurements of Spiro et al. [3] suggest the formation of polymer units containing ca 900 iron atoms in iron(III) nitrate solution. The K_{22} values measured at higher pH and temperature must, therefore, be treated with caution [9, 25, 26]. The experimental methods employed in the above work do not demonstrate whether the solution also contains polymers higher than the dimer. On the other hand, if the extent of polymerization is such that a superparamagnetic structure can also develop then Mössbauer spectroscopy will indicate this by the appearance of a sextet in the spectrum recorded at low temperature. As an example, Fig. 5.32 depicts a Mössbauer spectrum of

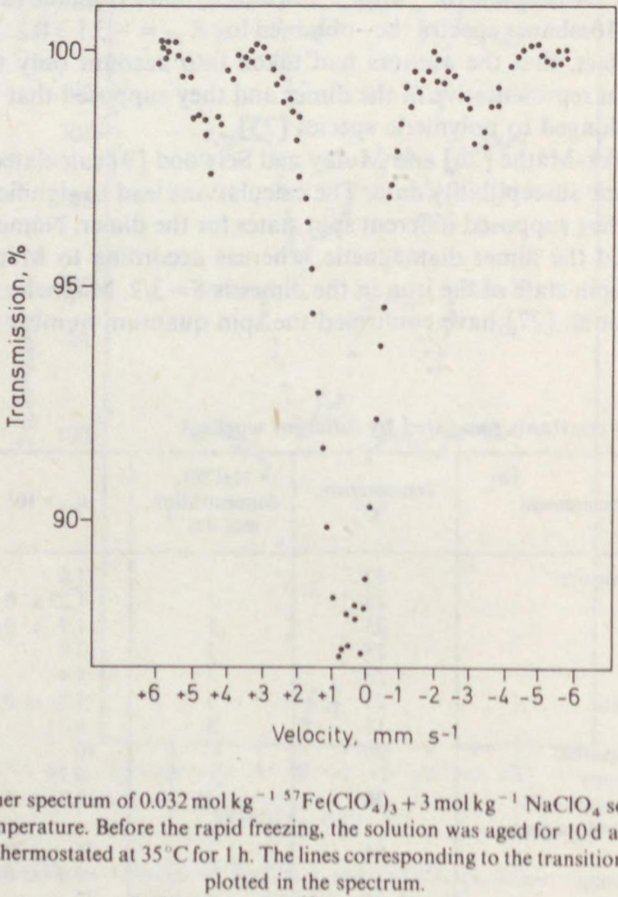

Fig. 5.32. Mössbauer spectrum of $0.032\,\mathrm{mol\,kg^{-1}}$ $^{57}Fe(ClO_4)_3 + 3\,\mathrm{mol\,kg^{-1}}$ $NaClO_4$ solution of pH 2.3, at liquid nitrogen temperature. Before the rapid freezing, the solution was aged for 10 d at room temperature and subsequently thermostated at 35 °C for 1 h. The lines corresponding to the transitions $m_{\mathrm{I}} = \pm 3/2$ are not plotted in the spectrum.
Radiation source: ^{57}Co in stainless steel

a frozen solution which was kept for 10 days at room temperature and subsequently thermostated for 1 h at 35°C and at pH = 2.3 [18].

In the Mössbauer spectra of polynuclear formations consisting of a smaller number of iron atoms, however, MHS does not appear even at low temperature, and thus the Mössbauer spectra do not yield any information about the presence of trimeric, tetrameric, etc. oligomers, i.e., no information can be obtained by this method on the initial stages of the polymerization (the Mössbauer parameters for these oligomers coincide with those for the spectrum of the dimer).

Table 5.23 gives the percentage distributions of the iron in superparamagnetic polymers exhibiting and not exhibiting magnetic structure obtained via intensities of the Mössbauer lines [18].

Table 5.23.
Distribution of iron in polymers exhibiting and not exhibiting magnetic hyperfine structure. The solutions were aged for 10 d at room temperature before the thermostating. The spectra were recorded at 80 K

Temperature of the thermostating for 1 hour (°C)	Percentage distribution of iron	
	In the magnetic polymer	In the paramagnetic polymer
35	34	66
45	51	49
55	68	32

The internal magnetic field strength in the polymer exhibiting magnetic splitting is 3.58×10^4 A m^{-1}. According to Watson and Freeman [28], the increase of the internal magnetic field strength produced by each unpaired d electron is 9.95×10^3 A m^{-1}. Taking this into account, it can be stated that the numbers of unpaired electrons in the iron atoms in the dimer and the polymer are equal.

The pH may have an effect on the structure of the aqueous solution of very complicated coordination compounds as well. The aqueous solution of *N*—[2-(salicylidenimino)ethyl] (*o*-hydroxyphenyl)glycine-iron(III) has dominant MHS at pH = 4.9 and pH = 9.8 but it has also a quadrupole doublet (0.95 mm s^{-1}) at pH = 7.2 beside MHS [28(a)]. The area percentage of the doublet is 21%. The MHS represents the species having mononuclear structure and the doublet corresponds to the dimer compound in the solution. The spectra were recorded in 5 : 1 glycerine/water solvent mixture at 4.2 K and at an applied magnetic field strength of 0.13 T parallel to the gamma beam [28(a)].

The effect of the hydrogen ion concentration can be observed even in the case of low spin compounds. The Mössbauer spectra of aqueous solution of protoporphyrin-iron(III)-cyanide at 80 K showed two doublets [28(b)]. The measured quadrupole splittings at pH = 12.5 were 1.51 mm s^{-1} and 0.73 mm s^{-1} and the area percentages were 36.2% and 63.8%, respectively. At pH = 10 these parameters changed to 1.73 mm s^{-1} and 0.79 mm s^{-1} for the quadrupole splitting and the corresponding area percentages were 25.5% and 75.5%, respectively [28(b)].

5.5.1.2. Anion effect on the hydrolysis of iron(III) salts

The anions present in iron(III) salt solutions may have considerable influence on the rate and mechanism of the hydrolysis, primarily, because certain anions, such as Cl^- [14, 29–32] and SO_4^{2-} [33], are able to coordinate with the iron(III) ion to a significant extent. Stability constants can be found, for example, in the monograph by Sillen and Martell [34].

Mössbauer spectra of iron(III) salt solutions containing nitrate anions, at liquid nitrogen temperature, are shown in Fig. 5.33. The Mössbauer spectra of frozen iron(III) nitrate solutions have been measured by a number of workers at the temperature of liquid nitrogen [20, 35–38].

Chaves and Garg [38] considered that the quadrupole doublet of ca 0.6 mm s^{-1} appearing at pH > 2 is due to the complex ion $[(H_2O)_5Fe—O—Fe(H_2O)_5]^{4+}$, and at lower pH (0.2–2) the two quadrupole doublets that appear with ca 1.6 and ca 0.4 mm s^{-1} are related to the coordination ion with an iron-hydroxide bridge and to the crystal hydrate, $Fe(NO_3)_3 \cdot nH_2O$, respectively. They found that the yield of $Fe(NO_3)_3 \cdot nH_2O$ increased while decreasing the velocity of freezing. During warming

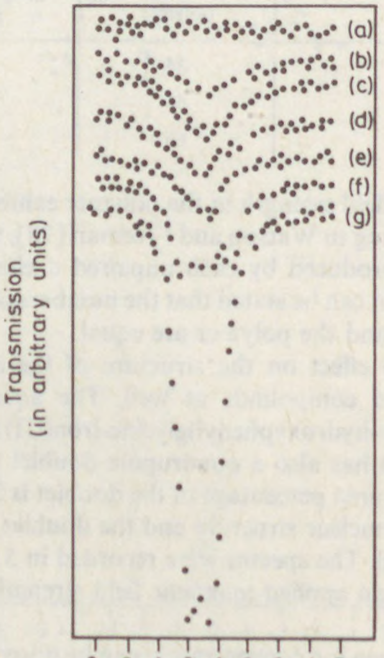

Fig. 5.33. Mössbauer spectra of 0.05 mol kg^{-1} $^{57}Fe(NO_3)_3$ solutions at liquid nitrogen temperature. (a) ^{57}Fe dissolved in 100% NHO_3; (b) ^{57}Fe dissolved in 49.5 wt.-% HNO_3; (c) pH = 0.5; (d) pH = 0.85; (e) pH = 1.5; (f) pH = 1.75; (g) pH = 2.1.
Radiation source: ^{57}Co in stainless steel

up of the quickly frozen solution, this crystal hydrate crystallized out at ca 180 K and a quadrupole doublet with a splitting of $\Delta \approx 0.4\,\mathrm{mm\,s^{-1}}$ was observed.

At lower pH values the iron in solution is present almost entirely in mononuclear form. In such instances the frequency of spin-spin relaxation decreases, and thus the spectrum exhibits MHS. Figure 5.34 shows spectra recorded under these conditions at the temperature of liquid nitrogen.

Filatova et al. studied the hydrolysis of iron(III) in the presence of phosphate ions [39]. The Mössbauer spectra of the frozen solution showed a quadrupole doublet or a very broad single line (half width $\Gamma = 1.4 - 1.7\,\mathrm{mm\,s^{-1}}$) without MHS. The concentration of iron(III) was between 0.01 and 0.1 mol dm^{-3} and the Fe^{3+}/PO_4^{3-} ratio was 2:1 during the experiments. The obtained isomer shift was 0.74 mm s^{-1} (relative to sodium nitroprusside) and the quadrupole splitting increased from 0.61 mm s^{-1} to 0.68 mm s^{-1} as the pH increased from 0.5 to 3.2. (The Mössbauer spectra of the quenched solution were recorded at 93 K.) The increase of the quadrupole splitting was interpreted as the effect of the polimerisation of the iron(III) specimen in the solution. The authors assumed that the following dimers were present before the polimerization: $[Fe_2HPO_4]^{4+}$ and $[Fe_2(OH)PO_4]^{2+}$.

Using the Mössbauer and spectrophotometrical results it was suggested [39] that the dimer had a hexamerous ring of the following structure:

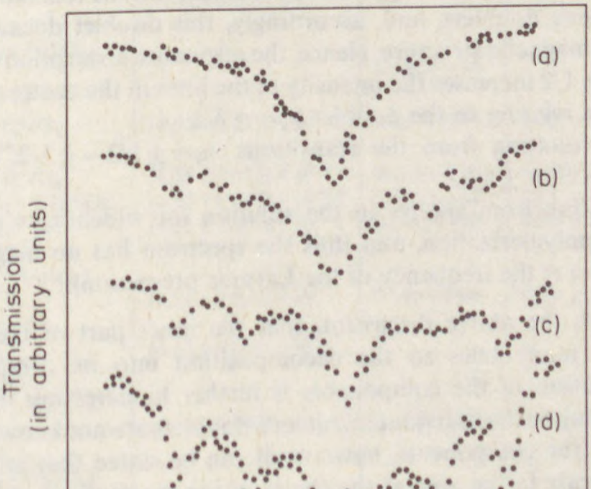

Fig. 5.34. Mössbauer spectra of ^{57}Fe dissolved in acid of 1 mol dm^{-3} concentration at liquid nitrogen temperature. Fe^{III} molality: 0.02–0.03 mol kg^{-1}. (a) Perchloric acid, (b) nitric acid; (c) sulfuric acid; (d) hydrochloric acid.
Radiation source: ^{57}Co in stainless steel

(Only the members of the ring are given in this scheme.)

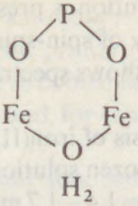

More exact information about the structure of solutions can be gained from spectra recorded at liquid helium temperature (4.5 K). At this temperature, the probability of spin-lattice relaxation decreases considerably (the frequency of spin-spin relaxation is independent of the temperature) and thus the spectral part relating to the monomer and exhibiting MHS can be readily distinguished in the spectrum. Parameters of the spectra are given in Table 5.24 and some of the spectra are shown in Fig. 5.35 [16].

Mössbauer spectra of $FeCl_3$ solutions of various pH values, recorded in order to study the hydrolysis process in the presence of chloride ions are presented in lines 1–7 of Table 5.24. The inner part of the spectra is due to the superposition of the following lines:

(*a*) τ_{SR} relating to $S_z = \pm 1/2$ is significantly shorter than the relaxation times for the other two Kramer's doublets, and, accordingly, this doublet does not, in general, exhibit hyperfine magnetic structure. Hence, the resonance absorption of the iron atom in the state $S_z = \pm 1/2$ increases the intensity of the lines in the centre of the spectrum.

(*b*) All the lines relating to the doublet $S_z = \pm 3/2$.

(*c*) The lines resulting from the transitions $m_i = \pm 1/2 \rightarrow \pm 1/2$, relating to the Kramer's doublet $S_z = \pm 5/2$.

(*d*) Lines resulting from species in the solution for which $\tau_{SR} < \omega^{-1}$ because of dimerization or polymerization, and thus the spectrum has no magnetic hyperfine structure (where ω is the frequency of the Larmor precession).

It is clear from the above discussion that the inner part of the spectrum is a superposition of many lines so the decomposition into its components is very uncertain. Separation of the components is further hindered by the fact that the populations relating to the individual Kramer's doublets are not known. Even without the separation of the components, however, it can be stated that an increase in pH results in an increase in the area at the centre of the spectrum, in the following area percentage proportions:

(in the same velocity interval)	$pH < 0$	$49.2 \pm 5\%$
	$pH = 1$	$55.5 \pm 6\%$
	$pH = 2$	$58.6 \pm 6\%$.

This definite progress of the area is connected with the fact that an increase in pH leads to an increase in the number of Fe—OH bonds, and the resulting coordination ions containing Fe—OH and Fe—Cl bonds undergo dimerization; these coordination entities belong to group (*d*) of the above classification.

Table 5.24.
Mössbauer parameters of iron(III) salt solutions

No.	Composition of solution (mol kg^{-1} in water)	Internal magnetic field strength $H_{5/2}$ A m^{-1}	Isomer shift δ* mm s^{-1}	Quadrupole splitting ΔE mm s^{-1}	Area of the outer line pair of $S_z = \pm 5/2$ Kramer's doublet (%)
1.	0.05 $FeCl_3 + 2\ HCl$	$(4.37 \pm 0.011) \times 10^7$	0.22 ± 0.05	0.10 ± 0.05	17.5 ± 2.4
2.	0.05 $FeCl_3 + 2\ (NaCl + HCl)$: pH = 1	$(4.36 \pm 0.010) \times 10^7$			16.1 ± 2.6
3.	0.05 $FeCl_3 + 2\ (NaCl + HCl)$: pH = 2				11.4 ± 2.1 5.04 ± 1.7
4.	0.2 $FeCl_3 + 2\ HCl$				14.2 ± 3.2
5.	0.2 $FeCl_3$		0.20 ± 0.02		
6.	0.5 $FeCl_3 + 1.0\ HCl$				10.1 ± 3.4
7.	1.0 $FeCl_3 + 0.5\ HCl$				2.5 ± 1.8
8.	0.025 $Fe_2(SO_4)_3 + 1.0\ H_2SO_4$	$(4.46 \pm 0.010) \times 10^7$	0.135 ± 0.017	0.03 ± 0.02	19.8 ± 3.0
9.	0.025 $Fe_2(SO_4)_3 + 1.0(Na_2SO_4 + H_2SO_4)$: pH = 1	$(4.46 \pm 0.013) \times 10^7$	0.135 ± 0.02	0.03 ± 0.025	13.0 ± 3.0
10.	0.025 $Fe_2(SO_4)_3 +$ $1.0(Na_2SO_4 + H_2SO_4)$: pH = 2	$(4.44 \pm 0.039) \times 10^7$			11.4 ± 4.0
11.	0.025 $Fe_2(SO_4)_3 +$ $1.0\ (Na_2SO_4 + H_2SO_4)$: pH = 2.4		0.147 ± 0.02		1.3 ± 1.1
12.	0.3 wt.-% $Fe^{III} +$ + 65 wt.-% HNO_3	$(4.53 \pm 0.011) \times 10^7$**	0.18 ± 0.01	0.00 ± 0.01	27.6 ± 1.1
13.	0.3 wt.-% $Fe^{III} +$ + 30 wt.-% HNO_3	$(4.54 \pm 0.012) \times 10^7$**	0.175 ± 0.003	0.022 ± 0.003	22.1 ± 1.6
14.	0.05 $Fe(NO_3)_3 + 2\ HNO_3$	$(4.52 \pm 0.017) \times 10^7$**	0.155 ± 0.02	0.03 ± 0.02	21.3 ± 3.0
15.	0.05 $Fe(NO_3)_3$	$(4.53 \pm 0.007) \times 10^7$**	0.14 ± 0.02	0.04 ± 0.02	20.4 ± 1.1
16.	0.05 $Fe(NO_3)_3 +$ $2.0\ (NaNO_3 + HNO_3)$: pH = 2	$(4.51 \pm 0.010) \times 10^7$	0.145 ± 0.04	0.05 ± 0.04	17.7 ± 2.6
17.	0.05 $Fe(ClO_4)_3 + 2.0\ HClO_4$	$(4.63 \pm 0.064) \times 10^7$			
18.	0.05 $Fe(ClO_4)_3 +$ $2.0\ (NaClO_4 + HClO_4)$: pH = 0.5	$(4.60 \pm 0.004) \times 10^7$	0.165 ± 0.01	0.02 ± 0.01	19.3 ± 1.7
19.	0.05 $Fe(ClO_4)_3 +$ $2.0\ (NaClO_4 + HClO_4)$: pH = 1				19.15 ± 1.70 3.24 ± 0.64
20.	0.05 $Fe(ClO_4)_3 +$ $2.0\ (NaClO_4 + HClO_4)$: pH = 2	$(4.64 \pm 0.005) \times 10^7$	0.155 ± 0.016	0.05 ± 0.02	20.5 ± 3.0
21.	0.05 $Fe(ClO_4)_3 +$ $2.0\ (NaClO_4 + HClO_4)$: pH = 2.3	$(4.63 \pm 0.012) \times 10^7$	0.17 ± 0.02		18.1 ± 2.4
22.	0.01 $Fe(ClO_4)_3 + 2.0\ HClO_4$	$(4.66 \pm 0.034) \times 10^7$			9.1 ± 3.1
23.	0.2 $Fe(ClO_4)_3$				6.0 ± 3.8
24.	0.5 $Fe(ClO_4)_3 + 1.0\ HClO_4$	$(4.64 \pm 0.048) \times 10^7$			6.5 ± 3.0
25.	1.0 $Fe(ClO_4)_3 + 0.5\ HClO_4$				3.1 ± 1.7

* The isomer shift refers to a $^{57}Co(Pt)$ radiation source and liquid helium temperature (4.5 K)
** Other authors measured $H_{5/2} \sim 4.61 \times 10^7$ A m^{-1} in the solution of $Fe(NO_3)_3$ [36, 39].

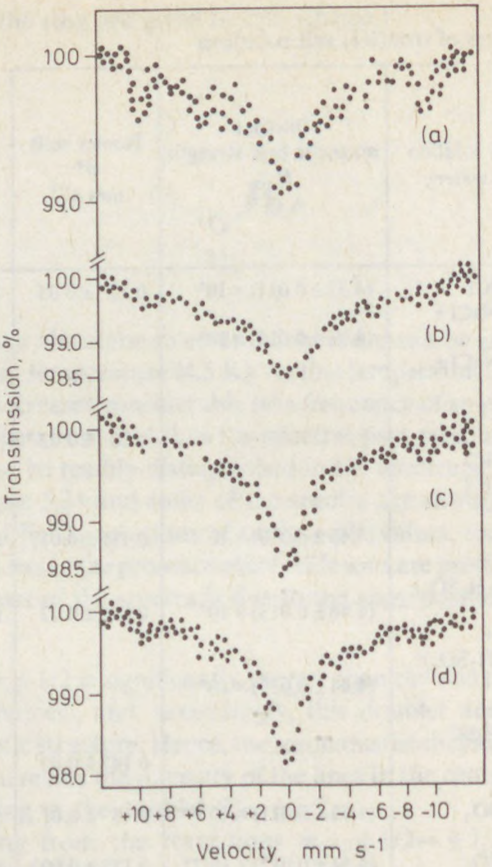

Fig. 5.35.. Mössbauer spectra of 0.025 mol kg^{-1} $^{57}Fe_2(SO_4)_3$ solutions at 4.5 K.
pH: (a) ~0, (b) 1.0, (c) 2.0, (d) 2.4.
Radiation source: $^{57}Co(Pt)$

Spectra of solutions containing SO_4^{2-} ions are shown in Fig. 5.35 and described in lines 8–11 of Table 5.24. From the value $H_{5/2} = 4.45 \times 10^4$ A m^{-1}, measured at pH ≈ 0, it can be concluded that the sulfate anion also participates in the inner ligand sphere of the iron. An increasing amount of the iron in the solution loses its magnetic hyperfine structure (MHS) with increasing pH. This indicates the development of the more covalent hydroxide bonds, and, consequently, dimerization. By decomposing the spectra into their components, the following values are obtained for the ratio of coordination iron ions that do not exhibit MHS in solutions of various pH:

pH < 0	0%
pH = 1.0	50 ± 12%
pH = 2.0	65 ± 8%
pH = 2.4	98.7 ± 6%.

The Mössbauer spectra of solutions containing NO_3^- ions recorded at 4.5 K are presented in Fig. 5.36 and lines 12–16 of Table 5.24. According to References [9, 40], in nitrate and perchlorate solutions of low pH the iron(III) is present in the form of the hexaaqua coordination entity in all cases. This agrees with the higher value of $H_{5/2}$ in these solutions. The measured spectra reflect that in nitrate solutions the population of the $S_z = \pm 5/2$ level is higher than that of the other two doublets, and it is associated with the lowest energy level. For the spectrum at pH = 2.0, the area proportion of the quadrupole line pair that does not possess MHS ($\Delta E = 0.43 \pm 0.03$ mm s^{-1}) is 21.8 ±5.6%; this result can be attributed to the formation of dimeric iron(III) ion. The corresponding equilibrium constant is $K_{22} = (0.42 \pm 0.17) \times 10^{-3}$. These results of the Mössbauer examination are in good accordance with the magnetic susceptibility measurements. (The concentration of the solutions in the magnetic measurements was

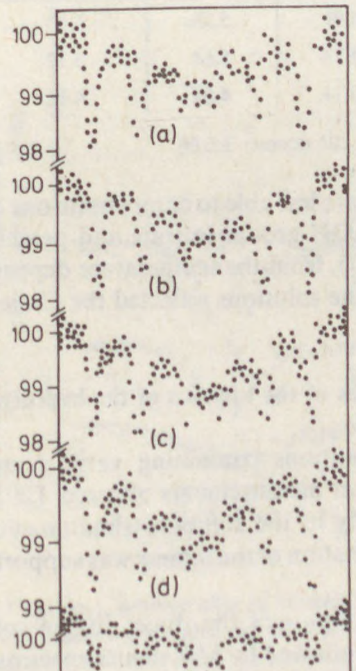

Fig. 5.36. Mössbauer spectra of 0.05 mol kg^{-1} $^{57}Fe(NO_3)_3$ solutions at 4.5 K. (a) 65 wt.-% HNO_3; (b) 30 wt.-% HNO_3; (c) 11.2 wt.-% HNO_3; (d) pH = 1.0; (e) pH = 2.0. The positions of lines relating to the various Kramer's doublets are also visible in the spectra.
Radiation source: $^{57}Co(Pt)$

chosen 0.5 mol kg^{-1} of iron(III) salt, because at lower concentrations the relative error of the susceptibility measurement is too high [41].)

From the values of molar paramagnetic susceptibilities (χ_M) obtained for the solutions, it is possible to calculate the average effective electromagnetic moments μ_{eff} (these values are given in Table 5.25).

From the "spin only" values in Table 5.25, it can be concluded that in the presence of chloride and sulfate anions (since the anion participates in polynuclear coordination entity also), the iron spins are less able to compensate one another than in the case with dimers that contain only OH groups (nitrate and perchlorate solutions).

Table 5.25.
Average effective electromagnetic moments of the iron(III) salt solutions at different pH [40]

pH	Anion			
	Chloride	Nitrate	Perchlorate	Sulfate
0.1	5.91	5.88	5.88	5.76
1.0	5.73	5.64	5.17	5.48
2.05	5.14	4.60	4.12	5.20

Error of the measurements: ±0.06.

In solutions of pH = 2.05, from the temperature dependence of the susceptibility it could be concluded that the solutions reflected the Curie–Weiss law for every anion.

5.5.1.3. Mössbauer studies of the kinetics of the hydrolysis of iron(III) salts

Increasing the pH of solutions containing various anions at pH = 0 by adding $NaHCO_3$, the Mössbauer measurements showed [20] that equilibrium was established relatively quickly in the solution (simultaneously with the dissolution of $NaHCO_3$). The quick formation of the dimers was supported by the paper of Wendt as well [42].

However, the decomposition of the dimer in the course of acidification of the solution could readily be followed by Mössbauer spectroscopy which means that this reaction is relatively slow [20]. For example Fig. 5.37 shows the variation with time, at 20 °C, of the Mössbauer spectrum of a 0.05 mol kg^{-1} $Fe(NO_3)_3$ solution with a constant 1 mol kg^{-1} NO_3^- concentration during the acidification of the solution with the calculated amount of acid from pH = 2.2 to pH < 0. Proportions of the solution were frozen to 80 K after various reaction times and the Mössbauer spectra were recorded at this temperature. Analogous examinations were also carried out with iron(III) solutions containing perchlorate, sulfate or chloride ions.

The measurements showed that the decomposition of the dimer (or polymer) can be regarded as a first-order reaction, so its concentration (c) at time t can be described by the equation

$$c = c_0 e^{-kt}.$$

Taking into account the surface density of the iron in the absorbers, the intensities of the Mössbauer lines of the polynuclear species can be used to determine the k values at 20 °C relating to the various anions. These values are listed in Table 5.26. The data reflect a significant anion effect, and show that the presence of the anion in the polynuclear iron coordination entity accelerates the decomposition.

Spectrophotometry was employed to study the decomposition of the dimer in the presence of perchlorate by Po and Sutin, and in the presence of perchlorate and chloride by Sommer and Margerum [43, 44].

It was found that the rate constant of the decomposition is several orders of magnitude higher ($k \approx 3\,s^{-1}$) than determined via the Mössbauer spectra. As the

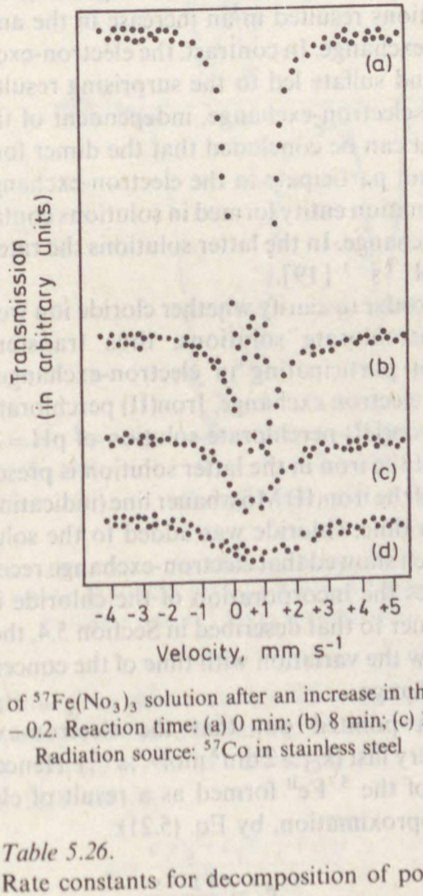

Fig. 5.37. Mössbauer spectra of $^{57}Fe(No_3)_3$ solution after an increase in the hydrogen-ion concentration from pH 2.2 to ca. −0.2. Reaction time: (a) 0 min; (b) 8 min; (c) 28 min; (d) 120 min. Radiation source: ^{57}Co in stainless steel

Table 5.26.
Rate constants for decomposition of polynuclear iron(III) ion

Anion	Rate constant, k s^{-1}
Perchlorate	8.0×10^{-4}
Nitrate	1.5×10^{-2}
Sulfate	1.7×10^{-3}
Chloride	1.0×10^{-2}

intensity of the quadrupole line pair changes only if, as a consequence of dissociation of the dimer, the frequency of spin-spin relaxation decreases and hence MHS shows up, Mössbauer spectroscopy does indeed indicate the dissociation of the dimer, while the spectrophotometric method indicates the protonation preceding dissociation. From a comparison of the results of the two methods, it can be stated that protonation during the decomposition of the dimer is a fast process, while the further steps that result in dissociation are substantially slower.

By electron-exchange reaction studies in chloride, sulfate and nitrate solutions at different pH values, in a similar manner to the studies with perchlorate solutions, further information can be obtained on the structure of the solutions [20].

As with perchlorate-containing solutions (cf. Fig. 5.31), an increase of the pH in nitrate-containing solutions resulted in an increase in the amount of the component not capable of electron-exchange. In contrast, the electron-exchange study of solutions that contain chloride and sulfate led to the surprising result that all of the iron(III) species take part in the electron-exchange, independent of the pH.

On the above basis, it can be concluded that the dimer formed in perchlorate and nitrate solutions does not participate in the electron-exchange reaction, whereas the polynuclear iron coordination entity formed in solutions containing chloride or sulfate is capable of electron exchange. In the latter solutions the rate constant of the electron exchange is $k > 2\,\mathrm{kg\,mol^{-1}\,s^{-1}}$ [19].

A study was made in order to clarify whether cloride ion would react with the dimer formed in iron(III) perchlorate solutions, thus transforming the polynuclear coordination entity not participating in electron-exchange reaction into a coordination ion capable to electron exchange. Iron(II) perchlorate prepared from natural iron was added to an iron(III) perchlorate solution of pH = 2 prepared from ^{57}Fe (a significant proportion of the iron in the latter solution is present in the form of dimer), and when the intensity of the iron(II) Mössbauer line (indicating the electron-exchange) no longer changed with time, chloride was added to the solution. A newly recorded Mössbauer spectrum then showed that electron-exchange recommenced (see Fig. 5.38). This result demonstrates the incorporation of the chloride ion into the dimer [18].

In an analogous manner to that described in Section 5.4, the intensity of the iron(II) line can be used to follow the variation with time of the concentration of iron(III) ions capable of electron-exchange.

It has already been pointed out that the electron-exchange of the chloro coordination entity is very fast ($k_{\mathrm{Cl}} > 2\,\mathrm{dm^3\,mol^{-1}\,s^{-1}}$). Hence the variation in time of the concentration (c_1) of the $^{57}\mathrm{Fe^{II}}$ formed as a result of electron-exchange can be described, to a good approximation, by Eq. (5.21):

$$c_1 = \frac{c_2 \cdot c_3}{c_2 + c_3} \tag{5.27}$$

where c_2 is the concentration of iron(III) capable of electron-exchange and c_3 is the concentration of natural $\mathrm{Fe^{II}}$ added to the solution at the beginning of the experiment (c_1 and c_2 are therefore functions of time). For c_2 we can write

$$c_2 = 2c + c_4 \tag{5.28}$$

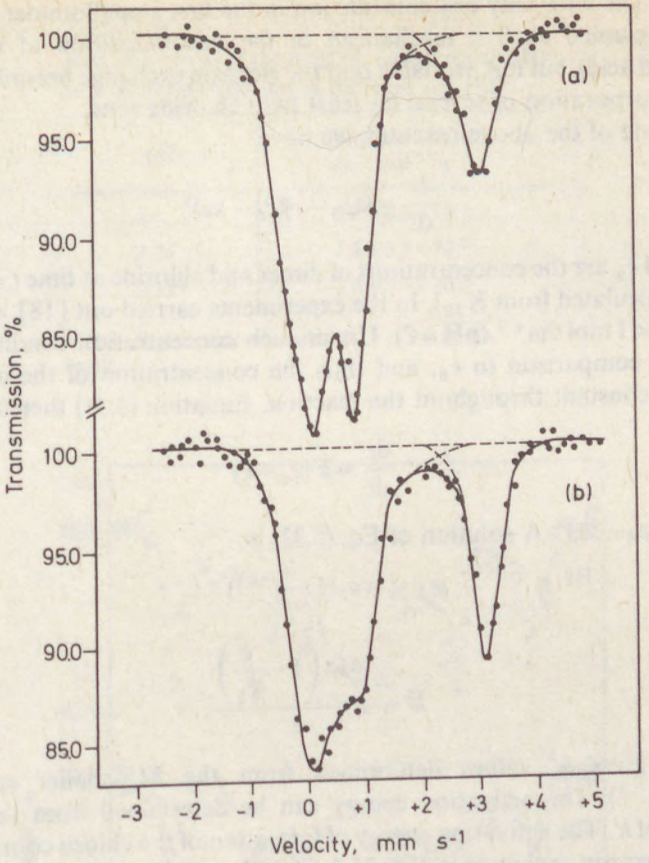

Fig. 5.38. Mössbauer spectra of solution containing 0.05 mol dm^{-3} $^{57}Fe(ClO_4)_3 + 0.05$ mol dm^{-3} $Fe(ClO_4)_2$ after addition of 1 mol dm^{-3} NaCl at pH = 2.3. Reaction time (at 20 °C): (a) 200 s; (b) 3 d [17]. Radiation source: ^{57}Co in stainless steel

where c is the concentration of the chloro coordination entity formed from the dimer (a time-dependent term), and c_4 is the concentration of non-dimerized monomeric $^{57}Fe^{III}$ in the solution (this concentration can be calculated from K_{22}) (cf. Section 5.5.1.1).

From Eqs (5.27) and (5.28) we get:

$$c = \frac{c_1c_3 + c_1c_4 - c_3c_4}{2(c_3 - c_1)} \tag{5.29}$$

where c_1 can be determined from the Mössbauer spectra.

The reaction between the dimer and the chloride ion, resulting in a coordination ion capable of electron exchange, can be described by the following overall reaction:

$$[Fe_2(OH)_2]^{4+} + xCl^- \rightleftharpoons [Fe_2Cl_x(OH)_y]^{(6-y-x)+} + (2-y)OH^- . \tag{5.30}$$

Naturally, it cannot be excluded that the coordination entity capable of electron exchange may possibly be formed in several steps. It is conceivable, for instance, that the dimer reacts with only one chloride ion in the first step (Sommer and Margerum [44] also assumed such a mechanism in the decomposition of the dimer with hydrochlorid acid), but it is probable that the electron exchange becomes possible only after the incorporation of several (at least two) chloride ions.

For the rate of the above reaction, we have

$$\frac{dc}{dt} = k(c_5 - c)(c_6 - xc)^x \tag{5.31}$$

where c_5 and c_6 are the concentrations of dimer and chloride at time $t = 0$, respectively (c_5 can be calculated from K_{22}). In the experiments carried out [18], c_5 was 8×10^{-3} and $0.5 < c_6 < 1$ mol dm^{-3} (pH = 2). Under such concentration conditions xc can be neglected in comparison to c_6, and thus the concentration of the chloride can be regarded as constant throughout the reaction. Equation (5.31) therefore reduces to

$$\frac{dc}{dt} = k'(c_5 - c) \tag{5.32}$$

where $k' = k(c_6 - xc)^x$. A solution of Eq. (5.32) is

$$c = c_5(1 - e^{-k't}) \tag{5.33}$$

or

$$k' = \frac{-\ln\left(1 - \dfrac{c}{c_5}\right)}{t}.$$

Table 5.27 gives k' values determined from the Mössbauer spectra (for $c_6 = 0.5$ mol dm^{-3}). The activation energy can be determined from the temperature dependence of k'. The activation energy of formation of the chloro coordination entity capable of electron exchange is $E_a = 25.2 \pm 6.3$ kJ mol^{-1}.

Table 5.27.
Temperature dependence of rate constants for iron(III)-chloro coordination formation

Temperature °C	Rate constant, k s^{-1}
0	0.67
20	1.03
43	3.07

The effect of incorporation of the chloride ion into the dimer has been detected with the aid of positron lifetime measurements [45]. In iron(III) perchlorate solutions, the rate constant of the interaction of iron(III) and the orthopositronium (^{T}Ps) decreased with increase in pH, indicating that formation of the dimer hinders the electron-transferring ability of the iron(III). When chloride was added to the solution, however, the average lifetime of the ^{T}Ps again decreased. The results are given in Table 5.28.

Table 5.28.
Rate constants for the reaction between iron(III) and orthopositronium at different pH [45]

pH	Rate constant, *k* dm^3 mol^{-1} s^{-1}
0.1	$5.7 \pm 0.5 \times 10^{10}$
2.35	$1.8 \pm 0.2 \times 10^{10}$
2.35*	$2.6 \pm 0.3 \times 10^{10}$

* The solution also contained 0.1 – 0.3 mol dm^{-3} of NaCl.

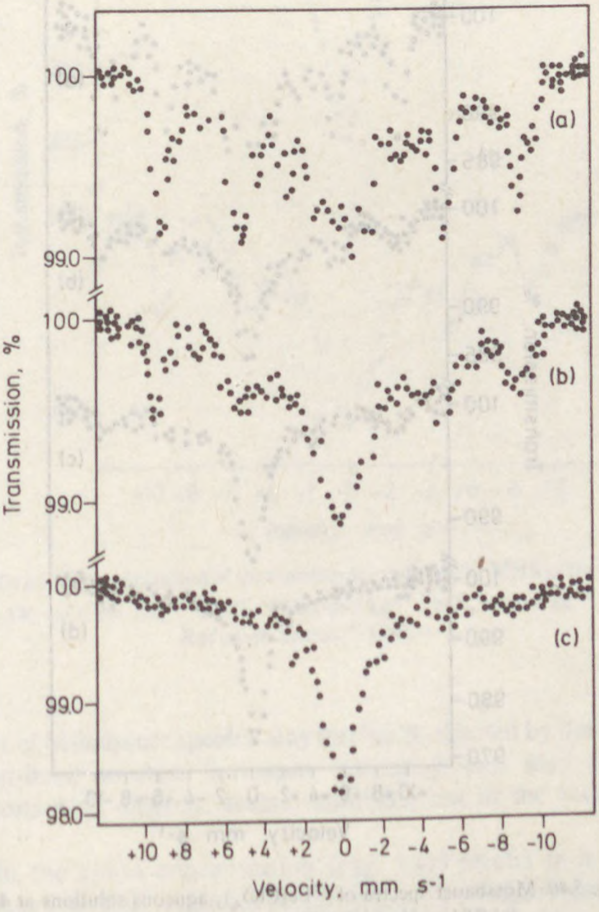

Fig. 5.39. Mössbauer spectra of ^{57}FeCl$_3$ aqueous solutions at 4.5 K.
(a) 0.05 mol kg^{-1} FeCl$_3$ + 2 mol kg^{-1} HCl; (b) 0.2 mol kg^{-1} FeCl$_3$ + 2 mol kg^{-1} HCl; (c) 0.5 mol kg^{-1} FeCl$_3$ + 1 mol kg^{-1} HCl.
Radiation source: ^{57}Co(Pt)

5.5.1.4. Effect of ionic strength on the hydrolysis of iron(III) salts and on the Mössbauer spectrum

The ionic strength influences the amounts of coordination ions formed during the hydrolysis of iron(III) salts [8], and an extreme increase in the ionic strength may even result in the formation of further coordination ionic species in the solution [14]. In addition, however, in iron(III) salt solutions the ionic strength may also affect the spin relaxation of the iron atom and hence the Mössbauer spectrum, too. This circumstance justifies the examination of the role of the ionic strength in connection with some results obtained in Mössbauer spectroscopic study of iron(III) salt solutions.

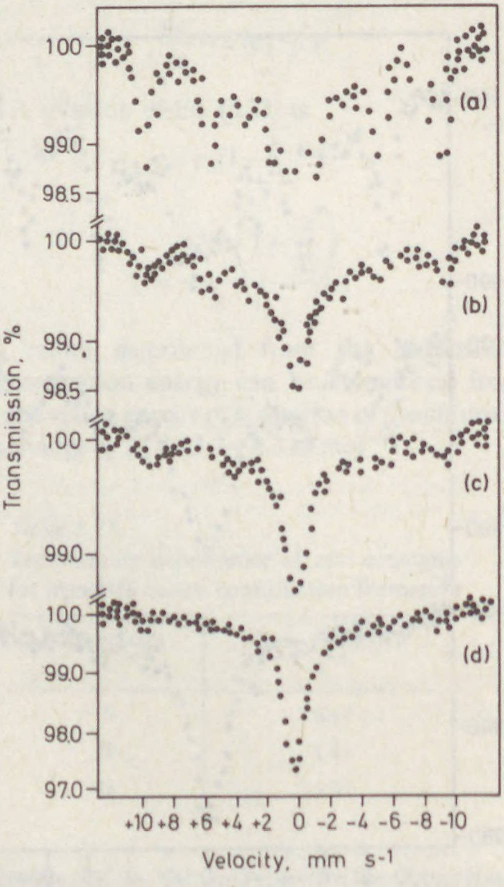

Fig. 5.40. Mössbauer spectra of $^{57}Fe(ClO_4)_3$ aqueous solutions at 4.5 K.
(a) 0.01 mol kg^{-1} $Fe(ClO_4)_3$ + 2 mol kg^{-1} $HClO_4$,
(b) 0.05 mol kg^{-1} $Fe(ClO_4)_3$ + 2 mol kg^{-1} $HClO_4$,
(c) 0.5 mol kg^{-1} $Fe(ClO_4)_3$ + 1 mol kg^{-1} $HClO_4$,
(d) 1.0 mol kg^{-1} $Fe(ClO_4)_3$ + 0.5 mol kg^{-1} $HClO_4$.
Radiation source: $^{57}Co(Pt)$

Figures 5.39 and 5.40 present Mössbauer spectra of solutions with almost the same anion concentrations, but with different iron(III) concentrations, recorded at the temperature of liquid helium. In these solutions, the average Fe–Fe distance varies in the range 1–5 nm. Accordingly, the frequency of spin-spin relaxation may also vary within wide limits, which has an effect on the Mössbauer spectrum.

It can be stated, that at lower concentrations reliable information can also be obtained from the MHS, while at higher concentrations only the determination of δ and ΔE can provide information.

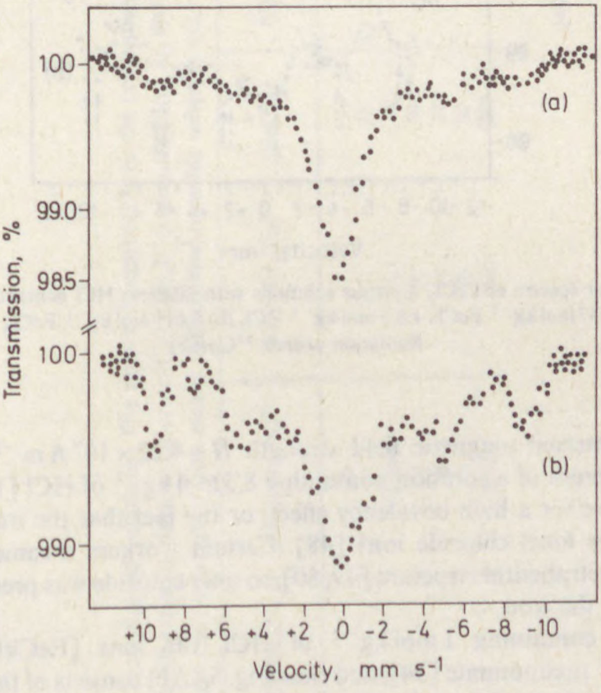

Fig. 5.41. Effect of the anion concentration of the aqueous solution on the MHS of the Mössbauer spectrum at 4.5 K. (a) 0.2 mol kg^{-1} FeCl$_3$; (b) 0.2 mol kg^{-1} FeCl$_3$ + 2 mol kg^{-1} HCl. Radiation source: ^{57}Co(Pt)

The character of Mössbauer spectra may further be affected by the concentrations of the other (non-iron) solutes. Spin-spin relaxation can also proceed between paramagnetic ions with different atomic numbers, but in the same spin state [40, 46, 47].

A decrease in the anion concentration (Fig. 5.41) results in an increase in the frequency of relaxation. This result can be interpreted by the assumption of segregation occurring during freezing at low ionic strengths, a phenomenon, however, inhibited at higher ionic strengths.

The effect of the hycrochloric acid concentration on the structure of the coordination ions formed in solution is illustrated in Fig. 5.42. A Kramer's doublet $S_z = \pm 5/2$

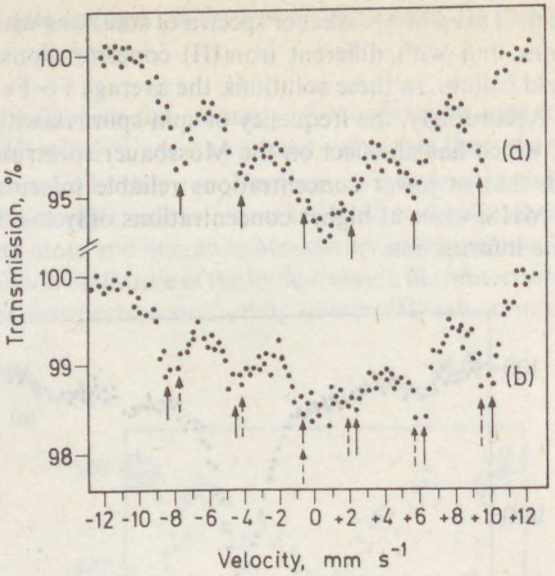

Fig. 5.42. Mössbauer spectra of $FeCl_3$ aqueous solutions with different HCl contents, at liquid nitrogen temperature. (a) 0.147 mol kg^{-1} $FeCl_3$ + 8.5 mol kg^{-1} HCl, (b) 0.011 mol kg^{-1} $FeCl_3$ + 1.0 mol kg^{-1} HCl. Radiation source: ^{57}Co(Cr)

possessing an internal magnetic field strength $H = 4.22 \times 10^7\ \mathrm{A\,m^{-1}}$ occurs in the Mössbauer spectrum of a solution containing 8.5 mol kg^{-1} of HCl [14]. This low H value is indicative for a high covalency effect, or the fact that the iron is bonded to several (probably four) chloride ions [48]. Certain workers assumed that the ion $[FeCl_4]^-$ has a tetrahedral structure [49, 50], so only chloride was present in the inner ligand sphere of the iron.

In solutions containing 1 mol kg^{-1} of HCl, the ions $[FeCl(H_2O)_5]^{2+}$ and $[FeCl_2(H_2O)_4]^+$ predominate [34], and thus Fig. 5.42(b) consists of the superposition of the Mössbauer lines of these ions.

There are also authors who supposed the presence of $[FeCl_5H_2O]^{2-}$ and $[FeCl_6]^{3-}$ octahedral ions in concentrated aqueous solution of HCl [51]. This conclusion was based on Raman studies.

X-ray diffraction measurements revealed that a relatively high ratio of iron is present as tetrachloroferrate(1-) ion in concentrated $FeCl_3$ solution [52]. These results are given in Table 5.29. (The Fe–Cl distances were measured to be between 0.223–0.23 nm in these solutions.)

5.5.1.5. Effect of ageing on the hydrolysis of iron(III) salts

The experimental results reported in Section 5.5.1.3 indicate that in iron(III) salt solutions an increase in pH is followed quickly (within a few minutes) by the establishment of equilibrium between the dimeric, monomeric, dihydroxo and hexa-

Table 5.29.
Distribution of coordination entities in the investigated solutions. The reported numbers give the percentage of the various coordination entities with respect to the total iron (iron coordination entities or chloride $[Cl(H_2O)_6]^-$ concentrations. $\bar{n}_{Cl}$ and $\bar{n}_{H_2O}$ are the average numbers of chloride ions and water molecules, respectively, bonded to iron atoms. Alternative possible schemes are reported in parentheses.)

Fe^{3+} concentration, mol dm^{-3}	Cl^-/Fe^{3+}	$[FeCl(H_2O)_5]^{2+}$	$[FeCl_2(H_2O)_4]^+$	$[FeCl_3(H_2O)_3]$	$[FeCl_4]^-$	$[Cl(H_2O)_6]^-$	$\bar{n}_{Cl}$	$\bar{n}_{H_2O}$
2.332	3	24	76			41	1.76	4.24
4.232	3		33	34	33		3.0	2.33
			(24)	(52)	(24)		(3.0)	(1.89)
5.882	3		20	30	50		3.3	1.7
2.308	3.97		20	60	20	24.5	3.0	2.6
2.205	4.68		. . .	70	30	29.5	3.3	2.1
			(10)	(60)	(30)	(31.6)	(3.2)	(2.3)

aqua ions in the solution. However, the literature also contains results (of ultracentrifugation, dialysis, potentiometric, electron-microscopic, etc. measurements) [3] indicating the possibility of polymer formation in iron(III) salt solutions even at room temperature [2]. These results, therefore, show that an apparent equilibrium develops rapidly after the adjustment of the pH and that a fairly slow polymerization process then commences. Mössbauer spectroscopy can be applied to the clarification of these phenomena, too.

Figure 5.43(a) shows the spectrum of a freshly prepared $^{57}Fe(ClO_4)_3$ solution containing $3 \, mg \, g^{-1}$ of iron, with a pH of 2.30, while Fig. 5.43(b) shows the corresponding spectrum after ageing at room temperature for 1 month. Figure 5.43 reveals that during 30 d ca 30% of the total amount of iron in the perchlorate solution is transformed into a polymer in which there is magnetic ordering.

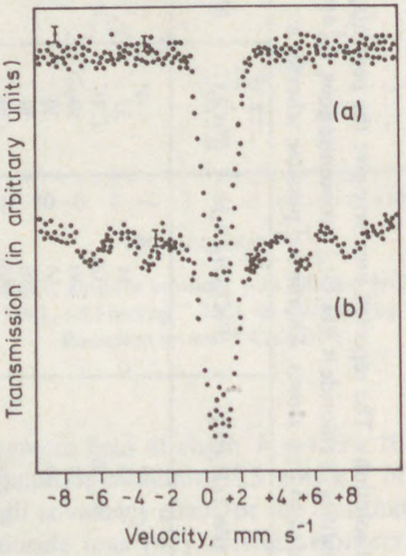

Fig. 5.43. Mössbauer spectra of 0.06 mol kg^{-1} $^{57}Fe(ClO_4)_3$ aqueous solution of pH 2.3, at liquid nitrogen temperature. (a) Immediately after preparation, (b) after standing for 1 month at room temperature. Radiation source: ^{57}Co in stainless steel

Table 5.30 gives internal magnetic field strength values (*H*) obtained from Mössbauer spectra recorded at liquid nitrogen temperature on iron(III) salt solutions with different anion contents, different pH values and different concentrations.

It should be pointed out that in certain cases MHS connected with the (individual) spin relaxation of paramagnetic substances and with the (collective) spin relaxation of magnetically ordered superparamagnetic species appear together in the spectrum (see Fig. 5.44). In this instance the heating of the solution results in polymerization, and a second sextet of lower effective magnetic field strength represents the superparamagnetic iron species in the spectrum (see Fig. 5.44(b)).

The particle size distribution of the polymers can be determined from the temperature dependence of the Mössbauer spectra of solutions containing superpara-

Table 5.30.
Internal magnetic field strength of superparamagnetic polymers formed in iron(III) salt solutions at different ageing time and pH
The spectra were recorded at 80 K.

Salt	Fe^{III} salts in water mol kg^{-1}	pH	Time d	Internal magnetic field strength, H A m^{-1}
$Fe(ClO_4)_3$	0.125	2.1	0	
	0.06	2.3	30	3.58×10^7
	0.125	2.1	91	3.54×10^7
$Fe(NO_3)_3$	0.123	2.2	0	*3.64×10^7
	0.123	2.2	82	
$Fe_2(SO_4)_3$	0.119	2.2	0	
	0.119	2.2	17	*3.40×10^7
	0.119	2.2	48	*3.20×10^7
$FeCl_3$	0.119	1.7	0	3.22×10^7
	0.119	1.7	83	
$FeCl_3$	0.070	2.0	0	*3.33×10^7
	0.070	2.0	79	

* Opalescent solution.

magnetic particles in the following way. The relaxation time characteristic of the transition state of the magnetic structure (τ_α) will be identical with the Larmor precession time: $\tau_\alpha = \frac{2\pi}{\omega_L}$, where ω_L is the Larmor precession angular frequency.

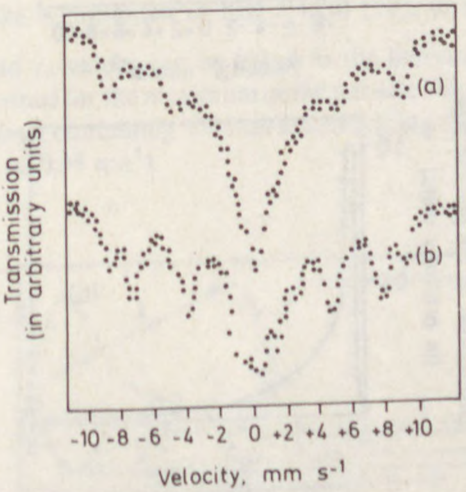

Fig. 5.44. Mössbauer spectra of 0.04 mol kg^{-1} $^{57}Fe(ClO_4)_3$ aqueous solution of pH 1.40, at liquid helium temperature (4.5 K). (a) Freshly prepared solution, (b) solution maintained at 60 °C for 45 min before freezing (to promote polymerization).
Radiation source: $^{57}Co(Pt)$

The ω_L can be calculated by the equation:

$$\hbar\omega_L = \frac{m_i}{I}\gamma\mu_N H \tag{5.34}$$

where m_i is the magnetic quantum number, I is the nuclear spin quantum number, γ is the gyromagnetic ratio, μ_N is the nuclear magneton and H is the effective magnetic field strength. Consequently, each measured H value gives a basis for the calculation of a τ_α value:

$$\tau_\alpha = \frac{hI}{m_i\gamma\mu_N H}\,. \tag{5.35}$$

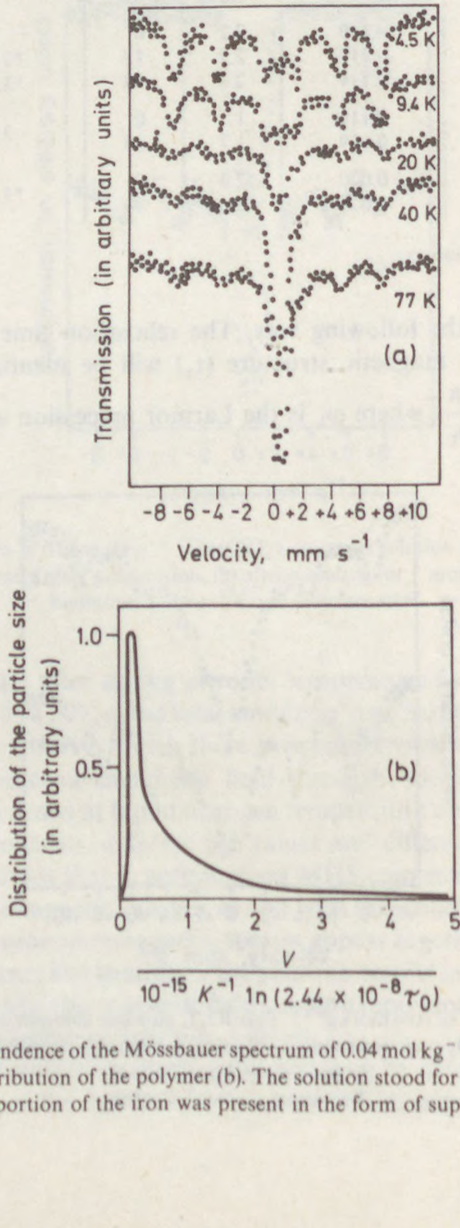

Fig. 5.45. Temperature dependence of the Mössbauer spectrum of 0.04 mol kg^{-1} ^{57}Fe(ClO$_4$)$_3$ solution of pH 2.3 (a) and particle size distribution of the polymer (b). The solution stood for 4 weeks before freezing, and thus a considerable proportion of the iron was present in the form of superparamagnetic polymer.

The internal magnetic field strength of the superparamagnetic particles in the 0.04 mol kg^{-1} $Fe(ClO_4)_3$ aqueous solution of pH = 2.3 is $H = 3.88 \times 10^7$ A m^{-1} (Fig. 5.45(a) [18]) and $\tau_\alpha = 2.44 \times 10^{-8}$ s.

On substitution of τ_α into equation (3.66) we obtain the following relationship for the temperature-dependence of the polymer particle volume (V_t) corresponding to the transition state:

$$V_t = \frac{kT}{K} \ln (2.44 \times 10^{-8} \tau_0) . \tag{5.36}$$

Using the spectra recorded at various temperatures, and Eq. (5.36), it is possible to construct graphically the function

$$I = f(V_t) \tag{5.37}$$

where I is the line intensity of the spectrum component with magnetic splitting relating to the superparamagnetic particles (which can be expressed, for example, as a percentage of the total line intensity of the spectrum).

Differentiation of Eq. (5.37) gives the particle volume distribution:

$$N = \frac{dI}{dV_t} \tag{5.38}$$

where N is the percentage proportion of the number of particles of volume V_t. Introducing the normalization $\int_0^\infty N(V_t) dV_t = 1$, then N is the probability of occurrence of a given particle volume.

The distribution of the particle volume determined in the above manner for the superparamagnetic polymer forming when a 0.04 mol kg^{-1} $Fe(ClO_4)_3$ solution of pH 2.3 stands for 4 weeks is presented in Fig. 5.45(b) [18], in units of $\frac{10^{-15}}{K} \ln (2.44 \times 10^{-8} \tau_0)$. The K and τ_0 values can be found in the literature [53–55]. About 1.5×10^{-20} cm^3 was obtained for the maximum of the particle volume distribution, which corresponds to a polymer containing 300 iron atoms (taking the spatial requirement of one FeOH group as ca 0.05 nm^3).

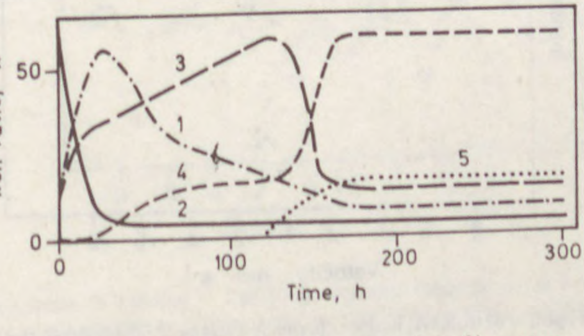

Fig. 5.46. Fe^{III} distribution in the particles containing different number of iron atoms. 1. $n \le 3$; 2. $2 < n < 13$; 3. $12 < n < 32$; 4. $n > 32$; 5. precipitate.

Andrianov and his co-workers studied the polymerization in the aqueous solution of 0.21 $\mathrm{mol\,dm^{-3}}$ $Fe(NO_3)_3$, 0.51 $\mathrm{mol\,dm^{-3}}$ $NaNO_3$ and 0.19 $\mathrm{mol\,dm^{-3}}$ NaOH [56]. The authors used and compared the techniques of gel-chromatography and Mössbauer spectroscopy. All the Mössbauer spectra were recorded at the temperature of liquid nitrogen and only paramagnetic components were detected. They supposed that the quadrupole doublet of 0.65 $\mathrm{mm\,s^{-1}}$ represented the polymer iron(III) species and the other doublet (1.64 $\mathrm{mm\,s^{-1}}$) belonged to the oligomer molecular fraction. The results obtained by gel-chromatography are given in Fig. 5.46.

5.5.1.6. Precipitate formation in iron(III) salt solutions

During the hydrolysis, uncharged coordination entities are formed in the solutions and coagulate. The rate of precipitation depends on the concentration of the iron(III) salt, the pH, the amounts and natures of foreign ions and the age of the solution. Precipitate formation is accelerated by an increase of the concentration or the pH and by the presence of certain anions as Cl^- and SO_4^{2-}. Even after the addition of stoichiometric

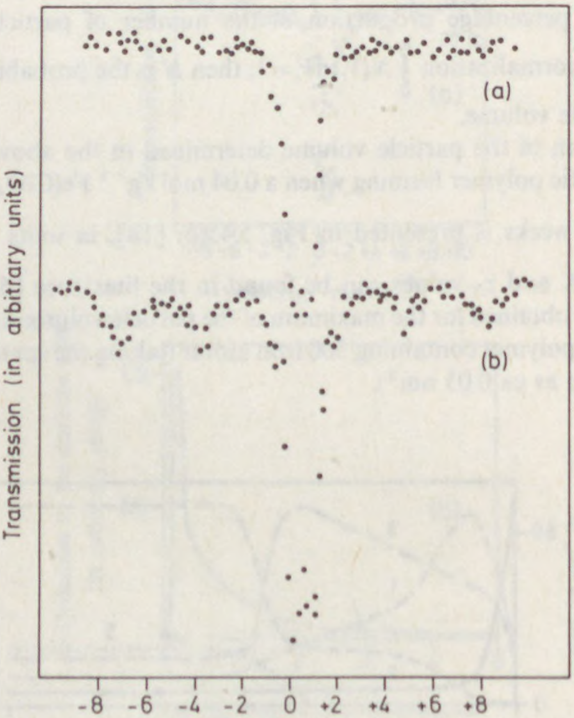

Fig. 5.47. Mössbauer spectra of iron(III) hydroxide precipitates at 80 K. (a) Fresh precipitate, (b) precipitate after an ageing of 90 d.
Radiation source: ^{57}Co in stainless steel

amount of $NaHCO_3$ or NaOH, however, several hours are required for quantitative precipitation of the iron(III) [57]. Figure 5.47 shows the Mössbauer spectrum of a precipitate produced with $NaHCO_3$ from an $Fe(ClO_4)_3$ solution. The freshly prepared amorphous $Fe(OH)_3$ precipitate ($\Delta E = 0.7\ \mathrm{mm\,s^{-1}}$) is progressively transformed during ageing into a structure that exhibits MHS. In the 90 days old precipitate, 25 ±3% of the iron has an internal magnetic field strength. The value of the internal magnetic field strength obtained at liquid nitrogen temperature ($H = 3.7 \times 10^7\ \mathrm{A\,m^{-1}}$) suggests that, on storing, amorphous $Fe(OH)_3$ is converted into β-FeOOH [58, 59] but it cannot be excluded that superparamagnetic α-FeOOH of poor crystallinity results in such an internal magnetic field strength [60]. The presence of α-FeOOH is supported also by the paper of Schindler et al. who supposed the formation of the α-modification of FeOOH from iron(III) chloride solution [61].

If iron(III) salt solutions are aged for a long period, so that a polymerization process accompanied by magnetic ordering may already begin in the solution phase, then the

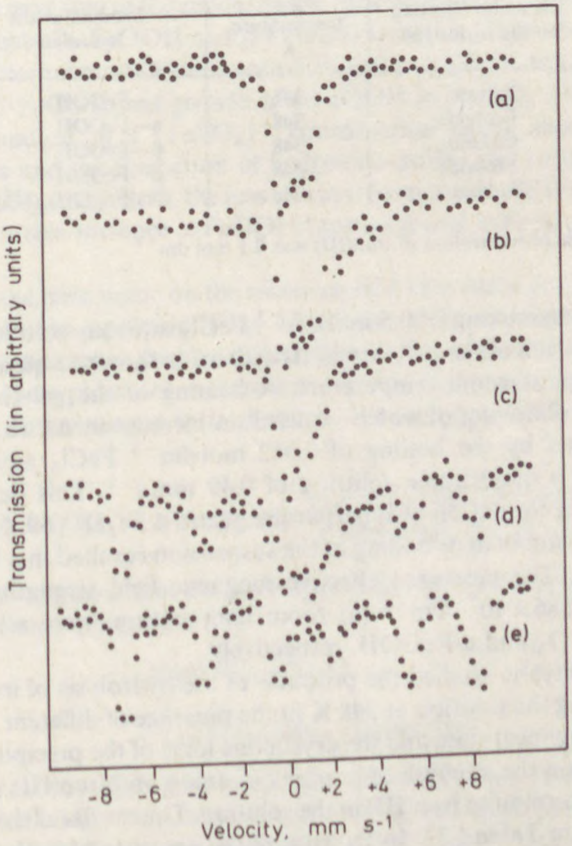

Fig. 5.48. Mössbauerspectra of 1 mol kg^{-1} $Fe(ClO_4)_3$ aqueous solution of pH 1.6 at 80 K. (a) Freshly prepared solution, (b) initial precipitate, (c) precipitate in 22 d solution, (d) precipitate in 110 d solution, (e) precipitate in 380 d solution.
Radiation source: ^{57}Co in stainless steel

precipitate also possesses MHS (see Fig. 5.48). These Mössbauer spectroscopic results are in agreement with the magnetic susceptibility measurements of Oosterhout [62], who found that the susceptibility of iron(III) hydroxide precipitated from a solution that had been kept for a long period at a comparatively high pH is lower than that of iron(III) hydroxide precipitated from a freshly prepared solution.

The structure of the precipitate also depends on the nature of the accompanying anion in solution. The internal magnetic field strength of the precipitate is very close to those obtained for the aged solutions and given in Table 5.31. Consequently the structures of the precipitate and of the polymer in solution are similar.

Applying Mössbauer spectroscopy, electron microscopy and IR analysis, Kauffman et al. [60, 63, 64] studied the hydrolysis products of iron(III) chloride. The hydrolysis was carried out by mixing of 0.5 mol dm^{-3} $FeCl_3$ aqueous solution with NH_3. The Mössbauer spectrum of the gel of iron(III) hydroxide showed a quadrupole splitting of 0.60–0.63 mm s^{-1} at room temperature. A heating of the gel to 200 °C for 64 h —that means a removing of water—caused an increase in ΔE to 0.76 mm s^{-1} [63]. The gel produced by the boiling of 0.012 mol dm^{-3} $FeCl_3$ aqueous solution for 90 min showed a quadrupole splitting of 0.49 mm s^{-1}. This decrease of ΔE was interpreted by the formation of superparamagnetic α-Fe_2O_3 [60, 64]. The heat treatment (e.g. 430 °C for 48 h) or boiling of the suspension resulted in a MHS in the Mössbauer spectrum. The measured effective magnetic field strengths 3.8×10^7 A m^{-1} and 2.47×10^7–2.86×10^7 A m^{-1} (at room temperature) were attributed to poorly crystalline α-Fe_2O_3 and α-FeOOH, respectively.

Table 5.31.
The effect of anions on the product of hydrolysis of iron(III)

The anion effecting on the hydrolysis	Ageing temperature K	Product of the hydrolysis
Nitrate	348	α—FeOOH
Bromide	348	α—FeOOH
Chloride	348	β—FeOOH
Fluoride	348	β—FeOOH
Sulfate	348	$Na[Fe_3(OH)_6(SO_4)_2]$

The concentration of iron(III) was 0.1 mol dm^{-3}

Ujihira and Ohyabu studied the products of the hydrolysis of iron(III) salts at pH 1.5–1.8 by heating the solution at 348 K in the presence of different anions [65]. They found that the chemical state and the crystalline form of the precipitate depend on the radius of anion, on the strength of bonding of anion and iron(III) species and on the molar ratio of the anion to iron(III) in the solution. The results of the experiments [65] are summarized in Table 5.31. In the case of the presence of both urea and sulfate a hydroxide salt of iron(III) sulfate was formed with the composition of $Fe_3NH_4(OH)_6(SO_4)_2$ (aminojarosite) [65].

Bhat and his co-authors found that the hydrolysis of diammonium iron(II) bis (sulfate) also resulted in aminojarosite ($\delta = 0.40$ mm s^{-1} and $\Delta E = 1.2$ mm s^{-1}) and goethite (α-FeOOH) [66]. The higher pH (>3.8) and lower concentration of diammonium iron(II) bis(sulfate) ($<10\%$) promoted the formation of the superparamagnetic goethite.

Musič et al. aged a 0.02 mol dm^{-3} $FeCl_3$ solution at pH = 2.15 and a 0.1 mol dm^{-3} $FeCl_3$ solution at pH = 1.76 for 600 h at room temperature. The Mössbauer parameters of the product of the hydrolysis, also at this case, gave evidence of the β-FeOOH formation [67]. The isomer shift was 0.39 mm s^{-1} relative to α-iron; the quadrupole splitting was 0.12 mm s^{-1} and the effective magnetic field strength was 3.74×10^7 A m^{-1} at 77 K. Measurements of the Mössbauer parameters of the precipitates formed by hydrolysis of iron(III) salts at 90 °C was carried out by Musič et al. [68]. The results are given in Table 5.32. The authors—in their conclusions—supported the findings of other papers cited in this chapter. They concluded that hydrolysis in the nitrate and chloride solutions proceeds by the formation of monomers and dimers of iron(III) ions, followed by the formation of polymeric species. The polymers formed in the chloride solution contain some chloride ions in the first ligand sphere of iron. The next step in the precipitation process is the formation of oxobridges and the development of α-FeOOH and β-FeOOH structures. This step is followed by loss of water and internal crystallization of α-FeOOH to α-Fe_2O_3 in nitrate solution or by dissolution of β-FeOOH and growth of α-FeOOH in chloride solution. In sulfate solutions the formation of a $[FeSO_4]^+$ coordination entity supresses the polymerization process and the formation of hydroxide-oxides and oxides.

Boiling an $Fe(OH)_3$ suspension, the loss of water from the iron(III) hydroxide can be accelerated and, in this instance α-FeOOH (goethite) and α-Fe_2O_3 (haematite) are formed [69].

Many studies have been made on the reactions that take place during the boiling of the $Fe(OH)_3$ suspension, applying X-ray diffraction, electron-microscopic examination, magnetic measurements, etc. A number of hypotheses have been put forward for the mechanism of these processes. According to one of these hypotheses, for instance, both goethite and haematite are formed in the solution phase [70] by the following mechanism:

$$2Fe(OH)_3+2OH^- \rightarrow 2[Fe(OH)_4]^- \begin{array}{l} \nearrow Fe_2O_3+3H_2O+2OH^- \\ \searrow 2FeOOH+2H_2O+2OH^- . \end{array}$$

Another hypothesis suggests that the haematite is formed in the solid phase and the goethite in the solution phase [71, 72]:

$$\begin{array}{l} 2Fe(OH)_3 \rightarrow Fe_2O_3 \\ \quad\downarrow \\ 2Fe(OH)_3(sln) \rightarrow 2FeO(OH) \end{array}$$

Mössbauer spectroscopy has been employed to clarify this problem [69]. The suspensions were boiled for 4 h, which was sufficient for quantitative transformation of the iron(III) hydroxide. The components of the Mössbauer spectra of the boiled suspension could be separated into two magnetic sextets, which can be ascribed to haematite and to goethite. Their proportions are shown in Fig. 5.49 as a function of the iron concentration of the suspension.

Table 5.32.
Mössbauer parameters of the precipitates formed by hydrolysis of iron(III) salt solutions at 90°C

No.	Temperature K	Lines	$\delta^{(a)}$ mm s^{-1}	$\Delta E^{(b)}$ mm s^{-1}	$H_{5/2}(c)$ A m^{-1}	$\Gamma^{(d)}$ mm s^{-1}	$A^{(e)}$ %	Experimental conditions for the precipitate preparation	pH start	pH final
1.	298	Q	0.311	0.689			100	0.1 mol dm^{-3} $Fe(NO_3)_3$ solution hydrolyzed for 80 min	1.66	1.48
	77	M$_1$	0.480	0.060	3.60×10^7	very broad	100			
2.	298	Q	0.369	0.644			100	Sample No. 1 hydrolyzed additionally for 2 d at room temperature	1.66	1.43
	77	M$_1$	0.498	−0.136	3.73×10^7	0.956	35.1			
		M$_2$	0.532	−0.062	3.31×10^7	0.956	37.5			
		M$_3$	0.483	0.010	2.81×10^7	0.956	27.4			
3.	298	Q	0.335	0.650			100	0.1 mol dm^{-3} $Fe(NO_3)_3$ solution hydrolyzed for 2 h	1.66	1.44
	77	M$_1$	0.468	−0.224	3.72×10^7	0.685	31.4			
		M$_2$	0.418	−0.144	3.39×10^7	0.910	42.6			
		M$_3$	0.388	−0.376	2.75×10^7	1.280	26.0			
4.	298	Q	0.370	0.802		1.195	30.4	0.1 mol dm^{-3} $Fe(NO_3)_3$ solution hydrolyzed for 6 h	1.66	0.92
		M$_1$	0.389	−0.156	3.80×10^7	1.409	27.1			
		M$_2$	0.384	−0.238	2.69×10^7	1.735	42.5			
	77	M$_1$	0.471	−0.242	4.20×10^7	0.312	19.4			
		M$_2$	0.470	−0.250	3.91×10^7	0.690	80.6			
5.	298	Q	0.385	0.700		0.571	11.9	0.1 mol dm^{-3} $Fe(NO_3)_3$ solution hydrolyzed for 24 h	1.66	0.79
		M$_1$	0.367	−0.214	3.97×10^7	0.571	70.0			
		M$_2$	0.396	−0.164	2.80×10^7	0.571	18.1			
	77	M$_1$	0.465	−0.204	4.22×10^7	0.363	64.1			
		M$_2$	0.480	−0.242	3.93×10^7	0.551	35.8			
6.	298	M$_1$	0.366	−0.236	4.10×10^7	0.396	66.0	0.1 mol dm^{-3} $Fe(NO_3)_3$ in 0.05 mol dm^{-3} HNO_3 solution hydrolyzed for 24 h		0.75
		M$_2$	0.303	−0.208	3.95×10^7	0.629	34.0			
	77	M$_1$	0.475	−0.198	4.22×10^7	0.394	67.9			
		M$_2$	0.478	−0.224	3.96×10^7	0.516	32.1			

Table 32. cont.

No.	Temperature K	Lines	$\delta^{(a)}$ mm s^{-1}	$\Delta E^{(b)}$ mm s^{-1}	$H_{5/2}(c)$ A m^{-1}	$\Gamma^{(d)}$ mm s^{-1}	$A^{(e)}$ %	Experimental conditions for the precipitate preparation	^{pH}start	^{pH}final
7.	298	Q	0.378	0.641			100	0.1 mol dm^{-3} $FeCl_3$ solution hydrolyzed for 3 h and additionally aged for 1 d at room temperature		
	77	M_1	0.498	0.020	3.75×10^7	0.245	4.8			
		M_2	0.477	−0.244	3.63×10^7	0.623	95.2			
8.	298	Q	0.345	0.670			100	0.1 mol dm^{-3} $FeCl_3$ solution hydrolyzed for 6 h		
	77	M_1	0.492	−0.120	3.81×10^7	0.456	67.6			
		M_2	0.449	−0.398	3.64×10^7	0.562	32.4			
9.	298	Q	0.394	0.648			100	0.1 mol dm^{-3} $FeCl_3$ solution hydrolyzed for 24 h	1.85	0.95
	77	M_1	0.488	−0.074	3.76×10^7	0.573	84.9			
		M_2	0.458	−0.324	3.56×10^7	0.557	15.1			
10.	298	Q	0.369	1.012			100	0.1 mol dm^{-3} $Fe_2(SO_4)_3$ solution hydrolyzed for 3 h and additionally aged for 1 d at room temperature		1.77 after one day
	77	Q	0.400	0.965			100			
11.	298	Q	0.369	1.012			100	0.1 mol dm^{-3} $Fe_2(SO_4)_3$ solution hydrolyzed for 8 h		
	77	Q	0.461	1.012			100			
12.	298	Q	0.382	0.689			100	0.1 mol dm^{-3} $Fe_2(SO_4)_3$ solution hydrolyzed for 24 h	1.65	1.38
	77	Q	0.507	0.736			100			
13.	298	Q_1	0.396	1.101		0.323	100	0.1 mol dm^{-3} $NH_4Fe(SO_4)_2$ solution hydrolyzed for 6 h		

(a) Isomer shifts are given relative to α-iron.
(b) Quadrupole splitting.
(c) Internal magnetic field strength.
(d) Half width.
(e) Area.

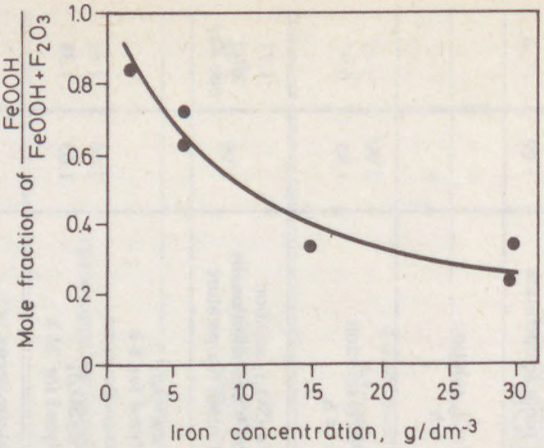

Fig. 5.49. Dependence of mole fraction of goethite on the concentration of the suspension

The fact that the proportion of goethite in the product increases with a decrease in the suspension concentration, suggests that the second of the above two hypotheses is correct, i.e. the goethite is formed in the solution phase and haematite in the solid phase.

5.5.2. HYDROLYSIS IN ANTIMONY CHLORIDE SOLUTIONS

The hydrolysis of antimony salts have been less extensively considered, than the hydrolysis of iron(III) salts. Some Mössbauer parameters are presented in Table 5.33 [73–75]. The radiation sources used were $BaSn(Sb)O_3$ and $Sn(Sb)O_2$. The results permit the following conclusions.

Table 5.33.
Mössbauer parameters of frozen antimony salt solutions at liquid nitrogen temperature

Composition of solution	Isomer shift, δ mm s^{-1}	Literature
$SbCl_3$ crystalline	-13.8 ± 0.2	[75]
in 8 mol dm^{-3} HCl solution	-17.4 ± 0.2	[73]
in 5 mol dm^{-3} HCl solution	-15.0 ± 0.2	
in 1 mol dm^{-3} HCl solution	-15.2 ± 0.2	
$Na[Sb(OH)_4]$	-9.8 ± 0.2	
$SbCl_5$	-3.5 ± 0.3	[74]
in 11 mol dm^{-3} HCl solution	-2.7 ± 0.2	
in 9 mol dm^{-3} HCl solution	-2.0 ± 0.2	
in 6 mol dm^{-3} HCl solution	-0.8 ± 0.2	
$H[SbCl_6] \cdot H_2O$	-3.0 ± 0.2	
$Na[Sb(OH)_6]$	$+0.5 \pm 0.2$	

In the aqueous solution of both Sb^{III} and Sb^{V} hydrolysis occurs in a stepwise fashion (δ varies progressively with the acid concentration). With Sb^{III}, the isomer shifts in solutions that contain 5 or 1 mol dm^{-3} of HCl agree within the limits of experimental error; this value is closer to the isomer shift measured in concentrated acid solution than to the isomer shift of $Na[Sb(OH)_4]$. This means that during the hydrolysis of Sb^{III} solutions the concentration of the monohydroxo coordination entity is higher than that of the dihydroxo one.

The conclusions drawn from the Mössbauer spectroscopic measurements are in qualitative agreement with the spectrophotometric results of Bonner and Goiski [76], who found that the spectrophotometric properties of Sb^{III} remain unchanged in the HCl concentration range 6–12 mol dm^{-3}, and accordingly hydrolysis begins only at a lower acid concentration.

As regards the electronic structures of Sb^{III} and Sb^{V} in solution, it can be stated that in both oxidation states an increasing extent of Cl^- coordination increases the density of the s electrons at the nucleus. If the value of δ for crystalline $SbCl_3$ is compared with that measured in concentrated HCl solutions of Sb^{III}, it can be concluded that chloride coordination is more pronounced in such solutions (e.g. $[SbCl_4]^-$) than in solid $SbCl_3$.

REFERENCES

1. Bose, A., *Proc. Ind. Acad. Soc., A*, **1**, 754 (1935).
2. Zvyagintsev, O. E., Lopatto, Yo. S., *Russ. J. Inorg. Chem.*, **6**, 439 (1961).
3. Spiro, T. G., Allerton, S. E., Renner, J., Terzis, A., Bills, R. and Saltman, P., *J. Am. Chem. Soc.*, **88**, 2721 (1966).
4. Schugar, H., Walling, C., Jones, R. B. and Gray, H. B., *J. Am. Chem. Soc.*, **89**, 3712 (1967).
5. Broersma, S., *J. Chem. Phys.*, **26**, 1405 (1957).
6. Mulay, L. N. and Naylor, M. C., *Advan. Chem. Coord. Comp. Proc. 6th. ICCC*, New York, p. 520 (1961).
7. Hedström, B. O. A., *Arkiv Khemi*, **6**, 1 (1938).
8. Milburn, R. M. and Vosburgh, W. C., *J. Am. Chem. Soc.*, **77**, 1352 (1955); Milburn, R. M., *J. Am. Chem. Soc.*, **79**, 537 (1957).
9. Mulay, L. N. and Selwood, P. W., *J. Am. Chem. Soc.*, **77**, 2693 (1955).
10. Knudsen, J. M., Larsen, E., Moreira, J. E. and Nielsen, O. F., *Acta Chimica Scandinavica, A*, **29**, 833 (1975).
11. Ohya, T. and Ono, K., *J. Chem. Phys.*, **57**, 3240 (1972).
12. Fordham, A. W., *Austral. J. Chem.*, **22**, 1111 (1969).
13. Rowley, J. K. and Sutin, N., *J. Phys. Chem.*, **74**, 2043 (1970).
14. Platchinda, A. S., Komor, M. and Vértes, A., *J. Radioanal. Chem.*, **10**, 89 (1972).
15. Dézsi, I., Gorobchenko, V. D., Lukashevich, I. I. and Vértes, A., *Chem. Phys. Lett.*, **2**, 665 (1968).
16. Vértes, A. and Parak, F., *J. Chem. Soc. Dalton Trans.*, 2062 (1972).
17. Dézsi, I., Gorobchenko, V. D., Komor, M., Lukashevich, I. I., Tzikishwili, K. F. and Vértes, A., *Acta Chim. Acad. Sci. Hung.*, **70**, 329 (1971).
18. Vértes, A., Komor, M. and Gelencsér, P., *Acta Chim. Acad. Sci. Hung.*, **77**, 55 (1973).
19. Komor, M., Vértes, A., Dézsi, I. and Ruff, I., *Proc. Conf. Appl. Mössbauer Effect, Tihany* (Hungary), 1969. Akadémiai Kiadó, Budapest, 1969, p. 713; *Magy. Kém. Folyóirat*, **76**, 402 (1970); *Acta Chim. Acad. Sci. Hung.*, **66**, 285 (1970).
20. Vértes, A., Komor, M., Dézsi, I., Burger, K., Suba, M. and Gelencsér, P., *Proc. 3rd Symp. Coord. Chem., Debrecen*, Hungary, Akadémiai Kiadó, Budapest, 1970, Vol. 1. p. 215.
21. Goldanskii, V. I., Stukan, R. A. and Tolmatsev, A. N., *Dokl. Akad. Nauk SSSR*, **191**, 380 (1970).
22. Dézsi, I., Vértes, A. and Komor, M., *Inorg. Nucl. Chem. Lett.*, **4**, 649 (1968).
23. Nikolskii, B. P., Kalyamin, A. V., Kuvshinov, V. A., Plachevskii, V. V., Tomilov, S. B. and Yakubov, Ch. M., *Dokl. Akad. Nauk SSSR*, **217**, 107 (1974).

24. Ropars, C., Rougéé, M., Momentean, M. and Lexa, D., *J. Chim. Phys. Physico-chim. Biol.*, **65**, 816 (1968).
25. Zvyagintsev, O. E. and Lyachmanov, S. B., *Zhur. Neorg. Khim.*, **13**, 1230 (1968).
26. Máthé, I. and Bakk-Máthé, E., *Revue Roumaine de Chimie*, **11**, 225 (1966).
27. Lázár, K., Pardavi-Horváth, M. and Vértes, A., *Acta Chim. Acad. Sci. Hung.*, **74**, 163 (1972); *Magy. Kém. Folyóirat*, **78**, 447 (1972).
28. Watson, R. W. and Freeman, A. J., *Phys. Rev.*, **123**, 2027 (1961).
28a. Carrano, C. I. and Spartalion, K., *Inorg. Chem.* **23**, 1994 (1984).
28b. Lukas, B., Peterson, J., Silver, J. and Wilson, M. T., *Inorganica Chimica Acta*, **80**, 245 (1983).
29. Bent, H. E. and Prench, C. L., *J. Am. Chem. Soc.*, **63**, 568 (1941).
30. Rabinowitsch, E. and Stockmayer, W. H., *J. Am. Chem. Soc.*, **64**, 335 (1942).
31. Gamlen, G. A. and Jordan, D. O., *J. Chem. Soc.*, 1435 (1953).
32. Katzin, L. J. and Gebert, E., *Nature*, **175**, 425 (1955); *J. Am. Chem. Soc.*, **72**, 5457 (1950).
33. Whitakar, R. A. and Davidson, N., *J. Am. Chem. Soc.*, **75**, 3081 (1953).
34. Sillen, L. G. and Martell, A. E., *Stability Constants of Metal Ion Complexes*. Chem. Soc. Spec. Publ. No. 17, London, 1964.
35. Knudsen, I. M., De Aranjo, F. T., Dufresne, A. and De Lima, C. G., *Chem. Phys. Lett.*, **11**, 134 (1971).
36. Mørup, S. and Thrane, N., *Chem. Phys. Lett.*, **21**, 363 (1973).
37. Du Fresne, A., Knudsen, J. M., Moreira, J. E. and Skeff-Nefo, K., *Chem. Phys. Lett.*, **20**, 108 (1973).
38. Chaves, F. A. B. and Garg, V. K., *J. Inorg. Nucl. Chem.*, **37**, 2283 (1975).
39. Filatova, L. N., Shelyakina, M. A., Platchinda, A. S. and Makarov, E. F., *Zh. Neorg. Chim.*, **21**, 2715 (1976).
40. Nozik, A. I. and Kaplan, M., *J. Chem. Phys.*, **49**, 4141 (1968).
41. Vértes, A., *Dissertation for the degree of Doctor of Sciences*, Budapest, 1972.
42. Wendt, H., *Inorg. Chem.*, **8**, 1527 (1969).
43. Po, H. N. and Sutin, N., *Inorg. Chem.*, **10**, 428 (1971).
44. Sommer, B. A. and Margerum, D. W., *Inorg. Chem.*, **9**, 2517 (1970).
45. Goldanskii, V. I., Lévay, B., Shantarovich, V. P., Komor, M. and Vértes, A., *Radiochem. Radioanal. Lett.*, **12**, 289 (1972).
46. Goldanskii, V. I., Novikov, G. V., Miklailov, A. I., Trukhtanov, V. A. and Andrashitov, E. F., *JETP Lett.*, **12**, 323 (1970).
47. Bhargava, S. C., Knudsen, J. E. and Mørup, S., *J. Phys. Chem. Solids*, **40**, 45 (1979).
48. Zeltmann, A. H. and Morgan, L. O., *J. Phys. Chem.*, **70**, 2807 (1966).
49. Friedman, H. L., *J. Am. Chem. Soc.*, **74**, 5 (1952).
50. Antipova-Karataeva, I. I., Zolotov, N. A. and Sheryakova, I. V., *Zhur. Neorg. Khim.*, **9**, 1712 (1964).
51. Shárma, S. K., Sehgal, V. N., Bomi, H. L. and Sharma, S. D., *J. Inorg. Nucl. Chem.*, **37**, 2417 (1975).
52. Magini, M. and Radnai, T., *J. Chem. Phys.*, **71**, 4255 (1979).
53. Kündig, W., Bömmel, H., Constabaris, G. and Lindquist, R., *Phys. Rev.*, **142**, 327 (1966).
54. Suzdalev, I. P., *Proc. Conf. Appl. Mössbauer Effect, Tihany* (Hungary), Akadémiai Kiadó, Budapest, 1971, p. 193.
55. Van der Kraan, A. M. and Van Loef, I. I., *Phys. Lett.*, **20**, 614 (1966).
56. Andrianov, V. A., Kalyamin, A. V. and Tomilov, S. B., *Zh. Obsh. Chim.*, **51**, 584 (1981).
57. Biedermann, G. and Schindler, P., *Acta Chim. Scand.*, **11**, 731 (1957).
58. Rossiter, M. J. and Hodgson, H. E. M., *J. Inorg. Nucl. Chem.*, **27**, 63 (1965).
59. Dézsi, I. and Fodor, M., *Phys. Stat. Sol.*, **15**, 247 (1966).
60. Kauffman, K. and Hazel, F., *J. Inorg. Nucl. Chem.*, **37**, 1139 (1975).
61. Schindler, P., Michaelis, W. and Feitknecht, W., *Helv. Chim. Acta*, **46**, 444 (1963).
62. Oosterhout, G. W. V., *Proc. Int. Conf. on Magnetism*. Nottingham, p. 529 (1964).
63. Kauffman, K. and Hazel, P., *J. Colloid Interface Sci.*, **51**, 422 (1975).
64. Kauffman, K. and Hazel, F., *Inorg. Nucl. Chem. Letters*, **10**, 595 (1974).
65. Ujihira, Y. and Ohyabu, M., *J. Physique Colloque*, **40**, C2–347 (1979).
66. Bhat, P. C., Sathyavathiamma, M. P., Puttaswamy, N. G. and Mallya, R. M., *Proceedings of the International Conference on the Application of the Mössbauer Effect* 14–18 December, 1981, Jaipur (India). Indian National Science Academy. New Delhi, pp 685–687 (1982).
67. Musič, S., Nagy–Czakó, I. and Vértes, A., *Colloid Polymer Sci.*, **258**, 469 (1980).
68. Musič, S., Vértes, A., Simmons, G. W., Czakó–Nagy, I. and Leidheiser, H., *J. Colloid and Interface Science*, **25**, 256 (1982)

69. Vértes, A., Lázár, K., Kelemen, K. and Bognár, L., *Radiochem. Radioanal. Lett.*, **3,** 375 (1970).
70. Wefers, K., *Ber. Deut. Keram. Ges.*, **43,** 677 (1966).
71. Feitknecht, W. and Michaelis, W., *Helv. Chim. Acta*, **45,** 212 (1962).
72. Schwertmann, M. and Fischer, W. R., *Z. Anorg. Allgem. Chem.*, **346,** 137 (1966).
73. Vértes, A. and Komor, M., *Acta Chim. Acad. Sci. Hung.*, **74,** 159 (1972); *Magy. Kém. Folyóirat*, **78,** 380 (1972).
74. Brukhanov, V. A., Iofa, B. Z. and Semyonov, S. I., *Radiokhimiya*, **11,** 362 (1969).
75. Bowen, L. H., Stevens, J. G. and Long, G. G., *J. Chem. Phys.*, **51,** 2010 (1969).
76. Bonner, N. A. and Goiski, W., *J. Am. Chem. Soc.*, **83,** 85 (1962).

6. AFTEREFFECTS OF NUCLEAR TRANSFORMATIONS IN FROZEN SOLUTIONS

6.1. INTRODUCTION

Mössbauer effect experiments usually require a radioactive source. In conventional absorption spectroscopy or scattering spectroscopy the function of the radioactive source is solely to ensure the greatest possible monochromaticity and intensity of the resonance line which is then employed for the investigation of Mössbauer nuclei in the absorber or scatterer. In an alternative experimental technique a monochromatic absorption or scattering line is used for analysis of the radiation produced by the source. This is the technique employed in Mössbauer emission spectroscopy (MES).

In comparison to absorption or scattering, Mössbauer emission spectroscopy shows the following essential differences.

First, the efficiency ab ovo limited by the resonance absorption cross-section in the case of absorption and scattering spectroscopy, can be improved by increasing the specific activity of the radioactive source (a merely technical problem) in MES. By this technique emission spectroscopy can be made more sensitive than conventional absorption spectroscopy. Second, MES makes it possible to extend the rather limited number of isotopes available for Mössbauer effect studies through the use of parent nuclei. Third, radiation of a Mössbauer quantum in the source is preceded by some radioactive transformation, such as α-decay, β-decay, electron capture (EC), converted isomer transition (CIT). Such nuclear transformations are likely to give rise to most diversified effects on the state of the daughter atom observed in the Mössbauer experiment, e.g. displacement of the atom from its initial site in the matrix of a crystal or a glass; local heating-up; ionization or excitation of the Mössbauer atom itself and of its immediate neighbourhood; change of the chemical nature of the atom and, consequently, their neighbourhood. Such effects and their consequences are described as aftereffects (AE) of nuclear transformations in solids.

The above effects are typical not only for nuclear tranformations but also for radiation-induced damage of solids as well as for processes involved in electron-beam and ion-beam techniques. This account for the extensive use of MES for simulating elementary acts of these processes. Problems associated with Mössbauer effect studies of AE of nuclear transformations have been considered in reviews [1, 2].

The main advantage of MES as a technique of investigating AE of nuclear transformation is that it provides evidence on the atoms immediately involved in these transformations.

As applied to frozen solutions (FS), the study of aftereffects of nuclear transformations is of additional interest, since its results may have direct bearing on conventional material of nuclear chemical technology, that is to say solutions of radioactive substances. Moreover, these results may contribute to the knowledge about the processes underlying separation of radioactive isotopes and isomers. The present account is a review of Mössbauer effect studies of aftereffects of radioactive transformations in frozen solution.

6.2. BASIC CONCEPTS OF MECHANISMS RESPONSIBLE FOR AFTEREFFECTS

The change of the charge of the nucleus, i.e. the change of the chemical nature of the atom, is the most evident consequence of many nuclear transformations. An example is the transformation of such a chemically active element as iodine to a noble gas xenon following β-decay or transformation of ^{57}Co to ^{57}Fe through EC common for Mössbauer spectroscopy. What follows from the change in the nature of the atom is a reaction to form new chemical bonds. Mössbauer effect studies of such reactions in solids have been recently reviewed by Goldanskii and Stukan [3].

A group of phenomena accompanying radioactive transformations of atoms in solids or in other condensed phases are termed the Szilárd–Chalmers effect. It will occur, if the change of the chemical state of the atom is not associated with the change of its nuclear charge. The Szilárd–Chalmers effect involves the displacement of the daughter atom from its initial site to be then fixed in a different site due to the emission of some particle by the parent atom due to local thermal spike or due to generation of structural effects in the neighbourhood of the radioactive atom, or due to ionization of the daughter atom. It is only in isomer transitions that these phenomena can appear in a pure form, yet they occur, apart from change of the nuclear charge, in other types of radioactive decay as well. Some mechanisms underlying the Szilárd–Chalmers effect will be described in the following.

One distinguishes two different mechanisms of displacements of atoms depending on whether the kinetic energy imparted to the atoms is larger or less than a certain value referred to as the threshold displacement energy, E_d. This value, as determined by bombarding the material by fast electrons is about 30 eV.

Should the kinetic energy of an atom exceed E_d, then it will leave its normal site as a vacancy and occupy a new site or collide with the neighbouring atoms causing secondary displacements and producing a so-called displacement cascade. Such concepts of the formation of displaced atoms and vacancies were proposed by Kinchin and Pease [4] as early as the 1950s. An important improvement of this theory has been provided by an account of so-called substitutional collisions [5] as a result of which a considerable portion of atoms involved in the displacement cascade are finally found at sites equivalent to the initial one. The role played by substitutional collisions is important in elementary monatomic lattices and becomes of less importance in complex matrices.

Recoil energy E_r of the radioactive nucleus emitting a particle can be obtained from the equation:

$$E_r = \frac{1}{2mc^2}(E^2 + 2m_0c^2E) \tag{6.1}$$

where E is the energy of a particle while m and m_0 are the mass of the daughter atom and rest mass of the emitted particle, respectively and c is the velocity of light. Among particles emitted in Mössbauer sources (α-particles in α-decay, β-particles and neutrinos in β-decay, neutrinos in electron capture, γ-quanta and conversion electrons in isomer transitions; rest masses of γ-quanta and neutrinos are equal to zero), only α-particles do impart to recoil atoms energy of the order of 10^4–10^5 eV by far exceeding displacement energy. In other cases the recoil energy is less or of the order of the displacement energy. In order to account for the displacement of atoms from their usual sites a number of special mechanisms have been suggested.

For ionic compounds it is common to refer to mechanisms of the Varley type [6] that assume ionization of the atom which, as a result, is found in an electrostatically unstable site and displaced from this latter to one that is energetically more advantageous. For molecular crystals such mechanisms assume ionization not only of the decayed atom but of the neighbouring atoms as well. As a result, the constituents of the molecule become positively charged, and disrupted by electrostatic repelling forces (fragmentation model [7]). Rather than ionization of atoms, some models [8] require localization of an exciton on one of the bonds. The result is an excited state quasi-molecule that disintegrates like a conventional pre-dissociated molecule.

For AE to occur, the atom that has undergone nuclear decay need not be displaced from its initial site. In order to alter the chemical state of the daughter atom it suffices to make alterations in its immediate surrounding. The heat wedge model suggests [9] that a portion of the energy released in radioactive decay leads to local thermal spike in the matrix and, therefore, to increased defect concentration in the vicinity of the daughter atom which changes its chemical state following interaction with defects. Another heat model [10] suggests melting and recrystallization of the microvolume around the hot atom.

The autoradiolysis model [11] has been applied for coordination molecules susceptible to radiolysis. According to this model, low energy Auger electrons and X-ray photons emitted by the daughter atom radiolyze ligands thus producing an oxidizing or reducing medium which changes the chemical state of the emitting atom.

The last model to be considered is a competing electron scavenger model which has found an extensive use to account for radiolysis phenomena [12] and of interpretation of MES [13], FS included. In accordance with this model, the preceding radioactive transformation results in a highly ionized state of the daughter atom. This process will be considered in detail for each type of decay separately. In a short time interval (much shorter than life times of conventional Mössbauer levels), multiply charged ions capture electrons from the surrounding medium to attain then a charge state typical for the chemistry of the daughter ion. The eventual fate of this ion, i.e. its final valence state and configuration of its immediate neighbourhood is determined by the competition of the ion with other electron scavengers in the particular matrix for free electrons emerging at internal radiolysis. Recourse to internal radiolysis is a feature common both to the competing electron scavenger models (CESM) and the aforementioned autoradiolysis model.

6.3. CHARACTERISTIC FEATURES OF EXPERIMENTS

Mössbauer emission experiments in FS have so far been carried out on five isotopes: ^{57}Fe with the parent nucleus ^{57}Co, ^{119}Sn with the parent nucleus ^{119m}Sn, ^{125}Te with the parent nuclei ^{125m}Te and ^{125}I, ^{129}I with the parent nucleus ^{129}Te, and ^{237}Np with the parent nucleus ^{241}Am. Diagrams of nuclear levels of these isotopes and diagrams of decay of parent nuclei are presented in Fig. 6.1 based on data borrowed from [14].

An important feature of emission experiments on FS is that it is required to handle open radioactive substances. Mössbauer absorption spectroscopy generally enables the experimentalist to manage with encapsulated commercially available sources. MES, on the other hand, requires that experimental samples, that is Mössbauer sources, be prepared in situ in a radiochemical laboratory. If the sources are solids they can be encapsulated and then taken to a conventional Mössbauer laboratory. In distinction, FS are not suitable to handle in such a way for consideration of radiation safety, because they should be stored in liquid nitrogen and melt when heated to room temperature. Consequently, Mössbauer measurements must also be made in or at least close to the radiochemical laboratory. This seems to be the reason why only a limited number of studies concerning MES in FS are available.

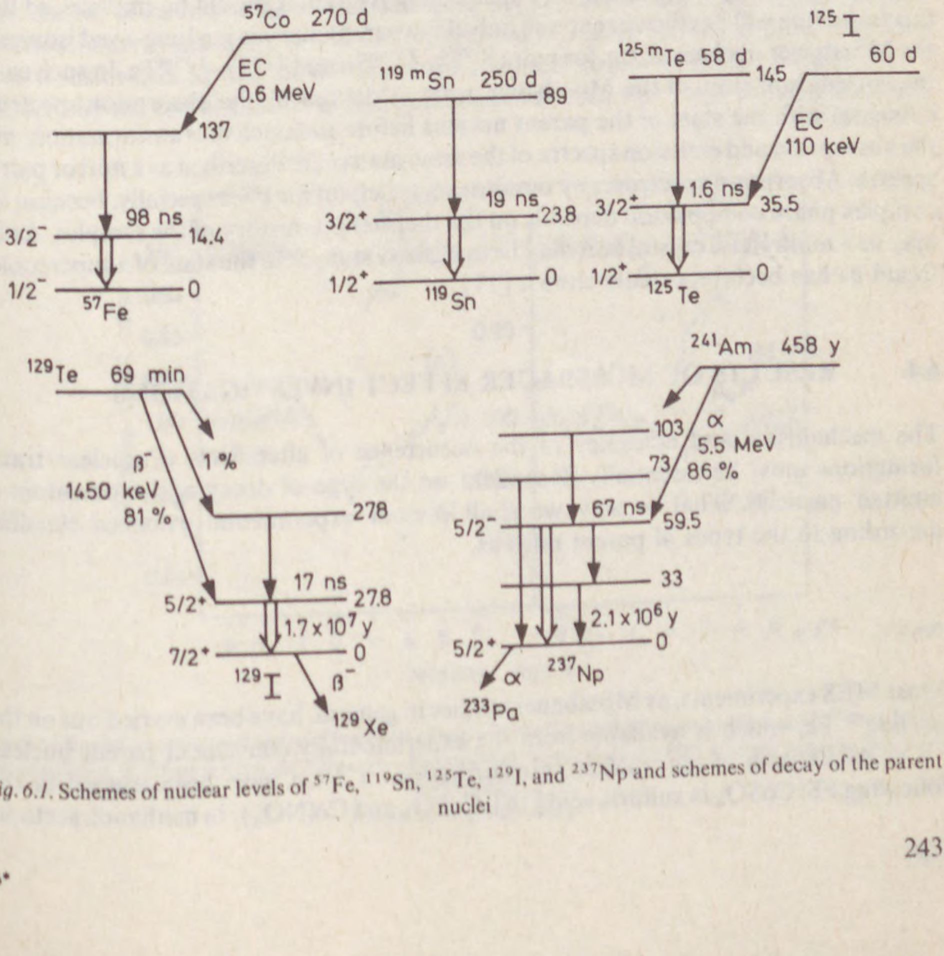

Fig. 6.1. Schemes of nuclear levels of ^{57}Fe, ^{119}Sn, ^{125}Te, ^{129}I, and ^{237}Np and schemes of decay of the parent nuclei

In such experiments sources are kept in holders made of a material inert with respect to the solvent used and transparent for Mössbauer radiation. The holders are filled with the solution to be investigated containing a radioactive isotope. The holder filled with the solution is cooled as a rule by liquid nitrogen. The holder is required to ensure tightness of the source and rigidity of its content to make it possible to mount the source at the drive of the Mössbauer spectrometer. For this reason, it is practicable to take the spectrum using a stationary source and moving the absorber. Spectra are generally taken with the source cooled to the temperature of liquid nitrogen if no lower temperature is required.

We have enumerated the principal features of the experimental techniques. Two more remarks of methodological character must be made at this point. In FS experiments as in MES, in general, it may prove most helpful to apply resonance detectors of Mössbauer radiation [15]. It will simplify the geometry of the experiment and reduce the time needed for taking the spectrum. [16] shows resonance detectors for ^{119}Sn to have currently the best parameters.

It must be, finally, noted that it is advantageous for comparison to measure, apart from emission spectra, also absorption spectra of the same solutions. Such a conclusion has been arrived at by Seregin et al. [1] with respect to Mössbauer effect investigations of aftereffects in any matrices. Absorption spectra permit to follow the equilibrium state of the Mössbauer atom in those cases in which this state does not appear to be evident or single and, thus, to prevent errors in detecting AE. Yet it should be emphasized that this technique will be efficient enough only if the parent nucleus is a long-lived isomer of the Mössbauer nucleus as, e.g. for pairs ^{119}Sn–^{119m}Sn and ^{125}Te–^{125m}Te. In such cases the equilibrium state of the Mössbauer atom evidenced by the absorption spectrum coincides with the state of the parent nucleus before radioactive transformation, and the absorption and emission spectra of the same matrix are described as a mirror pair of spectra. Absorption spectroscopy monitoring is helpful for FS, especially, because the complex phase composition depends on the thermal pre-history of the samples. As FS may be a multiphase crystal or it may be in a glassy state or in the state of a supercooled liquid as has been repeatedly shown [17].

6.4. RESULTS OF MÖSSBAUER EFFECT INVESTIGATIONS

The mechanisms and efficiency of the occurrence of aftereffects of nuclear transformations must be essentially dependent on the type of decay and momentum of emitted particles. That is why we shall present experimental evidence classified according to the types of parent nucleus.

6.4.1. ^{57}Co

Most MES experiments, as Mössbauer studies in general, have been carried out on the nuclide ^{57}Fe, which is available from the experimentally convenient parent nucleus ^{57}Co. Aftereffects of the nuclear transformation of ^{57}Co have been studied in the following FS: $CoSO_4$ in sulfuric acid [18], $CoSO_4$ and $Co(NO_3)_2$ in methanol, acetone, sulfuric and nitric acid [19], trisbipyridylcobalt (III) in nitromethane, acetone, ethyl acetate, acetonitrile, ethanol and methanol [20]; $CoCl_2$ in acetonitrile, acetone, dimethylformamide and dimethyl sulfoxide [21]; $CoCl_2$ in iodine alcoholic solutions [22] and $CoCl_2$ in water [23–27].

A diagram of ^{57}Co decay is presented in Fig. 6.1. ^{57}Co is transformed to ^{57}Fe by electron capture, a 0.7 MeV neutrino being released, the nucleus of ^{57}Fe obtains recoil energy of about 4.6 eV. This energy is insufficient to displace the atom, so Mössbauer emission spectra of ^{57}Co have shown no displaced atoms. However, EC in ^{57}Co gives rise to a vacancy in one of the inner shells of the daughter iron atom. The filling of this vacancy can be accompanied either by emission of a photon, the vacancy being shifted to an upper lying electron shell or by emission of an Auger-electron, with two vacancies formed in the upper lying shells. These newly formed vacancies must also be filled by electrons from outer shells, the higher the probability of the Auger process, the larger the principal quantum number of the shell. Such an Auger cascade results in a multiply charged iron ion, and emission of several Auger electrons and soft X-ray quanta responsible for ionization (internal radiolysis) of the immediate neighbourhood of the daughter atom. The iron ion charge state spectrum resulting from an Auger cascade (10^{-15}–10^{-14} s after the EC) has been calculated by Pollak [28]. According to this calculation the $^{57}Co^{2+}$ ions produce a set of iron ions with charges ranging from 2+ to 8+.

A number of studies (these are discussed, e.g. in [1]) have revealed that at the moment the Mössbauer γ-quantum is emitted (approximately after 100 ns), multicharge ions have transformed to one of the common chemical forms of iron, typically Fe^{3+}, followed by the establishment of an equilibrium between Fe^{3+} and the neighbouring

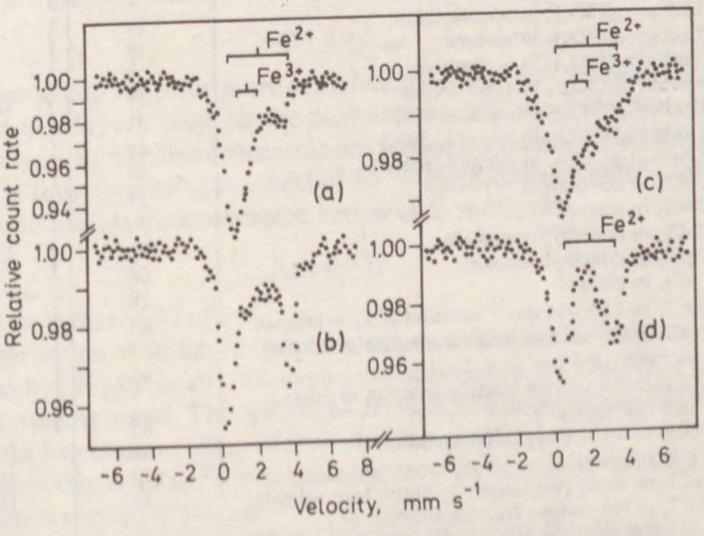

Fig. 6.2. Mössbauer emission spectra of frozen solutions of $^{57}CoCl_2$ [22]. (a) ethanol, glass, (b) 1.25 mol dm^{-3} iodine solution in ethanol, glass, (c) 80% ethanol solution in water, glass, (d) 80% ethanol solution in water, polycrystal

Absorber: $K_4[Fe(CN)_6]$

atoms, which is likely to result in a portion of iron atoms transforming into a different chemical form. Emission spectra of ^{57}Co predominantly show various proportions of Fe^{3+} and Fe^{2+}.

This feature is shown by emission spectra of FS as well. All of the aforementioned studies except [25–27] report on spectra as being a superposition of Fe^{3+} and Fe^{2+} quadrupole doublets. A characteristic shape of ^{57}Co spectra in FS is presented in Fig. 6.2. More complex spectra were reported in [21] showing two states of Fe^{2+} and two states of Fe^{3+}, attributable to the existence of two distinct initial forms of the Co parent atoms. The percentage of ^{57}Fe atoms in the form Fe^{2+} for diverse frozen solutions is given in Table 6.1. All the spectra considered have been taken at the temperature of liquid nitrogen.

All the studies interpret the evidence obtained in terms of CESM. An alternative autoradiolysis model is rejected for the following considerations:

Table 6.1.

Share of Fe^{2+} in emission spectra of ^{57}Co in frozen solutions

Solution	Percentage of Fe^{2+}	Literature
$CoSO_4$ in 3 mol dm^{-3} solution of H_2SO_4	87	[18]
$CoSO_4$ in 18.7 mol dm^{-3} solution of H_2SO_4	51	
$CoSO_4$ in H_2SO_4	41	[19]
$Co(NO_3)_2$ in HNO_3	28	
$CoSO_4$ in acetone	35	
$Co(NO_3)_2$ in acetone	47	
$CoSO_4$ in methanol	61	
$Co(NO_3)_2$ in methanol	67	
$[Co(bpy)_3](ClO_4)_3$ in nitromethane	14	[20]
$[Co(bpy)_3](ClO_4)_3$ in acetone	18	
$[Co(bpy)_3](ClO_4)_3$ in acetonitrile	21	
$[Co(bpy)_3](ClO_4)_3$ in ethyl acetate	31	
$[Co(bpy)_3](ClO_4)_3$ in methanol	41	
$[Co(bpy)_3](ClO_4)_3$ in ethanol (glass)	44	
$[Co(bpy)_3](ClO_4)_3$ in ethanol (polycr.)	60	
$CoCl_2$ in acetonitrile	73	[21]
$CoCl_2$ in acetone	76	
$CoCl_2$ in dimethylformamide	100	
$CoCl_2$ in dimethyl sulfoxide	66	
$CoCl_2$ in ethanol	28	[22]
$CoCl_2$ in 1.25 mol dm^{-3} solution of I_2 in ethanol	60	
$CoCl_2$ in 0.8 volume fraction solution of ethanol in water (glass)	40	
$CoCl_2$ in 0.8 volume fraction solution of ethanol in water (polycr.)	85	
$CoCl_2$ in water (very dilute solution, low velocity)	66 72	[24] [27]
$CoCl_2$ in water (very dilute solution, high velocity)	43	[25]
$CoCl_2$ in 0.5 volume fraction solution of glycerol in water (dilute solution)	83	[24]
$CoCl_2$ in water (0.06 mol dm^{-3})	57	
$CoCl_2$ in 0.5 volume fraction solution of glycerol in water (0.06 mol dm^{-3})	92	

(i) too short lapse of time for reactions to occur involving radicals at 80 K [19];

(ii) lack of correlation between the yield of Fe^{2+} and stability of solvent molecules to radiolysis [19, 20].

Table 6.1 shows the yield of various iron stabilization forms to be related to the solvent type. The observed correlation is not associated with the capability of sovent molecules for radiolysis. It is due to their aptitude to accept (scavenge) solvated electrons as known from pulse radiolysis experiments [12]. Solvents showing small reactivity with respect to the solvated electron, such as dimethylformamide permit a 100% yield of Fe^{2+} [21]. Both iron states, Fe^{2+} and Fe^{3+}, are shown by emission spectra of FS when use is made of cobalt parent atoms in a divalent [18, 19, 21, 22] as well as in a trivalent state [20].

According to CESM, electrons released as a result of internal irradiation participate in competing reactions as follows

$$Fe^{3+} + e = Fe^{2+}$$

$$\text{scavenger} + e = e_{\text{capt}}.$$

The velocity of the second channel must depend on the concentration of scavengers, and some experiments have attempted to control this concentration.

Kulikov et al. [18] have applied H^+ ions in sulfuric acid solution as scavengers that are capable of electron capture by the reaction:

$$H^+ + e = H$$

to obtain a dependence close to a linear one of Fe^{3+} yield on the sulfuric acid concentration over the range from 3 to 18.7 mol dm^{-3}. Moreover, this study has revealed electron traps identified as structure defects of a glassy matrix:

$$\text{trap} + e = e_{\text{capt}}$$

whose acceptor action becomes more pronounced at low H^+ concentrations.

Milgrom et al. [22] reported on the dual action of I_2 acceptor centres in iodine alcoholic solutions. Low iodine concentrations reduce the number of structure traps in a glassy matrix thus decreasing the yield of Fe^{3+}. High concentrations, on the other hand, lead to noticeable direct acceptor action of I_2 molecules:

$$I_2 + e = I_2^-$$

which results in higher yield of Fe^{3+}.

The acceptor action of structure traps in glassy matrices has been demonstrated by [22] as well as by [21] by means of comparison of emission spectra of the same FS in glassy and crystalline states. The spectra of crystalline samples show higher yield of Fe^{2+} due to the low concentration of their structure defects (see Table 6.1). Electrons captured on structure traps in ^{57}Co-containing samples have been detected in [22] by the thermoluminescence technique.

A somewhat modified CESM has been invoked to explain the decrease of the Fe^{3+} yield in the frozen aqueous solution of $^{57}CoCl_2$ when glycerol was added [24]. In an aqueous solution probably the most effective electron scavengers are the neutral $(OH)^{\cdot}$ radicals being present in the first hydrate shell of the nucleogenic iron ion. They tend to stabilize the Fe^{3+} species. If, however, an $(OH)^{\cdot}$ radical directly contacts a glycerol molecule the latter will passivate the $(OH)^{\cdot}$ radical reacting with it and producing a neutral peroxy radical:

$$C_3H_5(OH)_3 + (OH)^{\cdot} \rightarrow (C_3H_5(OH)_2)^{\cdot} + H_2O_2 .$$

It is, of course, also possible that the glycerol molecules directly act as scavengers.

It appears that all the experiments reported have been made on glassy materials, although it has not been specified in some cases. The concentration of structure traps in glasses must depend on the quenching mode of the solutions. This can account for certain discrepancies in values of the Fe^{2+} yield as determined in [18] and [19].

No use has been reported of absorption spectroscopy either to check samples for glassiness or to determine the equilibrium state of Fe atoms. Afanasov et al. have employed absorption spectra in order to identify the surrounding of the iron atoms resulting from the decay of ^{57}Co by comparing emission spectra with spectra of iron solutions [21].

The suitability of CESM to describe the mechanism of AE of EC in ^{57}Co in FS can, on the whole, be regarded as proved. A principal application of this model is that EC results in different charge states of iron atoms rather than in changes in the atomic structure of the environment of the daughter atom. It enabled the authors of [21] to apply MES to study the immediate surrounding of the parent Co atoms. The choice of the objects of study in the latter paper does not seem to be justified since the cobalt parent atoms in these solutions are found in two intitial structural positions, visually in $CoClL_5^+$ octahedra and in $CoCl_3L^-$ tetrahedra (where L is a solvent molecule). This fact prevents unambiguous interpretation of the spectra.

To conclude this topic, we consider the studies of Bondarevsky et al. [29], of the aftereffects of EC in ^{57}Co, in the eutectic NH_4NO_3—$LiNO_3$ rather than in conventional FS. The effective electron scavenger concentration in this system has been varied by incorporating KCl impurity, and the suitability of CESM has been shown to account for the observed state of the iron daughter atoms.

Unusual behaviour of the Fe^{3+} fraction was observed in a frozen aqueous solution of $^{57}CoCl_2$ [25]. In this case the relaxation of the Fe^{3+} spin is not fast enough. That is why a magnetic hyperfine structure was observed at 4.2 K. In applied magnetic field strength of $H \geqq 3$ T the spectra arising from the $m_s = +5/2$ and the $m_s = +3/2$ atomic Zeeman levels have been found at 4.2 K. At this temperature the contribution of these levels in thermal equilibrium would be less than 2 percent (see Fig. 6.3). This new kind of AE opened the way to study ligand field effects on excited states of the Fe^{3+} ion.

Since it was possible to independently evaluate the Fe^{3+} fraction of the spectra from their outer peaks where no contribution from Fe^{2+} ions was expected, the Fe^{2+} contribution could also be separated from that of the Fe^{3+} ions. The residual Fe^{2+} spectrum [26] (see Fig. 6.4) was almost identical with the absorption spectrum of a frozen aqueous solution of $FeCl_2$. This means, on the one hand, that no AE can be observed on the Fe^{2+} fraction and, on the other hand, that the environment of the nucleogenic Fe^{2+} ions in the $^{57}CoCl_2$ FS is the same as that of the Fe^{2+} ions in the $FeCl_2$ FS.

The spectra of the $^{57}CoCl_2$ FS clearly show the importance of accounting properly for Fe^{3+} relaxation effects when the contribution of one (e.g. Fe^{2+}) species is

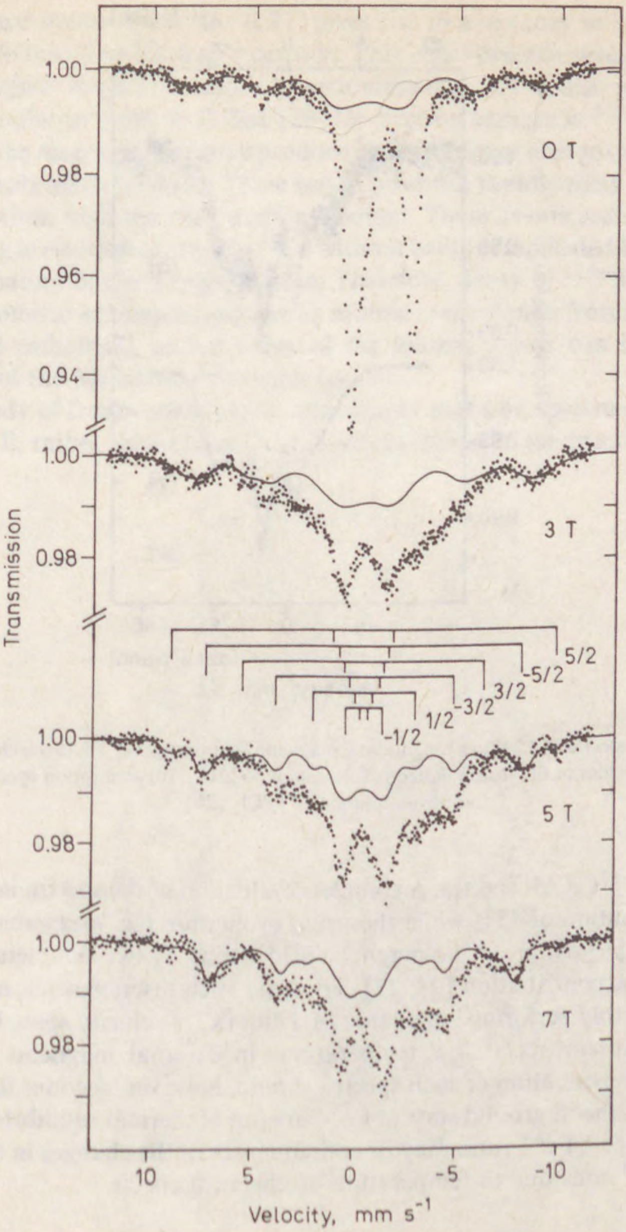

Fig. 6.3. Mössbauer emission spectra of a frozen aqueous solution of ^{57}CoCl$_2$ at 4.2 K in various longitudinal magnetic field strength. The schematic subspectra belong to Fe^{3+} ions in 5 T. The full line is the fit of the Fe^{3+} fraction from the outer part of the spectra [25]

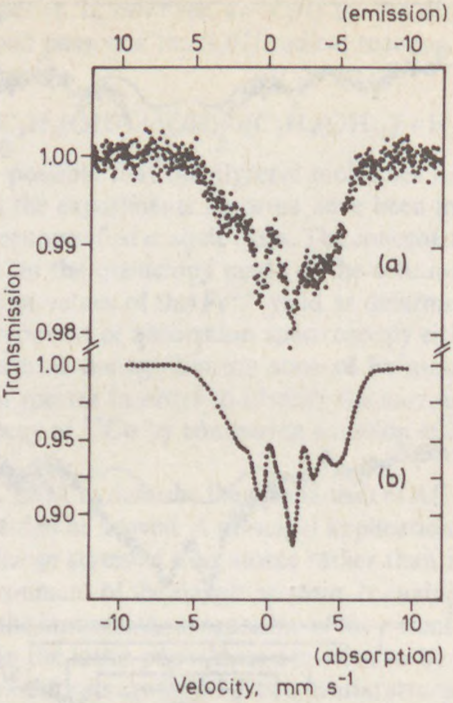

Fig. 6.4. Mössbauer spectra at 4.2 K in a longitudinal magnetic field strength of 5 T, (a) residual Fe^{2+} fraction of the emission spectrum of the frozen aqueous solution of $^{57}CoCl_2$, (b) absorption spectrum of a frozen aqueous solution of $FeCl_2$ [26]

determined from ^{57}Co AE spectra. A complete evaluation of the spectra in Fig. 6.3 gives an Fe^{2+} contribution of 43% while the usual evaluation (i.e. measurement in a low velocity span, e.g. ± 5 mm s^{-1}, no magnetic field, fitting by two doublets) results in ca 70% for the same contribution [24, 27]. To avoid such discrepancies, measurements should be preferably performed in a large (± 12 mm s^{-1}) velocity span. In some cases additional measurements at low temperatures in external magnetic field may be informative. The evaluation of such spectra should, however, account for the fact the Zeeman levels of the ^6S ground state of Fe^{3+} are out of thermal equilibrium. Apparent changes in the Fe^{2+}/Fe^{3+} ratio may be consequences of the changes in the relaxation time of the Fe^{3+} ions due to temperature or chemical effects.

6.4.2. ^{119m}Sn

^{119m}Sn is by far the most common parent nucleus for a 23.8 keV Mössbauer transition in ^{119}Sn. A diagram of ^{119m}Sn decay is presented in Fig. 6.1. Mössbauer level is populated by the (almost completely converted) 65 keV isomer transition. The recoil energy of conversion electrons does not exceed 0.3 eV and can be neglected if we are to gain insight into the mechanisms of the aftereffects. Like electron capture considered above, converted isomer transition (CIT) gives rise to a vacancy in the atomic inner electron shell followed by an Auger cascade. This latter cascade results in a multiply ionized tin daughter atom surrounded by an ionized region. For this case, however, no calculations similar to those by Pollak [28] for electron capture in ^{57}Co are available because in tin the Auger cascade may produce states of higher charge than in iron (8+) since tin has more electron shells. These states, however, rapidly relax to Sn^{4+}, which attains equilibrium with the surrounding medium. These events are quite similar to those occurring in electron capture in ^{57}Co without being complicated by the change of the chemical nature of the daughter atom. Therefore, decay of ^{119m}Sn may serve to simulate phenomena accompanying strong atomic ionization in frozen solutions (e.g. X-ray induced radiolysis), and the fate of the ionized atoms can be followed by measurement of the Mössbauer emission spectra.

The first study of frozen solutions by Mössbauer emission spectra of ^{119m}Sn [30], investigated AE, rather than converted isomer transition in the reaction ^{118}Sn (n, γ)

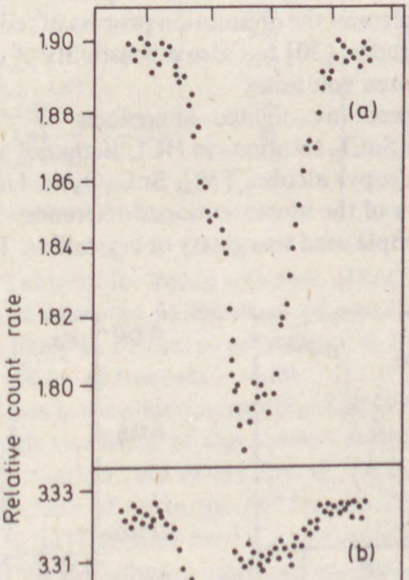

Fig. 6.5. Emission spectra [30] of reactor-irradiated ^{118}SnO sample (a) and of frozen solution of the same sample in HCl (b)
Absorber: $CaSnO_3$

^{119m}Sn typically yielding an isomer ^{119m}Sn. Murin et al. [30] have irradiated with reactor produced neutrons a sample of ^{118}SnO and compared the emission spectrum of this sample with that of a sample of SnO synthesized from previously irradiated tin. It was found that the spectrum of the irradiated SnO, apart from the principal Sn^{2+} line showed an additional Sn^{4+} line and the total intensity of the spectrum decreases in comparison to the emission spectrum of the sample not irradiated. The ratio between the intensities of the spectra of Sn^{2+} and Sn^{4+} was 3.5 at 80 K. The irradiated sample was then dissolved in concentrated HCl and the Mössbauer emission spectrum of this frozen solution was measured. The ratio between the intensities of the Sn^{2+} and Sn^{4+} lines was opposite to that observed for the irradiated SnO and amounted to 0.3. The spectra of the irradiated SnO and of the frozen solution of this sample in HCl are presented in Fig. 6.5. The authors [30] explained this result by assuming that a fraction of the tin atoms participating in the (n, γ) reaction experiences recoil and is found in a surrounding with quite a number of defects, and, consequently, do not contribute to the resonant line. On being dissolved these atoms go into solution as Sn^{4+} which is responsible for an increased intensity of the Sn^{4+} spectrum in frozen solutions. Not only the need to take into account the dissolution process in radiochemical analysis has been recognized in these studies [30] but also a possibility of aftereffects of an isomer transition of ^{119m}Sn in frozen solutions.

The studies that followed investigated aftereffects of ^{119m}Sn decay in frozen solutions, such as oxidized $SnCl_2$ solutions in HCl, methanol and acetone [31]; $SnCl_2$ in ethanol, acetone and propyl alcohol [32]; SnC_2O_4 in HCl and methanol [32]. Unfortunately, the authors of the aforementioned references have omitted to specify whether the state of the sample used was glassy or crystalline. To check the initial state

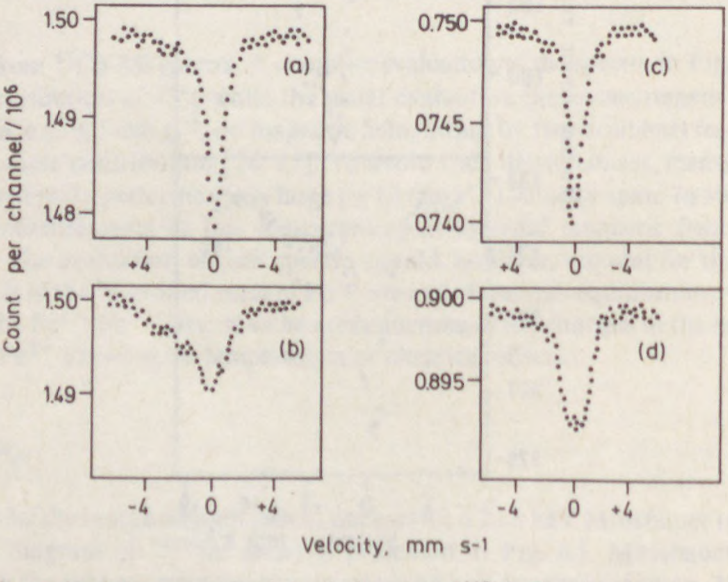

Fig. 6.6. Mössbauer absorption (a, c) and emission (b, d) spectra of $^{119m}SnCl_2$ solutions in methanol (a, b) and acetone (c, d), frozen on oxidation in air [31]
Absorber: $CaSnO_3$

of the tin atoms, Mössbauer absorption spectra have always been used with the same samples as sources in emission spectroscopy and absorbers in absorption spectroscopy (a standard source of high activity was applied). Typical mirror pairs of emission and absorption spectra are presented in Fig. 6.6. All emission spectra were superpositions of the initial line found in the absorption spectrum (Sn^{4+} and Sn^{2+} [31], [32]) and of the additional line belonging to oxidized (Sn^{4+}) or reduced (Sn^{2+}). The intermediate charge state Sn^{3+} tin form never occurred. The share of Sn^{2+} determined from the ratio of spectra areas is given in Table 6.2.

Table 6.2.
Share of Sn^{2+} in emission spectra of ^{119m}Sn in frozen solutions

Solutes	Percentage of absorption spectrum	Sn^{2+}, % emission spectrum	Literature
SnC_2O_4—HCl	100	20	[32]
SnC_2O_4—HCl—CH_3OH	100	100	
$SnCl_2$—HCl	100	30	
$SnCl_2$—HCl—$H_2C_2O_4$	100	40	
$SnCl_2$—CH_3—$[CH_2]_2$—OH	100	100	
$SnCl_2$—HCl—C_2H_5OH	100	90	
$SnCl_2$—HCl—C_2H_5OH—$(CH_3)_2CO$	80	70	
$SnCl_4$—HCl (oxidized in air)	0	0	[31]
$SnCl_2$—CH_3OH (oxidized in air)	0	30	
$SnCl_2$—$(CH_3)_2CO$ (oxidized in air)	0	0	

The data presented in Table 6.2 for frozen solutions of $SnCl_2$ in HCl indicate that the Sn^{2+}/Sn^{4+} ratio obtained from the Mössbauer spectrum of frozen solution of the irradiated SnO [30] are likely to be due to aftereffects of ^{119m}Sn decay in the frozen solution rather than to the (n, γ) reaction.

The intensity of Sn^{4+} lines in the emission spectra of all investigated frozen solutions is in good agreement with reactivity of the solvent molecules with respect to the electron. The higher the reaction rate of capture of the solvated electron by these molecules the higher the share of tin in the Sn^{4+} state. This is the reason why the experimental results in [31, 32] like those for ^{57}Co, are explained within the framework of CESM. Thus, the ^{119m}Sn Mössbauer emission spectroscopy may be considered suitable for investigations of the structure of tin-containing frozen solutions. For high tin concentrations it is unable to compete with the absorption spectroscopy.

6.4.3. ^{125m}Te

Isomer transition of ^{125m}Te populates the Mössbauer level of ^{125}Te (see Fig. 6.1). The 110 keV transition preceding the Mössbauer transition is almost totally converted (internal conversion coefficient is about 300). The recoil energy of conversion electrons is less than 0.5 eV. Parameters of this decay are close to those of competing isomer transition in ^{119m}Sn considered above. Hence similar mechanisms of the appearance of aftereffects can be expected. Spectrometric characteristics of ^{125}Te are less convenient for Mössbauer effect studies as compared with ^{119}Sn. However, it is of particular interest that tellurium atoms can be used as a model of processes resulting from competing isomer transition, since aftereffects of competing isomer transition are used to separate the radioactive isomer pairs ^{125m}Te–^{127}Te and ^{125m}Te–^{129}Te.

Mössbauer effect investigations of competing isomer transition in ^{125m}Te have only been made for frozen solutions of H_6TeO_6 in water. A tentative report on this work has been made by Lebedev et al. [33], and a more comprehensive one by Babeshkin et al. [34]. Both emission and absorption spectra of frozen solutions at 77 K have been taken. These spectra were found to agree with corresponding spectra of crystalline H_6TeO_6. No mention is made in the published papers on the state of the samples investigated. The coincidence of the spectra, however, indicates that the frozen solutions are polycrystalline or glassy-crystalline. Apart from Te^{6+} lines shown by absorption spectra, emission spectra exhibit a Te^{4+} doublet. The share of the Te^{4+} spectrum makes up 60% of the total spectral area. Moreover, the Lamb–Mössbauer factor as determined from the emission spectrum proved to be less than that determined from the absorption spectrum of the same solution by a factor of 6. The authors [33, 34] explain the appearance of an additional state of tellurium in the emission spectrum by the formation of defective states, i.e. change in the structure of the environment of part of Te atoms following competing isomer transition. The reduction of the Lamb–Mössbauer factor in the emission spectrum is associated in [33, 34] with the local heating-up in the neighbourhood of the tellurium daughter atom. The difference in the mechanisms of aftereffects of competing isomer transition in ^{125m}Te and ^{119m}Sn seems to be unexpected and can be accounted for by the specific chemical properties of H_6TeO_6 in which displacement of atoms takes place by a mechanism impossible in the case of tin compounds.

The authors of [33, 34] have also made a comparison between the data of Te^{4+} yield as obtained from the Mössbauer emission spectra of ^{125m}Te and those as deduced from radiochemical analysis of tellurium stabilization forms following competing isomer transition in ^{127m}Te. They have shown similarity between Te^{4+} as observed in the Mössbauer emission spectrum and as isolated by radiochemical techniques. They found that in radiochemical isolation partial annealing of defective states occurs.

6.4.4. ^{125}I

Electron capture of ^{125}I is another method for populating the Mössbauer level of ^{125}Te (see Fig. 6.1). This kind of decay differs from ^{57}Co electron capture by a lower energy (neutrino energy is 110 keV, recoil energy is 0.05 eV) and lack of isomer transition before emitting a Mössbauer γ-quantum. The processes of formation of a multiply charged tellurium ion and of ionization of its surrounding must be identical. A change in the chemistry of the daughter atom takes place like in the case of ^{57}Co electron capture.

The emission spectra of ^{125}I have been investigated in frozen solutions of NaI in water and of $Na_3H_2IO_6$ in 0.1 mol dm^{-3} solution of HNO_3 [34, 35]. The emission spectra of frozen solutions of NaI in water represented quadrupole doublets corresponding to Te in the Te^{2-} state and showed a similarity to those of $NaI \cdot 2H_2O$ crystal hydrate. This latter suggests that the samples are likely crystalline.

The emission spectrum of frozen solutions of $Na_3H_2IO_6$ in 0.1 mol dm^{-3} HNO_3 represented a strongly broadened asymmetric line attributed by the authors to a few tellurium forms resulting from ^{125}I decay, supposedly Te^{6+} and Te^{4+}.

The authors of [34, 35] did not explain the formation of tellurium in different states which seems to present some difficulties due to the pronounced difference between the chemical properties of the parent I atom and the daughter Te atom.

6.4.5. ^{129}Te

As distinct from all the cases considered above, the transformation of ^{129}Te of a Mössbauer isotope ^{129}I is achieved by β^--decay (see Fig. 6.1). The numerical calculation of recoil energy involved in emitting a β^--particle and an anti-neutrino [36] shows the maximum recoil energy to be 15 eV, the distribution maximum corresponding to ~9 eV. Such recoil energies appear to be insufficient to displacing atoms (see, e.g. [1]). The part played by ionization processes in β^--decay is insignificant, the calculation of the shake-off effect of electron shells in β^--decay [37] gives a 8% probability of this process for tellurium. Therefore, Mössbauer emission spectroscopy on ^{129}Te permits the consideration of aftereffects of nuclear transformations in conditions where no ionization of the daughter atom occurs.

The only study on emission spectra of ^{129}Te in frozen solution is that of Ablesimov et al. [38]. They investigated frozen solutions of a carrier-free preparation of tetravalent ^{129}Te in water (polycrystal), in concentrated HNO_3 (glass), in HCl (polycrystalline and glassy samples). The spectra of frozen solutions in water and nitric acid are shown in Fig. 6.7. Both spectra correspond to pentavalent iodine (for aqueous solutions the

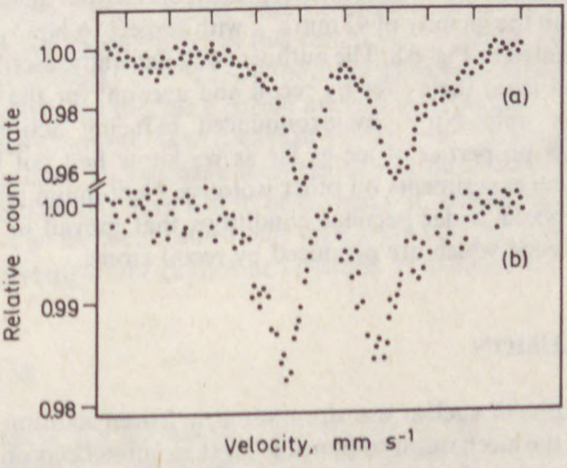

Fig. 6.7. Mössbauer emission spectra of frozen solutions of $^{129}Te^{IV}$ in water (a) and in concentrated HNO_3 (b) [38]
Absorber: KI

isomer shift is $\delta = 2.6\ \mathrm{mm\,s^{-1}}$ with respect to KI, the quadrupole interaction constant $e^2qQ = 745$ MHz and for HNO_3 solutions $\delta = 3.4\ \mathrm{mm\,s^{-1}}$, $e^2qQ = 745$ MHz) which corresponds to the I daughter ion retaining the electron configuration of the Te parent atom. For solutions in HCl two states of ^{129}I with 2.3 and 6.3 $\mathrm{mm\,s^{-1}}$ isomer shifts have been revealed. Both correspond to pentavalent iodine. Their formation was related to the existence of two initial forms of tetravalent tellurium. Unfortunately, no experiments have been made to verify this suggestion.

Thus, β^--decay of ^{129}Te retains the electron structure of the parent atom, hence Mössbauer emission spectroscopy on ^{129}Te can be used to investigate the state of tellurium atoms in frozen solutions [38].

6.4.6. ^{241}Am

^{241}Am is the parent nucleus for the Mössbauer nucleus of ^{237}Np. α-decay of ^{241}Am (see Fig. 6.1) is an example of nuclear transformation involving pronounced recoil (energy of α-particle is 5.5 MeV, recoil energy is 90 keV). Moreover, α-decay produces pronounced ionization due to the electron shell shake-off effect and internal conversion process. The spectrum of charges of the ^{237}Np daughter atom in vacuum has been determined experimentally [39] and found to include ions of 33+ charges. Mössbauer emission spectroscopy on ^{241}Am is, naturally, of much interest as viewed from the standpoint of investigating aftereffects of such strong actions on daughter atom.

The emission spectra of ^{241}Am in frozen solutions were studied by Gal et al. [40]. A study was made on frozen solutions of Am^{3+} in HNO_3 and H_3PO_4, of Am^{4+} in saturated NH_4F and in H_3PO_4, of Am^{5+} in HNO_3, and Am^{6+} (in AmO_2^{2+}) in HNO_3 and H_3PO_4 at 4.2 K.

Distinct from crystalline americium compounds that showed neptunium daughter atoms in the states 3+, 4+ and 5+, the emission spectra of all aformentioned frozen solutions exhibited only Np^{3+}. All spectra represent unresolved quadrupole multiplets with isomer shifts in the vicinity of 42 $\mathrm{mm\,s^{-1}}$ with respect to NpO_2. Spectra of some solutions are presented in Fig. 6.8. The authors [40], naturally, ascribed the spectra to atoms knocked off from their sites by recoil and account for the spectra of frozen solutions showing only Np^{3+} by pronounced reducing action of ice at low temperatures. Such properties of ice as far as we know had not been observed in Mössbauer emission experiments on other isotopes. Neptunium reducing to the 3+ state seems to proceed under peculiar conditions that prevail in the displacement cascade or heat wedge which are produced by recoil atoms.

6.5. CONCLUSION

A study of aftereffects of nuclear transformations in frozen solution permits to gain a better insight into the mechanism responsible for these aftereffects on one hand, since it makes it possible to place decaying atoms in a medium whose properties can be varied over a wide range. On the other hand, it permits recourse to Mössbauer emission spectroscopy in order to investigate the structure of the frozen solution.

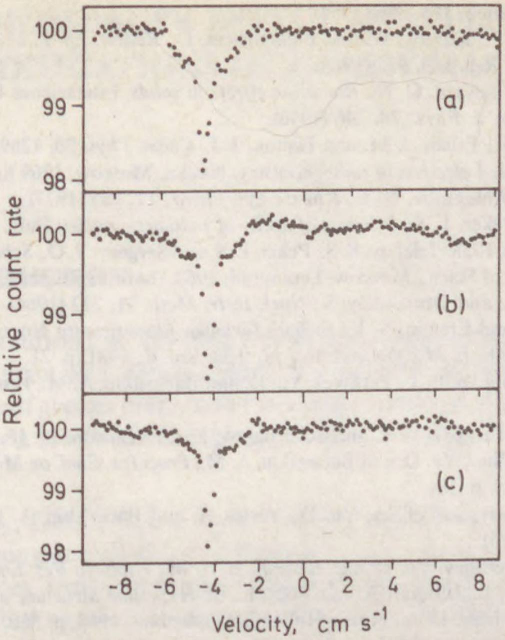

Fig. 6.8. Mössbauer emission spectra of ^{241}Am in frozen solutions [40] at 4.2 K. (a) Am^{6+} (in AmO_2^{2+}) in H_3PO_4, (b) Am^{4+} in H_3PO_4, (c) Am^{3+} in H_3PO_4
Absorber: NpO_2 at 4.2 K

Thus, the investigations suggest that the process of formation of aftereffects of ^{57}Co decay and ^{119m}Sn decay can be described in many cases, including frozen solutions in terms of the competing electron scavenger model (CESM) which, in turn, paved the way to using Mössbauer emission spectroscopy on these isotopes in order to study the structure of cobalt- and tin-containing frozen solutions. What remains open is the question as to the limits of suitability of this technique. A similar conclusion can be made with respect to β^--decay of ^{129}Te. On the other hand, consequences of α-decay of ^{241}Am prevent it from being used as a parent nucleus in Mössbauer investigations of the structure of frozen solutions. As to decays of ^{125m}Te and ^{125}I, the situation is much less clear. In fact, isolated studies have been performed on these isotopes, but more comprehensive investigations have still to be carried out. Indeed, emission spectra in frozen solutions have so far been studied only on a small number of Mössbauer nuclei. Thus, this field of investigations cannot be regarded as exhausted.

REFERENCES

1. Seregin, P. P., Nasredinov, F. S. and Vasiliev, L. N., *Phys. Stat. Sol.* (a) **45**, 11 (1978).
2. Bondarevsky, S. I., Murin, A. N. and Seregin, P. P., *Uspekhi Khimii*, **40**, 95 (1971).
3. Goldanskii, V. I. and Stukan, R. A., *Radiokhimia* **23**, 473 (1981).
4. Kinchin, G. N. and Pease, R. C., *Rep. Prog. Phys.*, **18**, 1 (1955).
5. Erginsoy, C., Vineyard, G. N. and Shimizu, A., *Phys. Rev.* **139**, 118 (1965).

6. Varley, T. O. N., *Nature*, **174**, 886 (1954).
7. Nath, A., Klein, M. P., Kündig, W. and Lichtenstein, D., *Radiat. Eff.* **2**, 211 (1970).
8. Hersh, H. W., *Phys. Rev.* **148**, 928 (1966).
9. Dienes, G. T. and Vineyard, G. N., *Radiation effects in solids*, Interscience Publishers, N. Y., 1957.
10. Brinkman, T. A., *Am. J. Phys.*, **24**, 246 (1956).
11. Baggio–Saitovitch, E., Friedt, J. M. and Danon, J. J., *Chem. Phys.* **56**, 1269 (1972).
12. Pikaev, A. K., *Solvated electron in radiochemistry*, Nauka, Moscow, 1969 (in Russian)
13. Bondarevsky, S. I., Ablesimov, N. E., *Khimia Vys. Energ.*, **11**, 285 (1977).
14. Jelepov, B. S. and Peker, L. S., *Schemes of decay of radioactiv nuclei*, Publ. by USSR Acad. of Scien., Moscow–Leningrad, 1958.; Jelepov, B. S., Peker, L. S. and Sergeev, V. O., *Schemes of decay of radioactive nuclei*. USSR Acad. of Scien., Moscow–Leningrad, 1963. (both in Russian).
15. Levy, L., Mitrani, L. and Ormandjev, S., *Nucl. Instr. Meth.* **31**, 233 (1964).
16. Bondarevsky, S. I. and Eremin, V. V., *Priborí Tekhnika Eksperimenta* No. 6. 57 (1975).
17. Ruby, S. L. and Pelah, J., *Mössbauer Effect Method*, Vol. 6., 1981, p. 21.
18. Kulikov, L. A., Bugaenko, L. T., Perfilyev, Yu, D. and Babeshkin, A. M., *Vestn. MGU, Khim.* No. 3, 347 (1972).
19. Bondarevsky, S. I., Tarasov, V. A. and Scherbakov, E. E., *Radiokhimia*, **15**, 895 (1973).
20. Afanasov, M. I., Perfiliev, Yu. D. and Babeshkin, A. M., *Proc. Int. Conf. on Mössbauer Spectrosc, Cracow*, Poland, Vol. 1., 1975, p. 381.
21. Afanasov, M. I., Nagy, S., Pefiliev, Yu. D., Vértes, A. and Babeshkin, A. M., *Radiochem. Radioanal. Letters*, **23**, 181 (1975).
22. Milgrom, Ya. M., Perfiliev, Yu. D. and Babeshkin, A. M., *Khimiya Vys. Energ.* **12**, 272 (1978).
23. Dézsi, I., Keszthelyi, L., Molnár, B. and Pócs, L., in: *Hyperfine Structure and Nuclear Radiations* eds Matthias, E. and Shirley, D. A., North-Holland, Amsterdam, 1968, p. 566.
24. Mulhem, J. K., Horváth, D., Molnár, B. and Nagy, D. L., *Nucl. Instr. Methods*, **199**, 277 (1982).
25. Nagy, D. L., Doerfler, R., Ritter, G., Waigel, J., Zeman, N. and Molnár, B., *Phys. Letters*, **95A**, 500 (1983).
26. Nagy, D. L., in: *Trends in Mössbauer Spectroscopy* eds Gütlich, P. and Kalvius, G. M., Johannes Gutenberg–Universität Mainz/FRG, 1983, p. 241.
27. Nagy, D. L., Doerfler, R., Molnár, B., Ritter, G., Waigel, J. and Zeman, N., *Hyp. Int.*, **15/16**, 1051 (1983).
28. Pollak, H., *Phys. Sat. Sol.*, **2**, 720 (1962).
29. Bondarevsky, S. I., Izotov, V. I. and Ozernoy, A. N., *Radiokhimiya*, **15**, 891 (1973).
30. Murin, A. N., Bondarevsky, S. I. and Seregin, P. P., *Radiokhimiya*, **11**, 474 (1969).
31. Bondarevsky, S. I. and Tarasov, V. A., *Radiokhimiya*, **14**, 162 (1972).
32. Murin, A. N., Bondarevsky, S. I., Jurdja, V. V. and Tarasov, V. A., *Khim. Vys. Energ.*, **6**, 494 (1972).
33. Lebedev, V. A., Babeshkin, A. M., Nesmeyanov, A. N. and Lamykin, E. V., *Vestn. MGU. Khim.*, No. 5, 45 (1969).
34. Babeshkin, A. M., Perfiliev, Yu. D., Lebedev, V. A., Lamikin, E. V., Kulikov, L. A., Lebedev, R. A. and Nesmeyanov, A. N., *Proc. Conf. on Appl. Mössbauer Effect, Tihany* 1969, Budapest, 1971, p. 697.
35. Babeshkin, A. M., Lamykin, E. V. and Lebedev, V. A. *Vest. MGU. Khim.*, No. 2., 1117 (1970).
36. Savin, E. P. and Seregin, P. P., *Fiz. Tverd. Tela*, **15**, 1291 (1973).
37. Carlson, T. A., Nestor, C. N., Tucker, T. C. and Malik, F. B., *Phys. Rev.*, **169**, 27 (1968).
38. Ablesimov, N. E., Bondarevsky, S. I., Kirin, I. S. and Tarasov, V. A., *Radiokhimiya*, **16**, 919 (1974).
39. de Wieclawik, W., *Comp. Rend. Acad. Sci.*, **266**, B577 (1968).
40. Gal, J., Hadari, Z., Yanir, E., Bauminger, E. R. and Ofer, S., *J. Inorg. Nucl. Chem.*, **32**, 2509 (1970).

7. MÖSSBAUER EFFECT AS APPLIED TO INVESTIGATIONS OF GLASSY MATERIALS

7.1. INTRODUCTION

The freezing of a solution may produce a solid which may or may not be crystalline. If not, the produced material is called a glass. The foregoing sections of this book discuss Mössbauer studies of glasses prepared by freezing aqueous and non-aqueous solutions. Glass is formed as a result of quenching, i.e. rapid freezing of certain types of melts, notably:

(i) Oxides (SiO_2, GeO_2, B_2O_3, P_2O_5, As_2O_3) and mixtures of these oxides with metal oxides forming so-called oxide glasses.

(ii) Chalcogenides, their compounds and melts described as chalcogenide glasses.

(iii) Aqueous solutions of acids, salts and alkalis described as hydrogen-bond glasses.

Problems involved in processes of the formation of oxide as well as chalcogenide glasses are similar to those already considered in the present book with reference to hydrogen-bond glasses. Reviews of particular problems of Mössbauer studies of oxide and chalcogenide glasses are available in the literature, e.g. [1–8]. The present account deals with available investigations on structural rearrangements involved with melt-glass-crystal transitions.

In experimental investigations of the local structure of vitreous materials by conventional methods of X-ray and electron diffraction a great number of difficulties are encountered. The bulk of structure information as obtained by the above methods is contained in the radial distribution function which, in the case of amorphous solids, has a series of maxima. These maxima can be used to determine average interatomic distances and local coordination numbers in the first, second and other spheres. It should be noted that bond angles cannot be determined from the radial distribution functions. Moreover, in the case of multicomponent vitreous systems even the determination of interatomic distances becomes ambiguous, due to a low resolution offered by the method. Therefore, a few versions of different arrangements of the atoms may lead to the same experimental radial distribution function.

In view of the difficulties to be faced in the interpretation of the radial distribution function for multicomponent glasses ever greater attention is being paid to indirect (structure–sensitive) methods of glass structure studies. Mössbauer effect has proved to be most promising. Although failing to provide immediate information on the structure, such as bond distances and angles, this method often facilitates unambiguous identification of close-range structure in amorphous materials.

7.2. OXIDE GLASSES

Of all the oxides, SiO_2, GeO_2, B_2O_3, P_2O_5 and As_2O_3 have the strongest tendency to form glasses in the process of quenching of their melts. Such oxides are termed glass-forming oxides, since they are responsible for a glass structure network. Any of these oxides if melted together with certain metal oxides may form a glass on cooling. Such metal oxides are for example the oxides of the alkali metals (R_2O) and the alkaline earth metals (RO) and are referred to as modifying oxides. Finally, a group of oxides exists that do not yield glasses by themselves, but being melted with modifying oxides they yield stable glasses. Such oxides are termed conventional glass formers, TeO_2, Al_2O_3 and others being typical.

The subject of most Mössbauer studies are silicate, germanate, borate and phosphate glasses because of their scientific and practical interest.

Vitreous silica (SiO_2) is a technologically important material. X-ray investigations by Warren [9] show vitreous silica which consists of tetrahedral (SiO_4), whose vertices are interconnected. The relative orientation of these tetrahedral sites, however, is varying. Consequently, the glass structure lacks long-range order. All the oxygen atoms in the SiO_2 glass are bonded to two silicon atoms. These oxygen atoms are termed bridging atoms. Addition of a modifying oxide to vitreous silica does not change the tetrahedral glass structure network in which the vacancies are randomly filled by the metal ions. Since oxygen atoms are likely to be introduced into the glass together with the metal ions, the O/Si ratio exceeds 2, and thus not all of the oxygen atoms are bonded to two silica atoms, consequently, non-bridging oxygen atoms occur in the glass structure.

The structure of glassy germanium dioxide GeO_2 is of vitreous silica type, i.e. all germanium atoms are fourfold-coordinated and the glass is made up of tetrahedral (GeO_4). Adding alkali metal oxide to glassy GeO_2 the density first increases up to a certain alkali concentration (10–20 mole%) and then decreases. Ivanov and Evstropyev [10] suggested that, in the composition range of less than 10–20 mole% alkali, non-bridging oxygen atoms are not formed, and the addition of alkali metal increases the local coordination number of the germanium atoms from 4 to 6 corresponding to GeO_4 and GeO_6, respectively. It is this fact that is responsible for the density increase. If the alkali metal concentration is increased beyond 20 mole% the contribution of the GeO_6 groups will decrease and non-bridging oxygen atoms will appear and as a result the density will decrease. It must be noted, however, that Murthy and Kirby [11], concluded from studies of IR spectra of $Na_2O—GeO_2$ glass that the role of the GeO_6 groups continues to increase even in the alkali metal concentration range exceeding 20 mole%.

For $Na_2O—B_2O_3$ glass anomalous effects have been discovered concerning the "property to composition" relations.

In contrast to the behaviour of other glasses where the addition of alkali oxide in the range 0–16 mole% decreases the thermal expansion coefficient, this is increased in the case of boron glasses ("boron anomaly"). Warren [12] drew the conclusion from X-ray structure analysis, that beyond the composition range of 0–16 mole% Na_2O the further increase of the alkali metal content does not lead to the forming of non-bridging oxygen but, rather, to the local increase of the coordination number of a fraction of the boron atoms from 3 (for pure B_2O_3) to 4. Warren showed in terms of simple model notions that the change of the local coordination number of the boron atoms must stop at the alkali metal content of 12 mole%. Experimentally this concentration limit was found to be 16 mole% in good agreement with the model calculations. On the other hand, Bray and O'Keefe showed by NMR technique that above the composition range of 0–30 mole% Na_2O the contribution of the fourfold-coordinated boron to the structure of Na_2O—B_2O_3 glass tends to increase. Hence, boron anomaly cannot be accounted for by the presence of non-bridging oxygen at alkali metal concentrations exceeding 16 mole%.

Three crystalline modifications of P_2O_5 are known (hexagonal, orthorhombic, tetragonal). The main elements of the structure of these modifications are (PO_4) tetrahedral, one of the oxygen atoms are non-bridging. P_2O_5 differs in this respect from other glass formers considered. In R_2O—P_2O_5 and RO—P_2O_5 binary glasses the coordination of the phosphorus ion is so stable as to render the phosphorus coordination number unchanged, no matter which modifier is involved. X-ray analysis shows the structure of such glasses to be similar to that of silicate glasses, i.e. tetrahedral groups (PO_4) form its basis and a modifier being added gives rise to an increase of the number of non-bridging oxygen atoms. It has to be pointed out, however, that in the case of RO—P_2O_5 systems in the 0 to 50 mole% composition range of RO the glass structure tends to be more rigid on addition of alkali metal (this evidence is obtained from studies of the expansion coefficient). This, according to Elyard et al. [14], poorly fits into the accepted model which suggests that added RO is to result in the destruction of the originally continuous spatial network made up of tetrahedral (PO_4).

7.2.1. SILICATE GLASSES

7.2.1.1. ^{57}Fe in silicate glasses

The number of Mössbauer studies of ^{57}Fe in silicate glasses is fairly great [15–47]. It was Pollak et al. [15] who carried out such investigations on vitreous silica and Pyrex glass. They used emission Mössbauer spectroscopy. The radionuclide ^{57}Co, a parent atom of the Mössbauer nuclide ^{57m}Fe, was introduced by diffusion into the glass and the samples served as Mössbauer sources. The Mössbauer spectrum showed a single line with the isomer shift $\delta = 0.27$ mm s^{-1} (here and elsewhere the isomer shift of Mössbauer spectra are presented with reference to α-iron). The authors [15] pointed out the anomalous broadening of Mössbauer spectra of glasses ($\Gamma_{exp} = 11\,\Gamma_{nat}$, where $\Gamma_{exp}, \Gamma_{nat}$ = experimental and natural half widths of the Mössbauer line). The broadening of the lines was accounted for by the lack of long-range order.

A detailed study of the $Na_2O \cdot 3SiO_2$ glass containing various amounts of Fe_2O_3 (ranging from 0.1 to 5 mole%) was made by Kirkjian and Buchanan [16–17]; they also refer to [19]. Although all the investigated glasses were found paramagnetic by magnetic susceptibility measurements, yet a hyperfine magnetic splitting (see Fig. 7.1) was observed in Mössbauer spectra at low temperatures only. Thus, for a glass containing 5 mole% Fe_2O_3 no magnetic splitting of Mössbauer spectrum occurred even at 4 K [Fig. 7.1(a)], whereas for a glass with 0.1 mole% Fe_2O_3 content pronounced

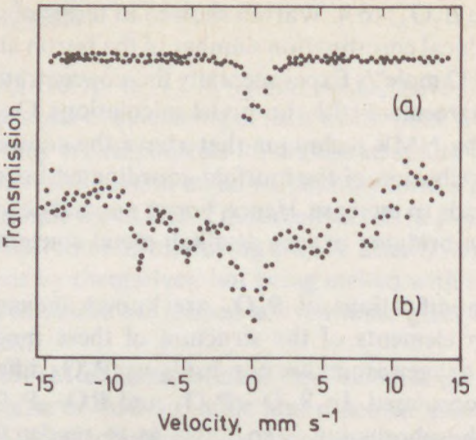

Fig. 7.1. Mössbauer spectra of ^{57}Fe in $Na_2O \cdot 3SiO_2$ with 5 mole% Fe_2O_3 glasses at 4 K (a) and in $Na_2O \cdot 3SiO_2$ with 0.1 mole% Fe_2O_3 glasses at 80 K (b) [16]

splitting was already observed at 80 K (see Fig. 7.1(b)]. This behaviour of the hyperfine structure of Mössbauer spectra is not due to the crystal phase precipitated from the glass but, rather, to relaxation effects. At fairly elevated temperatures Mössbauer spectra of glasses displayed a superposition of two quadrupole doublets that can by their parameters be referred to Fe^{3+}_{tet} and Fe^{2+}_{oct} ions (the share of Fe^{2+}_{oct} becomes noticeable in Mössbauer spectra of glasses prepared under reduction conditions). More recently, Lewis and Drickamer [22] proved this conclusion on the basis of measured results of Mössbauer spectra of $Na_2O \cdot 3SiO_2$ containing 5 mole% Fe_2O_3 glasses at high pressures.

A thorough investigation of R_2O—SiO_2—Fe_2O_3 glasses ($R_2O = Li_2O, Na_2O, K_2O$) has been made by Belyustin et al. [18]. Mössbauer spectra of the glasses showed a

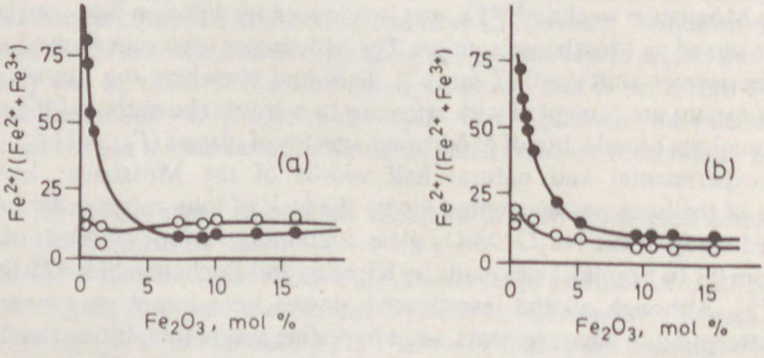

Fig. 7.2. Results of determination of relative Fe^{2+} content in Na_2O—SiO_2—Fe_2O_3 glasses by Mössbauer spectroscopy (●) and chemical analysis (○)

Spectra taken at 295 K [30], (a) glasses containing 16 mole% Na_2O, (b) 24 mole% Na_2O

superposition of two quadrupole doublets as coming from the Fe^{2+} and Fe^{3+} cations, the parameters of spectra depending neither on the type of the alkali ion involved nor on the concentration of alkali metal and Fe_2O_3. Broadened spectra were observed and it was suggested that both the spectrum of Fe^{2+} and that of Fe^{3+} actually correspond to the superposition of two quadrupole doublets (Fe^{2+}_{oct}, Fe^{2+}_{tet} and Fe^{3+}_{oct}, Fe^{3+}_{tet}). The relative content of Fe^{2+} in the glass decreases with increasing contents of the iron and the alkali metal and also in the order K_2O—Na_2O—Li_2O. It should be noted that Boon [27] revealed in the structure of Na_2O—SiO_2—FeO glasses two states for Fe^{2+} ions, both states having octahedral coordination. Labor and Gielen [30] compared the amount of Fe^{2+} in Na_2O—SiO_2—Fe_2O_3 glasses determined by Mössbauer spectroscopy and by chemical analysis (concentration of Na_2O was 16 and 24 mole%, that of the iron varied from 0.1 to 16 mole%). It was assumed that the spectra show a superposition of two quadrupole doublets coming from Fe^{2+}_{tet} and Fe^{3+}_{tet}. The findings obtained by the two methods differ only in the range of low iron concentrations (see Fig. 7.2), which is assigned to oxidation-reduction equilibrium between Fe^{2+} and Fe^{3+}, in the glass which gives preference to Fe^{2+} at lower iron concentrations.

Viewed in the context of comparison of the structures of glass and corresponding crystals, the interest is aroused by studies of Komatsu and Soga [41–42] who investigated crystalline and glassy compounds of $RFeSi_2O_6$ ($R = Na$, K, Cs) by Mössbauer spectroscopy. The coordination of iron in the respective crystals is known from X-ray structure analysis and, as follows from Table 7.1, there is an agreement between the Mössbauer and X-ray data. The transition of the compounds from a crystalline to a glassy state is a result of stabilization of iron atoms in a tetrahedral symmetry, i.e. in the case of $RFeSi_2O_6$ amorphization is accompanied by a rearrangement of the local symmetry for iron atoms with their local coordination number varying from 6 to 4. It is essential that for all compounds investigated the crystall-glass transition is also accompanied by a noticeable increase in the quadrupole

Table 7.1.
Parameters of Mössbauer spectra of ^{57}Fe in crystalline and glassy melts at 295 K [41–44]

Composition	State	Isomer shift, δ mm s^{-1} ($\alpha - Fe$)	Quadrupole splitting, ΔE mm s^{-1}	Charge and coordination state*	
				I	II
$NaFeSi_2O_6$	glass	+0.15	0.73	Fe^{3+}_{tet}	
	crystal	+0.31	0.28	Fe^{3+}_{oct}	Fe^{3+}_{oct}
$KFeSi_2O_6$	glass	+0.15	0.73	Fe^{3+}_{tet}	
	crystal	+0.16	0.44	Fe^{3+}_{tet}	Fe^{3+}_{tet}
$CsFeSi_2O_6$	glass	+0.15	0.78	Fe^{3+}	
	crystal	+0.16	0.73	Fe^{3+}_{tet}	Fe^{3+}_{tet}
$Fe_2O_3 \cdot 5Na_2O \cdot 8SiO_2$	glass	+0.38	0.76	Fe^{3+}_{oct}	
	crystal	+0.51	0.10	Fe^{3+}_{oct}	

Errors in δ were ± 0.01 mm s^{-1}, and ΔE ± 0.02 mm s^{-1}.
* I — data obtained by Mössbauer spectroscopy.
II — data of X-ray analysis.

splitting of Mössbauer spectra (see Table 7.1), i.e. deviation of the local symmetry from cubic symmetry is enhanced.

We shall not consider in great detail the studies of crystallization of multicomponent glasses by Mössbauer spectroscopy. It should be noted that crystallization of the $Fe_2O_3 \cdot 5Na_2O \cdot 8SiO_2$ glass does not result in varying the octahedral symmetry of the immediate neighbourhood of Fe^{3+} ions, however, the magnitude of the quadrupole splitting of the Mössbauer spectra decreases dramatically [41–42] which is in full agreement with the data on the effect of amorphization of the structure of the compounds (see Table 7.1). Investigating crystallization of a $26Fe_2O_3$ $37Na_2O \cdot 37SiO_2$ glass Collins and Mulay [25] found superparamagnetic particles β-Na[FeO_2]. Gorbachev et al. [44] showed that if the concentration of Fe_2O_3 exceeds 5 mole% the crystallization of the Na_2O—Al_2O_3—SiO_2—Fe_2O_3 glasses will produce magnetite. Substitution of Na_2O by CaO inhibits formation of magnetite at unchanged Fe_2O_3 concentrations.

Table 7.2.
Parameters of Mössbauer spectra of ^{57}Fe in silicate glasses [16, 17, 19, 21, 26, 30]

Charge and coordination state	Isomer shift, δ mm s^{-1} (α − Fe)	Quadrupole splitting, ΔE mm s^{-1}
Fe^{3+}_{tet}	−0.01–0.20	less than 1.60
Fe^{3+}_{oct}	0.30–0.55	less than 1.25
Fe^{2+}_{tet}	0.70–0.90	1.80–2.10
Fe^{2+}_{oct}	0.90–1.20	1.80–2.40

A pattern of intricate behaviour of iron was disclosed by Ivamoto et al. [38, 39, 45] for CaO—SiO_2—Fe_2O_3 glasses with 0.2 and 10 mole% Fe_2O_3 content. The synthesis of the glasses was carried out at different partial pressures of oxygen (from 101 325 to 0.03 Pa). At a high concentration of Fe_2O_3 the Mössbauer spectrum of the glass was assigned to three states of iron: Fe^{2+}_{oct}, Fe^{3+}_{oct} and Fe^{3+}_{tet}, and the $Fe^{3+}_{tet}/Fe^{3+}_{oct}$ ratio increased with increasing CaO/SiO_2 ratio. At a low concentration of Fe_2O_3 the Mössbauer spectrum corresponded to Fe^{2+}_{oct}, Fe^{2+}_{tet} and Fe^{3+} (its coordination state being not identified). The Fe^{3+}/Fe^{2+} ratio for all the glasses tends to increase as a function of the CaO/SiO_2 ratio and oxygen partial pressure. For CaO—SiO_2—Fe_2O_3 glasses Levy [36] found Fe^{3+}_{oct}, Fe^{3+}_{tet} and Fe^{2+} (the coordination state not identified). For the glass $Fe_2O_3 \cdot 3CaO \cdot 3SiO_2$ Knorr et al. [33] found magnetic short-range order to appear at temperatures below 7 K, the magnitude of the effective magnetic field on ^{57}Fe nuclei was not temperature-dependent and amounted to 3.1×10^7 A m^{-1}.

References [28, 35, 37, 43, 46, 47] are studies of multicomponent glasses. In particular, Varnek et al. [28] made a study of eight-component (K_2O—CaO—MgO—GaO—Al_2O_3—SiO_2—FeO—Fe_2O_3) glasses revealing two states for the Fe^{2+} ions in glasses synthesized under reduction conditions. Nolet [43] suggests that the Mössbauer spectra for six-component (CaO—MgO—Al_2O_3—TiO_2—SiO_2—Fe_2O_3) glasses also synthesized under reduction conditions be regarded as relating to Fe^{2+}_{oct} ions with permanently varying magnitude of the quadrupole splitting. For CoO—

Al_2O_3—SiO_2 (17 and 25 mole%) glasses at $T \approx 20$ K Bieman et al. [37] observed a hyperfine magnetic structure shown by the Mössbauer emission spectrum of ^{57}Co which, according to the authors, is due to a drastically reduced rate of spin relaxation at low temperatures.

An analysis of Mössbauer studies thus shows that under certain conditions iron is able to stabilize in silicate glasses in all possible valency and coordination states. Table 7.2 presents characteristic values of isomer shifts and quadrupole splittings for Fe^{2+}_{oct}, Fe^{2+}_{tet}, Fe^{3+}_{oct} and Fe^{3+}_{tet} in silicate glasses, the spread in values being determined both by the temperature of spectrum measurements and the composition of the glass.

Table 7.3.
Parameters of Mössbauer spectra of ^{119}Sn in silicate glasses at 295 K [50–53]

Glass composition	Sn^{IV}		Sn^{II}	
	Isomer shift, δ mm s^{-1} (SnO_2)	Quadrupole splitting, ΔE mm s^{-1}	Isomer shift, δ mm s^{-1} (SnO_2)	Quadrupole splitting ΔE mm s^{-1}
Li_2O—SiO_2—SnO_2	−0.19	1.15	2.5–2.8	1.75–2.00
Na_2O—SiO_2—SnO_2	−0.25	1.0		
K_2O—SiO_2—SnO_2	−0.27	0.95		

7.2.1.2. ^{119}Sn in silicate glasses

Like silicon, tin belongs to group IV elements, hence the interest in the behaviour of tin in silicate glasses. References [48–60] concern Mössbauer studies of tin-containing silicate glasses. Mitrofanov and Sidorov [50] were the first to undertake a detailed investigation of R_2O—SiO_2—SnO_2 ($R_2O = Li_2O, Na_2O, K_2O$) glasses. For the glasses the spectra appeared as single broadened lines with isomer shifts corresponding to tetravalent tin (see Table 7.3). The proximity of the isomer shift of tin spectra in glasses and that of SnO_2 made it possible to conclude that oxygen atoms are found in the immediate neighbourhood of tin in the glass. The weak temperature dependence of the Debye–Lamb factor f for ^{119}Sn in the glass ($f_{77\,K}/f_{296\,K} = 1.3$) shows that tin is sixfold-coordinated. The dependence of the isomer shift on the nature of the alkali ion enables us to have an insight into the influence on the tin electron state of atoms not directly associated with tin, such as lithium, sodium, potassium [54].

A thorough analysis of the dependence of f on the composition of Na_2O—SiO_2—SnO_2 glasses was carried out in publications [53, 56, 57]. It turned out that the value of f decreases with increasing content of alkali metal and SnO_2. It is suggested that isomorphous substitution of tin for silicon occurs in the glass structure and due to the difference of the radii of Si^{4+} and Sn^{4+} ions in the above substitution a distortion of the glass structure takes place which is, indeed, responsible for the increase of f with increasing concentration of SnO_2 [53, 56]. The authors of [53] do not rule out the alternative that the dependence of f on the concentration of SnO_2 in the glass may be due to the difference of the coordination numbers of silicon and tin. The dependence of

f on the Na_2O content in the glass may also be attributed to the looseness of the structural network of the glass induced by higher tin concentrations [53, 56].

Evstropyev et al. [53] point out that the temperature dependence of f in the case of Na_2O—SiO_2—SnO_2 glasses has two sections and cannot be described in terms of Debye's model. More recently, Bartenev et al. [58] revealed a similar effect for Na_2O—SiO_2—SnO_2 glasses doped with ZnO_2 and PbO. It is believed that tin in such glasses is involved in two different frameworks (i.e. the glass itself must be microheterogeneous) and this is the reason for the two sections of the temperature dependence of f [58].

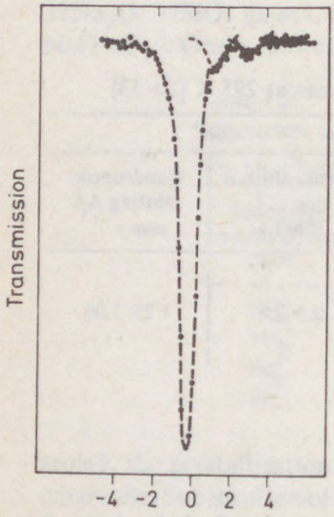

Fig. 7.3. Mössbauer spectrum of ^{119}Sn at 295 K in 22 mole% Na_2O, 73 mole% SiO_2 and 5 mole% SnO_2 [51]

Polozova and Seregin [52] first disclosed that tin in Na_2O—SiO_2—SnO_2 glasses can stabilize in part in a bivalent state (see Fig. 7.3). Then Evstopyev et al. [53, 60] detected bivalent tin in similar glasses synthesized in reductive processes (see Table 7.3). It is suggested that silicates of bivalent tin form in the glass.

Multicomponent silicate glasses are considered in [49, 55], the spectra only showing tetravalent tin to be present. It will be noted that [59] investigates the interaction of tin-containing glasses with sulfur dioxide.

7.2.1.3. Tm, Eu and Sb in silicate glasses

Of other isotopes in silicate glasses were investigated: Tm [61, 62], Eu [63, 64] and Sb [65]. Thallium is trivalent in glasses, its environment is like that in Tm_2O_3. Europium is also trivalent in silicate glasses. In Na_2O—SiO_2—Sb_2O_3 glasses antimony typically stabilizes in a Sb^{III} state although Sb^{V} is present, as well.

7.2.2. GERMANATE GLASSES

Evstropyev et al. [53] have made a study of a Na_2O—GeO_2—SnO_2 glass. Isomer shifts of Mössbauer spectra of ^{119}Sn in germanate glasses correspond to tetravalent tin ($\delta = -0.06\,mm\,s^{-1}$, isomer shifts of spectra of ^{119}Sn being given here and elsewhere with respect to SnO_2) and show a minor quadrupole splitting ($\Delta E = 0.50\,mm\,s^{-1}$). The distinction between the isomer shift of Mössbauer spectra of ^{119}Sn in germanate glasses and that of spectra of silicate glasses of a uniform composition is accounted for by the induction effect, i.e. glasses develop bonds —Sn—O—Si— and —Sn—O—Ge—, and silicon and germanium atoms not immediately associated with tin affect the electron state of tin atoms (induction effect). It is registered that the Debye–Waller factor f does not depend on the composition. This is due to isomorphous substitution of the Ge atoms by Sn atoms. It is considered that coordination polyhedra of Ge and Sn in glasses are identical and due to the proximity of ion radii of Ge and Sn such a substitution results only in a weak distortion of the glass structure network. Based on a Mössbauer investigation of Na_2O—GeO_2—SnO_2 glasses (tin concentration was 0.5 mole%, alkali metal concentration varied from 0 to 35 mole%) Seregina [66] draws a conclusion as to a sixfold coordination of tin in glasses of all compositions, no change is registered in coordination state of tin in the composition range over 20 mole% Na_2O.

7.2.3. BORATE GLASSES

7.2.3.1. ^{57}Fe in borate glasses

Iron-containing borate glasses have been the object of quite a number of Mössbauer studies [67–97]. For most elementary glasses in the B_2O_3—Fe_2O_3 system with Fe_2O_3 concentration ranging from 0.0028 to 0.05 mass fraction the result was obtained that Mössbauer spectrum of ^{57}Fe shows a superposition of a quadrupole doublet and a magnetic sextet [87]. The quadrupole doublet is attributed to Fe^{2+} ions in a high-spin state, and the sextet to the phase Fe_2O_3. Alkali metal addition seems to decrease the crystallite (Fe_2O_3) formation. Crystallization of a $Fe_2O_3 \cdot 8B_2O_3$ glass is shown due to formation of the compounds Fe_3BO_6 and $FeBO_3$ [69, 70].

Of greatest interest are studies of the glass in the R_2O—B_2O_3—Fe_2O_3 system (where $R_2O = Li_2O, Na_2O, K_2O$) [67, 68, 71, 72, 74, 75, 77, 82, 84, 86, 87, 93–97]. Buckrey et al. [67, 68] seem to be the first to have studied Na_2O—B_2O_3—Fe_2O_3 glasses over a wide concentration range of Fe_2O_3. Choice was made of a 33 mole% Na_2O + 67 mole% B_2O_3 with Fe_2O_3 of mass fraction $w = 0.10$–0.35 glass. The Mössbauer spectra of glasses at 298 and 77 K showed well-resolved quadrupole doublets the parameters of which displayed a weak dependence on iron concentration ($\delta = 0.09 - 0.25\,mm\,s^{-1}$, ΔE 1.0 mm s^{-1}). On slow cooling of the melt the Mössbauer spectrum of the glass developed a hyperfine magnetic structure that was referred to isolation of the phase Fe_2O_3. Chaumont et al. [96] point out that for $xLi_2B_2O_4$—$(100-x)LiFe_5O_8$ ($x = 1, 3, 10, 15$ mole%) glasses Mössbauer spectra at 4 K display a hyperfine magnetic structure, i.e. one observes a transition of the glass to a magnetic-ordered state.

Raman et al. [71, 75, 77, 82, 84] have made a Mössbauer study of R_2O—B_2O_3—Fe_2O_3 glasses aimed at detecting unbonded oxygen. For $xR_2O \cdot (94-x)B_2O_3 \cdot 6Fe_2O_3$ (where x is mole%) glasses the Mössbauer spectra taken at room temperature showed quadrupole doublets whose isomer shift gradually decreased with increasing concentration of the alkali metal over the range 0–20 mole% R_2O. This decrease becomes rather drastic at 22 mole% (see Fig. 7.4). It was concluded that iron as Fe^{3+} is incorporated into the glass structure network, and with varying x the polyhedron of oxygen atoms surrounding the Fe^{3+} ion changes from octahedral to tetrahedral. This structural change is due to non-bridging oxygen in alkali concentration ranges beyond 20 mole%. More recently, Nishida et al. [93, 95] reached a similar conclusion for $xK_2O \cdot (100-x)B_2O_3 \cdot 7Fe_2O_3$ ($0 < x$ mole% < 40) glasses. The Mössbauer spectra of the glasses showed the same quadrupole doublets. Moreover, at $x > 20$ mole% a drastic decrease occurred in the isomer shift and also in the quadrupole splitting which is believed to be induced by a change in the coordination state of Fe^{3+} ions owing to the presence of non-bridging oxygen. Nishida et al. [94] investigated the effect of γ-irradiation (^{60}Co) on $xK_2O \cdot 0.33Fe_2O_3 \cdot (100-x)B_2O_3$ ($15 \leq x$ mole% < 40) glasses showing non-bridging oxygen in their structure with $x > 20$ mole%. The Mössbauer spectra of the starting glasses show the quadrupole doublets coming from Fe^{3+}_{tet}. Irradiation gave rise to another quadrupole doublet corresponding to Fe^{2+}_{tet}, the intensity of this doublet first increasing with the irradiation dose to reach 5.16×10^4 C kg^{-1} then remaining constant. It is suggested that the appearance of the spectrum of Fe^{2+}_{tet} may be due to the transfer of the electron from the non-bridging oxygen to the ion Fe^{3+}_{tet} so that the intensity of the spectrum of Fe^{2+}_{tet} is associated with the contribution of

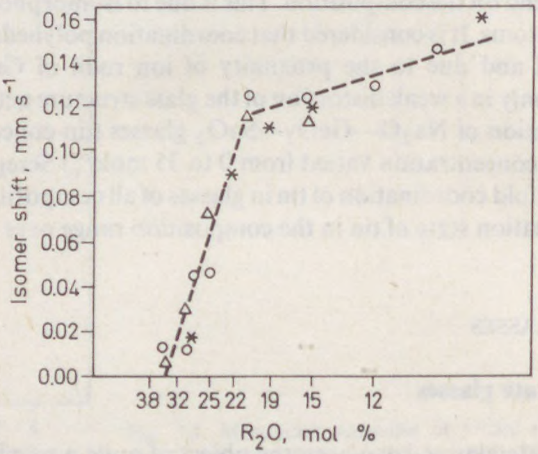

Fig. 7.4. Isomer shift of Mössbauer spectra of ^{57}Fe versus alkali metal concentration dependence in $xNa_2O \cdot 6Fe_2O_3 \cdot B_2O_3$ (○), $xNa_2O \cdot Al_2O_3 \cdot 6Fe_2O_3 \cdot B_2O_3$ (△) and $xK_2O \cdot 6Fe_2O_3 \cdot B_2O_3$ (✱) glasses [84]

R_2O: Na_2O and K_2O, resp.

non-bridging oxygen in glasses. Finally, Nishida et al. [97] have conducted a Mössbauer effect investigation of K_2O—B_2O_3 glasses with a low Fe_2O_3 content over the temperature range from room temperature to 80 K. As opposed to room temperature when the spectrum showed a quadrupole doublet corresponding to Fe^{3+}_{tet}, at 80 K, apart from the doublet, it exhibits a hyperfine pattern due to Fe^{3+}_{tet} ions resulting from the effects of paramagnetic relaxation. At a concentration of alkali below 20 mole% the isomer shifts of both spectra were not dependent on the glass composition, decreased with increasing alkali metal concentrations beyond 20 mole% K_2O. The area beneath the relaxation is independent of the composition of the glass at a K_2O concentration below 20 mole%, but increases with increasing K_2O concentration above this limit. These effects are attributed to non-bridging oxygen forming in the glasses at K_2O concentrations above 20 mole%.

Experiments on BaO—B_2O_3—Fe_2O_3 glasses were reported in [76, 78, 85, 88, 89, 92]. Over a composition range of 3–7 mole% Fe_2O_3 Mössbauer spectra exhibit Fe^{3+} ($\delta = 0.32$–$0.80\ \mathrm{mm\ s^{-1}}$, $\Delta E = 1.10$–$1.21\ \mathrm{mm\ s^{-1}}$). The authors in [78] consider that iron appears in clusters in the glass. Siono et al. [85, 88, 89] show that for $Fe_2O_3/BaO > 1$ a quadrupole doublet is observed at room temperature coming from Fe^{3+}_{tet} (see Table 7.4). At $T < 70$ K the spectra exhibit a magnetic hyperfine structure with $H_{eff} \approx 3.58 \times 10^7\ \mathrm{A\ m^{-1}}$ which is also typical of Fe^{3+}_{tet}. If $Fe_2O_3/BaO < 1$, the Mössbauer spectrum shows at room temperature two quadrupole doublets corresponding to Fe^{3+}_{tet} and Fe^{3+}_{oct} as well as an additional quadrupole doublet coming from Fe^{2+}. It is pointed out that the latter isomer shift is intermediate between those of Fe^{2+} and Fe^{3+} (see Table 7.4). Hence, it seems likely that this spectrum is assigned to the state induced by electron exchange between Fe^{2+} and Fe^{3+}. At $T < 140$ K the spectra of such glasses exhibit two sextets ($H_1 \approx 3.58 \times 10^7\ \mathrm{A\ m^{-1}}$ and $H_2 \approx 3.98 \times 10^7\ \mathrm{A\ m^{-1}}$) corresponding to Fe^{3+}_{tet} and Fe^{3+}_{oct} (the intensity of the sextet of Fe^{3+} proves too small and is not shown by experimental spectra). It is to be noted that the authors of [73], having investigated CaO—B_2O_3—Fe_2O_3 glasses revealed only Fe^{2+}_{oct}. After a prolonged annealing of such glasses the phase Fe_2O_3 precipitates.

Table 7.4.
Parameters of Mössbauer spectra of ^{57}Fe in BaO—B_2O_3—Fe_2O_3 borate glasses at room temperature [85, 88, 89]

Charge and coordination state	Isomer shift, δ $\mathrm{mm\ s^{-1}}$ (α-Fe)	Quadrupole splitting, ΔE $\mathrm{mm\ s^{-1}}$
Fe^{3+}_{tet}	0.23–0.35	0.84–0.97
Fe^{3+}_{oct}	0.37	0.32–0.42
Fe^{2+}, coordination state not identified	0.50–0.53	1.55–1.66

A similarly detailed study was made of glasses in the PbO—B_2O_3—Fe_2O_3 system [80, 81, 83, 90, 91]. For example Ardelean et al. [80, 81, 91] revealed for $(1-x)(PbO \cdot 3B_2O_3) \cdot xFe_2O_3$ ($0.10 \leqq x \leqq 0.50$) glasses Mössbauer spectra exhibiting three lines [see Fig. 7.5(a)]. The spectra were treated on the assumption that they show a superposition of four quadrupole doublets. The workers [80, 81, 91] believe these spectra to correspond to Fe^{3+}_{tet}, Fe^{3+}_{oct} their isomer shifts are identical, $\delta = 0.2$–$0.3\,mm\,s^{-1}$, the quadrupole splittings being different: 0.2–0.3 mm s^{-1} for Fe^{2+}(a), and 2.6–3.0 mm s^{-1} for Fe^{2+}(b). The $Fe^{3+}_{tet}/Fe^{3+}_{oct}$ ratio is actually independent of the ion concentration in the glass. The overall concentration of Fe^{3+}, on the other hand, increases almost linearly with the growth of the concentration of iron [see Fig. 7.5(b)]. At $T \approx 78$ K the spectra showed no magnetic hyperfine patterns which points to the absence of iron clusters in the glass.

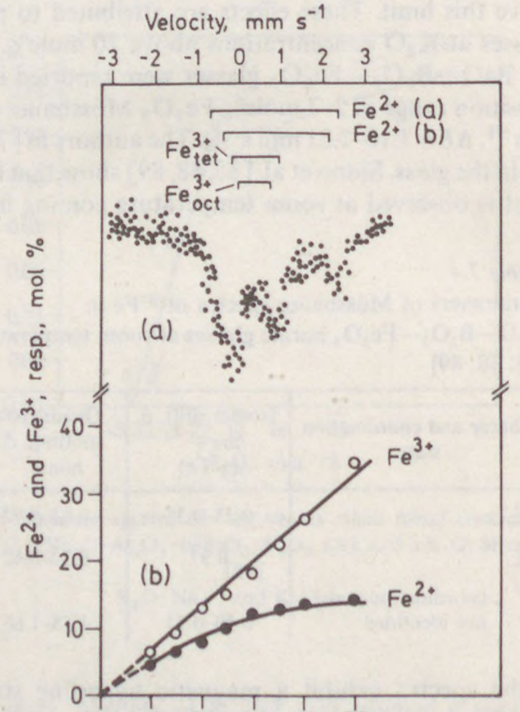

Fig. 7.5. Mössbauer spectrum of ^{57}Fe in 70 mole% $PbO \cdot 3B_2O + 30$ mole% Fe_2O_3 glass at 296 K. (a) Fe^{3+} [80] and Fe^{2+} concentration [81] versus iron content, (b) dependence in PbO—B_2O_3—Fe_2O_3 glasses [81]. Spectrum (a) shown is decomposed into four quadrupole doublets

Investigating $PbO \cdot 2B_2O_3$ glasses with mass fraction $w\,Fe_2O_3$ $(0.05 \leqq w \leqq 0.30)$ Sekhon and Kama [83] showed that the Mössbauer spectra have quadrupole doublets ($\delta = 0.24$–$0.31\,mm\,s^{-1}$, $\Delta E = 1.15$–$1.20\,mm\,s^{-1}$) coming from a high-spin Fe^{3+}, if $w < 0.20$. With $w > 0.20$ apart from the quadrupole doublet a sextet appears referable to the phase Fe_2O_3. The same authors [90] investigated $xPbO \cdot (1-x)B_2O_3$ with 10 mole% Fe_2O_3 ($0 \leqq x \leqq 0.85$ in steps of 0.05) glasses. Over the range $0.25 \leqq x \leqq 0.85$ the Mössbauer spectrum exhibited a quadrupole doublet, and with $x < 0.25$, a superposition of a quadrupole doublet and a sextet. The magnitude of the quadrupole splitting showed dependence on x. Interpreting this dependence the above authors [90] relied on the model according to which at $x > 0.25$ non-bridging oxygen is formed resulting in the variation of δ and ΔE. The magnetically split spectrum is attributable to the phase Fe_2O_3 consisting of small particles (≈ 20 nm).

Polyalkaline borate glasses are the object of Mössbauer investigations reported in [70, 79]. It is shown that in $w\text{Li}_2\text{O} \cdot (0.35-w)\text{PbO} \cdot 0.1\,\text{Fe}_2\text{O}_3 \cdot 0.55\,\text{B}_2\text{O}_3$ ($0 \leqq w \leqq 0.12$) glasses iron stabilizes as Fe^{2+} and Fe^{3+}, the contribution of Fe^{2+} decreasing with the growth of w and becoming zero at $w = 0.117$ [79]. For Na_2O—Li_2O—B_2O_3—Fe_2O_3 glasses the shape of the Mössbauer spectra depends on the concentration of iron [70]. At iron concentrations below 0.25 mass fraction the spectrum shows a superposition of two quadrupole doublets that markedly broaden at 4.2 K. At concentrations exceeding 0.25 mass fraction of iron, apart from the doublets, a complex pattern appears attributable to the phases Fe_3O_4, α-Fe_2O_3 and γ-Fe_2O_3.

7.2.3.2. Sn and Sb in borate glasses

Mössbauer spectroscopic studies of tin-containing borate glasses were published in [49, 53, 86, 99]. Mitrofanov et Sidorov [49] made a comparison of the Mössbauer spectra of ^{119}Sn in R_2O—SiO_2—SnO_2 and R_2O—B_2O_3—SnO_2 ($R_2O = Li_2O, Na_2O, K_2O$) glasses. The silicate glasses exhibited a single line; the borate glasses a quadrupole doublet ($\delta = -0.08 - -0.15\,\text{mm}\,\text{s}^{-1}$, $\Delta E = 0.65 - 0.90\,\text{mm}\,\text{s}^{-1}$). The difference in the magnitudes of the isomer shifts is accounted for by the formation of —Sn—O—Si— and —Sn—O—B— bonds, the atoms not immediately associated with tin, such as Si or B atoms, affecting electrons of tin state. In the borate glasses tin stabilizes in a tetravalent state. In the Li_2O—Na_2O—K_2O series the value is regularly shifted toward the region of negative rates. Also this shift can be attributed to the induction effect.

Evstropyev et al. [53], Eissa et al. [98] obtained for Na_2O—B_2O_3—SnO_2 glasses similar results, whereas Dannheim et al. [86], apart from Sn^{4+}, found Sn^{2+} in Na_2O—B_2O_3 glasses, the Sn^{4+}/Sn^{2+} ratio depending only on the composition of the glasses. Paul et al. [99] in a binary B_2O_3—SnO glass detected bivalent tin only. This effect is attributable to a higher ionicity of the tin-oxygen bond in a glassy medium. The value ΔE is independent of the glass composition, the value δ, on the other hand, increases with increasing SnO concentration and attains a peak value at the composition $SnO \cdot 4B_2O_3$ to decrease afterwards.

Paul et al. [65] made a study of Na_2O—B_2O_3—Sb_2O_3 glasses. The Mössbauer spectra of ^{121}Sb in such glasses correspond to Sb^{III} (the most intense line) and Sb^{V}. For a glass with $Na_2O/B_2O_3 = 1:2$ and Sb_2O_3 concentration from 2.5 to 25.7 mole% the value δ for Sb^{III} is independent of the composition and equal to δ of bulk Sb_2O_3. It is concluded that the interaction between Sb_2O_3 and the glass is weak in such glasses. For glasses containing 5 mole% Sb_2O_3 but with a different Na_2O/B_2O_3 ratio the magnitude of the isomeric shift of ^{121}Sb spectra is displaced to the negative rate region as the Na_2O content increases. This is accounted for by an increased ionicity of the antimony-oxygen bond.

7.2.4. PHOSPHATE GLASSES

7.2.4.1. ^{57}Fe in phosphate glasses

Iron-containing phosphate glasses have been investigated by Mössbauer spectroscopy on ^{57}Fe reported in [16, 22, 100–107]. A study of the influence of the crystal–glass transition on the structure and magnetic properties of the $\mathrm{Fe(PO_3)_3}$ compounds has been carried out by Kurkjian et al. [16]. The crystalline compound goes to an antiferromagnetic state at $T_N = 10\,\mathrm{K}$. As seen from Fig. 7.6, at 4 K the Mössbauer spectrum of (crystalline) $\mathrm{Fe(PO_3)_3}$ exhibits a well resolved magnetic splitting. Judged from the magnetic susceptibility data for a glass of the same composition the transition to a magnetic-ordered state occurs at $T = 1.2\,\mathrm{K}$. However, as can be inferred from Fig. 7.6, the Mössbauer spectrum of glassy $\mathrm{Fe(PO_3)_3}$ even at 4 K shows a magnetically unresolved structure which seems due to electron relaxation processes. It is essential, that even at $T > T_N$ there is a difference between the Mössbauer spectra of a crystalline and glassy $\mathrm{Fe(PO_3)_3}$. As seen from Fig. 7.6, the crystal Mössbauer spectrum is informative for one state of iron atoms, whereas the glass spectrum corresponds at least to two states, the crystal-glass transition being followed by a change in symmetry of the immediate neighbourhood of iron atoms (the crystal Mössbauer spectrum is a single line, that of the glass is a triple line). A similar effect has been discovered by the authors of [100, 101] investigating $\mathrm{RPO_3—Fe_2O_3}$ (R = Li, Na, K) glasses. They established that glass crystallization gives rise to a marked change in the quadrupole splitting of the Mössbauer spectra, even though the octahedral environment of $\mathrm{Fe^{3+}}$ atoms does not vary at this.

For alumophosphate glasses containing 10 mole% $\mathrm{Fe_3O_4}$ and 10 mole% $\mathrm{MgO \cdot 40Fe_3O_4 \cdot 50P_2O_5}$ the presence of $\mathrm{Fe^{3+}_{oct}}$ and $\mathrm{Fe^{2+}_{oct}}$ has been discovered [102, 105]. Similar states of iron atoms have been disclosed by Lewis et al. [22] investigating the effect of pressure on the parameters of the spectra of phosphate glasses (cf. also [107]).

Nishida et al. [106] have made a study of $x\mathrm{K_2O} \cdot (100-x)\mathrm{P_2O_5} \cdot 7\mathrm{Fe_2O_3}$ $(0 \leqq x \leqq 50$ mole%) glasses. The Mössbauer spectra of the glasses indicate the presence of $\mathrm{Fe^{3+}_{oct}}$ and

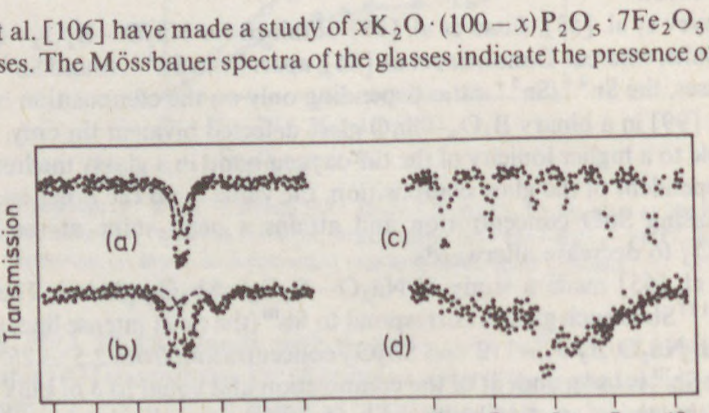

Fig. 7.6. Mössbauer spectra of $^{57}\mathrm{Fe(PO_3)_3}$ at 295 (a, b), and at 4 K (c, d) in crystalline (a, b) and glassy (c, d) states [16]

Fe^{2+}_{oct}. The quadrupole splitting of the spectra decreases with increasing concentration of the alkali metal over the range from 0 to 30 mole% dramatically increasing with a further increase of the K_2O content. Irradiation of the glasses with ^{60}Co γ-quanta at room temperature results in a smaller contribution of Fe^{2+}_{oct} attributable to the transfer of electrons from Fe^{2+}_{oct} to non-bridging oxygen atoms. Takashima et al. [104], studying the effect of reactor irradiation on the state of iron atoms in $FeO \cdot KPO_3$ and $Fe_2O_3 \cdot KPO_3$ glasses, showed that the reduction processes of Fe^{2+} to Fe^{+}, and Fe^{3+} to Fe^{2+} occur.

7.2.4.2. Sn and Sb in phosphate glasses

Evstropyev et al. [53] have investigated tin-containing phosphate glasses of the Na_2O—P_2O_5—SnO system. The Mössbauer spectra of ^{119}Sn showed well resolved quadrupole doublets assigned to bivalent tin ($\delta = 3.60\,\mathrm{mm\,s^{-1}}$, $\Delta E = 1.80\,\mathrm{mm\,s^{-1}}$). Glasses have also been prepared in the P_2O_5—SnO and P_2O_5—SnO_2 binary systems. The parameters of the Mössbauer spectra of ^{119}Sn in such glasses agreed with those of alkali metal-containing glasses.

In Na_2O—P_2O_5—Sb_2O_3 glasses the Mössbauer spectra of ^{121}Sn display the presence of Sb^{III}, even if antimony partially stabilizes as Sb^{V} [65, 108].

7.2.5. GLASSES CONTAINING A FEW GLASS FORMERS

7.2.5.1. ^{57}Fe

Burzo et al. [109] investigating 80 $[(1-x)PbO \cdot xGeO_2 \cdot 3B_2O_3] \cdot 20Fe_2O_3\,(x \leqq 0.25)$ glasses found the Mössbauer spectrum of ^{57}Fe to display a superposition of four quadrupole doublets corresponding to Fe^{2+}_{tet}, Fe^{2+}_{oct}, Fe^{3+}_{tet} and Fe^{3+}_{oct}. The relative concentration of Fe^{2+} in the glass decreases from 0.4 (at $x = 0$) to 0.3 (at $x = 0.25$). Menil et al. [100] have measured the Mössbauer spectra of ^{57}Fe in Na_2O—P_2O_5—NaF—Fe_2O_3 glasses (Fig. 7.7) that showed a superposition of three quadrupole doublets corresponding to one Fe^{3+}_{oct} state and two Fe^{2+}_{oct} states. The authors found no apparent correlation between the composition of the glasses and contribution of Fe^{2+} in the glass. For a $Fe_{0.39}Na_{0.61}P_{0.36}O_{1.22}F_{0.92}$ glass the Mössbauer spectra have been measured over a temperature range of 4.2–293 K. At $T < 7$ K the spectrum shows an unresolved magnetic splitting (see Fig. 7.7) which is associated with the transition of the glass to an antiferromagnetic state. Taragin and Eisenstein [111] have found Fe^{2+}_{tet} and Fe^{3+}_{tet} in boronsilicate glasses and made the conclusion that Fe^{3+}_{tet} ions substitute the silicon ions in the tetrahedral (SiO_4) structure.

Nishida et al. [112] have made a Mössbauer study of K_2O—$(100-x)$ $(B_2O_3 \cdot SiO_2)$—$7Fe_2O_3$ ($12 \leqq x$ mole% $\leqq 40$) glasses, the SiO_2/B_2O_3 ratio being 1 or 2. The Mössbauer spectra were found to show Fe^{3+}_{tet} in the glass. As the concentration of alkali metal increases over the range 0 to 18 mole% the values δ and ΔE decrease monotonously. This is attributed to non-bridging oxygen being formed.

7.2.5.2. ^{119}Sn

Takachinsky et al. [113] have conducted a study of Al_2O_3—SiO_2—B_2O_3—SnO_2 glasses by Mössbauer spectroscopy on the nuclide ^{119}Sn discovering in the glasses investigated both bivalent and tetravalent tin. The parameters of the spectra are $\delta = 3.40\,\mathrm{mm\,s^{-1}}$, $\Delta E = 1.84\,\mathrm{mm\,s^{-1}}$ for Sn^{II} and $\delta = 0.00\,\mathrm{mm\,s^{-1}}$ for Sn^{IV}. The substitution of SiO_2 by B_2O_3 (or Al_2O_3) results in an increase of the amount of Sn^{II} which is accounted for by the fourfold-coordination of the boron and aluminium in the glass (which results in "stripping" tin and Sn^{IV} transforming into Sn^{II}).

Bartenev et al. [114] have investigated crystallization of multi-component (Al_2O_3—MgO—TiO_2—SiO_2—B_2O_3—SnO_2) glasses. Tin is present in the glasses in two states (Sn^{II} and Sn^{IV}, see Table 7.5). No SnO_2 or SnO is formed in the crystallization process, but, rather, a solid solution of substitution (or incorporation) of tin in one or another phase (see Table 7.5). It should be noted, that this observation is inconsistent with the data reported by the authors of [49] who showed crystallization of Na_2O—Al_2O_3—SiO_2—SnO_2 glasses to give rise to the SnO_2 phase.

Table 7.5.

Parameters of Mössbauer spectra of ^{119}Sn in crystalline and glassy alloys in the Al_2O_3—MgO—TiO_2—SiO_2—B_2O_3—SnO_2 system at room temperature [114]

State	Sn^{IV}		Sn^{II}	
	Isomer shift, δ $\mathrm{mm\,s^{-1}}$ (SnO_2)	Half width, Γ $\mathrm{mm\,s^{-1}}$	Isomer shift, δ $\mathrm{mm\,s^{-1}}$ (SnO_2)	Quadrupole splitting ΔE $\mathrm{mm\,s^{-1}}$
Glass	0.03	1.91	3.58	1.85
Crystal	0.07	1.22	3.37	2.04
Error	±0.02	±0.02	±0.07	±0.07

7.3. CHALCOGENIDE GLASSES

Recent years have witnessed an ever-growing interest on the part of researchers in investigations of amorphous semiconductors, in particular, glassy semiconductors. This interest can be explained by both the practical value of the above type of semiconducting materials and the purely scientific singificance of information thus obtained.

All principal properties of semiconductors are known to be due to their intrinsic structure and the behaviour of impurity atoms [115, 116]. Amorphization of a compound or an alloy brings about changes in many of their properties, such as conductivity, carrier mobility and others. It is believed that these changes are associated with the disappearance of a long-range order and perhaps with a variation of the close-range order as well. In view of the challenge presented by the interpretation of the radial distribution function of glassy materials more and more studies appear dealing with the structure of glassy semiconductors using indirect techniques. It would be appropriate to remark that it is these indirect techniques that first made it possible to discover semiconductors for which melting is accompanied by short-range order rearrangement and that these conclusions were confirmed by X-ray analysis [117].

No clear-cut picture has yet been inferred of the behaviour of impurity atoms in glassy semiconductors. As early as 1965 Kolomiets et al. [118] showed amorphization of chalcogenide semiconductors to result in the disappearance of impurity conductivity. Addition of impurities in high concentrations to chalcogenide glasses is likely to noticeably change these electric properties. Although a great number of experiments and theoretical studies were made, the problem concerning the anomalous behaviour of impurities in amorphous semiconductors remains open. This is primarily due to the fact that direct methods of investigation of the state of the impurity atoms (such as the determination of their charge, electron structure, site in the matrix) in glassy materials are few, and the possibilities which they offer are limited. Since the parameters of the Mössbauer spectra are typically determined by the nature and symmetry of the immediate neighbourhood of the atoms under investigation, it can be hoped that Mössbauer effect will be used to best advantage to enable us to have insight into the structure of glassy semiconductors and the state of the impurity atoms.

7.3.1. CHALCOGENIDES AND THEIR COMPOUNDS

Arsenic telluride As_2Te_3 and the melt based on it $As_2Se_3 \cdot As_2Te_3$ were the first objects of Mössbauer studies of vitreous semiconductors (involving nuclides ^{129m}Te [119, 120] and ^{125}Te [120–124]). The compound As_2Te_3 has essentially been the object of a

Table 7.6.
Parameters of Mössbauer spectra of ^{125}Te of glassy and crystalline semiconductors at 80 K [120, 132, 160, 163]

Composition	State	Isomer shift, δ (ZnTe) mm s^{-1}	Quadrupole splitting, ΔE mm s^{-1}
As_2Te_3	crystal glass	0.10 0.50	2 7.75
$As_4Te_5I_2$	crystal glass	0.00	3.50
$TlAsTe_2$	crystal glass	0.00 and 0.05 0.46	2.0 and 7.00 8.60
$Si_{15}Te_{85}$	crystal glass	0.00 and 0.59 0.37	6.8 and 7.35 8.75
$Ge_{15}Te_{95}$	crystal glass	0.01 and 0.59 0.66	2.0 and 7.35 8.45
Si_2Te_3	crystal	0.00	6.80
GeTe	crystal	0.01	2.0
Te	crystal	0.59	7.35
Error		±0.15	±0.25

number of X-ray structure investigations of high sensitivity, and it is this very compound that has been responsible for an unambiguous interpretation of radial distribution curves for glassy samples.

The Mössbauer spectra of As_2Te_3 both on the isotopes ^{129}Te and ^{129m}Te (see Table 7.6) provide unambiguous evidence on the change of the local arrangement of tellurium atoms in the process of amorphization of As_2Te_3. The crystal-glass transition is accompanied by a pronounced increase in the quadrupole splitting of the Mössbauer spectra which can only be accounted for by a lowered symmetry in the immediate neighbourhood of the tellurium atoms. It is inferred from findings [123] of sensitive X-ray structure studies that tellurium atoms occupy three nonequivalent positions in the structure of crystalline As_2Te_3. According to the Mössbauer data, amorphization of As_2Te_3 results not only in a rearrangement of the short-range structure but in disappearance of one of the states of tellurium atoms as well. For an $As_2Se_3 \cdot As_2Te_3$ alloy, amorphization does not bring about any changes in the parameters of the Mössbauer spectra of ^{125}Te which points to a similarity (identity) between the structures of the glass and the crystal [120, 124].

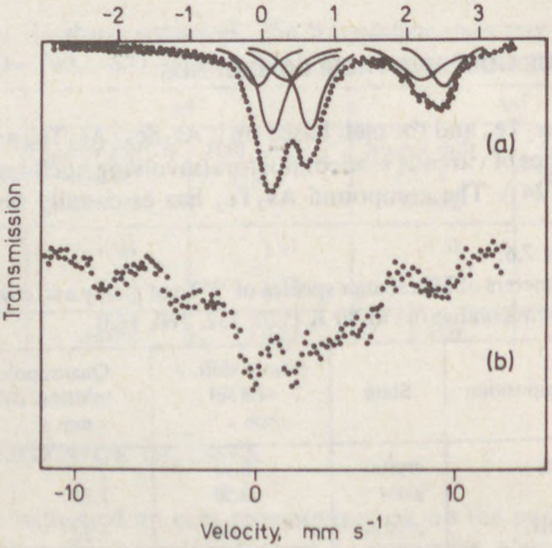

Fig. 7.7. Mössbauer spectra of ^{57}Fe in $Fe_{0.39}Na_{0.61}P_{0.36}O_{1.22}F_{0.99}$ glass at 293 (a) and at 4.2 K (b) [110]

A more complex semiconducting compound, $As_4Te_5I_2$, has been investigated both in the crystalline and the glassy state by Mössbauer spectroscopy on the two nuclides ^{125}Te and ^{127}I [125–127]. Like in the case of As_2Te_3, the crystal–glass transition in $As_4Te_5I_2$ is accompanied by a pronounced increase in the quadrupole splitting of the Mössbauer spectra (see Figs 7.8, 7.9 and Table 7.6). A conclusion is made that the result of amorphization of $As_4Te_5I_2$ is a lowered local symmetry around tellurium and iodine atoms. The authors of [121, 125] have made a similar comparison of the Mössbauer spectra of ^{127}I for AsIS and AsISe in a crystalline and vitreous state. In these

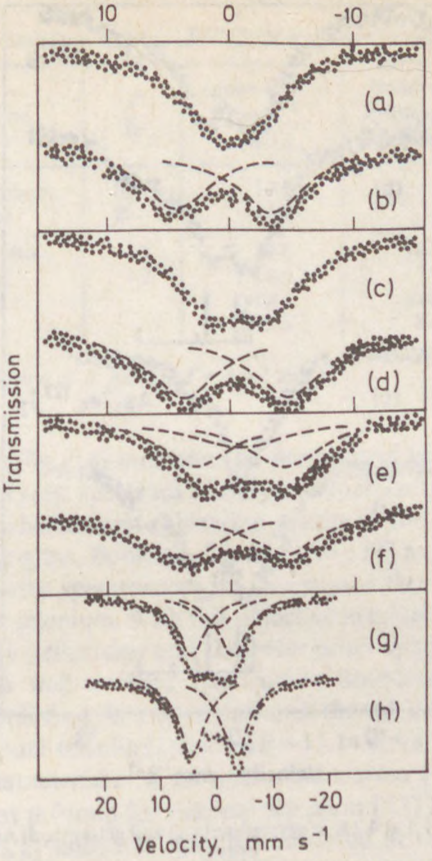

Fig. 7.8. Mössbauer spectra of ^{125}Te at 80 K in crystalline (a, c, e, g) and glassy (b, d, f, h) As_2Te_3 (a, b), $As_4Te_5I_2$ (c, d). $TlAsTe_2$ (e, f) and $Ge_{15}Te_{85}$ (g, h) [120, 121, 126]

compounds the crystal–glass transition does not cause any essential changes in the Mössbauer spectra of ^{127}I (see Fig. 7.9 and Table 7.7) which is indicative of the persistence of the close-range structure of AsIS and AsISe in this transition.

Antimony chalcogenides (Sb_2S_3 and Sb_2Se_3) have been studied by Mössbauer spectroscopy in crystalline and amorphous states on the isotope ^{121}Sb [128–130]. As opposed to Sb_2S_3 where amorphization does not bring about any marked change in the parameters of Mössbauer spectra (in both states *one* position has been detected for the antimony atoms), the amorphization of Sb_2Se_3 gives rise to a noticeable change in the fine structure of the Mössbauer spectra as two states of antimony have been observed in the crystalline compound which shows a fit to X-ray structure analysis data [131], but in the amorphous compound only one state appears (see Table 7.8).

As an illustration of the possibilities offered by the Mössbauer effect for structural investigations of glasses, reference should be made to the Mössbauer spectra of ^{125}Te for a crystalline and a glassy compound $TlAsTe_2$ [132]. Analysis of the spectra of the

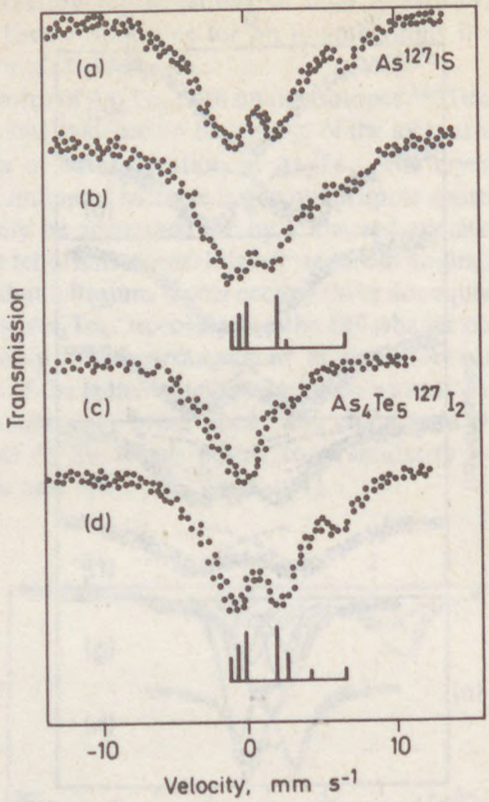

Fig. 7.9. Mössbauer spectra of ^{127}I at 4.2 K in crystalline (a, c) and glassy (b, d) AsIS (a, b) and $As_4Te_5I_2$ (c, d) [121]

The stick pattern shows the line positions of quadrupole multiplets for glasses

Table 7.7

Parameters of Mössbauer spectra of ^{127}I of glassy and crystalline compounds at 4.2 K [125–127]

Compound	State	Isomer shift, δ (ZnTe) mm s^{-1}	e^2qQ* mm s^{-1}
AsIS	crystal	−1.20	43.5
	glass	−1.30	45.0
AsISe	crystal	−1.25	42.6
	glass	−1.40	43.9
$As_4Te_5I_2$	crystal	−1.35	22.6
	glass	−1.50	31.4
Error		±0.25	±4.0

* e^2qQ = quadrupole interaction constant

Table 7.8.

Parameters of Mössbauer spectra of ^{121}Sb of antimony chalcogenides [128–129]

Compound	State	T K	Isomer shift, δ mm s^{-1} (SnO$_2$)	Quadrupole splitting, ΔE mm s^{-1}	Halfwidth, Γ mm s^{-1}
Sb_2S_3	amorphous	80	-12.7		5.2
	crystal	80	-14.3		4.3
Sb_2Se_3	amorphous	4.2	-13.6	10.9	
	crystal	4.2	-12.6 and 15.5	7.9 and 8.4	

Errors in determination of δ, ΔE and $\Gamma = \pm 0.2$ mm s^{-1}

crystalline compound (Fig. 7.8) indicates the presence of two tellurium states in the crystal structure (the crystal spectrum displays a superposition of a single line and a quadrupole doublet), whereas amorphization results in the stabilization of only one state of tellurium in the glass. Boolchand et al. [133–139] as well as Jones [140] have used Mössbauer impurity spectroscopy to investigate the short-range structure of crystalline and vitreous selenium. With this objective in mind selenium was doped with an isoelectron impurity (tellurium) and the Mössbauer spectra of ^{125}Te were taken. The spectra displayed well-resolved quadrupole doublets, but rather led to an increased quadrupole splitting. An extrapolation of the value ΔE for alloys of $Te_{1-x}Se_x$ glasses with $x = 1$ (for pure selenium) yields $\Delta E = 11.14$ mm s^{-1} [133], a value close to $\Delta E = 11.33$ mm s^{-1} characteristic of monoclinic selenium [137], yet different from $\Delta E = 10.44$ mm s^{-1} that is found for trigonal selenium [137] (experiments [133, 137] dealt with a $Se_{0.98}Te_{0.02}$ alloy). It can also be noted at this point that Blum and Feldman [141] used the Mössbauer effect to investigate crystalline and amorphous tellurium films on a nuclide ^{125}Te. For amorphous films the spectrum exhibited a poorly-resolved asymmetric doublet which proved to prevent an analysis of the spectrum obtained.

7.3.2. ALLOYS

Many Mössbauer studies have dealt with tin-containing chalcogenide alloys [142–157]. In all these experiments evidence on the valence state of tin and on the symmetry of its immediate neighbourhood was obtained in glassy alloys, such as arsenic—selenium—tin, arsenic—sulfur—tin, phosphorus—selenium—tin, phosphorus—sulfur—tin, germanium—selenium—tin, germanium—arsenic—selenium—tin, thallium—arsenic—selenium—tin.

Mössbauer investigations show tin to be only tetravalent in As—S—Sn, As—Se—Sn, Ge—Se—Sn glasses. Figure 7.10 presents typical Mössbauer spectra of ^{119}Sn for systems with an excess amount of chalcogen both in glassy and in crystalline state of the same composition. By its parameters the crystal spectrum agrees with that of a crystalline compound $SnSe_2$, i.e. crystallization of multicomponent glasses is followed by a compound $SnSe_2$ (SnS_2) being formed. The Mössbauer spectra of glasses exhibit single, somewhat broadened lines with the isomer shift close to that of the spectrum of $SnSe_2$ (or SnS_2) compound, the difference generally amounting to 0.20–0.25 mm s^{-1} (see Fig. 7.10).

This circumstance enabled the workers [142–147] to reach a conclusion as to the similarity in the chemical nature of the immediate neighbourhood of the Sn atom in a glass and in the crystal ($SnSe_2$ or SnS_2). We see that tin in the glass is bonded with chalcogenide atoms only and its local coordination number is close to six. The shift of the Mössbauer spectrum of the glass with respect to that of crystalline $SnSe_2$ (SnS_2) can be attributed to the induction effect, i.e. interaction between the tin atoms in the glass. This interaction results in a change of the electron density at the ^{119}Sn nuclei. Proceeding from the known calibrations of the isomer shifts of ^{119}Sn spectra it is concluded that the electron configuration of the atoms of tetravalent tin in chalcogen-containing glasses is close to $(4d)^{10}(5s)^1(5p)^3(5d)^2$, i.e. a sixfold coordination of the tin atoms is shown in the glass.

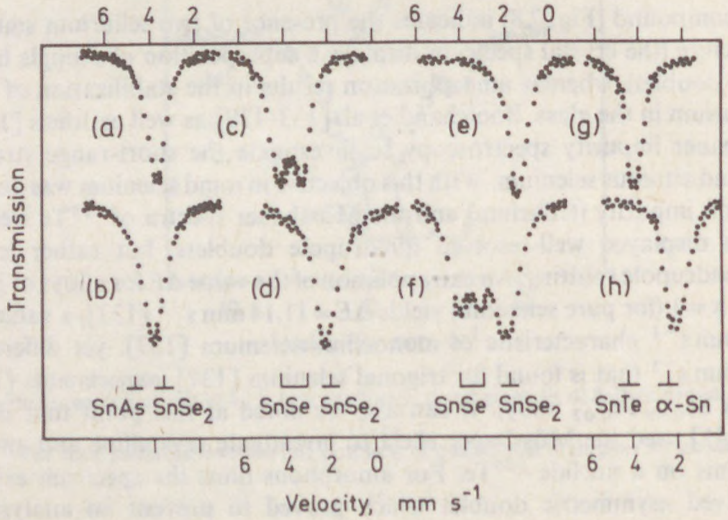

Fig. 7.10. Mössbauer spectra of ^{119}Sn in crystalline (a, c, e, g) and glassy (b, d, f, h) $Sn_{0.1}AsSe_4$ (a, b), $SnO_{0.05}AsSe$ (c, d), $3GeSe \cdot 3SnSe_2 \cdot 4As_2Se_3$ (e), $3GeSe \cdot 3SnSe \cdot 4As_2Se_3$ (f) and $Sn_{0.5}Ge_{14.5}Te_{85}$ (g, h) alloys at 80 K [144–155]

The sticks show the line positions of SnAs, SnSe, $SnSe_2$, SnTe and Sn

What is characteristic in Mössbauer spectra of tetravalent tin in germanate (Ge—Se—Sn, Ge—As—Se—Sn) glasses is their broadened half-width. The conclusion is reached in [142–147] that isomorphous substitution of germanium in glasses by tin is accompanied by distortion of groups of fourfold-coordinated germanium due to the difference of the local coordination numbers of germanium and tin.

The Mössbauer effect has widely been used for phase analysis of multicomponent crystalline and glassy tin-containing alloys. Figure 7.11 shows Gibbs' triangles of the systems As—Se—Sn and Ge—As—Se—Sn, for the latter in the As_2Se_3—GeSe—SnSe section determined by Mössbauer spectroscopy. Regions of the existence of various compounds of tin and alloy components can be seen in the Figure. In the case of the system As—Se—Sn, though the vitrification region overlaps the region of crystalline alloys containing bivalent tin in the glasses, no bivalent tin has been detected. In other words, rapid heat treatment of the alloy is favourable for the stabilization of entities of tetravalent tin in glasses of compositions thermodynamically disadvantageous. Spectra of ^{119}Sn characteristic of crystalline and glassy Ge—Te alloys are shown in Fig. 7.10. It can be seen that amorphization of the alloys gives rise to a pronounced change

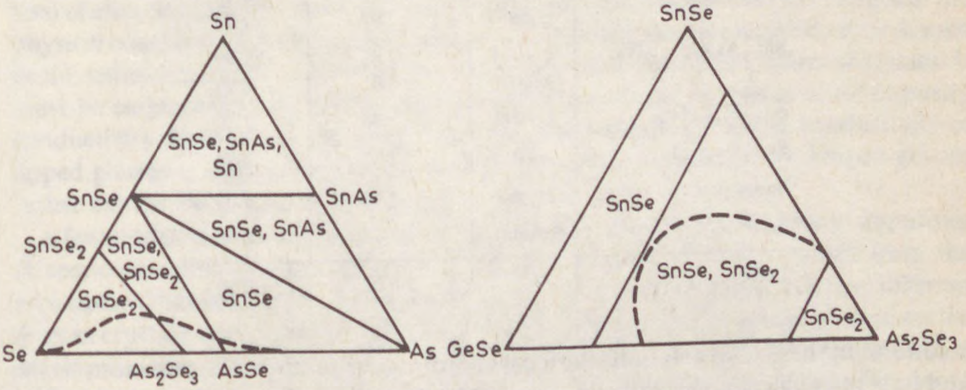

Fig. 7.11. Gibbs' triangles in As—Se—Sn and As$_2$Se$_3$—GeSe—SnSe systems
Dotted lines show region of vitrification, solid lines show regions of existence of various tin compounds [144, 155]

in the isomer shift of the Mössbauer spectra of ^{119}Sn, the isomer shift for glasses coinciding with one of the tin spectra in tetrahedral semiconductors (see Table 7.9). This made it possible to deduce a conclusion as to the realization in the glasses of sp^3 hybrid structural groups of tin (consequently, of germanium as well), and by making use of calibrations of the isomer shifts of the Mössbauer spectra of ^{119}Sn, the electron configuration of tin was determined in the structure of A^{IV}—Te alloys. A specific feature shown by the Mössbauer spectra of impurity atoms of ^{119}Sn in A^{IV}—Te glasses is their line broadening. Reference [158] considers two likely causes of such broadening, viz., due to distorted bond angles between tin atoms and other atoms of the glass, and to fluctuation of the distances between tin atoms to their closest neighbours with the persistence of a tetrahedral symmetry of the chemical bond system. The first cause gives rise to an increase of the half-width of the spectra because of the unresolved quadrupole splitting, the second, to a broadening induced by the non-uniform isomer shift. The second cause also leads to variation of the electron configuration of the tin in the glass in the range $(5s)^{0.92}(5p)^{2.76}$ to $(5s)^{1.15}(5p)^{3.45}$ the most likely configuration being $(5s)^{1.01}(5p)^{3.03}$.

From the analysis of parameters of ^{119}Sn spectra of A^{IV}—Te crystalline alloys it follows that crystallization of $Si_{1-x}Te_x$ glasses yields Si_2Te_3-based $Sn_xSi_{2-x}Te_3$ solid solutions, and crystallization of $Ge_{1-x}Te_x$ glasses, GeTe-based $Ge_{1-x}Sn_xTe$ solid

Table 7.9.
Parameters of Mössbauer spectra of ^{119}Sn impurity atoms in crystalline and glassy alloys at 80 K [158]

Composition of alloy	State	Isomer shift, δ mm s^{-1} (SnO_2)	Halfwidth, Γ mm s^{-1}
$Sn_{0.5}Si_{19.5}Te_{80}$	crystal	3.71	1.18
	glass	2.06	1.03
$Sn_{0.5}Ge_{14.5}Te_{85}$	crystal	3.52	1.10
	glass	2.07	1.03
$Sn_{0.5}As_4Ge_{14.5}Te_{81}$	crystal	2.85	1.09
	glass	2.05	0.98
$Sn_{0.5}Si_{19.5}Te_{30}$	crystal	3.70	1.20
$Sn_{0.5}Ge_{14.5}Te_{15}$	crystal	3.53	1.12
SnAs	crystal	2.70	1.03
SnTe	crystal	3.55	0.94
Error		±0.02	±0.03

solutions. In these solid solutions the local coordination number of the tin atoms is six, and so is their valency, since the tin atoms in Si_2Te_3 and GeTe substitute the bivalent and sixfold-coordinated Si and Ge atoms. Thus, the crystal–glass transition in A^{IV}—Te alloys is accompanied by a change in the valency and coordination states of silicon and germanium atoms.

Using Mössbauer impurity spectroscopy, the workers [158] have made a study of the crystalline and the glassy Ovshinsky alloy $As_4Ge_{15}Te_{85}$ (^{119}Sn was added and its atoms were believed to substitute the germanium atoms). Tin atoms (and, consequently, germanium atoms) have proved to form in the glassy alloy an sp^3 system of chemical bonds (like in the case of As^{IV}—Te glasses), whereas crystallization of the glass causes isolation of a SnAs microphase (see Table 7.9).

Boolchand et al. [170, 171] have made a Mössbauer effect study on the nuclide ^{125}Te in amorphous films of As_xTe_{1-x} $(0.10 < x < 0.57)$. The Mössbauer spectra of the amorphous films showed well-resolved quadrupole doublets. It must be noted that for compositions $As_{0.3}Te_{0.7}$ and $As_{0.5}Te_{0.5}$ the parameters of the amorphous films coincide with those of bulk glass samples. This is, in the opinion of the workers [170, 171] an indication of the similarity of the structures of these glasses and amorphous films. The isomer shift proved to be insensitive to the compositions of the film whereas the value of the quadrupole splitting is noticeably enhanced by increasing tellurium content, i.e. symmetry of the immediate environment of tellurium atoms varies as the composition changes.

Multicomponent tellurium-containing glasses have been investigated by Mössbauer spectroscopy on the nuclide ^{125}Te by Stukan et al. [172]. These authors demonstrated that the quadrupole splitting of the Mössbauer spectra increases during the process of amorphization of the alloys thus, for a crystalline $As_2Se_{1.5}Te_{1.5}$ alloy they obtained $\Delta E = 6.4$ mm s^{-1} (compare this with the value 8.2 mm s^{-1} for a glass). The authors also concluded that amorphization involves decrease of symmetry in the local environment of the tellurium atoms. This result can be compared with the data reported by the workers [173, 174] who have studied antimonide glasses on the nuclide ^{121}Sb by Mössbauer spectroscopy.

7.3.3. IMPURITIES IN CHALCOGENIDE GLASSES

All impurity atoms in glassy semiconductors can be conventionally divided into two groups, electrically active and electrically inactive. Even small mass fraction (0.001 and less) of electrically active atoms (copper, gold, silver) may cause marked changes of the physical constants of glassy semiconductors. Electrically inactive impurity atoms, such as tin, tellurium, on the other hand, do not change the electric properties of glasses. It must be emphasized that neither active nor inactive impurity atoms cause impurity conductivity. In other words, the temperature dependence of electric conductivity of doped glasses is different from that typical of impurity conductivity. Doped glasses rather exhibit behaviour characteristic of intrinsic semiconductors.

A few models have been suggested to explain the anomalous behaviour of impurities in semiconducting glasses (see, e.g. [175]). The simplest model proceeds from the assumption that impurity atoms occupy different sites and, consequently, play different roles in crystals and in glasses of the same composition. Another model is based on the assumption that the energy levels of the inactive impurities are fused into the bottom of the energy zone and therefore cannot supply current carriers into this zone. Similar to this model is still another one which considers levels created by impurity atoms to be neutralized by fluctuation of the levels of the glass. Finally, saturation of all valency bonds by impurity atoms might also be responsible for the loss of impurity conductivity in semiconducting glasses. The situation is aggravated by some theoreticians who do not rule out the possibility of impurity conductivity in doped glasses. Thus, the authors of [176] have proposed a modified method of doping glasses. As opposed to the conventional procedure where doping is involved in the process of preparation, the above researchers [176] have applied simultaneous sputtering of glass and metal from two individual sources. It appears that properties of such "modified" semiconducting glasses depend on the nature of the impurity and its concentration. It should be noted that in a few cases effects were observed very much similar to impurity conductivity as described above.

Not a smaller challenge than that presented by the lack of impurity conductivity in doped glasses is the problem of the mechanism of impurities affecting electric physical properties of glasses. No satisfactory theory is currently available to account for this mechanism. It is only due to Mössbauer spectroscopy that some of these problems have been somewhat clarified.

7.3.3.1. Mössbauer spectroscopy in the study of impurity atoms in semiconductors

In order to elucidate the reasons of the lack of impurity conductivity in doped glasses some special Mössbauer techniques were used which made it possible to identify charge states of impurity atoms, their sites in the matrix and the nature of their immediate environment. The theoretical possibility of determining the aforementioned properties by Mössbauer spectroscopy was practically not used up to quite recent times. Indeed, even if Mössbauer spectroscopy has been heavily involved in studies of impurities in crystalline semiconductors, none of the studies has registered dependence of parameters of the Mössbauer spectra on the state of the Fermi level, without any respect to the virtual charge state of the impurities. That is to say parameters of the Mössbauer spectra identified the impurity in one given state.

In some cases the fact that Mössbauer parameters of the impurity atoms are independent of the position of the Fermi level, can be attributed to electric inactivity of the impurity. In particular amongst such impurities are iron and silicon which was also demonstrated by Mössbauer spectroscopy [177, 179]. On the other hand, iron in $A^{III}B^{V}$ compounds being a deep acceptor, Bemski and Fernandes [180] have made an attempt to investigate the recharging process of impurity iron atoms in InAs. In contrast to expectation, the parameters of spectra proved to be independent of the type of conductivity of the starting sample. No dependence of Mössbauer spectrum parameters on impurity iron was observed for other $A^{III}B^{V}$ compounds at various carrier concentrations in the starting samples [181]. Such independence implied essential impossibility to determine the actual charge state of the impurity by means of the Mössbauer effect.

Authors [182] were first to undertake a successful attempt to associate Mössbauer parameters of impurity iron atoms with local levels which they exhibit in an $A^{III}B^{V}$ compound. The fine structure of the Mössbauer spectra of iron atoms in the subsurface region of broadband $A^{III}B^{V}$ proved to depend on the type of sample, conductivity and carrier concentration. In the case of n-type samples the spectra display poorly resolved doublets while in the case of hole-type samples the quadrupole splitting is markedly enhanced. Such a behaviour of the Mössbauer spectra is explained as follows. In n-type samples the spectra were assigned to iron impurity centres, the iron being associated with the vacancy, whereas in hole-type samples the impurity particles are not ionized and can be regarded as Fe^{3+} ions with an incomplete system of tetrahedral bond. This gives rise to an electronic component of the electric field gradient on ^{57}Fe nuclei and to an enhanced quadrupole splitting.

A correlation between the Mössbauer parameters of impurity iron atoms found in $A^{III}B^{V}$ and the position of the Fermi level has been shown by the workers [183, 184] in the cases of GaAs and GaP. It turns out that the Mössbauer spectra of the electron-type and the hole-type samples correspond to isolated iron atoms, the isomer shifts, however, being different in the case of these two types. The spectra are identified as assigned to Fe^{0} and Fe^{-1} states, the Fe^{0} to Fe^{-1} transition accompanied by a greater isomer shift owing to an increased population of the 3d shell of iron. Under favourable conditions it appears possible to observe even a subtle effect such as the process of recharging of ionized and neutral iron centres in GaP via the valence zone.

Thus the above brief account examplifies the fruitful use of Mössbauer spectroscopy for studies of impurity atoms in semiconductors.

7.3.3.2. Electrically inactive impurity atoms (tin)

Tin atoms are the only electrically inactive impurity atoms that have been studied in semiconducting glasses (on the nuclide ^{119}Sn) by Mössbauer spectroscopy [185–187]. Figure 7.12 presents Mössbauer spectra of ^{119}Sn impurity atoms in crystalline (b) and in glassy (a) As_2Se_3. The temperature dependence curve of electric conductivity shows a bend in the case of the crystalline phase (impurity conductivity with an energy level of ionization, 0.2 eV) but agrees with that for a pure As_2Se_3 glass in the case of a glassy phase with a tin concentration of 0.5 mole%. According to the workers [187–189], disappearance of impurity conductivity on amorphization of tin-doped As_2Se_3 can be explained by the rearrangement of the electronic structure of the tin atoms during the process of amorphization. And indeed, as follows from Mössbauer spectra shown in Fig. 7.12, for a crystalline sample the spectrum comes from Sn^{2+} (its electronic configuration is close to $(5s)^2\,(5p)^0$ so that 5s tin electrons can act as donor electrons and provide a level $E_c = 0.20$ eV). In the glassy phase, on the other hand, the impurity atoms become tetravalent since all chemical bonds of the tin atom are saturated and, consequently, unable to supply electrons to the conductivity band.

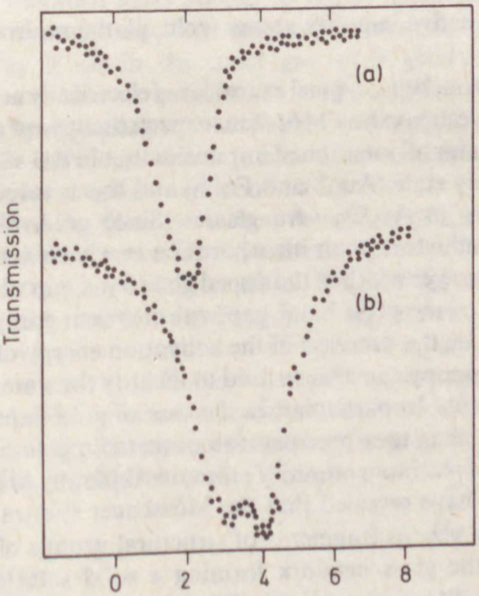

Fig. 7.12. Mössbauer spectra of ^{119}Sn impurity atoms glassy (a) and crystalline As_2Se_3 (b) at 80 K [187–189]

Similar investigations of ^{119}Sn impurity atoms have been conducted by the workers [158–162, 185–189] for quite a number of compounds and alloys (As_2S_3, As_2Te_3, AsIS, AsISe, $As_4Te_5I_2$, $TlAsS_2$, $TlAsSe_2$, $TlAsTe_2$, alloys As^{III}–Te, As^{IV}–Te and others) and in all tin-doped glasses the lack of impurity conductivity was experienced. Mössbauer spectra of tin impurity atoms clearly show the saturation of all valence bonds in the glass network, since the spectral parameters always indicate tetravalent tin. In other words, these results provide evidence for a staturated bond model in doped glasses.

The authors [155, 157] have investigated the state of tin impurity atoms with unsaturated chemical bonds in glassy alloys Ge—As—Se—Sn. As already noted, Mössbauer spectroscopy revealed in these glasses, apart from tetravalent, bivalent tin (see Fig. 7.10). It would be natural to expect that Sn^{2+} ions in a glass structure should lead to impurity conductivity in accordance with the influence in the optical properties. The attempts of the workers [157] to detect impurity conductivity in As_2Se_3—GeSe—SnSe glasses as well as impurity absorption in IR-spectra failed. In other words, the presence of unsaturated chemical bond impurity atoms in glasses does not lead to impurity conductivity. This fact is explained by them in terms of a model of doped glasses as solid solutions based on individual chemical compounds.

7.3.3.3. Electrically active impurity atoms (gold, platinum, iron)

Gold, platinum and iron, being typical examples of electrically active impurity atoms in glasses, have been investigated by Mössbauer spectroscopy on glassy semiconductors [190–193]. It is found for all mentioned impurities that in As—Se glasses they stabilize in a maximum valency state (Au^{3+} and Fe^{3+}) and this is responsible for the lack of impurity conductivity in As_2Se_3—Au glasses. Since gold, platinum and iron are narrow-band semiconductors, their incorporation in a glass resulting an As_2Se_3 solid solution, causes a narrower width of the doped glass band gap which is manifested both by narrowing width of the glass band gap with increasing impurity concentrations. This is accompanied by the decrease of the activation energy of electric conductivity.

Mössbauer spectroscopy can also be used to identify the state of the impurity atoms following crystallization. In particular, in the case of gold impurity atoms in As_2Se_3 glass, crystallization leads to a precipitation of metallic gold.

Study of the state of platinum impurity atoms in As_2Se_3 by Mössbauer spectroscopy on the nuclide ^{197}Pt have revealed that the Mössbauer spectra show platinum to be present in two states, viz., as fragments of structural groups of tetravalent platinum being contained in the glass network forming a solid solution in As_2Se_3, and as microinclusions of a $PtAs_2$ compound. Temperature dependence of such samples displays no impurity conductivity. This is accounted for by the workers [191] both by saturation of all of the platinum valence bonds (for platinum atoms in the glass network), and by blocking $PtAs_2$ microinclusions by the bulk of the glass.

The blocking effect of impurity microinclusions in the bulk of the glass is most apparent for iron impurity atoms in the glassy As_2Se_3 by diffusion technique [194]. Andreev et al. [195] in iron-doped Ge—Se glasses have observed a kink on the temperature versus electric conductivity curves assigning it to impurity conductivity. This suggestion is supported by the fact that the Mössbauer spectra show Fe^{I} in glasses, i.e. the iron does not use up all valent electrons and is, consequently, able to form a local energy level in the prohibited band. It will be noted, however, that the effect observed in [195] has so far been unique.

7.3.3.4. Modified glassy semiconductors

A simultaneous high frequency sputtering of glass and metal on a cold substrate gives rise to a "modified" glass the properties of which depend on concentrations of impurity atoms in such a glass. Averyanov et al. [196] were the first to recognize and solve the problem whether the properties of modified glasses are determined by the nature of the impurity being incorporated or, rather, by the technique of preparation of glasses. For this they prepared an As_2Se_3 glass modified with tin impurity atoms. Note that on doping glassy As_2Se_3 with tin impurity atoms during its synthesis, i.e. in the melt, no impurity conductivity was observed in glasses, nor was tin shown by optical spectra. It turned out that no bends are observed on the temperature versus electric conductivity curve in a tin-modified As_2Se_3 glass either, and the properties of a pure and a modified glass were identical (tin concentration attained 6 mole%). This result was accounted for within the framework of a "saturated bonds" model. The Mössbauer spectra of ^{119}Sn impurity atoms for a modified glass proved to exhibit tetravalent tin, i.e. the tin in modified glasses similarly to those doped in the melt saturates all chemical bonds and is unable to form energy levels in the band gap of a glassy semiconductor. The modification technique makes it possible to dope a glass with impurity up to concentrations markedly exceeding that attainable in doping a molten glass. This fact seems essential only for transition elements such as iron, nickel, cobalt, as it is these latter that poorly dissolve in glassy semiconductors.

Modified GeSe amorphous films have been the object of a study of iron impurity atoms [197]. These workers observed the Mössbauer spectra of ^{57}Fe for such samples to show at low temperatures (80 K) three states, Fe^{2+}_{tet}, Fe^{2+}_{oct} and Fe^{3+}. At elevated temperatures electron exchange between Fe^{2+}_{oct} and Fe^{3+}_{oct} states occurs, the Mössbauer spectrum at 295 K showing two iron states, a Fe^{2+}_{tet} and an averaged iron state. It is suggested by the above workers [197] that it is rapid electron exchange between Fe^{2+}_{oct} and Fe^{3+}_{oct} that is responsible for enhanced conductivity in modification-doped glasses. It should be noted that a similar interpretation is presented in [198] whose authors have made a study of iron-modified As_2Se_3 glasses.

7.4. CONCLUSIONS

Mössbauer spectroscopy has proved promising for investigations of iron- and tin-containing oxide glasses. Emphasis has been essentially placed in the studies under consideration on the states of the elements involved in a particular glass, their valence, site, chemical nature of the local surrounding. The number of studies dealing with a comparison of local structures in oxide systems is fairly limited, yet they indicate a difference of the short-range structures between crystals and glasses.

In contradiction, the bulk of Mössbauer investigations of chalcogenide glasses has been concerned with a comparison of structures of crystalline and glassy semiconductors. All the compounds and alloys studied fall into two groups, i.e. compounds and alloys characterized by rearrangement of a close-range order and, hence, lower local symmetry of Mössbauer atoms on amorphization, and, second, compounds and alloys for which the crystal-glass transition does not cause any marked change in the structure of short-range order. Semiconductors found to feature different short-range order structures in crystalline and glassy states and the latter should not be regarded as anomalous. It should be recalled that in experiments by Ioffe and Regel [117] a number of semiconductors were discovered for which the crystal–melt transition is concomitant with rearrangement of the structure of a close-range order, and, since a glass fixes certain momentary configurations of the melt, a change of the local structures of As_2Te_3 compounds on amorphization would indicate a difference in short-range order structures of the crystals and melts involved.

The analogy in the behaviour of semiconductors in terms of the crystal–melt and crystal-glass transitions can be also extended to the nature of changes in their electric and physical properties. In fact, pronounced anomalous changes of properties, such as density and electric conductivity are observed in the aforementioned transitions only for semiconductors that show different structures in crystalline and glassy (liquid) states. Such drastic changes of the properties are induced by rearrangement of the local structure, as it is this latter that predetermines principal properties of semiconductors.

Yet it is to be kept in mind, that analogy drawn between the crystal–glass and crystal–melt transitions is not absolute. In particular, in contrast to the crystal–melt transition accompanied by an increase of the local coordination number [117], the crystal–glass transition has as its result a decreased local coordination number [127].

The advent of Mössbauer spectroscopy has enabled the problem of doped semiconducting glasses to be solved. It appears that whatever its chemical nature, the impurity atom in a glass has its local surrounding rearranged in such a manner as to render all of its chemical bonds saturated. It is this very mechanism that is responsible for the lack of impurity conductivity in doped glasses.

REFERENCES

1. Kurkjian, C. R., *J. Non-cryst. Sol.*, **3,** 157 (1970).
2. Toneja, S. F., Kimball, C. W. and Shaffer, J. C., *Mössbauer Effect Methodology*, ed. Gruverman, I. J., Plenum, N. Y., 1973, Vol. 8, p. 41.
3. Kalvius, G. M., *Intern. Sum. Sch.* Frontier Probl. Nucl. and Solid State Phys., Predeal, Bucharest, 1973, p. 57.
4. Litterest, F. J. and Kalvius, G. M., *Proc. Intern. Conf. on Mössbauer Spectroscopy, Poland—Cracow*, 1975, Vol. 2., p. 189.
5. Regel, A. R. and Seregin, P. P., *Fiz. Techn. Poluprovodn.* **18,** 1153 (1984).
6. Bletry, J., *Rev. Phys. Appl.* **15,** 1019 (1980).
7. LaCaer, G. and Dubois, J. M., *Rev. Phys. Appl.* **15,** 1049 (1980).
8. Seregin, P. P., Andreev, A. A., Regel, A. R. and Nasredinov, F. S., *Phys. Stat. Sol.* (a) **74,** 377 (1982).
9. Warren, B. E., *J. Am. Ceram. Soc.* **21,** 259 (1938).
10. Ivanov, A. O. and Evstropyev, K. S., *Dokl. Akad. Nauk. SSSR*, **145,** 797 (1962).
11. Murthy, K. M. and Kirby, E. M., *Phys. Chem. Glasses*, **5,** 144 (1964).
12. Warren, B. E., *J. Appl. Phys.*, **13,** 602 (1942).
13. Bray, P. J. and O'Keefe, J. G., *Phys. Chem. Glasses*, **1,** 26 (1960).
14. Elyard, C. A., Baynton, P. L., Rawson, H., *Glasstechn. Ber.*, **32K**, 36 (1959).
15. Pollak, H., de Coster, M. and Amelinckx, S., *Proc. Internat. Conf. Mössbauer Effect. Saclay* (France), 1962, p. 295.
16. Kurkjian, C. and Buchanan, D., *Phys. Chem. Glasses*, **5,** 63 (1964).
17. Kurkjian, C. and Buchanan, D., *Revs. Mod. Phys.*, **36,** 397 (1964).

18. Belyustin, Yu., Ostanevich, M., Pisarevsky, A. M., Tomilov, S. B., Baishi, Yu. and Cher, A., *Fiz. Tverd. Tela*, **7**, 1447 (1965).
19. Gesselin, J., Shimony, U., Grodzins, L. and Cooper, A., *Phys. Chem. Glasses*, **8**, 56 (1967).
20. Temandl, G., Frischart, G. and Oel, R., *Glasstechn. Ber.*, **40**, 293 (1967).
21. Kurkjian, C. and Sigety, E., *Phys. Chem. Glasses*, **9**, 73 (1968).
22. Lewis, G. and Drickamer, H., *J. Chem. Phys.*, **49**, 3785 (1968).
23. Frischart, G. and Tomandi, G., *Glasstechn. Ber.*, **42**, 182 (1969).
24. Coleman, M., Duncan, J. and Sitharamarao, D., *Rev. Chim. Miner.* **7**, 1129 (1970).
25. Collins, D. and Mulay, L., *J. Am. Ceram. Soc.*, **53**, 74 (1970).
26. Frischart, G. H. and Tomandl, G., *Glasstechn. Ber.*, **44**, 173 (1971).
27. Boon, J. A., *Chem. Geol.*, **7**, 153 (1971).
28. Varnek, V. A., Verevkina, G. V. and Sokolov, V. K., *Neorg. Mat.*, **9**, 732 (1973).
29. Bhat, V. K., Manning, C. R. and Bown, L. N., *J. Am. Ceram. Soc.*, **59**, 459 (1973).
30. Laber, Ch. and Gielen, F., *J. Non-cryst. Sol.*, **13**, 107 (1973/74).
31. Peev, T. M., Kalyamin, A. V., Chakyrov, Khr. G. and Bozajiev, L. S., *Herald of Higher Chemical Technological Institute*, Burgas (Bulgaria) **10**, 307 (1974).
32. Levy, R. A., Lupis, C. H. P. and Flinn, P. A., *Phys. Chem. Glasses*, **17**, 94 (1976).
33. Knorr, K., Geller, R. and Prandl, W., *J. Magn. and Magn. Mater.*, **4**, 258 (1977).
34. Arif, S. K., *Proc. Intern. Conf. Mössbauer Spectroscopy, Bucharest–Romania*, 1977. Vol. 1, p. 241.
35. Hanga, E., Diamanderscu, L., Morariu, M., Popescu-Pogrion, N. and Taturu, E. *Proc. Internat. Conf. Mössbauer Spectroscopy, Bucharest*–Romania, 1977, Vol. 1, p. 423.
36. Levy, R. A., *Amorphous Magnetism*, ed. Levy, R. A., Plenum, New York, 1977, Vol. 2., p. 613.
37. Bieman, L. H., Kenealy, P. F., de Group, A. M., *Amorphous Magnetism*, ed. Levy, R. A., Plenum, New York, 1977, Vol. 2., p. 587.
38. Iwamoto, N., Tsunawaki, Y., Nakagava, H., Joshimura, T. and Wakabayashi, N., *J. Non-cryst. Sol.*, **29**, 374 (1978).
39. Iwamoto, N., Tsunawaki, Y., Nakagawa, H., Joshimura, T., Wakabayashi, N., *J. Physique*, **40**, 151, (1979).
40. Varret, F. and Naudin, F., *Rev. Phys. Appl.*, **14**, 613 (1979).
41. Hirao, R., Soga, N. and Kunugi, M., *J. Am. Ceram. Soc.*, **62**, 109 (1979).
42. Hirao, R., Komatsu, T. and Soga, N., *J. Non-cryst. Sol.*, **40**, 315 (1980).
43. Nolet, D. A., *J. Non-cryst. Sol.*, **37**, 99 (1980).
44. Gorbachev, V. V., Klyukin, A. B. and Filatov, T. A., *Fizika i khimia stekla* (Physics and Chemistry of Glass), **6**, 630 (1980); **7**, 402 (1981).
45. Sugimoto, M., Takahashi, T., Naya, K., Hitatsuka, N. and Soeno, Y., *I. Magn. Soc. Jap.* **9**, 167 (1985).
46. Yvanfu, H., Rongchvan, L., Jing, J., Gonser, U. and Engelmann, H., *Hyperfine Interaction*, **27**, 409 (1986).
47. Zhongshen, Z. and Yisong, Y., *J. Non-cryst. Sol.*, **84**, 34 (1986).
48. Bryukhanov, V. A., Goldansky, V. I., Delyagin, N. M., Koretko, L. A., Makarov, E. F., Suzdalev, I. P. and Shpinel, V. S., *Zh. Exp. Teor. Fiz.*, **43**, 448 (1962).
49. Gendler, T. S., Mitrofanov, K. P., Plotnikov, M. V., Tykachinsky, I. D. and Fedorovsky, Ya. A., *Neorg. Mat.* (Inorganic Materials), **2**, 1277 (1966).
50. Mitrofanov, K. P. and Sidorov, T. A., *Fiz. Tverd. Tela* (Sol. St. Physics) **9**, 890 (1967).
51. Bartenev, G. M. and Tsyganov, A. D., *Dokl. Akad. Nauk SSSR*, **181**, 627 (1968).
52. Polozova, I. P. and Seregin, P. P., *Fiz. Tverd. Tela* **10**, 2536 (1968).
53. Evstropyev, K. S., Bezrodny, V. G., Seregin, P. P. and Shipatov, V. T., *Neorg. mater.*, **6**, 781 (1970).
54. Bartenev, G. N., Brekhovsky, S. M., Varisov, A. Z., Landa, L. M. and Tsyganov, A. D., *Fiz. Tverd. Tela*, **12**, 1249 (1970).
55. Bartenev, G. M., Suzdalev, I. P. and Tsyganov, A. D., *Phys. Stat. Sol.*, **37**, 73 (1970).
56. Murin, A. N., Shipatov, V. T., Polozova, I. P. and Seregin, P. P., *Vestnik Leningradskogo Universiteta*, **16**, 157 (1971).
57. Seregin, P. P., Murin, A. N., Bezrodny, V. G. and Shipatov, V. T., *Vestnik Leningradskogo Universiteta*, **4**, 159 (1972).
58. Bartenev, G. M., Tsyganov, A. D., Ovchinnikov, A. I., Abrosimov, G. D., *Neorg. Mat.*, **8**, 2011 (1972).
59. Bartenev, G. M., Gorokhovsky, V. A., Tsyganov, A. D., Shcherbakova, V. P. and Ovchinnikov, A. I., *Neorg. Mat.*, **8**, 2192 (1972).

60. Kurbanova, L. and Seregin, P., *Fiz. Khim. Stekla*, **11**, 244 (1985).

61. Kurkjian, C. R., Sigety, E. A., *Proc. Internat. Congr. on Glass, Brussels*, Gordon and Breach, New York, 1964, p. 39.

62. Uhrich, D., Barnes, R., *Phys. Chem. Glasses*, **9**, 184 (1968).

63. Taragin, M. F. and Eizenstein, J. C., *Phys. Rev.*, *B2*, 3490 (1970).

64. Taragin, M. F. and Eizenstein, J. C., *J. Non-cryst. Sol.*, **11**, 395 (1973).

65. Paul, A., Donaldson, J. D. and Thomas, M. J. K., *J. Mater. Sci.*, **12**, 219 (1977).

66. Seregina, L. N., *Summary of Candidate of Science Thesis* (in Russian), Leningrad, 1981.

67. Bukrey, R., Kenealy, F., Beard, G. and Hooper, H., *J. Appl. Phys.*, **40**, 4289 (1969).

68. Bukrey, R., *Bull. Amer. Ceram. Soc.*, **51**, 371 (1972).

69. Jach, J., *J. Nonmetalls*, **1**, 155 (1973).

70. Jach, J., *J. Nonmetalls*, **2**, 89 (1974).

71. Raman, T., Nagesh, V. K., Chakravorty, D. and Rao, G. N., *Internat. Conf. Hyperfine Interact. Stud. Nucl. React. and Decay, Upsala*, 1974, p. 280.

72. Saini, M. S. and Kamal, R., *J. Non-cryst. Sol.*, **87**, 103 (1986).

73. Trieher, M. J., Thomos, J., Omar, M. H., Osman, A. and Bishay, A., *J. Mater. Sci.*, **9**, 1115 (1974).

74. Yuanfa, H. and Rongchuan, L., *Hypefine Interactions*, **27**, 285 (1986).

75. Raman, T., Nogesh, V. K., Chakravorty, D. and Rao, G. N., *J. Appl. Phys.*, **46**, 972 (1975).

76. Kishore, N., Bansal, T. K. and Kamal, R., *J. Non-cryst. Sol.*, **69**, 213 (1985).

77. Raman, T., Chakravorty, D. and Rao, G. N., *Proc. Nucl. Phys. and Solid State Phys. Symp., Ahmedabad*, 1976, p. 1.

78. Maccronel, R. K., Williams, J., Kim, K. and Maley, M. P., *The Structure of Non-crystalline Materials*, London, 1977, p. 121.

79. Barb, D., Nicula, A., Tarima, D. and Baican, K., *Proc. Intern. Conf. Mössbauer Spectroscopy, Bucharest–Romania*, 1977, Vol. 1., p. 425.

80. Burze, E. and Ardelean, I., *Proc. Intern. Conf. Mössbauer Spectroscopy, Bucharest–Romania*, 1977. Vol. 1., p. 245.

81. Ardelean, I., Burzo, E. and Pop, I., *Sol. State Commun.*, **23**, 211 (1977).

82. Raman, T., Rao, G. and Chakravorty, D., *Hyperfine Interact.*, **4**, 873 (1976).

83. Sekhon, S. S. and Kamal, R., *J. Non-cryst. Sol.*, **28**, 189 (1978).

84. Raman, T., Rao, G. and Chakravorty, D., *J. Non-cryst. Sol.*, **29**, 85 (1978).

85. Horie, O., Syono, Y., Nakagama, Y., Ito, A., Okamura, K. and Yakajima, S., *Sol. State Commun.*, **25**, 423 (1978).

86. Danheim, H. and Frey, T., *Borate glasses: structure, properties, application*, eds Pye, L. D., Frechette, V. D., Kreidl, N. J., Plenum-Press, N-Y, 1978, p. 227.

87. Sekhon, S. S. and Kamal, R., *J. Appl. Phys.*, **49**, 3444 (1978).

88. Syone, Y., Ite, A. and Horie, O., *J. Phys. Soc. Jap.*, **46**, 793 (1979).

89. Syone, Y. and Ite, A., *J. Physique Colloque*, **40**, C2–115 (1979).

90. Sekhon, S. S. and Kamal, R., *J. Non-cryst. Sol.*, **33**, 169 (1979).

91. Burzo, E. and Ardelean, I., *Phys. Chem. Glasses*, **20**, 15 (1979).

92. Friedt, J. M., *J. Physique*, **41**, 273 (1980).

93. Nishida, T. and Takashima, Y., *J. Non-cryst. Sol.*, **37**, 37 (1980).

94. Nishida, T., Shiotsuki, T. and Takashima, Y., *J. Non-cryst. Sol.*, **41**, 161 (1980).

95. Nishida, T., Hirai, T. and Nakayama, N., *Radiochem. Radioanal. Lett.*, **42**, 189 (1980).

96. Chaumont, C., Derory, A. and Bernier, J.-C., *Mater. Res. Bull.*, **15**, 771 (1980).

97. Nishida, T., Hirai, T. and Takashima, Y., *J. Non-cryst. Sol.*, **43**, 221 (1981).

98. Eissa, N. E., Shaisha, E. E. and Hussiun, A. L., *J. Non-cryst. Sol.*, **16**, 206 (1974).

99. Paul, A., Donaldson, J. D., Donoghue, M. T. and Thomas, M. J. K., *Phys. Chem. Glasses*, **18**, 125 (1977).

100. Berul, S. I., Yeits, B. N. and Ioffe, A. M., *Izv. Akad. Nauk. Latv. SSR* (physical-technical series), **2**, 66 (1969).

101. Veits, B. N. and Berul, S. L., *Izv. Akad. Nauk. Latv. SSR* (physical-technical series), **3**, 70 (1970).

102. Taragin, M. E., Eisenstein, J. C. and Haller, W., *Phys. Chem. Glasses*, **13**, 149 (1972).

103. Vaughan, J. G., Wilson, L. K. and Kinser, D. L., *Bull. Amer. Ceram. Soc.*, **52**, 384 (1975).

104. Takashima, Y. and Nishida, T., *J. Physique Colloque*, **37**, C12–919 (1976).

105. Sawicki, J., Savicka, B. and Growski, O., *Phys. Stat. Sol.*, (a) **41**, 173 (1977).

106. Nishida, T., Shiotsuki, T. and Takashima, Y., *J. Non-cryst. Sol.*, **43**, 115 (1981); **13**, 123 (1981).

107. Beltran-Porter, D., *Rev. Phys. Appl.*, **15,** 1155 (1980).
108. Vaivad, A. Ya., Veits, B. N., Grigalis, V. Ya., Dombrovskaja, V. K., Konstant, Z. A., Lisin, Yu. D. and Taksar, I. M., *Izv. Akad. Nauk. Latv. SSR* (chemical series), **4,** 504 (1969).
109. Burzo, E. and Ardelean, I., *Sol. State Commun.*, **31,** 75 (1979).
110. Menil, E., Fournes, L., Dance, J.–M. and Videau, J. J., *J. Non-cryst. Sol.*, **34,** 209 (1979), *J. Physique*, **41,** 271 (1980).
111. Taragin, M. F. and Eisenstein, J. C., *J. Non-cryst. Sol.*, **3,** 311 (1970).
112. Nishida, T., Hirai, T. and Takashima, Y., *Phys. Chem. Glasses*, **22,** 94 (1981).
113. Tykachinsky, I. D., Fedorovsky, D. A., Jakhva, N. G., Ovchinikov, A. I. and Tsyganov, A. D., *Neorg. Mater.*, **10,** 2198 (1974).
114. Bartenev, G. M., Mogimedov, G. M. and Taganov, A. D., *Neorg. Mater.*, **12,** 742 (1976).
115. Mott, N. F. and Davis, E. A., *Electronic Processes in Non-crystalline Materials*, Clarendon Press, Oxford, 1971.
116. Zakharov, V. P. and Gerasimenko, V. S., *Specific Features in Structure of Amorphous Semiconductors* (in Russian), Naukova dumka, Kiev (1976).
117. Ioffe, A. F. and Regel, A. R., *Progress Semicond.*, **4,** 237 (1960).
118. Kolomiets, B. T., Mamontova, T. N. and Stepanov, T. I., *Fiz. Tverd. Tela*, **7,** 1630 (1965).
119. Seregin, P. P. and Vasilyev, L. N., *Fiz. Tverd. Tela*, **13,** 2699 (1971).
120. Wells, I. and Boolchand, P., *I. Non-cryst. Sol.*, **89,** 31 (1987).
121. Seregin, P. P., Sagatov, M. A., Nasredinov, F. S., Krylnikov, Yu. V., Kamolov, A. and Vasilyev, L. N., *Fiz. Tverd. Tela*, **16,** 2441 (1974).
122. Vincze, I. and Van der Woude, F., *J. Non-cryst. Sol.*, **42,** 499 (1980).
123. Cornet, J. and Rossier, D., *J. Non-cryst. Sol.*, **12,** 85, (1973).
124. Jones, C. H. W. and Tse, A., *J. Appl. Phys.*, **49,** 4598 (1978).
125. Seregin, P. P., Krylnikov, Yu. V., Nasredinov, F. S., Vasilyev, L. N., Sagatov, M. A. and Turaev, E. Yu., *Letters to J. E. T. F.*, **20,** 132 (1974).
126. Seregin, P. P., Vasilyev, L. N., Nasredinov, F. S., Seregina, L. N. and Krylnikov, Yu. V., *Problems of Physics of Semiconductors* (in Russian) Kaliningrad, 1975, Vol. 1., p. 37.
127. Seregin, P. P., Sivkov, V. P., Nasredinov, F. S., Vasilyev, L. N. and Krylnikov, Yu. V., *Structure of Non-Crystalline Semiconductors* (in Russian), Nauka, Leningrad, 1976, p. 139.
128. Ruby, S. L., Gilbert, L. R. and Wood, C., *Phys. lett.*, **37**A, 453 (1971).
129. Stevens, J. G. and Bowen, L. H., *Mössbauer Effect Methodology*, Plenum, New York, 1969, Vol. 5., p. 27.
130. Aleksandrov, A. Yu., Baltrunas, D. I., Belyaev, A. M., Lyubutin, I. S. and Lyakhovitskaya, V. A., *Kristallografia*, **17,** 332 (1978).
131. Tideswell, W., Kruse, F. and McCullough, J., *Acta Cryst.*, **10,** 99 (1957).
132. Vasilyev, L. N., Krylnikov, Yu. V., Kamolov, A. and Seregin, P. P., *Neorg. Mat.*, **12,** 350 (1976).
133. Boolchand, P., Tenhover, M. and Neufville, J. *Structure and Properties of Non-crystalline Semiconductors*, Nauka, Leningrad, 1976, p. 144.
134. Boolchand, P. and Suranyi, P., *Phys. Rev. B*, **7,** 57 (1973).
135. Boolchand, P., *Sol. State Commun.*, **12,** 753 (1973).
136. Boolchand, P., *Amorph. Magnetism. Proc. Internat. Symp., Detroit*, N-Y–London, 1973, p. 149.
137. Honneberger, T. and Boolchand, P., *Sol. State Commun.*, **13,** 1619 (1973).
138. Boolchand, P., Honneberger, T. and Oberschmidt, J., *Phys. Rev. Lett.*, **30,** 1292 (1973).
139. Kim, C. S. and Boolchand, P., *Phys. Rev. B.*, **19,** 3187 (1979).
140. Jones, C. H. V., *J. Chem. Phys.*, **67,** 1587 (1977).
141. Blum, N. A. and Feldman, C., *Sol. State Commun.*, **15,** 965 (1974).
142. Vasilyev, L. N. and Seregin, P. P., *Symposium on Vitreous Chalcogenide Semicond.*, Leningrad, 1970, p. 43.
143. Borisova, Z. U., Vasilyev, L. N., Seregin, P. P. and Shipatov, V. T., *Fiz. Tv. Prov.*, **4,** 533 (1970).
144. Vasilyev, L. N., Seregin, P. P. and Shipatov, V. T., *Neorg. Mat.*, **7,** 2069 (1971).
145. Bartenev, G. M., Tsyganov, A. D., Dembovsky, S. A. and Mikhailov, V. I., *Zh. Strukt. Khim.*, **12,** 926 (1971).
146. Seregin, P. P., Vasilyev, L. N. and Pronkin, A. A., *Neorg. Mat.*, **8,** 376 (1972).
147. Seregin, P. P., Vasilyev, L. N. and Borisova, Z. V., *Neorg. Mat.*, **8,** 567 (1972).
148. Seregin, P. P. and Vasilyev, L. N., *Neorg. Mat.*, **8,** 1238 (1972).

149. Tanejeva, S. P., Dwight, A. E., Gilbert, L., Harper, W. C., Kimball, C. and Wood, C., *Phys. Chem. Glasses*, **13**, 153 (1972).
150. Enzweiler, R. N. and Boolchand, P., *Hyperfine Interaction*, **27**, 393 (1986).
151. Niederriter, C. F., Cappelletti, R. L. and Boolchand, P., *Sol. State Commun.*, **61**, 527 (1987).
152. McNeil, L. E., Mikrut, J. M. and Peters, M. J., *Sol. State Commun.*, **62**, 101 (1987).
153. Krylnikov, Yu. V., Bakhtiyarov, A. Sh., Seregina, L. N. and Vasilyev, L. N., *Chemical Bunds in Crystals and their Physical Properties* (in Russian). Nauka i teknika, Minsk, 1976, Vol. 2, p. 193.
154. Belozersky, G. N., Gitsovich, V. N., Shkolnikov, E. A. and Borisova, Z. U., *Fiz. Tverd. Tela*, **18**, 310 (1976).
155. Vasilyev, L. N., Bakhtiyarov, A. Sh., Makeeva, K. B., Sivkov, V. P. and Seregina, L. N., *Fiz. Khim. Stekla*, **3**, 77 (1977).
156. Shkolnikov, E. A. and Seregin, P. P., *Neorg. Mat.*, **12**, 818 (1976).
157. Regel, A. A. and Seregin, P. P., *Fiz. Khim. Stekla*, **7**, 154 (1981).
158. Seregina, L. N., Nasredinov, F. S., Melekh, B. T., Maslova, Z. V., Turaev, E. Yu. and Seregin, P. P., *Fiz. Khim. Stekla*, **3**, 328 (1977).
159. Nasredinov, F. S., Melekh, B. T., Vasilyev, L. N. and Seregina, L. N., *Fiz. Tverd. Tela*, **17**, 633 (1975).
160. Seregin, P. P., Sivkov, V. P., Nasredinov, F. S., Vasilyev, L. N., Krylnikov, Yu. V. and Kostikov, Yu. P., *Phys. Stat. Sol.*, (a) **39**, 437 (1977).
161. Bordovskii, G., Seregina, L. and Podchaluzin, V., *Fiz. Khim. Stekla*, **12**, 373 (1986).
162. Andreev, A. A., Ablova, M. S., Melech, B. T., Nasredinov, F. S., Seregin, P. P. and Turaev, E. Yu., *Proceedings of the 7th International Conference*, ed. Spear, W. E., University of Edinburgh, 1977, p. 44.
163. Seregin, P. P., Turaev, E. Yu., Melekh, B. T. and Andreev, A. A., *Fiz. Khim. Stekla*, **5**, 659 (1979).
164. Seregin, P. P., Turaev, E. Yu., Andreev, A. A., Melekh, B. T. and Nistiryuk, P. V., *Fiz. Khim. Stekla*, **7**, 283 (1981).
165. Boolchand, P., Triplett, B., Hanna, S. S. and de Neufville, J. P., *Mössbauer Effect Methodology*, Vol. 9, Plenum, N-Y, 1974, p. 53.
166. Nath, P., Suri, S. and Chopra, K., *Phys. Stat. Sol.*, (a) **30**, 771 (1975).
167. Kamna, A., *J. Non-cryst. Sol.*, **23**, 357 (1977).
168. Hafemeister, D. and de Ward, H., *J. Appl. Phys.*, **43**, 5205 (1972).
169. Minaev, V. S. and Shipatov, V. T., *Neorg. Mat.*, **16**, 1526 (1980).
170. Boolchand, P., Tenhover, M. and Flasc, R. E., *Structure and Excitations of Amorphous Solids*, Amer. Inst. of Phys. Inc., 1976, p. 102.
171. Boolchand, P., Tenhover, M., Hersman, W., Flasch, R. E. and de Neufville, J. P., *J. Physique Colloque*, **37**, 782 (1976).
172. Stukan, R. A., Yurlova, G. A., Gorbachev, V. V. and Linsky, V. A., *Teor. Eksp. Khim.*, **8**, 884 (1972).
173. Paul, A., *Mater. Sci.*, **12**, 219 (1977).
174. Teslenko, S. M., *Fiz. Khim. Stekla*, **5**, 61 (1979).
175. Mott, N. F. and Davis, E. A., *Electron Processes in Non-crystalline Materials*, Clarenol Press, Oxford, 1979.
176. Flask, R., Izu, M., Sapru, K., Anderson, T., Ovshinsky, S. R. and Fritzche, H., *7th Intern Conf. on Amorphous and Liquid Semicond., Edinburgh*, 1977, p. 524.
177. Norem, F. and Wertheim, G., *J. Phys. Chem. Sol.*, **23**, 111 (1962).
178. Bemski, G., Ganzaler, F. and Peyre, J., *Phys. Lett.*, **31** A, 231 (1970).
179. Nistryuk, I. V., Boltaks, B. I. and Seregin, P. P., *Fiz. Tverd. Tela*, **17**, 592 (1976).
180. Bemski, G. and Fernandes, J., *Phys. Lett.*, **6**, 10 (1963).
181. Belozersky, G. N., Nemilov, Yu., Tomilov, S. B. and Shvedchikov, A., *Fiz. Tverd. Tela*, **7**, 307 (1965).
182. Seregin, P. P., Kamalov, A. and Blashku, A. I., *Fiz. Tverd. Tela*, **16**, 2013 (1974).
183. Seregin, P. P., Nasredinov, F. S. and Demakov, Yu. P., *Fiz. Techn. Poluprovodn.*, **10**, 20009 (1976).
184. Seregin, P. P., Nasredinov, F. S. and Bachtyarov, A. Sh., *Phys. Stat. Sol.*, (b) **91**, 35 (1979).
185. Seregin, P. P. and Vasilyev, L. N., *Fiz. Tverd. Tela*, **14**, 1640 (1972).
186. Sagatov, M. A., Boltaks, B. I., Vasilyev, L. N. and Seregin, P. P., *Fiz. Tverd. Tela*, **16**, 462 (1974).
187. Seregin, P. P., Sivkov, V. F. and Vasilyev, L. N., *Fiz. Techn. Poluprovodn.*, **8**, 2270 (1974).
188. Seregin, P. P., Sagatov, M. A., Masets, T. F. and Vasilyev, L. N., *Phys. Stat. Sol.*, (a) **28**, 127 (1975).
189. Seregin, P. P., Sagatov, M. A., and Sivkov, V. P., *Problems of Physics of Semiconductors* (in Russian), Kaliningrad, 1975, Vol. I. p. 46.

190. Seregin, P. P., Sivkov, V. P., Nasredinov, F. S., Kartenko, N. F., Vasilyev, L. N. and Bakhtiyarov, A. Sh., *Fiz. Techn. Poluprovodn.*, **10,** 1325 (1976).
191. Nasredinov, F. S., Seregin, P. P., Vasilyev, L. N., *Fiz. Khim. Stekla*, **5,** 324 (1979).
192. Boltaks, B. I., Dzhafarov, T. D., Khudoyarova, V. Kh., Nasredinov, F. S. and Seregin, P. P., *Amorphous Semiconductors–78* (in Russian), 1978, p. 166.
193. Belozerskii, G. N., Beljakov, N. N., Borisova, Z. V. and Vlasov, Yu. G., *Fiz. Khim. Stekla*, **12,** 20 (1986).
194. Khudoyarova, V. Kh., Nasredinov, F. S. and Seregin, P. P., *Fiz. Khim. Stekla*, **8,** 350 (1982).
195. Andreev, A. A., Borisova, Z. U., Benkov, E. A. and Vlasov, Yu. G., *J. Non-cryst. Sol.*, **35–36,** 901 (1980).
196. Averyanov, V. L., Nasredinov, F. S., Nistiryuk, P. V., Prihodko, O. I. and Seregin, P. P., *Fiz. Khim. Stekla*, **8,** 541 (1982).
197. Shtotsel, H., Seregin, P. P., Nasredinov, F. S. and Andreev, A. A., *Fiz. Tverd. Tela*, **25,** 1528 (1983).
198. Lyubin, V. M., Averyanov, V. L., Nasredinov, F. S., Nistiryuk, P. V., Prikhodko, O. I. and Seregin, P. P., *Fiz. Techn. Poluprovodn.*, **17,** 353 (1983).

SUBJECT INDEX

The book starts out by reviewing the physical background and technical details of Mössbauer spectroscopy.

Although the Mössbauer effect can occur only in solids the aim here is to demonstrate how to apply Mössbauer spectroscopy to the investigation of the chemical structure of solutions.

Solutions can be brought to a frozen state and in this state if they include Mössbauer-active atoms it is possible to record Mössbauer spectra. The process of freezing can be carried out in a way that the ice formed preserves the most significant chemical features of the solutions. In that case the Mössbauer method can serve as a rich source of information on the geometrical, chemical and magnetic structure of solutions.

The Mössbauer spectra of solutions and liquids can also be recorded at room temperature if they are diffunded in "thirsty glass" with a pore diameter of 4 nm. This recently developed measuring technique and the related principles are also discussed in this volume.

The second part of the book shows several applications of the Mössbauer technique for the study of hydration, solvation and hydrolysis of salts containing Mössbauer active elements. Some examples of the investigations of electron exchange reactions and coordination compound formation in solutions are also demonstrated.

The glasses can be considered as frozen solutions and the Mössbauer study of these kinds of materials are also discussed.

This book will be most useful for experts dealing with solution and glass structures who would apply Mössbauer spectrum as a method. It is also recommended to those dealing with chemical and physical research who are ready to extend their method in these fields.

ISBN 963 05 5347 3

Mössbauer Spectroscopy of Frozen Solutions